DNA 6501H-4-2

NUCLEAR GEOPLOSICS SOURCEBOOK

Volume IV, Part II, Empirical Analysis of Nuclear and High-Explosive Cratering and Ejecta,

General Electric Company—TEMPO
DASIAC
816 State Street
Santa Barbara, California 93102

1 March 1979

Handbook

Prepared for

Director

DEFENSE NUCLEAR AGENCY

Washington, D. C. 20305

Destroy this report when it is no longer
needed. Do not return to sender.

SECURITY CLASSIFICATION OF THIS PAGE *(When Data Entered)*

REPORT DOCUMENTATION PAGE		READ INSTRUCTIONS BEFORE COMPLETING FORM
1. REPORT NUMBER DNA 6501H-4-2	2. GOVT ACCESSION NO. *AD-AC45096*	3. RECIPIENT'S CATALOG NUMBER
4. TITLE *(and Subtitle)* NUCLEAR GEOPLOSICS SOURCEBOOK Volume IV, Part II- Empirical Analysis of Nuclear and High-Explosive Cratering and Ejecta		5. TYPE OF REPORT & PERIOD COVERED Handbook
		6. PERFORMING ORG. REPORT NUMBER
7. AUTHOR(s) Jacques E. Schoutens, Editor		8. CONTRACT OR GRANT NUMBER(s) DNA 001-79-C-0081
9. PERFORMING ORGANIZATION NAME AND ADDRESS General Electric Company-TEMPO DASIAC 816 State St., Santa Barbara, California 93102		10. PROGRAM ELEMENT, PROJECT, TASK AREA & WORK UNIT NUMBERS Subtask P99QAXDC008-09
11. CONTROLLING OFFICE NAME AND ADDRESS Director Defense Nuclear Agency Washington, DC 20305		12. REPORT DATE 1 March 1979
		13. NUMBER OF PAGES 464
14. MONITORING AGENCY NAME & ADDRESS*(if different from Controlling Office)*		15. SECURITY CLASS. *(of this report)* Unclassified
		15a. DECLASSIFICATION/DOWNGRADING SCHEDULE N/A

16. DISTRIBUTION STATEMENT *(of this Report)*

Approved for public release; distribution unlimited.

17. DISTRIBUTION STATEMENT *(of the abstract entered in Block 20, if different from Report)*

19. KEY WORDS *(Continue on reverse side if necessary and identify by block number)*

Acceleration	Ejecta	Hard rock	Non-linear region
Alluvium	Explosion phenomenology	HE explosion	Particle velocity
Areal density	Ground motion	Hydrodynamic region	Plastic region
Craters	Granite	Modeling	
Displacement	Geologic effects	Nuclear explosion	

20. ABSTRACT *(Continue on reverse side if necessary and identify by block number)*

This sourcebook is a compendium of nuclear and high-explosive empirical data and analysis of ground motion, cratering, and ejecta. It is a revised and greatly expanded version of the Nuclear Geoplosics Sourcebook published by DNA in 1964 (DASA 1285-IV). It is not meant to be a handbook but rather an authoritative sourcebook on explosion-produced ground-behavior phenomena.

DD FORM 1473 1 JAN 73 EDITION OF 1 NOV 65 IS OBSOLETE

19. KEY WORDS (Continued)
     Particle-size distribution
     Prediction technique
     Salt
     Soviet
     Strain
     Stress
     Trajectory
     Tuff
     Waveforms

PREFACE

This volume of the Nuclear Geoplosics Sourcebook is a revised and greatly expanded version of the previous edition published by DNA in 1964 (DASA 1285-IV). The Nuclear Geoplosics Sourcebook is comprised of five volumes:

Volume I   Theory of Directly Induced Ground Motion

Volume II-1   Mechanical Properties of Earth Materials - Soils

Volume II-2   Mechanical Properties of Earth Materials - Rocks

Volume III   Test Sites and Instrumentation

Volume IV   Empirical Analysis of Ground Motion, Cratering and Ejecta

Volume V   Effects of Underground Structures and Equipment

Volume IV consists of two parts and five chapters:

Part I

Chapter IV-1   Ground Motion from Aboveground Nuclear Explosions

Chapter IV-2   Ground Motion from Underground Explosions

Part II

Chapter IV-3   Characteristics of Nuclear and High-Explosive Craters

Chapter IV-4   Ejecta

Chapter IV-5   Review of the Soviet Work in Cratering and Associated Ground Motion

The philosophy of the first edition of the Nuclear Geoplosics Sourcebook has been kept. In the words of F. Sauer, author of the original edition, the following quotation remains true in this edition:

"This book is not meant to be a handbook of design specifications. It is meant to be an authoritative sourcebook. Between these two is the difference, for example, between the laboratory course and the lecture course. It contains more philosophy than figures, more hypotheses than certainties. These hypotheses are given whenever possible with the empirical information and the theory upon which they are based so that the reader can make his own judgment of their validity. We strive to avoid the temptation to speculate

intuitively without factual or theoretical foundation for the arguments presented, and we attempt to present objectively all approaches, favored and unfavored, with the reasons for preference of one or another type of analysis or procedure clearly stated. So that the sourcebook need not be classified, a few relevant references are not discussed. In addition new material appearing during the late stages of compilation of the sourcebook is not referenced. It is hoped that these deficiencies will be corrected in future editions."

TABLE OF CONTENTS

LIST OF ILLUSTRATIONS

LIST OF ILLUSTRATIONS (Continued)

LIST OF ILLUSTRATIONS (Continued)

LIST OF ILLUSTRATIONS (Continued)

LIST OF ILLUSTRATIONS (Continued)

LIST OF ILLUSTRATIONS (Continued)

LIST OF ILLUSTRATIONS (Continued)

LIST OF ILLUSTRATIONS (Continued)

LIST OF ILLUSTRATIONS (Continued)

LIST OF ILLUSTRATIONS (Continued)

LIST OF ILLUSTRATIONS (Continued)

LIST OF ILLUSTRATIONS (Continued)

LIST OF ILLUSTRATIONS (Continued)

LIST OF ILLUSTRATIONS (Continued)

LIST OF ILLUSTRATIONS (Continued)

LIST OF ILLUSTRATIONS (Continued)

LIST OF ILLUSTRATIONS (Continued)

LIST OF TABLES

LIST OF TABLES (Continued)

LIST OF TABLES (Continued)

CHAPTER IV-3
CHARACTERISTICS OF NUCLEAR AND HIGH EXPLOSIVE CRATERS[*]

IV-3.0 INTRODUCTION

The explosion of a charge at, or near, the free surface separating a solid from the atmosphere may leave a permanent record of the event in the form of a crater. If the height of the detonation above the surface is great enough, no crater will form. Craters will form for lower heights of burst (HOBs) and for detonations at the surface or in the solid. For sufficiently large depths of burst (DOBs) a closed cavity will form instead of a crater. Pokrovskii and Federov (Reference IV-3.1) pointed out that the definition of an explosion, including nuclear detonations, can be sufficiently broad to include phenomena ranging from collapse of cavitation bubbles in fluids to meteor impacts on Earth or on the Moon. This chapter presents a discussion of craters and their formation by nuclear and high-energy explosives. It includes experimental results and correlation of data between nuclear and high-energy explosives, as well as analytical methods used in predicting crater dimensions. To give the reader a feeling for the similarities of explosive craters and meteor craters, a summary of some of the theory and observational data available for Lunar and Earth meteor craters is presented in the appendices.

IV-3.1 CRATER FORMATION MECHANISMS

There is ample experimental evidence to show that craters are formed during an explosion by two principal mechanisms: The scouring and ejection of ground material by the exploding device, and by the compaction, plastic deformation and flow of the ground beneath the true crater boundary. Compaction, plastic deformation and flow of the crater produces a slight increase in material density as well as considerable brittle and plastic failure of the ground material. The combination of these mechanisms causes a radial displacement with overturning of crater material around the edge of the crater. The top of the mound is termed the crater lip. After the detonation, the crater is partially refilled by

---

material falling back into the crater, by slumping, and by late-time rebound. This is called the fallback material. The ramaining material ejected from the crater is thrown out around and beyond the crater lip. This material, called ejecta, forms a layer aboveground whose thickness diminishes with radial distance from the burst point. The boundary below the original ground surface that separates the fallback and the air, in the case of a dry crater, or between the fallback and the water, in the case of a flooded crater, defines the apparent crater. Most of the recommended crater terminology is shown in Figure IV-3.1 (Reference IV-3.2). The most important parameters used in crater studies, and used most often in this chapter, are the apparent radius, depth and volume, and the height or depth of the explosive device prior to detonation. Despite many explosive cratering experiments in the field with nuclear and high-explosive (HE) devices, and in the laboratory with small explosive charges, the quantitative dynamics of crater formation is not fully understood.

This section introduces, in a qualitative manner, some of the mechanisms of energy and momentum transfer from the explosive device to the cratering medium. Some fundamentals of crater formation mechanisms and their relationships to the detonation altitude or depth also are introduced.

IV-3.1.1 Energy Partition and Transfer

Airblast estimates for near-surface bursts are frequently related to ideal airbursts in which the blast is assumed spherically symmetric about the source (usually a point source) without the complications introduced by the air-earth interface. The airblast from an explosion at the interface would look like an equivalent free-air burst of twice the device yield if the earth were perfectly rigid. The earth does not act as an ideal reflector, however, and computations performed by the Air Force Weapons Laboratory (AFWL) indicate that in a surface burst the kinetic energy is predominantly in the upward direction (Reference IV-3.3).

Energy sinks cannot be precisely quantified, but the energy partitions into numerous elements such as, for example, the thermal losses to the earth through fireball radiation, quenching of fireball interior temperatures as a result of injected crater debris, and losses due to earth motion and crater formation. Although precise partition of device energy remains a subject of controversy for nuclear surface bursts, about 5 percent of the total device yield is a currently accepted value for the amount of energy deposited in the

RECOMMENDED CRATER NOMENCLATURE

D_a	Maximum depth of apparent ground surface measured normal to the preshot ground surface.*	R_{zt}	Distance between the zero point and the true crater surface measured in any specified direction. When measured in a direction below the zero point is equivalent to lower cavity radius.
D_{al}	Depth of apparent crater below average apparent crater lip crest elevation.		
Dob	Normal depth of burst (measured normal to preshot ground surface).	S_a	Apparent crater surface, e.g. rock air or rubble-air interface.
Dt	Maximum depth of true crater below preshot ground surface.	S_{al}	Apparent lip surface.
		SGZ	Surface ground zero.
		S_d	Displaced ground surface
D_{tl}	Depth of true crater lip crest below apparent crater lip crest.	S_p	Preshot ground surface.
		S_t	True crater surface, e.g. rock-air or rock rubble interface.
Ejecta	Material above and or beyond the true crater and includes: (1) foldback; (2) breccia—ballastic trajectory; (3) dust-aerosol transport; etc.	V_a	Volume of apparent crater below ground surface.
		V_{al}	Volume of apparent crater below apparent lip crest.
Fallback	Material fallen inside the true crater and includes: (1) slide blocks; (2) breccia and stratified fallback—ballastic trajectory; (3) dust—aerosol transport; (4) talus; etc.	V_t	Volume of true crater below preshot ground surface.
		V_{tl}	Volume of true crater below true crater lip crest.
H_{al}	Apparent crater lip crest height above preshot ground surface.	Z	Vertical depth of burst (equivalent to dob when crater is formed on a horizontal surface).
H_{tl}	True crater lip crest height above preshot ground surface.	ZP	Zero Point effective center of explosion energy.
L_{ac}	Apparent crater lip crest.	Note:	The following definitions apply to linear craters only. Linear crater refers to the excavation formed by overlapping crater effects resulting from a row of charges. All above terms applicable to single craters apply also to linear craters with the exception of the radius terms which are replaced by the width terms below.
L_{tc}	True crater lip crest.		
R_a	Radius of apparent crater measured on the preshot ground surface.		
Note:	The radius measurements pertain only to single charge craters and represent average dimensions. If crater shape deviates substantially from circular, the direction of measurement must be specified. An average radius value can also be determined by dividing the plan area by and taking the square root.	W_a	Width of apparent linear crater measured on the preshot ground surface.
		W_{al}	Width of apparent lip crest measured across linear crater.
		W_{ds}	Width of displaced surface measured across linear crater.
R_{al}	Radius of apparent lip crest to center.	W_{eb}	Width of outer boundary of continuous ejecta measured across linear crater.
R_{ds}	Outer radius of displaced surface.	W_{lb}	Width of true crater outer lip boundary measured across linear crater.
R_{eb}	Radius of outer boundary of continuous ejecta		
R_{lb}	Outer radius of true lip boundary.	W_t	Width of true linear crater measured on the preshot ground surface.
R_t	Radius of true crater measured on the preshot ground surface.	W_{tl}	Width of true linear crater lip crest measured across crater.
R_{tl}	Radius of true lip crest to crest to center.		

*All distances, unless specified otherwise, are measured parallel or perpendicular to preshot ground surface.

Figure IV-3.1. Recommended crater nomenclature.

ground directly from the source region. This value is a function of the device design and the chemical composition of the soil, and is independent of the purely hydrodynamic contributions of the airblast occurring at late times and over relatively large ground ranges. HE devices produce larger craters than equivalent nuclear devices.

The energy contribution to crater development is strongly dependent upon explosive type as well as burst position. For a nuclear device, energy is transferred to the ground predominantly by photon and neutron absorption. Early estimates by Brode and Bjork (Reference IV-3.4) of the energy transfer mechanism for cratering were based on the assumption that hydrodynamics of the device debris dominated the transfer mechanism. Subsequent investigations have shown the debris to have a less important role, acting primarily as a reflector to inhibit energy losses from the earth. However, this is not a unanimous point of view. For a HE device, radiation is a relatively insignificant energy transport mechanism and energy transfer is almost exclusively hydrodynamic. Because of these differences in energy transfer mechanisms, the relative energy transported to the earth is markedly different for nuclear and HE explosions. For a half-buried spherical charge, energy permanently transferred to the ground is calculated to be approximately one-third of the total energy released (Reference IV-3.5). However, it should be noted that HE coupling may be material dependent; in other words, energy coupling depends on the geology.

The effect of burst position on energy transferred to the ground for a nuclear event is very pronounced. The shock breakaway radius in air (the range at which the energy transport mechanism undergoes a transition from radiation diffusion to hydrodynamic shock propagation) is between 40 to 50 meters for a typical 1-MT device or 4 to 5 $m/KT^{1/3}$ (Reference IV-3.6). For HOBs greater than this magnitude, energy transfer is dominated by airblast loading of the earth. For high explosives, a phenomenon similar to shock breakaway occurs when the HE is no longer in contact with the earth. For HOB above one equivalent charge radius, or approximately 5 $m/KT^{1/3}$, the intervening air acts as a buffer to the HE and energy transfer is primarily through airblast loading. Figure IV-3.2 shows the calculated results for the relative energy transferred to the ground

for a 100-ton sphere of TNT as a function of HOB (Reference IV-3.5). This curve indicates an exponential decrease in the energy transmitted to the ground. At a burst height of one charge radius (tangent sphere), the coupled energy has been reduced from approximately 33 percent when the device center of mass is coincident with the ground surface to approximately 7 percent. Increasing the elevation to 1.5 charge radii reduces the coupled energy to less than 3.5 percent. Therefore, for HE, as for nuclear explosions, the reduction in coupled energy with HOB is quite dramatic.
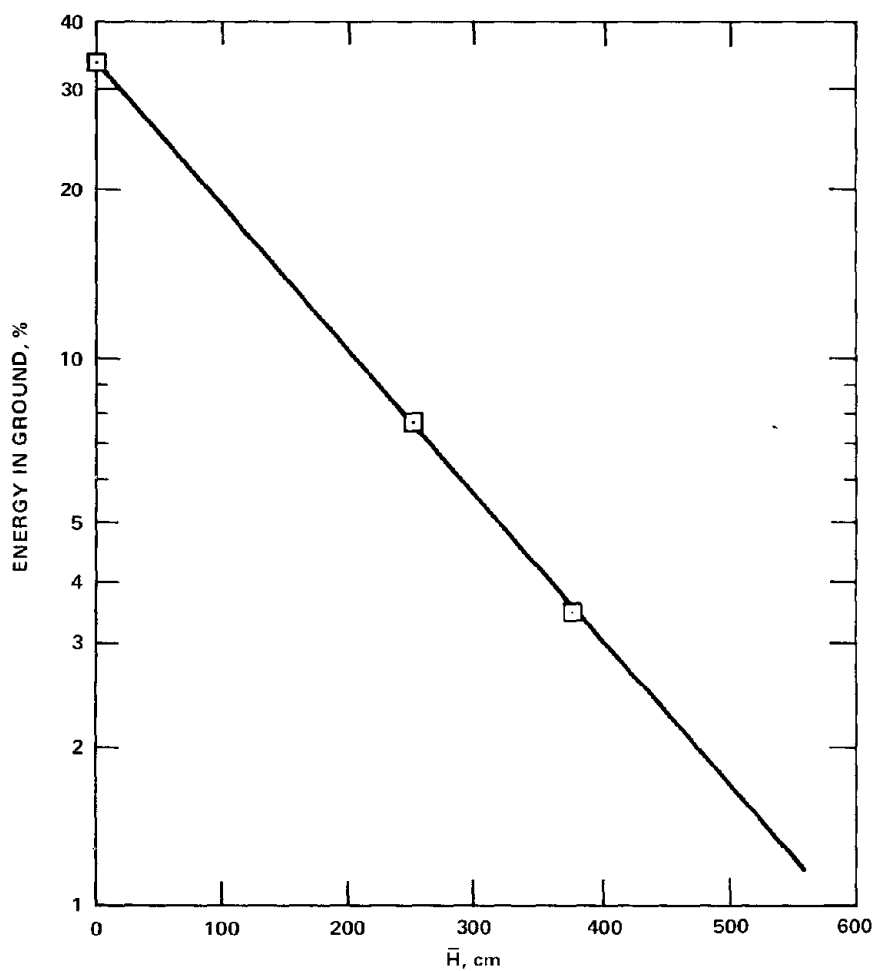
Figure IV-3.2. Computed fraction of total energy deposited in the ground from a 100-ton TNT sphere detonated at height H̄ (center of mass) above the ground.

Typically, the time required for the transfer of energy from the device to the earth and the air is small compared to the time required for the growth of the crater. Figure IV-3.3 shows a typical calculated history of the relative energy transferred to the air for a slightly buried nuclear burst for which the prompt radiation was contained below the surface. This particular calculation estimates that approximately 60 percent of the device energy (about 85 percent of the total that can be delivered) is delivered to the air within 1 msec. This occurs either by direct gas venting or through kinetic energy loss, with only about 30 percent of the device energy being ultimately available for the production of ground shock. For buried nuclear devices, the equivalent shock breakaway radius in the soil is roughly proportional to the electron density of the earth material. Consequently, radiation transport terminates within a few inches from the device and the dominant energy transfer mechanism thereafter is hydrodynamic. Temperatures and pressures of the vaporized earth in which the energy is deposited will be extremely high. The temperatures are on the order of tens of millions of degrees kelvin, and pressures are on the order of tens of megabars.[*] For subsurface bursts first-order estimate of the energy transmitted to the earth may be made by observing the reduction in airblast equivalent energies with DOB. Observations of airblast from buried bursts (Reference IV-3.8) indicate that the fractional effective energy delivered to the atmosphere decreases exponentially with DOB in accordance with:

$$\frac{W_{eff}}{W} = e^{-0.024 \, \rho \lambda_d} \tag{IV-3.1}$$

for $\lambda_d \leqslant 250$ ft/kt$^{1/3}$. Thus the fractional energy delivered to the ground is, by inference,

$$\frac{W_g}{W} = 1-e^{-0.024 \, \rho \lambda_d} \tag{IV-3.2}$$

where ρ is the specific gravity of the soil and λ_d is the scaled DOB measured in ft/kt$^{1/3}$. The relative fraction of energy that is transmitted to the ground from a near-surface explosion is amenable to experimental modeling. Such work has been reported by Alekseyenko (Reference IV-3.8). The basic idea behind the experimental technique is quite simple. Careful measurements and calculations

---

[*]1 bar = 14.5 psi = 0.987 atmosphere = 10^5Pa

are performed for the surface bursts where the surface is a mathematically rigid semi-infinite solid. A series of scaled explosions is carried out on a material in question, leading to a determination of an effective yield that is then compared to the results expected for a rigid half-space. Charges weighing from 1.6 to 25 kg were detonated on concrete, compacted sand, and loose sand. The experiments on concrete were surface tangent shots above the surface. On the compacted sand the configurations were surface tangent above the surface, zero DOB and surface tangent below the surface. The explosions in loose sand were surface tangent above the surface and zero DOB. Table IV-3.1 shows the results of this work. Energy in the air was inferred by measuring the shock propagation properties from each experiment at various radial positions for the various charge weights. Note that the amount of energy transmitted to the air is a function of the DOB and the properties of the solid half-space.
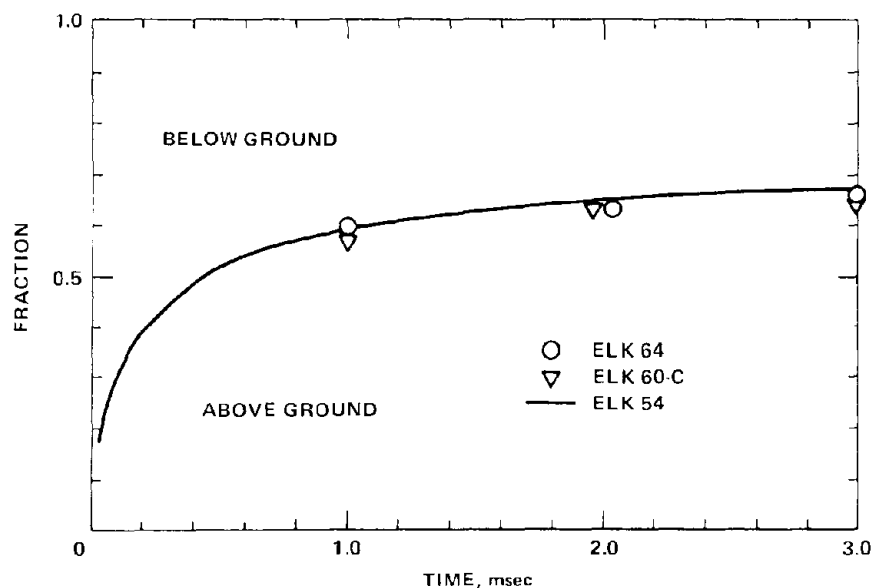
Figure IV-3.3. Fractional energy above ground for slightly buried nuclear devices versus time. Comparison for ELK 64 and two previous calculations (Reference IV-3.5).

Table IV-3.1. Partition of energy between air and ground in a contact burst.

Energy Fraction into	Explosion on Concrete - Charge on Surface	Explosion on Undisturbed Sand			Explosion on Loose Sand	
		Charge on Surface	Charge Level With Surface	Center of Charge Radius Below Surface	Charge at Surface	Center of Charge Level With Surface
Atmosphere	0.9	0.8	0.65	0.53	0.7	0.56
Ground	0.1	0.2	0.35	0.47	0.3	0.44

IV-3.1.2 Cratering Processes

The effects of DOB on the crater profile are idealized in Figure IV-3.4. The crater radius is maximized by a different DOB than the DOB that will maximize the crater depth. This is indicated in Figures IV-3.5 and IV-3.6. Optimizing the DOB is thus a matter of choosing the dimensions one wishes to maximize. It is common practice to define the optimum DOB as that value which yields the maximum crater volume.

The four fundamental processes which take place during crater formation from buried bursts were first qualitatively described by Nordyke (Reference IV-3.9) and form the backbone of this section. These processes are:

1. Compaction and elastic and plastic deformation.
2. Spall.
3. Gas acceleration.
4. Subsidence.

These processes are schematically illustrated in Figure IV-3.7. The early-time phenomenologies of nuclear and HE explosions are quite different in that the energy released from a buried nuclear device is deposited within a very short time and short distance from the device. This results in an extremely high-pressure and high-temperature gas bubble of vaporized earth and device material. These pressures typically reach values on the order of megabars. As this high pressure moves away from the burst point in the form of a shock front, the gas bubble grows and simultaneously cools. Since the gas is mostly vaporized earth
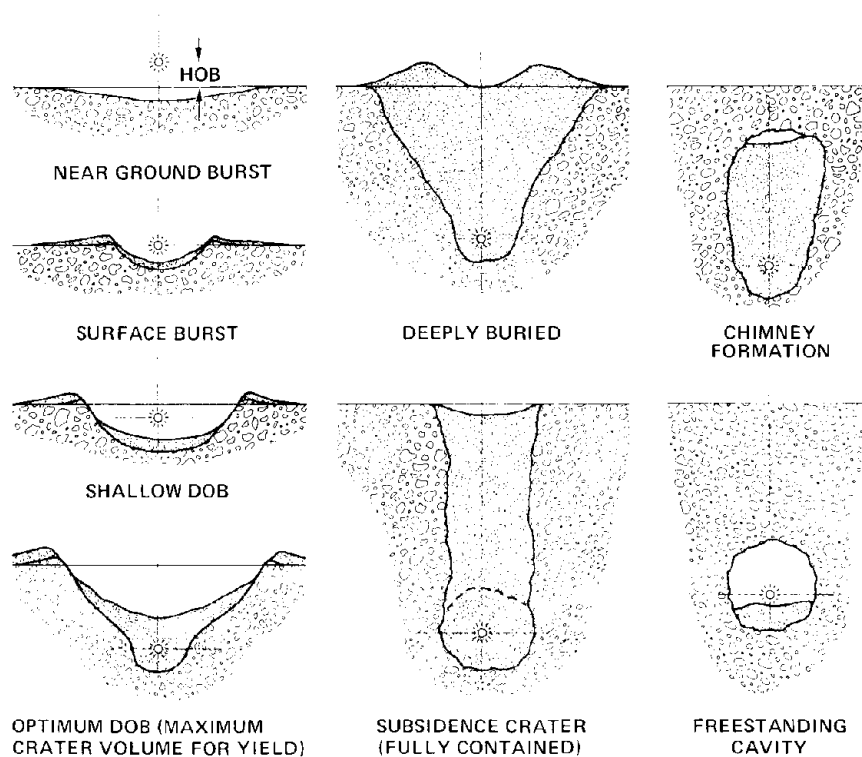
Figure IV-3.4. Primary types of craters resulting from a
variety of burst positions.

material, the cooling process will result in condensation of the vaporized rock,
thereby altering the growth of the cavity from that predicted on the basis of
an adiabatic process involving a perfect gas. In the case of an HE detonation,
maximum pressures are on the order of 50 to 200 kbar. The gases contain the
products of chemical reactions and will not generally condense as the cavity
increases in volume, the only cooling being that of the pressure-volume work
done against the surrounding material. For nuclear and high explosives, cavity
growth continues by compaction and elastic and plastic deformation of the geo-
logic material. This growth continues until a combination of the plastic stress
limits of the medium and the lithostatic pressure* exceed the internal pressure
of the gas bubble and the associated inertial stress due to the motion of the
surrounding material. The compressive shock front radiated by the explosion will

---

*The words "lithostatic pressure" are a contraction for the phrase "lithosphere
hydrostatic pressure."
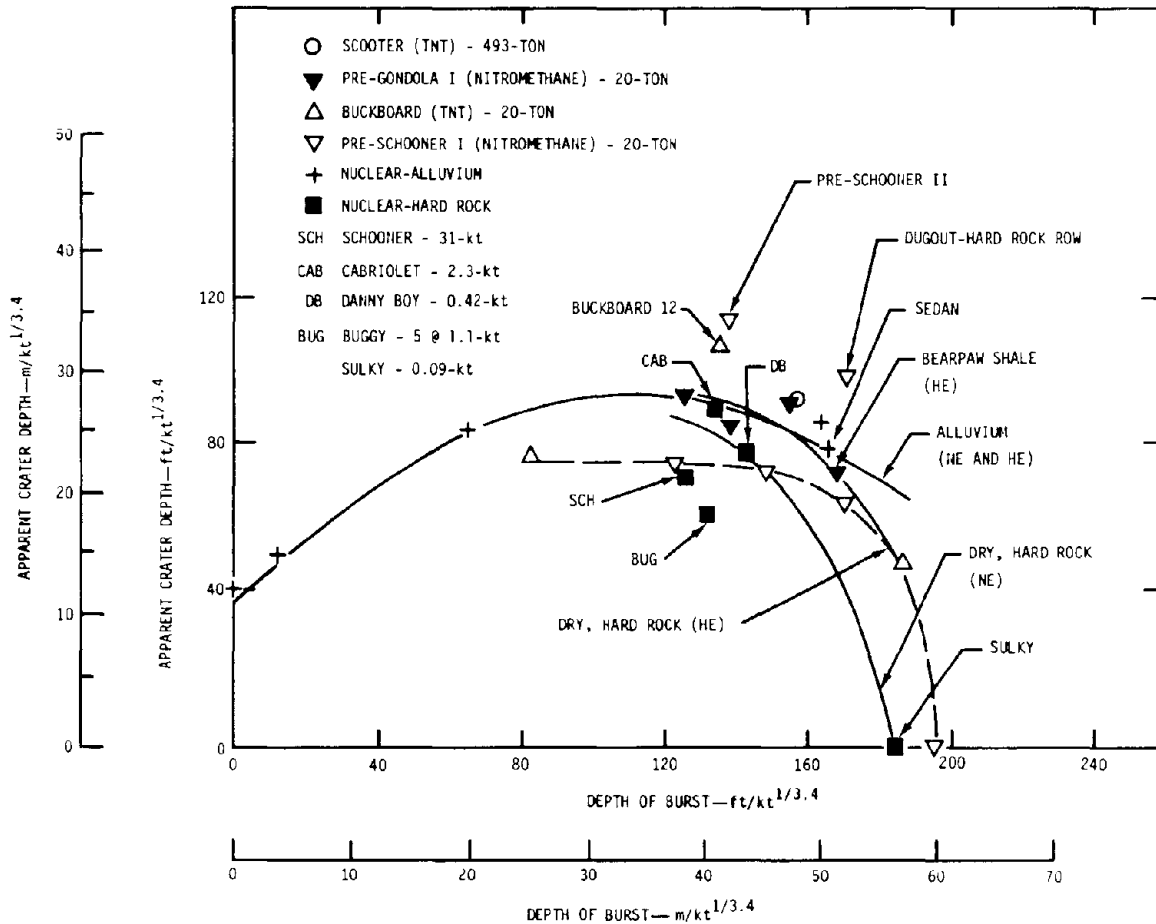
Figure IV-3.5. Scaled crater depth curves.

NOTE: 1/3.4 yield scaling is used for W ranging from 10^2 lb to 10^6 lb; 1/3 yield scaling is applicable for W < 10^2 lb; and 1/4 yield scaling applies for W > 10^6 lb (Reference IV-3.3).
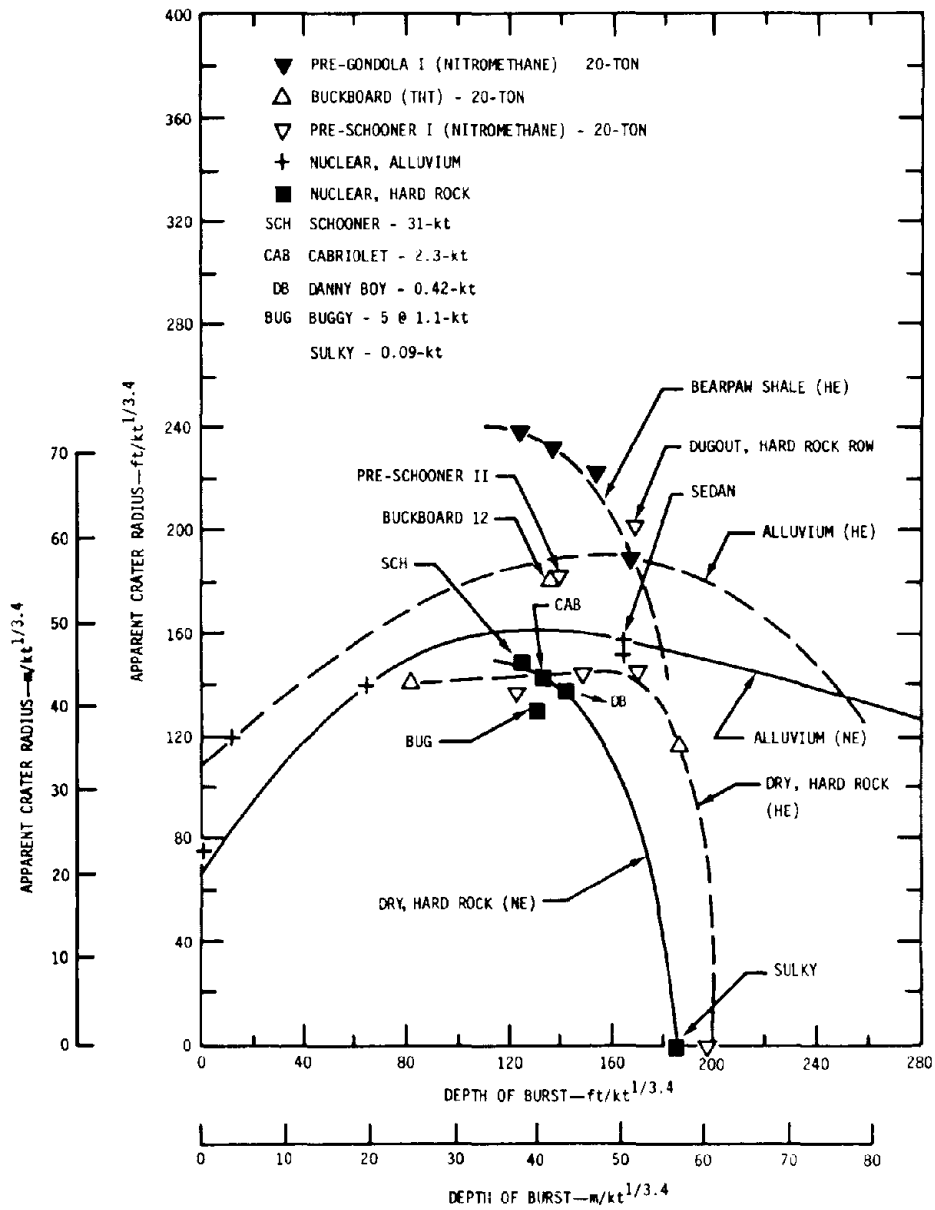
Figure IV-3.6.   Scaled crater radius curves.

(See Note on Figure IV-3.5.)
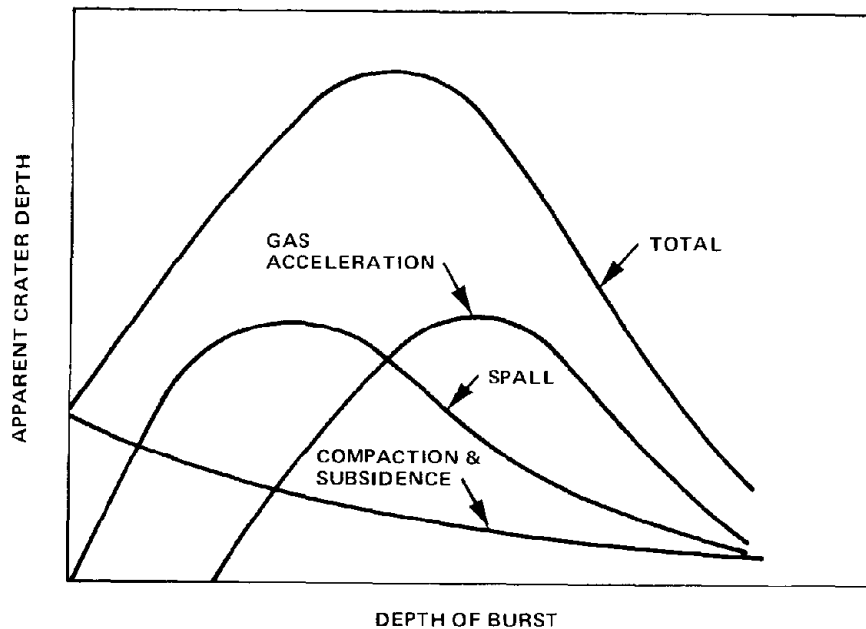
Figure IV-3.7. Estimated relative contribution of
various cratering mechanisms to
changes in the apparent crater depth
(near optimum bursts).

eventually reach the free surface of the earth, which will reflect the incident
wave as a tensile stress wave. When the magnitude of this tensile stress is
greater than the tensile strength of the earth material, the surface will move
in the direction of the incident wave and spalling will occur as shown in Figure
IV-3.8. The upward velocity of the spalled surface is characteristic of the
momentum imparted to it by the incident wave. Tensile strengths of nearly all
geologic materials are small, particularly for alluvial soils. (It is interesting
to note that in very weak soil, loss mechanisms are such that the shock front
thickness may spread out over a large enough distance that the reflected tensile
wave will not reach a large enough magnitude to spall the surface.) In hard,
high-impedance rock, the initial disturbance may maintain its shock character.
Upon reflection the tensile wave will be quite strong and the rock will fail
along existing joint planes having low tensile strength. These joints are often
closely spaced and near the surface, and are typically the result of weathering.
In any case, the reflected tensile wave will tend to reduce the mean stress of
the earth material (that is, the effective lithostatic stress in the material
above the expanding gas bubble), allowing the gases within the cavity to expand
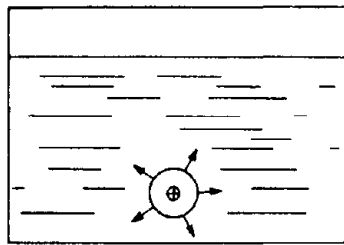
(a) Detonation of device, shock wave vaporizes and melts surrounding medium
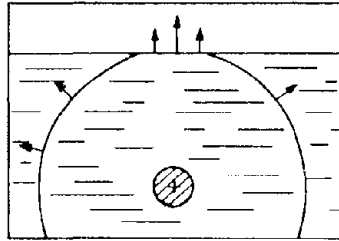
(b) Shock wave reaches surface causing spalling; simultaneous spherical cavity growth
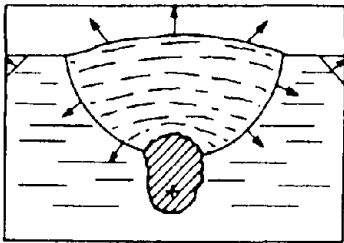
(c) Rarefaction from surface reaches cavity and asymmetrical growth towards surface begins
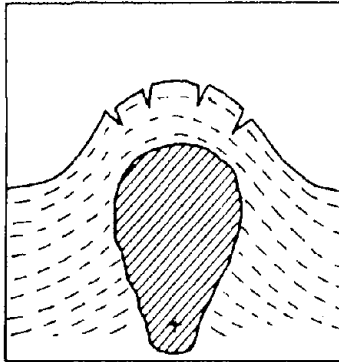
(d) Mound grows and begins to dissociate, vapor filters through broken material
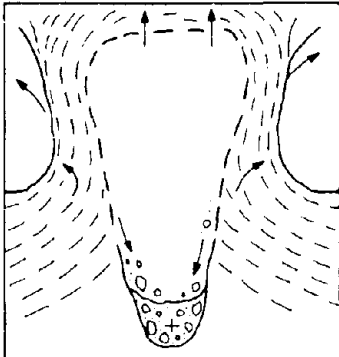
(e) Maximum development of mound, some material slumps from cavity walls, major venting
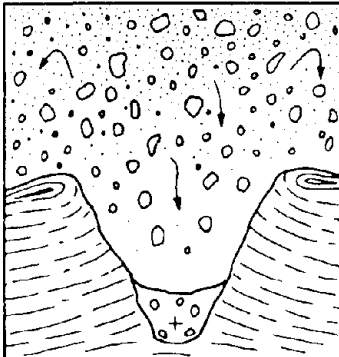
(f) Complete dissociation of mound, ejection and fallback of material to form apparent crater
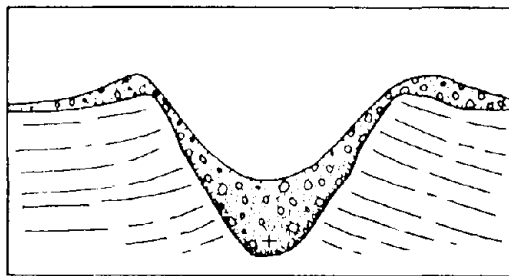
(g) Final crater configuration

Figure IV-3.8.   Sequential stages of crater formation for buried bursts.

more rapidly. For want of better terminology, this is called the gas acceleration phase. The duration of the phase is much longer than that of the compaction and spalling mechanisms which are associated with the shock front. Gas acceleration phase duration is on the order of seconds for device yield ranging from kilotons to megatons. As the cavity volume increases, cracks form in the covering over-burden permitting the trapped gases to vent to the atmosphere. For shallow DOBs, spall accelerations are considerably larger than gas acceleration. For deeply buried bursts, the weight of the overburden and the attenuation of the shock front become so great that gas acceleration is inhibited and may be reduced to the level of a negligible crater production mechanism.

For equal energy release, the mechanism of gas acceleration for buried bursts (gas acceleration is unimportant for surface bursts) may not be as effective for nuclear detonations as it is for chemical explosions. The reasons for this are quite simple. The high temperature and pressure within the expanding cavity in the nuclear case create a large percent of internal energy that is not useful for doing mechanical work. For the chemical explosion, the chemical detonation products are noncondensable gases at much lower temperature than for the nuclear case and more mechanical energy is available. Thus, in general, chemical explo-sives of the same yield are more effective at producing craters than are nuclear devices. The same holds for surface bursts as well. There is one condition for which the two explosives appear very similar in their cratering capabilities: where the surrounding material is saturated with water and is highly porous. The Hugoniot shock vaporization pressure of water is approximately 150 kbar. This means that all water inside a radius corresponding to the stress from the nuclear explosion higher than 150 kbar is vaporized. This gas will then remain within the camouflet* as noncondensing gas. It also should be noted that the Chapman-Jouguet pressure of many high explosives is around 150 kbar. Therefore, the primary difference between the two explosions is the difference between the momen-tum imparted to the surrounding material at the radius corresponding to the shock front peak pressure of 150 kbar.

For greater DOBs, at which the gas acceleration does not have an appreciable effect in cratering, the wave reflected from the surface still will lead to

*Camouflet is defined as an underground explosion of a bomb or mine that does not break the surface, but leaves an enclosed cavity of gas and smoke. It is also the pocket formed by such an explosion.

fracture and failure of the ground above the cavity. There also will be failure in the rock around the cavity due to the compaction. When these two failure regions connect, there is a possibility of producing a subsidence crater with the result that a standing, but unstable, cavity is created. Rubble from the cavity ceiling will then begin to fall into the cavity bottom. This collapse proceeds upwards until bridging occurs or bulking of the collapsed material fills the initial cavity volume, or until the collapsed zone extends all the way to the surface. It has been found that subsidence craters have been produced within a few minutes to several days after the explosion. For greater DOBs the shock wave may have been attenuated to the extent that the reflected tensile wave is not strong enough to fracture material near the surface. In that case a chimney may be created in which the failed material above the cavity falls into it, with the collapse proceeding upward to a region that has not been fractured or until all of the initial cavity volume has been filled by debris.

From the abundance of data generated by deeply buried explosions in Nevada Test Site (NTS) alluvium and tuff an extensive investigation of the time of formation of a subsidence crater was conducted by Orphal (Reference IV-3.10). Several different parameters were investigated, including the scaled DOB, the DOB minus the cavity radius, and the unscaled DOB. Among these, the best correlation came from using the absolute DOB. This correlation is shown in Figure IV-3.9. Although the data for both tuff and alluvium are widely scattered, they show a clear trend. Other materials show more dispersion. A classic example of this dispersion is the subsidence crater formed by the event GREELY conducted under the welded tuff and basalt of the Pahute mesa. Many months after the event, a single block dropped vertically from the ground surface. This left a crater with vertical sides having a diameter substantially smaller than the diameter of the cavity created by the event. It is suspected that the failure of the surface was triggered by other nuclear events in the area.

Several circumstances may conspire to create an inverted crater, or what is termed a "retarc." As noted above, hard high-impedance rocks may allow a very strong tensile wave to be reflected from the surface, thus producing substantial amounts of cracking and spalling of the surface. When the DOB is sufficiently great as to prevent the crater from forming by spallation alone, gas acceleration must be present in order to obtain a crater. Moreover, the gas acceleration phase is strongly dependent upon the amount of noncondensable gas remaining within the camouflet. If the nuclear explosion has occurred in a very dry siliceous
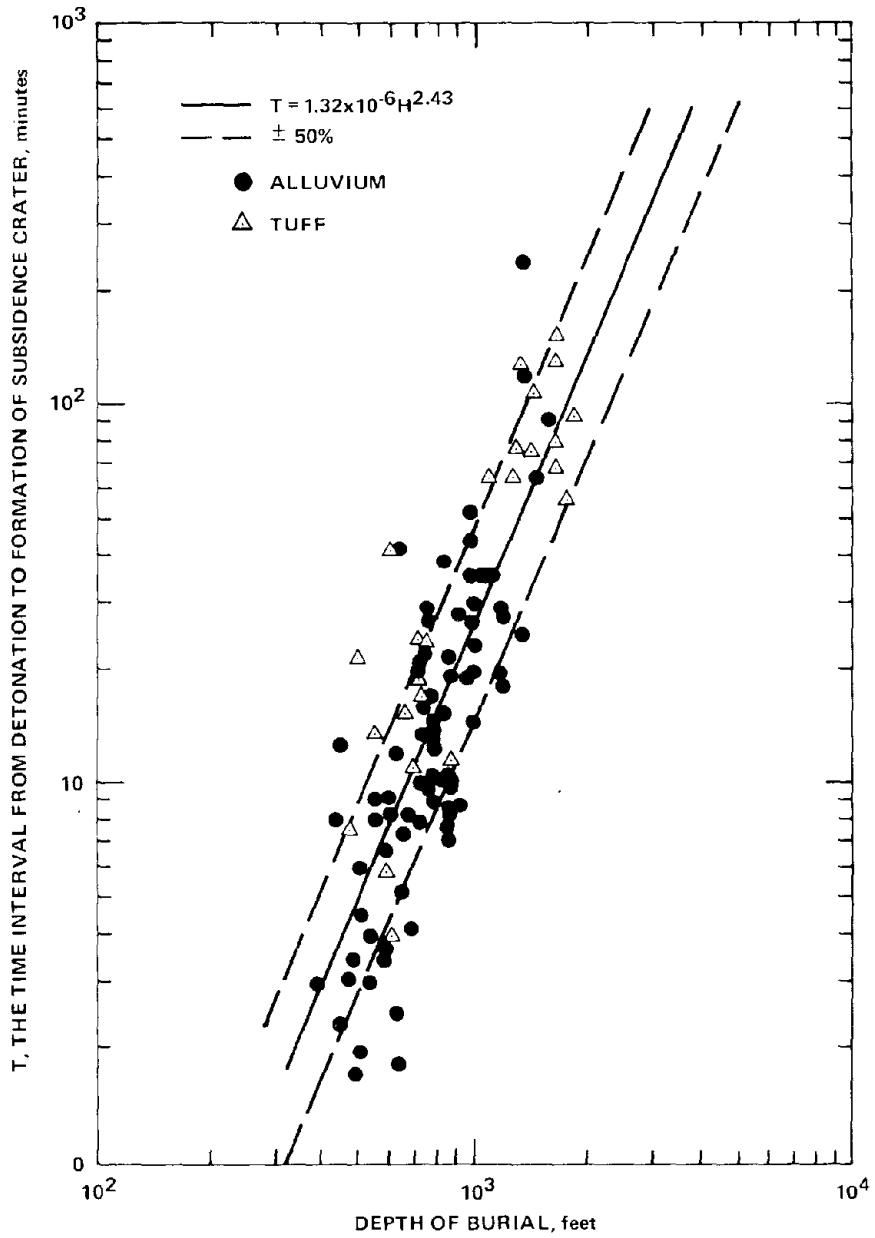
Figure IV-3.9. Time interval from detonation to formation of subsidence crater versus depth of burst.

rock, the expanding gas bubble may have condensed a substantial fraction of the initial vaporized silicates by the time the reflected tensile wave reaches the cavity. Then, the gas acceleration can no longer operate effectively; the spall mechanism will upthrust a certain amount of fractured rock, but not sufficiently to eject it any great distance from the crater area. The nuclear event SULKY (Reference IV-3.11) in dry basalt is an example of this type of event.

For above-ground detonations where HOBs are larger than the shock breakaway radius (4 to 5 meters/kt$^{1/3}$), the crater is formed almost exclusively by compaction with plastic flow. Scouring results from the airblast overpressure and the airblast associated winds. As implied in Figure IV-3.4, there is little fallback in the crater. True and apparent craters may be thought of as essentially identical in this case. Analysis of craters resulting from surface and near-surface nuclear bursts is complicated by a variety of factors which have affected the experimental results. Examples are the energy coupling, the soil type, HOB and DOB effects and water washing of craters at the Pacific Proving Grounds (PPG). Qualitatively, however, compaction, plastic deformation, and flow are the dominant mechanisms in the nearly hydrodynamic processes of near-surface crater formation. It has been postulated that a substantial portion of the ejecta resulting from surface and above-surface bursts have their origin in the splash of the crater lip. Folding of the material in the crater lip has been observed for the surface events such as PRAIRIE FLAT (Reference IV-3.12) and DIAL PACK conducted in Canada. There the material is a clay-like substance which tends to flow without fracture. Folding also has been observed at the NTS, where the surface is composed of dry alluvium.

IV-3.2 EXPERIMENTAL RESULTS

This section is primarily a qualitative and quantitative description of the nuclear and high-explosive cratering experiments conducted to date.[*] Nuclear experiments have been conducted by the United States at the PPG and at the NTS. A single complex geology exists at the PPG, namely the coral atolls of Bikini and Enewetak. The NTS geology is sufficiently diverse that cratering experiments have been conducted in four general rock types as well as several alluvial soils. The rock types at NTS are basalt, granite, limestone, and welded tuff.

---

[*] A cutoff date for this review is April 1976. Because of the usual delays in publication of reports, definitive information on late events is not available as of the writing of this document.

The alluvial soil is composed of the detritus of these four rock types, each deposit within the NTS having a somewhat different composition.

Radiation hazards have limited the range of nuclear device yields for the tests conducted at the NTS. The largest cratering event conducted there was the nearly optimally buried 100-kt SEDAN; the smallest events were on the order of 20 tons. Tests in the PPG have all been at or above the surface of the earth with yields ranging from a few tens of tons to 15 megatons.

In addition to the disparity between the yields of the events conducted at these two locations, the differences in the environment played a substantial role in the ultimate measurement of crater dimensions. Several of the events at the PPG were detonated on barges floating several feet above the coral. The resulting water washing of the craters made their measurement very difficult, and some of the data are of questionable value. There are few craters in the PPG which were not immediately flooded with water. In two of the events, SEMINOLE and KOA, although emplaced a few feet above the surface of the ground, the devices were submerged in large tanks filled with water (Figure IV-3.10). This had the effect of tamping the explosion and of altering the radiation transport and apparent mass of the device. This has made the question of assigning a realistic HOB to these events extremely difficult. On the other hand, events conducted at the NTS resulted in craters that were relatively easy to measure, but sometimes the measurements were made late after the events. A wide range of heights and depths of burst have also been investigated at the NTS. For these reasons the nuclear cratering events in the two geographic locations will be discussed separately in this section.

IV-3.2.1 Nuclear Events in the PPG

It should be recognized that nearly all of the PPG tests utilized devices that were under development. Consequently, a varying amount of instrumentation in support of diagnostics was placed in close proximity to the device to determine the characteristics of the detonation. The effects of these environmental masses have not been determined satisfactorily and will probably never be generalized adequately for all shots.

As mentioned above, a problem which complicates the utilization of the PPG data is that nearly all events were detonated on islands or sections of reef with land areas too small to contain the craters. Consequently, these craters were exposed to the eroding action of water waves. Various estimates of the influence
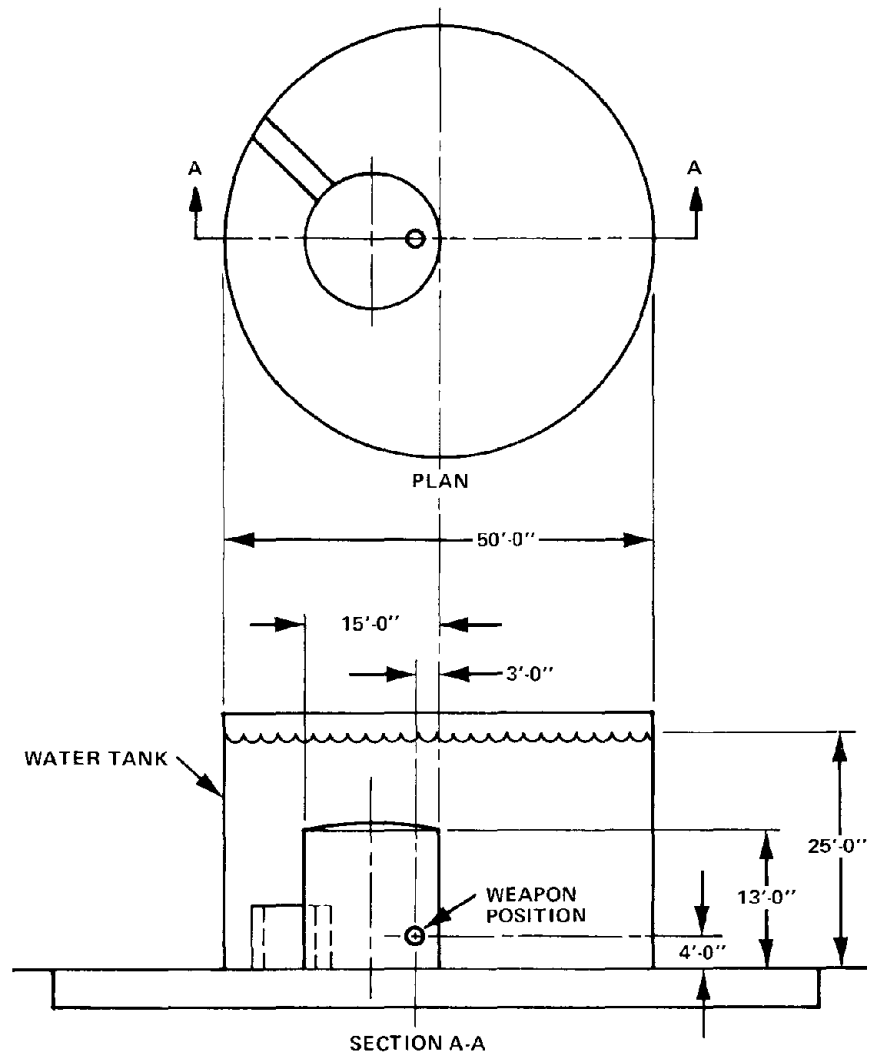
Figure IV-3.10. Emplacement geometry for shot SEMINOLE.

of the wave action have been based on an assumption of equal crater volume before
and after washing and considerations of the crater radii to have been increased
from about 10 percent to approximately 33 percent. For some of the barge shots,
the device was detonated against or near the edge of the coral reef. The asym-
metry of the geology may have contributed to energy focusing leading to a strong
asymmetry in the crater (Figure IV-3.11).* Estimates of the volume of these

---

*The reader should note that the horizontal scale on Figure IV-3.11 has been
deliberately foreshortened, thereby conveying a somewhat erroneous picture of
the crater profile.
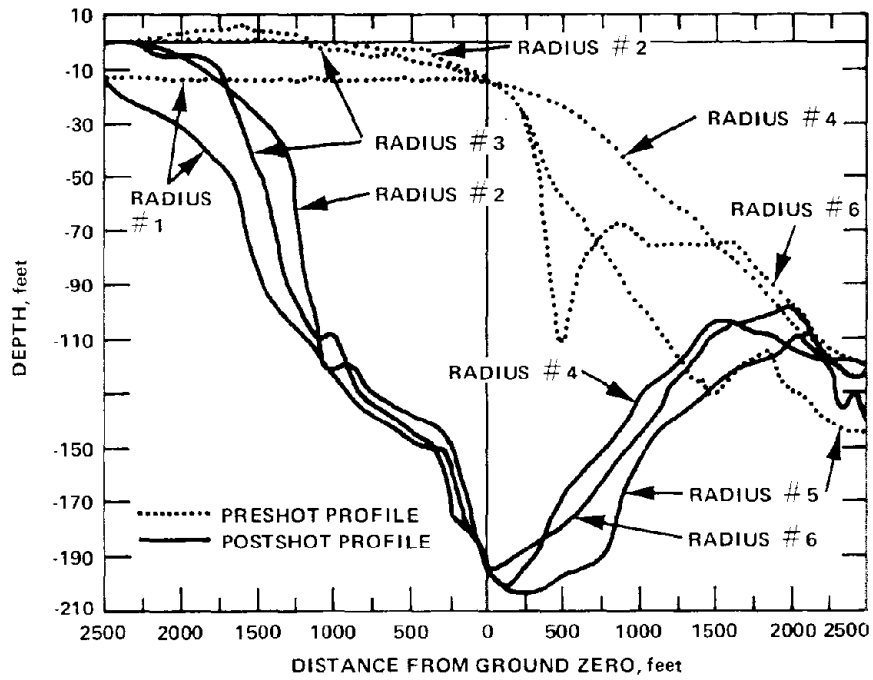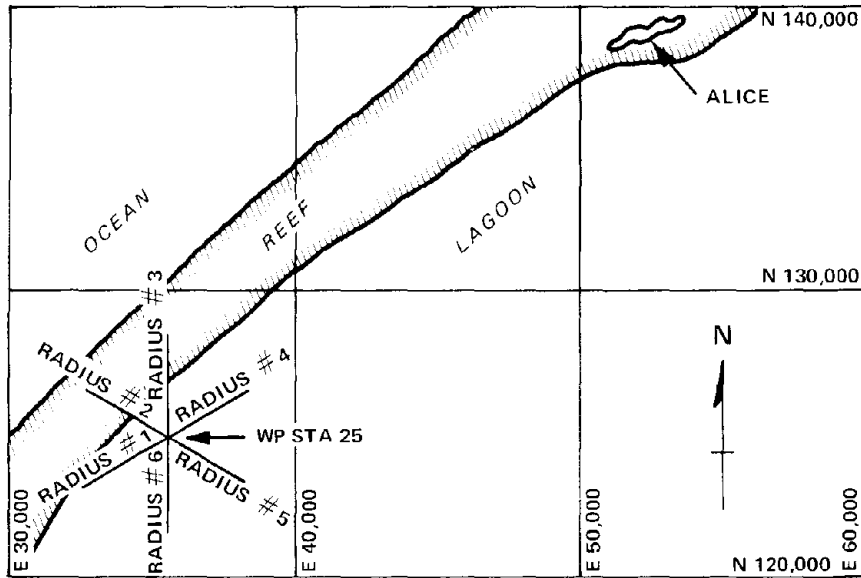
Figure IV-3.11. Pre- and post-shot cratering surveys, Event OAK.

craters range from those based on experimental measurements to calculations as to what the craters would have been if they had been produced in a uniform half-space of material. Finally, measurement techniques for determining depths have contributed to uncertainty in the crater profiles. When conditions allowed, standard recording echo fathometers were used for crater depth determination. Where post-shot radiation intensity did not permit surface work, helicopters were used. A third method, that of leadline measurements, suffered from slow settlement of the material in the bottom of the crater. Frequently no clear-cut line of demarcation between fluid and solid could be determined. In general, post-shot work included only a few soundings at the center of the crater and along one or two radii. Very recently, however, a reexamination of six nuclear craters (IVY-MIKE, OAK, KOA, SEMINOLE, LACROSSE, CACTUS) produced at Enewetak Atoll in the early 1950's was performed by the AFWL. The AFWL personnel reexamined pertinent field books and records, including photographic and other data, and carried out field measurements of these craters. Considerable environmental masses were present at detonation time, as for example the large (285,000 lbs) cryogenic facilities near IVY-MIKE. It is not surprising, therefore, that the crater data as interpreted and averaged by several investigators at different times appear to be inconsistent. Table IV-3.2 is a summary of the recorded values of yield, HOBs, crater dimensions, and volumes for the most frequently referenced PPG craters. A review of the tabulated results will show that there is no single event upon which all of the investigators agree completely. Each nuclear cratering event had its own unique set of characteristics that has made generalization for cratering analyses difficult. Each major cratering event, with experimental conditions and results, is described in the following subsections.

IV-3.2.1.1 IVY-MIKE. The HOB for event IVY-MIKE has been the subject of controversy. Originally reported as 35 feet, subsequent review of pre-shot photos has indicated that the device was 10 feet above the floor of a supporting structure. The structure was located on a fill above the general level of the surface of the island. Ten feet has become widely accepted as the HOB value.

IV-3.2.1.2 CASTLE-1 (BRAVO). BRAVO was detonated at the end of a long narrow strip of land. Although most of the crater was formed within the reef, approximately 40 percent of the perimeter breached into the open water of the lagoon. A post-shot fathometer survey of the crater, taken six days after the shot, showed the maximum crater depth as 170 feet. Leadline soundings taken several weeks later indicated the crater depth as 240 feet, while the AFWL value is 250 feet. The early

Table IV-3.2. Comparative reported Pacific nuclear crater dimensions.

Event	Laupa	Carlson	Cicero Reference IV-3.14	Cooper	AFWL Reference IV-3.13
Radius (ft)[*]					
IVY-MIKE	2800	3120	2800	2800	2910
CASTLE-1 (BRAVO)	3000	3000	3000	3320	3255
CASTLE-3 (KOON)	470	400	400	490	495
LACROSSE	202	202	202	199	200
ZUNI	1155	1240	1240	1540	1165
SEMINOLE	330	330	255-390	321	324
TEWA	-	2000	2000	2380	1915
CACTUS	170	170	185	169	173
KOA	2000	2000	1825	2260	2160
OAK	-	2200	2200	2860	2870
Depth (ft)					
IVY-MIKE	164	187	164	164	187
CASTLE-1 (BRAVO)	240	240	240	225	250
CASTLE-3 (KOON)	75	75	40	75	40
LACROSSE	44	44	44	44.5	55.5
ZUNI	103	103	115	95	113
SEMINOLE	47	31	31	32	32.2
TEWA	-	129	129	129	133
CACTUS	34.5	34.5	36	34.5	37.2
KOA	171	171	135	148	170
OAK	-	183	183	195	204

Table IV-3.2 (continued)

Event	Laupa	Carlson	Cicero Reference IV-3.14	Cooper	AFWL Reference IV-3.13
	Yield (kT)				
IVY-MIKE	10,400	10,500	10,400	10,400	-
CASTLE-1 (BRAVO)	15,000	14,500	15,000	15,000	-
CASTLE-3 (KOON)	150	130	110	150	-
LACROSSE	39.5	39.5	39.5	39.5	-
ZUNI	3,380	3,530	3,530	3,380	-
SEMINOLE	13.7	13.5	13.5	13.7	-
TEWA	-	5,010	5,010	4,600	-
CACTUS	18	17	18	18	-
KOA	1,300	1,300	1,370	1,380	-
OAK	-	8,900	8,900	9,000	-
	Height of Burst (ft)				
IVY-MIKE	20	10	35	10	10
CASTLE-1 (BRAVO)	15.4	7	15.5	15.4	7
CASTLE-3 (KOON)	13.6	13.6	13.6	13.6	9.6
LACROSSE	15	7	17	8	8
ZUNI	9.3	9.25	9	9.3	10
SEMINOLE	4.5	4.5	4.5	4.5	7
TEWA	-	6.5	20	15	10
CACTUS	3	3	3	3	3
KOA	3	3	3	3	2.67
OAK	-	6.5	6.5	6.5	5.75

Table IV-3.2 (continued)

Event	Laupa	Carlson	Cicero Reference IV-3.14	Cooper	AFWL Reference IV-3.13
			Volume (ft^3)[†]		
IVY-MIKE	-	1.44^{+9}	-	1.39^{+9}	1.236^{+9}
CASTLE-1 (BRAVO)	-	2.89^{+9}	-	2.05^{+9}	2.025^{+9}
CASTLE-3 (KOON)	-	1.03^{+7}	-	1.50^{+7}	1.41^{+7}
LACROSSE	-	3.12^{+6}	-	3.03^{+6}	3.06^{+6}
ZUNI	-	1.55^{+8}	-	3.03^{+8}	2.018^{+8}
SEMINOLE	-	4.75^{+6}	-	7.12^{+6}	6.99^{+6}
TEWA	-	4.04^{+8}	-	9.25^{+8}	7.418^{+8}
CACTUS	-	1.94^{+6}	-	2.03^{+6}	1.99^{+6}
KOA	-	6.44^{+8}	-	8.14^{+8}	7.451^{+8}
OAK	-	7.29^{+8}	-	1.68^{+9}	1.825^{+9}

*The radius is measured at tide level from zero difference contours, the depth is the difference between the foundation elevation and the deepest point in the crater, and the HOB is above foundation elevation or water level for barge detonations.

†The notation 1.44^{+9} means 1.44×10^9.

fathometer readings were probably an indication of the depth to the unsettling layer of suspended mud and sand. The fathometer results thus exhibit typical problems associated with their use in determining submerged crater profiles soon after the events.

IV-3.2.1.3 CASTLE-3 (KOON). KOON was detonated near the end of an island. Approximately 40 percent of the crater perimeter breached into the open water of the lagoon. Before post-shot crater surveys were conducted, the waves from another nuclear event (UNION) washed over the KOON crater. Measurements of the crater showed a flat-bottomed profile, undoubtedly influenced by wave washing from the two events, KOON and UNION.

IV-3.2.1.4 LACROSSE. LACROSSE was detonated on a man-made, earth-filled causeway built over the reef. The center of the device was 8.5 feet above the causeway, itself 8.5 feet above the original reef surface. The majority of analysts have

considered the HOB to be approximately 17 feet. For consistency with IVY-MIKE results, HOB of 8.0 feet would also be acceptable. The LACROSSE crater did not breach to the open water of the lagoon and hence was not water washed. In fact, the water level in the crater immediately following the shot was 20 feet below the level of the water on the reef. LACROSSE is one of the few Pacific craters showing a definable lip and evidence of ejecta.

IV-3.2.1.5 ZUNI. ZUNI was detonated on the same island as KOON, about 100 feet from the edge of the KOON crater. This was probably near enough to the KOON crater for the material properties of the ZUNI site to have been substantially altered over pre-KOON characteristics. The ZUNI crater was smaller than anticipated in both radius and depth and has been considered anomalous by most investigators. The crater partially breached the KOON crater and was severely water washed. A perplexing aspect of the crater is its unusually large asymmetry with respect to ground zero. Although the crater appears to be reasonably circular in profile, the center of the crater is skewed heavily towards the island side of ground zero and away from the breached opening into the KOON crater.

IV-3.2.1.6 SEMINOLE. As indicated previously, SEMINOLE was the prototype of the devices fired inside of water-filled tanks. The crater formed was notable for its flat bottom, having a radius of 150 to 200 feet at approximately the maximum depth of the crater. On this largely land-enclosed event, a lip was formed with a height of approximately 7 feet above ground level. The volume of this crater is approximately 3.5 times that of CACTUS, an event of approximately the same yield without the tamping effect of the water tank. The depths of the SEMINOLE and CACTUS craters are between 30 and 40 feet. This is slightly less than the 40-foot depth of the cemented reef rock underlying the entire reef ring of the atoll.*

IV-3.2.1.7 TEWA. TEWA was detonated on a barge in 20 feet of water over the sloping bottom of the Bikini lagoon. Most of the resulting crater was formed beneath the deep waters of the lagoon. Although the crater was formed in the sloping portion of the reef, the greatest depth of the crater is within the reef. At a depth of 129 feet, the crater bottom was approximately 50 feet below the ridge forming the lagoon-side boundary of the crater. The radius of the crater was defined from reef-side measurements only. No lip was formed above water for the event.

---

*For the most recent details on the geology at the Enewetak Atoll craters (OAK, IVY-MIKE, KOA, SEMINOLE, LACROSSE, CACTUS), see Reference IV-3.13.

IV-3.2.1.8 <u>CACTUS</u>. CACTUS was detonated on the end of a small island about 300 feet from the edge of the LACROSSE crater. At that distance, ground zero for CACTUS was approximately 2½ LACROSSE crater radii. Although the effects were not as pronounced as they were for ZUNI (which was located within 1¼ KOON crater radii), the CACTUS crater dimensions were smaller than had been anticipated. Like LACROSSE, CACTUS was not water washed and was completely contained within the island and the reef rock. A distinct lip was formed around the crater, with sections of the lip as high as 25 feet on all sides of the crater except north which opened onto the water-washed reef.

IV-3.2.1.9 <u>KOA</u>. Like SEMINOLE, KOA was fired within a water tank. The tank was somewhat smaller than for SEMINOLE, and the KOA device yield was approximately an order of magnitude larger than SEMINOLE. The tamping effects of the water were similar for the two events. The craters for both events are nearly twice the size expected for non-tank events. Moreover, KOA was fired close to the IVY-MIKE crater. Ground zero for KOA was 3200 feet from ground zero for IVY-MIKE, a separation of approximately 1.1 IVY-MIKE crater radii. The KOA crater radius has been variously reported as ranging from 1825 feet to 2260 feet. The 1825-feet radius was obtained from measurements of the crater profile within the island. The 2260-feet dimension comes from reef-side measurements of the crater profile. Predictably, the IVY-MIKE and KOA craters coalesced and the KOA crater was severely water washed.

IV-3.2.1.10 <u>OAK</u>. The OAK event was a barge shot detonated near the sloping lagoon edge of the reef in approximately 10 feet of water. The major part of the crater was formed within the downward sloping portion of the reef. However, like TEWA, the deepest portion of the crater, which is approximately 200 feet below the water surface, was approximately 80 to 100 feet below the high point of the ridge marking the lagoon side boundary of the crater.

IV-3.2.2 Non-PPG Nuclear Cratering Events

The wide disparity of test conditions evidenced in the PPG carries over to the tests conducted at the NTS. For example, those events which were primarily device-development tests had associated with them numerous diagnostic instrumentations. Others were detonated in specially prepared areas that could have influenced the resulting crater. In general, those events within the PLOWSHARE program (aimed at peaceful uses of nuclear explosives) were conducted for the express purpose of investigating cratering and the engineering uses of nuclear

explosives. Materials at the NTS that have been cratered by nuclear explosives are basalt, welded tuff, alluvium, and playa. The many mountain ridges at the NTS contributing to the alluvium deposits are composed of limestone, granite, basalt, and tuff. Thus, each test area within the site is unique because it has a slightly different material composition. For a full description, the term "alluvium" must also be related to the area within the test site where the test was conducted. Some of the alluvial deposits are more than 1,000 feet thick and without significant water content for most of the year.

The only nuclear cratering event of the United States which was not conducted at either NTS or PPG was TRINITY, the first nuclear explosion conducted near Alamagordo, New Mexico. Other events discussed in this chapter are Events T1, 1003, and 1004, conducted by the Soviet Union and published as part of their studies on the engineering uses of nuclear explosives. Those events having special characteristics are discussed in the following paragraphs.

IV-3.2.2.1 SEDAN (Reference IV-3.15). On 6 July 1962 a 100-kt device was detonated at a depth of 635 feet (193 meters) in the moist alluvium at the northern end of Yucca Flat within the NTS. The first venting of gas occurred approximately 3 seconds after detonation, when the rising dome of material above the explosion was at a height of about 290 feet and had a diameter between 600 and 800 feet (183 to 244 meters). The venting was not symmetric and appeared randomly distributed around the top of the dome. The resulting crater had an apparent diameter of about 1222 feet (372 meters), a maximum apparent depth of 323 feet (98.5 meters), and an apparent volume of 1.8×10^8 cubic feet ($5.1 \times 10^6 m^3$). This was the first major nuclear explosion conducted in the PLOWSHARE series. The SEDAN crater is shown in Figure IV-3.12.

IV-3.2.2.2 HOLE 1004 (Reference IV-3.16). The date and the yield of this Soviet explosion are uncertain. References quote the yield to be greater than 100 kt. This device was detonated at a depth of about 200 meters in a complicated sedimentary geology. The point of detonation appears to have been in a clay shale, sandstone type material. The area is highly layered with the bedding planes steeply dipping. The shot point was intentionally located well below a shallow water table and the crater was subsequently filled with water. The largest of the reported Soviet experiments was designed exclusively for engineering studies. This crater had an apparent diameter of 400 to 430 meters and an apparent depth of 83 meters. The volume of the apparent crater was $6.4 \times 10^6 m^3$. With the exception of the geology and hydrology, it closely matches the SEDAN event.
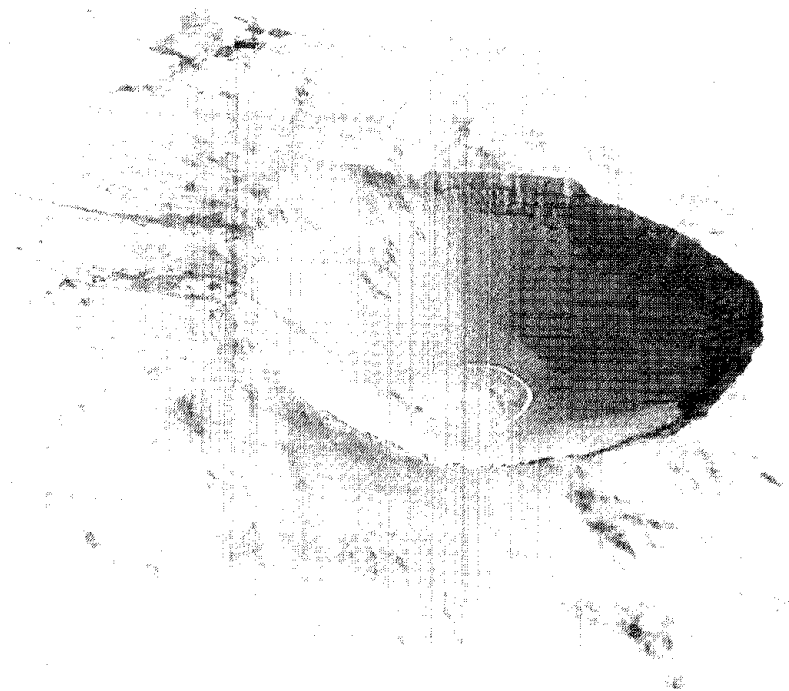
Figure IV-3.12. The SEDAN crater.

IV-3.2.2.3 SCHOONER (Reference IV-3.17). This event, conducted in December of 1968, had two unique characteristics. First, it was the final nuclear cratering event in the PLOWSHARE program, and second, it was conducted in a geology that consisted of a top layer of hard, welded tuff (or rhyolite) overlying a thick, soft, porous layer of tuff. The explosion was detonated in a third underlying layer of dense, strong welded tuff. The device having a yield of 31 ± 4 kt was detonated at a depth of 355 feet (108 meters). The resulting apparent crater radius was 426 feet (130 meters), the apparent depth was 208 feet (63 meters), and the resulting crater volume was 5.94×10^7 cubic feet (1.68×10^6 meters). Although the high porosity layer was about 200 feet (61 meters) thick, its lower boundary was only a few feet above the working point. Further, it contained 28 percent water by weight. Thus, there was a large amount of water (noncondensable gas) in the developing cavity, leading to an enhanced gas acceleration phase in the production of this crater.

IV-3.2.2.4 JOHNIE BOY. A half-kiloton device slightly buried in the NTS Area 18 was detonated in July of 1962. The center of mass of this device was buried at a

depth of about 0.58 meters. The device was surrounded by a large, thin, oblate spheroid shell. The pit in which the shell was partially buried was backfilled with alluvium from the area.

A number of other nuclear tests have been conducted at the NTS: Cabriolet, Danny Boy, Teapot Ess, to mention a few.

IV-3.2.3 High-Explosive Tests

High-explosive cratering tests are numerous and varied and a great deal of selectivity has been exercised for their inclusion in this section. A summary of the projects and/or events which contribute to the discussion below is given in Table IV-3.3. Excluded are events which were conducted with explosive yields too small to be statistically significant for extrapolation to high yield. Tests using explosives that are poorly characterized and tests that are nonspherical, single-charge events, or tamped charges also have been excluded from this discussion. Experimentation has included a large number of events with equal explosive yields in identical media. This work permits the development of reasonably well-defined DOB curves for several soils. A wide range of soil and rock media are included in the shots discussed here. Explosive yields range from approximately 10 pounds to 10^6 pounds in soil, and from 100 pounds to an excess of 100,000 pounds in rock. HOBs ranging from approximately 6 charge radii above the ground to well below the optimum cratering depth have been included. Tabulated dimensions, volumes and other data are given in Appendix IV-3B for nonnuclear shots up to April 1976. A comprehensive compendium of up-to-date cratering data is maintained by the United States Army Engineer Waterways Experiment Station (WES) (Reference IV-3.18).

In addition to the experiments conducted to determine the effect of DOB and yield in a medium, there have been several experiments conducted in unique media. These include, among others, the MINE SHAFT series in Cedar City Tonalite (a granite-like material); FLAT TOP I, a half-buried sphere in limestone; the PRAIRIE FLAT, DIAL PACK, and DISTANT PLAIN 6 Events conducted in layered clay of the Watching Hill Test Range in Canada; the MIDDLE GUST series detonated in wet and dry clay/shale; the MIXED COMPANY Event conducted on soil and sandstone near the Glade Park area in Western Colorado; the MINE THROW I Event detonated in desert alluvium at the NTS; and the ESSEX Phase I Events detonated at the Fort Polk Military Reservation in Louisiana. Some of these unique events are discussed individually.

Table IV-3.3. Summary of some HE cratering experiments.[a] Single-charge events (spherical).

Project or Event	Medium[b]	Number of Shots	Explosive Type	Range of Equivalent Yields[c] (lbs)	Scaled Range of Depth of Burst $(ft/lb^{1/3.4})$
DUGWAY	Dry Sand (Utah)	15	TNT	8 - 40,000	-0.64 - 3.85
DUGWAY	Wet Clay (Utah)	20	TNT	8 - 320,000	-0.64 - 3.85
DUGWAY	Wet Clay (Utah)	5	TNT	8 - 2,560	0.46 - 1.36
DUGWAY	Limestone (Utah)[d]	2	TNT	320	0.46 - 1.21
DUGWAY	Granite (Utah)[d]	12	TNT	320 - 2,560	-0.46 - 4.58
DUGWAY	Sandstone (Utah)[d]	19	TNT	320 - 320,000	-0.46 - 2.29
JANGLE HE	Alluv - 10	10	TNT	216 - 40,000	-0.2 - 0.68
JANGLE HE	Alluv - 10	3	Pentolite	220	0.183 - 0.654
MOLE	Alluv - 10	13	TNT	256	-0.16 - 1.24
MOLE	Dry Clay (Utah)	7	TNT	256	-0.16 - 1.24
MOLE	Wet Sand (Cal)	10	TNT	256	-0.16 - 0.93
MOLE	Moist Clay (Cal)	3	TNT	256	-0.16, 0.62
TOBOGGAN	Playa (YL)	24	TNT	8	0 - 2.71
SANDIA I	Alluv - 10[e]	11	TNT	256	1.86 - 4.97
SANDIA II	Alluv - 10	13	TNT	256	0, 2.56 - 5.83
STAGE COACH	Alluv - 10	3	TNT	40,000	0.76, 1.51, 3.54
SCOOTER	Alluv - 10	1	TNT	987,410	2.16
LITTLE DITCH	Alluvium (Alb)	10	TNT	256	0.62 - 2.49
BUCKBOARD	Basalt - NTS	13	TNT	1000 and 40,000	0.63 - 3.23
ROWBOAT	Alluv - 10	2	TNT	278	2.85
PRE-BUGGY	Alluv - 10	7	NM	1,000	1.96 - 2.79
PRE-BUGGY II	Alluv - 5	4	NM, TNT	1,000	2.44 - 2.60
PRE-SCHOONER	Basalt - NTS	4	NM	40,000	1.86 - 2.93
PRE-SCHOONER II	Rhyolite (Idaho)	1	NM	171,000	2.05

Table IV-3.3. (continued).

Project or Event	Medium[b]	Number of Shots	Explosive Type	Range of Equivalent Yields[c] (lbs)	Scaled Range of Depth of Burst $(ft/lb^{1/3.4})$
FLAT TOP I	Limestone (NTS)	1	TNT	40,000	0
FLAT TOP II, III	Playa (FF)	2	TNT	40,000	0
AIR VENT I	Playa (FF)	1	TNT	40,000	0.76
AIR VENT II	Playa (FF)	20	TNT	256	-0.17 - 4.97
AIR VENT III	Playa (FF)	9	TNT	64 - 6000	0
UNNAMED	Alluvium (NTS)	1	TNT	5,000	0
UNNAMED	Alluvium (Alb)	11	TNT	64	1.77, 2.06
PRE-CAPSA	Alluvium (Alb)	2	TNT	256	1.86
CAPSA	Alluvium (Alb)	13	TNT, NM	1000 and 30,500	1.31 - 2.29
TTR-211	Playa (TTR)	11	TNT	8 - 1000	0 - 2.06
MTCE	Basalt (YFC)	5	TNT	4000 and 16,000	0
MTCE	Basalt (YFC)	4	TNT	4,000	-0.19 - 0.19
SANDIA TUFF	Tuff	5	TNT	256	1.35 - 2.03
PRE-GONDOLA I	Bear Paw Shale (DCI)	8	NM	1000 and 40,000	1.60 - 3.05
DISTANT PLAIN	Silt (DRES)	5	TNT	40,000 - 200,000	-1.31 - 0
PRAIRIE FLAT	Silt (DRES)	1	TNT	1,000,000	-0.23
DIAL PACK	Silt (DRES)	1	TNT	1,000,000	-0.23
MINE SHAFT CALIB	Granite (CC)	10	TNT	1,000	-0.35 - 0.05
MINE SHAFT	Granite (CC)	3	TNT	200,000	-0.43, -0.19
PRE-GONDOLA III	Bear Paw Shale (DCI)	8	NM	2,000	0.64 - 2.78
ANFO IV	Layered Clay (DRES)	1	AN/FO	50,000	-0.20
ANFO V	Layered Clay (DRES)	1	AN/FO	47,000	0.0
DIAMOND ORE-IIA	Bear Paw Shale (DCI)	3	Aluminized AN Slurry	32,000	1.94, 1.94, 0.95

Table IV-3.3. (continued).

Project or Event	Medium[b]	Number of Shots	Explosive Type	Range of Equivalent Yields[c] (lbs)	Scaled Range of Depth of Burst $(ft/lb^{1/3.4})$
PLEX NO. 6	Playa (Alb)	1	TNT	1,000	-0.30
MIDDLE GUST	Wet Alluvium (OT)	5	TNT	40,000 - 200,000	-0.44 - 0.0
MIXED COMPANY	Sand (GJC)	3	TNT	$40,000 - 10^6$	-0.23 - 0.0
PACE	Coral Sand (PPGE)	12	TNT	1,000	-0.35 - 0.17
SUFFIELD	Silt and Sand (DRES)	4	TNT	10,000 - 40,000	-0.26

Notes:

[a]References for these experiments may be obtained from Appendix IV-3B.

[b]Site locations and materials defined as: (Utah) Dugway Proving Grounds, Utah; (YL) Yucca Lake, NTS; (Idaho) Bruneau Plateau, Southwestern Idaho; (FF) Frenchman Flat, NTS; (Alb), Albuquerque, N.M.; (TTR) Tonapah Test Range, Nevada; (YFC) Yakima Firing Center, Washington; (DRES) Defence Research Establishment Suffield, Canada; (CC) Cedar City, Utah; Alluv-10, Desert Alluv, Area 10, NTS; Alluv-5, Desert Alluvium, Area 5, NTS; (Cal), Mouth of the Santa Ynez River, California; (DCI), Duck Creek Inlet at Fort Peck Reservoir, Montana; (OT) Ordway Test Site, 50 mi. east of Pueblo, Colorado; (GJC) Grand Junction (Glade Park area), Colorado; (PPGE) Enewetak, Pacific Proving Ground.

[c]Scaled to equivalent energy TNT.

[d]True crater dimensions only.

[e]Includes one shot (209) in Albuquerque alluvium.

IV-3.2.3.1 PRAIRIE FLAT, DISTANT PLAIN 6, and DIAL PACK. The PRAIRIE FLAT Event
and its related shots, DISTANT PLAIN 6 and DIAL PACK, were executed in the Canadian
Test Range on a bed of layered clay and sandy loam. PRAIRIE FLAT had extensive
dynamic instrumentation and a sizeable investigation was conducted after the event.
The explosion consisted of a surface-tangent sphere made from stacked blocks of TNT
totaling a weight of 500 tons. The resulting crater was cylindrically symmetric
and exhibited several concentric ridges on the crater floor, but no central mound.
The crater can be seen in Figure IV-3.13. Careful excavation through the crater
showed a folding back of material in the region of the crater lip. This is clearly
defined by the layering of the clay. It was also found that, contrary to common
experience, the boundary of the true crater lip was depressed below the pre-shot
ground surface with the high lip being composed of folded material and ejecta. The
same comments apply to the DIAL PACK Event, except that instead of the concentric
rings observed in the PRAIRIE FLAT event the central mound was shown to be composed
of folded material and not fallback. DISTANT PLAIN 6 exhibited a central mound and
showed an uplifted, rather than depressed, crater lip. The magnitude of the
PRAIRIE FLAT explosion and the careful attention given to the measurements have
made this event a key data point serving for extrapolations to higher explosive
yields. The apparent crater radius was approximately 100 feet and the apparent
volume 3.12×10^5 cubic feet. Because of the concentric ring structure in the
crater floor, no depth is quoted here. The photograph of Figure IV-3.13 showing
the crater after it had begun to fill with water clearly indicates the ring struc-
ture.

IV-3.2.3.2 MINE SHAFT (Reference IV-3.19). MINE SHAFT is the designation given
a series of four explosions conducted in and above a granite-like material called
Cedar City tonalite. This series is unique because it is the only set of large-
scale high-explosive experiments conducted in hard rock with the exception of the
20-ton FLAT TOP I explosion conducted in limestone at the NTS. Cedar City tonalite
is a highly fractured material with block faulting in preferred directions. The
explosive charges were detonated at three different heights with respect to the
ground surface. Two identical experiments were conducted with the sphere of explo-
sives penetrating the rock surface for one-tenth of its radius. The third test was
conducted with the center of mass of the explosive at 2 charge radii above the
ground surface. The fourth test consisted of approximately 14 tons of slurry
detonated at a depth of 100 feet below the ground surface. This latter shot was
fully contained, producing no crater. The three charges above the ground surface
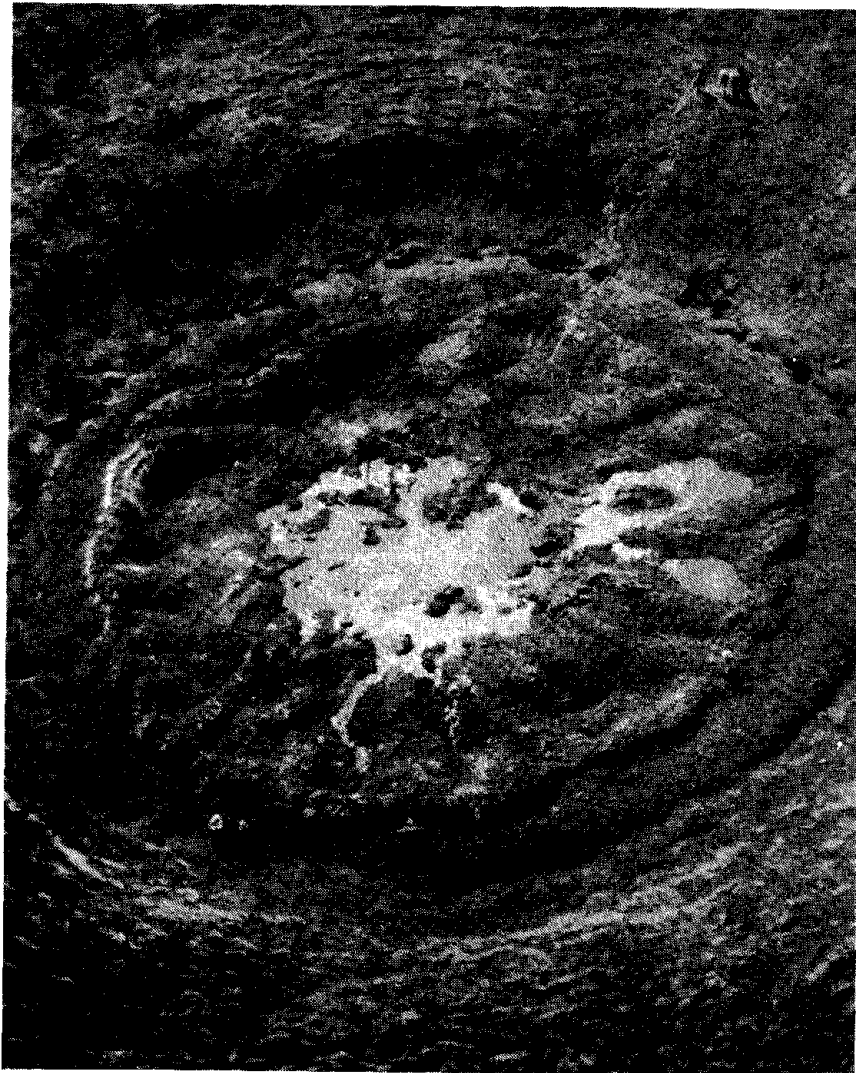
Figure IV-3.13. Aerial photograph of the PRAIRIE FLAT crater
several days after detonation.

were 100-ton spheres of TNT. The craters formed by the surface and above-surface
explosions were highly asymmetric because of the pre-shot faulting planes in the
tonalite. Large blocks of material were strewn around each crater. Some of these
blocks had dimensions that were commensurate with those of the crater. It should
be noted that similar effects were observed after the FLAT TOP I Event.

IV-3.2.3.3 FLAT TOP I (Reference IV-3.20). The FLAT TOP I Event consisted of a
half-buried sphere of TNT weighing 20 tons detonated in competent limestone at NTS.
Drill samples of the rock formation indicate that joint spacings vary between 3 and
12 inches with the joints filled with clay or calcite. As observed in the MINE

SHAFT series conducted in granite material, the resulting crater was asymmetric with the shape being strongly influenced by the pre-shot fracture patterns. Several large undamaged sections postulated to correspond with pre-shot fracture planes were observed in the crater floor. Ejecta and fallback had size distributions characteristic of the pre-shot joint spacing with a substantial amount of fine material included.

IV-3.2.3.4 MINE THROW I (Reference IV-3.21). Event MINE THROW I consisted of an approximate ellipsoidal shape charge of a mixture of ammonium nitrate and fuel oil weighing 118 tons. The charge was designed to simulate the cratering effects and ground motion of the JOHNIE BOY nuclear event. The charge was emplaced just below the surface in desert alluvium at the NTS. The top of the charge was tangent to the surface. Apparent crater dimensions and surface displacements were measured by conventional topographic survey methods and by aerial photography. True crater dimensions and subsurface displacements were measured by exposing colored sand columns that had been emplaced before detonation with elevation markers seeded into the columns. These elevation markers also served as artificial ejecta when thrown from the crater. Comparison with the JOHNIE BOY nuclear event showed similarities in most crater dimensions, although MINE THROW I showed a slightly larger crater. However, there appeared to be differences in cratering mechanisms between these two events; compaction volume was larger and plastic flow volume was smaller than for the JOHNIE BOY event.

IV-3.2.3.5 MIDDLE GUST. Project MIDDLE GUST was a series of HE detonations designed to provide free-field ground motion, cratering and ejecta, and structure-medium interaction data for surface and near-surface explosions in a layered clay-shale geology. Between March 1971 and August 1972 five main events and fourteen 1000-pound TNT calibration events were detonated at two test sites in southeastern Colorado near Crowley, Colorado. The main events were two 20-ton half-buried charges with zero HOB, two 100-ton tangent-above surface charges, and one air burst at two charge radii above the surface. The 100-ton charge for the air burst was surported by a massive wooden tower weighing 14 tons. Each of the charges for the main event consisted of 32.6-pound TNT blocks stacked in a spherical configuration. The calibration charges were cast spheres of TNT. Figure IV-3.14 shows the charge configurations and their relative locations with respect to the ground surface.

MIDDLE GUST

MAIN

EVENTS

"Wet" Site

II 100 tons

III 100 tons

I 20 tons

4'

9'

— Clay —

Water Table

Shale

IV 100 tons

V 20 tons

1

2'

Clay

Shale

"Dry" Site

1000 POUND TNT EVENTS

3 3a 3b 3c 3d 4

5 6 6a

7 8

9

4'

9'

Clay

Water Table

8'
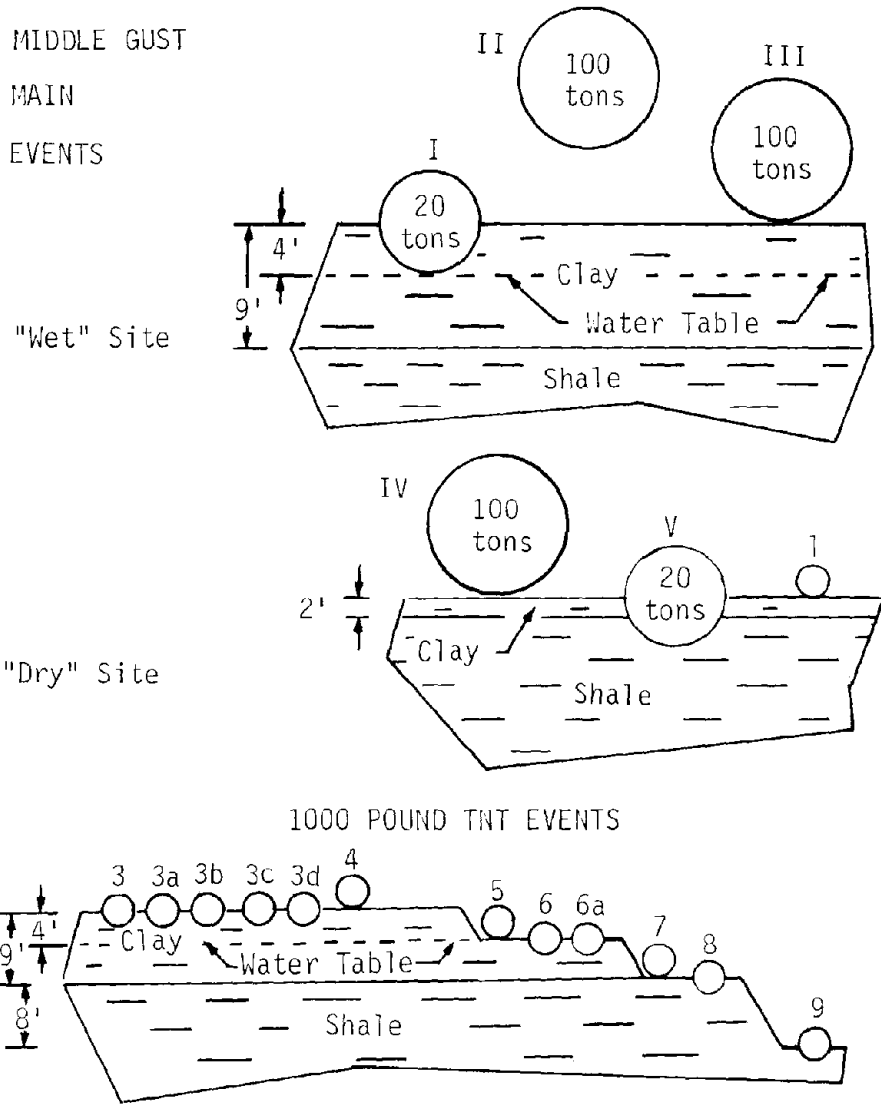
Shale

Figure IV-3.14.   Test configurations for the MIDDLE GUST
                   HE events (Reference IV-3.22).

The geology of the MIDDLE GUST test sites consisted of layered clay soil over weathered shale which graded into competent Pierre shale at depth shown in Figure IV-3.14. At the test site for the main events I, II and III and the calibration events 2 through 9, a perched water table existed in the test medium above the competent shale. This site was referred to as the "wet" site. The water table was encountered at about four feet below the surface of the test bed in the clay soil. At a depth of approximately 8 to 9 feet the soil transitioned into weathered shale and between 16 to 23 feet depth to competent shale. In order to determine the cratering response of each of these layers independently, a portion of the wet site was isolated from the influx of water by driving sheet piling through the test bed down to the competent shale. This test site was then progressively excavated to expose the water table, the weathered shale surface and the hard shale surface. As shown on Figure IV-3.14 cratering tests were conducted on each of the exposed layers with the 1000-pound calibration charges. At the wet site, the surface clay soil above the 4-foot water table was 80 percent saturated with 14 percent by weight water content. Between the 4-foot depth and the hard competent shale, the material was 97 percent saturated with about 20 percent water by weight.

About five miles from the wet site a similar geologic environment of layered clay soil and shale existed, but no water table was present near the surface. Main events IV and V were conducted at this location, which is referred to as the "dry" site. Here the clay soil at the surface graded into highly weathered shale at about the 2- to 3-foot depth, and this transitioned gradually into competent Pierre shale at about 28 feet. The material above the hard shale averaged about 70 percent saturation with 13 to 14 percent water content by weight. The 1000-pound Event 1 was detonated in dry area adjacent to the "wet" site where about 1 foot of dry alluvial soil overlay dry weathered shale. Results of postshot investigations showed that the cratering efficiencies were as much as a factor of 3.7 higher for the "wet" site than for the "dry" site (Reference IV-3.22).

IV-3.2.3.6 MIXED COMPANY. The MIXED COMPANY program was a specially designed series of high-explosive detonations to provide free-field ground motion, cratering and ejecta, and some structure-medium interaction data for surface and near-surface explosions in a layered sand over sandstone geology. Between June 1972 and November 1972 three main events and five 1000-pound cratering calibration events were detonated near Grand Junction in west central Colorado. The main events were a 20-ton half-buried charge at zero HOB, a 20-ton surface-tangent charge, and 500-ton

surface-tangent charge at one charge radius above the surface. The explosive charges for each of these main events were spherical in shape and made from 32.6-pound TNT blocks. The smaller 1000-pound explosive charges were cast TNT spheres. Figure IV-3.15 shows the charge configurations and their relative locations with respect to the ground surface.

The geology of the MIXED COMPANY test site consisted of an alluvial sandy soil, varying in thickness from several inches to over 10 feet, overlying the fluvial Kayenta sandstone. The upper several feet of the Kayenta formation consisted of a transitional zone of weathered sandstone. The Kayenta sandstone is a very competent sandstone forming the caprock for the cliffs and the monoliths in the nearby Colorado National Monument. The surface alluvial soil and weathered Kayenta sandstone in the test area site normally contain 3 to 5 percent water by weight. For Event I approximately four feet of alluvial soil existed above the weathered sandstone, so that the base of the half-buried charge was in contact with the sandstone. In Event II approximately 2.5 feet of soil was present above the weathered sandstone. Surface alluvial soil was at a depth of 6.5 feet, and the dense competent Kayenta sandstone appeared at a depth of 12 feet.

The MIXED COMPANY test bed was excavated in one location to expose the surface of the weathered sandstone in order to provide a test surface for two of the 1000-pound calibration events (Events III and IV). Two other 1000-pound calibration events were detonated on the alluvial soil surface material at a location where the craters would not intersect the weathered sandstone. Event V was detonated on a specially prepared surface of 0.65 feet-thick alluvial soil packed over the excavated weathered sandstone surface. This attempted to provide a scaled down version of the geologic layering at the Event III ground zero.

IV-3.2.3.7 ESSEX. Project ESSEX is a long-range program designed to simulate the various effects associated with the employment of low-yield nuclear devices. The ESSEX I Phase I program was designed to study methods to realistically simulate nuclear cratering detonations using high explosives. The Phase I project involved four large-scale detonations having shot geometries considered appropriate to current concepts of atomic demolition munition (ADM) employment (Reference IV-3.23) using varying emplacement configurations in a wet, weak soil (Reference IV-3.24). One of its purposes was to investigate the potential of such detonations to produce crater obstacles to surface mobility. These tests were conducted at the Fort Polk Military Reservation in Louisiana. Permanent surface and subsurface

MIXED COMPANY

MAIN EVENTS
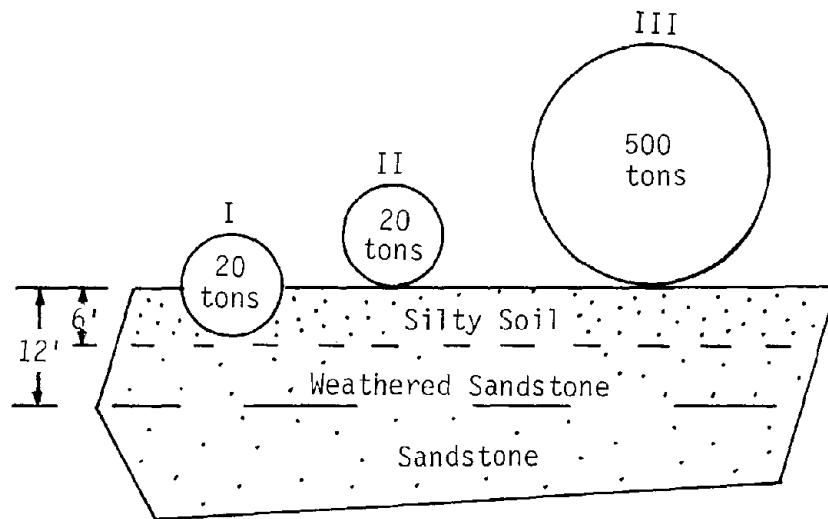
1000 POUND TNT EVENTS
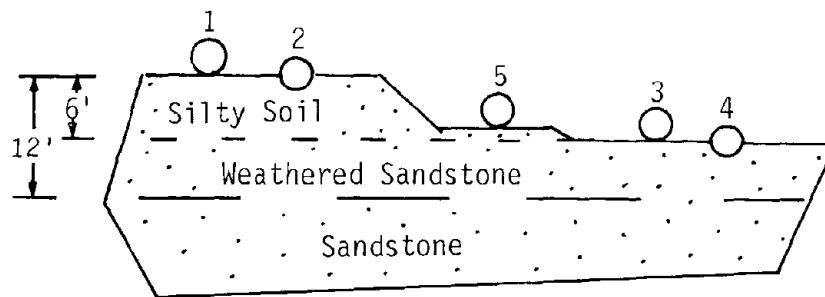
Figure IV-3.15. Test configurations for the MIXED COMPANY
HE events (Reference (IV-3.22).

displacements were measured on three large HE cratering tests intended to simulate the effects associated with the detonation of low-yield nuclear devices. The test events consisted of: a 10-ton (equivalent TNT) charge at a 12-meter DOB, stemmed (Event 12MS); a 10-ton charge at 6-meter DOB, stemmed (6MS); and an 8-ton charge at 6-meter DOB, unstemmed (6MU). The cratering medium consisted of a layered system of sands, silts, and clays, with a water table that for the most part was encountered at depth in the range of 3 to 5 meters below the surface. From the displacement data, the radius of the true crater and the radial extent of permanent deformation at ground surface were determined for each event. Dimensions of the true crater and associated displacement for 12MS were satisfactorily predicted. Both 6-meter events produced larger true craters than had been anticipated. It is believed that soil mass instabilities, such as soil creep, subsidence, and perhaps to some degree slope failures, caused the anomalously wide craters in the cases of the 12MPS, 6MS, and 6MU events. (Reference IV-3.25).

The Phase 2 program consisted of detonating four charges with a nominal yield of 10 tons each (Reference IV-3.26). Permanent surface and subsurface displacements were measured in four large HE cratering tests intended to simulate the effects associated with the detonation of a low-yield nuclear device. The test events consisted of: a 10-ton charge at a 6-meter (~20-foot) DOB and water-stemmed (6MWS); an 11.5-ton and a 9-ton charge at 3-meter (9.8-foot DOB, stemmed and un-stemmed, respectively (3MS and 3MU); and an 8-ton charge at 12-meter (~39-foot) DOB and unstemmed (12MU). The cratered medium consisted of a layered system of sedimentary sands, silts, and clays, with a water table that lay generally at or above the charge elevation. From the displacement data, the radius of the true crater and the radial extent of permanent deformation at ground surface were determined for each event. The true crater radius of 6MWS was about as predicted. The shallower events would normally be expected to provide smaller craters. The fact that they did not may be attributed to the charge position relative to the water table and to the layering of the cratered medium. The small radius of 12MU indicates that its DOB for the unstemmed condition may have exceeded optimum. Azimuthal variations in surface displacements indicate significant anisotropic characteristics of the cratered medium.

IV-3.2.4 Comparative Geologic Effects on HE Cratering

In this section a brief analysis is made of the comparative geologic effects on HE cratering. The material presented was adapted from Reference IV-3.22. The

cratering efficiency data for the various geologic materials permit a comprehensive comparison to be made of the macroscopic effects of earth materials on the cratering processes for near-surface detonations. One convenient point of comparison is the zero HOB: comparing the mean craters formed by unit explosive charges set into the media with the center of mass of the charge at the earth's surface. This assures a valid, meaningful comparison between the various events and the geologic materials. A tabular listing of the zero HOB cratering efficiencies for eleven geologic materials is presented in Table IV-3.4. An order of magnitude difference in the cratering efficiencies can be noted between the wet coral sand of Enewetak or the wet clay soil of the MIDDLE GUST events and the hard granitic and basaltic rocks of the MTCE and MINE SHAFT events. This means that for the same size explosive charges, crater volumes in the weak water-saturated sands and soils are ten times larger than those in hard granitic or basaltic rocks. The information given in Table IV-3.4 can be made more visual by plotting the cratering efficiencies as a function of earth material strength. This is shown in Figure IV-3.16. The high-yield-strength materials (hard rock) shown on the left of the graph gradually decrease to lower strength rocks and dense soils, and finally to the weak unconsolidated sands and soils shown on the right. Materials which are essentially void of water, shown on the left of the graph, change to materials with moderate water content and finally change to completely water saturated. The largest incremental increase in cratering efficiency is seen to occur as the earth materials change from a relatively high water content to fully saturated, as occurred with the shale test media in southeastern Colorado.

By combining the semi-logarithmic plots of cratering efficiencies deduced for all of these near-surface high-explosive tests, there emerges the dependence of cratering on geologic materials as shown in Figure IV-3.17. The cratering efficiency lines are markedly parallel, the only exceptions being low cratering efficiency playa and hard rock. The slopes of the lines tend to increase and become systematically steeper with increasing strength of the geologic materials. With increasing cratering efficiencies, the geologic media becomes progressively weaker in strength and wetter in percent water by weight as well as percent saturation. This effect involves the interrelationship of material strengths and moisture, at least insofar as the increased water content decreases the shear strengths. The playa data seem to exhibit a somewhat anomalous behavior with a markedly steeper slope. It should be noted that there is much more scatter in the data than implied by the lines in Figure IV-3.17.

Table IV-3.4. HE cratering efficiencies for various earth materials at a zero height of burst (Reference IV-3.22).

Material	Test Area/Project	Cratering Efficiency $(ft^3/ton)^*$
Coral Sand (saturated)	Enewetak Atoll (PACE)	4,000
Clay Soil/Shale (saturated)	SE Colorado (MIDDLE GUST)	4,000
Clay Soil/Shale Claystone	Montana (DIAMOND ORE)	1,900
Glacial Soil	Alberta, Canada (DRES)	1,500
Clay Siltstone	Louisiana (ESSEX)	1,200
Clay Soil/Shale	SE Colorado (MIDDLE GUST)	1,100
Alluvial Soil	Nevada (NTS)	1,000
Sandy Clay Soil	New Mexico (CERF)	950
Playa	Nevada, New Mexico (NTS, PLEX)	900
Soil/Sandstone	W Colorado (MIXED COMPANY)	500
Basalt-Granite	Washington, Utah (MTCE, MINE SHAFT)	400

*These numbers are not all of equal confidence.

On the high end of the cratering efficiency scale the PACE and MIDDLE GUST "wet" site cratering efficiency lines are essentially identical. While the materials are geologically quite different—unconsolidated calcium carbonate coral sand (PACE) versus cohesive clay soil and clay shale (MIDDLE GUST)—the individual data points are almost indistinguishable from one another within the scatter of the data of both test series. These materials were nearly 100 percent saturated, so that this physical property may have dominated the cratering process. The same phenomenon was observed among the different saturated geologic layers of the MIDDLE GUST site, but it was not as dramatic as when the shale is compared with the unconsolidated coral sand of Enewetak.

For the dry soils (MIDDLE GUST "dry" site, NTS alluvium, and CERF dry soil) the cratering efficiency lines do not differ appreciably in the near-surface region. The scatter in the data from each of these tests is sufficiently large that a number of parallel lines (e.g., approximately the NTS alluvium line) would be used to
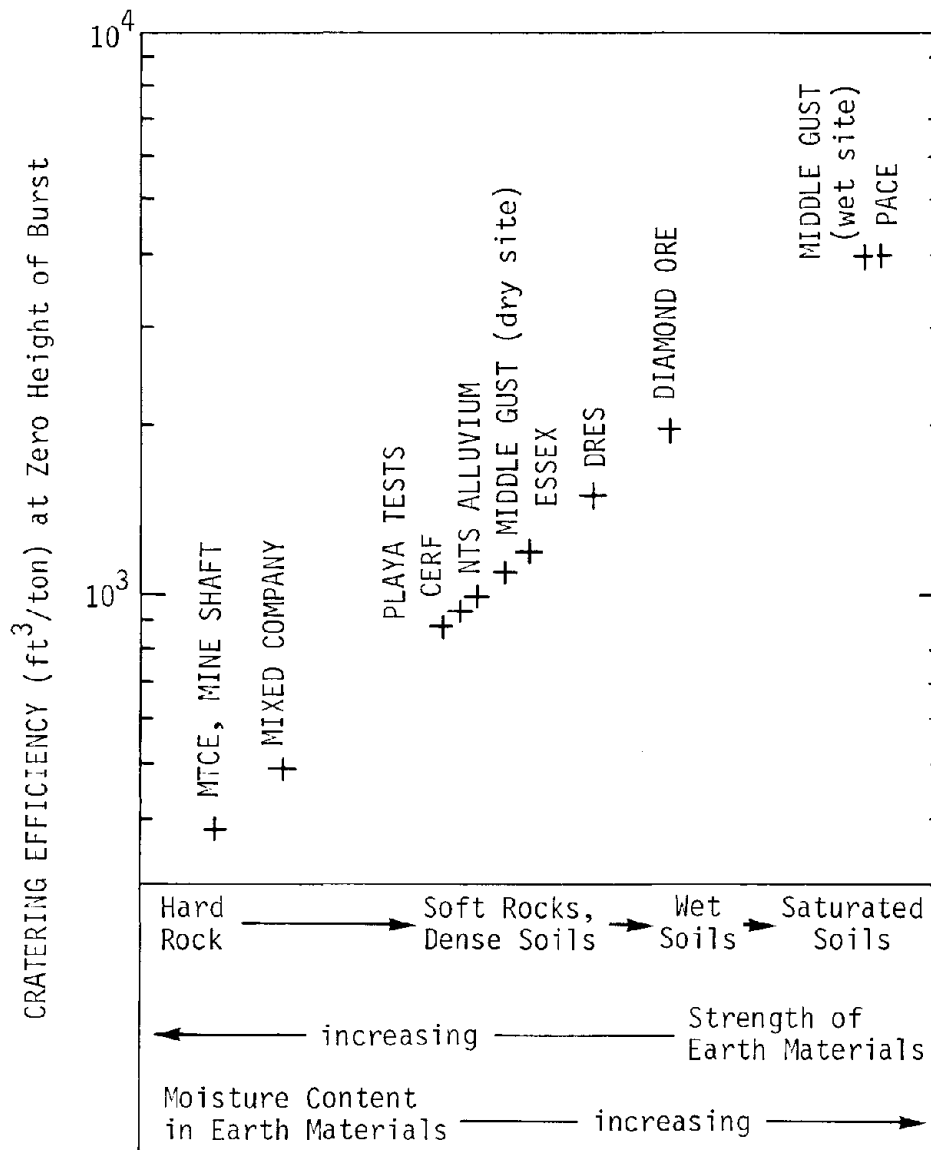
Figure IV-3.16. Descriptive geologic effect on HE cratering
efficiency (Reference IV-3.22).
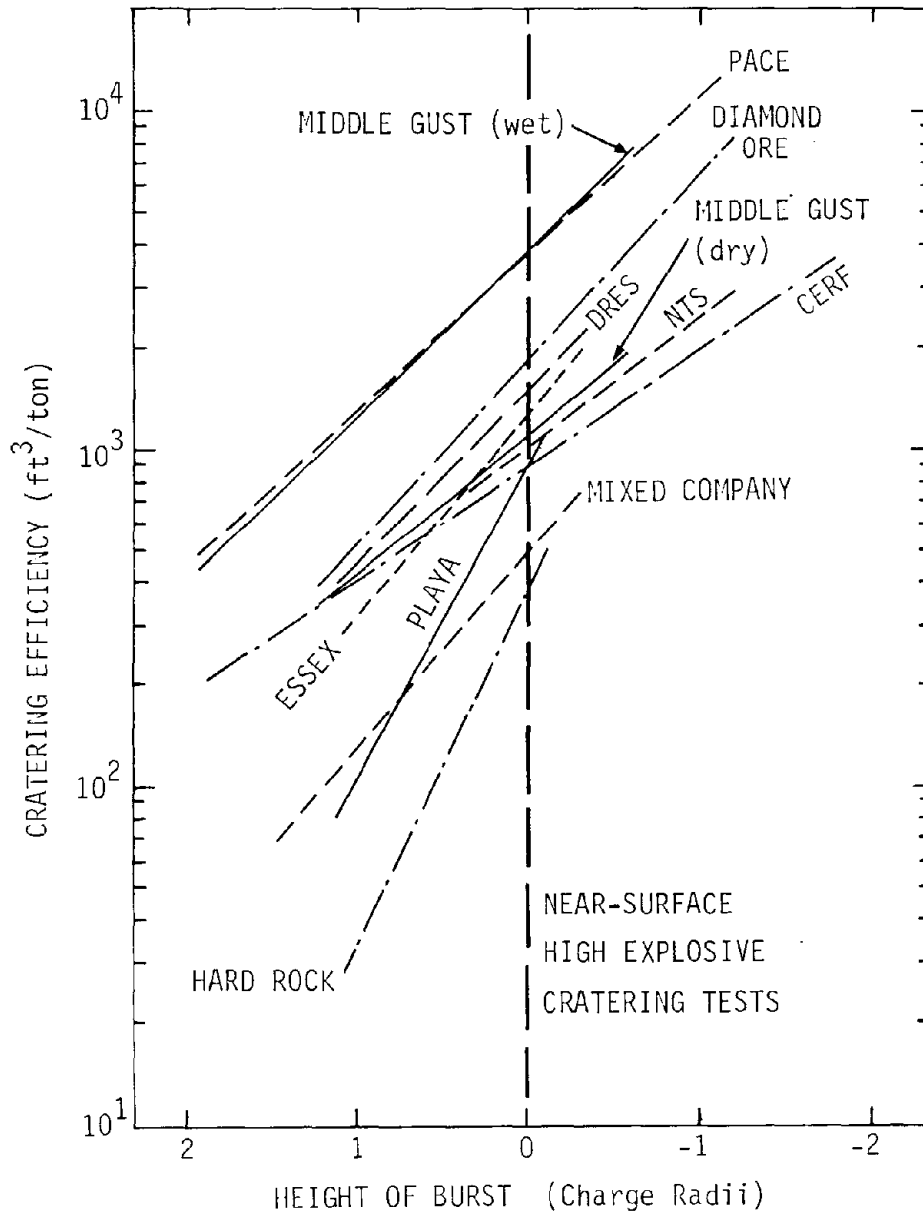
Figure IV-3.17. Comparative cratering efficiency for
eleven geologic media (Reference IV-3.22).

represent all of the dry soils. The DRES and MIDDLE GUST "dry" test sites contain approximately the same amount of water (12 to 14 percent).

IV-3.2.5 Multiple Charge Events—HE and Nuclear Linear Craters

One of the prime objectives of the PLOWSHARE program conducted by the Lawrence Livermore Laboratory was the investigation of the use of nuclear explosives to create a sea-level transisthmian canal. Multiple small-scale charges have been used for many years in the mining industry. Early experiments with line charges such as the TOBOGGAN events of 1959 to 1960 (Reference IV-3.27) demonstrated the feasibility of excavating large quantities of earth with chemical explosives. In addition to the TOBOGGAN series conducted in the Yucca Lake playa at the NTS, the PRE-BUGGY series was conducted in alluvium and basalt at the NTS, and the PRE-GONDOLA series was conducted in Bear Paw shale at Fort Peck, Montana. Subsequent to these experimental shots, engineering use was made of the multiple charge concept in clearing the Sergis Narrows in Alaska (granite) and in Project TUGBOAT in Hawaii where a boating harbor was created in coral. These two projects were conducted by the Explosive Excavation Research Laboratory of the Waterways Experiment Station located at the Lawrence Livermore Laboratory. A compendium of line and multiple explosive cratering events is given in Tables IV-3B.7 and IV-3B.8 in Appendix IV-3B.

The United States has conducted only one multiple-charge nuclear cratering event, BUGGY (Reference IV-3.28). This experiment was conducted in a complicated basaltic mesa (Chukar) at the NTS. This site is composed of multiple flows of volcanics having densities ranging from 1.8 to 2.7 gm/cc and porosities ranging from near zero to greater than 30 percent. Five 1.1-kt charges were detonated simultaneously at a depth of 135 feet (41.2m). The separation between charges was 150 feet (45.7m) or corresponding to a DOB of 1.11. The resulting crater was smooth-walled and of fairly uniform depth. Longitudinal and transverse cross sections of the crater are given in Figure IV-3.18.

One nuclear row charge experiment has been reported by the Soviet Union (Reference IV-3.16). A set of three 0.2-kt charges were emplaced in holes to a depth of 103 feet (31.4m) with a separation of 134 feet (40.8m) or corresponding to a DOB of 1.3. The geology of the area is a sedimentary deposit, including gritstone, sandstone, and extrusives, and is overlaid by a strata of clay, loam, and sand to a depth of about 7 meters, the approximate depth of the water table. Qualitatively, the resulting crater was essentially the same as that of the BUGGY
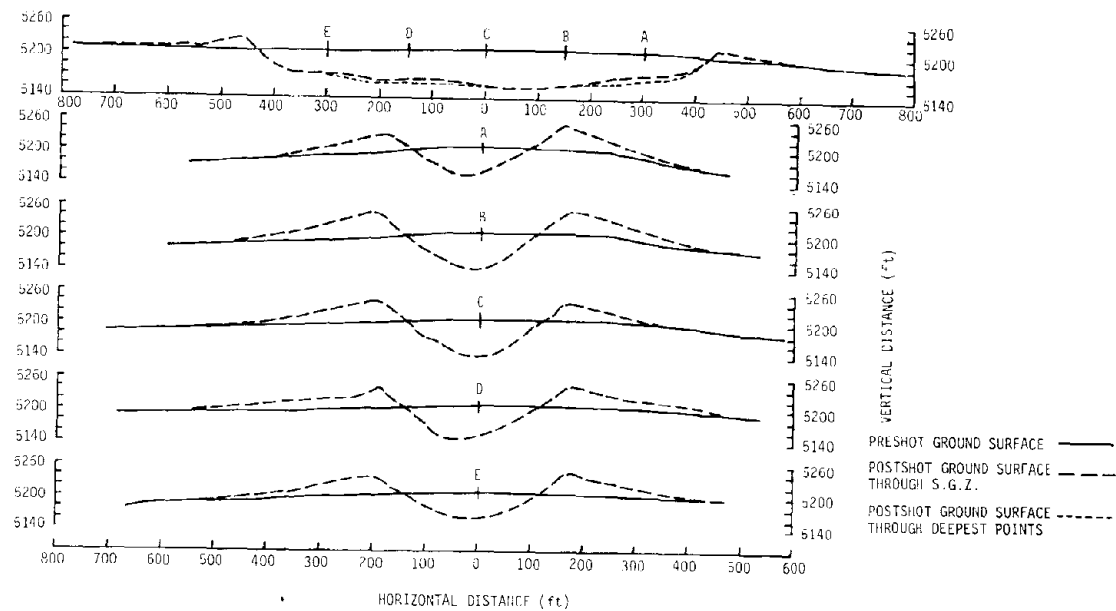
Figure IV-3.18. BUGGY crater topographic profiles.

experiment—smooth sides and a relatively flat bottom along the length of the crater. The length of the trench at ground level was 466 feet (142m) and the width at ground level was between 200 and 226 feet (61 and 69m). The depth of the trench from the original ground surface varied between 49 and 66 feet (15 and 20m). There appears to be somewhat more crater lip at the end of the trench than was observed in the BUGGY experiment. The sides of the trench yielded a crater lip height between 29.5 and 52.5 feet (9 and 16m) and at the end of the trench the lip was about 23 feet (7m) high. The total volume of the crater measured from the original ground surface was 2.72 x 10^6 ft^3 (7.7 x 10^4m^3). Vortman stated (Reference IV-3.3) that with an increasing number of charges the lip size at the trench ends compared to the sides tends to decrease.

In the limit of a large number of discrete charges detonated simultaneously, the effects are like those produced by a continuous line charge. To determine the cratering behavior of this limiting case, the TOBOGGAN events were carried out during 1959 and 1960 in the Yucca Lake playa of the NTS. This particular medium was chosen because of its unusually high degree of uniformity of material properties over a great depth. It was expected that the line charge cratering process could be determined without ambiguities from nonuniformities of the test site. Craters resulting from linear charges were then related directly to these limiting-case line charges. Vortman (Reference IV-3.29) published a complete review of the status

IV-3-46

of high-explosive cratering research at the end of 1968. In addition to a discussion of cratering produced by single charges, an extensive analysis of the relationship between multiple linear charges and line charges was also presented. An example of the results of this work is seen in Figure IV-3.19. Line charge equivalence is defined as the crater having uniform width and depth between the first and the last charge in the linear sequence. Greater separation between charges resulted in a linear crater having greater dimensions at the positions of the charges and smaller dimensions at positions between the charges. The plane defined by charge spacing and charge DOB is divided into four overlapping regions as shown in Figure IV-3.19. These regions separate cratering and containment (cross-hatched) of the explosion. A line shows the demarcation of the region of line-charge equivalence. Figure IV-3.19 also shows the cratering behavior with respect to crater width (dashed lines). A similar diagram was developed by Vortman to describe crater depth. It was found that the demarcation line separating the region of line-charge equivalence for crater depth was different from that shown in Figure IV-3.19. The data points shown in Figure IV-3.19 reveal that these boundaries are only approximate. Furthermore, the scaled depth as a function of scaled spacing within the region of line-charge equivalence gives a crater of maximum volume for a given yield per charge. This must be obtained from a further manipulation of the data. When related to the dimensions of the optimum crater produced by a single charge of the same yield, Vortman derived the rules given in Table IV-3.5. He assumed that the individual charges in the linear array are at the same depth of burst as the single charge used to define the optimum single-charge crater.

One method for designing a multiple-charge row cratering experiment is to determine the optimum DOB for a single charge in the medium to be cratered. Past experience indicates that if the multiple charges are then emplaced at this optimum depth with a spacing between the charges of 1.3 times the DOB, a linear crater having lateral dimensions equal to that of the optimum single-charge crater would result. It was postulated, and later experimentally verified, that smaller yield charges when placed at smaller DOB and at closer relative spacing would result in a linear trench having the same transverse dimensions as the trench produced by larger charges. In order to create the same trench length a larger number of charges of lower yield would be required. This so-called yield enhancement concept has been considered by Redpath (Reference IV-3.30). It was also shown that the enhancement concept could reduce the total yield required to produce a given linear
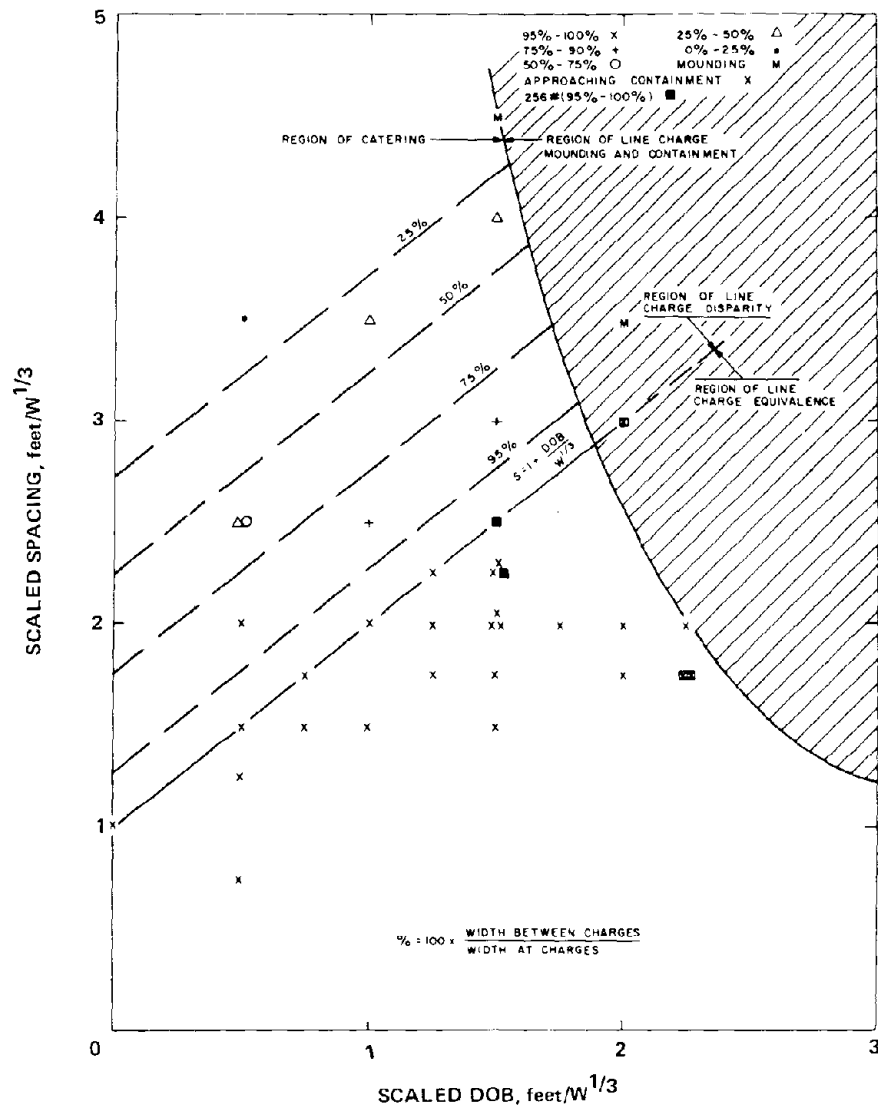
Figure IV-3.19. Regions of line-charge equivalence for crater width as a function of scaled spacing and scaled depth of burst.

Table IV-3.5. Maximum volume linear crater parameters related to optimum single-charge crater dimensions.

Condition Predicted	Parameter		
	$W_r/2R_s$	D_r/D_s	S/R_s
Uniform Width	1.05	1.20	1.3
Uniform Depth	1.15	1.25	1.1

W_r = width of row crater

D_r = row crater depth

R_s = radius of single-charge optimum crater

D_s = depth of single-charge optimum crater

S = separation between charges

crater. Experiments leading to that conclusion consisted of a series of six row charges placed at varying depths and varying charge spacings detonated in the Bear Paw shale of Fort Peck, Montana. All charges consisted of one ton of nitromethane. Additionally, a series of single charges were detonated in the same medium to obtain the properties of the crater resulting from an optimally buried single charge of the same yield. It was found that the transverse crater dimensions precisely scaled to the optimum single charge crater dimensions if the charge spacing S and DOB, D_r, were related as

$$S = \left(\frac{4}{\pi}\right) R_a \left(\frac{D_s}{D_r}\right)^2 \qquad (IV-3.3)$$

where R_a is the apparent crater radius of the optimum single crater and D_s is the corresponding DOB. As long as Equation IV-3.3 holds, the trench transverse dimensions are given by

$$\frac{DOB/2}{D_r} = \frac{R_a}{D_s} \quad \text{and} \quad \frac{d_r}{D_r} = \frac{d_a}{D_s} \qquad (IV-3.4)$$

where d_r is the apparent depth of linear crater and d_a is the depth for a single crater.

Unfortunately, no experiments were conducted in which Equation IV-3.3 was not obeyed. Thus, it is impossible, from these experiments, to claim that the spacing defined by Equation IV-3.3 is a unique method of obtaining Equation IV-3.4.

Myasnikov et al., (Reference IV-3.16) briefly described a series of HE tests designed to investigate the effects of DOB and charge spacing in linear multiple-charge detonations. Several dozen tests were performed in which the individual charges weighed between 600 and 650 kgm. Emplacement depths were between 5.6 and 6.6 meters. The cratered medium consisted of a sandy loam with alternating layers of loam and clay. Emplacement holes for each shot were generated through the technique of hole springing.* The effect of charge spacing was determined for the ratio of spacing-to-DOB ranging from 1.1 to 1.8. Results of these tests are shown in Figure IV-3.20. These data substantiate the rule of thumb that the relative charge spacing of 1.3 will give a crater cross section equal to that of a single charge at the same DOB and that the longitudinal crater dimensions will have minimal departure from uniformity. Another interesting observation made my Myasnikov is that the ground surface motion normal to the axis of the multiple-charge array is the same as that from a single explosion having the same total yield. He limited his observations to the ground surface motions of Rayleigh waves. However, such motion does not develop within several characteristic crater dimensions from the shot point (Reference IV-3.3).[†]

---

*Hole springing is a mining industry phrase used to describe the following process: a hole is drilled and a small charge is detonated in that hole thus producing a cavity; this cavity is then filled with explosives to generate a larger cavity which in turn is filled with explosives, and so on, until a large enough earth mass has been excavated.

[†]Nakano (Reference IV-3.32), who studied the buried line source problems, discovered that the Rayleigh wave does not appear near the epicenter. Its beginning is not sharply defined but an approximate "origin" is given by

$$X_{pR} = C_R h \left(c_p^2 - c_R^2 \right)^{-\frac{1}{2}}$$

for the compressional wave source, and

$$X_{SR} = C_R h \left(c_s^2 - c_R^2 \right)^{-\frac{1}{2}}$$

for a shear wave source. Here, X is the epicentral distance, h is the source depth, C_R is the Rayleigh wave speed, C_p is the compressional wave speed, and C_s is the shear wave speed. The Rayleigh wave does not suddenly appear at these distances but grows gradually and approaches a recognizable form at $X = X_{pR}$ or $X = X_{SR}$, and becomes completely developed at distances where $X \gg h$.
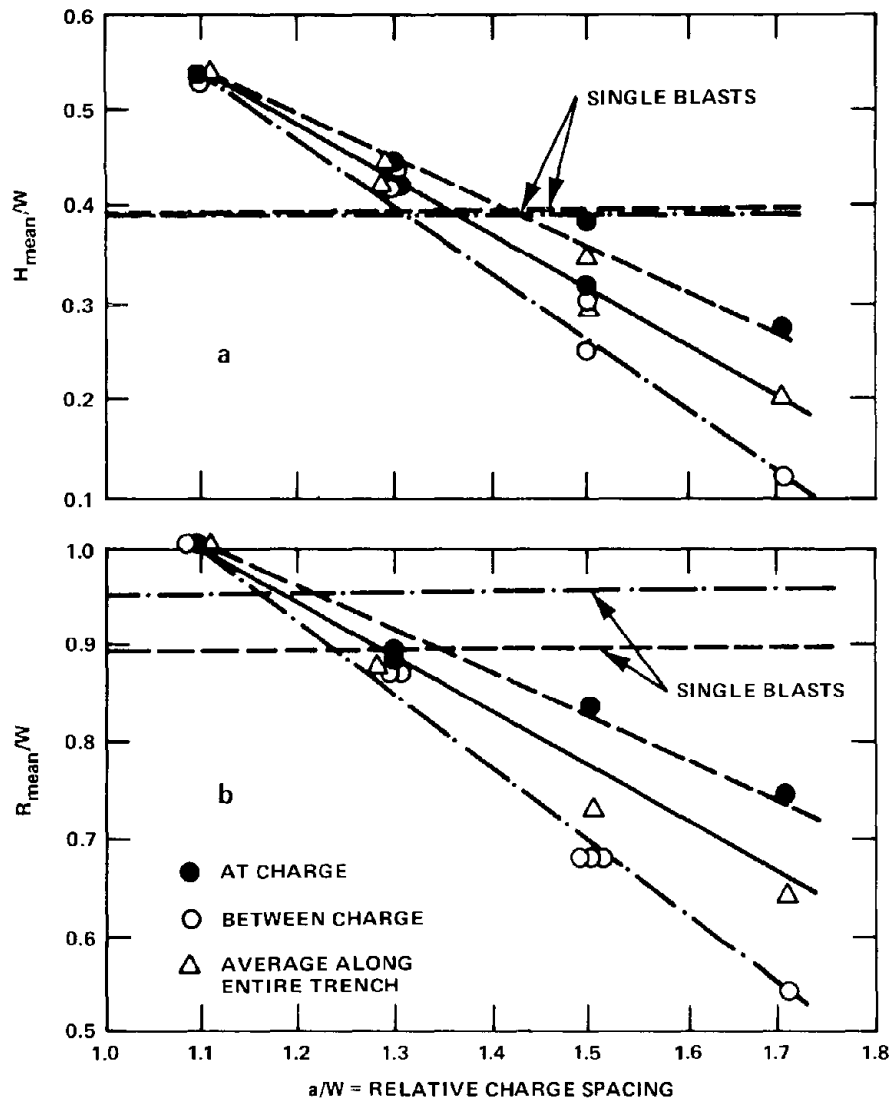
Figure IV-3.20.   Relative trench depth (a) and ejective index (b) as functions
of the relative charge spacing. Here DOB is the depth of
burst, H is the crater depth, and R is its half-width.

He further notes that the close-in motion is asymmetric with a maximum in intensity normal to the axis of the crater and a minimum in intensity along the axis. Some of the early work of Vortman noted a net inward permanent displacement along the axis of the crater for material near the crater rim.

IV-3.2.6 Repeated Cratering Experiments

Beginning in 1963 (Reference IV-3.33) a number of tests were conducted in which charges were detonated along a vertical axis in the following manner: the first charge was half-buried at surface ground zero (GZ), the second charge was half-buried at the bottom of the apparent crater produced by the first charge, and so on for n charges. Strange and Rooke (Reference IV-3.34) report the results of two test series: one involves the detonation of five 4-lb and the other of five 21-lb TNT charges along a common vertical axis. These detonations occurred in sandy clayey silt in the region of the west bank of the Big Black River near Vicksburg, Mississippi. The material was determined to be quite homogeneous with depth, generally moist but not sufficiently so to exhibit a sheen or "free water." However, moisture content increased slightly with depth and the water table was at a depth greater than 10 feet. The preliminary conclusions reached by Strange and Rooke were that the increase in the size of the apparent crater was significant even after the fifth shot. The results for the 21-lb shot series indicated that as the number of shots increased the amount by which the crater enlargement increased tended toward an asymptotic value. For example, the normalized apparent crater depth increased by a factor of about two as the number of 21-lb shots increased from one to five.

By 1967 and 1968 these types of tests had considerably expanded in scope over the earlier tests. O'Brien et al, (Reference IV-3.35) reported on a series of tests conducted at Yakima in Washington where a series of 4000-lb and 16,000-lb TNT charges were detonated in basalt along a common vertical axis. Their research program compared successive craters formed by HE charges with single explosions equivalent in yield to the sum of the multiple charges. These studies included craters and ejecta distribution; energy coupling of cratering explosions at and near the ground surface; charge shape effects on craters and related phenomena; and distribution, size, and weight of discrete ejecta missile. Their results indicated that the excavated crater depth may be increased by a fourth half-buried charge. The increase in depth ranges between zero and 25 percent depending on the technique used. However, results were inconclusive. Excavated craters formed by the successive emplacement of hemispherical charges were smaller than those produced by half-buried spherical charges. In 1968, Chew et al. (Reference IV-3.36)

performed laboratory experiments to provide a qualitative estimate of the cratering and subsurface damage mechanisms involved in repeated surface explosions along a common vertical axis. They used hemispherical charges of lead azide weighing 0.40 and 0.85 grams to produce craters at various air-soil interfaces and to enlarge these by repeated explosions at the bottom of the apparent craters produced by the previous detonation. Sequences of five charges were detonated in dry and saturated sand and dry and soaked grout, with the water table at the original ground surface in the wetted conditions. The crater was measured following each shot and the dimensions from each sequential shot were compared with those of the first shot and the preceding shot. Crater dimensions were also compared with those from detonation of a single charge of equivalent weight. Volumetric measurements were made to define the mechanisms contributing to crater formation. The sand craters appeared to scale with explosions produced by charges having weights 4 or 5 orders of magnitude greater than those expected from an equivalent single shot at the ground surface. Explosions in a medium where the water table was at the surface produced craters substantially larger than those in the same medium in a dry state.

The most recent experiments were conducted by Stephanson and Hooks (Reference IV-3.37) at the Civil Engineering Research Facility (CERF) of the University of New Mexico. They experimented with ten small-scale spherical shots of 1-lb center-fired C-4 charges detonated along a vertical axis. The first charge was fired half-buried in a sand-clay medium. Each subsequent charge, placed vertically below the first, was also half-buried in the bottom of the apparent crater produced by the previous shot. Crater profiles were measured and these data, combined with data from earlier experiments (References IV-3.34, IV-3.35, and IV-3.36), showed that the logarithms of apparent crater volumes and radii are linearly related to the logarithms of the corresponding number of successive shots. These relations led to a general method for predicting volume, depth, and radius for multiple cratering with arbitrary-sized spherical charges half-buried in various geologic media.

The CERF data were plotted in Figure IV-3.21 as a function of the shot number. The crater depth increased through shot 4 then decreased through shot 8, for which the depth is almost that of shot 2. There was then another increase in depth which would continue to a maximum value at N = 12. The relationship between the first and second peaks of the depth curve may only be conjectured, but a decaying oscillation superimposed on a monotonically increasing curve with a decreasing slope seems likely. (Note that only integer values of N have meaning in this figure; the
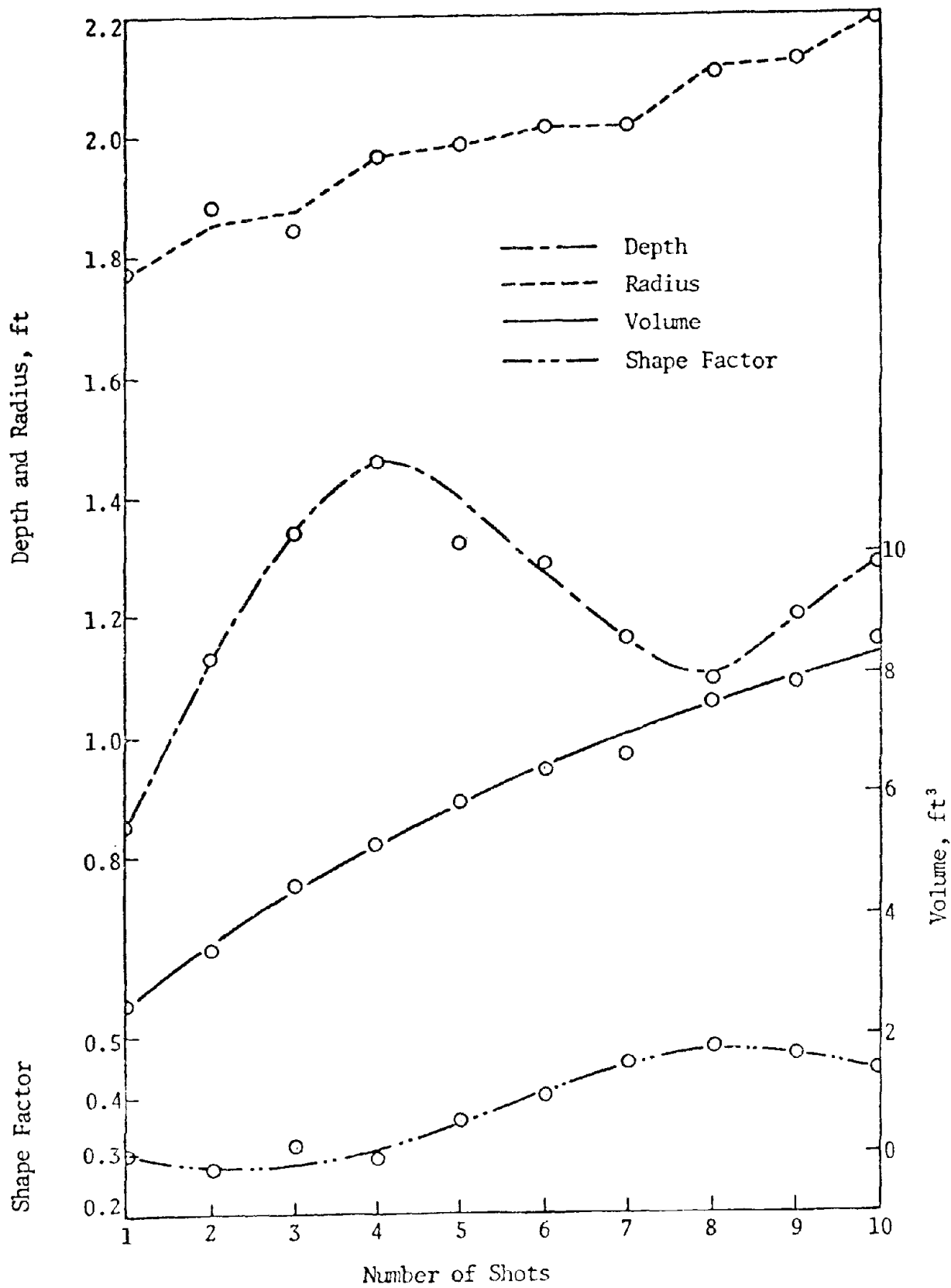
Figure IV-3.21. Parameter curves for RCE (Reference IV-3.36).

smooth curves are shown only for ease of visualization, and for the determination of approximate equations representing the data.) Figure IV-3.21 shows that the volume increased monotonically with decreasing slope as N increased. One major cause of volume data scatter was that a few craters were formed with undercut lips (kettle-shaped), and the CERF profilometer data approximate these craters as having the overhanging lips by blasting them away or causing them to slump. Slumping, in fact, seemed to be the major cause of crater radius increase with N. Figure IV-3.21 also shows that the average apparent radius increased unevenly with N, but that it did not undergo the long-period (N $\approx$ 12) oscillation that D did.

The shape of the crater volume curve suggests a nondimensionalized log-log plot of the volume data. Table IV-3.6 gives the dimensionless crater data and Figure IV-3.22 shows a log-log plot of the normalized volume as a function of N. The straight-line relationship is an excellent fit to the data and can be represented by

$$\frac{V_N}{V_1} = N^a, \quad (a = 0.526) \tag{IV-3.5}$$

in which a is the slope of the volume fit. Stephanson and Hooks then conjectured that other crater volume data from multiple cratering experiments might have the same form. In that case, media differences would appear as changes of exponent since it is the only free variable in Equation IV-3.5. Table IV-3.7 shows the crater data from WES and Boeing for multiple-cratering experiments.

Figure IV-3.23 demonstrates the generality of the crater volume correlation (CVC) for half-buried multiple cratering experiments with N $\leq$ 10. of the 10 sets of data in Table IV-3.7 (nine half-buried series and one surface-tangent series), eight sets of half-buried data in addition to the CERF data are well approximated by Equation IV-3.5. Thus, using the appropriate a values from Figure IV-3.23 in Equation IV-3.5, the quantity V_N/V_1 may be estimated for N $\leq$ 10 for repeated half-buried shots in a variety of media. As a crude model, one could consider that repeated shots in a crater cause it to grow in size while remaining geometrically self-similar. The radius and depth of the growing crater would then obey Equation IV-3.5 in the same way the volume does, since the shape factor a would be constant. The exponent on N for both radius and depth would be one-third of the N exponent for volume. This approach provided the motivation for plotting R_N/R_1 and D_N/D_1 versus N. The D_N/D_1 values could not be plotted to exhibit any systematic regularity, either on a log-log plot or by any other method. However, the R_N/R_1 values

Table IV-3.6. Normalized crater data from RCE.

Number of Shots	Normalized Radius (R_N/R_1)	Normalized Depth (D_N/D_1)	Normalized Volume (V_N/V_1)
1	1.00	1.00	1.00
2	1.06	1.35	1.37
3	1.03	1.60	1.79
4	1.11	1.74	2.09
5	1.12	1.57	2.36
6	1.14	1.52	2.59
7	1.14	1.38	2.69
8	1.19	1.36	3.04
9	1.20	1.42	3.15
10	1.24	1.52	3.43

for the nine test series for which the V_N/V_1 data obeyed Equation IV-3.5 plot as a straight line on a log-log plot with the exception of the WES 0.85-gm charge tests in dry sand. Figure IV-3.24 shows the R_N/R_1 data and the approximating lines with their corresponding power exponent values in the equation

$$\frac{R_N}{R_1} = N^c, \quad (c = 0.00773), \quad N \leq 10 \qquad (IV-3.6)$$

where c is the slope of the radius fit. The c values in Figure IV-3.24 were not found to be one-third of the corresponding a values in Equation IV-3.5.

IV-3.3 EMPIRICAL ANALYSES

This section will begin with an historical perspective of the work done by many investigators who have contributed significantly to the cratering predictive capability. To the extent possible the presentation will be in chronological order. The primary purpose of this section is to discuss the accumulated information that has led to the existing scaling rules. Work on the problem of scaling rules was begun much earlier than the first reference cited here; however, the interested reader can find these earlier discussions from the references cited.
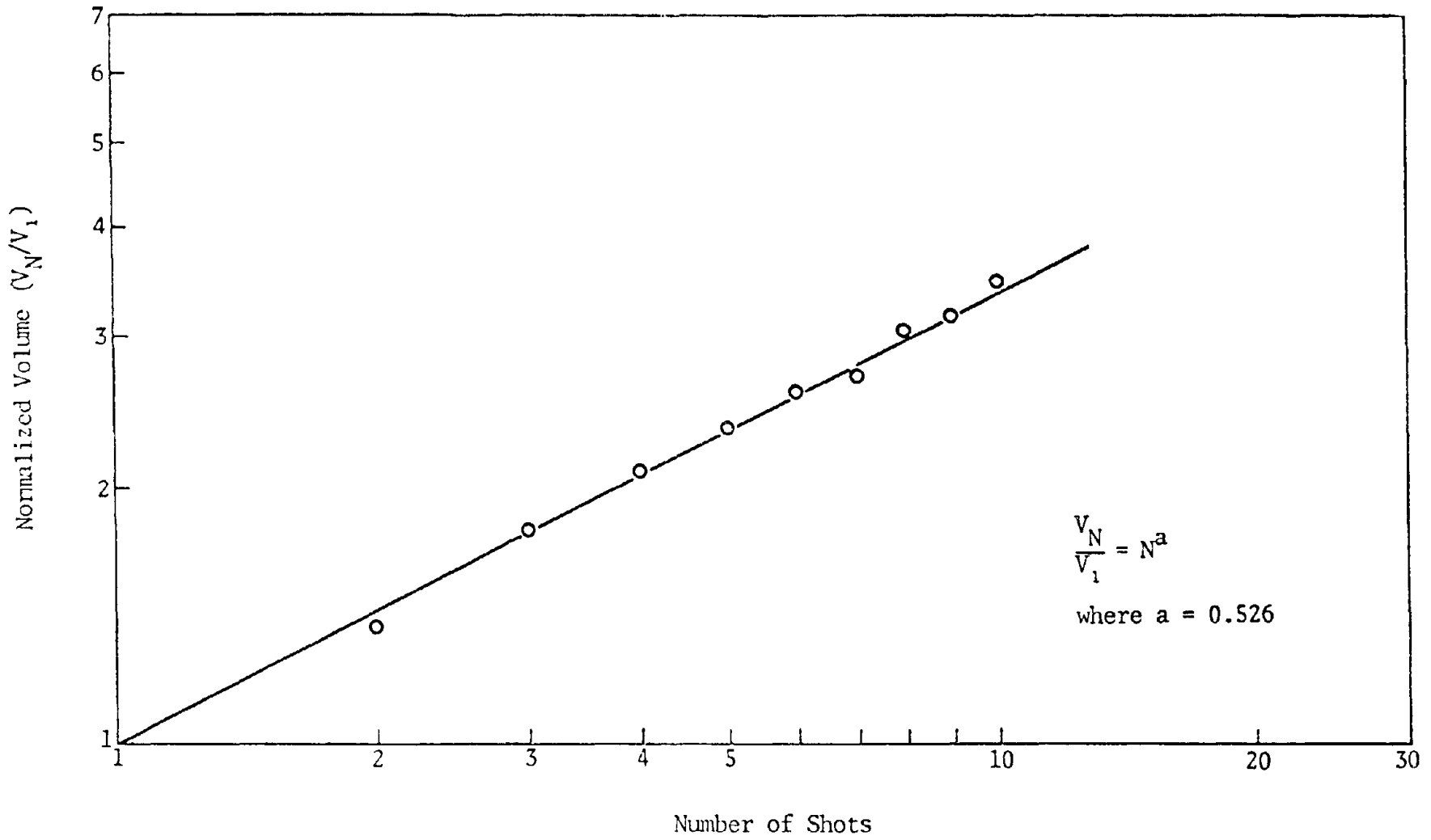
Figure IV-3.22.   Crater volume correlation of RCE data (Reference IV-3.36).

Table IV-3.7. Crater data from WES and Boeing multiple-cratering experiments.

Number of Shots	Charge	Figure Designation	Apparent Radius (R)	Apparent Depth (D)	Apparent Volume (V)	Shape Factor (α)	Data Source
1	4-lb spherical TNT charges half-buried in moist sand/clay silt.	□ IV-3.23	1.94 ft	1.10 ft	6.5 ft^3	Assumed to be 0.5 to calculate V	WES IV-3.34
2			2.30 ft	1.30 ft	10.8 ft^3		
3			2.70 ft	1.50 ft	17.2 ft^3		
4			3.17 ft	1.75 ft	27.6 ft^3		
5			3.30 ft	2.35 ft	40.2 ft^3		
1	21-lb spherical TNT charges half-buried in moist sand/clay silt.	■ IV-3.23, IV-3.24	4.21 ft	2.62 ft	73 ft^3	Assumed to be 0.5 to calculate V	WES IV-3.34
2			4.81 ft	3.03 ft	110 ft^3		
3			5.42 ft	3.95 ft	182 ft^3		
4			5.75 ft	4.37 ft	227 ft^3		
5			5.95 ft	4.90 ft	272 ft^3		
S4a	4000-lb spherical TNT charges half-buried in basalt.	△ IV-3.23, IV-3.24	10.4 ft	4.0 ft	605 ft^3	0.445	Boeing IV-3.35
S4b			12.2 ft	5.8 ft	1178 ft^3	0.434	
S4c			13.5 ft	5.9 ft	1577 ft^3	0.460	
S4d			14.8 ft	8.4 ft	2081 ft^3	0.360	
ST3a	4000-lb spherical TNT charges surface tangent in basalt.	▲ IV-3.23	4.5 ft	1.2 ft	25 ft^3	0.327	Boeing IV-3.35
ST3b			9.2 ft	2.4 ft	324 ft^3	0.508	
ST3c			12.3 ft	3.3 ft	560 ft^3	0.357	
1	0.4-gm lead azide (PbN$_6$) hemispherical charges half-buried in soaked grout half-space bounded by vertical plastic wall. All volumes given in Reference IV-3.41 (postulated) complete crater.	▷ IV-3.23, IV-3.24	3.0 cm	0.9 cm	11 cm^3	0.432	WES IV-3.36
2			3.7 cm	1.3 cm	25 cm^3	0.447	
3			4.7 cm	1.8 cm	55 cm^3	0.440	
4			5.0 cm	1.9 cm	106 cm^3	0.710	
5			5.7 cm	3.0 cm	148 cm^3	0.483	

Table IV-3.7 (continued)

Number of Shots	Charge	Figure Designation	Apparent Radius (R)	Apparent Depth (D)	Apparent Volume (V)	Shape Factor (α)	Data Source
1	0.85-gm lead azide (PbN$_6$)	▶ IV-3.23,	2.6 cm	1.1 cm	20 cm^3	0.856	WES
2	hemispherical charges half-	IV-3.24	4.4 cm	1.5 cm	52 cm^3	0.570	IV-3.36
3	buried in soaked grout. All data		5.4 cm	1.6 cm	114 cm^3	0.778	
4	in Reference IV-3.41 obtained in		6.4 cm	3.9 cm	182 cm^3	0.363	
	half-space with charge separated						
	from plastic wall by ¼-in. pillow						
	disk 1.2 in. in diameter.						
1	0.4-gm lead azide (PbN$_6$)	▽ IV-3.23,	3.4 cm	0.7 cm	12 cm^3	0.472	WES
2	hemispherical charges half-	IV-3.24	3.7 cm	1.0 cm	24 cm^3	0.558	IV-3.36
3	buried in dry grout.		4.0 cm	1.6 cm	41 cm^3	0.510	
4			4.1 cm	1.7 cm	49 cm^3	0.546	
5			4.1 cm	2.2 cm	68 cm^3	0.585	
1	0.85-gm lead azide (PbN$_6$)	▼ IV-3.23,	2.5 cm	1.6 cm	14 cm^3	0.446	WES
2	hemispherical charges half-	IV-3.24	3.0 cm	2.1 cm	30 cm^3	0.505	IV-3.36
3	buried in dry grout.		4.1 cm	3.0 cm	87 cm^3	0.549	
4			4.3 cm	4.5 cm	94 cm^3	0.360	
5			4.3 cm	4.0 cm	126 cm^3	0.542	
1	0.85-gm lead azide (PbN$_6$)	◁ IV-3.23	9.0 cm	2.0 cm	221 cm^3	0.434	WES
2	hemispherical charges half-		9.0 cm	4.0 cm	472 cm^3	0.464	IV-3.36
3	buried in dry sand.		9.0 cm	5.7 cm	498 cm^3	0.343	
4			9.9 cm	5.3 cm	632 cm^3	0.387	
5			10.8 cm	5.7 cm	848 cm^3	0.406	

Table IV-3.7 (continued)

Number of Shots	Charge	Figure Designation	Apparent Radius (R)	Apparent Depth (D)	Apparent Volume (V)	Shape Factor (α)	Data Source
1	0.86-gm lead azide (PbN_6)	◄ IV-3.23,	5.1 cm	2.4 cm	88 cm^3	0.449	WES
2	hemispherical charges half-	IV-3.24	7.7 cm	4.0 cm	336 cm^3	0.451	IV-3.36
3	buried in saturated sand.		10.5 cm	5.2 cm	645 cm^3	0.358	
4			12.0 cm	3.9 cm	1030 cm^3	0.584	
5			13.0 cm	6.4 cm	1495 cm^3	0.440	
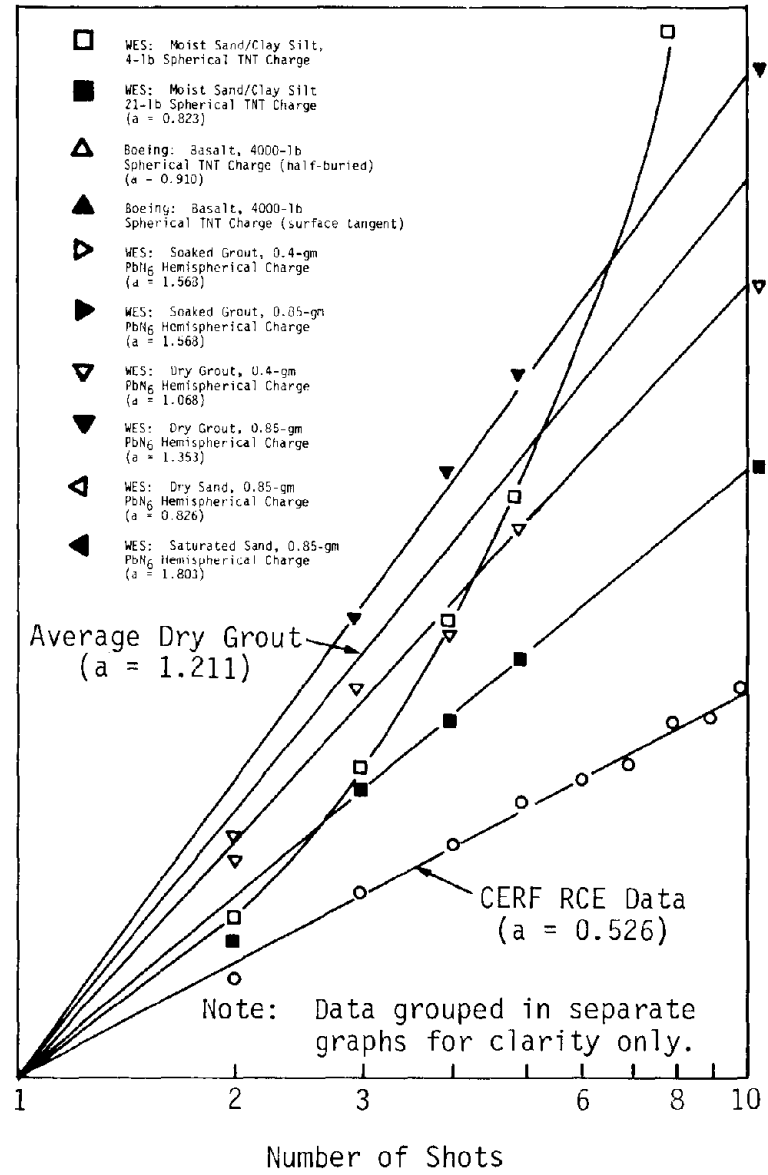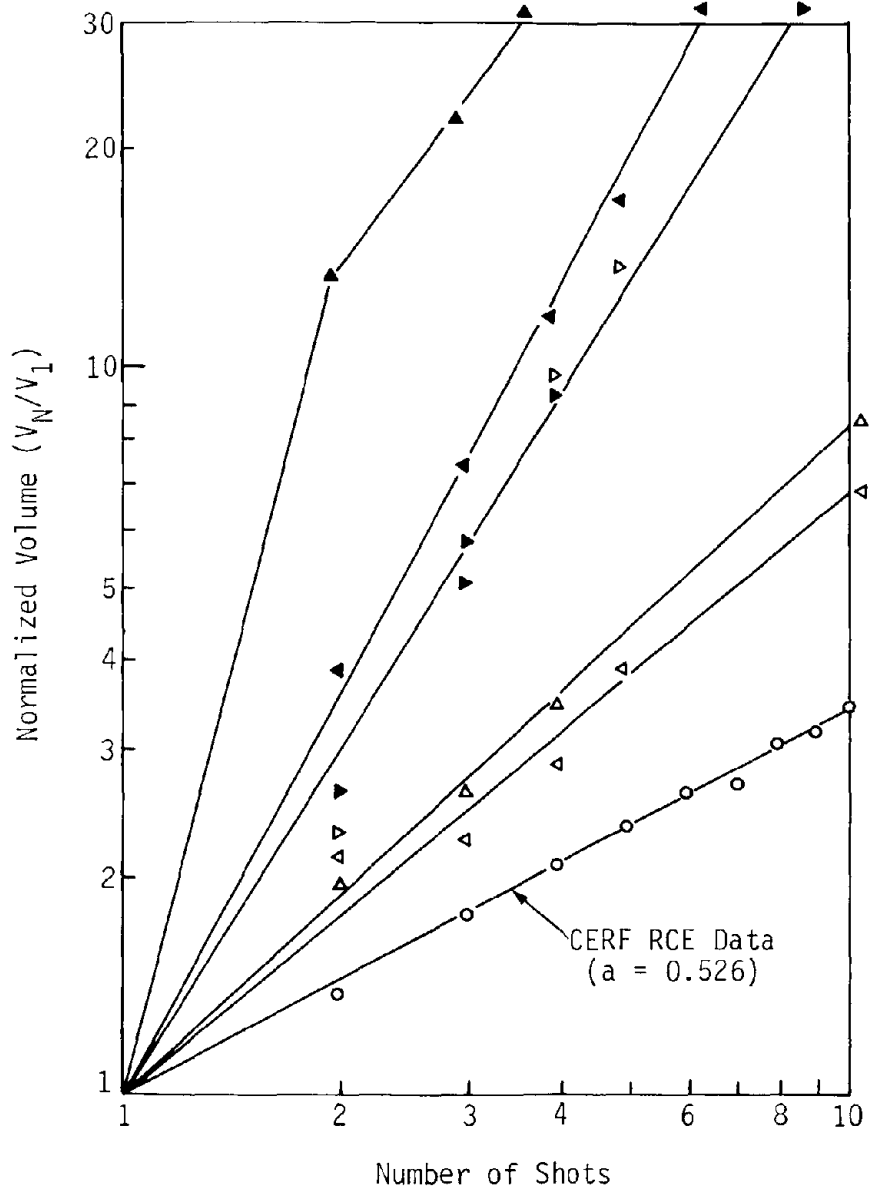
Figure IV-3.23. Comparison of crater volume correlations (Reference IV-3.36).
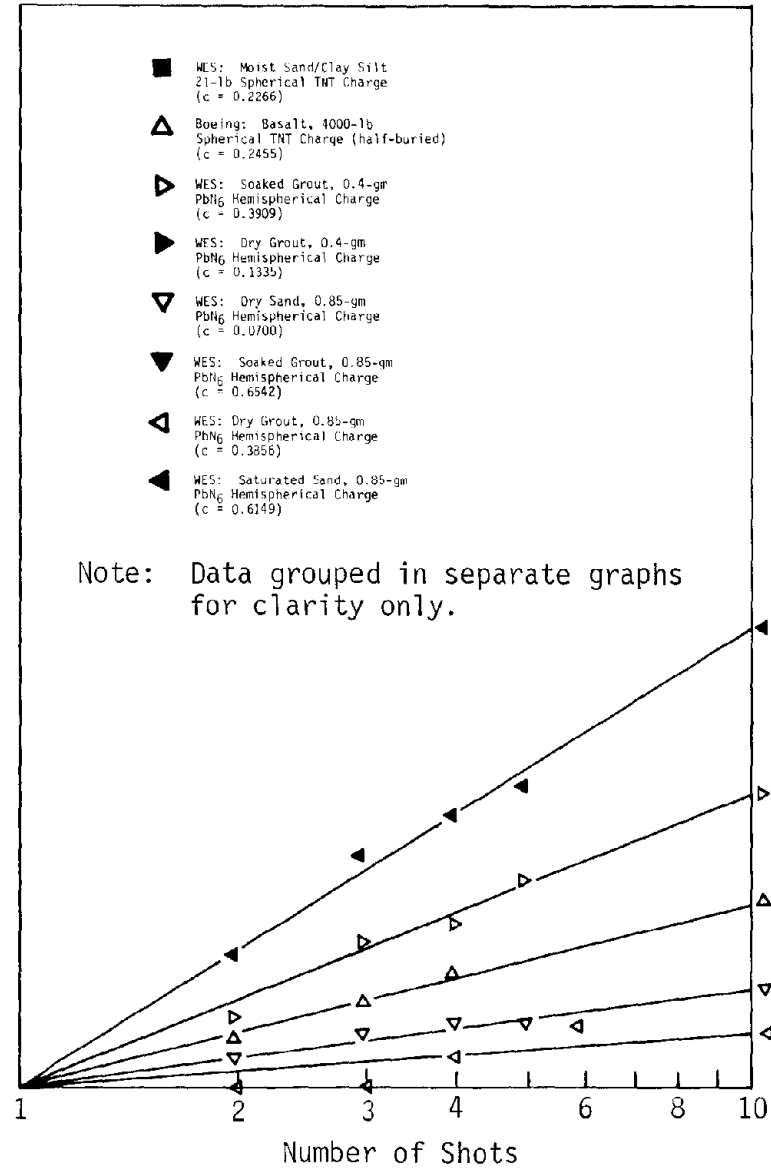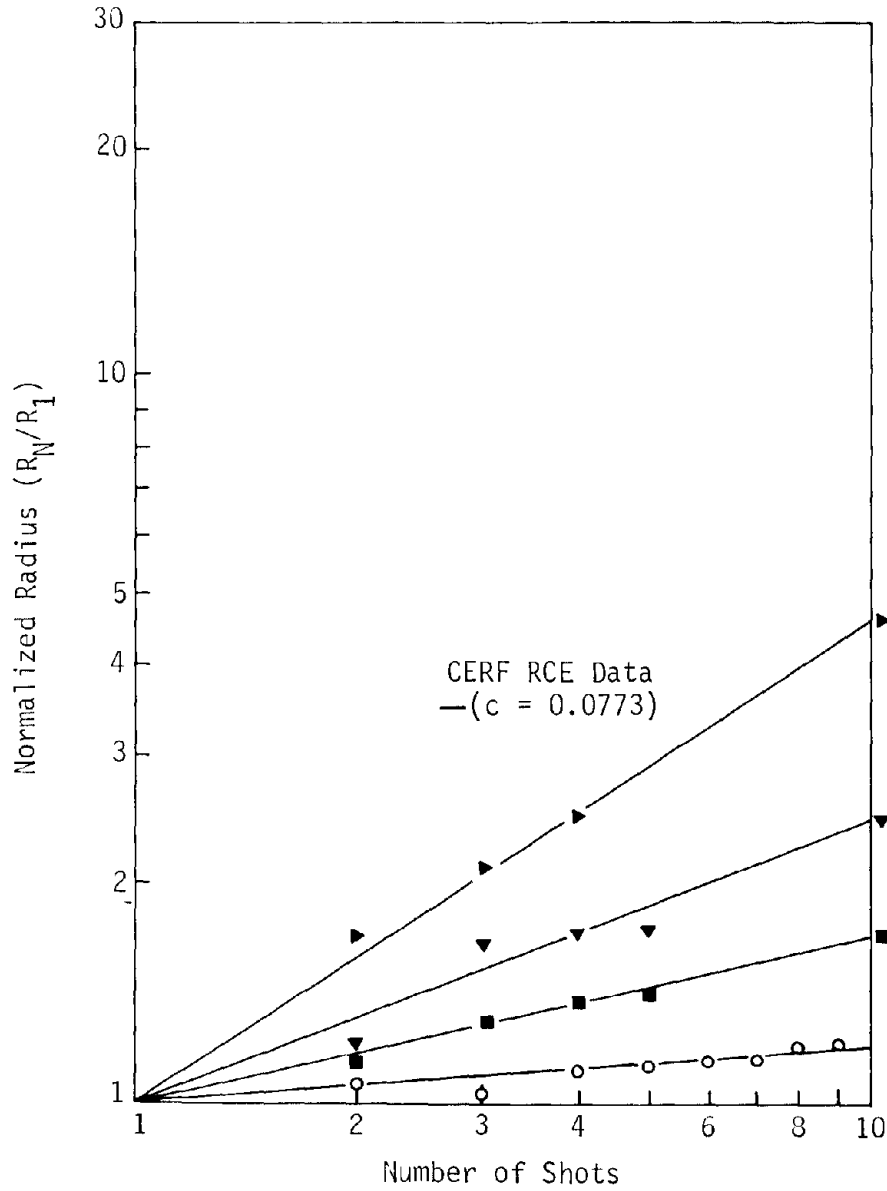
Figure IV-3.24. Comparison of crater radius correlations (Reference IV-3.36).

In the past, three broad and overlapping areas of empirical analysis have been pursued. The desired goal was the ability to predict crater dimensions over a wide range of weapon yields. Included in these analyses were parameters such as the explosive yield, the effects of the gas acceleration phase in buried shots, the DOB, the effects of the gravitational acceleration, and the effects of the atmospheric overpressure. Investigative techniques employed were mainly statistical analysis, small-scale experimental modeling and similarity analysis. These three areas overlap and they will be discussed separately whenever possible.

IV-3.3.1 Statistical Analyses

Based on much of the data available in 1961, Vaile (Reference IV-3.38) arrived at nomograph curves for predicting crater radii as a function of DOB or HOB and yield. One of these nomographs is shown in Figure IV-3.25. However, Vaile did not give a predictive method for determining crater depth. In this work, as in many others, it was postulated that the crater radius was proportional to the explosive yield to the 1/m power, the cratering exponent. Vaile proceeded to determine the value of m for several ground materials. The values he derived are given in Table IV-3.8. As noted in the introduction to this chapter, crater dimensions are not monotonic functions of DOB. There exists a DOB for which the explosion is fully contained.

Chabai's works on scaling in 1960 (References IV-3.39 and 3.40) were followed by Nordyke's in 1962 (Reference IV-3.9). Nordyke also made a systematic analysis of cratering to obtain the cratering exponent and other crater dimensions as a function of DOB for bursts deeper than the optimum. Using a regression analysis, Nordyke concentrated his attention on nuclear and HE explosions in NTS alluvium. His results were that the yield scaling exponent of 1/3.4 best fit the data of the crater radius and depth for DOBs between zero and the depth where no crater is produced. This is shown graphically in Figures IV-3.26 and IV-3.27. To perform the regression analysis, Nordyke assumed that the scaled radius and depth were power law functions of the scaled DOB. These cratering equations are given as

$$R_s = 112.5 + 0.77\ Z_s - (9.6 \times 10^{-6})\ Z_s^3 - (9.11 \times 10^{-12})\ Z_s^5 \qquad \text{(IV-3.7)}$$

$$D_s = 32.7 + 0.851\ Z_s - (2.5 \times 10^{-5})\ Z_s^3 + (1.78 \times 10^{-10})\ Z_s^5 \qquad \text{(IV-3.8)}$$
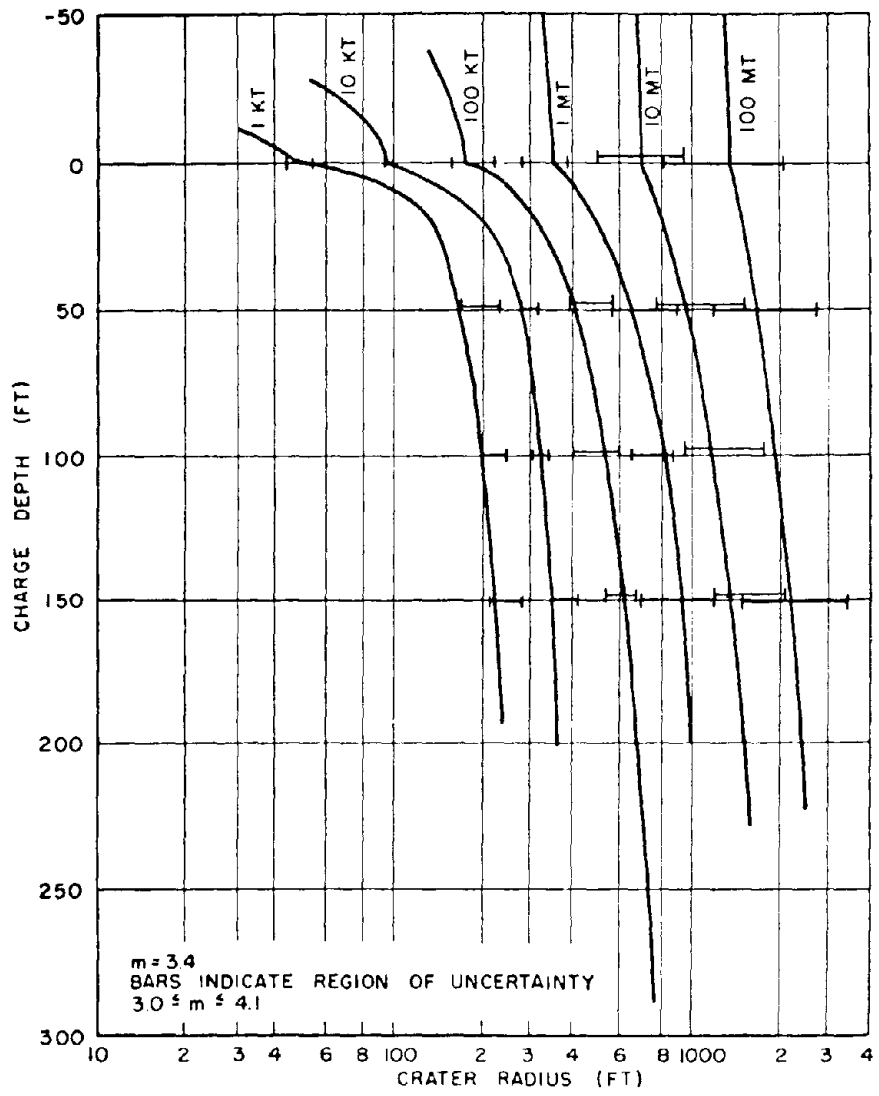
Figure IV-3.25. Nomograph for predicting crater radius versus charge depth in Nevada alluvium (Reference IV-3.38).

Table IV-3.8. Crater radius versus yield. Vaile scaling
exponents[a] (Reference IV-3.38).

Soil Type	Exponent (m)	Maximum Value	Minimum Value
NTS Alluvium	3.4	4.1	3.0
Dry Clay	2.9	3.2	2.9
Wet Clay	2.5	3.3	2.0
Dry Sand	2.7	3.2	2.6
Sandstone	3.6	4.1	3.4

Note:

[a] Exponent "m" is defined in equation $R_a Y^{-1/m} = $ constant.
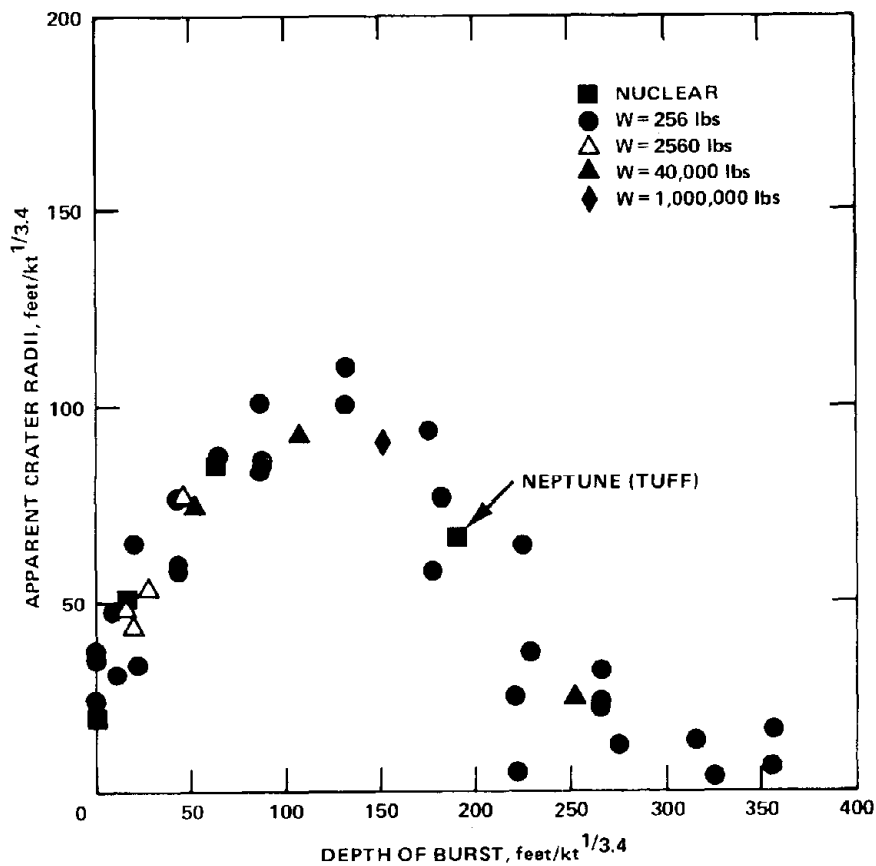
Figure IV-3.26. Plot of apparent crater depth versus depth of burst
using $W^{1/3.4}$ scaling (Reference IV-3.9).
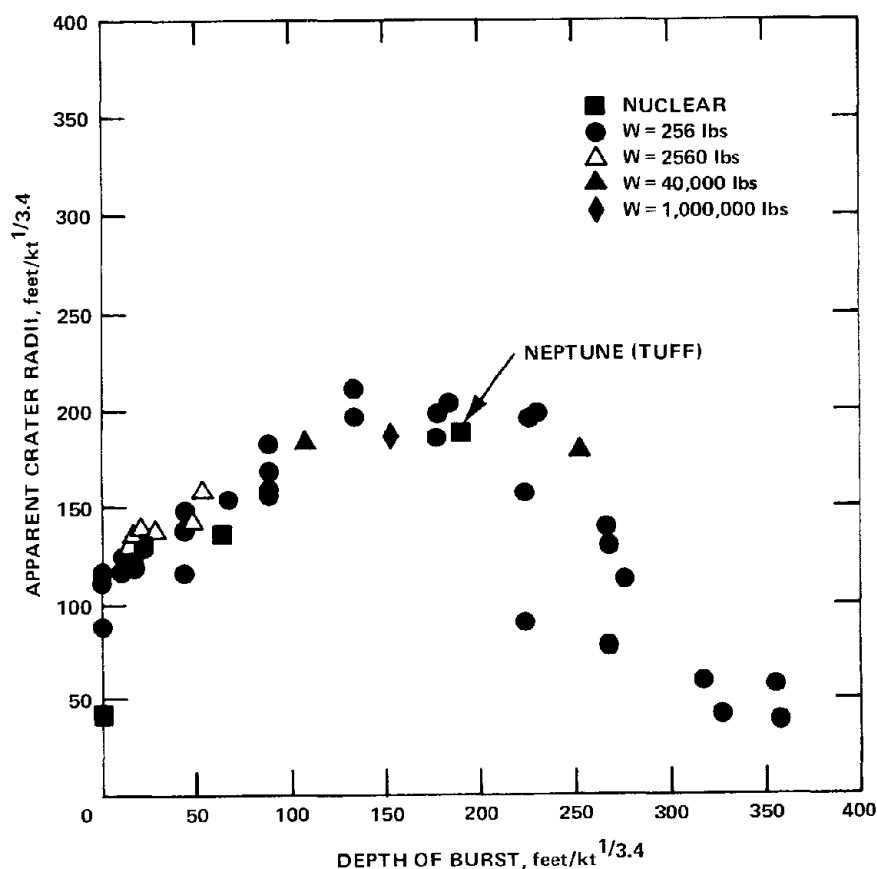
Figure IV-3.27. Plot of apparent crater radius versus depth of burst using $W^{1/3.4}$ scaling (Reference IV-3.9).

where R_s, D_s, and Z_s are the radius, depth, and DOB, respectively, for a 1-kt explosion. Dimensions for another yield are given by

$$R = R_s \, W^{1/3.4} \quad , \quad D = D_s \, W^{1/3.4} \qquad\qquad (IV-3.9)$$

It must be remembered that Nordyke concentrated only on NTS alluvium and that these cratering equations do not apply to other media.

In 1968 Vortman (Reference IV-3.41) published results of an investigation of surface bursts on several media. The media considered were NTS alluvium, NTS playa, clay silt at the Suffield Experiment Station, limestone, basalt, and PPG coral sand. By at least squares analysis, he obtained the yield-scaling exponents for crater radius, depth, and volume. These are summarized in Table IV-3.9. Vortman reached the conclusion that, for symmetric surface burst craters, the apparent crater volume is very nearly proportional to the explosive yield, the scaling exponent for most

Table IV-3.9. Yield scaling exponents for near-surface bursts
for crater dimensions (Reference IV-3.41).

Soil Type	Radius	Yield Exponents[a] Depth	Volume
NTS Playa	0.375 ± 0.006	0.342 ± 0.019	1.111 ± 0.018
Canadian Shield Silt	0.408 ± 0.005	0.259 ± 0.019	1.04 ± 0.05
Basalt	0.371 ± 0.056	0.262 ± 0.042	1.18 ± 0.17
PPG Coral	0.387 ± 0.023	0.215 ± 0.054	0.885 ± 0.073[b]

Notes:

[a]The yield exponent n is defined in equation RY^{-n} = constant, DY^{-n} = constant, VY^{-n} = constant.

[b]It is claimed that when volumes are normalized to surface bursts, using PPG height of burst data this exponent becomes 1.00 ± 0.07 and may be preferable to the value of the table.

materials being approximately to 1.1. The exception to this includes those data from the PPG for yields between 14 kt and about 14 MT, where the crater volume is linearly proportional to the yield to within the experimental errors. Vortman further suggested that it is the strain rate effect on the failure conditions that leads to crater volume being a nonlinear function of explosive yield. The inclusion of strain rate as an important term of the equation of state is analogous to the inclusion of viscosity terms or the inclusion of the acceleration of gravity in fluid flow equation of motion. The effect of the strain rate is intuitively understood by the following arguments:

1. For many materials it is observed that shear strength is an increasing function of strain rate for a given value of mean stress.

2. The dimensions of the true crater are strongly dependent on the failure of the material.

3. If geometric similarity was exactly obeyed, the stresses at a given scaled position for one yield should be identical to those at the same scaled position for a different yield. However, if strain rates are important, 1 and 2 above lead to the conclusion that the true crater dimensions should scale so that yields larger than some standard yield produce craters larger than would be predicted by geometric scaling.

Dillon (Reference IV-3.42) recently carried out a statistical analysis on crater dimensions. A very general regression analysis was performed including DOB, yield,

and several ground material properties for experiments conducted in alluvium, basalt, shale, playa, and limestone. A functional form for the DOB curves was assumed. Preliminary examination of the data used by Dillon indicated that the crater radii were best fit when scaled by the yield to the 5/16 power. He also found that for every set of data except one, the scaling exponent of 7/24 produced the best overall fit to the data. For surface burst data, cube root scaling was found to fit best. Figure IV-3.28 shows the crater radius as a function of the DOB from Dillon's regression analysis for the NTS alluvium craters. The data points shown in Figure IV-3.28 were not individually defined by Dillon.
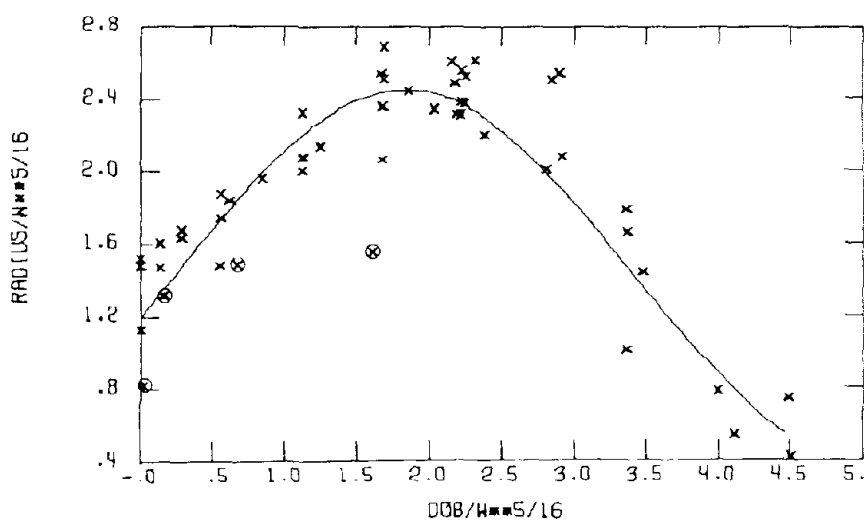
Figure IV-3.28. Crater radius as a function of charge depth for desert alluvium (Reference IV-3.42).

IV-3.3.2 Similarity Techniques

The separation of this section from the one following on experimental modeling is an arbitrary and subjective separation by the authors. Therefore, only the main ideas will be presented in this section.

A standard reference textbook on dimensional analysis was written by Sedov (Reference IV-3.43). Not only is the mathematical foundation of dimensional analysis presented, but its application to many natural phenomena is also discussed. Of particular interest here is an extensive section on explosions and the effects of shock waves on the surrounding medium.

It is possible that two long-recognized classes of exact similarity solutions might apply to cratering. The first of these is Cauchy scaling (1/3) that is valid when the only restoring force is due to the elastic properties of the material. The second is Froude scaling (1/4) that is valid when the only restoring force is that of gravity. These two similarity laws are mutually incompatible but both play important roles in cratering. Thus, if similarity is to be used as a predictive method, some compromise must be made between Cauchy and Froude scaling.

Buried explosions are required to do work against the sum of the lithostatic pressure and the atmospheric overpressure in order to generate a crater. Chabai (Reference IV-3.44) took for the scale length the cube root of the ratio of the total explosive yield to the total mean stress at the DOB. Gravity was assumed to play no role in the crater formation process beyond its contribution to the lithostatic stress. Results from the use of this parameter as a length scale are graphically shown in Figure IV-3.29. Although substantial improvement in correlating capability over that of Nordyke was not observed, the scaling rule was shown not to be that of Cauchy (geometric similarity) but strongly implied 1/4 scaling to be fundamental. Not only is this intuitively more pleasing than the purely empirical method of Nordyke, it can also lead to an estimate of the relative contribution to the cratering process of the constitutive properties of the cratered medium. In 1970 Westine (Reference IV-3.45) showed that the statistical results obtained by Nordyke were not inconsistent with small-scale experiments conducted at Wright-Patterson Air Force Base. The same conclusion was reached simultaneously by Saxe and Del Manzo (Reference IV-3.46), who discussed only the results of cratering in desert alluvium while Westine discussed data obtained in small-scale experiments. The papers by Westine and Saxe and Del Manzo concluded that the crater dimensions could be well fitted by functions of yield to the 7/24 power. This exponent is an arithmetic average of the Cauchy and Froude scaling. Table IV-3.10 shows crater data obtained from small-scale experiments conducted by Viktorov and Stepanov (Reference IV-3.47). These experiments were carried out under high acceleration to determine the effects of the acceleration field on the cratering process.

It should be added that White published a note (Reference IV-3.48) describing the shortcomings of previous efforts in finding crater scaling rules. He stated that cratering is not a scalable phenomenon because the gravitational constant cannot be scaled in field experiments where cratering varies from a small to a large crater size because the value of g remains constant. However, he recognizes that a simple power law on yield correlates experimental data reasonably well but that
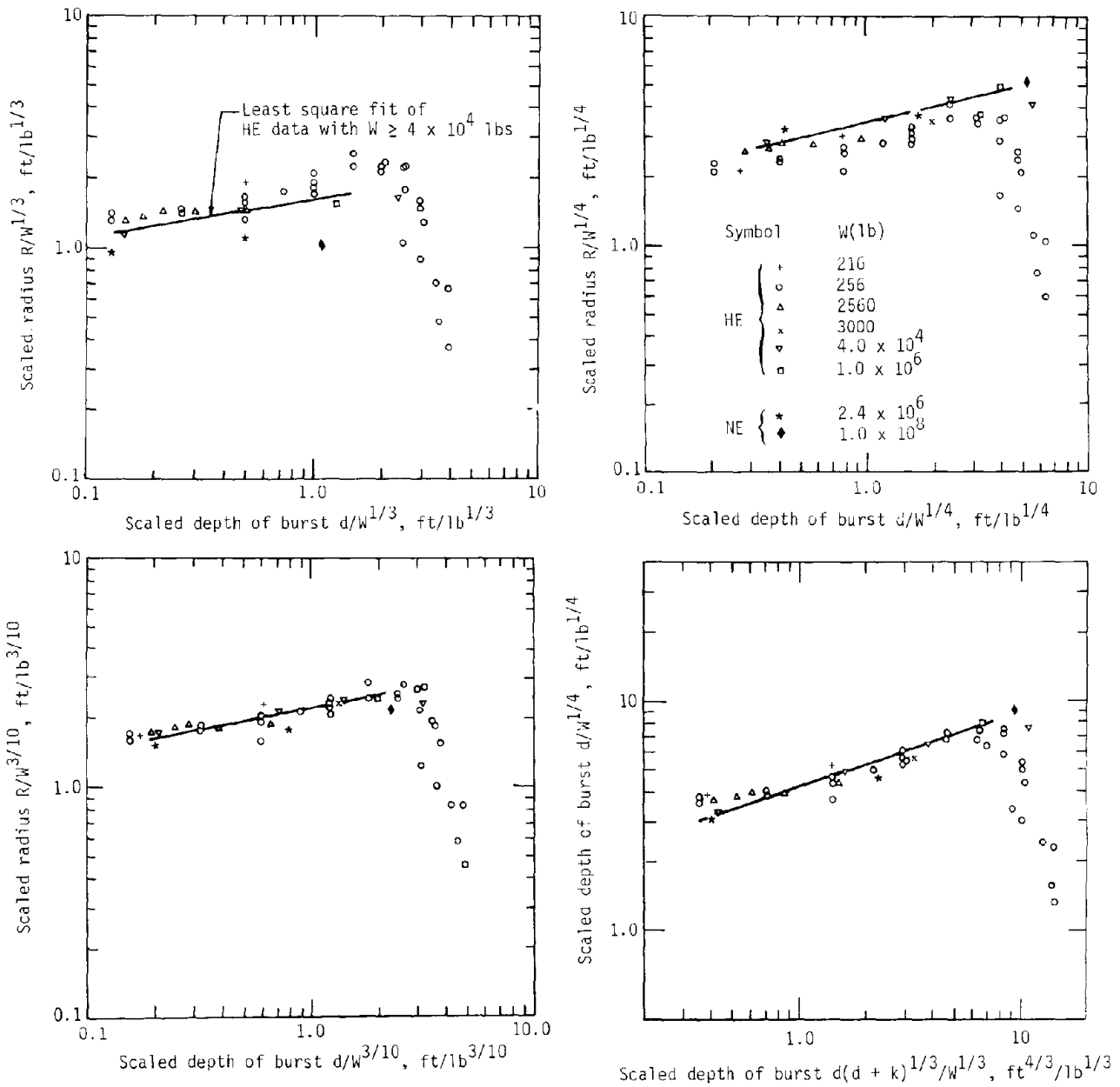
Figure IV-3.29. Various scaling rules relating depth of burst to crater radius (Reference IV-3.44).

Table IV-3.10. Crater data from high-g linear acceleration sled (Reference IV-3.47).

DoB (cm)	Charge Mass (gm)	Acceleration (g)	Apparent Crater Dimensions		
			Depth (cm)	Radius (cm)	Volume (cm^3)
10	3.06	25	7.5	13.4	1800
10	4.59	25	8.5	16.6	2900
10	6.12	25	9.5	17.5	3950
15	4.59	25	4.0	12.3	900
15	6.12	25	5.0	16.0	1500
15	7.65	25	4.0	18.0	2050
20	6.12	25	3.1	19.7	300
20	9.18	25	3.6	13.5	950
10	3.06	45	5.4	13.0	1000
10	4.59	45	6.5	14.1	1600
10	6.12	45	8.0	16.4	2250
15	4.59	45	2.8	9.4	350
15	6.12	45	3.1	10.5	700
15	7.65	45	3.5	14.5	1000
20	7.65	45	2.5	8.4	100
20	9.18	45	3.0	9.5	300
10	3.06	65	5.0	12.0	700
10	4.59	66	3.0	13.6	1000
10	6.12	66	3.4	15.3	1450
15	4.59	66	1.0	9.0	150
15	6.12	66	-	-	-
15	7.65	66	-	-	-
10	3.06	1	12.5	17.0	-
10	6.12	1	14.7	21.4	-

different curves are needed for different kinds of explosive energy sources and that new scaling rules are needed when a new cratering medium is used (Reference IV-3.49).

IV-3.3.3 Small-Scale Experimental Modeling

This section treats one particular aspect of small-scale experiments aimed at understanding the effects of gravity and atmospheric overpressure on the formation of craters. This will be followed by a brief discussion of more conventional small-scale experiments designed to understand cratering in various media and cratering in multilayered media.

Successful small-scale laboratory experiments rely on similarity techniques for their design. In this section experiments that were conducted in laboratories in contrast to field experiments are discussed. In general, the laboratory experiments were designed to obtain information on the effect of the gravitational field and on the effects of the atmospheric overpressure. These parametric investigations were conducted in the United States and the USSR. Lunar exploration gave the impetus to this work in the United States, while in the USSR the determination of the effects of gravitational acceleration and atmospheric overpressure were apparently dictated by a requirement to verify scaling laws pertaining to cratering on the surface of the earth. The cratering medium used by Viktorov and Stepanov (Reference IV-3.47) consisted of moist sand. Accelerations of 1, 25, 45, and 65 g's were attained on a linear acceleration sled during the detonation of small test charges. DOB and explosive yield were varied with the results given in Table IV-3.10. Acceleration levels of less than 1 g were obtained in experiments by Johnson et al. at Wright Patterson Air Force Base (Reference IV-3.50). The acceleration fields were 0.17 g (lunar gravity), 0.38, 1 and 2.5 g's during the detonation of small charges. A test bed of dry sand was flown in an aircraft performing carefully controlled maneuvers to obtain these acceleration values. DOB varied from 0 to 13 cm and the charge used was quite small, about 6 grains of explosive. The results of these experiments in various acceleration fields are represented in Figures IV-3.30 and IV-3.31. It can be seen that the scaling exponent of gravity for the crater diameter varies from 1/8 (0.125) at very shallow DOB to almost 1/6 (0.166) for very large DOB. Some of the experiments shown in these figures were conducted at greater than optimum DOB. Data presented by Johnson (Reference IV-3.50) indicate that the optimum DOB for the crater diameter was about 4 cm and independent of the static acceleration and that the optimum DOB for the crater
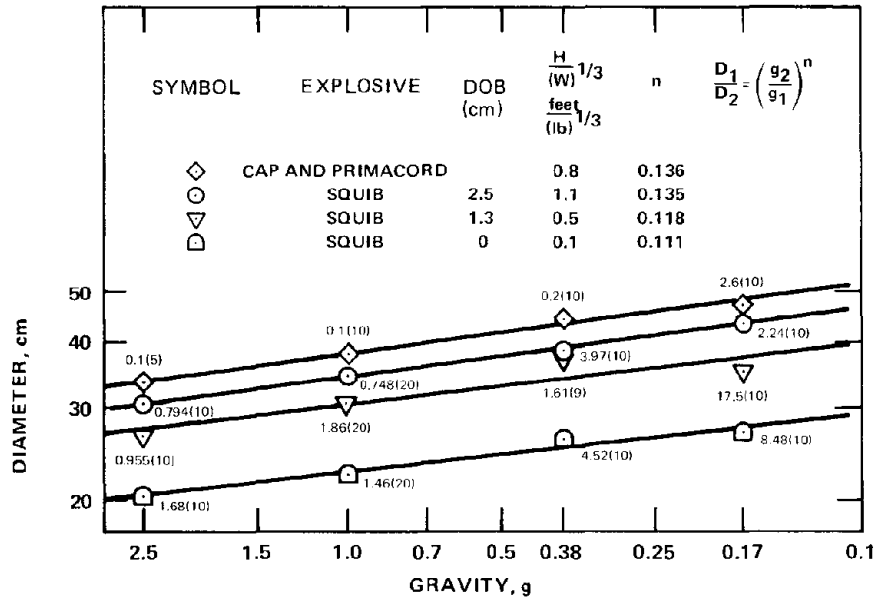
Figure IV-3.30. Logarithmic plot of crater diameter versus gravity for depth of burst < 3.8 cm.
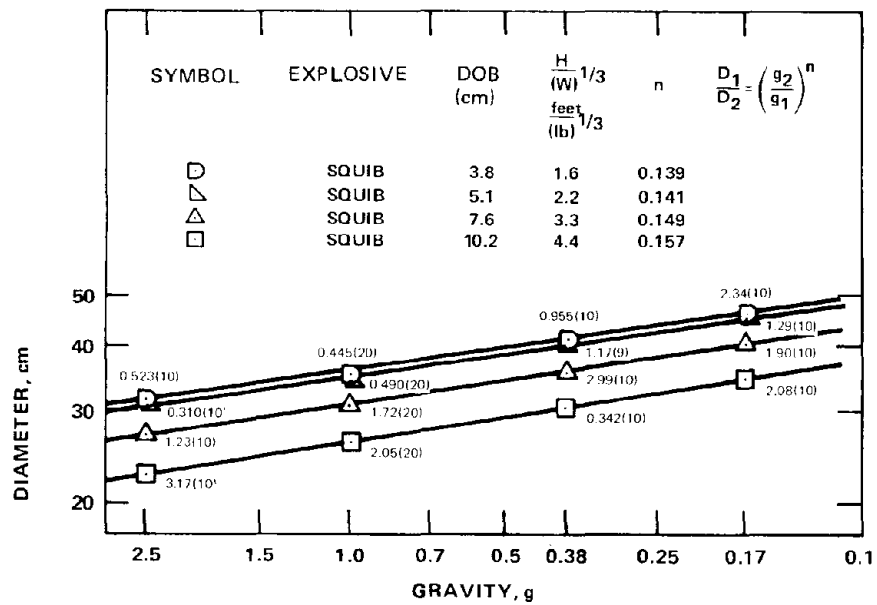
Figure IV-3.31. Logarithmic plot of crater diameter versus gravity for depth of burst > 3.8 cm.

depth was between 2 and 3 cm also independent of the static acceleration. From the data presented in these figures it can be noted that a scaling exponent for gravity of 1/8 is quite appropriate for DOB less than or equal to the optimum, either for the crater diameter or the crater depth. At this point it is interesting to note that the high-explosive cratering experiment SCOOTER[*] was near the optimum DOB (see Figure IV-3.5). SCOOTER would scale according to Cauchy's geometric scaling to a depth of approximately 3 cm compared to the experiments under discussion (Reference IV-3.51).

As long as the DOB is large enough so that the gas acceleration phase is a significant portion of the cratering process, it is reasonable to expect that the atmospheric overpressure will affect the crater production. Three experimenters have investigated this question. In conjunction with their work on the variation of the crater production with the gravitational field, Johnson et al. (Reference IV-3.50) performed some studies on the effect of different atmospheric overpressures. The small HE charges (about 6 grains) were used in a sand test bed placed inside a vacuum chamber. The DOB was held constant and shallow (about 2 cm) on all of the shots fired. The resulting effect of the overpressure is shown in Figure IV-3.32. The effects of atmospheric overpressure are seen to be quite weak, as one would expect for near-surface burst events. There is only a 7 percent change in going from zero overpressure to atmospheric overpressure.

A more extensive investigation was performed at NASA-Langley by Herr (Reference IV-3.52). He considered a wide range of DOBs and atmospheric overpressures. Additionally, four different cratering media were considered: dry sand; loose, dry ground limestone; and a mixture of the powdered limestone and sand. This latter mixture most closely approximates NTS alluvium. For that reason, the following discussion uses, for comparison with high-yield data, only the information derived from the limestone-sand mixture. Herr developed the length scale defined by

$$[L] = \frac{Y^{\frac{1}{4}}}{\rho g} \qquad (IV-3.10)$$

where Y is the charge yield. Using this scaling length the data generated are plotted in Figure IV-3.33. The solid lines through the data points are at fixed values of the ratio of the atmospheric overpressure to the lithostatic pressure, or $\frac{p}{\rho g D}$ where D is the DOB.

_____

[*] The SCOOTER event was 987,410 lbs of TNT detonated at a depth of 125 feet in the NTS area-10 alluvium.
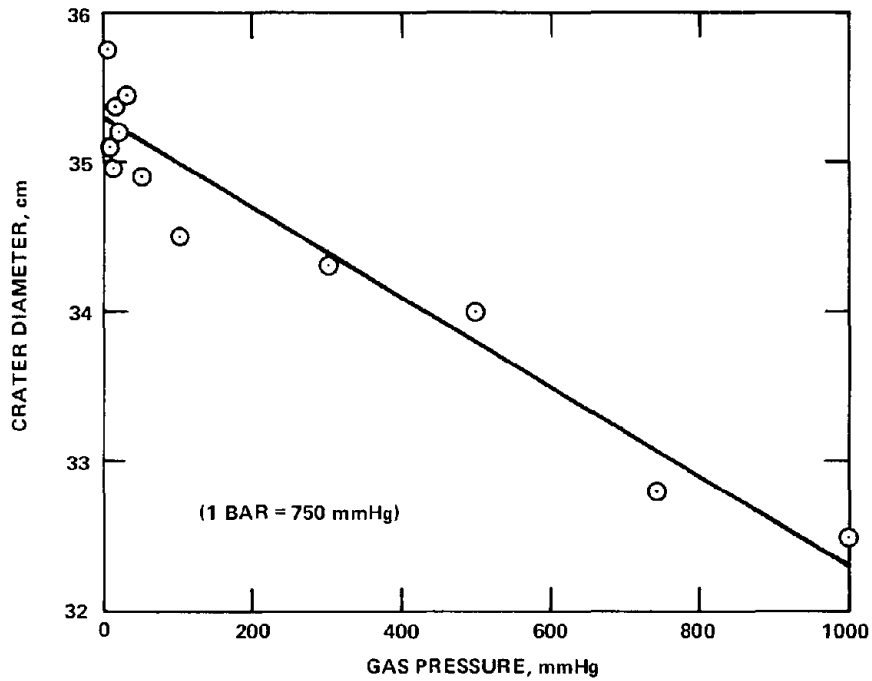
Figure IV-3.32. Effect of atmospheric overpressure on crater radius from shallow explosions.
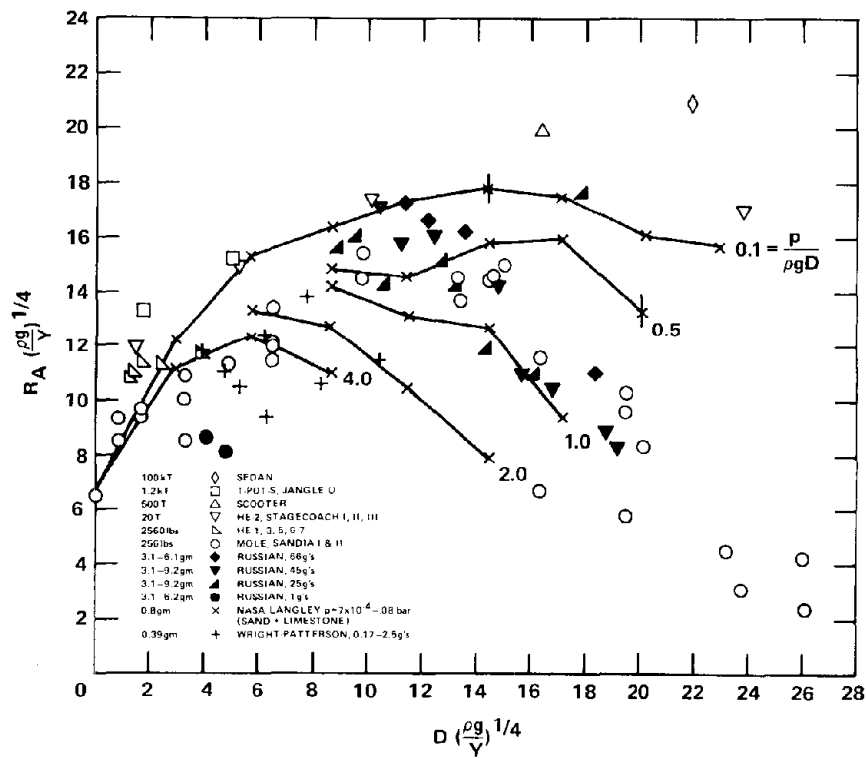
Figure IV-3.33. Crater radius versus depth of burst scaled according to Herr (Reference IV-3.52).

As a part of the present review, the work of Herr was extended in an attempt to obtain an empirical rule which would tend to collapse all of his data to a single curve or band. The simplest extension was to assume a scaling length that includes the above ratio raised to some power or

$$[L]_1 = \left(\frac{Y}{\rho g}\right)^{\frac{1}{4}} \left(\frac{p}{\rho g D}\right)^m \qquad (IV-3.11)$$

where m was to be determined. A best fit occurs when m = -1/8 resulting in

$$[L]_1 = \left(\frac{Y^2 D}{\rho g p}\right)^{\frac{1}{8}} \qquad (IV-3.12)$$

The same experimental data shown in Figure IV-3.33, when scaled by $[L]_1$, are shown in Figure IV-3.34. Included in this figure are high-yield events in desert alluvium, the high-acceleration field experiments conducted in moist sand by Viktorov and Stepanov, and the data of Johnson et al., for the largest DOB. The behavior of the Herr data at large DOB are somewhat suspect. He carefully adjusted the depths of his test bed to exclude tests in which the bottom boundary would influence the crater formation. Such tests did not involve DOB much greater than 13 cm. However, the largest DOB Herr reported (38.8 cm) is greater than one-half the total thickness of his test bed (61 cm). Therefore, the influence of the reflections from the test bed boundary cannot be ruled out in this case. The significant observation is that for atmospheric-to-lithostatic pressure ratios between 0.1 and 2, and for DOB greater than the optimum, the scaling factor used for Figure IV-3.34 appears to give a good correlation between the radii of craters produced by explosives having yields between 0.4 grams and 100 kt and for gravitational accelerations between 0.2 and 66 g's. Attempts were made to include the Chabai formalism, that is, by using $\sigma = (p + \rho g D)$ as one of the scaling parameters, where σ is the lithostatic stress. However, no combination was found for which the very small-yield and the very high-yield data could be collapsed as well as by the use of $[L]_1$ given by Equation IV-3.12. It can be concluded from this work that when the DOB, the acceleration of gravity, the atmospheric overpressure, and the yield are taken into account, the craters resulting from large enough DOB for the gas acceleration phase to be dominant scale according to Froude scaling (proportional to yield to the one-quarter power).

The third group to conduct experimental modeling to investigate the effects of atmospheric overpressure was led by Rodionov (Reference IV-3.53). He recognized the importance of being able to separate the gas acceleration phase of cratering from the effects of shock transmission and spall. To model the gas acceleration
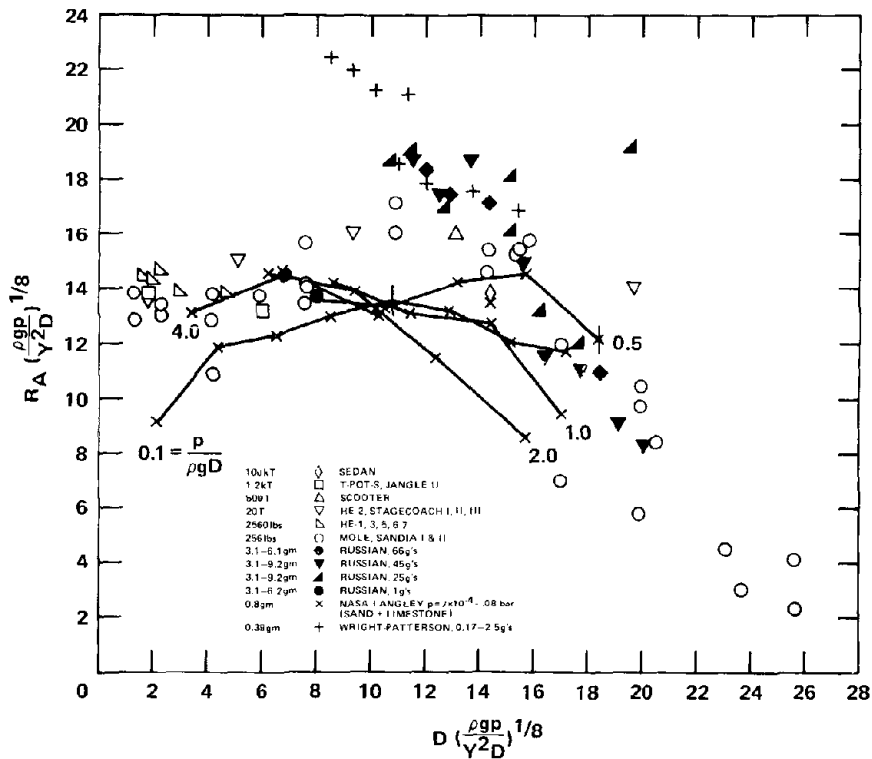
Figure IV-3.34. Data of Figure IV-3.33 with scaling length modified to include atmospheric overpressure.

phase only, an inflated balloon was buried to a specified depth in a test bed of sand. The entire test was placed in a vacuum chamber and the balloon burst. The DOB (D) and the overpressure in the vacuum chamber (p_0) were varied. Figure IV-3.35 shows the comparison of the best-fit straight line to Rodionov's experimental data. In this work the critical parameter is the dimensionless ratio given by the following equation, where E is the total energy released. All laboratory experimental data are grouped around the empirical relationship

$$\frac{R_A}{D} = 0.5 + 0.85 \log \overline{E} \qquad (IV-3.13)$$

with
$$\overline{E} = \frac{E}{(p_0 + \rho gD)\, D^3} \qquad (IV-3.14)$$

where log is the logarithm to the base 10 and D = DOB. A comparison of this relationship and the data obtained from large-scale field experiments is shown in Figure IV-3.36. In addition to obtaining a good fit to the crater radius, Rodionov also
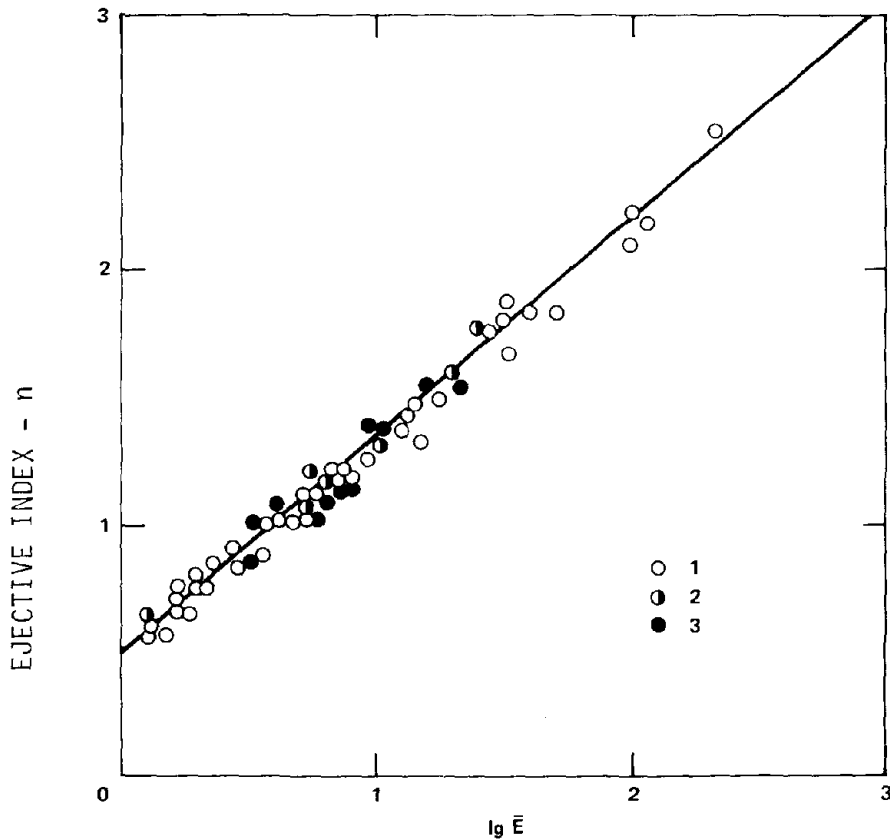
Figure IV-3.35. Index of ejection n (n = R_A/D) as a function of $\bar{E}$.
1. p/p_0 = 100; 2. p/p_0 = 20; 3. p/p_0 = 5.

obtained the rate of rise of the dome above the expanding gas bubble, using the following two scaling rules for velocity and time

$$\frac{V_N}{V_M} = \frac{\sqrt{gD_M + \dfrac{p_{oM}}{\rho_M}}}{\sqrt{gD_N + \dfrac{p_{oN}}{\rho_N}}} \qquad \qquad (IV-3.15)$$

$$\frac{t_N}{t_M} = \frac{D_M}{D_N}\frac{V_M}{V_N} \qquad \qquad (IV-3.16)$$

where N denotes the predicted quantity while M denotes the parameters in the experimental tests. Rodionov estimated the rise rate history of the domes above SEDAN, SCOOTER, and a one-ton HE shot conducted in loess[*] in southern Kazakhastan. These

---
[*] Webster's New Collegiate Dictionary defines loess as follows: an unstratified usually buff to yellowish brown loamy deposit found in North America, Europe and Asia and believed to be chiefly deposited by the wind.
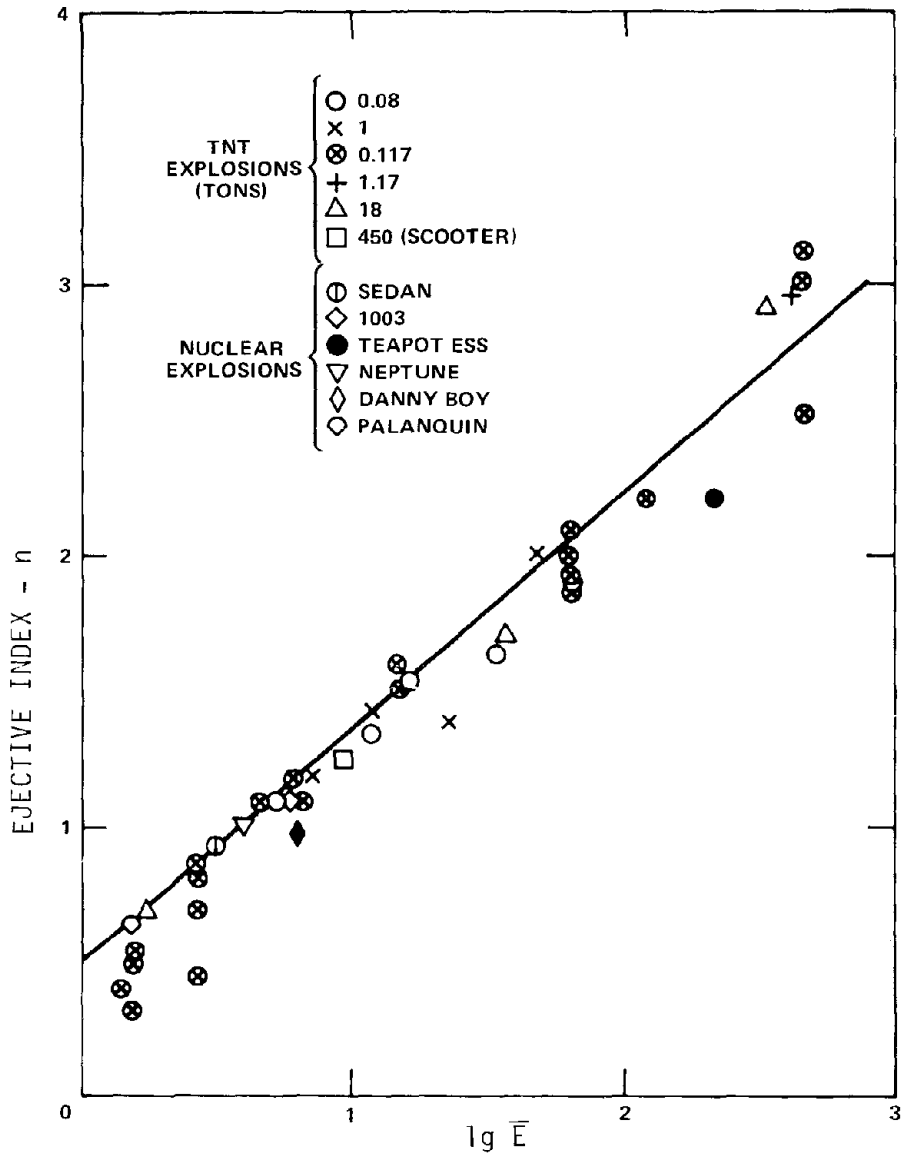
Figure IV-3.36. Comparison of crater dimensions in model experiments (solid line) with field experiments. n is the ratio of ambient to vacuum chamber pressure and E is the energy released.

predicted waveforms are shown in Figure IV-3.37. The early spall and gravitational collapse phases were not present in any of the exploding balloon experiments, and scaling curves could not reproduce these phenomena. Caution is required in interpreting Figure IV-3.37 because none of the U.S. reports on SCOOTER and SEDAN give data on the time the dome reaches its peak velocity. For these shots, venting occurred prior to the estimated time shown in Figure IV-3.37. Alternatively, the time to gas venting could be taken arbitrarily as the time of termination of mound growth.
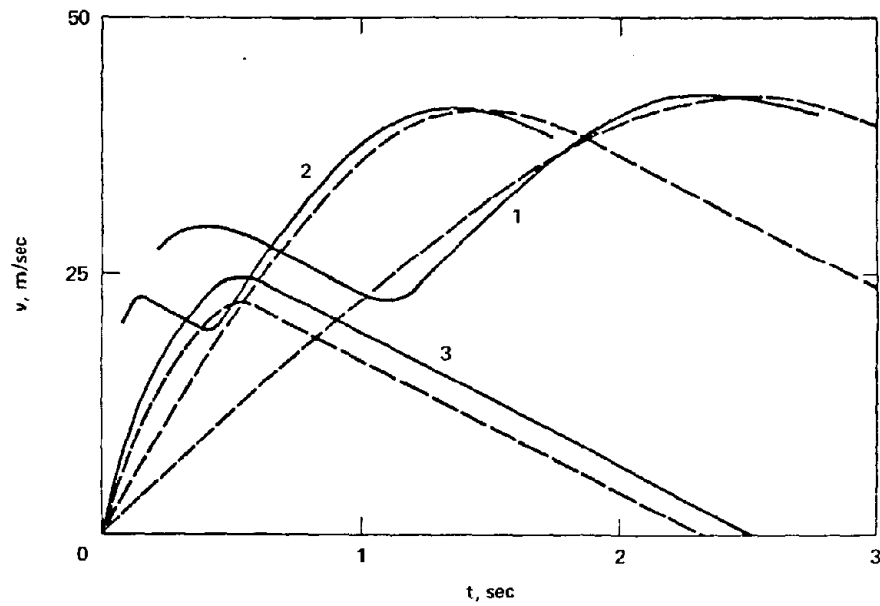
Figure IV-3.37.   Comparison of the curves for the rate of rise of
                  the free surface above the shot point as a func-
                  tion of time in field experiments (solid lines)
                  and model experiments (dashed lines). 1. SEDAN;
                  2. SCOOTER; 3. 1-ton, DOB = 7m, in loess.

It may be concluded from the experimental work discussed that a critical scaling parameter must include the total mean stress at the DOB as postulated by Chabai. The good agreement between not only the crater dimensions, but also the velocity history of the rise of the dome at ground zero, gives credence to the validity of the critical scaling parameter (p + ρgD). This would appear to be in conflict with the results of Herr.

Finally, a brief discussion follows of recently conducted small-scale laboratory experiments that had a different objective than those of Herr, Johnson,

Rodionov, and others. For those HE cratering experiments conducted in natural soils little data has been reported on the relationship between the physical properties and the dynamical behavior of the cratering medium and the final crater dimensions. In general, investigators have concluded that the effects of material properties on crater dimensions are somewhat obscure. As stated previously, several theories concerning various aspects of the formation of craters have been advanced, including attempts to scale these dimensions over a wide range of detonation yields. Piekutowski at the University of Dayton Research Institute (Reference IV-3.54) contends that if an analysis of cratering phenomenology is to be made, it would be advantageous to control or at least measure specific cratering medium properties for each experiment or event. His group designed and constructed a cratering facility for the purpose of conducting carefully controlled, laboratory-scale, high-explosive cratering experiments using selected cratering media and explosive materials. Three objectives were chosen during the initial phase of the program:

1. Construct a workable facility in which a reasonable number and variety of experiments could be performed.
2. Conduct a Benchmark Series of experiments in a "standard" soil bed.
3. Obtain pressure-time histories at soil-structure interface for various charge configurations and distances from the charge.

The purpose of the Benchmark Series would be to establish a set of reference data to provide a base for comparison with future data in which selected cratering media or explosion parameters had been varied. Moreover, this series would determine a realistic level of repeatability that could be expected for a given set of experimental conditions, and concentration of effort would be on several selected DOBs and HOBs of the charge. Primary concern was placed on obtaining accurate measurements of significant dimensions of the apparent craters. Other post-event measurements included the weight of far-field ejecta collected at various distances from the center of the explosion. A study of initial mound growth for subsurface detonations was also performed, and selected surface particles were photographed with high-speed motion picture cameras. Subsequent examination of this data resulted in early-time velocity and ejection angle histories for these surface particles. The ejecta aspect of these experiments will be discussed in Chapter IV-5.

Piekutowski reported the results of the first 57 events conducted at the Cratering Facility (Reference IV-3.54). These events were conducted in dry Ottawa sand with centrally-initiated spherical lead azide charges. DOBs and HOBs ranged up to 5 charge radii from the surface. The standard sandbed had an in-situ density

of 1.801 gm/cm^3. Apparent crater volumes were found to vary ±5 to 6 percent for the events of the Benchmark Series, while the apparent crater average maximum depth and radius varied ±4.5 percent and ±2.5 percent, respectively. Additional events requiring specialized experimental techniques with layers of colored sand also were performed. No attempts were made to scale the crater dimensions with charge energy. However, an attempt was made to obtain a simple mathematical relationship that could be used to describe the various apparent crater dimensions as a function of charge configuration. Plotted data suggested the use of a third-order polynomial to describe these data. A fifth-order polynomial also was fitted. Results for the apparent crater radius as a function of HOB and DOB are shown in Figure IV-3.38.

Chabai (Reference IV-3.44) in discussing cube-root, fourth-root, and other empirical methods of scaling cratering experiments indicated that all results of cratering experiments might be explained by the influence of certain variables not included in his analysis. Besides gravitational and overpressure effects discussed earlier, an anisotropy resulting from variations in density, moisture content, and porosity with depth also influences cratering. In-situ density of sandbed appears to be a material property which significantly affects final crater dimensions. This was shown most dramatically by one of the events detonated in the loose sandbed (Event S-11-32). Localized sandbed density variations, which resulted when closely spaced subsurface layers of dyed sand were placed in the sandbed, seriously affected the final crater dimensions of the near-surface bursts. An indication of localized density variation was also observed in the grid pattern placed on the surface of the sand for below-surface bursts. The intersections of the grid pattern were assumed to accurately follow the motion of a particle that would be on the surface of a plain sandbed. Localized density variations vitiate these techniques and assumptions. The completed grid pattern and/or subsurface layers could be vibrated at their resonant frequency to produce a sandbed of uniform density. A correlation between crater size and charge weight variation could not be detected. However, oblique-angle, high-speed films were made of two above-surface events. These films showed the lead-azide charge immediately after detonation and before oxidation of the gases had occurred. The fireball, as observed for these detonations, was composed of many jets of hot gas which appeared to cause the raying and occasional abnormalities observed in or around the craters. The effect of medium grain size is uncertain when an attempt is made to scale the craters produced in Piekutowski's study with craters produced in larger scale events.

APPARENT CRATER RADIUS - MM

THIRD ORDER POLYNOMIAL FIT TO EXPERIMENTAL DATA

EXPLOSIVE-SPHERICAL, CENTRALLY-INITIATED LEAD AZIDE
10.16 MM DIAMETER—1.7 GRAMS

CRATERING MEDIUM—OTTAWA SAND IN-SITU
DENSITY—1.801 gm/cm^3 (112.4 lb/ft^3)

FIFTH ORDER POLYNOMIAL FIT TO
EXPERIMENTAL DATA

THIRD ORDER POLYNOMIAL:
PREDICTED APPARENT CRATER RADIUS $= 99.3513 + 7.2198R_c$
$+ 0.207452R_c^2 - 0.0329943R_c^3$

FIFTH ORDER POLYNOMIAL:
PREDICTED APPARENT CRATER RADIUS $= 100.118 + 10.7234R_c$
$+ 0.0701507R_c^2 - 0.171463R_c^3 + 0.0151212R_c^4 - 0.000413541R_c^5$

FOR COMPUTATIONAL PURPOSES, ABOVE SURFACE
EVENTS HAVE A NEGATIVE R_c

R_c IS THE HOB OR DOB EXPRESSED IN CHARGE
RADII (in this case 5.08 mm)

HEIGHT OF BURST (HOB)   DEPTH OF BURST (DOB)   IN CHARGE RADII

Figure IV-3.38. Apparent crater radius as a function of charge configuration
for the overall series (Reference IV-3.54).

Piekutowski published results of further work carried out at the Cratering Facility of the University of Dayton Research Institute (Reference IV-3.55). He performed 68 cratering experiments designed to examine the effect of test media density on apparent crater dimensions. Spherical lead-azide charges weighing 1.7 grams having a density of 3.1 gm/cm^3 and a diameter of 10.16 mm were detonated at several near-surface depths. The detonations were in dry Ottawa Sand at various in-situ densities. Crater volume and depth were shown to increase as the sandbed in-situ density decreased from a very dense state to a loose state. However, a slight increase in the crater radius occurred for the events in the loose sandbeds. Figure IV-3.39 shows the apparent crater volume as a function of HOB and DOB for various sandbed densities. This figure shows rather large increases in crater volumes with decreasing densities—at one DOB an increase of nearly a factor of two corresponding to a density decrease of only 1.11. Cratering efficiencies were determined for each event for the various densities and the results are shown in Figure IV-3.40. A TNT-equivalent value for lead azide of 0.39 was used to convert the individual charge weights. Note that a factor of about two increase in cratering efficiency can accompany a reduction of 1.11 in density. Finally, the value of the ratio $R_a/V_a^{1/3}$, where R_a is the apparent crater radius and V_a is its apparent volume, was computed for each event. These results are presented in Figure IV-3.41.

Further studies conducted by Piekutowski (Reference IV-3.56) consisted of a series of cratering experiments using 400-mg silver azide-PETN composite charges, equivalent to 1.7 gm lead azide. These tests were conducted in dense dry Ottawa sand. Apparent crater dimensions from this series were compared with similar data from earlier studies using 1.7 gm of lead-azide charges detonated in the same medium. These experiments were conducted to examine the effect a difference in energy release per unit mass or volume of source material has on these data. Figure IV-3.42 shows a comparison in the apparent crater volume as a function of HOB or DOB for events using 1.7 gms of lead azide and 400 mgs of equivalent silver azide-PETN. Although both charges released the same caloric energy, the cratering efficiency of the more energy dense composite charges was significantly less than for the lead-azide charges. Figure IV-3.43 shows the variation of the ratio $R_a/V_a^{1/3}$ with HOB or DOB for events in the Benchmark Series and the 400-mg equiva-lent PETN series. A failure model that treats initial crater growth of a near-surface event as an earth pressure problem was developed to explain the differences and similarities in the apparent crater dimensions for the near-surface events in both series.
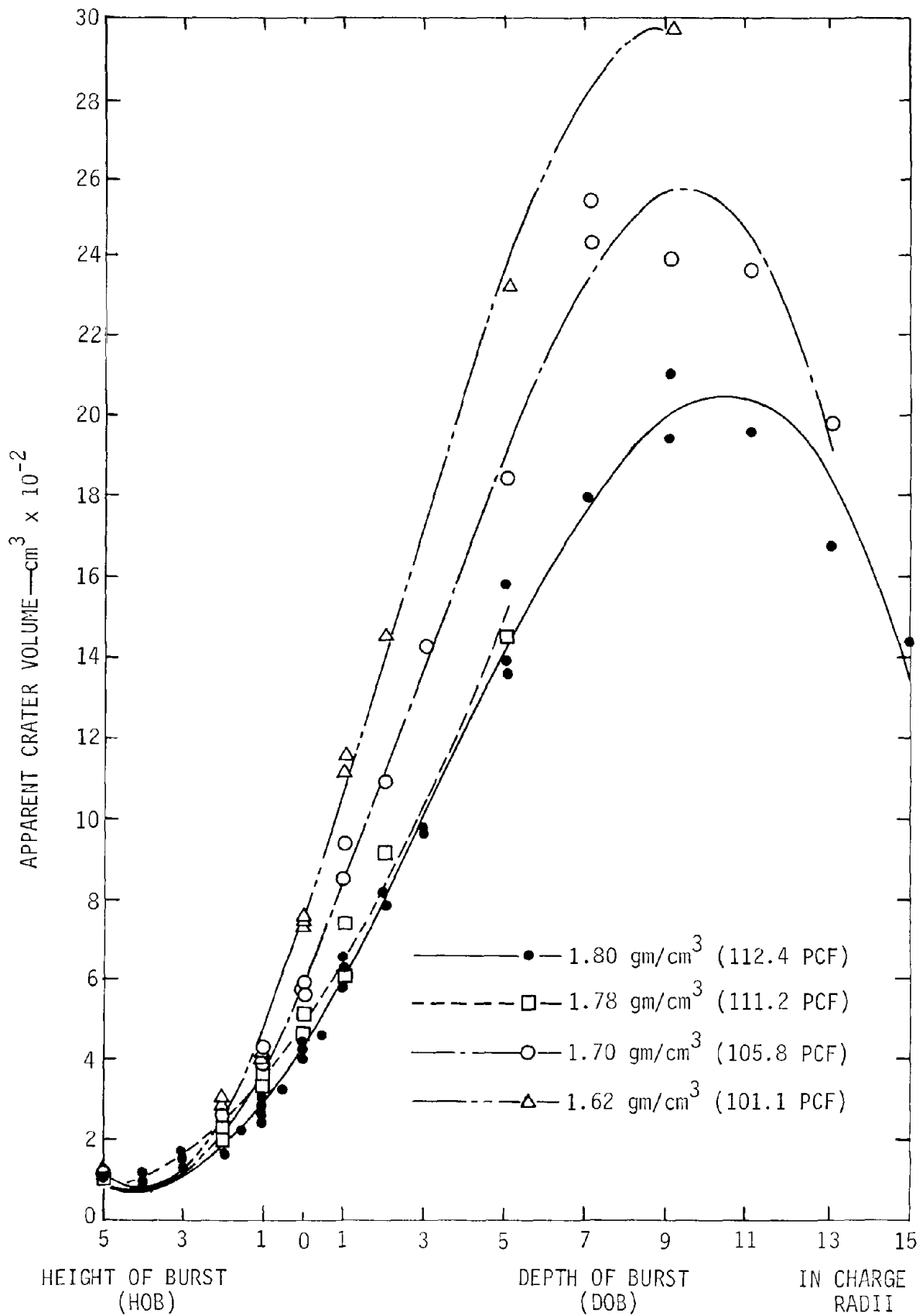
Figure IV-3.39. Apparent crater volume as a function of charge
configuration for various density sandbeds.
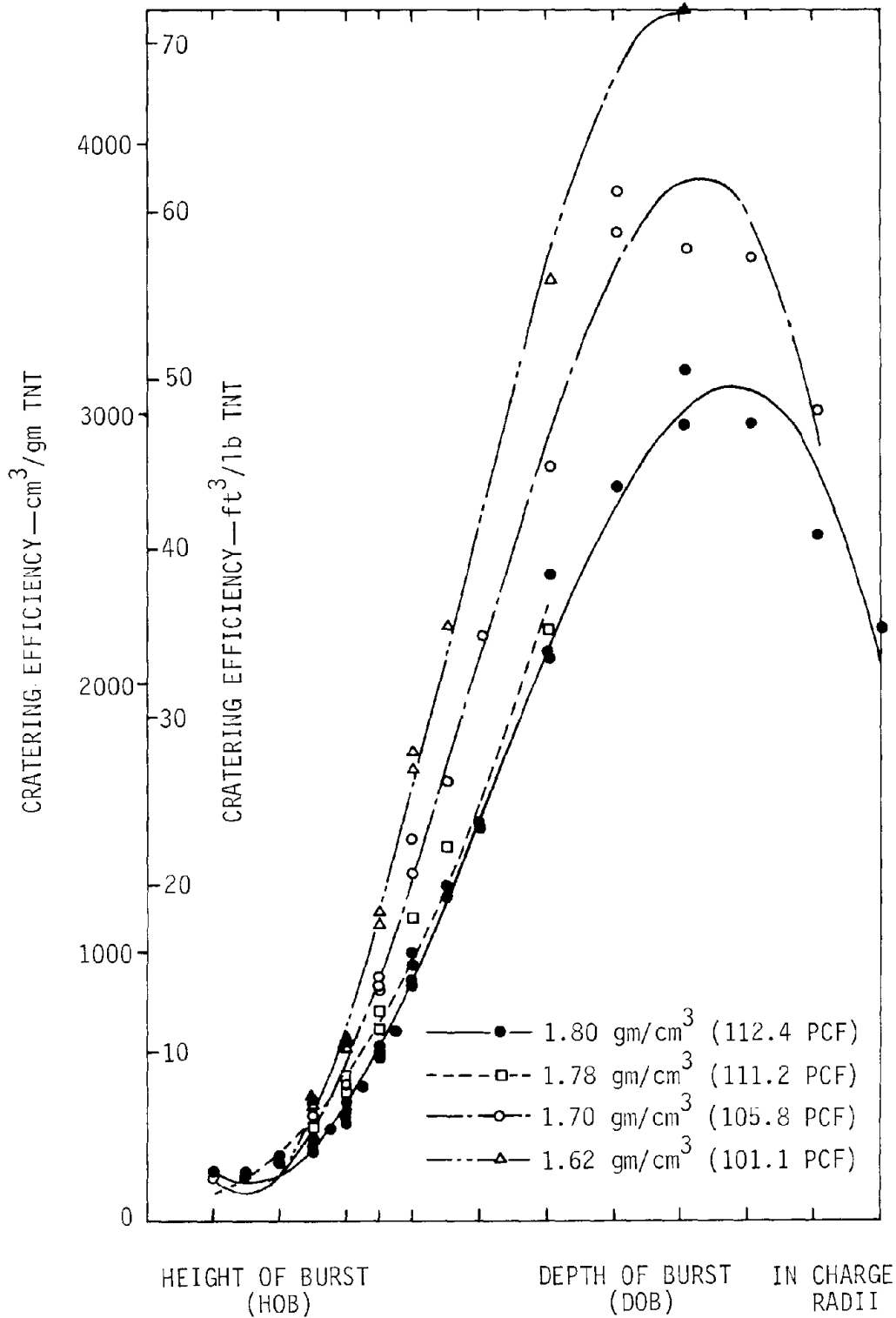
Figure IV-3.40. Cratering efficiency as a function of charge
configuration for various density sandbeds.
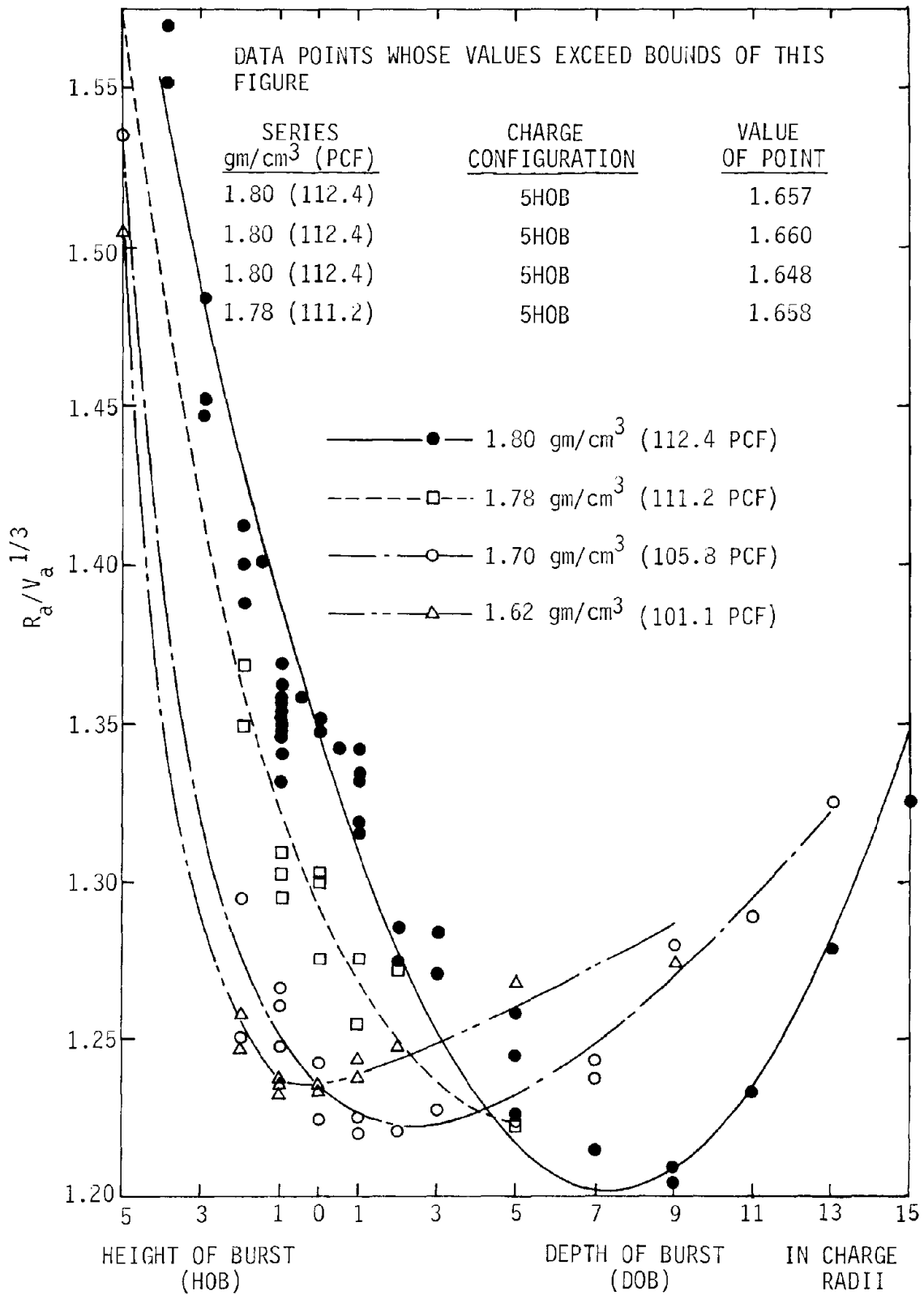
Figure IV-3.41. Value of Ratio $R_a/V_a^{1/3}$ as a function of charge configuration for various density sandbeds.
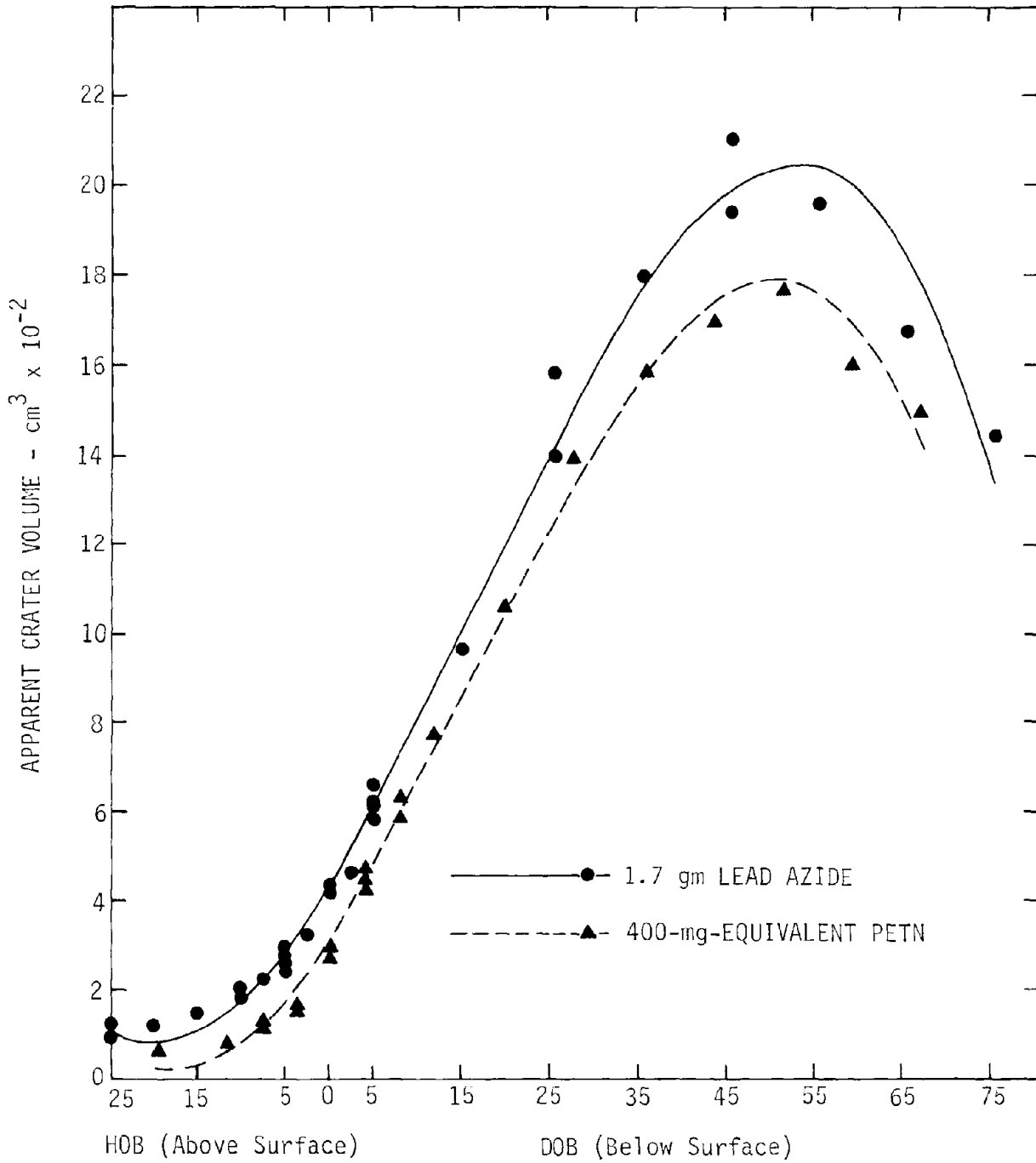
Figure IV-3.42. A comparison of apparent crater volume as a
function of charge center HOB or DOB for
events detonated using 1.7 gm lead azide and
400-mg equivalent PETN charges.
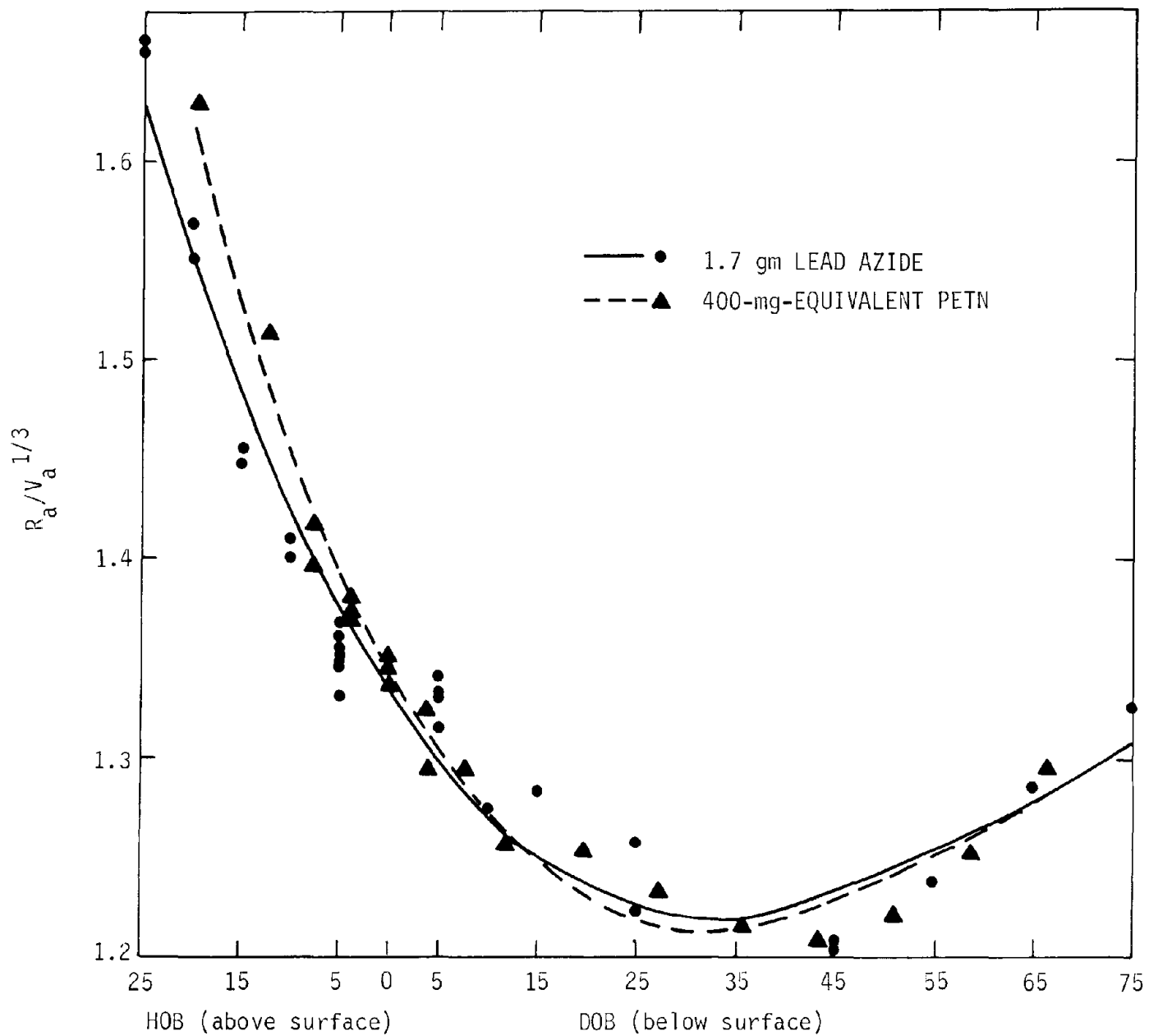
Figure IV-3.43. Variation of ratio $R_a/V_a^{1/3}$ with HOB or DOB for events in standard data series and 400-mg equivalent PETN series.

In December 1975, Piekutowski released two reports: one concerning the effects of a layered medium on the apparent crater dimensions (Reference IV-3.57) and the other summarizing four laboratory-scale, high-explosive cratering parametric sensitivity analyses (Reference IV-3.58). The latter report summarizes the preceding studies discussed above. A total of 194 events were detonated in dry Ottowa sand. The first series of 68 experiments examined the effect of in-situ density of the cratering medium on apparent crater dimensions. A series of 32 events examined the differences in the cratering effects of two explosives. The third series, 73 events, was the first phase of a two-part detailed study to determine the effects of an interface between geologic stratum on cratering. The last series, 21 events, concerned itself with defining the origin and the distribution of ejecta.

The former report discusses the results of three series of cratering experiments performed in layered media to examine the effect on apparent crater dimensions from an interface between geologic strata. Unconsolidated loose and dense Ottawa sand were used as overburden on a weakly cemented Ottawa sandstone man-made layer. This sandstone was made from 92 percent by weight of dry Ottawa sand cemented with 4 percent by weight of high early strength cement and 4 percent by weight of water (Reference IV-3.57). An additional series of experiments were performed using loose unconsolidated Ottawa sand over dense unconsolidated Ottawa sand as the cratering medium. The interface in these layered media had the effect of reducing the apparent crater size. A decrease in crater dimensions was observed as the interface began to affect the crater formation process. Figure IV-3.44 shows the apparent crater dimensions as a function of the thickness of the low-density sand overburden. The initial decrease was followed by a brief increase in crater dimensions and then a decrease as the interface approached the preshot surface. Evidence was obtained that indicated that mound-like features which were observed near the crater bottom were produced by elastic rebound of shock waves.

It was mentioned earlier that several investigators have examined the effects of an interface in a cratering medium. Strange (Reference IV-3.59) performed a series of 36 experiments at Waterways Experiment Station using dry to moist sand over a concrete base slab. The nature of this series did not offer the opportunity for detailed study of the effects of the interface because three types and weights of explosive charges were used in three near-surface DOB configurations with only a limited number of overburden depths. Vesic et al. (Reference IV-3.60) employed deeply buried gram-size lead-azide charges in a mixture of cement and sand over a cemented sandstone. In addition, a large number of field-scale, HE events have been
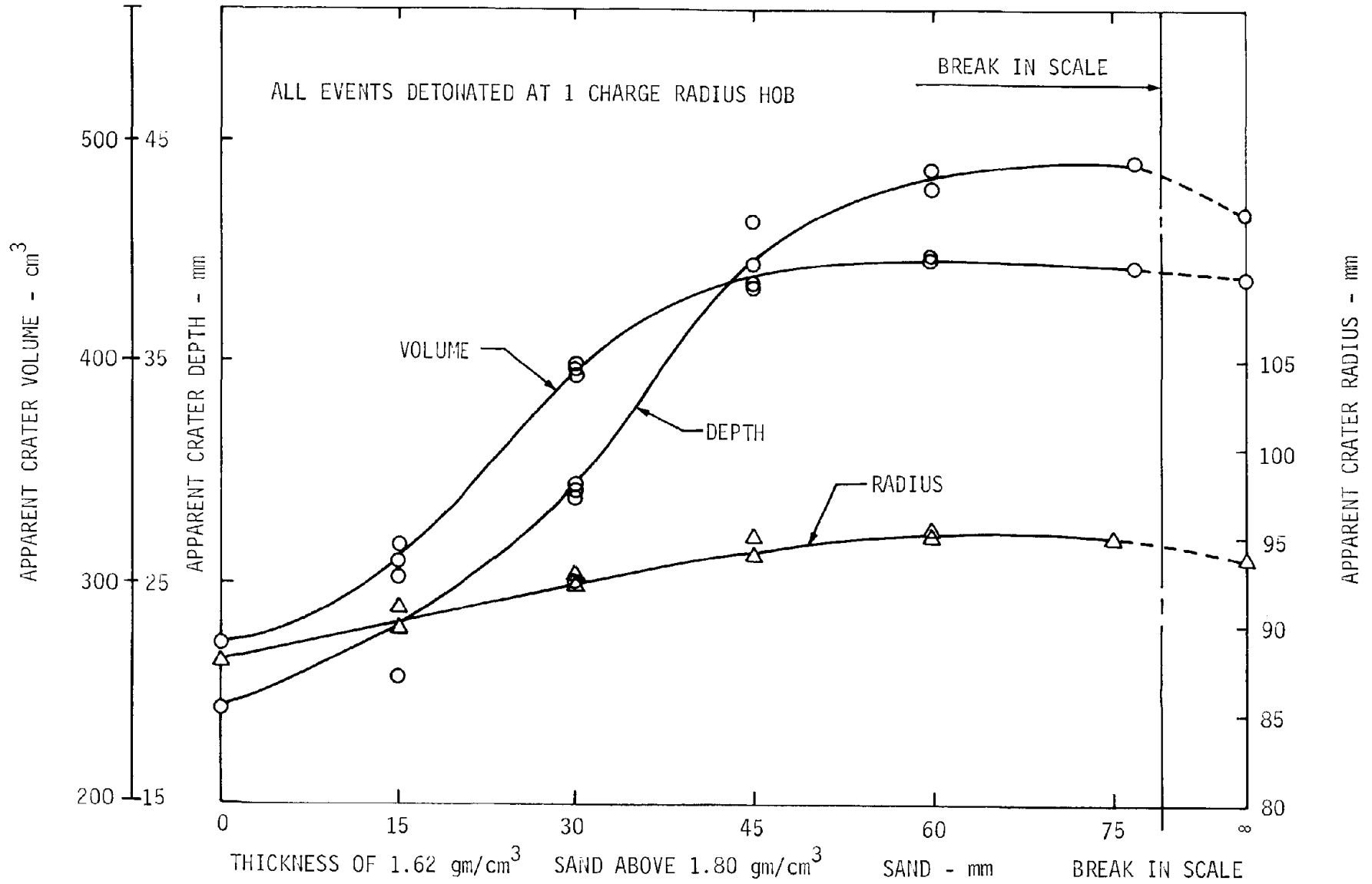
Figure IV-3.44. Apparent crater dimensions as a function of thickness of low-density sand above high-density sand.

detonated in strongly layered media. Finally, the University of New Mexico, Eric H. Wang Civil Engineering Research Facility (CERF) designed and built a cratering facility for the purpose of performing small-scale, HE cratering experiments (Reference IV-3.61). Twenty-seven experiments were conducted with 1-lb centrally initiated spherical C-4 charges detonated in a dry soil mixture of two parts concrete sand and one part clay. Charge configurations ranged from 2 charge radii HOB to 2 charge radii DOB. These experiments provided benchmark data for comparison of cratering effects with other experiments to be conducted in the future at CERF in a soil medium. Stephenson compared his results with those of Fulmer (Reference IV-3.62) and Dillon (Reference IV-3.42). This comparison is shown in Table IV-3.11 where the values have been scaled by the yield to the 5/16 power. In this table the comparison is based on the curve fits and material constants developed by Dillon (Reference IV-3.42) for shots detonated in sand.

Table IV-3.11. Comparison of Fulmer, Dillon, and CERF studies (Reference IV-3.61).

HOB or DOB	$R_a/W^{5/16}$			$D_a/W^{5/16}$			$V_a^{1/3}/W^{5/16}$		
	Dillon	CERF	Fulmer	Dillon	CERF	Fulmer	Dillon	CERF	Fulmer
-1.5R	2.35	1.30	2.07	1.8	0.64	0.48	2.40	1.077	1.368
-1 R	0.303	1.19	1.93	1.038	0.17	0.23	--	0.339	0.916
0	1.326	1.10	1.684	0.485	0.40	0.322	1.05	0.650	1.07
+1 R	2.42	1.19	1.93	1.629	1.30	0.46	2.4	0.921	1.249
+2 R	1.837	1.59	2.07	0.522	0.86	0.66	4.44	1.359	1.508

Under controlled conditions in a cratering facility, such as the one used in the experiments conducted by CERF, data scatter can be held to a minimum. However, it was found that inherent variations in the tests and the test medium set that limit. Averaging and determining density dependence reduces this scatter for predictions based on curve fits. The reliability of the HOB versus crater power curve fit equations is excellent if the HOB and DOB are varied and the charge size, the placement of the soil medium, and the properties of the soil are controlled as well as possible.

IV-3.3.4 Summary

In attempting to arrive at a predictive capability, two methods of analyzing cratering phenomena have been employed. Statistical techniques have been applied to data from buried- and surface-burst experiments. The primary application of dimensional analysis has been to data from buried explosions. This work has been augmented by small-scale laboratory experiments designed to determine the effects of the acceleration of gravity and the atmospheric overpressure as well as to develop carefully controlled experiments that could serve as benchmark crater dimensions for future experiments.

Drawbacks to both techniques are evident. Statistical analysis requires a large body of information which is quite costly and, in some instances, difficult to obtain. Furthermore, extrapolation to yields beyond those investigated cannot be made with confidence. On the other hand, the statistical methods allow only an interpolation of data with true confidence. Dimensional analysis suffers from the fact that the equations of motion cannot be made self-similar when the gravitational acceleration and the properties of the cratered material must be taken into consideration simultaneously.

To apply dimensional analysis to the cratering problem, a formalism was required in which either the elastic properties or the acceleration of gravity was included as part of the scaling parameters but was assumed to have little or no influence in the actual dynamics of the cratering process. As an example of this approach, Chabai examined the influence of the total mean stress at the DOB. This included the atmospheric overpressure and the lithostatic stress. Both are considered unscalable since the atmospheric overpressure and the acceleration of gravity cannot be altered with the explosive yield for large cratering experiments conducted on earth. Modeling experiments were conducted by Rodionov to examine the role of the gas acceleration phase in cratering. It was his conclusion that the total mean stress at the DOB was indeed a valid scaling parameter for craters whose production was primarily brought about by the gas acceleration phase. The rules he proposed, Equations IV-3.15 and IV-3.16, for scaling velocity and time from the modeling experiments to large scale tests correspond to Froude scaling (1/4 scaling). If Figure IV-3.37 is to be believed, there is excellent agreement. Caution must be exercised though, since no clear observation of the time of peak velocity has been reported in the U.S. literature.

Herr conducted an extensive series of experiments that closely matched those of Rodionov, the difference being that Herr examined explosively produced craters while Rodionov examined craters generated by the gas acceleration phase only using buried balloons. The conclusion of Herr's experiments was that crater dimensions were well approximated through Froude scaling, that is, quarter-root scaling of the yield. The current situation is one in which four different prediction techniques (that is, Dillon, $E^{5/16}$; Herr, $[E/pg]^{1/4}$; Chabai, $[E/pg]^{1/3}$; Rodionov, log $[E/(pgD + P_0)D^3]$) give equivalently good fits to the existing experimental data.

At this point, a few comments on the mean stress parameter used by Chabai and Rodionov are in order. Intuitively, this pressure term is of importance to the gas acceleration phase of cratering, since the gas within the expanding cavity must work against the confining medium. This confining medium exerts a pressure composed of the atmospheric overpressure and the lithostatic stress (p_0 + ρgD). Although the material above the expanding gas cavity may have been pulverized by the initial shock wave, it should maintain some cohesive strength. For the sake of argument, assume that this material behaves as a von Mises[*] solid. The remaining strength in the material will add an additional confining stress. Thus, the pressure term of Rodionov and Chabai should be modified to include an apparent additional pressure due to the strength of the material around the expanding gas bubble (Reference

---

[*] R. von Mises defined a yield condition by a single equation which is referred to as the energy-to-distortion condition. It states that yielding occurs when the principal stress reaches a critical value. This condition is (Reference IV-3.63)

$$(\sigma_1 - \sigma_2)^2 + (\sigma_2 - \sigma_3)^2 + (\sigma_3 - \sigma_1)^2 = k^2$$

where σ_1, σ_2, σ_3 are the principal stresses and k is an experimentally determined constant. For simple tension and pure shear we have, respectively, that

$$k^2 = 2\sigma_0 \quad , \quad k^2 = 6\overline{K}^2$$

This condition predicts that the yield shear stress in pure shear, $\overline{K}$, is related to the maximum elastic shear in simple tension, $\sigma_0/2$, by

$$\overline{K} = \frac{2}{\sqrt{3}}\left(\frac{\sigma_0}{2}\right)$$

In terms of a geometric representation, the von Mises yield condition is an ellipse in the σ_1, σ_2 space. The equation of this ellipse is obtained by setting $\sigma_3 = 0$ in the von Mises yield condition so that

$$\sigma_1^2 + \sigma_2^2 - \sigma_1\sigma_2 = \sigma_0^2$$

The major axis is $2\sigma_0\sqrt{2}$ and the minor axis is $2\sigma_0\sqrt{2/3}$. Therefore, from the above discussion, a von Mises solid is one that obeys the von Mises yield condition.

IV-3.64). This pressure may or may not be of the same order as the atmospheric pressure. One would intuitively expect it to be small for such materials as NTS alluvium, while it may be measurably larger than the atmospheric pressure in materials which can heal, such as moist clay and halite.

Under the assumption that the final crater dimensions are the end product of the ground motion, it is reasonable to search for scaling rules in the ground motion data and vice-versa. The earliest work along this line was performed by Soviet workers on a series of scaled experiments in a clay-loam-loess material in Kazakhstan. Although they found the ground motions of the surface to scale approximately as Froude scaling, there were mitigating experimental circumstances which precluded arriving at a definitive conclusion. First, the geology in which the experiments were conducted is highly layered. This could result in the trapping of seismic energy in certain preferred layers, thus creating a confusion in the search for whatever scaling rules may be operative. Second, the explosions were conducted in nonspherical cavities that were produced either by hole-springing or mining. Finally, the explosive used was a slurry. There has been ample indication on the uses of slurries in the United States that the energy yield per unit mass of explosive is dependent not only on the amount of explosive present but also on the method used to emplace the slurry. Since little information is available on the explosive used in the Soviet experiments, this comment is not a criticism.

IV-3.4 NUMERICAL ANALYSES OF CRATERING

Brode and Bjork (Reference IV-3.4) published in 1961 the first significant report on numerical analyses of cratering. Since then many sophisticated analyses of cratering and ground motion have been conducted in two broad classes of calculations, those for deeply buried bursts and those for near-surface bursts. Some of the most impressive successes in cratering calculations for deeply buried bursts have been accomplished by the Department of Energy (DOE)[*] at the Lawrence Livermore Laboratory. The other broad class of calculations is the effort to predict near-surface cratering from nuclear and HE explosions as well as meteoric and hyper-velocity projectile impacts.[+] Studies are currently underway to demonstrate the ability to correlate calculated and experimental HE cratering events in several media. A brief resume of the status of progress and the principal conclusions

_____
[*]Formerly Energy Research and Development Agency (ERDA) and Atomic Energy Commission (AEC).
[+]An overview of theory and observational data on lunar and earth meteor cratering is given in Appendix IV-3.A.

reached concerning important cratering mechanisms identified through these studies is presented in this section. Also included is a brief summary of calculational techniques.

IV-3.4.1 Numerical Techniques

The equations of motion, that is, the conservation laws, applied to rock and soil continua have long been known, and closed-form analytic solutions to some of the simplest problems have been obtained (Reference IV-3.65). However, even the simplest of the non-ideal constitutive equations preclude their analytic solution in closed form. Therefore, it became apparent long ago that numerical techniques were required. In dealing with shock phenomena, the equations of motion written in finite difference form are the most amenable to numerical solution. In all forms of the equations of motion the three conservation laws—mass, momentum and energy— are obeyed. In the Lagrangian coordinate frame, mass is intrinsically conserved in that the calculational grid distorts with the material, each grid cell being defined by the mass contained within it. The other major form of the equations of motion is for the finite difference grid to remain fixed in space while the material flows through the grid. This is the Eulerian coordinate system. Conservation of mass in this system must include a mass flow, or diffusion term, across the grid cell boundaries. Sometimes, certain types of problems require a combination of the Lagrangian and Eulerian coordinate systems. The earliest work performed on coupled Lagrangian-Eulerian calculations was discussed by Noh (Reference IV-3.66). His work considered the problem to be separable into several regions, each region de- fined by a particular coordinate system, either Lagrangian or Eulerian.

The particle-in-cell (PIC) codes developed at the Los Alamos Scientific Labora- tories (LASL) have the characteristics of the Lagrangian and the Eulerian codes, and are quite useful for some applications. In this case, the conservation laws deter- mine the flow of fixed-mass particles from one cell to another in an Eulerian grid. The mass in any given Eulerian cell is determined by the number of particles in that cell. As one particle crosses the cell boundary, the mass in that cell changes by a discontinous amount corresponding to the loss or gain in particles. Correspond- ingly the pressure in going from one cell to another experiences a discontinous jump. In order to reduce the computational numerical noise in the PIC-type codes, it is necessary for the particle density in these cells to be maintained at a high level. The early work by Brode and Bjork initially allowed 20 particles in each computational cell.

Another modification of the Lagrange and Euler coupling is that used by Applied Theory, Inc. (ATI) for their two-dimensional calculations. In this code, rows are defined in a Lagrangian grid and the columns are defined by an Eulerian formulation. Problems can arise with this formulation when large material flow must be considered. The Lagrangian portion of the grid may distort to such an extent that the Eulerian cells are emptied of mass, resulting in a discontinuity in the calculation. This may be overcome by paying careful attention to the progress of the calculation, either through manual or automatic rezoning at appropriate time intervals.

A standard method of calculating nuclear or HE surface-burst cratering events is to start to zone the problem in an Eulerian coordinate frame. At the time when the stresses in the shock front fall below the hydrodynamic limit (when the stress is no longer a scalar point function) the problem is coupled to a Lagrangian coordinate frame. Two methods of performing this coupling are currently in use. One is to map the entire flow and stress field from the Eulerian calculation onto a Lagrangian grid. The calculation then proceeds as an exclusively Lagrangian calculation. This is the technique used at Shock Hydrodynamic, Inc. (SHI). The second technique is to maintain an overlay of the Eulerian grid and a Lagrangian grid, and allow a dynamic coupling between the two grids as outlined by Noh in Reference IV-3.66. The computation is then run with both the Eulerian and the Lagrangian grids until such time as significant activity in the Eulerian grid has ceased. At this time the Eulerian grid may be removed and the problem continued as a purely Lagrangian calculation. This is the method currently in use at Physics International (PI).

The use of two different formulations of the equations of motion is a purely practical one. The size of the real-time step required for the stable integration of the equations of motion is, in general, much smaller for the Eulerian system than for the Lagrangian system. Thus, the computer resources required for a given real-time calculation are greater for the Eulerian approach than for the Lagrangian approach. However, for nearly hydrodynamic flow calculations, which may or may not be turbulent, the Lagrangian grid (with a network of points which follows and distorts with the flow) often becomes hopelessly tangled and the calculation cannot proceed without experienced help.

As discussed by Noh, other formulations are possible in which the coordinate frame of the problem may move with respect to a fixed coordinate system or with respect to the mass particles in the flow. In any case, one is required

simultaneously to calculate the elements of strain and stress. The equations of motion allow only the calculation of either stress or strain alone. Some connection must be made between an element of stress and the elements of strain. Such a connection is called variously an equation of state, or the constitutive property, or the material model. This is discussed in detail in Volume II of this Handbook.

IV-3.4.2 Calculation of Buried Explosions

The requirements of cratering calculations in support of the PLOWSHARE program have centered on the efforts of the Lawrence Livermore Laboratory (LLL) for the computation of deeply buried explosions. A reasonable degree of reliability has been demonstrated by LLL in the preshot calculations of craters from buried nuclear and HE events. The numerical analyses have been performed by using Lagrangian calculations in one-dimensional spherical symmetry and two-dimensional cylindrical symmetry. The techniques used for the calculations of the craters are as follows. The one-dimensional SOC code was used to determine the validity of the equation of state employed, the timing of the shock waves at the surface, and the general time step required for the calculation. It was also used to verify the input to the two-dimensional calculation performed with the TENSOR code. Typically a calculation is started by placing all of the released energy within a sphere corresponding to the bubble as described by Butkovitch (Reverence IV-3.67). Computations are continued well into the gas acceleration phase or until large pressure and velocity gradients no longer exist. At this time the calculation enters a different phase wherein all of the particles that have undergone extensive shearing and can follow a free-fall ballistic trajectory out of the crater region are allowed to do so in the computations. The material calculated to leave the grid is located and stacked in the final location as though on the original ground surface. The stacked material is then distributed within the final crater volume or on the crater lip so that the fallback in the true crater and the apparent crater dimensions can be estimated. At the time the cratering calculations are turned off in the TENSOR code, there still is residual motion in the true crater wall. The wall is allowed to complete its motion assuming linear viscosity for damping. Material that falls back into the crater is allowed to bulk to a density considered to be reasonable for the soil under consideration. Comparisons of calculated and measured results (Reference IV-3.68) for SEDAN and DANNY BOY are shown in Figures IV-3.45 and IV-3.46. A general agreement between calculated and measured GZ surface velocity is satisfactory (Figure IV-3.47). The basic phases of the cratering motion—shock, spall, gas
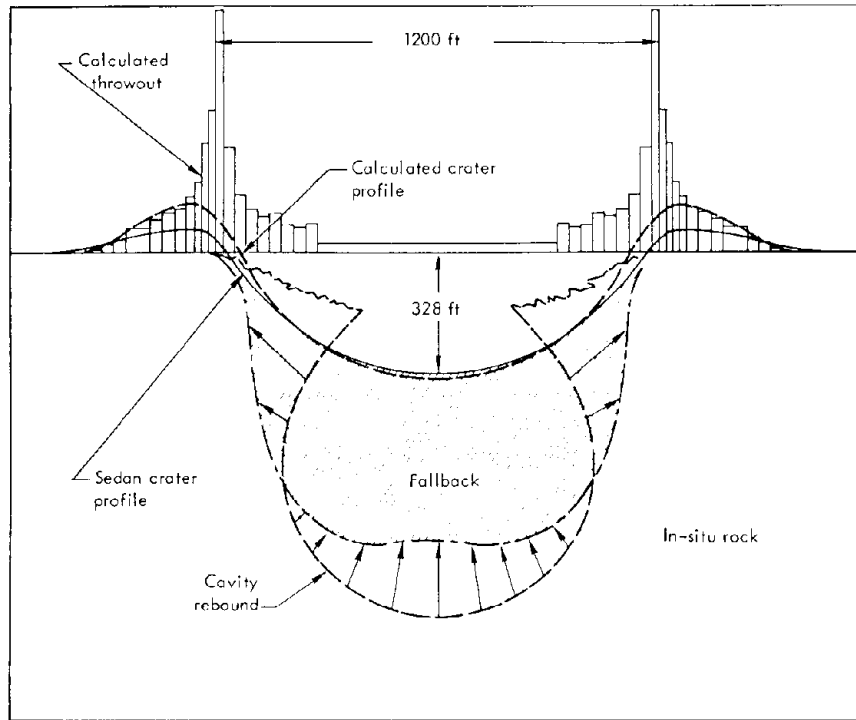
Figure IV-3.45. SEDAN crater profile at t = 2.4 seconds.
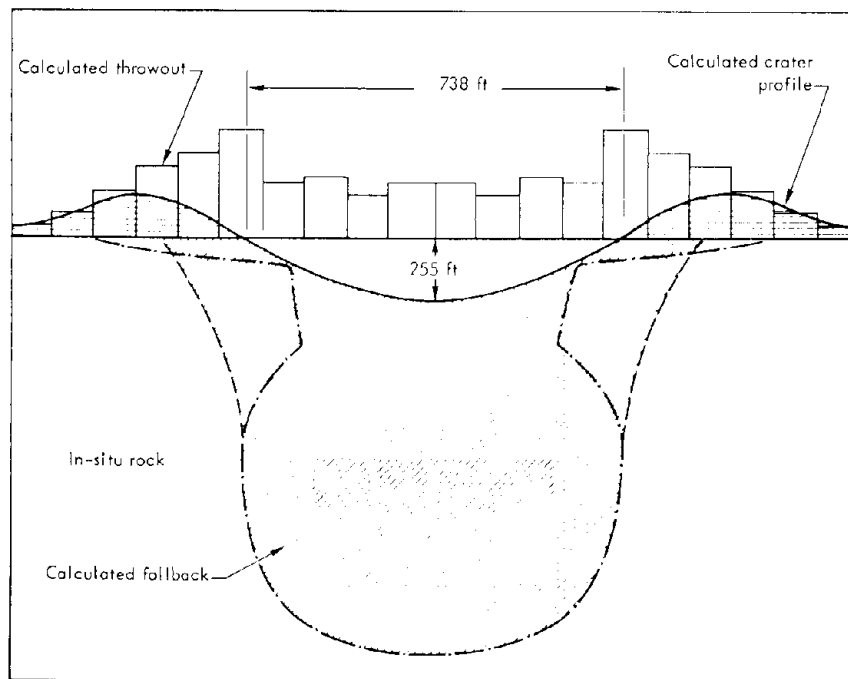
Figure IV-3.46. Calculated crater profile for DANNY BOY at t = 0.1 second.
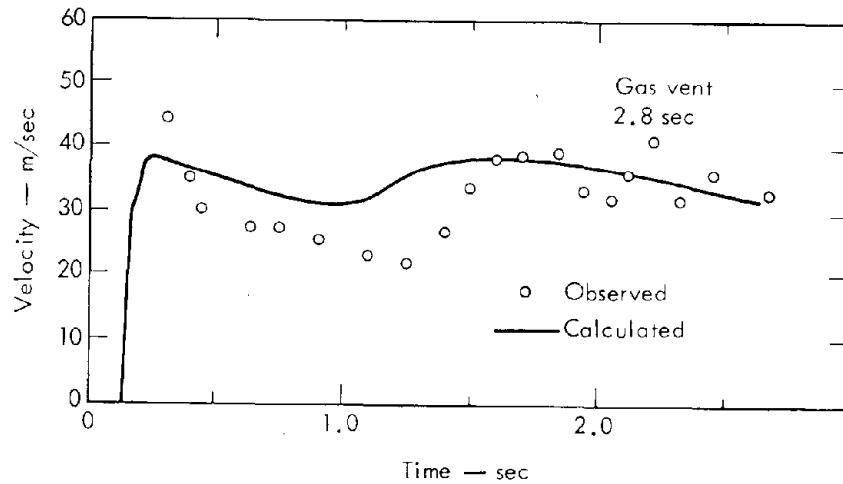
Figure IV-3.47. Calculated and observed ground zero surface
velocity for SEDAN.

acceleration, and ballistic trajectory—show reasonable correspondence between cal-
culated and observed values. The correspondence between the postshot calculated
and measured crater dimensions on SEDAN is good, with the crater dimensions within
2 percent of the measured value. Similarly, close correspondence can be noted for
the DANNY BOY calculations where the computed crater radius is within 1 percent of
the measurement values and the depth within 11 percent of the measured values. In
the DANNY BOY calculation (0.42 kt at 110 feet DOB), spalling was the primary mode
of crater formation. It should be pointed out that the calculations for DANNY BOY
and SEDAN were performed after the shot. These calculations were terminated at a
fairly early real time. The motion of the crater walls was allowed to continue
until it was expected that there would be no compaction in the upper regions. The
assumption was made that on the crater axis the gravitational forces would stop the
rebound of the crater wall. Bulking of the fallback material was maintained to
within limits obtained by experiment. However, the bulking was adjusted to give a
reasonable fit to the measured crater.

Preshot calculations for event SCHOONER are compared with experimental results
in Figure IV-3.48. Considering the rather poor estimates of the material properties
and the complicated layered geology, the agreement between predicted and observed
results is reasonable. The SCHOONER device (35 kt) was detonated approximately 25
feet into a hard welded tuff layer. This was overlain by a soft porous tuff
approximately 200 feet thick. The topmost layer extending to the surface consisted
of a fairly hard layer of welded tuff. Inadequate information on the tuff equation-
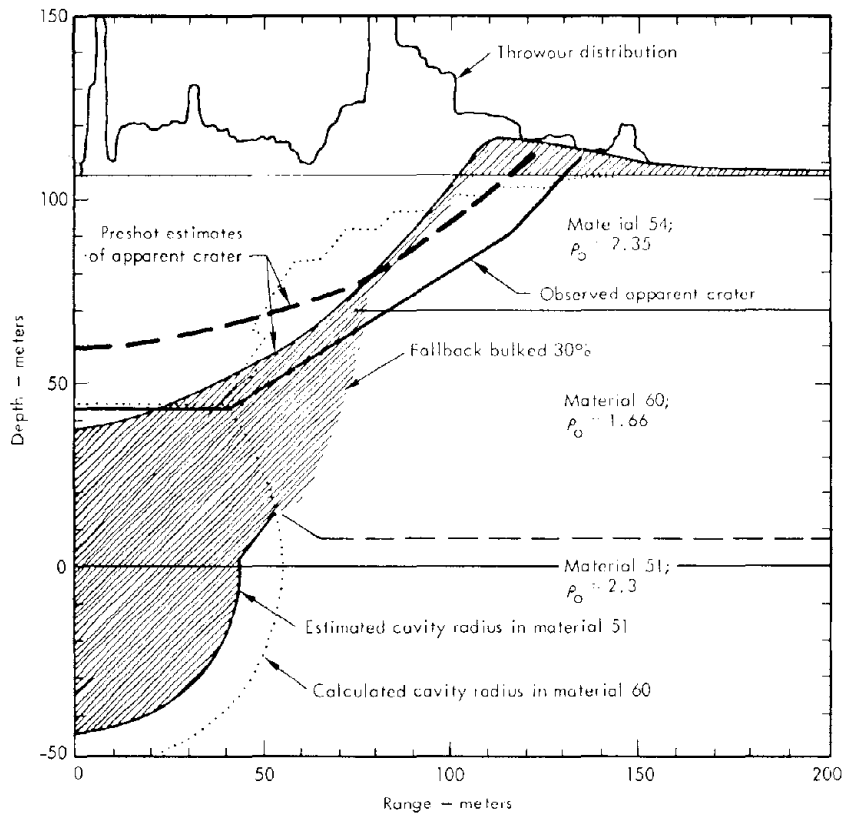
Figure IV-3.48. Calculated and observed crater profiles
for the SCHOONER crater.

of-state could easily account for the fact that the predicted radius was 25 percent
smaller than the measured values, and the predicted depth approximately 8 percent
greater than the measured values. Although it is apparent that preshot calculations
have not provided exact correspondence with measured values for these complex media,
it should be remembered that the calculated values can be no better than the mate-
rial models used in the calculations. Also, there is evidence that the differences
are on the same order as the experimental variations for similar tests in similar
media. A demonstration of this is shown in Figure IV-3.49. This figure shows the
crater volumes as a function of DOB resulting from the detonation of 256-lb TNT
spheres in NTS Area 10 alluvium. These are the data obtained during the MOLE 200,
MOLE 400, SANDIA I and SANDIA II test series (see Appendix IV-3.B).

In summary it can be said that the reliability and validity of calculational
methods for predicting crater dimensions from buried bursts have been substantially
demonstrated. Refinement in measurement of dynamic earth constitutive properties
may be expected to improve the numerical prediction capabilities. The material
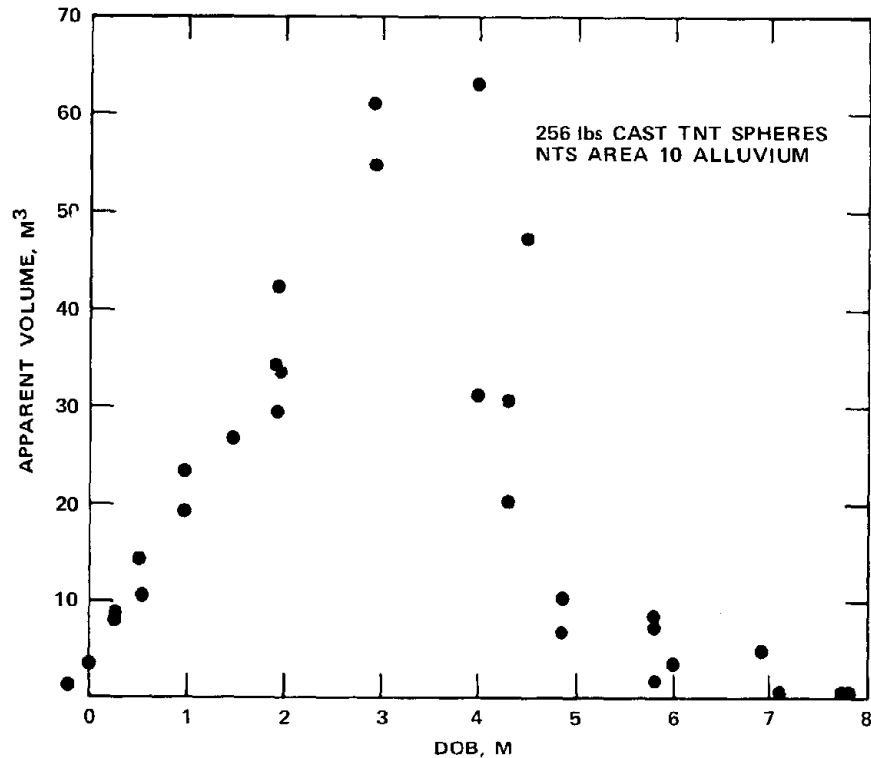
Figure IV-3.49.   Apparent crater volume as a function of
depth of burst in NTS Area 10 alluvium.

properties that had the greatest effect on the cratering behavior from buried bursts
are listed below in the order of their importance:

1. Water content.
2. Shear strength.
3. Dry porosity.
4. Compressibility.

Water content was found to be of primary importance because it decreases the rock
shear strength. Moreover, water provides an additional source of noncondensable
gas within the expanding camouflet. Compressibility and porosity were found to be
the dominant factors in determining the energy delivered to a point within the
medium. The shear strength and length of time the shear stress operated were found
to be the primary determinants of the velocity field behind the shock.

IV-3.4.3   Near-Surface Burst Calculations

The earliest work of Brode and Bjork (Reference IV-3.4) used the PIC code dis-
cussed above. Very coarse zoning was required due to the limited size of the com-
puters available at that time. Particle densities within the 20 x 20 rectangular

array were such that material density change was limited to increments of 5 percent. By rezoning, the mass points were frequently rearranged so that they were maintained in the vicinity of the shock front where the principal density gradients were observed. Because of this coarse zoning, details of the actual cratering process were lost. With present-day computers such extreme computational frugality is not required. However, retaining adequate zonal detail in the vicinity of the crater is still a problem. For megaton bursts a number of recent calculations have been carried to times equivalent to one to several seconds. This is more than an order of magnitude longer than the 0.1 second for the early Brode and Bjork calculations. Brode and Bjork used the velocity field at 0.1 second to estimate the final crater dimensions. As shown in Figure IV-3.50, reasonable agreement occurred between this early-time velocity vector field and the typical crater dimensions recommended in Reference IV-3.69. Although it is now recognized that much of the crater formation occurs at a much later time (full crater formation requires one to several seconds for a 1-MT surface burst), the practice of estimating crater dimensions from early-time ($\approx$0.1 to 0.2 seconds) velocity fields is still common and useful. This was mentioned in the previous section in connection with the DOE method of predicting crater dimensions for buried bursts. One of the more significant results of these calculations was the recognition of the sensitivity of the cratering process on the details of the detonation of the nuclear device and its coupling of energy to the ground. Brode and Bjork assumed that the coupling was primarily hydrodynamic, that is, a momentum transfer of the explosive debris to the ground. These early calculations assumed that the role of radiation energy coupling to the ground was insignificant in comparison with the purely hydrodynamic coupling. However, it has recently been recognized that the surface ablation resulting from massive radiation deposition in the ground is a very significant, if not a dominant, mode of momentum transfer for nuclear explosions.

As part of an investigation of the various numerical techniques for crater calculation, DNA sponsored the calculation of two very similar cratering experiments. These were performed by ATI and SHI. The ATI technique was a combined Euler-Lagrange method in which the ground surface was assumed to be a Lagrange line. The calculation of SHI used a modified PIC code. Perhaps the largest difference between these two calculations was that of the velocity field near the boundaries of the crater. Tha ATI solution indicated that for the most part motion has ceased around 400 msec, while the SHI solution shows that there are still upward velocities in excess of 100 ft/sec at the same time. When the results of the computations were
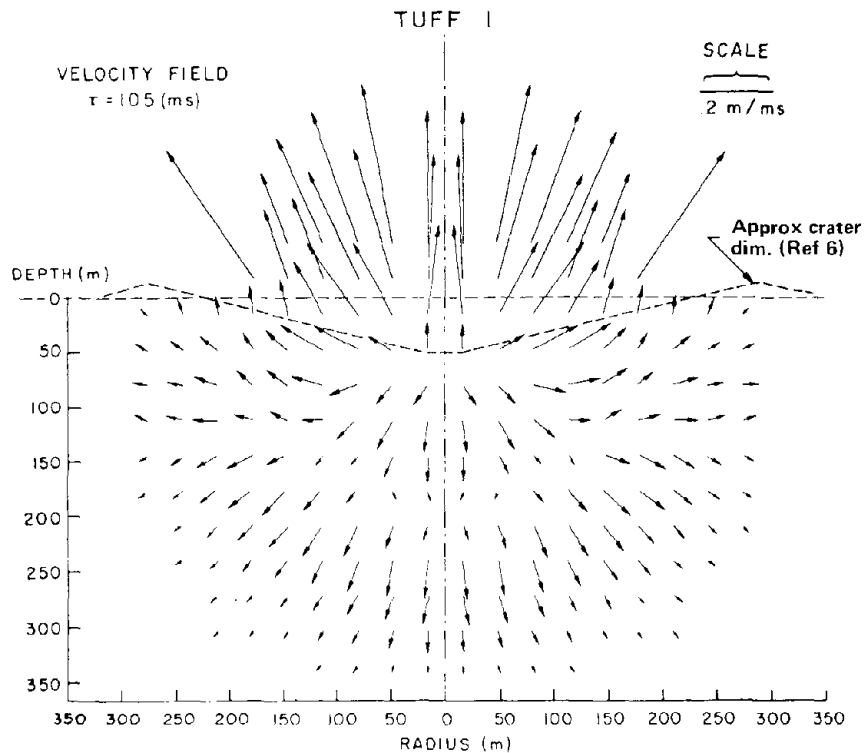
Figure IV-3.50.   Computed particle velocity field at 0.1 second
resulting from a 1-MT surface burst (Reference
IV-3.4).

first published it was felt by some investigators that the differences in the re-
sults arose from the differences in the structure of the codes. As discussed
earlier, the ATI code (AFTON) has a formulation in which the rows are defined in a
Lagrangian grid while the columns are defined in an Eulerian grid. This has the
effect of making the ground surface a continuous Lagrange line which can distort
and will partially map out the boundaries of the crater. It was then suggested
that the requirement that the ground surface in the AFTON code be a continuous
Lagrange line precluded the formation of a crater lip and resulted in the subsequent
loss of mass from the calculated boundaries. Perhaps a more direct cause of the
discrepancies between these two calculations lies in the material property models
used in the two codes. The ATI calculation found peak stresses falling below 0.1
kbar within 90 feet from ground zero. In the SHI calculation, the stresses are
maintained above 0.1 kbar for distances exceeding 600 feet.

Several computations have been performed at PI to check calculational methods
against actual experimental results. The experiments calculated included the

DISTANT PLAIN 6 Event a 100-ton TNT surface tangent sphere on layered clay and sandy silt of the Watching Hill test range in Canada; the MINE UNDER Event (Reference IV-3.70), a 100-ton sphere of TNT supported two charge radii above Cedar City tonalite; and the Sierra Madera meteor impact crater in Texas (Reference IV-3.71). The Sierra Madera calculation was performed by assuming that the impact corresponded to approximately 1200 megatons of initial kinetic energy in the basalt of the Sierra Madera Caldera. Other calculations associated with nuclear events included TINY TOT and JOHNIE BOY. Each of the above nonnuclear events had a central uplifted or mound region. The physical explanations for each, although related, are unique.

The calculations were all performed with the PI ELK program, an Euler-Lagrange coupled finite-difference code. The operation of this code begins by defining the entire problem in an Eulerian grid. When the problem progresses to the point where the stress is no longer a scalar point function, the calculation is then dynamically coupled to an overlying Lagrange grid. Then the calculation is allowed to continue until most of the activity in the hydrodynamic (Eulerian) portion of the coupled grid has ceased. Subsequently, the problem is continued as a purely Lagrangian calculation. DISTANT PLAIN 6 produced a crater with a measured radius of about 40 feet. The maximum depth was about 17 feet with a 1½ foot central upthrust diminishing the crater depth below GZ to about 15.5 feet. Details of the calculations (Reference IV-3.72) of this event are shown in Figure IV-3.51. It appears that the flow leading to the central upthrust was initiated quite early in the calculation. Figure IV-3.52 shows the velocity vector field at 220 msec when most of the motion had nearly ceased. The upward flow on the central axis of the crater is quite apparent in the velocity vector field. The significant observation is that the occurrence of a central mound in the crater for the DISTANT PLAIN 6 Event is not necessarily associated with gravity-induced flow at late time. Gravitational forces were included in this calculation. Figure IV-3.53 shows the profile at 223 msec as predicted by the computations. In the experimental and the computational analysis, the soil ejecta is almost nonexistent. The computed maximum depth and shape at the crater bottom agreed with the experiment. However, the computed radius was about 80 percent of the value of the experimental radius.

The same flow pattern observed in the DISTANT PLAIN 6 calculation was again observed in the calculation of the MINE UNDER event. Details of the calculation can be found in Reference IV-3.70.
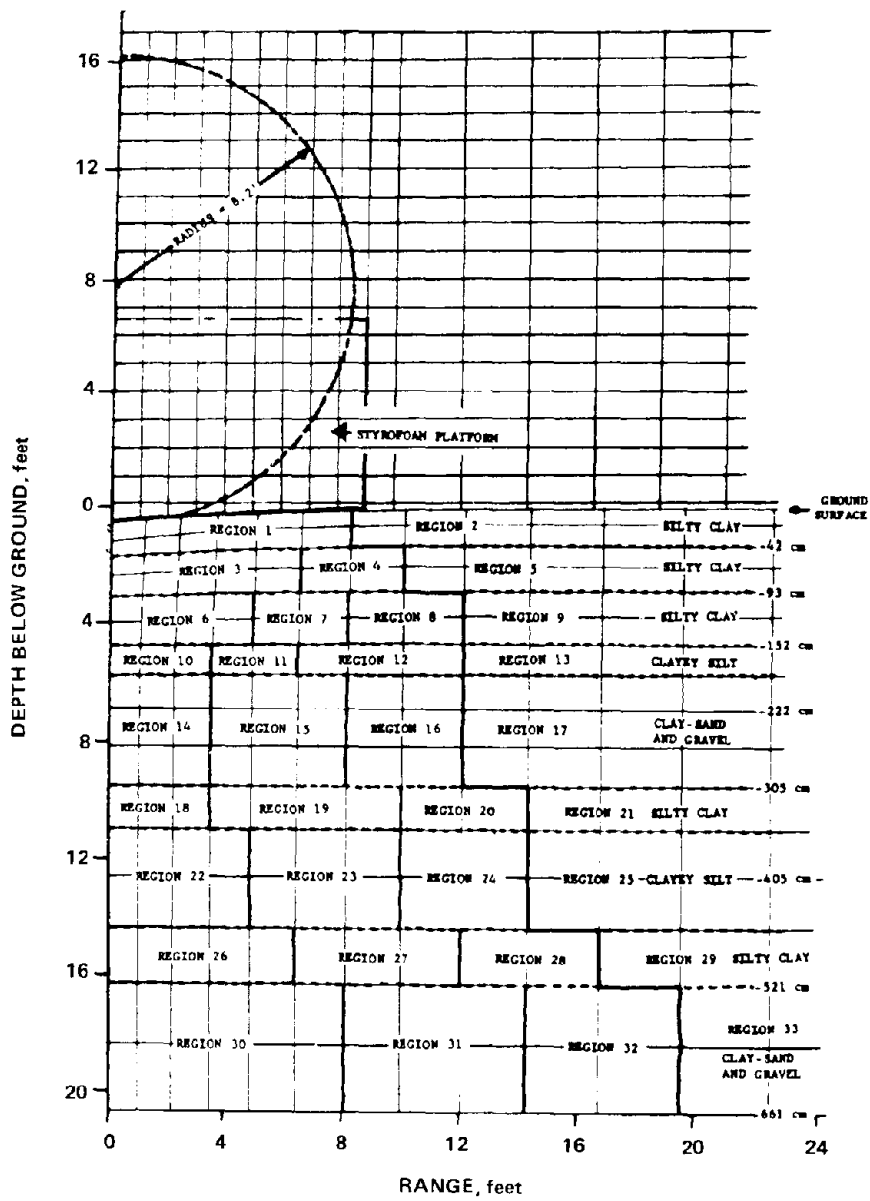
Figure IV-3.51. DISTANT PLAIN 6—theoretical calculation:
Euler-Lagrange grid at zero time.
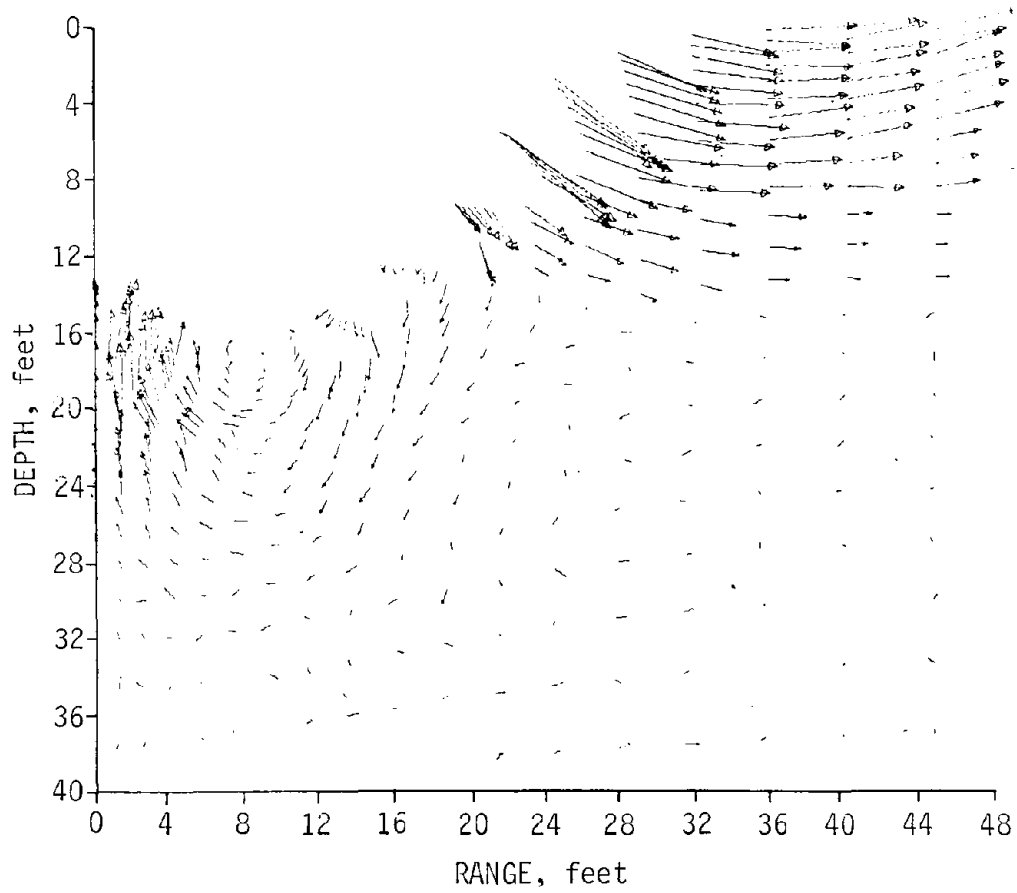
Figure IV-3.52.   DISTANT PLAIN 6—theoretical crater calculation:
velocity vectors at t = 220 msec.
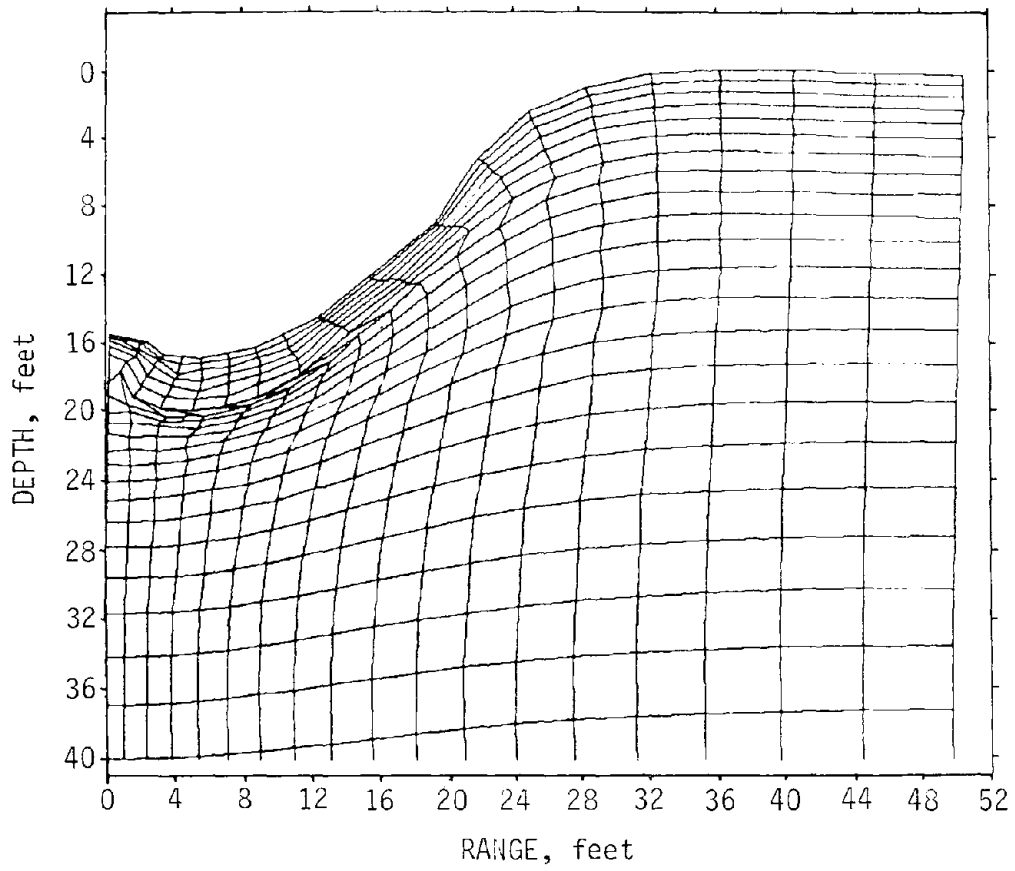
Figure IV-3.53. DISTANT PLAIN 6—theoretical crater calcu-
lation: Lagrange grid at t = 223 msec.

In the Sierra Madera calculation (Reference IV-3.71) substantial flow occurred
at great distances and for long periods of time, with the strength of jointed rock
being relatively unimportant compared to the gravity-induced overburden pressures
released by the crater excavation process. Because of severe weathering, gross
assumptions as to the production mechanism of this crater were required. It was
assumed that an impacting spherical meteor with a radius of 100 meters and an impact
velocity of 30 km/sec was responsible for the crater. The kinetic energy was equiv-
alent to a nuclear detonation having a yield of 1200 MT. The calculated particle
trajectories indicated a vortex flow field similar to that of Figure IV-3.52. The
calculated crater exhibits the principal features of the Sierra Madera structure
with a well-developed central uplift region and a surrounding ring depression
(Figure IV-3.54). The computed magnitudes (Figure IV-3.55) of the physical features
are smaller than might be inferred from the eroded surface structural features of
the Sierra Madera, suggesting either that the actual impact energy may have been
somewhat larger than the value assumed for the calculations or, just as likely, that
the equation of state used in the calculation was in error. The pertinent conclu-
sion is that the central mound had its origin in the release of lithostatic stresses
causing material to flow toward the crater axis.
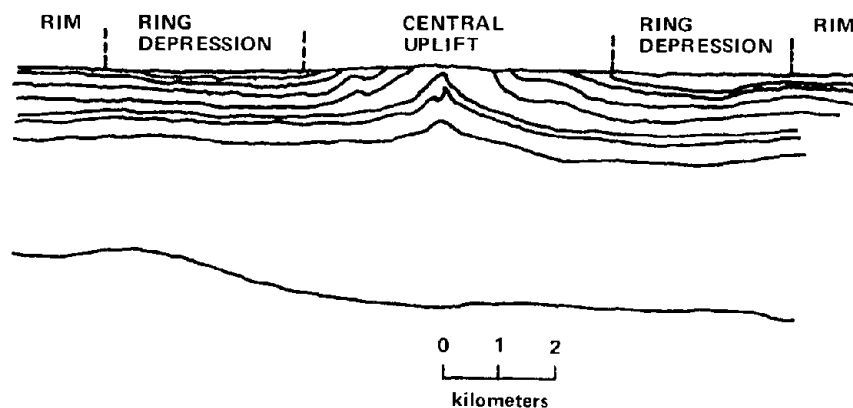
Figure IV-3.54. Geologic cross section of the Sierra Madera
                 Caldera showing the ring depression around
                 the central uplift.

IV-3-109
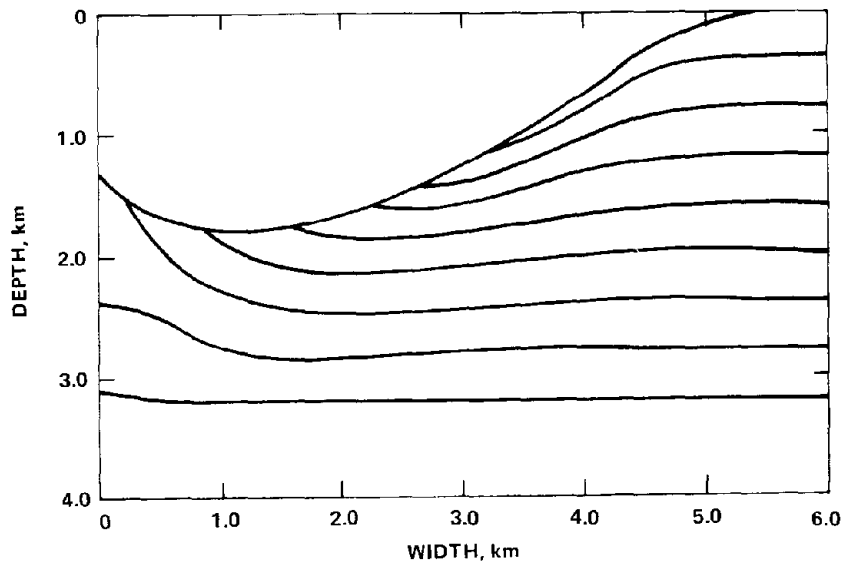
Figure IV-3.55.   Computed crater profile of the Sierra
Madera meteor impact event.

It should also be remarked that the velocity gauges implanted on the PRAIRIE
FLAT Event, a 500-ton TNT explosion conducted under identical conditions as the
DISTANT PLAIN 6 experiment, show a gross inward motion fairly early in the time
history of the event (Reference IV-3.72).   Such inward motion decreases slightly
with decreasing depth of the gauge.   This is suggestive of the gravitational stress
relief flow presumed for the Sierra Madera crater.   One may surmise that the flow
field initiated early in the DISTANT PLAIN 6 Event is not the full story in the
creation of the central mound.

Ullrich (Reference IV-3.73) performed a series of numerical simulations of
ground response to a HE detonation to examine the influence of material models on
calculated central-peak formation in shock-produced craters.   One simulation of the
20-ton HE detonation MIXED COMPANY II showed that computed motions at 16.4 msec,
when ballistically extrapolated, were consistent with the observed crater and forma-
tion of the central mound.   Compaction, layering, and material yield models were
varied in additional numerical simulations.   The results indicated that the occur-
rence of a central mound is primarily dependent on material properties of the medium.

IV-3.4.4   Summary of Calculations of Explosive and Impact Craters

Computations and investigations of craters from deeply buried bursts have
demonstrated the physical process first postulated by Nordyke.   These are compaction

and plastic flow, spall, and gas acceleration. Material properties in order of
decreasing significance to the cratering process are water content, shear strength,
porosity and compressibility. The role played by the ground water is to reduce the
shear strength of the material, increase the material density and sound velocity,
and in the case of underground nuclear explosions increase the mass of noncondens-
able gases in the expanding cavity, thus enhancing the gas acceleration phase. This
is closely associated with the constitutive properties of the material (see Volume
II of this Handbook). The calculations of craters from deeply buried explosions
have been sponsored by the DOE at LLL through the PLOWSHARE program. The primary
computational tool in this work has been a two-dimensional Lagrangian formulation
code named TENSOR.

Calculations of surface and near-surface burst events have been sponsored by the
Defense Nuclear Agency (DNA). The computer codes used have included Eulerian and
Lagrangian formulations. In some cases these are used separately and in other cases
they are coupled in the same calculation. The need for major improvements in the
calculation of explosion- and impact-produced craters appears to be in the defini-
tion of the equation of state of the material. In all of the existing codes the
mass, the momentum, and the energy are conserved. The precise formulation of the
finite difference coding scheme, that is, Eulerian or Lagrangian, or a combination
of these two, determines the precision and the computer resource requirements for
the particular problem. Conversely, a particular problem may determine the formu-
lations to be used for the most efficient solution of that problem. Table IV-3.12
is a compilation of two-dimensional, finite difference codes currently employed in
cratering and ground motion calculations. Because of the great proliferation of
one-dimensional codes, they have not been included in this list. Neglect of any
significant two-dimensional code is inadvertent and not intended as a judgment
against them. The PIC-type codes (one of which was used by Brode and Bjork) are
used primarily for incompressible, fluid flow calculations and are no longer exten-
sively used in cratering and ground motion calculations. For these reasons they
are not included in the table. MIDDLE GUST and MIXED COMPANY calculations showed
comparisons between the AFTON, TOODY, LAYER, and SHEP codes and a small DISPL code.
Ground motion and crater calculations were in better agreement with each other than
with the data.

Table IV-3.12. Two-dimensional, finite difference codes in use for ground motion and cratering calculations.

Code Name	Types of Calculations	Source
CSQ	Eulerian; hydrodynamic-elastic-plastic	Sandia
HELP	Eulerian; hydrodynamic-elastic-plastic	SSS
OIL	Eulerian; hydrodynamic-elastic-plastic	General Atomic
OIL-RPM	Eulerian; hydrodynamic-"rigid plastic"	General Atomic
PISCES-2DE	Eulerian; hydrodynamic-elastic-plastic	PI
SHESAM	Eulerian; hydrodynamic-elastic-plastic	SHI
HEMP*	Lagrangian; hydrodynamic-elastic-plastic	LLL
LAYER	Lagrangian; hydrodynamic-elastic-plastic	PWA
PISCES-2DL	Lagrangian; hydrodynamic-elastic-plastic	PI
SHEP	Lagrangian; hydrodynamic-elastic-plastic	SHI
TENSOR	Lagrangian; hydrodynamic-elastic-plastic	LLL
TOODY	Lagrangian; hydrodynamic-elastic-plastic	Sandia
AFTON Series	Mixed Eulerian-Lagrangian; hydrodynamic-elastic-plastic	ATI
CEL	Coupled Eulerian-Lagrangian; hydrodynamic-elastic-plastic	LLL
ELK	Coupled Eulerian-Lagrangian; hydrodynamic-elastic-plastic	PI

*This code has been used primarily in impact studies; it is the forerunner of nearly all the existing two-dimensional Lagrangian codes.

IV-3.5 REFERENCES

IV-3.1 Pokrovskii, G. I., and I. S. Federov, Action of Shock and Explosion in Deformable Media, Moscow State Publisher of Literature on Construction Materials, Moscow, 1957; translated by S. Shewchuck, Library of Congress, NOS. QA935; p. 585.

IV-3.2 Nordyke, M. D., "Cratering Experience with Chemical and Nuclear Explosives," Proceedings of the Third PLOWSHARE Symposium on Engineering with Nuclear Explosives, Lawrence Livermore Laboratory, TID 7695, April 1964.

IV-3.3 Vortman, L., Sandia Laboratories, Personal Communication, June 1976.

IV-3.4 Brode, H. L., and R. L. Bjork, "Cratering from a Megaton Surface Burst," Proceedings of the Geophysical Laboratory-Lawrence Radiation Laboratory Cratering Symposium, UCRL-6438, Part II, March 1961.

IV-3.5 Christensen, D. M., C. S. Godfrey, and D. E. Maxwell, Calculations and Model Experiments to Predict Crater Dimensions and Free-Field Motion, Physics International Company, San Leandro, California, PIFR-072, September 1968.

IV-3.6 Brode, H. L., "Review of Nuclear Weapons Effects," Annual Review of Nuclear Science, Vol. 18, 1968.

IV-3.7 Maxwell, D., J. Reaugh, and B. Gerber, JOHNIE BOY Crater Calculations, Physics International Company, San Leandro, California, PIFR-365, DNA-3048F, April 1973.

IV-3.8 Alekseyenko, V. D., "Experimental Investigation of the Energy Distribution in a Contact Explosion," Fiz. Goreniya i Veryva, Vd. 3, pp. 152-155, 1967.

IV-3.9 Nordyke, M. D., "An Analysis of Cratering Data from Desert Alluvium," Journal of Geophysical Research, Vol. 67, p. 1965, 1962.

IV-3.10 Orphal, D. L., Cavity Collapse, Chimney Growth, and the Time Interval from Detonation of an Underground Nuclear Explosion to Formation of the Subsidence Crater, Environmental Research Corporation Report (Unpublished).

IV-3.11 Videon, F., Project SULKY: Crater Measurements, U.S. Army Engineer Nuclear Cratering Group, Lawrence Radiation Laboratory, Livermore, California, Final Report PNE-713F, October 1965.

IV-3.12 Roddy, D. J., "Geological Survey Activities, Project LN303," Operation PRAIRIE FLAT Preliminary Report, Vol. 1, January 1969.

IV-3.13 Couch, R. F., et al., Drilling Operations on Enewetak Atoll During Project EXPOE, Air Force Weapons Laboratory, AFWL-TR-75-216, 1975.

IV-3.14 Cicero, L. J., Nuclear Cratering Experience at the Pacific Proving Ground, Lawrence Berkeley Laboratory, UCRL 12172, November 1964.

IV-3.15 Nordyke, M. D., and M. M. Williamson, The SEDAN Event, Lawrence Livermore Laboratory, Livermore, California, PNE-242Γ, April 1965.

IV-3.16 Myasnikove, K. V., L. B. Prozorov, and I. E. Sitnikov, "Mechanical Effects of Single and Multiple Underground Nuclear Cratering Explosions and the Properties of the Excavations Dug by Them," Nuclear Explosions for Peaceful Purposes, Lawrence Berkeley Laboratory, Berkeley, California, Atomizdat Moscow, UCRL-Trans-10517, 1970.

IV-3.17 Tewes, H. A., "Results of the SCHOONER Excavation Experiment," Proceedings of the Symposium on Engineering with Nuclear Explosives, ANS Publication (Unpublished).

IV-3.18 Rooke, A. D., Jr., B. L. Carnes, and L. K. Davis, Cratering by Explosions: A Compendium and an Analysis, Waterways Experiment Station, Technical Report N-74-1, January 1974.

IV-3.19 Davis, L. K., MINE SHAFT Series, Events MINE UNDER and MINE ORE, Subtask N-121, Crater Investigations, Waterways Experiment Station, Report TR-N-70-8, March 1970.

IV-3.20 Davis, L. K., FERRIS WHEEL Series, FLAT TOP Event, Crater Measurements, Waterways Experiment Station, Report POR-3008, 9 August 1966.

IV-3.21 Carnes, B. L., and J. A. Conway, Event MINE THROW I: Cratering Effects of a Multiton Near-Surface Detonation in Desert Alluvium, U.S. Army Engineer Waterways Experiment Station, Vicksburg, Mississippi, Technical Report N-73-3, May 1973.

IV-3.22 Lamping, N. E., A Determination of the Geologic Effects on Nuclear Crater Formation by High Explosive Simulation Technique, M.S. Thesis, Air University, Maxwell Air Force Base, Alabama, May 1974.

IV-3.23 Rooke, A. D., Jr., ESSEX-DIAMOND ORE Research Program; True Crater and Permanent Displacement Measurements Associated with Simulated Low-Yield Nuclear Explosions, U.S. Army Engineer Waterways Experiment Station, Vicksburg, Mississippi, Report No. WES MP N-75-5, July 1975.

IV-3.24 Harvey, W. T., Summary Report, ESSEX I, Phase 1: Nuclear Cratering Simulation, U.S. Army Engineer Waterways Experiment Station - Explosive Excavation Research Laboratory, Livermore, California, Report No. WES TR-E-75-3 (Unpublished).

IV-3.25 Vortman, L. J., and J. A. Beyeler, Results of Ground Motion and Airblast Measurements, Project ESSEX I, Phase 1, Vol. 1, pp. 47, 94, 124, and 159, Sandia Laboratories, Albuquerque, New Mexico, Report No. SLA-73-0918, November 1974.

IV-3.26 Rooke, A. D., Jr., ESSEX-DIAMOND ORE Research Program; True Crater and Permanent Displacement Measurements for Simulated Low-Yield Nuclear Explosions, Phase 2, U.S. Army Engineer Waterways Experiment Station, Vicksburg, Mississippi, Report No. WES MP N-76-1, February 1976.

IV-3.27 Carlson, R. H. High Explosive Cratering from Linear Charges, Sandia Corporation, SC-4483, July 1961.

IV-3.28 Toman, J., "Project BUGGY: A Nuclear Row-Excavating Experiment," Nuclear Applications and Technology, Vol. 7, pp. 243-252, 1969.

IV-3.29 Vortman, L. J., "Ten Years of High Explosive Cratering Research at Sandia Laboratory," Nuclear Applications and Technology, Vol. 7, pp. 11 269-304, 1969.

IV-3.30 Redpath, B. B., "A Concept of Row Crater Enhancement," Proceedings of the Symposium on Engineering with Nuclear Explosives, ANS Publication (Unpublished).

IV-3.31 Rodean, H. C., Nuclear-Explosion Seismology, Lawrence Livermore Laboratory, TID-25572, September 1971.

IV-3.32 Nakano, H., "On Rayleigh Waves," Jap. J. Astr. Geophys., Vol. 2, p. 233, 1925.

IV-3.33 Vortman, L. J., Craters from Repeated Direct Hits at the Same Aiming Points, Sandia Laboratories, Albuquerque, New Mexico, Report Number SC-4760 (RR), January 1963.

IV-3.34 Strange, J. N., and A. D. Rooke, Jr., Craters Resulting from Repeated Explosions along a Common Vertical Axis, U.S. Army Engineer Waterways Experiment Station, Vicksburg, Mississippi, Technical Report No. I-665, November 1964.

IV-3.35 O'Brien, T. E., J. E. Seknicka, R. H. Carlson, and G. D. Jones, Multiple Threat Cratering Experiment, Vol I—Successive Cratering in Hard Rock, Air Force Weapons Laboratory, Report AFWL-TR-76-8, Vol. I, April 1967.

IV-3.36 Chew, T. D., A. D. Rooke, Jr., L. W. Pitman, A Small-Scale Study of Craters Resulting from Repeated Explosions Along a Common Vertical Axis, U.S. Army Engineer Waterways Experiment Station, Vicksburg, Mississippi, Report. No. Miscellaneous Paper N-68-1, September 1968.

IV-3.37 Stephanson, D. E., and L. E. Hooks, Repeated Cratering Experiments: Data and Analysis, Air Force Weapons Laboratory AFWL-TR-73-102, February 1974.

IV-3.38 Vaile, R. B., Jr., "Pacific Craters and Scaling Laws," Journal of Geophysical Research, Vol. 66, pp. 3413-3438, 1961

IV-3.39 Chabai, A. J., and D. M. Hankins, Gravity Scaling Laws for Explosion Craters, Sandia Laboratories, Albuquerque, New Mexico, Report No. SC 4541 (RR), December 1960.

IV-3.40 Chabai, A. J., Crater Scaling Laws for Desert Alluvium, Sandia Laboratories, Albuquerque, New Mexico, Report No. SC 4391 (RR), December 1960.

IV-3.41 Vortman, L. J., "Craters from Surface Explosions and Scaling Laws," Journal of Geophysical Research, Vol. 73, pp. 4621-4636, 1968.

IV-3.42 Dillon, L. A., The Influence of Soil and Rock Properties on the Dimensions of Explosion-Produced Craters, AFWL-TR-71-144, Air Force Weapons Laboratory, February 1972.

IV-3.43 Sedov, L. I., Similarity and Dimensional Methods in Mechanics, Fourth Russian Edition, M. Friedman, editor, Academic Press, New York, New York, 1959.

IV-3.44 Chabai, A. J., "On Scaling Dimensions of Craters Produced by Buried Explosives," Journal of Geophysical Research, Vol. 70, pp. 5075-5098, 1965.

IV-3.45 Westine, P. S., "Explosive Cratering," J. Terramech., Vol. 7, pp. 9-19, 1970.

IV-3.46 Saxe, M. C., and D. D. Del Manzo, Jr., "A Study of Underground Explosion Phenomena in Desert Alluvium," Proceedings of the Symposium on Engineering with Nuclear Explosives, ANS Publication (Unpublished).

IV-3.47 Viktorov, V. V., and R. D. Stepanov, "Modeling of the Action of an Explosion with Concentrated Charges in Uniform (Homogeneous) Ground," Engineering Collection of the Institute of Mechanics of the Academy of Sciences of the USSR XXVIII, Sandia Corporation Translation SC-T-392, pp. 87-95, 1960 (out of print).

IV-3.48 White, J. W., "Examination of Cratering Formulas and Scaling Methods," Journal of Geophysical Research, Vol. 76, No. 35, pp. 8599-8603, 1971.

IV-3.49 White, J. W., "An Empirically Derived Cratering Formula," Journal of Geophysical Research, Vol. 78, No. 35, pp. 8623-8633, 1973.

IV-3.50 Johnson, S. W., et al., "Gravity and Atmospheric Pressure Scaling Equations for Small Explosions Craters in Sand," Proceedings of the Working Group on Extraterrestrial Resources, NASA SP-177, February 1968.

IV-3.51 Perret, W. R., et al., Project SCOOTER, Sandia Corporation, Sandia, New Mexico, SC-4602, October 1963.

IV-3.52 Herr, R. W., Effects of the Atmospheric-Lithostatic Pressure Ratio on Explosive Craters in Dry Soil, NASA-Langley Research Center Report, NASA TR R-366, September 1971.

IV-3.53 Rodionov, V. N., Methods of Modeling Ejection with Consideration of the Force of Gravity, USSR State Committee on the Uses of Atomic Energy, Moscow, Lawrence Radiation Laboratory Translation, UCRL-Trans-10476, 1970.

IV-3.54 Piekutowski, A. J., Laboratory-Scale High-Explosive Cratering and Ejecta Phenomenology Studies, Air Force Weapons Laboratory, AFWL-TR-72-155, April 1974.

IV-3.55 Piekutowski, A. J., The Effects of Variations in Test Media Density on Crater Dimensions and Ejecta Distributions, Air Force Weapons Laboratory, AFWL-TR-74-326, April 1975.

IV-3.56 Piekutowski, A. J., A Comparison of Cratering Effects for Lead Azide and PETN Explosive Charges, Air Force Weapons Laboratory, AFWL-TR-74-182, May 1975.

IV-3.57 Piekutowski, A. J., <u>The Effect of a Layered Medium on Apparent Crater Dimensions and Ejecta Distribution in Laboratory-Scale Cratering Experiments</u>, Air Force Weapons Laboratory, AFWL-TR-75-212, December 1975.

IV-3.58 Piekutowski, A. J., <u>A Summary of Four Laboratory-Scale High-Explosive Cratering Parametric Sensitivity Studies</u>, Air Force Weapons Laboratory, AFWL-TR-75-211, December 1975.

IV-3.59 Strange, J. N., <u>Effects of a Soil-Rock Interface on Cratering</u>, U.S. Army Engineer Waterways Experiment Station, Vicksburg, Mississippi, Report Numbers 2-498 and AFSWP-1056, May 1958.

IV-3.60 Vesic, A. S., N. M. F. Ismael, and K. Bhushan, <u>Cratering in Layered Media</u>, U.S. Army Engineer Waterways Experiment Station, Explosive Excavation Research Laboratory, Livermore, California, Technical Report No. E-72-31, December 1972.

IV-3.61 Stephenson, D., <u>Small-Scale Cratering Studies in Sand/Clay Soil</u>, Air Force Weapons Laboratory, AFWL-TR-73-99, August 1975.

IV-3.62 Fulmer, C. V., <u>Cratering Characteristics of Wet and Dry Sand</u>, The Boeing Company, Seattle, Washington, October 1965.

IV-3.63 Scipio, L. A., <u>Principles of Continua with Applications</u>, John Wiley and Sons, Inc., New York, 1967.

IV-3.64 Sadovskii, M. A., et al., "A Method of Modeling Large Cratering Explosions," <u>Fiz. Goreniya i Vzryva, Vol. 3</u>, pp. 119-127.

IV-3.65 Fung, Y. C., <u>Foundations of Solid Mechanics</u>, Prentice-Hall Publishing Company, New York, New York, 1965.

IV-3.66 Noh, W. F., <u>CEL: A Time Dependent, Two Space Dimensional Coupled Eulerian-Lagrange Code</u>, Lawrence Radiation Laboratory Report UCRL-7463, August 1963.

IV-3.67 Butkovich, T. R., <u>The Gas Equation of State for Natural Materials</u>, UCRL-14729, January 1967.

IV-3.68 Terhune, R. W., T. F. Stubbs, and J. T. Cherry, "Nuclear Cratering on a Digital Computer," <u>Proceedings of the Symposium on Engineering with Nuclear Explosives</u>, ANS Publication (Unpublished).

IV-3.69 Glasstone, S. (editor), The Effects of Nuclear Weapons, USAEC Publication, Revised Edition, February 1964, U.S. Government Printing Office.

IV-3.70 Maxwell D., and H. Moises, Prediction Calculation of MINE UNDER and MINE ORE, DASA-2526, June 1970.

IV-3.71 Maxwell, D. E., and H. Moises, Hypervelocity Impact Cratering Calculations, Physics International Company, San Leandro, California, PIFR-190, February 1971.

IV.3-72 Hoffman, H. V., F. M. Sauer, and B. Barclay, Operation PRAIRIE FLAT, Project Officer's Report - Project LN-308, Strong Ground Shock Measurements, Stanford Research Institute, POR 2108 (WT-2108), April 1971.

IV-3.73 Ullrich, G. W., The Mechanics of Central Peak Formation in Shock Wave Cratering Events, Air Force Weapons Laboratory, AFWL-TR-75-88, May 1976.

APPENDIX IV-3A

OVERVIEW OF METEOR-PRODUCED CRATERS

This Appendix briefly discusses craters produced by meteor impact on the earth and on the moon. It introduces the reader to the relationship between explosively formed craters and craters produced by meteor impact or other crater formation methods. The field of meteor impact is extensive and the author did not have at his disposal extensive references; this overview is perforce rather narrow. For example, craters produced by the impact of hypervelocity projectiles into metallic or other target materials will not be discussed.

This Appendix briefly reviews the papers presented at the Geophysical Laboratory/Lawrence Radiation Laboratory (now LLL) Cratering Symposium held in 1961 (Reference IV-3A.1) and then proceeds to several recent papers from the Journal of Geophysical Research. Finally, as a matter of completeness and interest a new approach to cratering studies using laser techniques is presented.

At the cratering symposium, Shoemaker and Eggleton discussed the terrestrial features originating from meteor impact (Reference IV-3A.1). Craters produced by meteor are now known from eleven widely-scattered regions in the world. Most of these craters and their meteoritic origin were discovered and documented from about 1930 to 1950. Some of these craters were discovered in the course of geologic mapping and some by aerial photography. The formation by a meteor of the Sikhote'-Aline craters in the USSR was witnessed in 1947. Studies of the size distribution of craters indicate that during any given period of time the small craters far outnumber the large ones. However, the smaller the crater the quicker it is buried or eroded away. Therefore, there is a selective attrition of smaller craters with time. It follows that recent impact craters will be predominantly small, whereas most of the ancient features preserved and exposed will be from comparatively large craters.

Shoemaker and Eggleton gave particular attention to geological evidence for discriminating meteorite craters from craters formed by other structural processes. The major known meteorite craters are briefly described, as are other craters that on the basis of less conclusive evidence are considered probable or possible meteorite craters. Separate tabulations are given of topographic features either known to be meteor craters or considered as possible meteor craters through lack

of conclusive evidence to the contrary, and of topographic features once considered to be possible meteor impact craters but which are now believed to be of other origin.

At the same symposium (Reference IV-3A.1) Shoemaker and Chao presented new evidence for the impact origin of the Ries Basin, Bavaria, Germany. The Ries Basin is a shallow, nearly circular depression about 17 miles in diameter lying between the Schwäbian and Fränken plateaus of Southern Germany. Great masses of breccia and a system of thrust sheets associated with the Ries Basin have been studied by German geologists for approximately one century. Some investigators have suggested the Ries to be an impact crater while others have suggested that the basin was formed by some sort of volcanic explosion. Shoemaker and Chao analyzed the evidence of magnetic activity and concluded from an examination of the local breccia, called suevit, that the occurrence of the same phases in sintered rock fragments at Meteor Crater, Arizona suggests that the glassy components of suevit are of impact rather than volcanic origin.

Beals and Innes (Reference IV-3A.1) have conducted studies of Canadian aerial photographs that revealed the presence of three hitherto unexplained circular depressions with geographic locations and dimensions as follows: Holleford, Ontario, diameter 7700 ft, depth 100 ft; Bent, Ontario, diameter 12,000 ft, depth 300 ft; Deep Bay, Saskatchewan, diameter 40,000 ft, depth 700 ft. Gravity, geo-magnetic, and seismic observations have indicated the presence under the three craters of circular volumes of rock from several hundred to several thousand feet thick, of lower density, lower magnetic susceptibility, and lower seismic velocity than the surrounding rock. Diamond drilling at Holleford and Bent has identified this material as partly sedimentary but mainly re-cemented breccia assumed to be due to meteorite impact and explosion. Deep Bay has not yet been drilled, but the geophysical evidence leaves little doubt that the origin of this crater is also due to meteorite impact. Geological evidence indicates that the craters at Bent and Holleford are of Precambrian or early Paleozoic age (2 to 5 x 10^8 years ago), while the Deep Bay crater is of Mesozoic age (1.6 x 10^8 years ago). In addition to the three craters for which definite evidence points to meteorite impact, there have also been observed in Canada 15 or more additional circular features ranging in diameter from 3300 ft to 300 miles for which a meteorite impact origin has been considered as a possibility. Beals and Innes give the locations of these features together with brief descriptions containing available scientific information.

Evans performed investigations of Odessa meteor craters (Reference IV-3A.1) formed simultaneously by a meteoritic shower during the late Pleistocene time (less than 7×10^7 years ago). These craters consist of the main crater, which is 550 ft in average rim diameter and about 100 ft in maximum depth, and a second crater, 70 ft in diameter and 17 ft in depth. Three smaller, but poorly preserved, craters from 6 to 10 ft in depth are located near the main crater. These Odessa craters are located 10 miles southwest of the city of Odessa in Ector County, Texas, in the extreme southwestern part of the Llano Estacado. The main crater was nearly filled by post-impact deposits, and the other craters were completely filled. Extensive excavations and test drilling resulted in the discovery of the previously unknown smaller craters, and in the accumulation of a large body of detailed information concerning the dimensions and characteristics of the several craters. Maps of the main crater and the 70-ft diameter crater have been drawn within close limits of accuracy. These maps, along with other illustrations and a brief discussion of the history of the investigations, geology, and the more interesting crater features are presented in Evans' paper.

Bjork (Reference IV-3A.1) performed a theoretical study of the cratering process accompanying the impact of a 12,000-ton iron projectile on a semi-infinite half-space of soft rock at a velocity of 30 km/sec. The soft rock constituents and impact velocity approximated those involved in the formation of Meteor Crater in Arizona. The assumption was made that the process is hydrodynamic in nature, since the pressures generated greatly exceeded the strengths of the materials. At these high pressures the compressibilities of the materials must be taken into account. The motion was solved numerically and graphs showing details of the motion were presented. Although Bjork's paper was preliminary, he concluded that the meteor had a mass between 30,000 and 194,000 tons, the range being due to the uncertainty in the impact velocity.

Shoemaker presented (Reference IV-3A.1) an analysis of the ballistics and ejecta for the lunar crater Copernicus. He stated that discrimination between lunar craters of impact origin and volcanic origin may be possible on the basis of the distribution pattern of the ejecta, a feature that is also observable on earth. The ejecta from a maar type of volcano (a volcano whose crater resembles lunar craters) are almost invariably thrown out along high-angle trajectories, and shower down in a diffuse, more or less uniform, pattern around the crater. Ejecta from large impact craters, on the other hand, are expected (by analogy with

nuclear explosion craters) to be thrown out along high and low trajectories, having a pattern containing distinct streaks or rays. From the ray pattern and the ballistic trajectories of the fragments that form the rays it is possible to reconstruct the fragmentation pattern of the ground (the interior ballistics of crater formation).

Öpik also presented his theory of impact craters (Reference IV-3A.1). He pointed out that despite similarities between terrestrial explosion and meteorite impact in the formation of craters, there is a basic difference. This difference is that the terrestrial explosion is the result of a gaseous expansion without initial translational motion, whereas in meteorite impact the primary agent that produces the crater is the translational motion of the impacting body. The action of the expanding detonation gases is similar in both cases but the mass involved in the formation of an impact crater is not simply proportional to the kinetic energy of the projectile. He states that there is no direct way of applying quantitative results of explosions to meteorite impact, although the geometry of the craters may be similar. There is another difference, minor in import, between the two types of craters, namely in the spatial and temporal distribution of the source of the shock due to the motion of the projectile compared with the fixed position of the explosive charge. For given materials the volume efficiency of impact cratering is mainly proportional to the momentum of the projectile and not to its kinetic energy. Öpik presents a simplified impact cratering model and its application to known craters and compares these results with calculations performed by others. From his model, and from independent consideration of the size of surviving fragments, and consistent values of mass and velocity of the Canyon Diablo meteorite, he obtained values of 2×10^6 tons and 15 km/sec, respectively. The close order of magnitude of these estimates is further supported by the agreement between predicted and observed numbers of craters in Mare Imbrium. In 1971, Öpik published an extensive review article treating all aspects of lunar cratering and related topics (Reference IV-3A.2).

Gault and others (Reference IV-3A.3) published a paper dealing with some comparisons of impact craters on Mercury and the Moon. They stated that the morphologies of these craters are remarkably similar, although comparisons of ejecta deposition, interior structure, and changes in morphology with size reveal important differences between these two crater populations. These differences are attributable to the different gravity fields in which the craters were formed and have significant implications for the interpretation of cratering processes.

For lunar craters, two mechanisms—the base surge and the ballistic transport—have been proposed by Oberbeck for transport of crater ejecta (Reference IV-3A.4). Formation of base surges associated with underwater and underground explosion craters and with volcanic events all require the presence of an atmosphere in the area where ejecta impacts. Ejecta impacts and mixes with the air to form an aerosol cloud carrying the dust outward and deposits this dust on preexisting terrain. Because the moon has no appreciable atmosphere, Oberbeck concludes that the base surge mechanism of separation and transport of fine-grained ejecta is not a viable lunar process. Studies of laboratory impact craters, high-explosive and nuclear craters, and lunar craters, and theoretical studies of formation of impact craters indicate that material is ejected from impact craters at low angles to the surface. He then proceeds to develop a model of this cratering process including the formation of secondary craters produced by the ejecta. Considerable discussion is then devoted to the role of ballistic erosion and sedimentation due to these mechanisms and their effect on the lunar stratigraphy.

Focused laser radiation has been suggested as a possible method of investigating related physical phenomena of the cratering process under well-controlled laboratory conditions. The initial energy density in the deposition region or the energy coupled into the solid medium was identified as one of the important cratering parameters. Kuhl and Wuerker (Reference IV-3A.5) carried out an experimental investigation to determine the maximum energy density achievable by this method, as well as such other contributions as this technique might make to the understanding of the nuclear cratering problem. The technique consisted of depositing laser energy at a wavelength of 1.06 μm into a circular carbon foil target having a thickness of 1 μm and a diameter of 3 mm. This target was immersed in a transparent test medium (CCl_4/SiO_2 powder) having physical properties approximating that of wet sand. Breakdown of the medium caused by the formation of small vaporization centers was averted by maintaining the laser power flux below the critical value of 5×10^9 watts/cm^2. Initial deposition volumes were computed from photographs of the events. These results indicated that energy densities as high as 700 to 900 kilojoules/cm^3 were experimentally achieved. This compares to energy densities of 1 kilojoule/cm^3 for TNT explosions and 10 megajoules/cm^3 for nuclear detonations. Thus, Kuhl and Wuerker demonstrated that the laser deposition technique developed provides a feasible method of investigating certain physical phenomena of cratering together with the associated flow fields.

IV-3A   REFERENCES

IV-3A.1   Nordyke, M.D., ed., <u>Proceedings of the Geophysical Laboratory/Lawrence</u>
<u>Radiation Laboratory Cratering Symposium</u>, UCRL-6438, Parts I and II,
March 28-29, 1961.

IV-3A.2   Öpik, E.J., "Cratering and the Moon's Surface," in <u>Advances in Astronomy</u>
<u>and Astrophysics</u> (Z. Kopal, ed.), Vol. 8, Academic Press, 1971.

IV-3A.3   Gault, D.E., et al., "Some Comparisons of Impact Craters on Mercury and
the Moon," <u>Journal of Geophysical Research</u>, Vol. 80, No. 17, pp. 2444-2460,
1975.

IV-3A.4   Oberbeck, V.R., "The Role of Ballistic Erosion and Sedimentation in Lunar
Stratigraphy," <u>Rev. of Geophys. and Space Phys.</u>, Vol. 13, No. 2, pp. 337-
362, 1975.

IV-3A.5   Kuhl, A.L. and R.F. Wuerker, <u>Laser Cratering Research Technique</u>, TRW
Redondo Beach, California, Report No. DNA 3442F, September 1974.

APPENDIX IV-3B

TABULATION OF HIGH-EXPLOSIVE CRATER DATA

Table IV-3B.1 Single charges, surface bursts (soil).

Series Name	Designation	Sponsor	Date	Medium	Type of Ex-plosive	Charge Weight (lb)	Apparent Crater Radius (ft)	Apparent Crater Depth (ft)	Apparent Crater Volume (ft³)	Ref.	Re-marks
TOBOGGAN	E1a	Sandia Lab.	11/23/59	Yucca Flat Playa	TNT	8	1.88	0.91	2.33	B.1	
	E1b		11/23/59			8	1.47	0.67	1.76		
	E1c		11/24/59			8	1.31	0.05	1.54		
AIR VENT	III 1A		1/31/64	Frenchman Flat		64	3.41	1.57	24.02	B.2	
	III 1B		1/31/64	Playa		64	3.41	1.82	28.10		
	III 1C		1/31/64			64	3.26	1.81	22.79		
	III 1D		1/31/64			64	3.52	1.87	28.33		
	II 2A		1/30/64			256	5.54	2.39	95.46		
	II 2B		1/29/64			256	5.40	2.43	93.22		
	III 2A		1/11/64			1 000	9.36	4.27	442.0		
	III 2B		1/11/64			1 000	10.12	4.55	517.8		
	III 2C		1/13/64			1 000	8.92	4.27	440.0		
	III 3A		1/8/64			6 000	16.44	6.57	2 820		
	III 3B		1/9/64			6 000	17.52	9.91	2 703		
TTR 211-	51	Sandia Lab.	7/7/67	Playa (Tonopah Test Range)	TNT	64	3.62	1.55	25.7	B.3	
	52		8/10/67			1 000	9.38	4.14	399		
	53		1/9/68			64	3.21	1.46	20.3		
	56		4/20/68			1 000	9.66	4.78	593		
FLAT TOP	II	Sandia Lab.	2/17/64	Frenchman Flat Playa	TNT	40 000	35.8	12.9	24 030	B.4	
	III		3/24/64			40 000	38.80	18.6	37 800		
UNNAMED	11 through 20	SES*	1958-1959	Salt Drowning Ford	TNT	8	1.15	0.9	--	B.5	Average of 10 shots
	51 through 60	SES	1958-1959			60	2.51	2.2		B.5	Average of 10 shots
DISTANT PLAIN		SES	7/28/66			39 960	35.72	16.53	--	B.6	
SANDIA SERIES II		Sandia Lab	7/59 8/59	Alluvium (NTS Area 10)	TNT					B.7	
	S-12					256	8.57	2.49	161		
	S-13					256	8.34	2.60	267		
UNNAMED		Sandia Lab.	1960	Alluvium NTS	TNT	5 000	18.5	4.75	2 950		
DIAL PACK		SES	8/8/68	Silt	TNT	10⁶	100	16	2.5x10⁵	B.8	
PRAIRIE FLAT		SES	7/23/76	Drowning Ford	TNT	10⁶	105	15	3.1x10⁵	B.8	

*Suffield Experimental Station

Table IV-3B.2 Single charges, surface bursts (rock).

Series Name	Shot Designation	Sponsor	Date	Medium	Type of Ex-plosive	Charge Weight (lb)	Apparent Crater Radius (ft)	Apparent Crater Depth (ft)	Apparent Crater Volume (ft³)	Ref.	Re-marks
FLAT TOP	1	DNA*	6/22/64	Limestone (NTS)	TNT	40 000	27	12.7	10 000	B.4	
MULTIPLE THREAT CRATERING EXPERIMENT	S1 (C1)	AFWL*	6/21/65	Basalt (Yakima Firing Center)		4 000	12.1	3.6	733	B.9	
	S2a		6/17/65			4 000	10.7	4.0	672		
	S3a		7/16/65			4 000	11.4	4.0	853		
	S4a		7/10/65			4 000	10.4	4.0	605		
	LS		7/8/65			16 000	18.7	5.6	3 650		
OSO	1	Boeing Co.	8/63	Argillite		64	3.3	1.4	36.2	B.13	
	2		8/63			64	4.7	1.6	55.8		
MINE SHAFT	MINE ORE	DNA	11/13/68	Granite	TNT	2x10⁵	23	5.9	5.9x10³	B.9	
	MINERAL ROCK	DNA	10/69	Granite	TNT	2x10⁵	31.5	8.5	8.1x10³	B.10	

*Formerly the Defense Atomic Agency (DASA), now the Defense Nuclear Agency (DNA).
*Air Force Weapons Laboratory

Table IV-3B.3 Single charges, buried bursts (alluvium).

Series Name	Shot Designation	Sponsor	Date	Medium	Type of Explosive	Charge Weight (lb)	Charge Burial Depth (ft)	Apparent Crater Radius (ft)	Apparent Crater Depth (ft)	Apparent Crater Volume (ft³)	Ref.
JANGLE HE	HE-1	DOD/SRI[a]	8/25/51	Alluvium (NTS Area 10)	TNT	2 560	2.05	18.50	6.70	2 010	B.11
	HE-2		9/3/51			40 000	5.13	39.00	15.00	35 000	
	HE-3		9/15/51			2 560	6.84	20.27	10.80	6 000	
	HE-4		9/9/51			2 560	-2.05	6.90	1.90	110	
	HE-5		9/31/51			2 560	4.10	19.40	7.50	4 000	
	HE-6		10/2/51			2 560	3.01	19.80	6.10	3 600	
	HE-7		10/4/51			2 560	2.60	19.00	6.70	3 300	
	HE-8		10/13/51		TNT	216	1.08	Not Measured			
					Pentolite	177	1.08	9.04	3.40	271	
	HE-9		10/14/51		TNT	216	0.84	8.30	4.00	270	
					Pentolite	177	0.84	8.76	3.50	255	
	HE-10		10/14/51		TNT	216	3.00	11.30	5.50	860	
					Pentolite	177	3.00	10.13	5.00	500	
MOLE	202	DNA/SRI[b]	9/14/52	Alluvium (NTS Area 10)	TNT	256	6.35	11.30	5.50	1 044.8	B.12
	203		9/19/52			256	3.18	8.35	3.95	355.6	
	204		10/4/52			256	1.65	9.45	2.60	363.6	
	205		10/8/52			256	0.83	9.05	2.05	299.8	
	206		10/11/52			256	0.00	6.35	1.70	129.3	
	207		10/15/52			256	-0.83	4.05	1.40	37.4	
	212		10/24/52			256	6.35	11.70	5.85	1 206.9	
	401		10/23/54			256	3.18	10.6	5.5	824.4	
	402		10/26/54			256	4.77	11.05	6.2	942.7	
	403		10/28/54			256	0.83	8.3	3.4	293.3	
	404		10/30/54			256	6.35	11.75	6.0	1 190.5	
	405		11/2/54			256	1.65	9.2	4.55	498.2	
	406		11/4/54			256	3.18	9.85	4.0	672.7	
SANDIA SERIES I	8	Sandia Lab	1/20/59	Alluvium (NTS Area 10)	TNT	256	6.35	13.13	7.30	1 489	B.7
	2		1/21/59			256	9.53	15.12	7.86	2 146	
	9		1/23/59			256	9.53	14.14	7.16	1 930	
	10		1/23/59			256	12.70	13.40	4.10	1 093	
	16		?			256	12.70	14.19	6.70	2 220	
	4		1/26/59			256	15.90	11.32	1.77	368	
	11		1/24/59			256	15.90	6.53	0.38	236	
	12		1/27/59			256	19.05	9.36	2.30	256	
	17		12/15/58 ?			256	19.05	5.68	1.70	55	
	15		12/16/58 ?			256	25.40	4.18	0.45	31	
SANDIA SERIES II		Sandia Lab	7/59 8/59	Alluvium (NTS Area 10)	TNT						B.7
	11					256	13.10	14.69	5.43	1 670	
	10					256	16.10	14.10	4.55	1 077	
	9					256	16.40	14.29	2.61	716	
	8					256	19.00	10.07	1.60	297	
	7					256	19.70	8.13	1.01	121	
	6					256	22.60	4.39	1.00	170	
	5					256	23.30	3.03	0.30	18	
	4					256	25.50	2.35	1.15	16	
	3					256	26.10	32.30	-1.03[c]	-1 187[c]	
	2					256	28.50	37.70	-0.83[c]	-1 079[c,d]	
	1					256	29.80	31.00	-0.63[c]	-584[c]	
STAGECOACH	1	Sandia Lab	3/15/60	Alluvium (NTS Area 10)	TNT	40 120	80.0	57.0	7.9	49 145	B.13
	2		3/19/60			40 240	17.1	50.5	23.6	83 650	
	3		3/25/60			40 070	34.2	58.6	29.2	144 600	
SCOOTER			10/13/60			987 410	125.0	153.8	74.5	2 642 000	B.14

[a] Department of Defense/Stanford Research Institute.
[b] Formerly Defense Atomic Support Agency (DASA) and Armed Forces Special Weapons Project (AFSWP)/Stanford Research Institute, now SRI International.
[c] Negative sign indicates formation of a raised surface mound.
[d] Cavity volume = 118.

Table IV-3B.3 (continued)

Series Name	Shot Designation	Sponsor	Date	Medium	Type of Explosive	Charge Weight (lb)	Charge Burial Depth (ft)	Apparent Crater Radius (ft)	Apparent Crater Depth (ft)	Apparent Crater Volume (ft³)	Ref.
ROWBOAT	7a	LLL[c]	6/26/61			278	14.9	22.1	2.9	Not given	B.15
	8a		6/28/61			278	14.9	28.7	2.5	Not given	
PRE-BUGGY	Test	NCG[f]		Alluvium (NTS Area 10)	Nitro-methane	1 017	15.0	22.7	10.9	--	B.16
	1		12/5/62			1 003	15.0	21.0	9.7	6 560	
	2		12/10/62			1 011	16.6	21.8	9.1	7 560	
	3		12/11/62			1 011	18.2	20.9	7.8	5 830	
	4		12/13/62			1 009	19.8	20.6	9.4	6 530	
	5		12/18/62			1 016	21.4	19.7	4.1	2 650	
	6		12/19/62			1 015	19 6	20.7	8.3	6 080	
PRE-BUGGY II	F1	NCG	8/6/63	Alluvium (NTS Area 5)	Nitro-methane	1 000	19.8	22.7	11.8	7 860	B.17
	F2	NCG	8/6/63		Nitro-methane	1 000	19.8	21.2	11.8	6 030	
	F3	NCG	8/6/63		TNT	950	18.5	21.1	11.0	6 950	
	F4	NCG	8/6/63		TNT	950	18.33	22.1	10.8	7 560	
209	209	Sandia Lab	1959	Alluvium (Albuquerque)	TNT	256	12.7	~17	3.8	945	B.18
LITTLE DITCH	III-0.5		6/8/60			256	3.17	10.1	4.5	643	B.19
	III-0.75		6/17/60			256	4.76	10.7	7.0	913	
	III-1.00		6/13/60			256	6.35	11.1	5.5	983	
	III-1.25		7/19/60			256	7.94	11.7	5.7	1 210	
	62-34		7/16/62			256	7.94	11.7	5.1	904	
	III-1.50		6/15/60			256	9.52	12.65	3.5	824	
	62-35		7/18/62			256	9.53	11.9	4.9	1 172	
	III-2.00a		7/26/60			256	12.7	11.6	2.8	550	
	III-2.00b		8/22/60			256	12.7	11.9	2.6	438	
	III-1.25b		8/8/60			256	7.94	11.4	5.2	1 139	
UNNAMED SERIES	C1		6/14/66			64	6	7.96	3.94	425	B.20
	C2		6/14/66			64	6	8.24	4.44	504	
	1		6/1/66			64	6	8.18	4.29	454	
	6-1		10/7/66			64	6	7.98	3.94	354	B.21
	7-1		10/11/66			64	7	7.71	3.21	318	
UNNAMED SERIES	8-1	Sandia Lab	10/18/66	Alluvium (Albuquerque)	TNT	64	7	8.36	3.97	513	B.21
	9-1		10/21/66			64	6	8.41	4.25	411	
	10-1		10/25/66			64	5	7.97	4.90	405	
	62-60		11/19/63			64	7	6.90	2.70	173	B.22
	62-62		11/26/63			64	7	7.40	2.05	182	
	62-64		12/2/63			64	7	6.90	2.05	162	
	Pad 1		9/11/67			256	6	9.01	4.50	517	
	Pad 2		9/22/67			64	6	8.85	3.70	388	
	Pad C		2/9/68			64	6	8.05	2.90	303	
	Pad D		5/15/68			64	6	8.31	3.44	338	
PRE-CAPSA	1		5/3/65			256	9.5	13.46	6.98	1 905	B.23
	2		5/6/65			256	9.5	12.82	6.72	1 783	B.23
CAPSA	1	Sandia Lab	8/16/66	Alluvium (Albuquerque)	TNT	1 000	15.0	18.82	7.10	4 045	B.18
	2		8/18/66			1 000	12.5	18.11	10.27	4 840	
	3		8/24/66			1 000	10.0	17.89	10.49	4 557	
	4		8/26/66			1 000	17.5	19.15	7.07	3 930	
	5		8/31/66			1 000	15.0	19.87	7.10	4 172	
	6		9/2/66			1 000	17.5	19.72	10.58	5 936	
	7		9/13/66			1 000	10.0	16.12	9.12	3 661	
	8		9/16/66			1 000	12.5	19.43	10.63	5 781	
	9		5/21/68			1 000	12.5	18.45	10.43	5 339	
	10		5/29/68		Nitro-methane	1 000	12.5	19.40	11.33	6 470	
	11		6/13/68		Comp B	30 478	47.9	57.03	28.74	121 746	
	12		7/25/68		Nitro-methane	977	12.5	19.89	9.44	5 737	
	13		7/25/68		Nitro-methane	981	15.0	19.33	9.65	5 182	

[c]Formerly Lawrence Radiation Laboratory (LRL).
[f]Nuclear Cratering Group.

Table IV-3B.4 Single charges, buried bursts (other soil).

Series Name	Shot Designation	Sponsor	Date	Medium	Type of Explosive	Charge Weight (lb)	Charge Burial Depth (ft)	Apparent Crater Radius (ft)	Apparent Crater Depth (ft)	Apparent Crater Volume (ft³)	Ref.
DUGWAY	101	DOD[a]		Dry Sand (Utah)	TNT	320	-3.5	4	0.5	--	B.24
	102		6/7/51			320	0	7.63	2.5	250	
	103		6/7/51			320	1.3	10.88	6	720	
	104					320	3.5	12	6.5	1 300	
	105		6/19/51			320	7.0	15.5	8.5	2 600	
	106		6/27/51			320	14.0	16.75	4.5	1 100	
	107					320	21.0	13.5	3.5	790	
	108		7/10/51			2 560	2.6	19	9.75	5 200	
	109					2 560	7.0	24.75	8.5	8 200	
	110		8/13/51			320	3.5	13	7.5	1 600	
	112		7/27/51			2 560	7.0	30	12	13 000	
	115		8/8/51			40 000	17.5	75	23	180 000	
	111					8	2.5	6	4	140	
	113					320	3.5	14	6.75	1 900	
	114					8	2.5	6	3.5	150	
	116					320	8.75	18.5	9	3 500	
	0.029A-15					8	2.5				
	0.04A-16					20	2.5				
	0.05A-17					40	2.5				
	301			Dry Clay (Utah)		320	-3.5	2.5	1	--	
	302		3/29/51			320	0	7.25	4	240	
	303		4/2/51			320	1.3	9	5.5	600	
	304		4/4/51			320	3.5	10.5	6	820	
	305		4/6/51			320	7.0	11.75	7	1 300	
	306		4/12/51			320	14.0	15	1	236	
	307		4/10/51			320	21.0	10	1	100	
	308		4/16/51			2 560	2.6	20	12	5 400	
	309		4/18/51			2 560	7.0	21.5	15.5	7 300	
	310		4/23/51			320	3.5	11	7	900	
	312		5/4/51			2 560	7.0	26	15	13 000	
	315		5/10/51			40 000	17.5	64	42	190 000	
	318					320 000	35.0	120	60	1 100 000	
	311					8	2.0	4	2.5	66	
	314					8	2.5	4.5	3	86	
	316					110	2.45	9	6	740	
	313					320	3.5	12.75	8	1 500	
	317					2 560	7.0	23	15.5	11 000	
	319			Dry Clay (Utah)		2 560	7.0	23	13.5	7 800	
	Dry Clay Symmetry Test			Dry Clay (Utah)		320	7.0	12.5	7	1 300	
	402		8/23/51	Wet Clay (Utah)		320	2.5	18.75	10	4 100	
	403		8/11/51			2 560	5.0	41.75	12.75	29 000	
	401					8	2.5	7	5	310	
	405					8	2.5	6	4.1	270	
	404		8/21/51			320	2.5	17.5	11.5	3 900	
MOLE	101	DNA/ SRI[b]	6/28/52	Dry Clay (Utah)	TNT	256	6.35	10.55	5.40	742.4	B.12
	102					256	3.18	10.25	6.4	810.4	
	102A		7/6/52			256	3.18	9.6	5.35	588.2	
	104		7/13/52			256	-0.83	5.4	1.47	60.2	
	105		7/17/52			256	6.35	10.80	5.80	856.7	
	106		7/19/52			256	1.65	9.1	6.2	538.2	
	107		8/20/52			256	0.00	6.6	3.9	232.1	
	301		9/15/53	Wet Sand (California)		256					
	302		9/18/53			256	3.18	20.0	6.2	3 387.4	
	304		9/23/53			256	4.77	19.5	6.6		
	305		9/26/53			256	1.65	16.1	6.3	2 070.0	
	306		10/8/53			256	0.83	13.1	3.8	1 375.3	
	307		10/10/53			256	0.00	12.9	4.7	1 317.2	
	308		10/13/53			256	-0.83	8.9	4.0	447.2	
	309		10/16/53			256	3.18	16.7	6.1	2 718.5	
	310		10/17/53			256	3.18	17.5	5.2	2 598.0	
	311		10/20/53	Moist Clay (California)		256	3.18	15.5	11.2	3 147.5	
	313		10/24/53			256	-0.83	6.1	3.4	163.3	
	312		10/22/53			256	3.18	17.5	9.1	3 345.3	

[a] Department of Defense/Stanford Research Institute.
[b] Formerly Defense Atomic Support Agency (DASA) and Armed Forces Special Weapons Project (AFSWP)/Stanford Research Institute, now SRI International.

Table IV-3B.5 Single charges, buried bursts (rock).

Series Name	Shot Designation	Sponsor	Date	Medium	Type of Ex-plosive	Charge Weight (lb)	Charge Burial Depth (ft)	Apparent Crater Radius (ft)	Apparent Crater Depth (ft)	Apparent Crater Volume (ft³)	Ref.
DUGWAY	501	DOD[a]		Limestone	TNT	320	6.6	11.2	9.1	–	B. 25
	502					320	2.5	8.3	3.9		
	601			Granite		320	-2.5	1.20	0 175		
	602					320	0.0	8.43	1.7		
	603					320	2.5	9.70	2.6		
	604					320	5.0	14.5	5.0		
	605					320	12.5	17.1	6.1		
	606					320	25.0	5.20	2.0		
	607					320	2.5	14.4	5.3		
	608					320	2.5	14.0	4.6		
	609					2 560	5.0	25.2	10.2		
	610					2 560	5.0	23.1	8.7		
	611					320	2.5	13.4	5.0		
	612					320	17.0	13.2	7.6		
	801			Sandstone		320	-2.5	0.0	0.0		
	802					320	0.0	5.6	2.3		
	809					1 080	3.75	19.0	8.6		
	812					2 560	5.0	23.3	11.0		
	813					10 000	7.9	39.4	16.1		
	815					40 000	12.5	70.5	26.9[b]	125 000	
	816					40 000	12.5	53.6	27.5[b]		
	817					320 000	25.0	94.8	47.0	512 000	
	818					320	2.5	17.5	6.0		
	819					320	2.5	15.6	6.5	1 440	
	803		11/13/51			320	2.5	11.6	4.8	810	
	804		10/31/51			320	5.0	14.0	2.04	1 440	
	805		11/6/51			320	12.5	9.3	14.9	1 190	
	807		4/15/52			320	2.5	14.3	5.1[b]	1 460	
	808		5/3/52			320	2.5	13.1	5.8	1 620	
	810		4/9/52			2 560	5.0	32.6	9.7	8 650	
	811		4/30/52			2 560	5.0	25.1	10.5	7 050	
	814		6/4/52			40 000	12.5	56.5	26.9	108 000	
	806					320	25.0	0			
BUCKBOARD	1	Sandia Lab	6/23/60	Basalt (NTS)	TNT	1 000	24.6	–	–	–	B. 26
	2		6/21/60			1 000	18.9	4.63	1.40	45	
	3		6/30/60			1 000	14.7	15.65	5.20	1 800	
	4		8/16/60			1 000	9.6	16.70	6.50	2 620	
	5		7/1/60			1 000	4.8	15.00	7.50	1 890	
	6		6/27/60			1 000	24.0	6.10	5.20	185	
	7		6/30/60			1 000	18.6	10.67	3.80	654	
	8		6/24/60			1 000	14.7	16.92	8.80	3 500	
	9		8/16/60			1 000	9.6	12.15	4.80	800	
	10		7/6/60			1 000	4.8	15.80	7.00	2 660	
	11		9/14/60			40 000	25.5	44.66	24.90	54 220	
	12		9/27/60			40 000	42.7	57.00	34 70	135 000	
	13		8/24/60			40 000	58.8	36.80	16.20	23 200	
PRE-SCHOONER	Alpha	NCG	2/6/64	Basalt (NTS)	Nitro-methane	39 250	58.0	50.3	22.9	75 800	B. 27
	Bravo		2/13/64			39 450	50.2	49	25.5	73 900	
	Charlie		2/25/64			39 840	66.1	mound	-1.3	mound	
	Delta		2/27/64			39 590	41.8	46.1	25.6	64 800	
PRE-SCHOONER	II	NCG	9/30/65	Rhyolite (Idaho)	Nitro-methane	171 000	71.1	95.2	60.7	669 000	B. 28
MULTIPLE THREAT CRATERING EXPERIMENT		Air Force Weapons Lab		Basalt (Yakima Firing Center)	TNT						B. 29
	C2		6/25/65			4 000	2.2	14.0	5.3	1 500	
	St1		6/11/65			4 000	-2.2	3.7	1.3	37	
	St2a		7/14/65			4 000	-2.2	6.8	1.9	139	
	St3a(C3)		6/23/65			4 000	-2.2	4.5	1.2	25	
TUFF	1	Sandia Lab	Spring 1959	Tuff	TNT	256	7.37	15	4.9	1 266	B. 30
	2					256	9.62	13.9	4.2	1 100	
	6					256	6.92	11.7	4.3	591	
	7					256	10.37	6.9	2.3	112	
	11					256	9.32	11.6	1.8	357	

[a]Department of Defense.
[b]Crater shape was estimated; the breakthrough volume is not included.
[c]The damage did not extend to the surface and is not comparable with other rounds; the sides of the original charge hole were damaged up to an average slant distance of 5.6 ft from the center of gravity of the charge.

Table IV-3B.5 (continued)

Series Name	Shot Designation	Sponsor	Date	Medium	Type of Ex- plosive	Charge Weight (lb)	Charge Burial Depth (ft)	Apparent Crater Radius (ft)	Apparent Crater Depth (ft)	Apparent Crater Volume (ft³)	Ref.
PRE- GONDOLA I	Bravo	NCG	10/25/66	Bear Paw Shale (Montana)	Nitro- methane	39 240	42.49	80.4	32.6	277 550	B.16
	Charlie		10/28/66			38 720	46.25	78.5	29.5	241 260	
	Alpha		11/1/66			40 700	52.71	76.1	32.1	235 300	
	Delta		11/4/66			40 480	56.87	65.1	25.2	133 880	
	SC-4		6/21/66			1 000	12.2	24.5	13.0		
	SC-2		6/22/66			1 000	15.8	27.3	12.5		
	SC-1		6/20/66			1 000	19.1	7.1	2.8		
	SC-3		6/23/66			1 000	23.3	14.6	3.4		
MINE SHAFT	MINE UNDER	DNA	10/22/68	Granite	TNT	$2x10^5$	-2	6.5	2.2	190 ft³	B.9

Table IV-3B.6 Single charges, buried bursts (playa).

Series Name	Shot Designation	Sponsor	Date	Medium	Type of Explosive	Charge Weight (lb)	Charge Burial Depth (ft)	Apparent Crater Radius (ft)	Apparent Crater Depth (ft)	Apparent Crater Volume (ft³)	Ref.
TOBOGGAN	E1a	Sandia Lab.	11/23/59	Playa (Yucca Lake)	TNT	8	0	1.55	0.91	2.33	B.1
	E1b		11/23/59			8	0	1.47	0.67	1.76	
	E1c		11/24/59			8	0	1.31	0.65	1.54	
	E2a		11/24/59			8	0.5	2.55	1.11	11.55	
	E2b		11/24/59			8	0.5	2.25	1.06	8.00	
	E2c		11/24/59			8	0.5	2.43	1.44	11.56	
	E3a		11/24/59			8	1.0	2.78	1.60	15.69	
	E3b		11/24/59			8	1.0	3.02	1.54	17.03	
	E3c		11/24/59			8	1.0	2.70	1.75	15.68	
	E3.5a		6/16/60			8	1.5	2.85	1.71	18.1	
	E4a		11/24/59			8	2.0	3.43	1.77	26.64	
	E4.5a		6/18/60			8	2.5	3.75	1.48	27.4	
	E4b		11/24/59			8	2.0	3.56	1.94	34.32	
	E4.5b		6/18/60			8	2.5	3.31	1.01	13.0	
	E4c		11/24/59			8	2.0	3.68	1.81	36.37	
	E5a		11/14/59			8	3.0	3.68	0.80	16.82	
	E5b		11/15/59			8	3.0	4.00	1.79	38.70	
	E5c		11/15/59			8	3.0	3.66	0.67	13.72	
	E5.5a		6/18/60			8	3.5	3.16	0.34	7.05	
	E6a		11/15/59			8	4.0	1.91	0.20	1.24	
	E6b		11/15/59			8	4.0	1.50	0.12	0.52	
	E6c		11/15/59			8	4.0	2.40	0.11	2.22	
	E6.5a		6/18/60			8	4.5	0	0	0	
	E7a		6/18/60			8	5.0	0	0	0	
AIR VENT	I	DNA[a]/ Sandia Lab	12/14/63	Playa (Frenchman Flat)	TNT	40 000	17.19	47.61	22.5	72 500	B.2
AIR VENT	II-1		1/30/64			256	-0.865	3.20	0.82	13.13	
	II-2A		1/30/64			256	0	5.54	2.39	95.46	
	II-2B		1/29/64			256	0	5.40	2.43	93.22	
	II-3		1/29/64			256	0.865	6.72	3.38	235.4	
	II-4		1/29/64			256	1.59	7.62	3.72	247.0	
	II-5A		1/28/64			256	3.175	8.84	4.13	426.0	
	II-5B		1/28/64			256	3.175	8.50	4.35	381.0	
	II-6		1/28/64			256	4.76	9.58	4.64	517.0	
	II-7A		1/27/64			256	6.35	9.82	4.36	505.7	
	II-7B		1/27/64			256	6.35	9.94	4.49	544.0	
	II-8		1/27/64			256	7.94	10.32	3.98	483.0	
	II-9A		1/24/64			256	9.53	10.98	3.63	486.0	
	II-9B		1/23/64			256	9.53	11.02	2.34	332.0	
	II-10A		1/24/64			256	12.7	22.9	-3.81	-1 178.0	
	II-10B		1/23/64			256	12.7	26.4	-4.13	-2 500.0	
	II-11A		1/16/64			256	15.9	22.6	-4.11	-2 678.0	
	II-11B		1/16/64			256	15.9	22.3	-4.41	-2 722.0	
	II-12		1/17/64			256	19.05	22.0	-2.67	-1 878.0	
	II-13		1/17/64			256	22.2	23.4	-1.35	-1 003.0	
	II-14		1/17/64			256	25.4	24.7	-0.63	-900.0	
TTR 211-	40	Sandia Lab	8/11/66	Playa (Tonopah Test Range)	TNT	64	4	7.28	4.17	260	B.3
	42		10/25/66			64	6.9	7.33	2.92	195	B.32
	47		5/18/67			64	5	7.96	3.82	326	B.3
	48		5/24/67			64	6	8.39	4.16	369	
	49		6/8/67			64	7	7.69	3.02	206	
	54		1/19/68			8	3	3.64	0.97	16.1	
	55		3/21/68			256	9.5	11.9	4.84	907	
211-A					TNT	256	6.35	11.52	6.51	1007	
211-B					TNT		7.94	10.20	3.75	484	
211-C					TNT		9.53	0.91	0.11	0.06	

[a]Formerly the Defense Atomic Agency (DASA), now the Defense Nuclear Agency (DNA).

Table IV-3B.7 Line charges.

Series Name	Shot Designation	Sponsor	Date	Medium	Type of Explosive	Explosive Length (ft)	Chg Wt (lb/ft)	Total Chg Wt (lb)	Chg Burial Depth (ft)	Average Apparent Crater Width (ft)	Average Apparent Crater Depth (ft)	Apparent Crater Volume (ft³)	Ref.
			(1959)										
TOBOGGAN Phase I	A1a	Sandia Lab.	10/30	Playa	TNT	7.5	1.81	13	0	2.14	0.27	2.93	B.1
	A1b		10/31			7.5	1.81	13	0	1.90	0.35	3.36	
	A1c		10/31			7.5	1.81	13	0	2.17	0.33	3.51	
	A2a		10/31			9.4	1.81	17	0.33	3.53	0.92	16.51	
	A2b		11/1			9.4	1.81	17	0.33	4.20	1.15	24.38	
	A2c		11/1			9.4	1.81	17	0.33	4.52	0.78	20.26	
	A3a		11/1			11.3	1.81	20.5	0.65	4.79	1.14	37.23	
	A3b		11/1			11.1	1.81	20.0	0.65	5.35	1.04	39.88	
	A3c		11/3			11.3	1.81	20.5	0.65	4.70	1.10	34.86	
	A4a		11/16			15.0	1.81	27.0	1.31	6.27	1.89	88.14	
	A4b		11/18			15.5	1.81	28.0	1.31	6.67	1.63	97.28	
	A4c		11/19			15.2	1.81	27.5	1.31	5.66	1.89	103.5	
	A5a		11/19			18.5	1.81	33.5	1.97	6.35	2.21	139.1	
	A5b		11/21			18.8	1.81	34.0	1.97	7.46	2.40	169.2	
	A5c		11/21			18.8	1.81	34.0	1.97	7.43	2.12	157.4	
	A6a		11/16			22.9	1.81	41.5	2.62	4.39	2.26	262.8	
	A6b		11/20			26.5	1.81	48.0	2.62	6.30	1.42	224.2	
	A6c		11/20			26.8	1.81	48.5	2.62	7.10	1.47	230.0	
	B1a		11/3			19.3	10.8	208	0	5.90	1.19	73.56	
	B1b		11/3			18.5	10.8	198	0	6.33	1.23	74.00	
	B1c		11/4			18.5	10.8	198	0	6.04	1.30	72.71	
	B2a		11/4			23.8	10.8	257	0.82	8.52	1.68	175.6	
	B2b		11/5			23.8	10.8	257	0.82	10.52	2.22	276.6	
	B2c		11/9			29.4	10.8	317	0.82	9.08	1.96	271.2	
	B3a		11/10			38.6	10.8	416	1.64	11.55	3.09	812.7	
	B3b		11/11			38.6	10.8	416	1.64	10.96	2.82	611.1	
	B3c		11/11			38.6	10.8	416	1.64	11.93	2.60	805.6	
	B4a		11/18			53.1	10.8	574	3.28	12.60	3.32	1 410.0	
	C1a		11/12			38.9	42.7	1640	0	12.74	2.10	635.0	
	C1b		11/12			38.9	42.7	1640	0	11.82	2.78	615.9	
	C1c		12/2			42.6	42.7	1800	0	12.51	2.31	702.3	
	C2a		12/7			60.0	42.7	2517	1.65	19.16	3.55	2 391.0	
	C2b		12/7			60.0	42.7	2517	1.65	17.18	4.30	2 434.0	
	C2c		12/9			60.0	42.7	2517	1.65	21.03	3.41	2 730.0	
	C3a		12/11			75.0	42.7	3157	3.30	28.52	4.05	7 608.0	
	C3c		12/15			75.0	42.7	3157	3.30	30.67	5.20	8 628.0	
	D1a		12/12		Primacord	4	0.23	0.92	0	0.90	0.15	0.30	
	D1b		12/12			4	0.23	0.92	0	0.90	0.17	0.32	
	D2a		12/12			6	0.23	1.38	0.12	0.74	0.31	1.36	
	D2b		12/12			6	0.23	1.38	0.12	1.28	0.32	1.59	
	D3a		12/12			8	0.23	1.84	0.24	1.98	0.45	4.05	
	D3b		12/12			8	0.23	1.84	0.24	1.80	0.50	3.93	
			(1960)										
TOBOGGAN Phase II	A1a	Sandia Lab.	12/15[a]	Playa	TNT	12.0	1.81	21.8	0.0	1.7	0.20	3.25	
	A2a		4/2			14.7	1.81	27.5	0.33	3.72	0.74	19.20	
	A3a		4/13			20.0	1.81	37.0	0.65	3.87	0.79	27.5	
	A4a		5/6			30.2	1.81	55.0	1.34	6.04	1.63	156.0	
	A5a		5/10			40.1	1.81	73.0	2.04	6.78	1.79	227.2	
	A6a		5/11			50.0	1.81	91.0	2.67	7.18	1.51	356	
	A7a		5/13			60.2	1.81	108.5	3.36	6.78	0.89	280	
	A8a		5/16			70.3	1.81	128.0	4.02	NA	NA	125	
	B1a		6/17			25.4	10.8	267.0	0.0	6.00	1.30	89.1	
	B1b		12/15[a]			25.4	10.8	267.0	0.0	5.49	1.14	74.0	
	B2a		4/4			34.6	10.8	363.8	0.81	7.65	2.00	230	
	B2b		4/4			34.6	10.8	363.8	0.83	9.45	2.60	347	
	B3a		4/13			41.6	10.8	436.2	1.64	11.60	2.50	632	
	B3b		4/12			41.9	10.8	436.2	1.64	11.70	2.80	759	
	B4a		4/18			53.6	10.8	563.9	3.27	15.50	4.00	1 768	
	B4b		4/1			52.1	10.8	565.2	3.27	15.50	4.26	1 762	
	B5a		4/19			67.9	10.8	712.9	4.90	18.70	4.89	3 540	
	B5b		4/21			67.0	10.8	702.2	4.90	18.40	4.66	3 312	
	B6a		4/20			82.0	10.8	861.8	6.54	19.39	3.95	4 437	
	B6b		4/20			81.3	10.8	851.2	6.54	21.03	4.50	5 275	
	B7a		4/29			95.2	10.8	1003.9	8.19	21.18	4.00	5 580	
	B7b		5/3			95.2	10.8	1014.6	8.22	22.11	5.07	7 560	
	B8a		5/27			111.3	10.8	1170.4	9.80	19.40	3.58	4 600	
	B8b		6/16			111.6	10.8	1170.4	9.70	18.40	2.96	4 550	

[a]1959

Table IV-3B.7 (continued)

Series Name	Shot Desig-nation	Sponsor	Date	Medium	Type of Explosive	Ex-plosive Length (ft)	Chg Wt (lb/ft)	Total Chg Wt (lb)	Chg Burial Depth (ft)	Average Apparent Crater Width (ft)	Average Apparent Crater Depth (ft)	Apparent Crater Volume (ft³)	Ref.
			(1960)										
TOBOGGAN Phase II	C1a	Sandia Lab.	12/15[a]	Playa	TNT	45.0	42.7	1920.0	0.0	11.94	2.30	598	B.1
	C2a		4/7			60.0	42.7	2519.0	1.62	19.70	4.33	2 962	
	C3a		4/8			75.3	42.7	3160.0	3.25	26.49	5.30	6 150	
	C4a		6/9			100.9	42.7	4223.0	6.50	29.6	7.83	14 300	
	C5a		6/9			125.0	42.7	5240.0	9.75	39.4	11.4	30 000	
	C6a		6/7			151.5	42.7	6356.0	13.10	38.3	7.34	33 600	
	C7a		6/7			177.1	42.7	7423.0	16.50	41.1	6.62	29 300	
	C8a		6/22			201.3	42.7	8447.0	19.92	32.8	6.27	26 000	
	D1a		12/15[a]		Prima-cord	4.0	0.23	0.92	0.0	0.90	0.13	0.38	
	D1b		12/15[a]			4.0	0.23	0.92	0.0	1.70	0.18	0.43	
	D2a		4/2			6.0	0.23	1.38	0.12	1.50	0.28	1.35	
	D2b		4/2			6.0	0.23	1.38	0.12	1.45	0.28	1.16	
	D3a		4/13			8.0	0.23	1.84	0.24	1.69	0.36	3.06	
	D3b		4/13			8.0	0.23	1.84	0.24	1.87	0.39	3.51	
	D4a		5/5			10.0	0.23	2.30	0.48	2.58	0.56	9.60	
	D4b		5/6			10.0	0.23	2.30	0.48	2.85	0.76	8.25	
	D5a		5/6			11.8	0.23	2.76	0.72	2.80	0.74	11.44	
	D5b		5/6			12.1	0.23	2.76	0.72	2.50	0.71	7.52	
	D6a		5/7			15.0	0.23	3.45	0.96	2.80	0.56	17.5	
	D6b		5/7			15.0	0.23	3.45	0.97	2.88	0.52	20.2	
	D7a		5/9			17.0	0.23	3.91	1.20	2.26	0.35	15.8	
	D7b		5/9			17.0	0.23	3.91	1.20	2.33	0.27	13.9	
	D8a		5/13			19.0	0.23	4.37	1.44	3.10	0.38	22.4	
	D8b		5/13			19.0	0.23	4.37	1.45	2.45	0.03	8.4	
	F1a		5/19		TNT	26.0	10.8[b]	283.4	0	5.53	1.00	72.8	
	F1b		5/20			26.0	10.8[b]	283.4	0	6.48	1.18	82.4	
	F1c		5/20			26.0	10.8[b]	283.4	0	6.37	0.99	83.2	
	F4a		5/25			54.0	10.8[b]	591.6	3.26	16.40	3.90	2 196.0	
	F4b		6/1			53.8	10.8[b]	591.6	3.28	14.85	4.25	1 917.0	
	F4c		5/31			54.0	10.8[b]	591.6	3.27	17.42	4.31	2 448.0	
	F6a		6/16			80.12	10.8[b]	872	6.64	22.5	5.48	5 900.0	
	F6b		6/3			80.04	10.8	872	6.55	21.75	4.88	5 737.0	

[a] 1959

[b] Circular cross section

Series Name	Shot Designation	Sponsor	Date	Medium	Type of Explosive	Chg. Wt. (lb)	Chg. Burial Depth (ft)	Spacing Between Charges (ft)	Average Apparent Crater Width (ft)	Average Apparent Crater Depth (ft)	Apparent Crater Volume (ft³)	Apparent Crater Volume per lb of Explosive (ft³/lb)	Ref.
LITTLE DITCH	IIE-3.0	Sandia Lab	12/9/59	Alluvium (Albuquerque)		7 ea 8 lb	2.0	3.0	8.3	1.75	192.08	3.43	B.19
	IIE-4.0		3/10/60			7 ea 8 lb	2.0	4.0	7.7	2.40	268.80	4.8	
	IIE-5.0		5/24/60			7 ea 8 lb	2.0	5.0	6.0	1.60	184.80	3.3	
	IIE-7.0		5/27/60			7 ea 8 lb	2.0	7.0	5.3	0.85	128.80	2.3	
	IIF-3.5		11/13/59			7 ea 8 lb	2.5	3.5	8.01	1.85	203.84	3.64	
	IIF-4.0		3/11/60			7 ea 8 lb	2.5	4.0	8.05	2.10	260.96	4.66	
	IIF-4.5		3/30/60			7 ea 8 lb	2.5	4.5	8.02	2.30	330.96	5.91	
	IIG-3.0		1/29/60			7 ea 8 lb	3.0	3.0	9.32	2.40	239.68	4.28	
	IIG-3.5		11/10/59			7 ea 8 lb	3.0	3.5	8.9	1.80	224.00	4.00	
	IIG-4.0A		12/11/59			7 ea 8 lb	3.0	4.0	8.1	1.20	165.76	2.96	
	IIG-4.0C		2/16/60			7 ea 8 lb	3.0	4.0	9.03	2.60	334.88	5.98	
	IIG-4.0B		4/4/60			7 ea 8 lb	3.0	4.0	9.47	2.80	381.92	6.82	
	IIG-4.5		2/19/60			7 ea 8 lb	3.0	4.5	8.45	2.55	372.96	6.66	
	IIG-4.5		2/25/60			7 ea 8 lb	3.0	4.5	8.47	2.40	379.68	6.78	
	IIG-6.0		3/4/60			7 ea 8 lb	3.0	6.0	7.68	1.95	359.52	6.42	
	IIG-8.0		3/9/60			7 ea 8 lb	3.0	8.0	6.36	1.20	263.20	4.70	
	IIG-9.0		5/25/60			7 ea 8 lb	3.0	9.0	Same as IIJ-7.0 with mounds between charges				
	IIH-4.0		3/28/60			7 ea 8 lb	3.5	4.0	9.59	2.10	286.16	5.11	
	IIJ-3.5		3/3/60			7 ea 8 lb	4.0	3.5	10.1	2.55	357.84	6.39	
	IIJ-4.0		4/6/60			7 ea 8 lb	4.0	4.0	9.93	1.37	244.72	4.37	
	IIJ-5.0		6/2/60			7 ea 8 lb	4.0	5.0	8.0	1.95	276.08	4.93	
	IIJ-6.0		3/14/61			9 ea 8 lb	4.0	6.0	5.11	0.50	134.64	1.87	
	IIJ-7.0		5/20/60			7 ea 8 lb	4.0	7.0	Fall back filled crater leaving an uneven surface at original ground level.				
	IIL-4.0		6/1/60			7 ea 8 lb	5.0	4.0	9.4	1.75	272.16	4.86	
	IIL-4.0B		3/20/61			7 ea 8 lb	5.0	4.0	Mound with max height of 2.2 ft				
	V-14.3 -9.52		8/17/60			8 ea 256 lb	9.52	14.3	28.8	6.50	13148.16	6.42	
	V-15.87 -9.52		12/30/60			8 ea 256 lb	9.52	15.87	24.5	6.00	10526.72	5.14	
	II-K-3.5A		3/1/61			9 ea 8 lb	4.5	3.5	9.32	0.67	254.88	3.54	
	II-K-3.5B		3/6/61			9 ea 8 lb	4.5	3.5	9.72	0.32	216.72	3.01	
	II-K-4.0		3/9/61			9 ea 8 lb	4.5	4.0	8.51	1.04	259.20	3.60	

Table IV-3B.8 (continued)

Series Name	Shot Designation	Sponsor	Date	Medium	Type of Explosive	Chg. Wt. (lb)	Chg. Burial Depth (ft)	Spacing Between Charges (ft)	Average Apparent Crater Width (ft)	Average Apparent Crater Depth (ft)	Apparent Crater Volume (ft³)	Apparent Crater Volume per lb of Explosive (ft³/lb)	Ref.
PRE-CAPSA	3	Sandia Lab	3/19/65	Alluvium (Albuquerque)	TNT	2 ea 256 lb	9.5	13.6	25.5	6.20	3 055	5.97	B. 23
	4		6/14/65			3 ea 256 lb	9.5	13.6	27.7	7.23	4 604	6.00	
	5		5/27/65			5 ea 256 lb	9.5	13.6	28.8	6.59	7 659	5.98	
TOBOGGAN	A1	Sandia Lab	Spring 1959	Playa (NTS Yucca Lake)	TNT	6 ea 8 lb	2.0	3.0	10.0	2.04	179.0	3.73	B. 1
	B2					6 ea 8 lb	2.0	3.5	7.09	2.01	187.0	3.90	
	C3					6 ea 8 lb	2.0	4.0	7.00	1.65	160.2	3.33	
	D4					6 ea 256 lb	6.34	12.7	23.01	5.21	5 507.0	3.59	
	E5					6 ea 8 lb	2.0	5.0	5.8	2.04	153.0	3.19	
	F6					6 ea 8 lb	2.0	6.0	6.48	1.41	1 charge misfired		
TTR-211	1	Sandia Lab	5/12/64	Playa (Tonapah Test Range)	TNT	6 ea 64 lb	5	8	17.18	4.83	1551	4.04	B. 18
	2		5/12/64			6 ea 64 lb	6	8	19.76	5.74	3184	8.29	
	3		5/12/64			6 ea 64 lb	7	8	21.04	5.78	2245	5.85	
	10		8/20/64			11 ea 64 lb	6	8	18.06	4.85	4 485	6.37	B. 31
	13		3/3/65			11 ea 64 lb	6	8	16.94	3.94	3 583	5.09	
	16		5/27/65			5 ea 64 lb	6.9	5.25	20.04	5.78	2 012	6.29	
	41		10/5/66			2 ea 64 lb	6	8	16.74	4.16	657	5.13	
	43		11/18/66			25 ea 64 lb	6	8	18.34	4.86	10 116	6.32	
	44		11/22/66			5 ea 64 lb	6	8	17.40	5.02	1 953	6.10	
	45		2/24/67			11 ea 64 lb	6.9	5.25	20.86	6.55	4 823	6.85	
	46		3/27/67			2 ea 64 lb	6.9	5.25	18.24	5.14	793	6.20	
DUGOUT	--	LLL[d]	6/24/64	Basalt (NTS)	Nitro-methane	5 ea 40 000	59.0	45	136.4	35.1	567 800	5.68	B. 33

[d]Formerly Lawrence Radiation Laboratory

Table IV-3B.8 (continued)

Series Name	Shot Desig- nation	Sponsor	Date	Medium	Type of Ex- plosive	Chg. Wt. (lb)	Chg. Burial Depth (ft)	Spacing Between Charges (ft)	Average Apparent Crater Width (ft)	Average Apparent Crater Depth (ft)	Apparent Crater Volume (ft³)	Apparent Crater Volume per lb of Explosive (ft³/lb)	Ref.
PRE- GONDOLA II		NCG	6/28/67	Bear Paw Shale	Nitro- methane	C					1 312 631ᵉ	4.78	B. 34
			6/28/67			E77 200	59.7	105.5	206.5	55.5			
			6/28/67			F39 400	49.4	79.8	152.5	37.5			
			6/28/67			G39 100	48.8	79.9	164.0	36.9			
			6/28/67			H79 120	59.9	79.9	214.5	57.0			
			6/28/67			I 40 000	48.8	79.9	173.0	33.5			
PRE- GONDOLA IIIᶠ		NCG	10/30/68	Bear Paw Shale	Nitro- methane			93.3			2 350 000	5.57	
						M60 000	56		196	54			
								86.0	190	55			
						N58 800	50		185	46			
								86.6	191	49			
						060 200	55		182	53			
								86.0	187	47			
						P60 500	52		182	46			
								87.1	199	49			
						Q61 000	51		212	50			
								52.6	223	52			
						R60 600	50		202	57			
								52.1	217	52			
						S60 500	54		216	46			

ᵉVolume added by 5 charges

ᶠAll dimensions are preliminary.

IV-3B.1   REFERENCES

IV-3B.1   Carlson, R. H., Project TOBOGGAN: High-Explosive Ditching From Linear Charges, SC-4483 (RR), Sandia Laboratory, Albuquerque, New Mexico, July 1961.

IV-3B.2   Flanagan, T. J., Crater Studies, Project AIR VENT, SC-RR-64-1704, Sandia Laboratory, Albuquerque, New Mexico, April 1966.

IV-3B.3   Carlson, R. H., and R. T. Newell, Ejecta from Single-Charge Cratering Explosions, The Boeing Company, Albuquerque, New Mexico, SC-RR-69-1, Sandia Laboratory, Albuquerque, New Mexico, 1969.

IV-3B.4   Rooke, A. D., Jr., and L. K. Davis, Crater Measurements Project FLAT TOP, POR-3008, Waterways Experiment Station, Vicksburg, Mississippi, August 1966.

IV-3B.5   Jones, G. H. S., N. Spackman, and F. H. Winfield, Cratering by Ground Burst TNT, Suffield Technical Paper, No. 158, Suffield Experimental Station, Ralston, Alberta, Canada, 1959.

IV-3B.6   Rooke, A. D., Jr., and L. K. Davis, "Monitor Crater Studies," in Operation Distant Plain Symposium, Vol. 1, DASA Information and Analysis Center, Santa Barbara, California, September 1967.

IV-3B.7   Murphey, B. F., High Explosive Crater Studies: Desert Alluvium, SC-4614 (RR), Sandia Laboratory, Albuquerque, New Mexico, May 1961.

IV-3B.8   Roddy, D. J., "U.S. Geological Survey Activities," Project LN 303, Event Dial Pack Symposium, Report, Volume II (Unpublished).

IV-3B.9   Davis, L. K., and B. L. Carnes, Operation Mine Shaft, Cratering Effects of a 100-Ton Detonation on Granite, U.S. Army Engineers, Waterways Experimental Station, Misc. Paper N-72-1, February 1972.

IV-3B.10   Davis, L. K., Mine Shaft Series, Events Mine Under and Mine Ore, Subtask N121, Crater Investigations, U.S. Army Engineers, Waterways Experimental Station, Tech. Report N-70-8, March 1970.

IV-3B.11   Campbell, D. C., Some HE Tests and Observations on Craters and Base Surges—Operation JANGLE, WT-140, Armed Forces Special Weapons Project, Kirtland AFB, New Mexico, November 1951.

IV-3B.12   Sachs, D. C., and L. M. Swift, <u>Small Explosion Tests, Project MOLE</u>, Vols. I and II, AFSWP-291, Stanford Research Institute, Menlo Park, California, December 1955.

IV-3B.13   Vortman, L. J., et al., <u>Twenty Ton HE Cratering Experiment in Desert Alluvium, Project STAGECOACH</u>, SC-4596 (RR), Sandia Laboratory, Albuquerque, New Mexico, May 1962.

IV-3B.14   Perret, W. R., A. J. Chabai, J. W. Reed, and L. J. Vortman, <u>Project SCOOTER Final Report</u>, SC-4602 (RR) Sandia Laboratory, Albuquerque, New Mexico, October 1963.

IV-3B.15   Myers, B., <u>Summary Report—Project ROWBOAT</u>, UCRL-12118, Lawrence Radiation Laboratory, Livermore, California, October 1964.

IV-3B.16   Rooke, A. D., Jr., <u>Project PRE-BUGGY: Emplacement and Firing of High-Explosive Charges and Crater Measurements</u>, PNE-302, Waterways Experimental Station, February 1965.

IV-3B.17   Spruill, J. L., and F. F. Videon, <u>Project PRE-BUGGY II: Studies of the PRE-BUGGY II Apparent Craters</u>, PNE-315F, Final Report, U.S. Army Engineer Nuclear Cratering Group, Lawrence Radiation Laboratory, Livermore, California, June 1965.

IV-3B.18   Unpublished data, Sandia Laboratory, Albuquerque, New Mexico.

IV-3B.19   Vortman, L. J., and L. N. Schofield, <u>The Effect of Row Charge Spacing and Depth on Crater Dimensions</u>, SC-4730 (RR), Sandia Laboratory, Albuquerque, New Mexico, November 1963.

IV-3B.20   Vortman, L. J., <u>Crater from an Individually Detonated Multiple-Charge Array</u>, SC-RR-67-727, Sandia Laboratory, Albuquerque, New Mexico, November 1967.

IV-3B.21   Vortman, L. J., <u>Comparison of Craters from Rows of Charges Detonated Simultaneously and One at a Time</u>, SC-RR-67-728, Sandia Laboratory, Albuquerque, New Mexico, November 1967.

IV-3B.22   Vortman, L. J., <u>Craters from Two Charges Buried in Vertical Array</u>, SC-RR-64-1239, Sandia Laboratory, Albuquerque, New Mexico, November 1964.

IV-3B.23 Vortman, L. J., <u>Craters From Short-Row Charges and Their Interaction with Pre-Existing Craters</u>, SC-RR-66-324, Sandia Laboratory, Albuquerque, New Mexico, July 1966.

IV-3B.24 <u>Underground Explosive Test Program, Final Report, Vol. 1, Soil</u>, Engineering Research Associates, Inc., Arlington, Virginia, August 1952.

IV-3B.25 <u>Underground Explosive Test Program, Final Report, Vol. 2, Rock</u>, Engineering Research Associates, Inc., Arlington, Virginia, April 1953.

APPENDIX IV-3C

TABULATION OF SOME NUCLEAR CRATER DATA

The table shown in this Appendix presents some of the nuclear crater data for detonations that occurred as early as 1951 through 1968. The four Soviet tests listed are those that were obtained from them under an agreement for information exchange on the peaceful uses of nuclear explosives.

Table IV-3C.1. Nuclear crater data.[a]

Event	Date	Site	Medium	Yield	D_{oB}[b]	R_a	D_A	V_A	Ref.
JANGLE S	11/51	NTS	Alluvium	1.2	-3.5	45	17	4.93×10^4	1
JUNGLE U	11/51	NTS	Alluvium	1.2	17	129	5.3	9.73×10^5	1
IVY MIKE	10/52	Enewetak	Sat Coral	$(0.4\text{-}14) \times 10^3$[c]	-20[c]	2900	164	1.4×10^9	-
CASTLE-1	2/54	Bikini	Sat Coral	1.5×10^4[c]	-15.4[c]	3000	240	2.9×10^9	-
CASTLE-3	4/54	Bikini	Sat Coral	100	-13.6	400[c]	75	1×10^7	-
TEAPOT ESS	3/55	NTS	Alluvium	1.2	67	146	90	2.6×10^6	2
LACROSSE	5/56	Enewetak	Sat Coral	39.5	-15	202	44	3.1×10^6	-
ZUNI	5/56	Enewetak	Sat Coral	3.53×10^3	-9.3	1240	103	1.5×10^8	-
SEMINOLE[d]	6/56	Enewetak	Sat Coral	13.5	-4.5[d]	330	31	4.8×10^6	-
TEWA	7/56	Bikini	Sat Coral	5×10^3	-6.5[e]	1000	129	4×10^8	-
CACTUS	5/58	Enewetak	Sat Coral	18	-3	170	34.5	1.9×10^6	-
KOA[d]	5/58	Enewetak	Sat Coral	1.38×10^8	-3[d]	2000[c]	171	6.4×10^8	-
CAK	6/58	Enewetak	Sat Coral	8.9×10^3	-6.5[e]	2200	183	7.3×10^8	-
NEPTUNE	10/58	NTS	Tuff	0.115	100	100	35	5.9×10^5	3
DANNY BOY	3/62	NTS	Basalt	0.43	110	107	62	9.13×10^5	-
SMALL BOY	7/62	NTS	Playa	1.6	-10	180	4.5	9.2×10^4	-
LITTLE FELLER I	7/62	NTS	Alluv-18	0.018	-3?	6	1.1	38	-
LITTLE FELLER II	7/62	NTS	Alluv-18	0.022	-3	9	2.0	120	-
JOHNIE BOY	7/62	NTS	Alluv-12	0.5	1.9	61	30.5	1.45×10^5	4
SEDAN	7/62	NTS	Alluvium	100	635	610	323	1.8×10^8	5
TINY TOT[f]		NTS	Granite	0.02	0[f]	13[f]	55[f]	1.44×10^3[f]	6
SULKY	12/64	NTS	Basalt	0.087	90	29[g]	-9.2[g]	-2.5×10^4[g]	7
PALANQUIN[h]	4/65	NTS	Rhyolite	4.3	250	119	78.8	1.3×10^6	8
CABRIOLET	1/68	NTS	Rhyolite	2.3	170	181	117	4.9×10^6	9
BUGGY[i]	3/68	NTS	Basalt	$5 \cdot 1.1$[i]	135	855x254[i]	65	7.1×10^6	10
SCHOONER	12/68	NTS	Tuff	35	355	426	208	6.1×10^7	11
T-1	NR	Russia	Wet Sandstone	0.2	103	121	66	NR	12
1003	NR	Russia	Siltstone	1.1	158	204	95	3.92×10^6	12
1004	NR	Russia	Sat Sandstone	100	650-660	670	328	2.33×10^8	12
T-2[i]	NR	Russia	Sat Sandstone	$3 \cdot 0.2$[i]	106	233x107[i]	52.5	2.72×10^6	12

(a) All dimensions are in units of kt and ft.
(b) A negative DOB indicates height of burst (above ground).
(c) The value in dispute—see Table IV-3.2.
(d) Fired inside water tank.
(e) Fired from barge—DOB assumed.
(f) Fired on the surface of an underground cavity.
(g) Mounding event (RETARC).
(h) Significant stemming failure—crater data may be effected.
(i) Multiple-burst linear array.

IV-3C.1   REFERENCES

IV-3C.1   Vortnam, L. J., JANGLE True Crater Measurements, Sandia Lab Report
          SC-RR-64-19, February 1964.

IV-3C.2   Lewis, J. G., Crater Measurements, Operation TEAPOT, Project 1.6,
          WT-1105, May 1955.

IV-3C.3   Shelton, A. V., M. D. Nordyke, and R. H. Goeckerman, The NEPTUNE
          Event — A Nuclear Explosive Cratering Experiment, UCRL-5166, Lawrence
          Livermore Laboratory, April 1960.

IV-3C.4   Goode, J. B., and A. L. Mathewes, Soils Survey, Shot JOHNIE BOY,
          POR-2285, U.S. Army Engineers Waterways Experiment Station, Vicksburg,
          Mississippi, May 1963.

IV-3C.5   Nordyke, M. D., and M. M. Williamson, The SEDAN Event, Lawrence
          Radiation Laboratory, PNE-242F, April 1965.

IV-3C.6   Weart, W. D., Reentry and Crater Measurements, TINY TOT Project 1.9,
          POR-3019, Lawrence Livermore Laboratory.

IV-3C.7   Videon, F. F., Crater Measurements, Project SULKY, Lawrence Livermore
          Laboratory, PNE-713F, October 1965.

IV-3C.8   Videon, F. F., Project PALANQUIN: Studies of the Apparent Crater,
          PNE-904, April 1966.

IV-3C.9   Tewes, H. A., "Results of the CABRIOLET Excavation Experiment,"
          Nuclear Applications and Technology, Vol. 7, p. 232, September 1969.

IV-3C.10 Toman, John, "PROJECT BUGGY: A Nuclear Row-Excavation Experiment,"
          Nuclear Applications and Technology, Vol. 7, p. 243, September 1969.

IV-3C.11 Tewes, H. A., "Results of the SCHOONER Experiment," Symposium on
          Engineering with Nuclear Explosives, January 14-16, 1970, Las Vegas,
          Nevada (Unpublished).

IV-3C.12 Myasnikov, K. V., L. B. Prozorov, and I. E. Sitnikov, "Mechanical
          Effects of Single and Multiple Underground Nuclear Cratering Explosives
          and the Properties of the Excavations Dug by Them," Nuclear Explosions
          for Peaceful Purposes, I. D. Morokhov, ed., Atomizdat, UCRL-Trans-10517,
          Moscow, 1970.

CHAPTER IV-4

EJECTA*

IV-4.0 INTRODUCTION

The size and shape of an explosively generated crater and the attendant pro-
duction of ejecta are dependent on numerous factors. These factors can be divided
into two categories: the environmental parameters and the explosive parameters.
The environmental parameters include the density, composition, and strength of the
medium in which the crater is formed, the moisture content of the medium, the
jointing or layering of the medium, and the atmospheric conditions at the time of
detonation.† The explosive parameters include the quantity and type of explosive
used, the geometry of the charge, the method of charge emplacement and the position
of the charge relative to the air-medium interface. The actions and interactions
of these independent variables on crater and ejecta formation are complex, and
only the major influencing factors are examined here. Appendix IV-4A provides
additional references to the interested reader to supplement those listed in this
chapter.

IV-4.0.1 Relationship Between TNT and Other Explosives

Besides the nuclear devices, approximately 10 different kinds of explosive
have been widely used for different test programs, depending upon the requirements
of the test and/or the convenient availability of various types of explosives.
For this discussion, all explosives are converted to an equivalent TNT yield where
each equivalent TNT weight is assumed to be a sphere of cast explosive.

The explosives that have been most commonly used for cratering and ejecta
research are TNT, nitromethane (NM), ammonium nitrate/fuel oil mixtures (AN/FO),
and ammonium nitrate (AN) slurries. TNT is considered the basic explosive due to
its widespread use and a result of the fact that it is readily available to mili-
tary users. Moreover, it can be cast in various sizes and shapes and it is a
relatively insensitive explosive and, therefore, relatively safe to handle. NM is
a liquid which is classed as a solvent rather than an explosive. It has been

---

*Author: J.E. Schoutens (General Electric—TEMPO).
†For example, winds will affect the distribution on the ground of fine particles
 thrown out of the crater by the detonation.

widely used in cratering experiments because of the fact that a large volume of NM (up to 100 tons) can be poured into an underground emplacement chamber from the surface through small-diameter fill pipes. This greatly simplifies the problem of charge emplacement for large deeply buried shots. AN/FO has also been used for many years for cratering. It is classed as a blasting agent, and can be mixed on-site prior to placement in its cavity or container. AN slurry has been used increasingly in recent years. It is also classed as a blasting agent and can be pumped into deeply buried emplacement chambers. Its higher viscosity in most instances eliminates the need for extensive lining of the chamber to prevent seepage. Unfortunately, very few data exist that permit performance comparisons of the crater-forming abilities of different types of chemical explosives compared to TNT. In the absence of more definitive research on cratering performance, a list of common explosives and their TNT equivalents has been compiled from References IV-4.1 and IV-4.2 and is presented as Table IV-4.1. Table IV-4.1 does not take into account the effects of different soils or rocks on cratering. The interested reader might also wish to consult Reference IV-4.3.

Table IV-4.1. Comparison of explosive cratering efficiency with that of TNT (References IV-4.1 and IV-4.2).

Explosive	Conversion Factor*
TNT†	1.00
Amatol	0.94
Dynamite (40%)	0.68
Pentolite	1.23
C-4, C-3	1.34
Ammonium Nitrate	1.00
Nitromethane	1.10

*To determine relative cratering efficiency (TNT), multiply weight of explosive charge by conversion factor.

†TNT explosive energy is approximately 10^9 calories/ton heat of detonation or approximately 10^{12} calories/kt.

IV-4.0.2 Origin and Compositions of Ejecta

Crater ejecta consists of the soil or rock debris thrown beyond the boundaries of the apparent crater by an explosion. Together with the fallback, which is the ground material lying between the true and the apparent crater boundaries, the ejecta comprises all material completely dissociated from the parent medium by the explosion. It may represent a significant hazard at considerable distances from the crater.

For a buried explosion, the ejecta mainly originates in the dome of earth material which is forced upward by the expanding gas bubble. As the dome disintegrates and gas venting occurs as shown in Figure IV-4.1, taken from Reference IV-4.4, discrete particles of ejected material follow trajectories that are, except for very small windborne particles, essentially ballistic. For near-surface explosions, where the fireball obscures the cratered region, the mechanics of ejection are not so well known. Observations of near-surface explosions show an early, fast-moving corona of material ejected from a position near the charge and at a steep angle to the ground surface. However, the ejection process is known to take place over a longer period of time and to include lower exit angles.

Material fractured by the compression wave may be dislodged and ejected by the explosion gases, as visualized in Figure IV-4.2. However, attempts to predict ejecta ranges by consideration of shock-front conditions and by calculation from early trajectory parameters have not been entirely satisfactory.

Theoretical studies indicate that in large near-surface detonations, ejecta particles of considerable size may be captured by the thermal updrafts and lofted into high nonballistic trajectories. Figure IV-4.3 illustrates origins and relative ranges for general classes of high explosive (HE) charge geometries, as determined from field observations.

The ejecta field is divided into two zones: the crater lip or what is also called the continuous ejecta surrounding the apparent crater, and the discontinuous or missile ejecta comprising the discrete natural missiles falling beyond the crater. The principal parameters used to describe the ejecta are the average lip crest height (H_{al}) (see Figure IV-3.1 for recommended crater nomenclature); the radial extent of the crater lip (R_{eb}) from ground zero (GZ); the depth of deposition, ejecta mass density, and missile size or distribution defined as functions of radial distance from GZ; and the maximum missile range (R_m). The principal
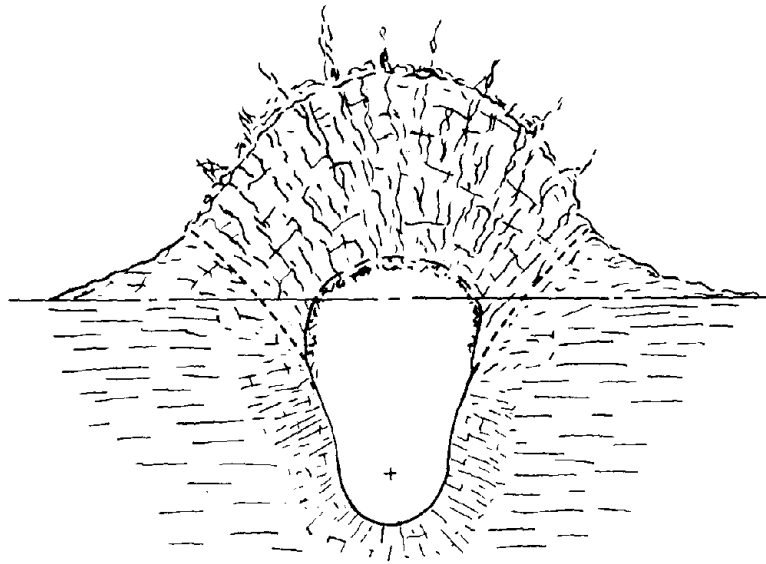
a. Cavity and dome immediately prior to venting.
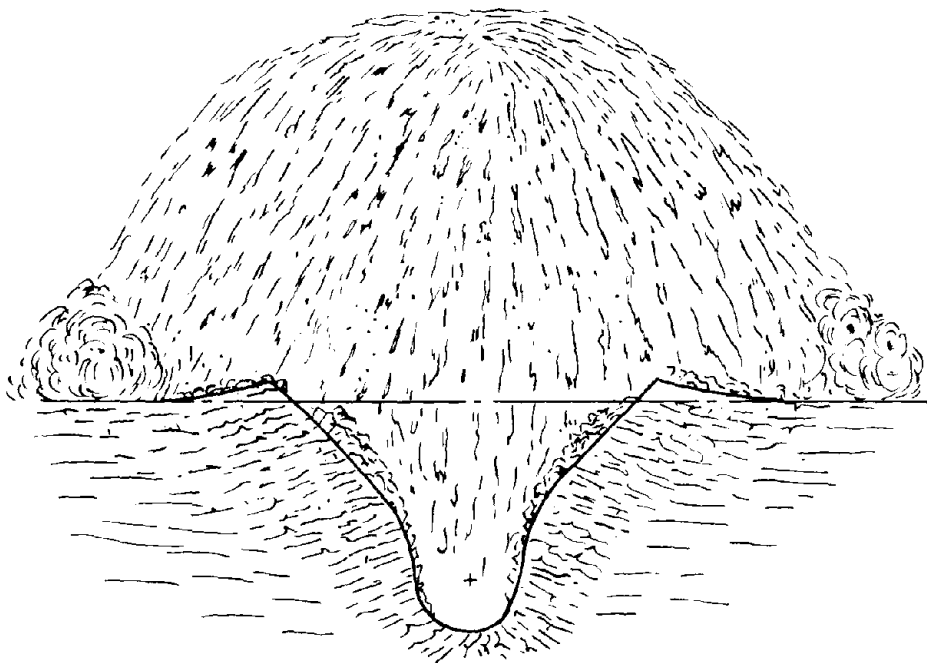
b. Venting and ejection of in-situ material.

Figure IV-4.1. Ejection process for a buried explosion (Reference IV-4.4).
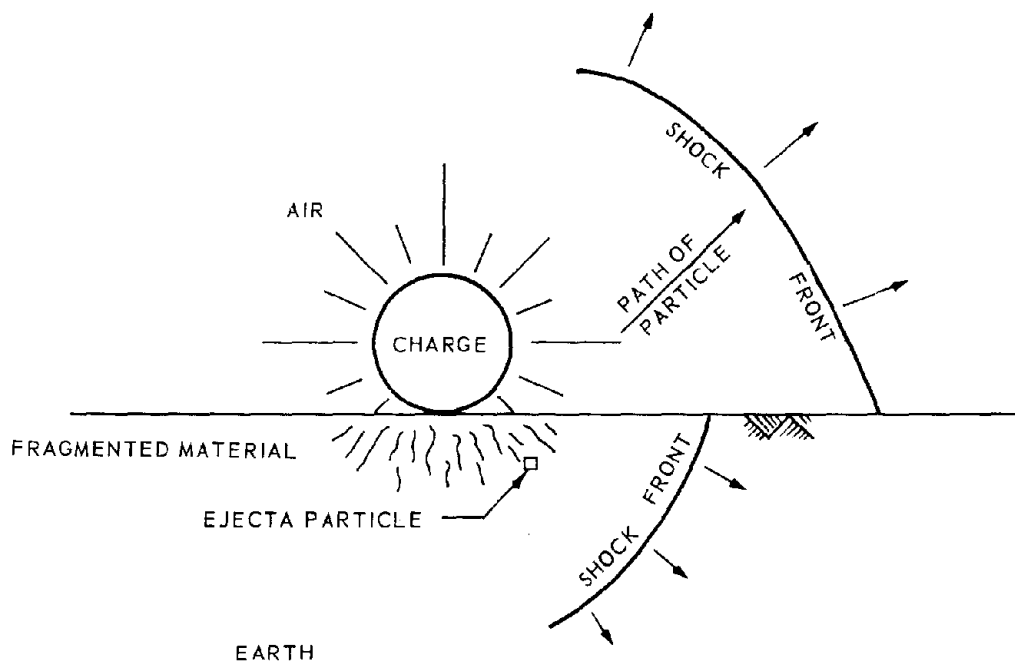
Figure IV-4.2. Ejection process for a near-surface
explosion (Reference IV-4.4).
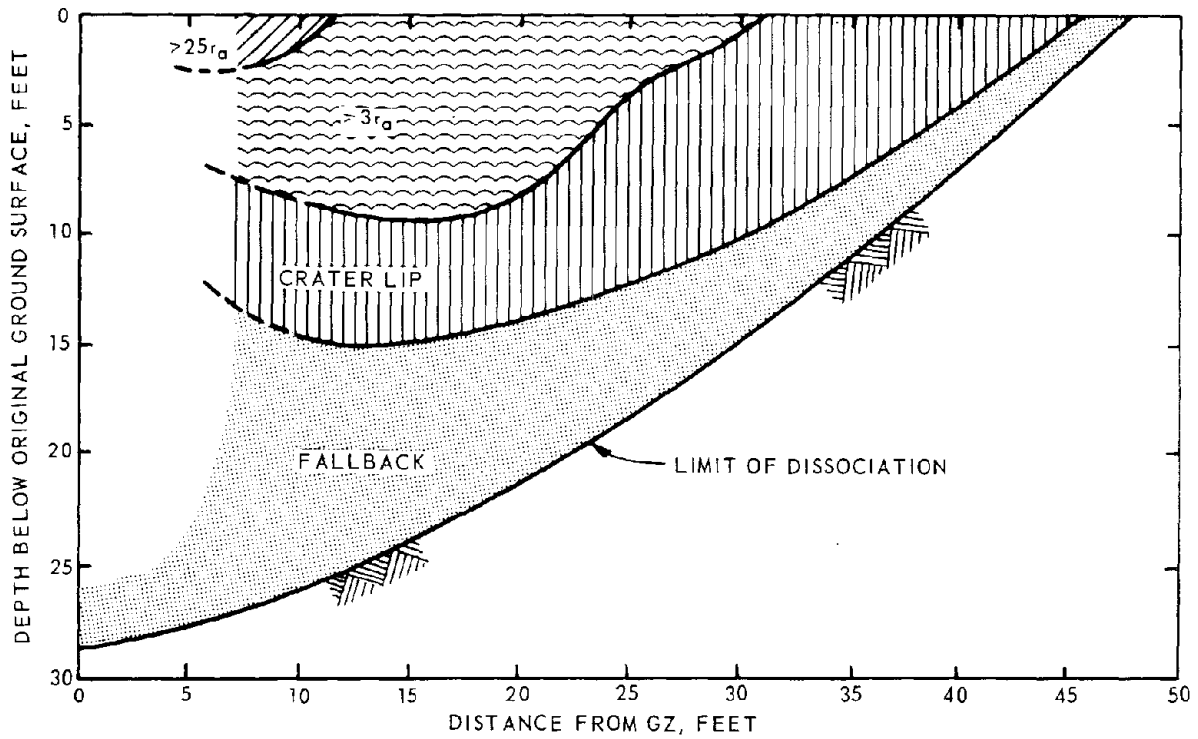
a. Buried detonation (20 tons)
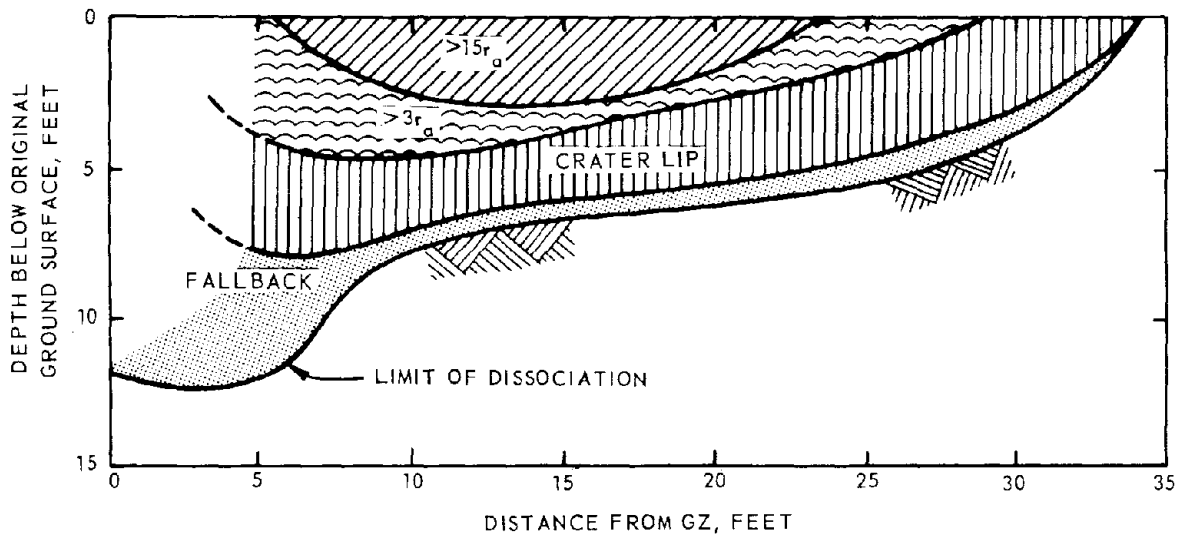
b. Near-surface detonation (100 tons)

Figure IV-4.3. Ejecta origins and relative ranges for HE
detonations (Reference IV-4.4).

variables which control the ejecta parameters are the shot yield and geometry and the physical nature of the earth medium.

The amount and extent of the continuous ejecta in the crater lip are determined primarily by the shot yield and geometry. The radial extent of the continuous ejecta will usually vary from about 2 to 4 apparent crater radii. The maximum depth of this ejecta occurs at or near the lip crest, and its height above the original ground surface can be estimated as about one-fourth to one-third the apparent crater depth for near-surface bursts. For deeper bursts, the lip height is usually one-fifth to one-fourth the apparent crater depth. The depth of continuous ejecta will decrease rapidly with increasing radial distance from GZ. In general, the volume of continuous ejecta varies from about 40 percent to over 90 percent of the total material thrown out, the latter figure being based on near-optimum depth of bursts (DOBs) in cohesive media. Deeper bursts may result in a continuous ejecta containing all of the ejected material surrounding an apparent crater of insignificant size. Figure IV-4.4 illustrates the fraction of total deposition with range from GZ.
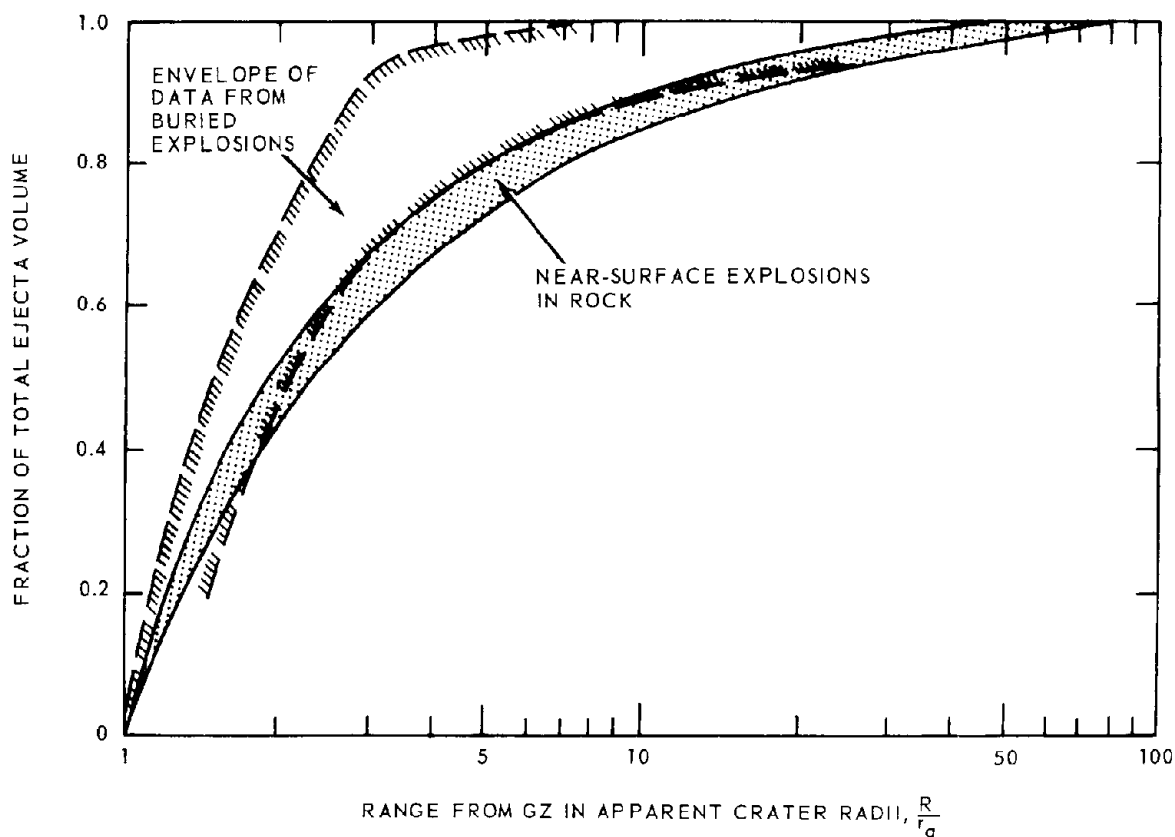
Figure IV-4.4. Fraction of total ejecta volume as a function of range from GZ (Reference IV-4.4).

The discontinuous or missile ejecta beyond the continuous ejecta is usually described by a real mass density in kg/m^2 or lb/ft^2, and a numerical density number of missiles per square meter. Both parameters decrease with increasing radial distance from GZ. A wide circumferential variation is usual which is mainly the result of medium inhomogeneities. Ejecta missile size and quantity within the continuous ejecta region and within the missile ejecta field, depend primarily on the characteristics of the earth medium. For example, the cohesiveness of a soil with a high clay content often results in missiles of substantial size, while a noncohesive material such as sand will produce almost no missiles of significant size. Explosions in glacial tills will produce a large number of long-range missiles. In rock, the spacing of joints is a controlling factor in determining missile size. Means of predicting natural missile-size distribution, either analytically or empirically, are currently considered tentative.

For buried charges, maximum missile range is approximately proportional to the yield to the 1/6 power, and is shown graphically as a function of depth of burst (DOB) in Figure IV-4.5 (from Reference IV-4.5). Surface or near-surface bursts produce maximum missile ranges which more nearly scale as the yield to the 0.3 power. It has been observed that, for near-surface HE geometries, the periphery of the ejecta field consists of predominantly small (less than about 0.5 kg) particles.

IV-4.0.3 Effects of the Environment

In many situations it may be necessary to detonate explosives in a medium containing some environmental anomaly, such as a water table at a shallow depth, a layering of one type of soil over another, parallel planes of distinct jointing in rock, or a steeply sloping ground surface. All of these factors can influence the formation of a crater and the production of ejecta and, in some cases, radically change its size or characteristics.

Terrain slopes of about 5 degrees or greater will affect crater formation for a surface explosion, the venting process for a buried explosion, and ejecta distribution. For gentle slopes, the total volumetric effects will be about the same as for craters on level ground, but the resulting crater will be asymmetrical, wider upslope and with a larger lip downslope. For the field of discrete ejecta particles, greater maximum ranges will occur downslope, assuming that the wind is not a significant factor.
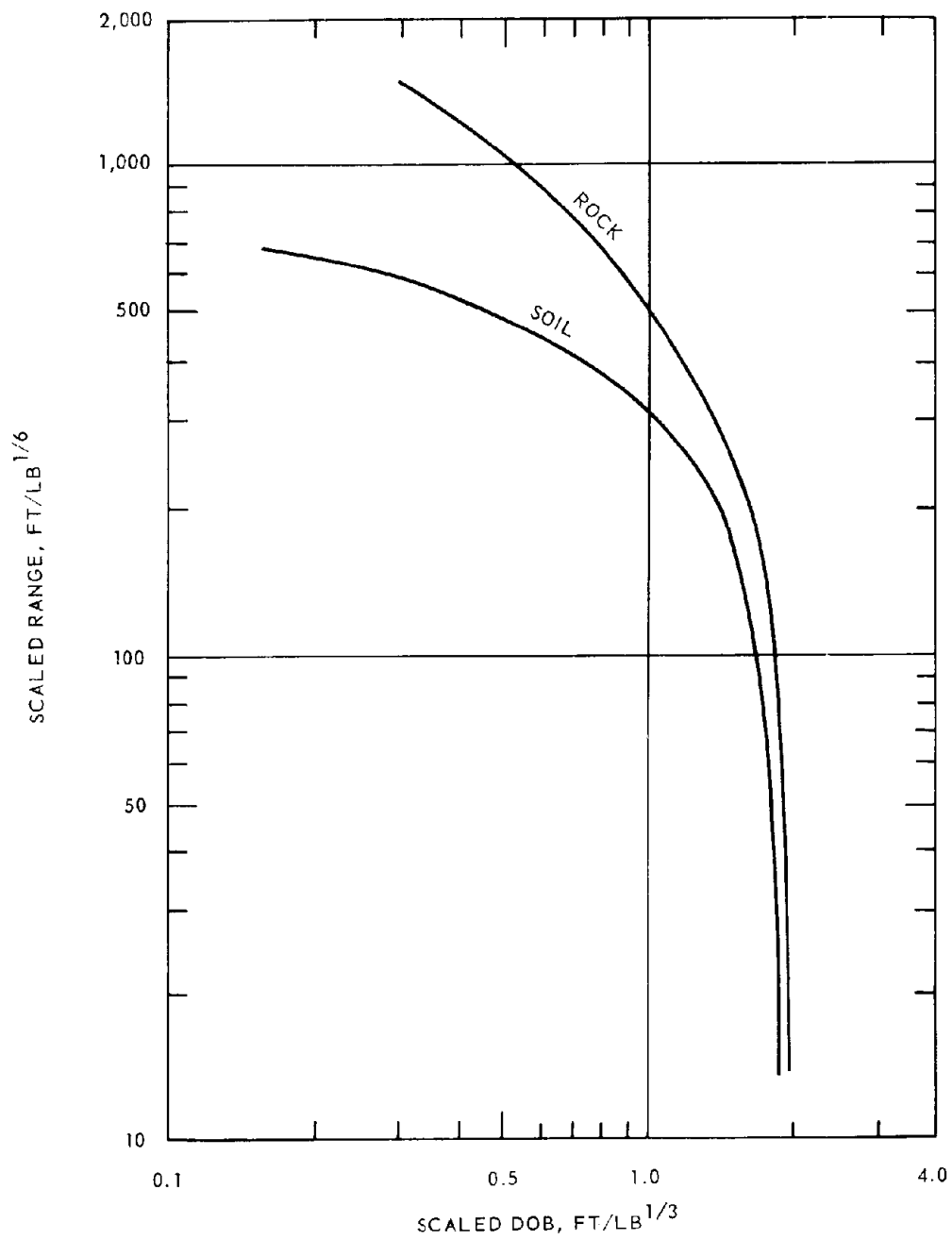
Figure IV-4.5. Maximum missile range for buried
charges (Reference IV-4.5).

Limited small-scale cratering experiments have been conducted in moist, sandy soil and in desert alluvium on slopes ranging from 40 degrees to vertical wedges, the latter representing the extreme in sloping topography. For charges buried on severe but nonvertical slopes, with DOB measured normal from the sloping surface and with the vertical depth of overburden being greater than containment depth, crater dimensions decrease with increasing slope. Optimum vertical DOB and optimum distance from the free, vertical face of a wedge appear roughly the same, and perhaps larger by about one-third than optimum DOB on level terrain. For this geometry, ejecta distribution is preponderantly directed toward the free face, with about three-fourths of the total ejecta mass falling in this direction when DOB is optimum for crater volume. The disparity in ejecta distribution increases with further increase in DOB.

Based upon HE experiments (for example, MIDDLE GUST) a subsurface water table in a soil medium will begin to influence the size and shape of the crater when its depth below the surface is equal to or less than three-fourths the predicted apparent crater radius. Its effect is to flatten and widen the crater. As the water table depth decreases, its effect becomes more evident. For a water table depth of one-fourth to one-fifth the predicted crater radius, the final radius may be as much as 50 percent greater and the depth as small as one-third that of the predicted crater dimensions.

The influence of a bedrock layer below a soil medium is similar to that of a water table, although somewhat less pronounced. For HE explosions at the surface, the bedrock layer may increase the crater radius (within scatter of the data) slightly (5 - 10 percent), and may decrease the final depth by as much as one-third when the overburden layer is as shallow as one-fourth the predicted apparent crater radius.

For low-yield nuclear devices and high-yield HE detonations at or very near the surface, the bedding or jointing planes in rock can influence the shape of the crater produced, as well as the direction of the ejection process. The formation of the crater will tend to follow the direction of the predominant joints, thereby increasing the crater radius by as much as one-third in the direction parallel to the joints, or decreasing it by as much as one-third normal to the joints. Such joints tend to be associated with ejecta rays. The magnitude of the crater depth is usually not affected significantly, but the deepest point may be shifted to one side of the crater. As the yield or DOB is increased, the influence of rock jointing is reduced.

The dip of bedding planes will influence energy propagation, causing the maximum crater depth to be offset in the down-dip direction. Little overall effect is noted in regard to crater radius, but differences in ejection angles cause the maximum lip height and ejecta radius to occur in the down-dip direction.

IV-4.1 NUCLEAR EVENTS

This section contains a discussion of the data from nuclear events. For convenience, these data have been separated into near-surface and deeply buried events.

IV-4.1.1 Near-Surface Events

The ejecta produced by nuclear devices detonated at or near the ground surface is discussed in this subsection. Table IV-4.2 summarizes the list of devices discussed in the subsections that follow.

Table IV-4.2. Summary of near-surface nuclear events.

Code Name	Yield (kt)	DOB (m)	Scaled DOB $(m/kt^{1/3.4})$
JANGLE S	1.2	-1.07*	-1.01
JANGLE U	1.2	5.18	4.91
JOHNIE BOY	0.5	-0.39	-0.48
*A negative sign for the DOB means that the device center of mass was above the ground plane by the amount indicated.			

For the sake of completeness, some of the Pacific Proving Ground (PPG) events will be mentioned only briefly. However, it is well to remember that the PPG events were mainly device development tests and as such not specifically instrumented for ejecta measurements. Craters were measured but only to the extent which was needed to determine the explosive capabilities of these devices. Moreover, many events resulted in underwater craters for which crater measurements were not extensively carried out, and no ejecta measurements were ever made. In fact, a megaton device has never been detonated by the United States with a cratering experiment as its primary objectives. Moreover, the United States has never detonated a megaton device in such a configuration as to create a crater in hard rock or soil. From the point of view of cratering, these PPG events exhibit various undesirable features that lead to ambiguities in the interpretation and

analysis of these data. The fact that six craters produced by megaton yield devices have been measured is in itself significant.

The choice of the events chosen for discussion as shown in Table IV-4.2 was based on availability of data. LITTLE FELLER I and II were left out because they had yields lower than JOHNIE BOY and the author felt no new additional information would be added by including their description in the discussion. The ejecta data available from the events listed in Table IV-4.2 were extracted from the original Operation Officer's Reports.

Table IV-4.3 summarizes the type ejecta information if any is available for the events listed in Table IV-4.2.

Table IV-4.3. Summary of ejecta data available for
events listed in Table IV-4.2.

Event Name	Type of Data
PPG Events	No ejecta data
JANGLE S and U	Some general crater measurements
JOHNIE BOY	Detailed Mass distribution measurements

IV-4.1.1.1 The PPG Events. There were 10 major nuclear devices detonated at the PPG. The detonations occurred over saturated coral and resulted in underwater craters. Most of these craters were subsequently severely water-washed making their measurements less accurate. These devices ranged in yield from 13.4 kt to 14.5 Mt. One of these events was CACTUS, detonated on the end of a small island with the crater dimensions smaller than had been anticipated. CACTUS was not water-washed and was completely contained within the island and the reef rock. A distinct lip was formed around the crater, with sections of the lip as high as 7.6 meters on all sides of the crater except north which opened onto the water-washed reef. It was observed that even after a few tidal cycles, the crater lip changed considerably. In the summer of 1974, it was observed that little silt deposit had occurred in that crater due to the tidal cycles even though the Islands were hit twice by a typhoon, one in 1968 and the other in 1971. This lack of silt deposit was attributed to the crater lip remaining from the shot.

LACROSSE was detonated on a man-made earth-filled causeway built over the reef. The center of the device was 2.6 meters above the causeway, itself 2.6 meters above the original reef surface. The LACROSSE crater did not breach to the open water of the lagoon and hence was not water-washed. LACROSSE is one of the few Pacific craters showing a definable lip and evidence of ejecta.

IV-4.1.1.2 JANGLE S and U. The JANGLE U was an underground nuclear event and JANGLE S was a surface event: both events were carried out at the Nevada Test Site (NTS) in November 1951 with the general objective of determining the properties of surface and underground nuclear detonations. Both devices had a yield of 1.2 kt with the JANGLE U device detonated at a depth of 5.18 meters and with the JANGLE S device detonated at 1.07 meters above the ground surface. Among the basic phenomena measured, only the crater shape and size were measured. Thus, no crater ejecta measurements for these nuclear devices are available. However, data were obtained from discrete missile ejecta produced by concrete and roadway material that were emplaced in the vicinity of GZ of JANGLE U.

For the underground JANGLE U Event, the maximum height of the crater lip above the original ground surface was determined to be 2.4 meters. Crater lip height measurements were made using topographic methods and the lip volume was established at 4570 m³, and using the average soil density of 1.49 gm/cm³, the lip volume was determined to be 6800 metric tons. A profile on an east-west line across the crater and the lip taken at the crater's deepest point is shown in Figure IV-4.6.

For the surface JANGLE S Event, the height of the crater lip was 1.5 meters above the original ground surface. The volume of earth comprising the crater lip was estimated to be 344 m³. This represents, using the same soil density as for JANGLE U, approximately 513 metric tons of earth. Figure IV-4.7 shows a profile of the surface shot crater taken across the crater's deepest point.

The missile experiment performed as part of the JANGLE U explosion test demonstrated that reinforced concrete walls and highways located approximately 12 meters to 43 meters from GZ were broken and thrown out as missiles. Material nearer than 12 meters was vaporized or pulverized to the extent that it was largely windborne. Missiles were found over a range from 120 to 1000 meters from GZ. The missiles of major significance were found in the range from 120 to 460 meters. From this experiment, it was concluded that for shallow undergound nuclear explosions, the airblast damage extended farther than the damage produced by missiles and, therefore, no further missile experiments of this kind appeared necessary (References IV-4.6 and IV-4.7).
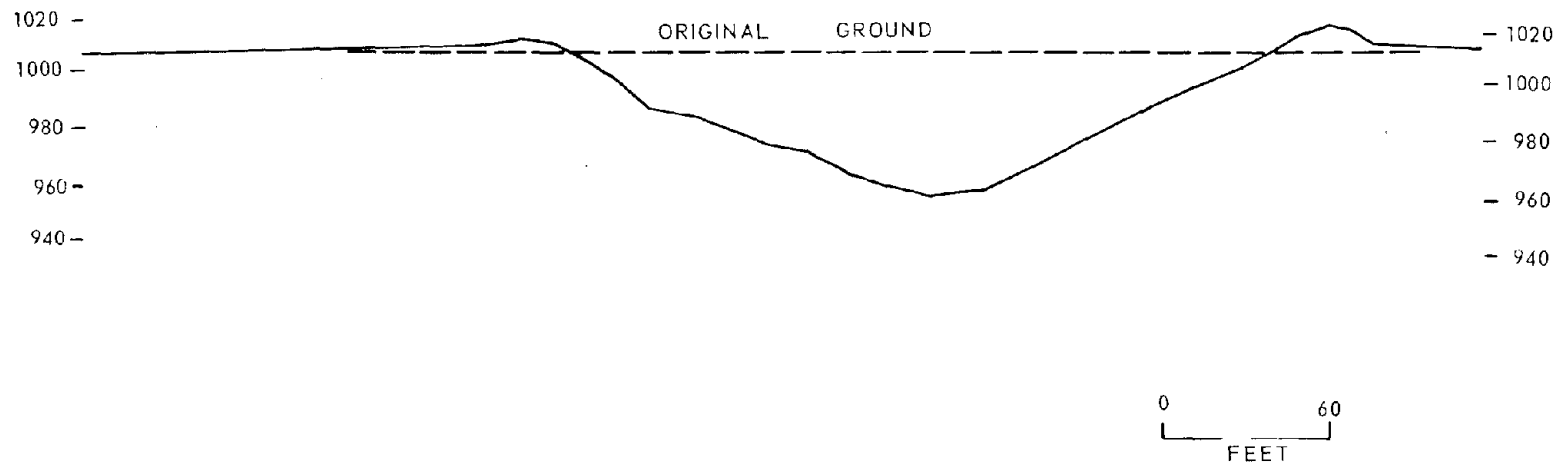
Figure IV-4.6. Crater centerline profile - underground shot, east-west.
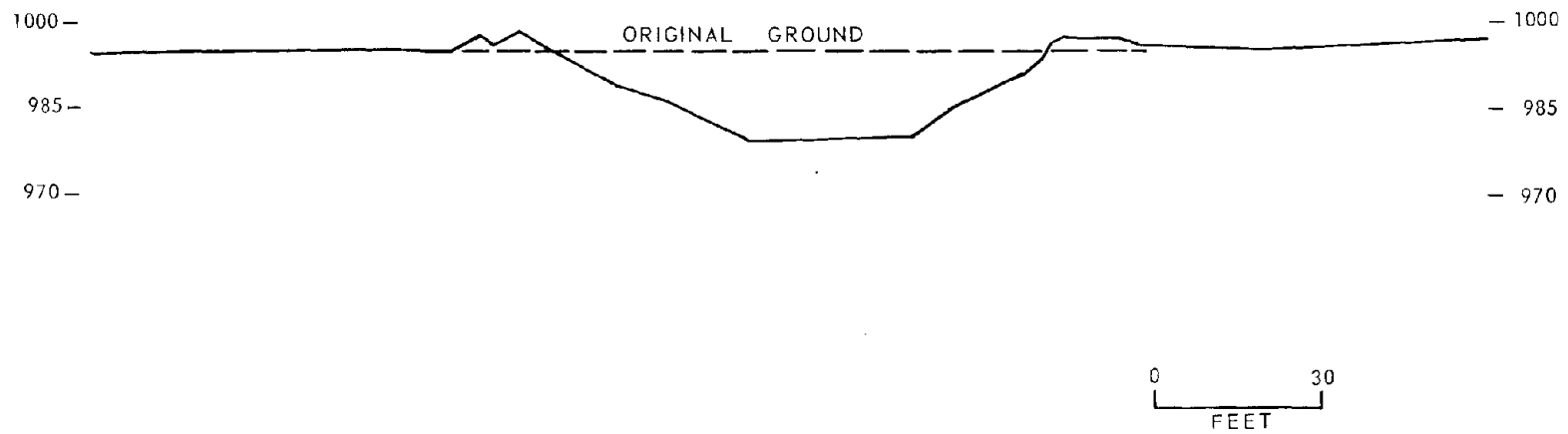
Figure IV-4.7. Crater centerline profile - surface shot, bearing N62°30'W.

IV-4.1.1.3 <u>JOHNIE BOY</u>. The JOHNIE BOY Event was a nuclear device with a yield of 0.5 kt detonated at the NTS at a DOB of 0.58 meter. Because of the objectionable level of radiation following the detonation, the early crater measurements were made by aerial stereophotography from which contour maps were drawn. Comparison of preshot and postshot maps enabled an early determination of the dimensions of the crater to be made. Ground surveys of the crater were undertaken some 7 months after the event. This survey yielded two profiles of the crater, one on the north-south and the other on the east-west axes. These profiles are shown in Figure IV-4.8 which includes the elevation markers above mean sea level. An investigation of the ejecta and the postshot ground surface in the crater lip was also made.

Ground survey showed that the average lip height was approximately 3.35 meters above the preshot ground surface. The maximum and the minimum lip crest heights were determined to be 4.9 and 2.4 meters, respectively. Detailed analysis gave the JOHNIE BOY crater and ejecta characteristics reproduced here in Table IV-4.4.

Table IV-4.4. JOHNIE BOY crater and ejecta volumes.

Volume	Values (m^3)
True crater, V_t	6010
Apparent crater, V_a	4110
Dissociated material, V_{dis}	~3590
Fallback, V_{fb}	~1900
Lip, V_ℓ	~5200
Ejecta, V_e (as measured) (including 1 percent fallout)	2975 3005
Compression, V_c	~77
Upthrust, V_u, or flowage, V_f	~2370
Vaporization, V_v	Negligible
Permanent deformation, V_d	1.158×10^5
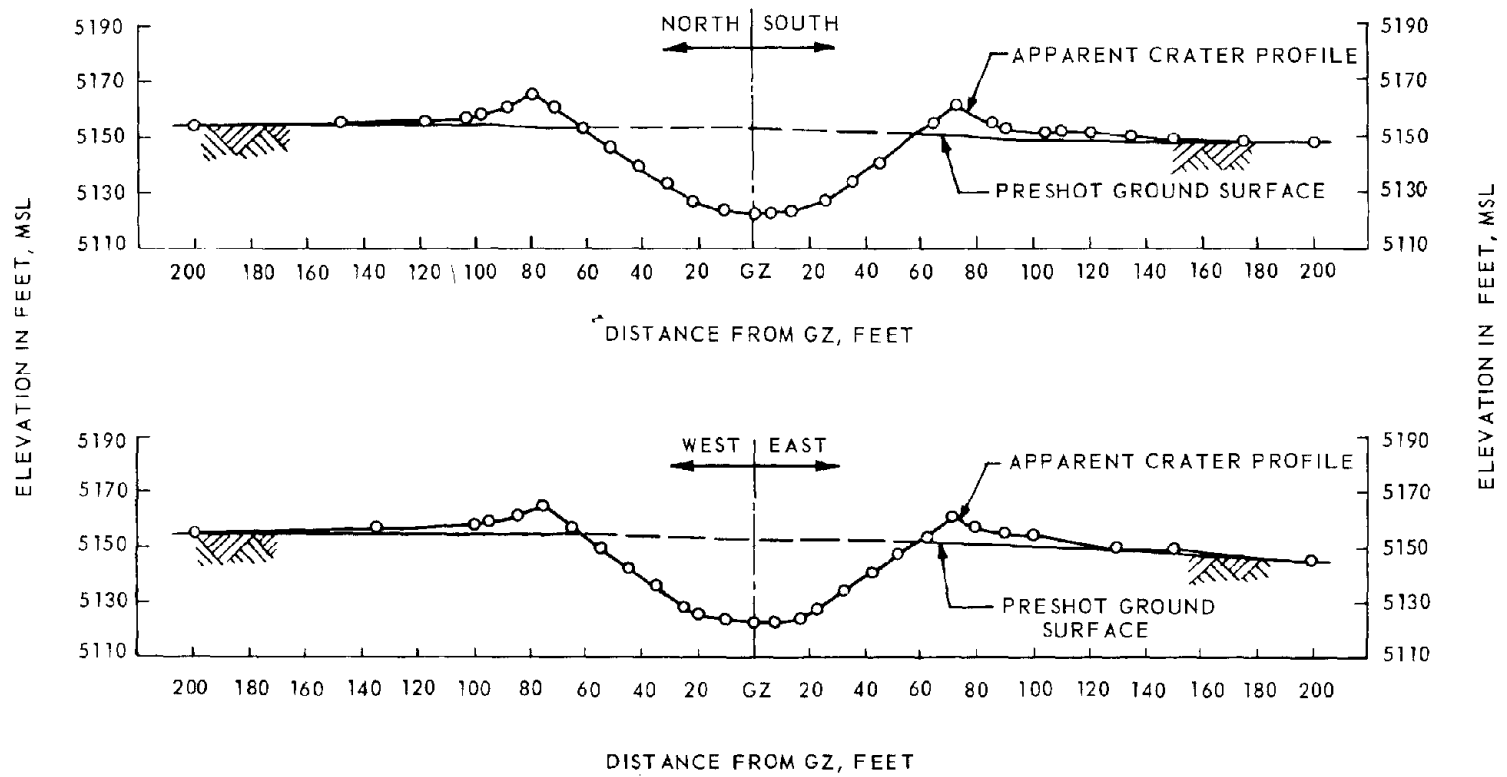
Figure IV-4.8. Apparent crater profiles (two diameters).

One of the objectives of the test was to determine the distribution of the crater ejecta that resulted from the JOHNIE BOY detonation. This included the determination of the distribution by weight or mass and grain size. To perform measurements in keeping with this objective, a circular pattern of ejecta collectors was chosen and arranged along seven circles concentric with GZ. The circular pattern was chosen because of somewhat unpredictable wind pattern and because of the random circumferential variation in ejecta deposition that was known to have occurred in previous experiments. The greatest radial distance was 600 meters and represented 30 predicted crater radii. This was the maximum distance at which recovery of identifiable ejecta samples was anticipated. The minimum distance was 50 meters, selected as the range slightly outside the predicted crater lip. Since it was observed in past tests that ejecta deposition decreases with range from GZ, the radial distance of each circular pattern was based on a geometric progression having a common ratio $r \simeq 1.5$. The number of collectors on each ring was approximately proportional to the circumference of the ring, beginning with a minimum number of 12 collectors on the three inner rings. The total array included 186 collectors.

Each collector consisted of a 0.70 m^2 (0.76 x 0.91 meter) metal pad. The collectors on the three innermost rings were set in concrete to prevent their dislodgement by blast and shock. The rings were coded in alphabetical order commencing with "A" nearest GZ and numbered clockwise with the first number beginning east of true north. To guard against preshot accumulation of debris, regular cleaning of the collectors was made until just prior to shot time.

Recovery began one day after shot time and continued intermittently until 15 days later at which time 135 collectors had been examined and 73 samples recovered. Three months later the remainder of the recovery work was accomplished. Of 186 collectors, 100 samples were obtained, 21 collectors were destroyed or buried by debris, and 3 collectors were found to be useless. The remaining 62 collectors contained no identifiable deposition. Several of the close-in pads had been dislodged by the blast, but the concrete bases were found in place so that samples were collected from them.

Recovery of ejecta samples from the A ring was poor because of the effects of the blast and because of the ejecta thickness, which made it difficult to locate the collectors. The recovery for rings B through G was satisfactory although some of the collectors on the F ring and most of those on the G ring had no discernible

ejecta deposited on them. The ejecta areal density data are presented graphically
on an ejecta distribution map shown as Figure IV-4.9. Although at shot time a 7-mph
wind was blowing, it appears to have had no effect on the ejecta distribution.
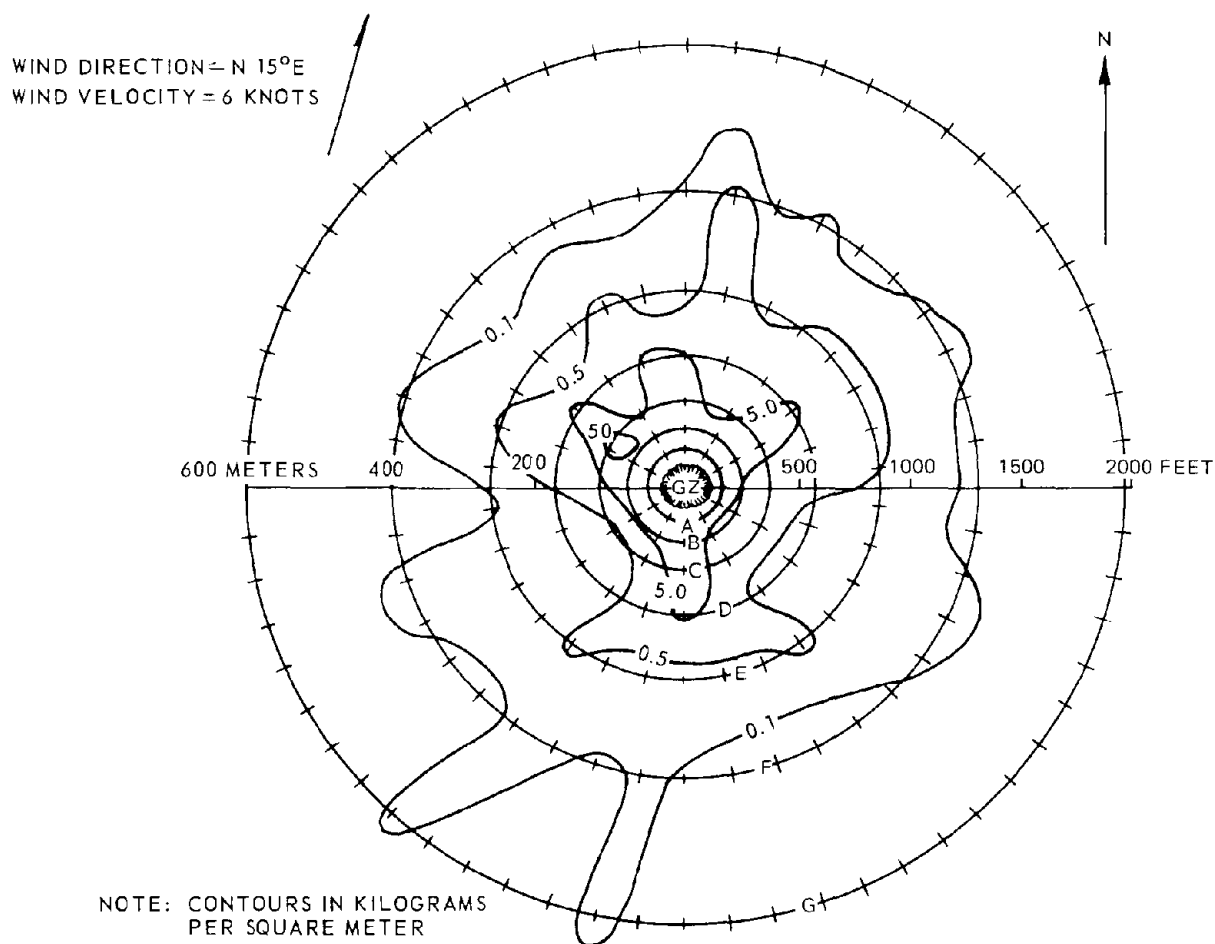
Figure IV-4.9. Ejecta distribution contours.

The observed pattern of ejecta deposition for JOHNIE BOY is shown in Figure
IV-4.9 and the pattern shown conforms to those obtained from similar experiments.
Ejecta deposition quantities on the order of 5 kg/m² generally occurred within a
radial distance of less than 200 meters or ten apparent crater radii. The ejecta
distribution is plotted logarithmically as a function of radial distance from GZ
and shown in Figure IV-4.10. Average values of ejecta thicknesses were used

assuming a soil density of 1.5 gm/cm³ to compute the ejecta mass inside a 50-meter ring. The total mass of ejecta, M_e, was computed from the equation

$$M_e = 2\pi \int_{R_0}^{\infty} \delta(R)R\,dR \qquad \text{(IV-4.1)}$$

where $\delta(R)$ is the ejecta areal density function shown in Figure IV-4.10. Thus, $\delta(R)$ is a power law of the form

$$\delta(R) = k\,R^m \qquad \text{(IV-4.2)}$$

where k is determined from the data and m is the slope. If the JOHNIE BOY data is plotted on a semilogarithmic paper, Figure IV-4.11 shows that the data can be represented by two power laws. The first would apply for the range $23 \leq R \leq 50$ meters from GZ while the second for $50 \leq R < 600$ meters. The same data is also presented in dimensionless form in Figure IV-4.12. Finally, the fraction of total ejecta volume V_i/V_e as a function of ground range in units of crater radii is shown in Figure IV-4.13. This figure shows that 53 percent of the JOHNIE BOY ejecta was deposited within two crater radii, 75 percent within three crater radii, and approximately 90 percent within five crater radii.

IV-4.1.2 Deeply Buried Events

This section presents a summary discussion of the nuclear devices detonated at scaled depths of burst greater than 10 $m/kt^{1/3.4}$, but not so deep as to produce a completely contained cavity (camouflet). Table IV-4.5 summarizes a list of these events, their code names, yields, DOB, and scaled DOBs.

Table IV-4.5. Summary of deeply buried nuclear events.

Code Name	Yield (kt)	DOB (m)	Scaled DOB $(m/kt^{1/3.4})$
CABRIOLET	2.3	51.82	40.56
DANNY BOY	0.43	33.5	42.94
SCHOONER	35.	108.0	37.96
SEDAN	100.	194.0	50.07
TEAPOT ESS	1.2	20.4	19.34
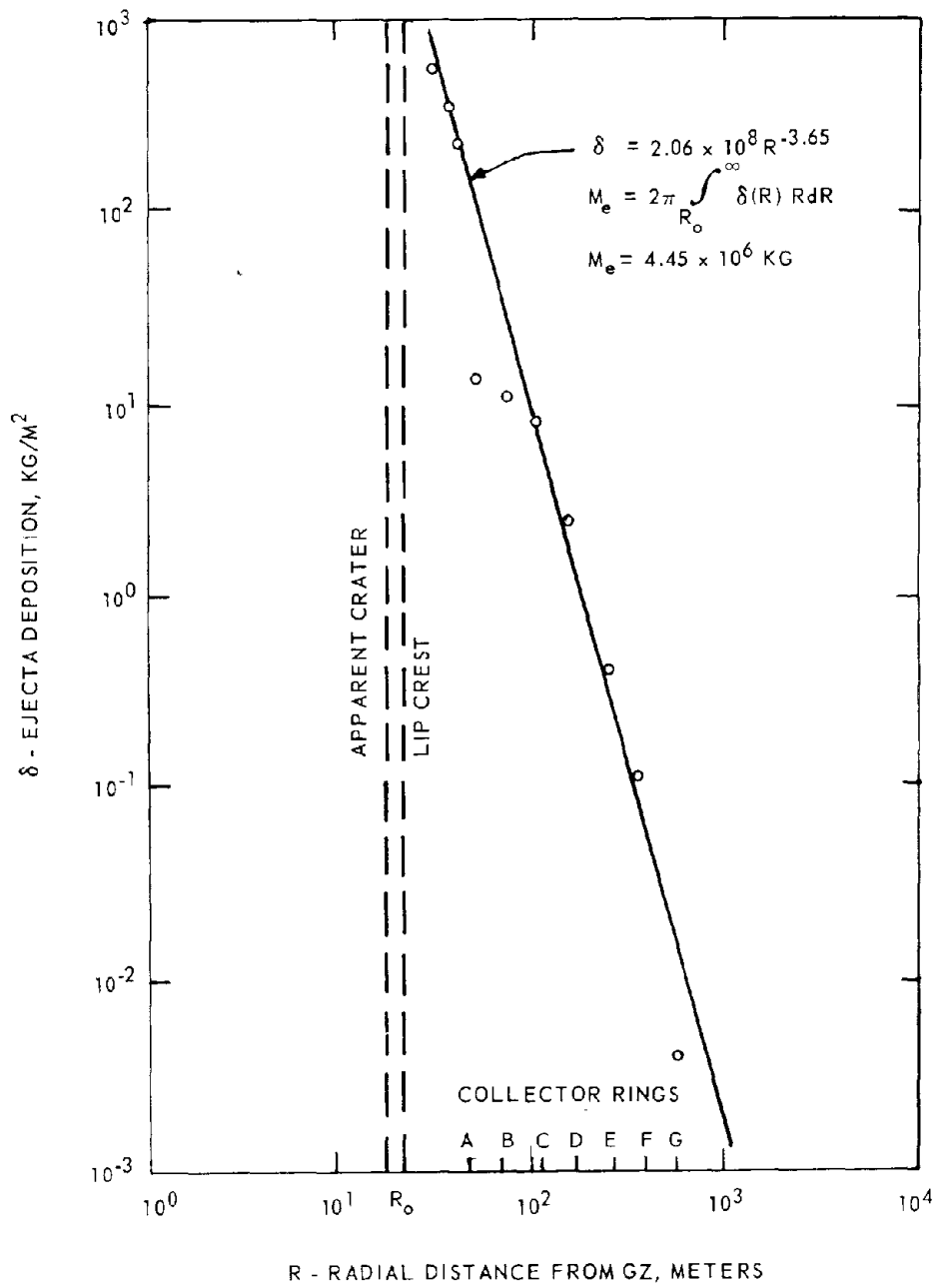
Figure IV-4.10. Ejecta distribution, JOHNIE BOY. (Data points represent arithmetic means of recoverable samples. One data point, 1,890 kg/m² at 24.4 meters, is not shown. Data points for rings A and B were not used in computation of curve.)
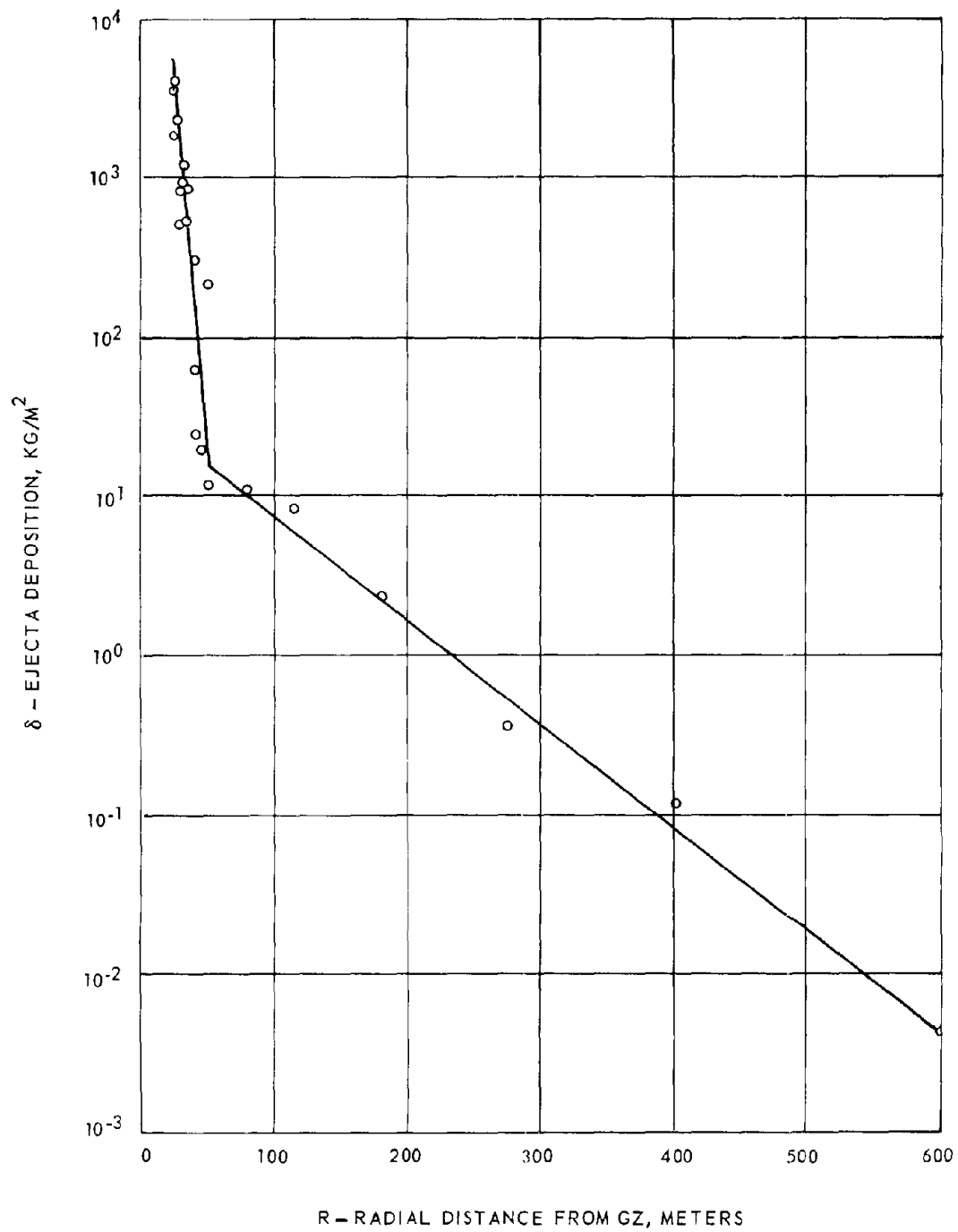
Figure IV-4.11.   Exponential distribution of ejecta, JOHNIE BOY.

The equation shown on the plot:

$$\frac{\delta r_a d_a}{w} = 1.89 \left(\frac{R}{r_a}\right)^{-3.65}$$

Vertical axis: $\dfrac{\delta r_a d_a}{w}$

Horizontal axis: $\dfrac{R}{r_a}$ (CRATER RADII)
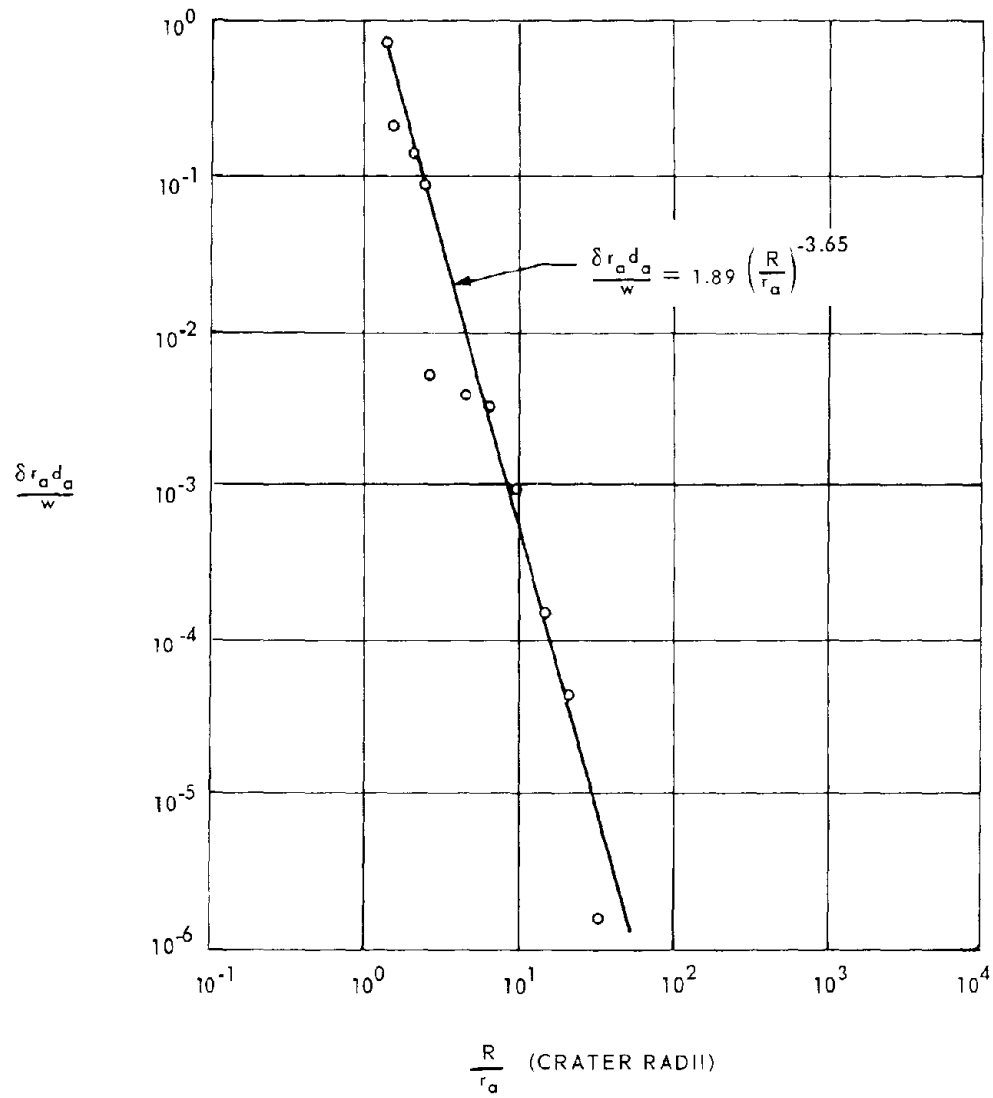
Figure IV-4.12. Dimensionless plot of ejecta deposition versus range for JOHNIE BOY.
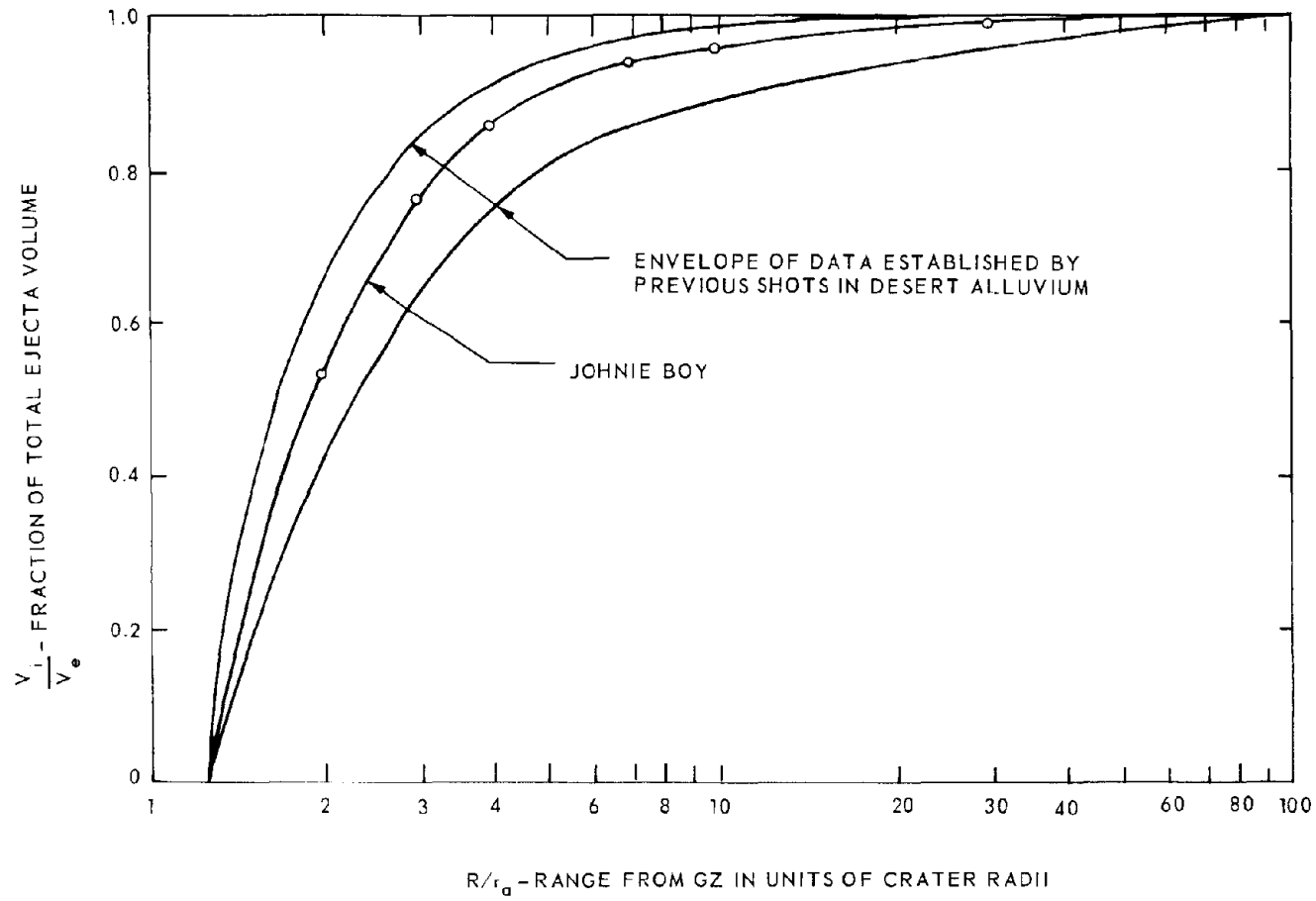
Figure IV-4.13.   Fraction of total ejecta volume as a function of range from GZ.

All of these devices except TEAPOT ESS were detonated as part of the PLOWSHARE Program. For some of these events little useful ejecta information could be obtained. Table IV-4.6 summarizes the type of information that could be obtained from available reports. The DANNY BOY, SCHOONER and the SEDAN Events were well instrumented to measure continuous ejecta field and the missiles ejecta. Only one continuous ejecta profile could be found for the CABRIOLET Event. In the sections that follow, the data about each event listed in Table IV-4.5 are presented in alphabetical order for convenience.

Table IV-4.6. Summary of ejecta and crater data available on events listed in Table IV-4.5.

Code Name	Type of Data
CABRIOLET	One profile of crater and continuous ejecta.
DANNY BOY	Extensively instrumented for continuous and missile ejecta.
SCHOONER	Well instrumented for ejecta.
SEDAN	Extensively instrumented for continuous and missile ejecta.
TEAPOT ESS	Only crater measurements and near crater edge ejecta data could be found.

IV-4.1.2.1 CABRIOLET. The CABRIOLET device was detonated at a depth of approximately 52 meters in the Pahute Mesa media at the NTS. The site media consisted of a dry dense porphyritic trachyte overlain by a thin soil layer. Investigations reported in Reference IV-4.8 deal with the results of a single-trench excavation of the crater lip to determine the engineering properties of the ejecta material. While the in-situ density within the true crater was estimated to be 2.19 gm/cm^3, the measured bulk density of the ejecta was 1.98 gm/cm^3, giving a bulking factor of 1.10. The average particle size in the ejecta determined by mechanical screening was found to be approximately 4 cm. The maximum upthrust in the excavated trench measured 4.3 meters and the true crater radius inferred from observations in this trench is 64 meters. Table IV-4.7 summarizes crater and ejecta dimensions and volumes.

Table IV-4.7. CABRIOLET crater dimensions.

Measurement	Value
Apparent Crater Radius, m	54.68
Maximum Apparent Crater Depth, m	35.48
Average Height of Apparent Crater Lip Crest, m	9.69
Apparent Lip Crest Radius, m	65.15
Radius of Outer Continuous Ejecta Boundary, m	201
Apparent Lip Volume, m^3	184,900
Apparent Crater Volume, m^3	137,600

The measured profile of the crater at the trench location is shown in Figure IV-4.14. It shows that the maximum uplift along the trench is approximately 4.27 meters occurring at a distance of about 61 meters from surface ground zero (SGZ) and decreases to zero at a distance of about 142 meters from SGZ. No other information on the ejecta could be found for this event.

IV-4.1.2.2 DANNY BOY. The DANNY BOY Event was a nuclear device having a yield of 0.42 kt detonated at the near optimum depth of 33.5 meters in basalt at the NTS. The mesa surface consists of numerous loose, weathered basaltic rocks of small boulder size, and the thin overburden consists of an unconsolidated, very fine-grained material resembling silt. The basalt is largely vesicular becoming more consolidated with depth.

One of the experiments on operation DANNY BOY was designed to measure the ejecta from this underground nuclear detonation. A series of 1145 objects were placed at predetermined locations both on the ground surface, at shallow-buried depths (0.3 meter) and at available drill holes in the crater region. The objects emplaced on the surface and at 0.3-meter depth included a wide range of geometric shapes and sizes: "ideal" geometric solids and such debris as bricks and lumber.

The initial locations of these objects, which affect their initial velocities and drag coefficients can be expected to influence their trajectories and ranges.
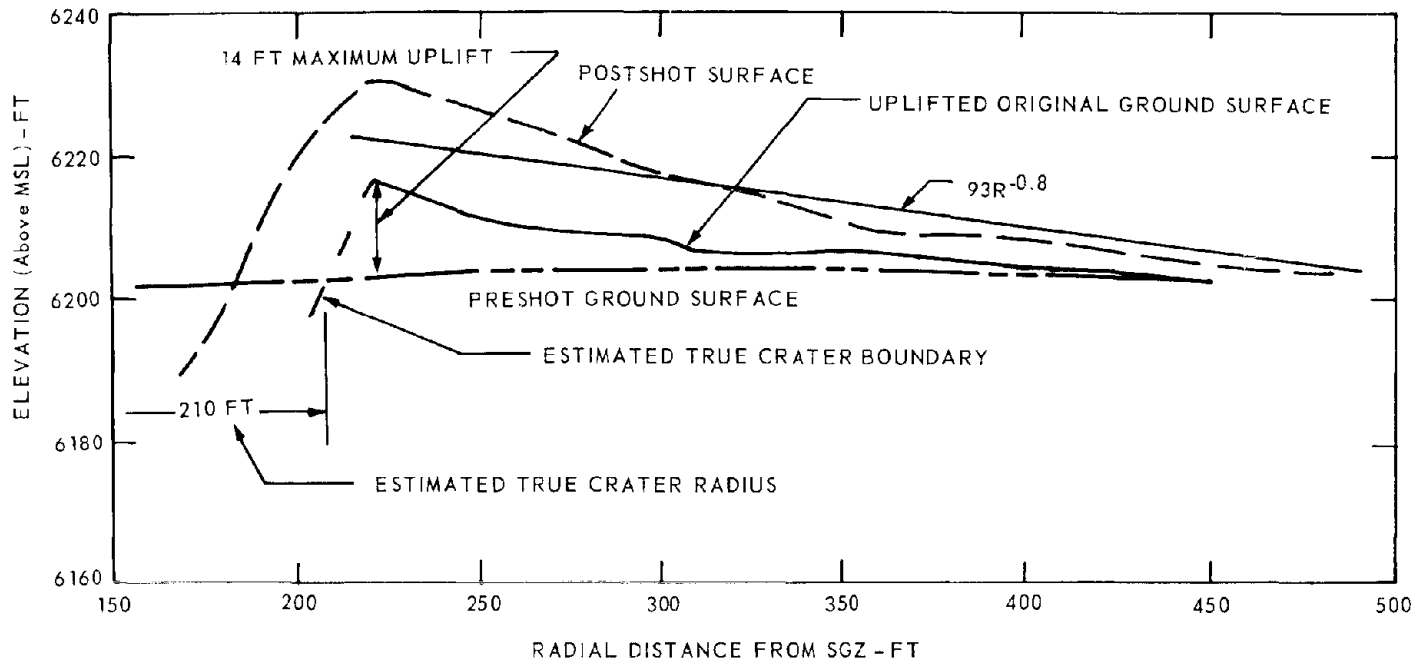
Figure IV-4.14. Post-trenching profiles.

Therefore, an array of ideal objects was placed in the predicted crater region to provide for a broad range of these parameters. All objects, except the wood and brick piles, were serialized for identification of their initial positions. The piles of bricks and the wood blocks were color-coded to identify their initial locations.

Besides deeply buried objects, the placement of surface objects was planned to provide for the following conditions: coverage of ground range to range just beyond the preshot estimate of the crater diameter, placement of objects in all quadrants so that any cratering asymmetry could be analyzed, doubling up of differently shaped objects along various radial lines so that the effects of shape factors could be compared, and clustering of materials in piles for posttest measurements of dispersion of items having nearly identical initial locations. Deeply buried objects were placed in existing drill holes.

After the detonation the apparent crater radius was measured at 32.6 meters with an apparent depth of 18.9 meters. The apparent crater volume was estimated to be approximately 27,600 m^3 and the average lip height was measured at 7.32 meters (Reference IV-4.9). Figure IV-4.15 shows the shot geometry and the crater dimensions.

Terminal locations of the ideal objects were found by visual search of the postshot area. The positions of the objects sighted were marked with stakes and their locations determined. Objects found by this method included those found at the surface in the lip region (continuous ejecta) and beyond the edge of the lip to a ground range of about 120 meters (approximately 3 crater radii).

Posttest collection of data was limited to visually located objects. Beyond the edge of continuous ejecta this means essentially complete recovery. Figure IV-4.16 shows three areas beyond the continuous ejecta boundary selected for measuring the distribution of ejecta. The edge of the continuous ejecta was considered to be the limit beyond which the ejecta did not completely obscure the area surveyed by compass and tape methods.

Of the 1145 ideal objects emplaced only 186, or 16.2 percent of the total, were located and their terminal positions determined by survey methods. The recovery rate was highest for surface objects and lowest for deeply buried objects. Table IV-4.8 shows the percentage of all objects recovered.
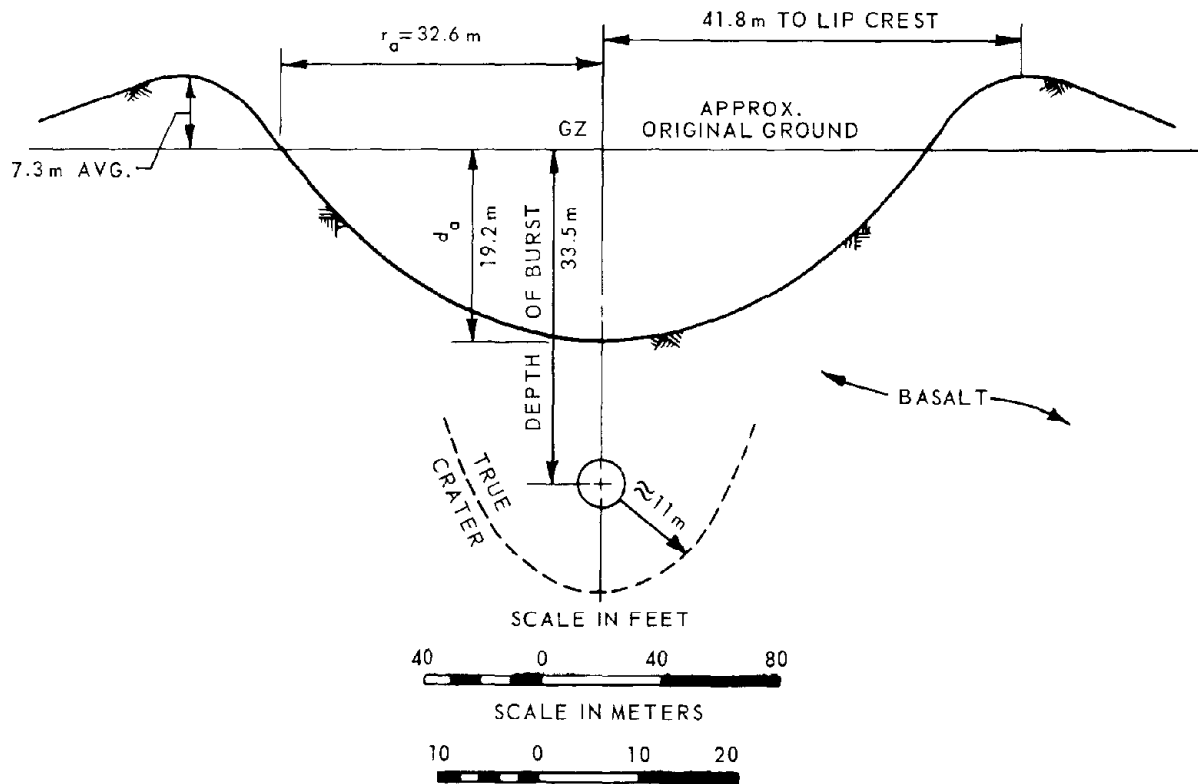
Figure IV-4.15. Shot geometry and crater dimensions, DANNY BOY.

Table IV-4.8. Number of objects recovered.

Placement	Number Placed	Number Recovered	Percent Recovery
Surface	889	161	18.1
Near-Surface	132	20	15.2
Deeply Buried	124	5	4.0
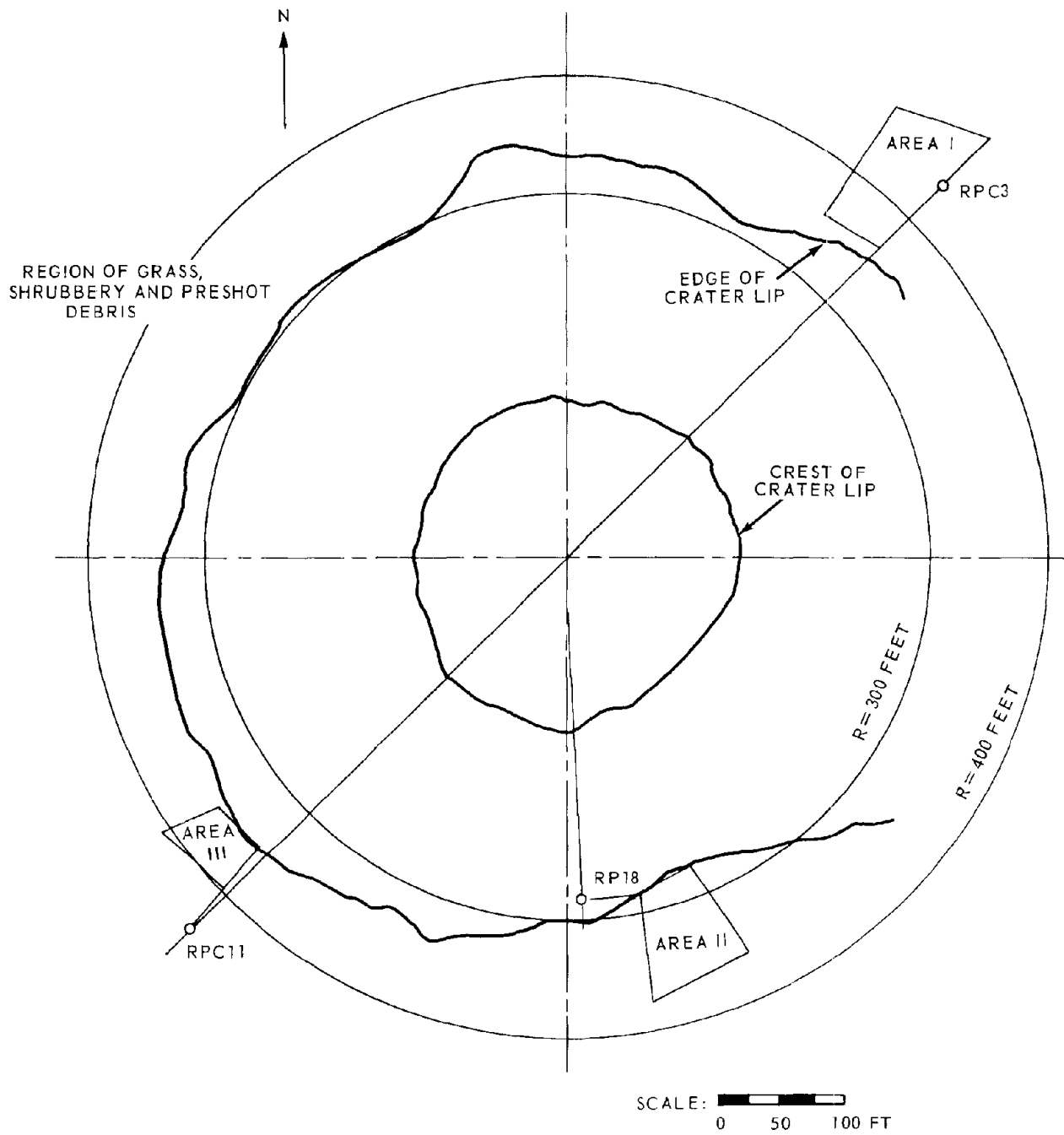
Figure IV-4.16. Areas selected for measurement of natural throwout material.

The ideal objects were found on the surface of the continuous ejecta and beyond the continuous ejecta boundary to a maximum range of approximately 120 meters from SGZ (see Figure IV-4.16). Many objects that remained undiscovered are undoubtedly concealed within the continuous ejecta. The relatively short terminal range at which most objects were found, and the large number of ideal objects remaining concealed in the lip and in the fallback material in the crater, is thought to be due to the considerable depth of burial of the device. The resultant trajectories of the ejecta were found to have pronounced vertical components.

The percentage recovery of objects placed along various azimuths is shown in Figure IV-4.17. Although recovery appears higher along the northeast and southwest directions, the actual quantities recovered along most azimuths are small and the nature of this relationship is quite random.

Trajectory computations for the ideal objects recovered were performed and are fully discussed in Reference IV-4.10. Suffice to state here that a simple model was used which takes account of the measured values of the range, assuming initial velocity directions in accordance with Hess's observations that the blast winds can interact with the trajectory to substantially alter the impact point of ejecta (Reference IV-4.11), and the assumption of unimpeded flight for each individual object.

The total distances surface and near-surface objects were thrown are shown in Figure IV-4.18 plotted against the initial position of these objects. The plot shows that the range of values of the distances the objects were thrown is quite dispersed for objects originating from the same initial positions. An envelope of maximum value is shown in Figure IV-4.18 which was estimated on the basis of maximum value curves for initial velocity and flight duration. The curve labeled "equivalent maximum ground range" shown is obtained by adding the initial position to the maximum distance thrown. This assumes that the objects were thrown radially and differs somewhat from the distances at which the objects were actually recovered. This is considered a better measure of thrown range since the causes of asymmetrical behavior were not determined.

An attempt was also made to determine the effect of atmospheric drag on the ideal objects by plotting distance thrown versus minimum and average values of the ballistic coefficient, and also versus the weight of the objects. The results of this analysis were inconclusive.

SYMBOLS:
● SURFACE OBJECTS
× NEAR-SURFACE OBJECTS
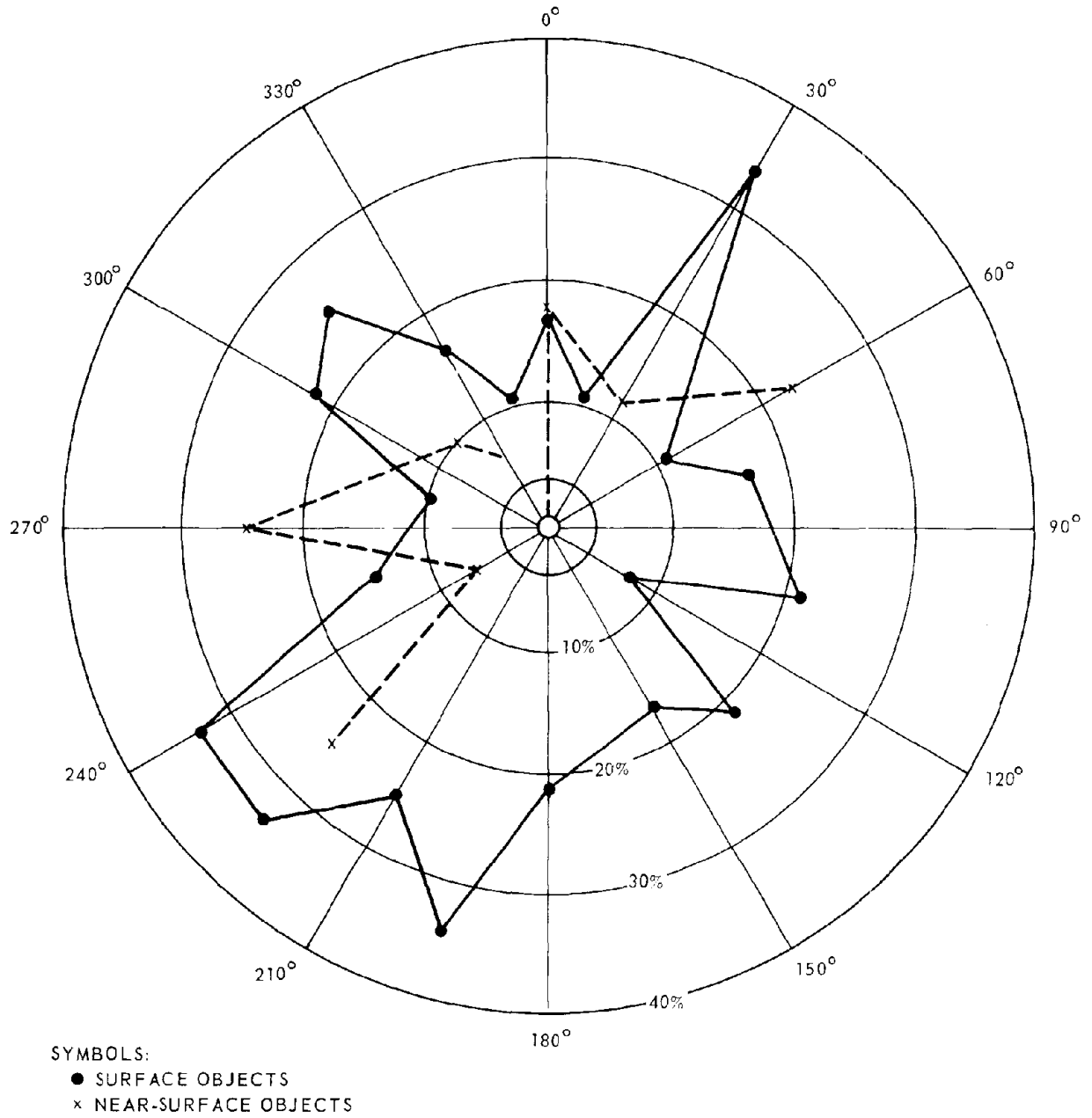
Figure IV-4.17. Recovery of ideal objects versus azimuth.
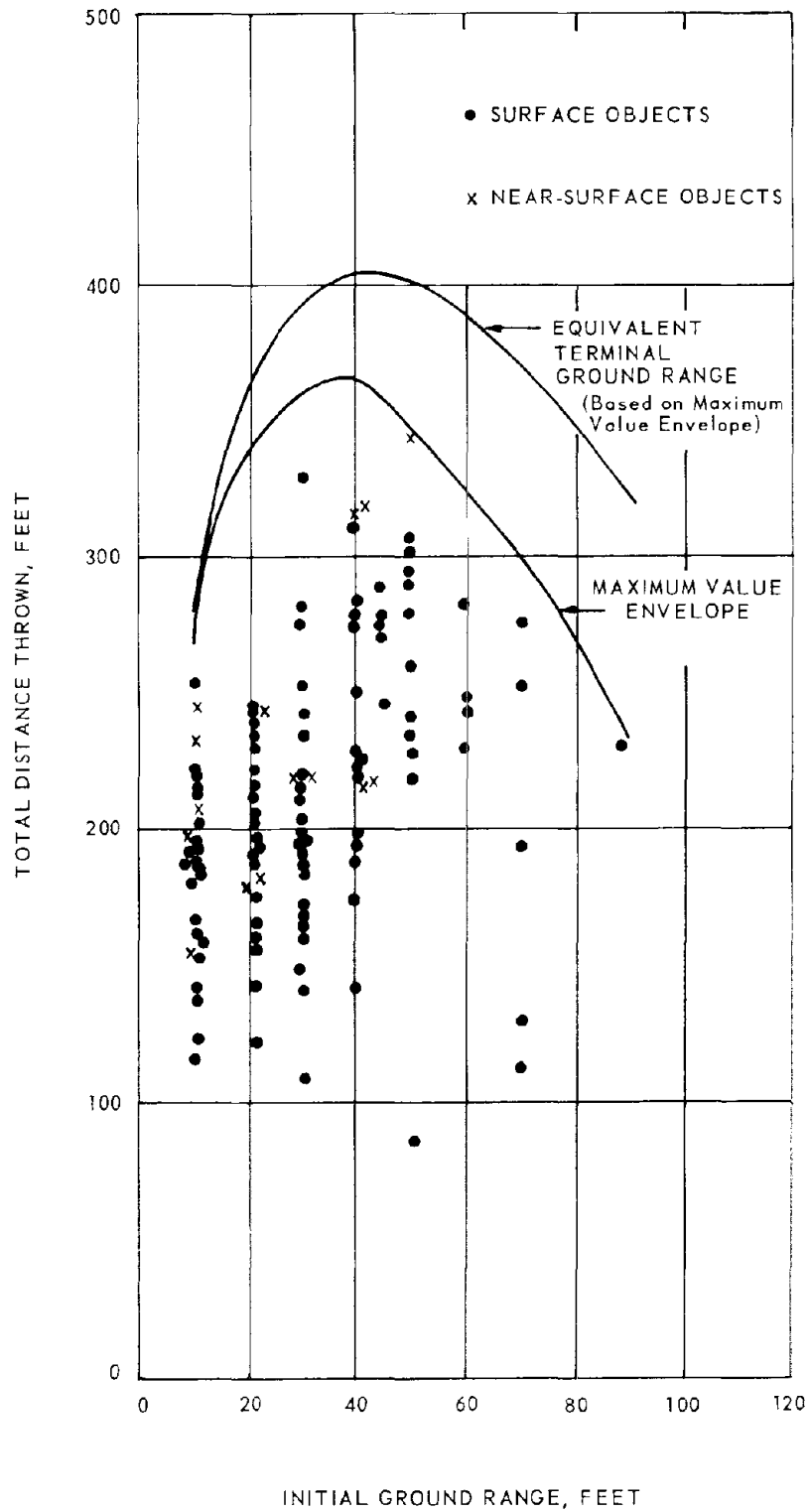
Figure IV-4.18. Total distance thrown from initial position for all objects except bricks and lumber.

Figure IV-4.19 shows the initial velocities of all objects except bricks and lumber for the case of a flat plane neglecting air drag, and for the case of a sloping terrain including air drag. Note the proximity of both curves at large initial ground ranges. Figure IV-4.20 shows the maximum height of the trajectory as a function of the initial ground range of the objects for the case of a flat plane without air drag and for the case of a sloping terrain and air drag. Figure IV-4.21 shows the flight time data for both cases mentioned.

In general, from these figures one can see that the data of all surface and near-surface objects show initial velocities, maximum trajectory heights and total flight time decreasing monotonically with increasing values of the initial position of these objects. These figures also show that by considering the sloping terrain and the effects of air drag, there results larger values of the initial velocities, a somewhat higher maximum trajectory altitude and a somewhat longer flight duration.

Additional analysis indicated that the loss of energy between the initial and the final conditions was from 10 to 20 percent for steel objects, from 50 to 90 percent for wood objects, approximately 50 percent for bricks, and ranged from about 30 to 90 percent for empty spheres and empty storage drums.

No extensive analysis of the deeply buried objects could be made because of the low recovery for these objects (4 percent). However, trajectory characteristics were computed and some comparisons made with the behavior of surface objects. The initial velocity vectors for these deeply buried objects are shown in Figure IV-4.22, together with the initial velocities for corresponding surface objects. The latter values were taken from the maximum value envelope shown on Figure IV-4.19 for a flat plane and no air drag. The trajectory characteristics, initial velocities, trajectory heights and time-of-flight of deeply buried objects were also analyzed and plotted in dimensionless form (Reference IV-4.10). The dimensionless form was obtained by normalizing the deeply buried object data to the surface and near-surface object data.

The distribution of the ejecta thrown out of the crater was measured for three sectors beyond the continuous ejecta boundary shown in Figure IV-4.16. The collected data included the distribution pattern for approximately 220 boulders, over 0.03 m^3 in volume each, covering a total area of approximately 1490 m^2. Data records include the distribution of the smaller fragments (2.5 to 46 cm in equivalent diameter) over selected portions of the three sectors shown in Figure IV-4.16.
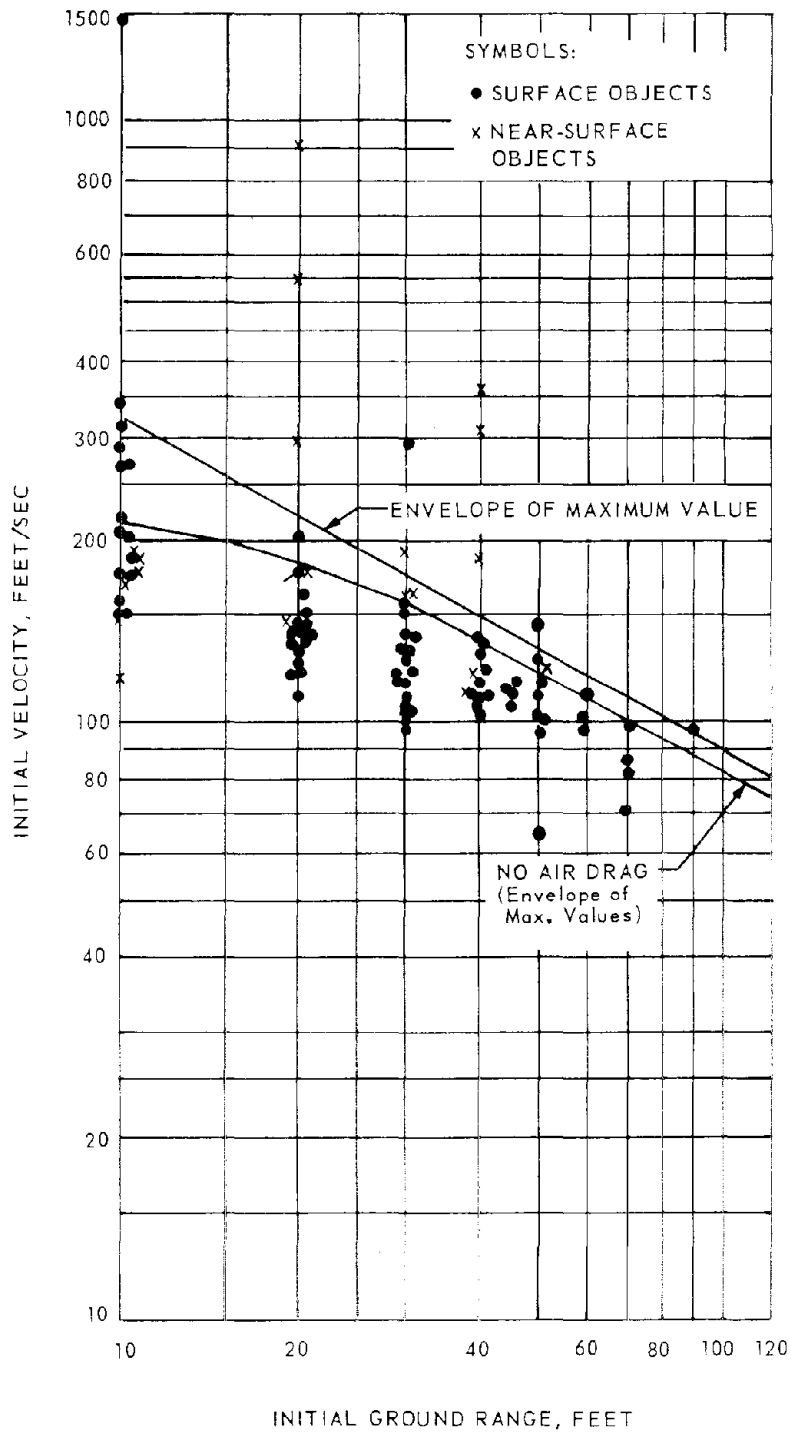
Figure IV-4.19. Initial velocity versus initial
ground range for all objects
except bricks and lumber.
(Analysis considering sloping
terrain and effect of air drag.)
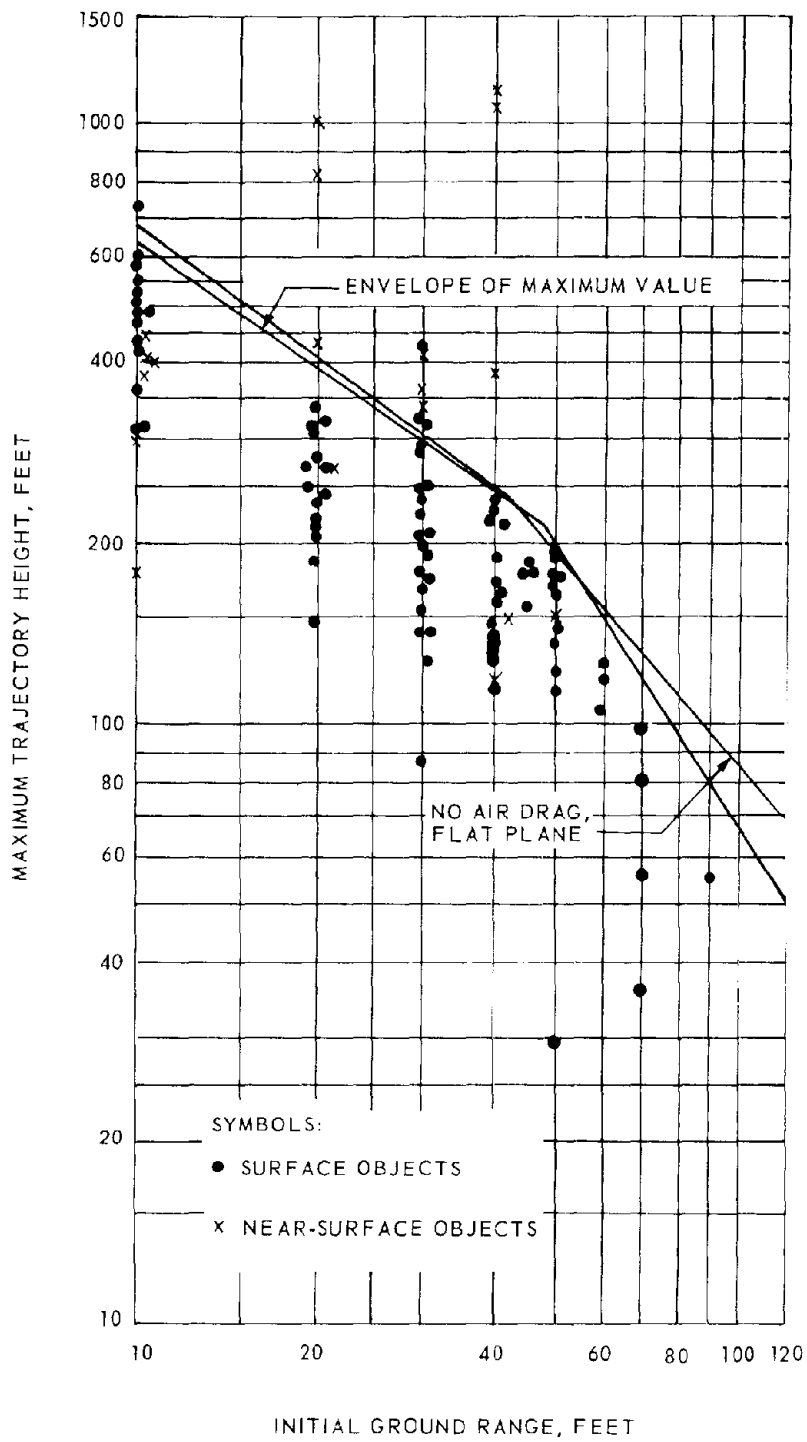
Figure IV-4.20.   Maximum trajectory height versus
initial ground range for all
objects except bricks and lumber.
(Analysis considering sloping
terrain and effect of air drag.)
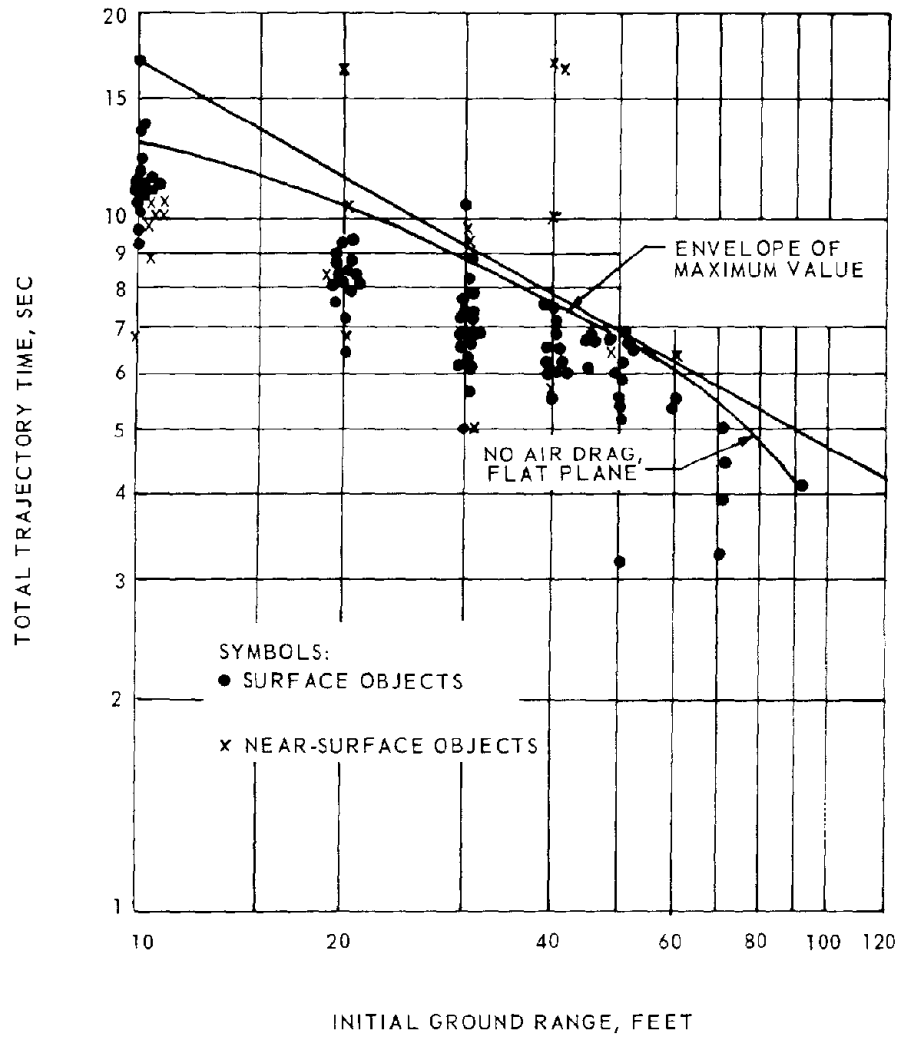
Figure IV-4.21. Total trajectory time versus initial ground range for all objects except bricks and lumber. (Analysis considering sloping terrain and effect of air drag.)
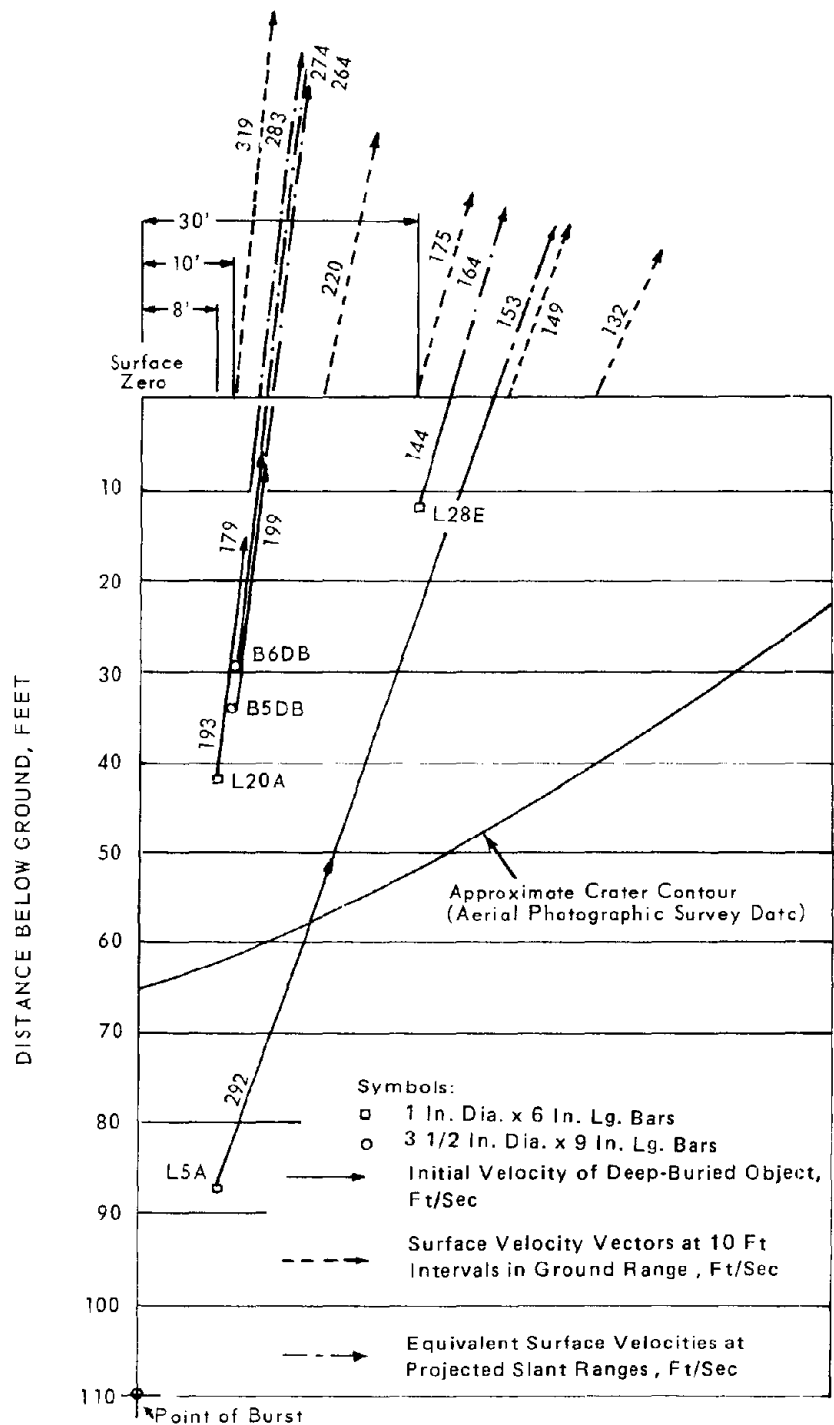
Figure IV-4.22. Initial velocities of deep-buried
objects and corresponding maximum
initial surface velocities.

These data are representative of approximately 10,000 objects thrown out over an area of about 280 m^2. The range covered in the distribution of missile ejecta is from about 90 to 150 meters. Ejecta was measured only beyond the limit of continuous ejecta, that is, beyond the contour where continuous ejected material completely obscured the ground surface. Posttest inspection showed that the limit of continuous ejecta extended from about 88 to 107 meters from GZ at the three selected sectors. It was also observed that no appreciable amount of ejecta was thrown beyond 150 meters. This accounts for the relatively narrow band in which distribution measurements were made. Numerous aerial density plots are given in Reference IV-4.10 that show, quantitatively, the relative amounts of various ejected object sizes found at various ranges. From these plots, the pronounced drop in fragment density with increasing fragment size is apparent. The extreme slope of the density curves and the relatively narrow band of ejected material is consistent with the high trajectories the ejected material was observed to follow on photographic records. The high trajectories coupled with the DOB appear to support the contention that initial velocities of much of the material were radial from the burst point. Figure IV-4.23 shows the continuous ejecta depth and the missile ejecta depth. Figure IV-4.24 shows the cumulative distribution of the fragment sizes for Area II shown in Figure IV-4.16.

Debris dispersion in the angular direction was also noted. It was observed that objects initially placed in the sector from E30°S to W30°S were thrown with a predominant clockwise direction from their original bearings. Objects placed in the sector from N60°W to N75°E were thrown somewhat counterclockwise from their original bearings relative to surface GZ. Figure IV-4.25 shows the angular dispersion of ideal objects versus the azimuth angle. For the most part, it was observed that on any one initial bearing, the directions of travel tended to be within a total angle of about 40 or 50 degrees, although the median directions were generally not in line with the original bearings. Counterclockwise deviations are maximum at about N30°E where the median deviation is approximately 30 degrees. Analysis of dispersion shows that the angular dispersion of ideal objects as a function of their initial preshot positions decreases.

Recovery of surface and near-surface objects placed within 15 meters of GZ amounted to about 40 percent of the total. Only five deep-buried objects were recovered, which is a low but not unexpected return of only 4 percent. In addition to the low-recovery expectation resulting from the lack of posttest excavation of
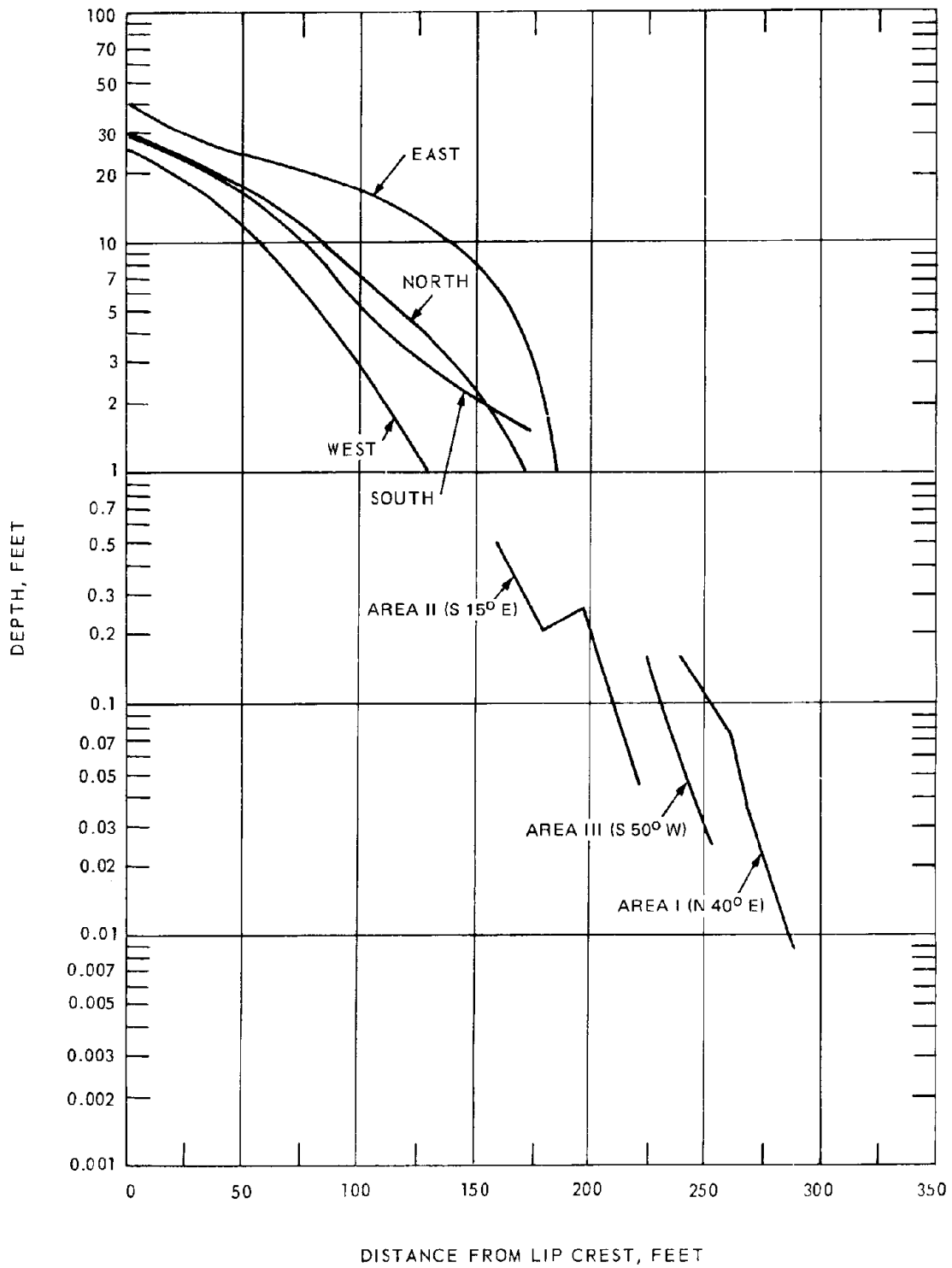
Figure IV-4.23. Crater lip and equivalent throwout depths (semilog plot).
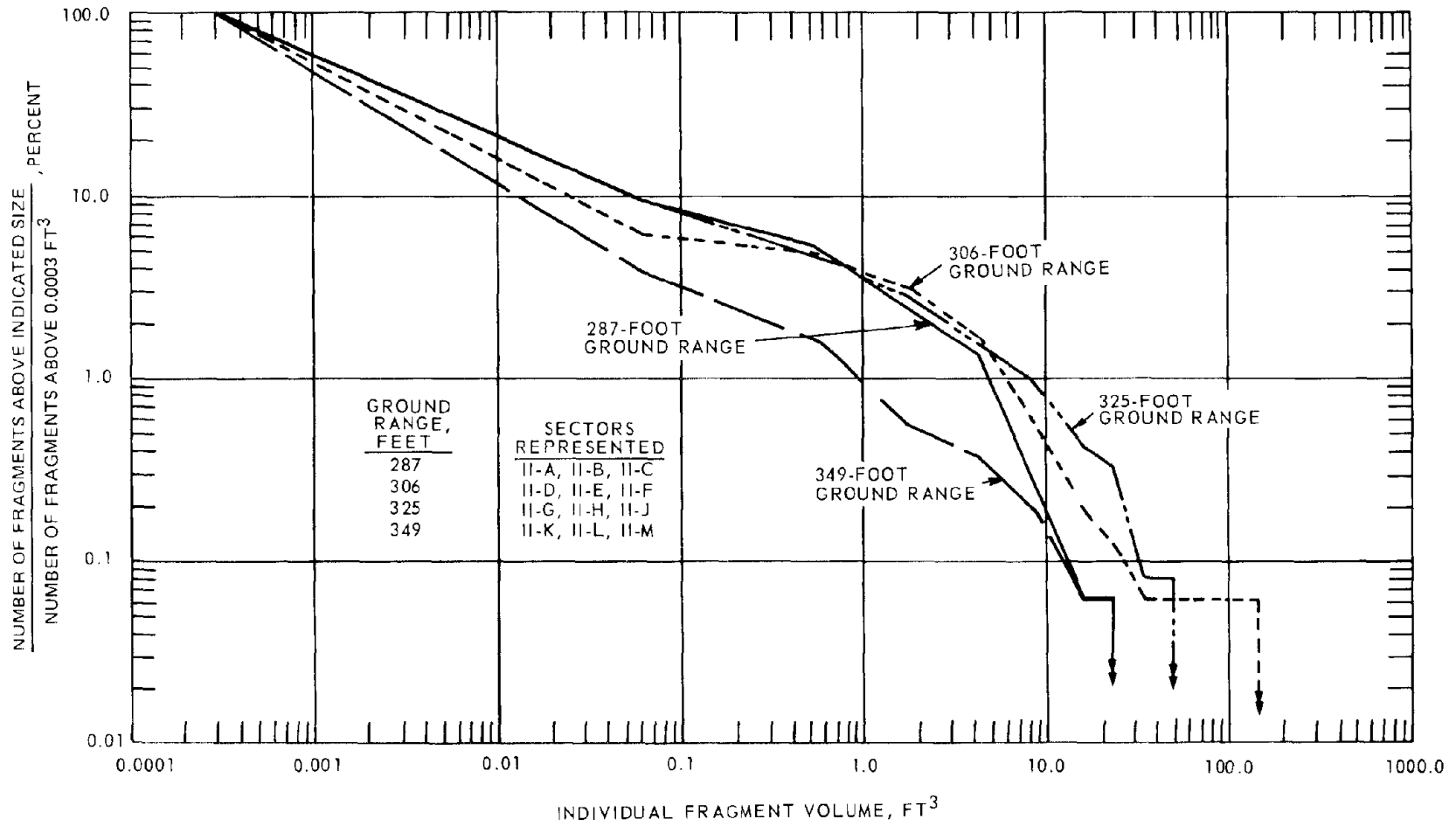
Figure IV-4.24. Cumulative distribution of fragment size, Area II.
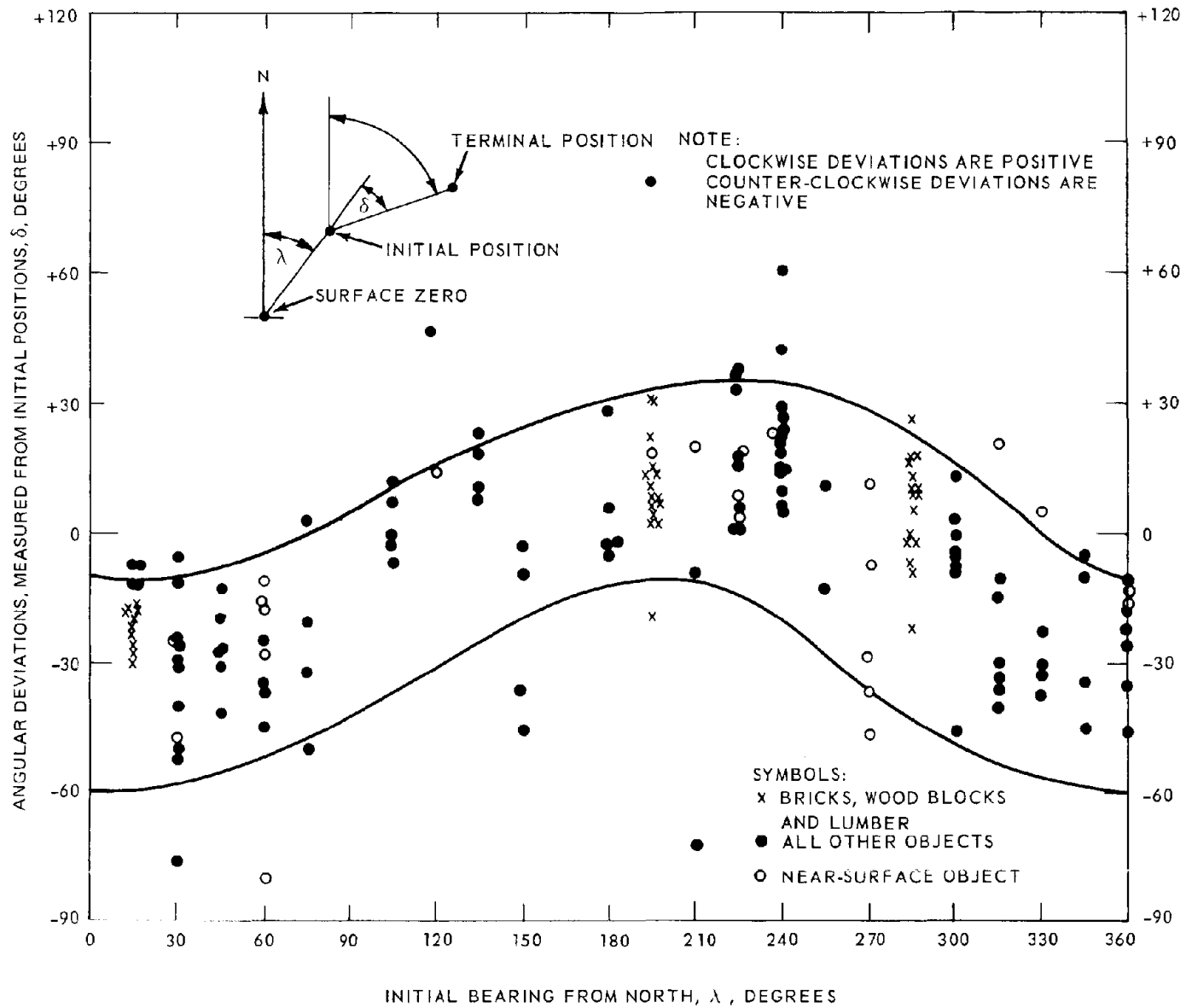
Figure IV-4.25. Angular dispersion of ideal objects versus azimuths.

the continuous ejecta, many deep-buried objects lie grouted within large boulders, reducing visual recognition even further.

One conclusion of potentially great significance is that the deposition pattern of ejected material was not symmetrical. Furthermore, the lack of symmetry was not random; there was a definite pattern to the movements. This lack of symmetry is a secondary effect of minor importance in predicting ejecta.

Another objective of the DANNY BOY Event (Reference IV-4.12) was to determine the distribution of ejecta and dust. For this purpose, 158 waterproof tarpaulins, each $1.5\,m^2$ in area, were placed in a pattern around GZ at radial distances varying from 67 to 2160 meters from GZ. This array of tarps was symmetrical and circular except for that portion described by the 2160-meter radius, which was a circular sector centered on the north axis. This corresponded to the approximate direction in which the prevailing winds might transport dust thrown up by the detonation.

It was important to the objectives of the experiments that particulate deposition on these tarps be measured at the earliest possible time after the shot so that redistribution of fine material by winds could be minimized. Recovery began as early as 4 hours after detonation and was limited to areas lying off the mesa because of the residual radiation level and continued into the 36th day. Only 27 samples were recovered and because of this small number, all of them were analyzed for particle-size distribution.

Figure IV-4.26 shows a straight-line fit for mass-distribution averages on all collector rings as a function of the distance from GZ. These averages are based upon arithmetic means that includes all recovered stations. Figure IV-4.27 shows the contours of the mass distribution, and Figure IV-4.28 shows profiles of the lip prepared from a topographic map of the crater. Also on the latter figure is the average lip profile, and the ring locations are shown for reference to illustrate the approximate thicknesses of deposition on nonrecoverable collectors. The cumulative ejecta mass distribution for DANNY BOY shown in Figure IV-4.29 is different from that of any other shot for which data are available. This will be compared with the other events.

The mass-distribution measurements presented here are for the samples that were recovered and do not take into consideration any weight changes that might have occurred as a result of changes in the moisture content between the detonation and the recovery time. These differences, however, are probably minor in view of the arid Nevada climate.

CRATER RADII

$$\delta = 2.69 \times 10^{18}\ R^{-8.55}$$
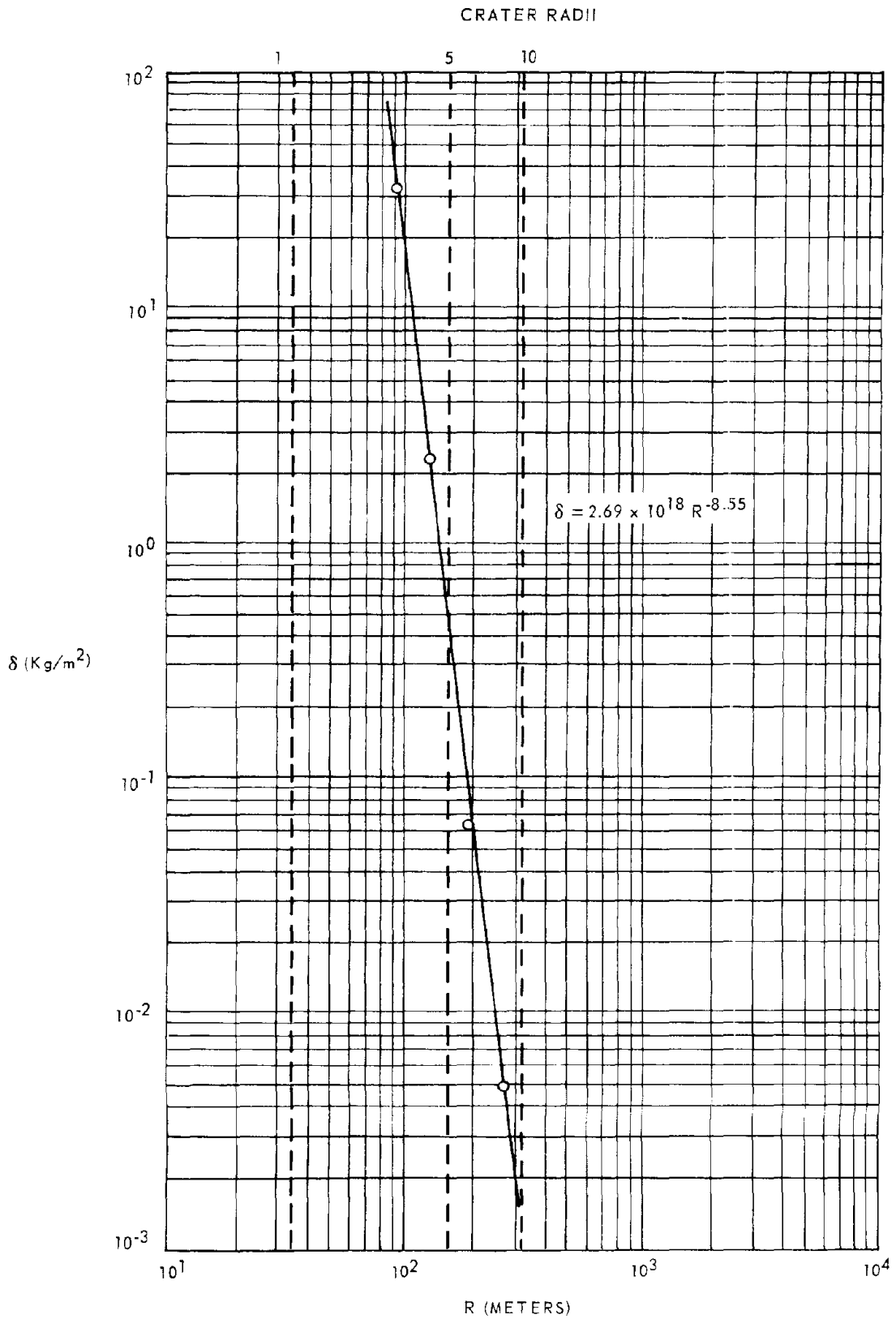
Figure IV-4.26. Average mass distribution (δ) versus radial distance from GZ (R) for DANNY BOY.
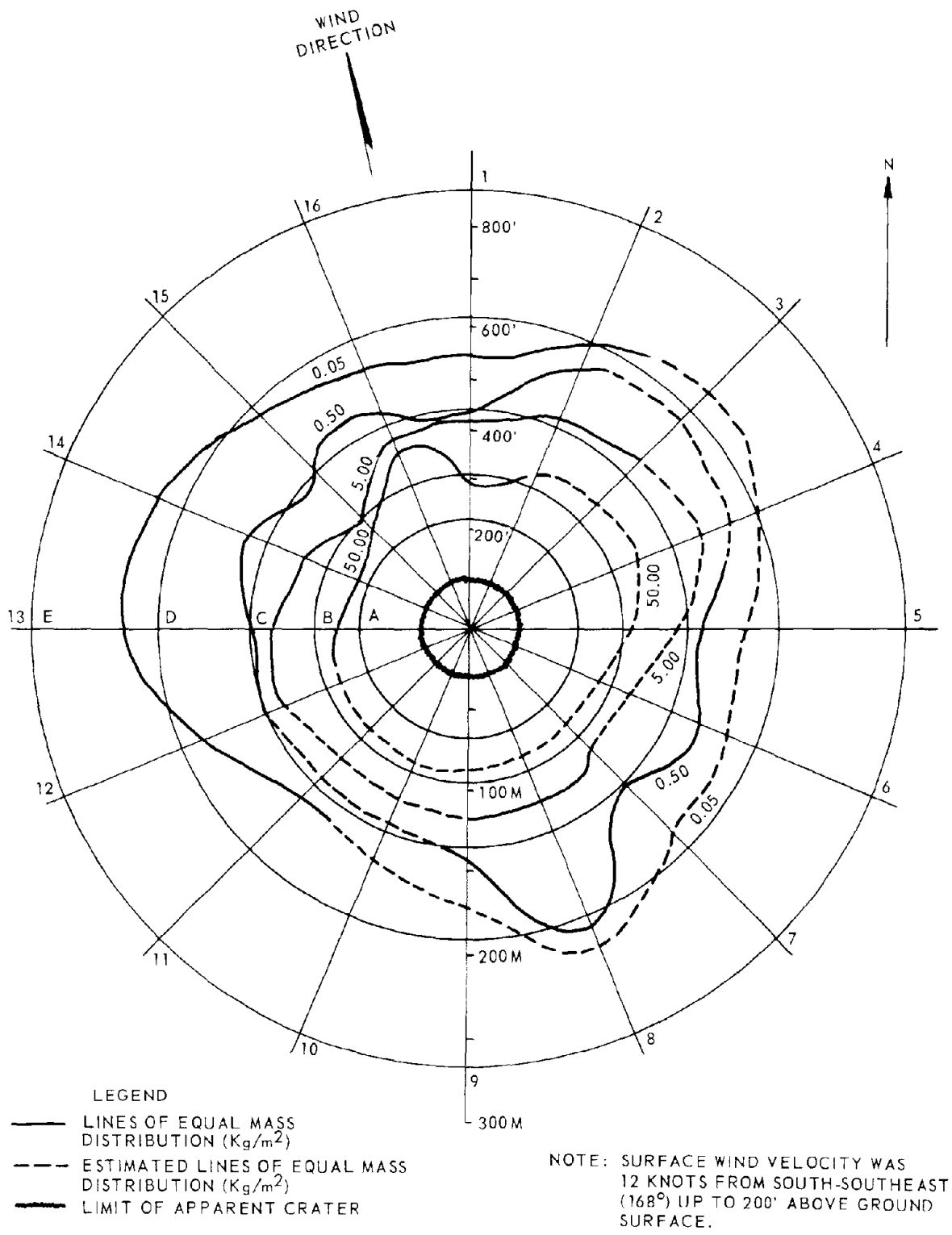
Figure IV-4.27. Mass distribution contours, in kg/m², for DANNY BOY.
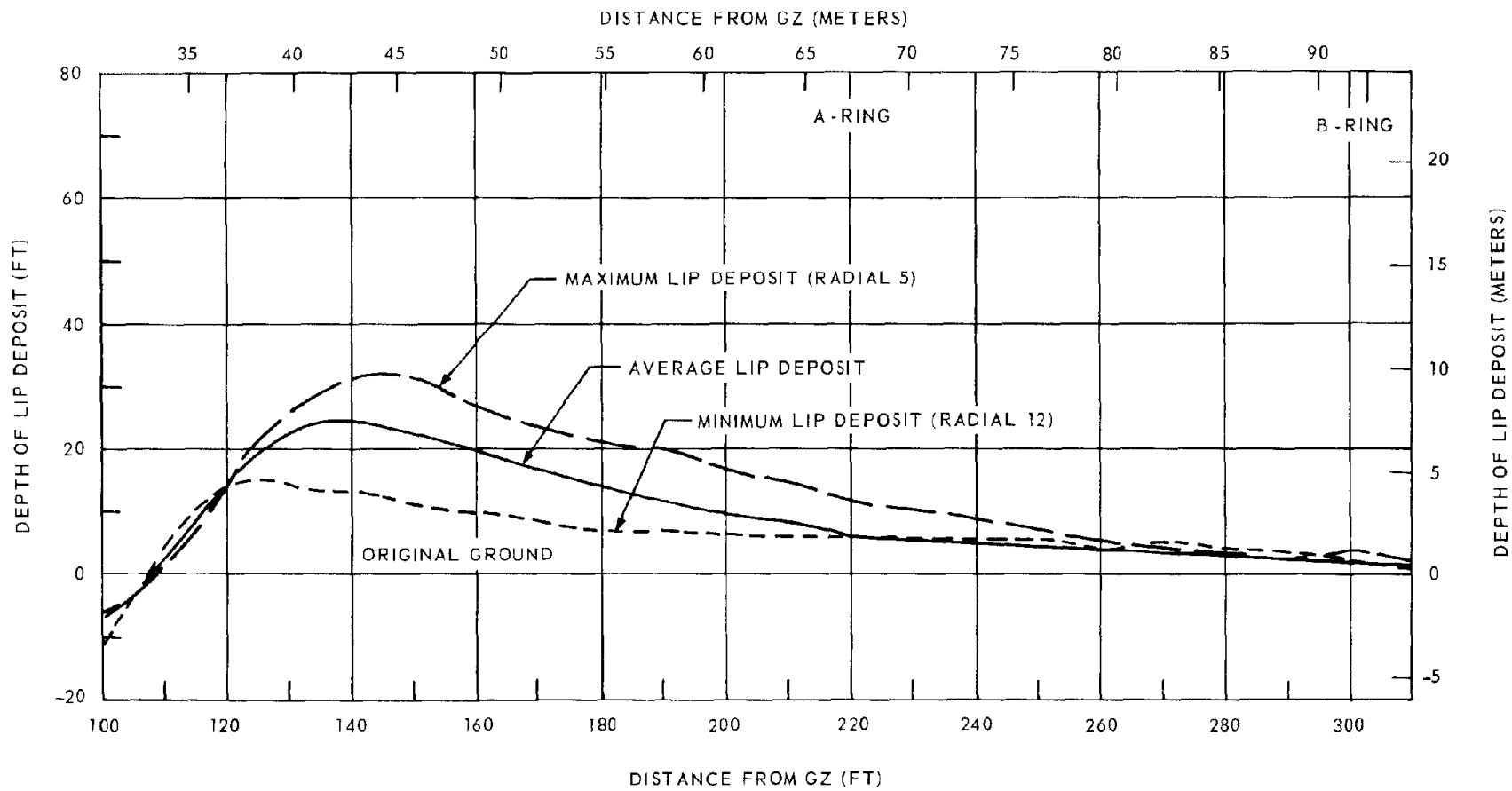
Figure IV-4.28. Ejecta deposition in the region of the lip for DANNY BOY.
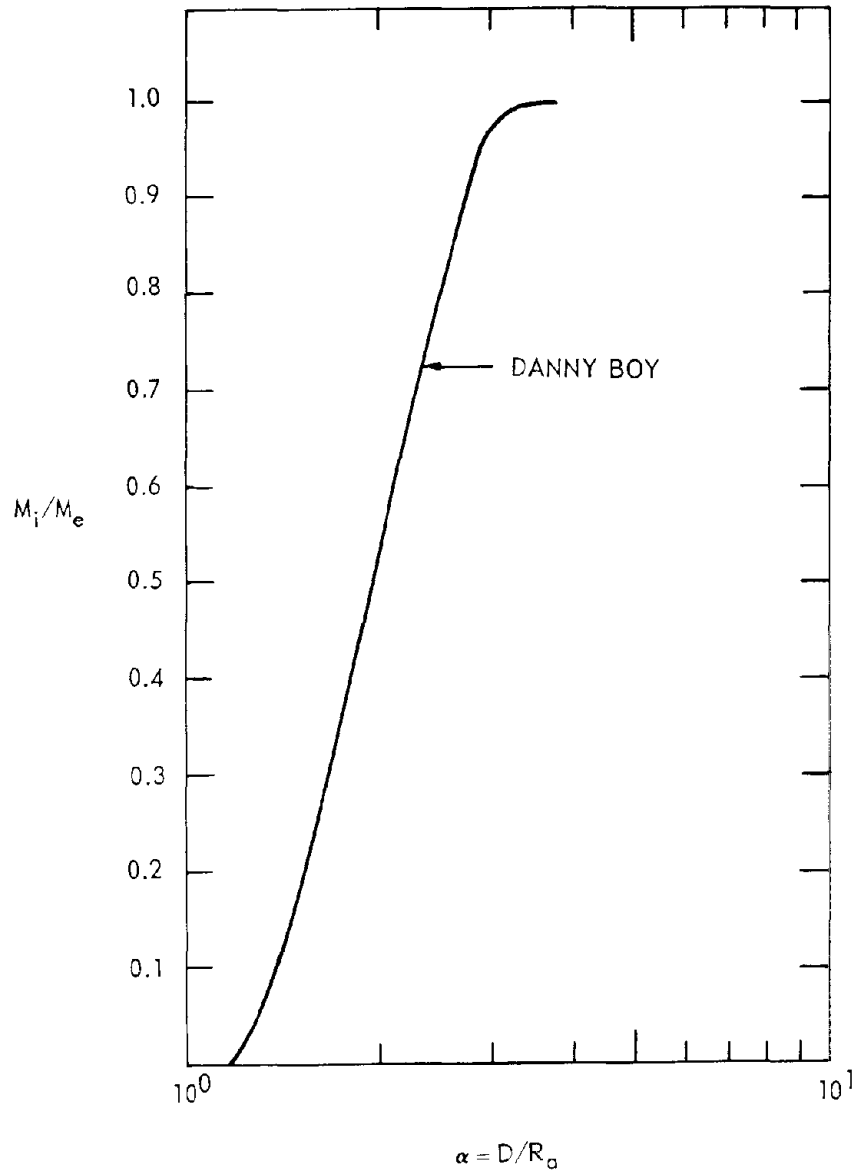
Figure IV-4.29. Ejecta mass distribution curve for
DANNY BOY.

In conclusion, a relatively simple experiment made it possible to obtain valuable information on the distribution of ejecta from this cratering event in hard rock. Although radiation levels and unfavorable weather conditions limited the success of the sample recovery, good data were obtained. All of the observed and measured ejecta was deposited within approximately 8 crater radii from GZ. The continuous ejecta extended out to a radial distance less that 3 crater radii.

IV-4.1.2.3 SCHOONER. The SCHOONER Event was part of the PLOWSHARE program. It was a nuclear device with a yield of 35 kt detonated at a depth of 108 meters in a layered tuffaceous medium of the NTS. The resulting crater had an apparent radius of 130 meters and an apparent depth of 63.4 meters. AFWL-CERF* participated in Event SCHOONER with the primary objective of studying the site, the crater, and the resulting continuous and missile ejecta (References IV-4.13, IV-4.14 and IV-4.15). The stratigraphy consists of a layered sequence of welded and bedded tuffs and ash flows in nearly horizontal position overlayed by 0.3 to 1.2 meter of soil. The water table at the SCHOONER test site was located between 240 and 310 meters below the ground surface. Two predominant, nearly vertical dipping joint sets were also observed.

For the collection of ejecta, three radial and three concentric tar-oil strips 3 meters wide by 1 cm thick were emplaced. This was done to locate the original ground surface and to provide an ejecta collection and trenching surface. To collect the ejecta fines, 85 1- x 1-meter canvas tarps and 247 0.3- x 0.3-meter trays were emplaced.

The aerial stereophotographs were sufficient for crater and continuous ejecta analysis. However, it was not found to be sufficient for the identification of small discrete missiles of approximately 1/4-kg size.

Results of measurements of the crater and ejecta are summarized in Table IV-4.9.

At shot time the visibility was adequate but not optimum for photography because of a thin cloud cover. A CERF official aboard the photography helicopter made a number of observations. Among these, the following are relevant:

1. Ejecta exhibited strong vertical movement indicating a significant gas boost phase.

2. Most discrete missiles that came out of the fireball were incandescent and some were seen to impact when still in an incandescent condition.

3. Continuous and missiles ejecta could be followed throughout various phases of these trajectories. Many discrete

_____
*Eric H. Wang Civil Engineering Research Facility.

missiles impacted in front of the developing base surge.*

4. The base surge developed and reached 610 to 1220 meters south of GZ and exceeded a height of 460 meters.
5. The ejecta was deposited in an asymmetrical pattern with large area of fine material being evident.
6. Many missiles exceeding a volume of 28 m^3 were observed.
7. Maximum missile range exceeding 1830 meters.
8. Formation of many secondary craters due to missile ejecta impact.

Table IV-4.9. SCHOONER crater data and ejecta.

Measurement	Value
Apparent Crater Radius, m	129.8
Apparent Crater Depth, m	63.4
Apparent Lip Height, m	13.4
Apparent Lip Crest Radius, m	147.2
Continuous Ejecta Limit, m	518 to 823
Maximum Missile Range, m	1830 +
Maximum Missile Size, m	9 x 6 x 6
Apparent Crater Volume, m^3	1.745 x 10^6
Apparent Lip Volume, m^5	2.099 x 10^6

---

*When material thrown upward as a dirt column from an underground crater-explosion falls back to earth, it produces a secondary expanding cloud of fine particles known as the base surge. This secondary cloud moves outward from the center of the explosion eventually settling over a large area. The extent of the base surge area depends on the burst depth, geologic medium, energy released, and so on. Because of the significance of the base surge in connection with the PLOWSHARE cratering projects, its extent on the SEDAN Event was documented. Similar documentation is available for the TEAPOT ESS Event.

Postshot aerial photographs and on-site measurements showed the crater to be nearly circular in appearance. Figure IV-4.30 shows three profiles through the apparent crater. Note the slumped sides and flat bottom of this crater.

In general, the ejecta population can only be termed as immense (Reference IV-4.14). The volume and extent appeared to be twice that predicted. Within 610 meters of GZ, missiles on the order of 0.3 m^3 were plentiful out to a range of about 900 meters. The base surge deposit southwest of GZ was found to be a few inches deep at 900 meters.

Figure IV-4.31 shows the apparent crater and the continuous ejecta boundary drawn from aerial photographs. Superimposed are the tar-oil strips and the outer-most ejecta pads. Field trips indicated that the continuous ejecta boundary usually extended from about 150 to 300 meters beyond the point indicated by aerial photo-graphs. At approximately 460 meters along the S 35°W radial line at least 0.9 meter of ejecta and blocks over 1.5 meters across were observed. The ejecta population is bimodal consisting of discrete and fine particles. It was hypothesized that nearly all the discrete missiles originated from the upper welded tuff and the fine parti-cles originated from the bedded tuff and the overburden.

IV-4.1.2.4 SEDAN. This event is important because a considerable amount of cra-tering and ejecta data were collected. The SEDAN Event was a 100-kt nuclear device detonated at the NTS. The geologic medium is desert alluvium, a recent sedimentary deposit of poorly sorted clay, silt, sand and occasional lenses of gravel containing rock fragments ranging in size from pebbles to boulders. The shot was detonated at the near optimum depth of 194 meters. The apparent crater was measured to be about 182 meters in radius and about 99 meters in depth. The primary objective of the SEDAN Event was to obtain quantitative data on the cratering and the distribution of ejecta on the ground surface surrounding the crater (Reference IV-4.16).

Ejecta collector stations were located in a circular pattern on the basis of a predicted crater radius of 213 meters. Basically two methods were used to obtain data on mass distribution of crater ejecta. Areal density was determined by weigh-ing ejecta samples obtained from tarps and tray stations. These collectors were designed to sample approximately 0.2 percent of the ejecta in the radial directions and 1.2 percent along the circumferential direction.
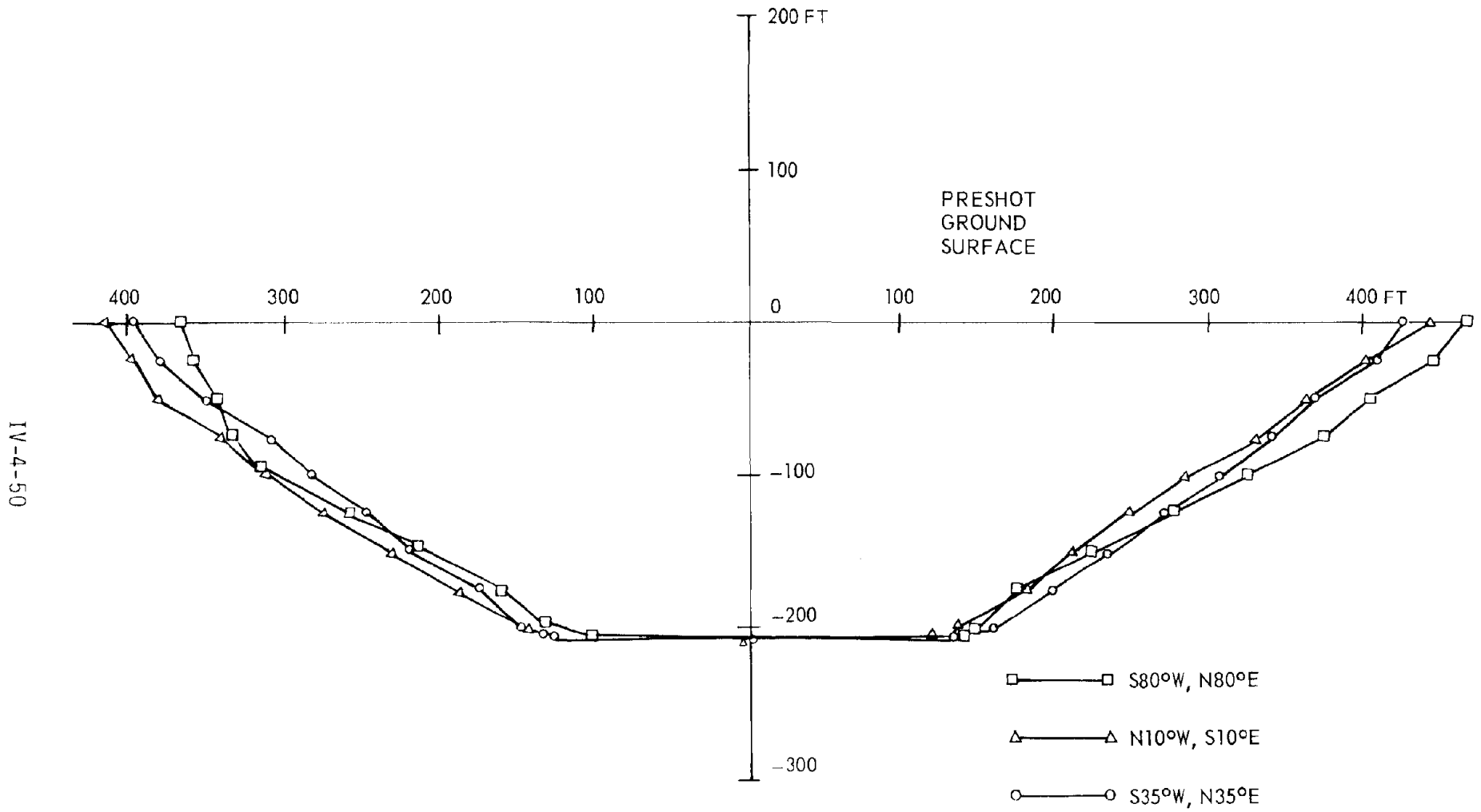
Figure IV-4.30. SCHOONER apparent crater cross sections (Reference IV-4.14).
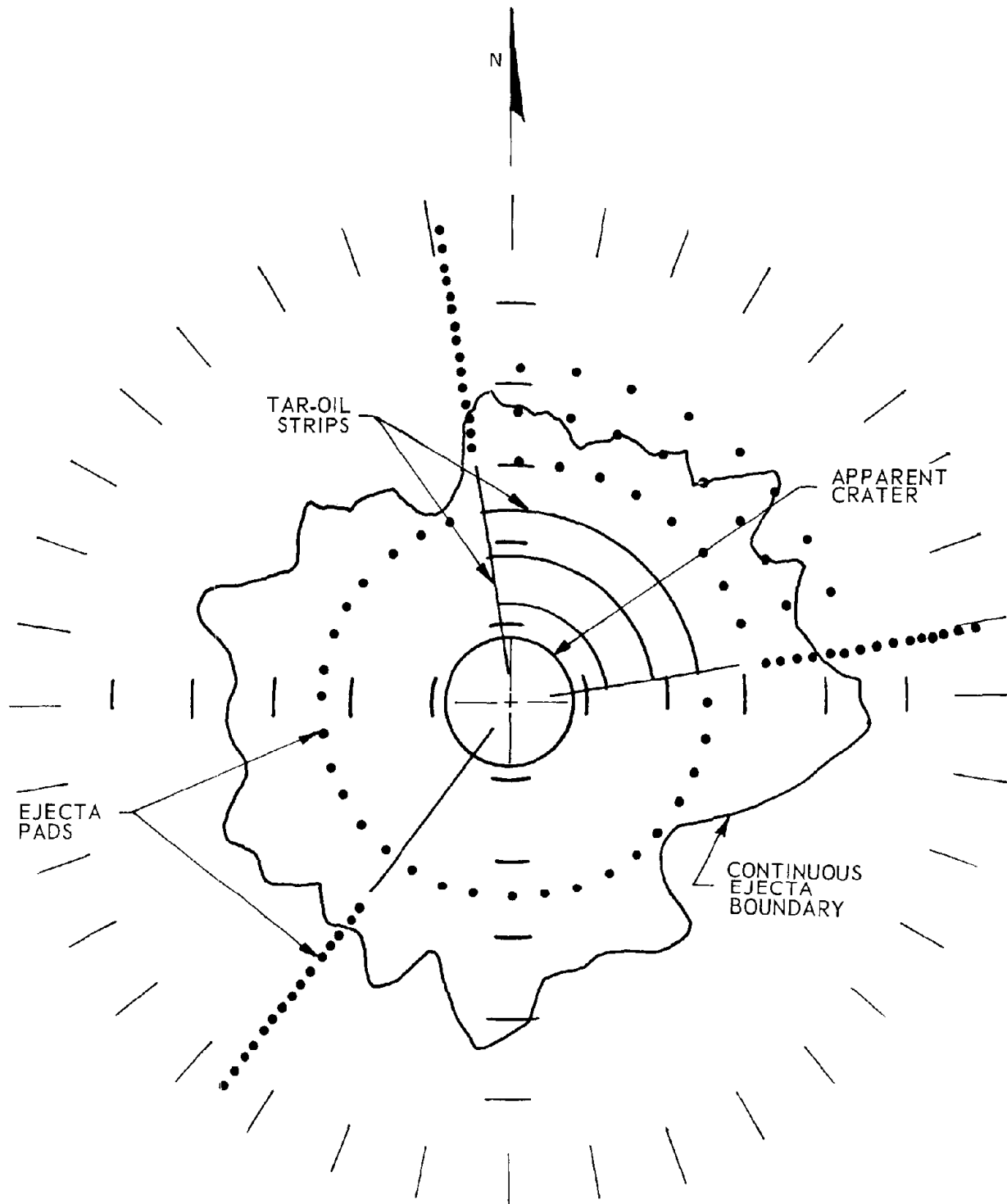
Figure IV-4.31. Apparent crater and continuous ejecta boundary (Reference IV-4.13).

Another objective of the SEDAN Event was to investigate the manner in which the earth is ejected ballistically by the underground detonation. From a knowledge of the initial and the final positions of radioactive pellets, it would be possible to approximate crater ejecta trajectories. For this purpose, 88 Co^{60} radioactive pellets were buried at known locations and depths within the estimated crater volume prior to the event. No Co^{60} radioactive pellet sources were recovered after the detonation (Reference IV-4.17) so that no initial ejection angles could be obtained from this experiment.

Figure IV-4.32 shows an isopach map of the ejecta thickness made from postshot measurements. It shows the ejecta distribution to be fairly isotropic covering an area up to 1300 meters in radius from SGZ with dust ranging in thickness from 1 cm on the edge up to 10 meters in the general area of the lip.

The original ground surface was identified at several locations along the inner edge of the crater. The location of the original ground surface before the shot was established by the preshot topographic map. Figure IV-4.33 shows the pre-shot and postshot ground surface, and establishes an approximate value of 3 meters for the permanent uplift at the crater edge. Note the considerable variations in the elevation of the lip crest. Note also that the original ground surface, and the postshot ground surface, shows a gentle slope from west to east. Vertical layering of the ejecta was observed beyond the crater edge. Figure IV-4.34 dia-grammatically shows a section through the SEDAN crater. At the lip crest, the layering is multiple and marked by particle sorting. Beyond the lip crest, multi-ple layering does not appear to be present. In general, two distinct layers were observed; a third layer was also noted and is uppermost in the sequence. This layer was deposited from the base-surge cloud and later almost completely removed by winds. Henny (Reference IV-4.14) observes that while it is suspected and faintly observed in the isopach map that the ejecta was controlled to some extent by the joint system, the base surge and the ejecta fires appear to partially counteract this effect. Observations in the field showed that missile shapes and sizes were strongly controlled by pre-existing fractures and joint. Most missiles exceeding 4.5 kg exhibited at least one control face, while larger missiles exhibited an increase in these controlled faces. The maximum missile observed had a dimension of 9 x 6 x 6 meters. It was found lying on the edge of the crater and showing an almost perfectly shaped hexagon. Figure IV-4.35 shows a plot of cumulative percent as a function of missile weight, missile volume, and nominal size for each 30-meter range interval, and Figure IV-4.36 shows the areal density as a function of the radial distance from GZ.
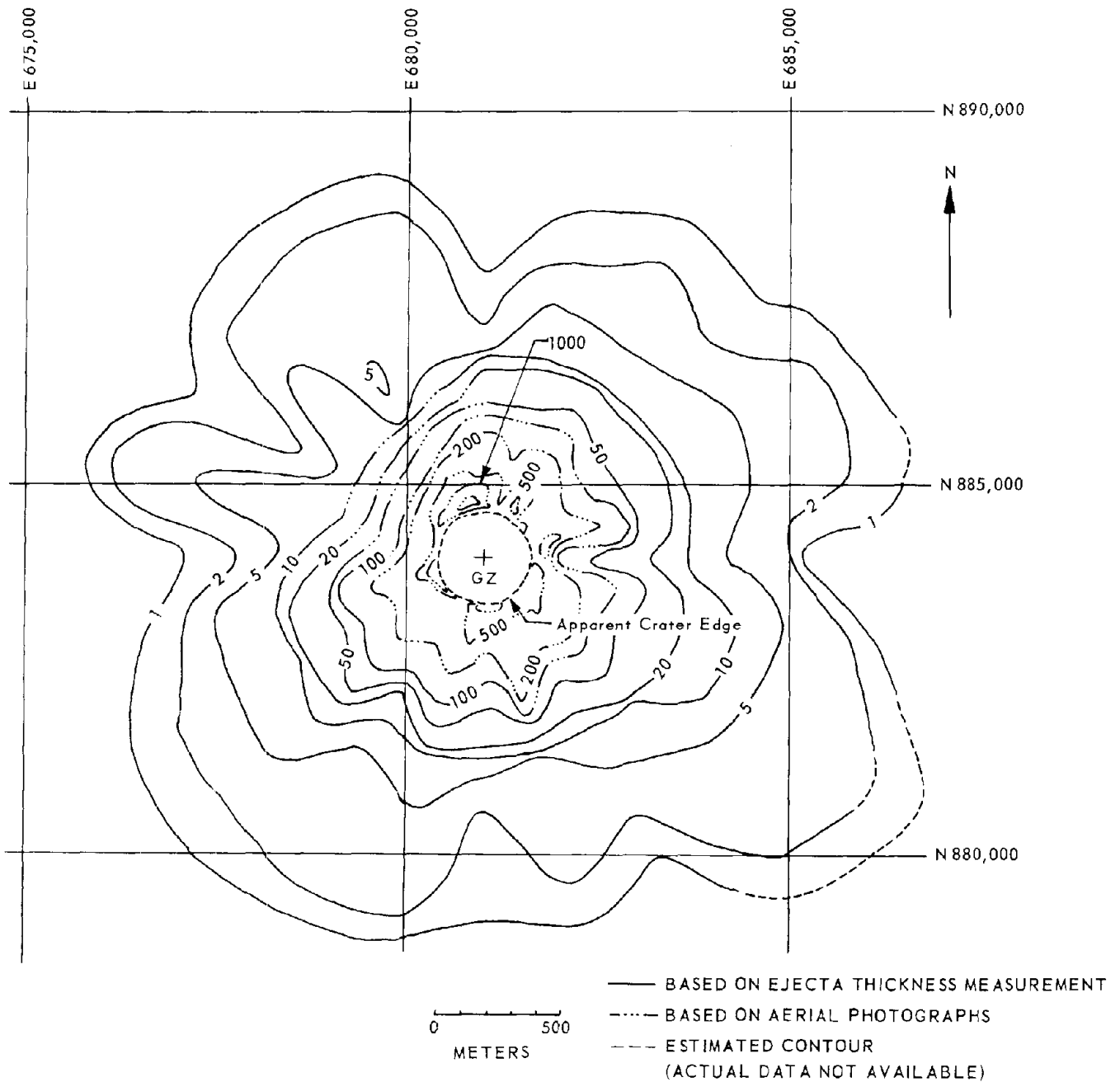
Figure IV-4.32. Isopach map of ejecta thickness (Reference IV-4.16).
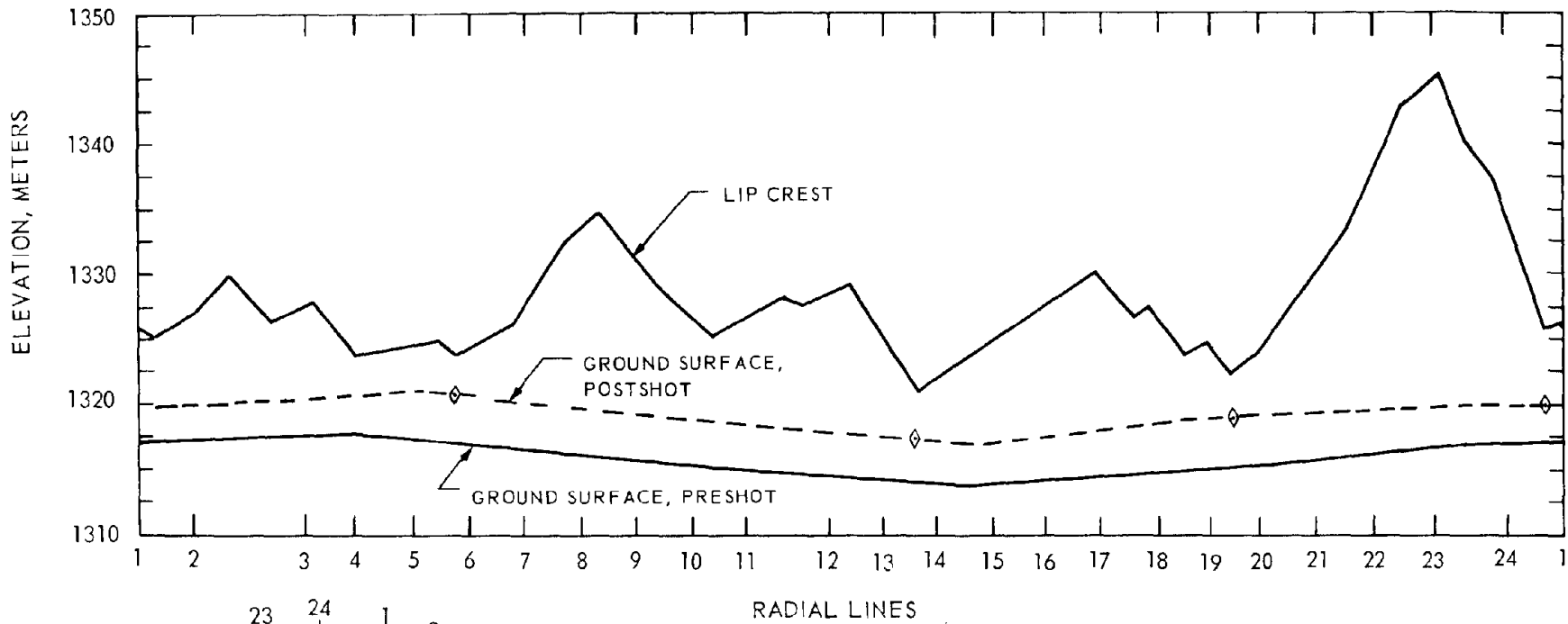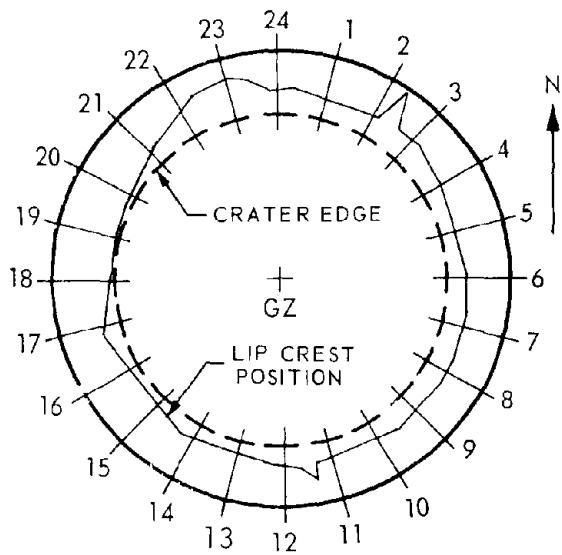
Figure IV-4.33. SEDAN lip crest (Reference IV-4.16).
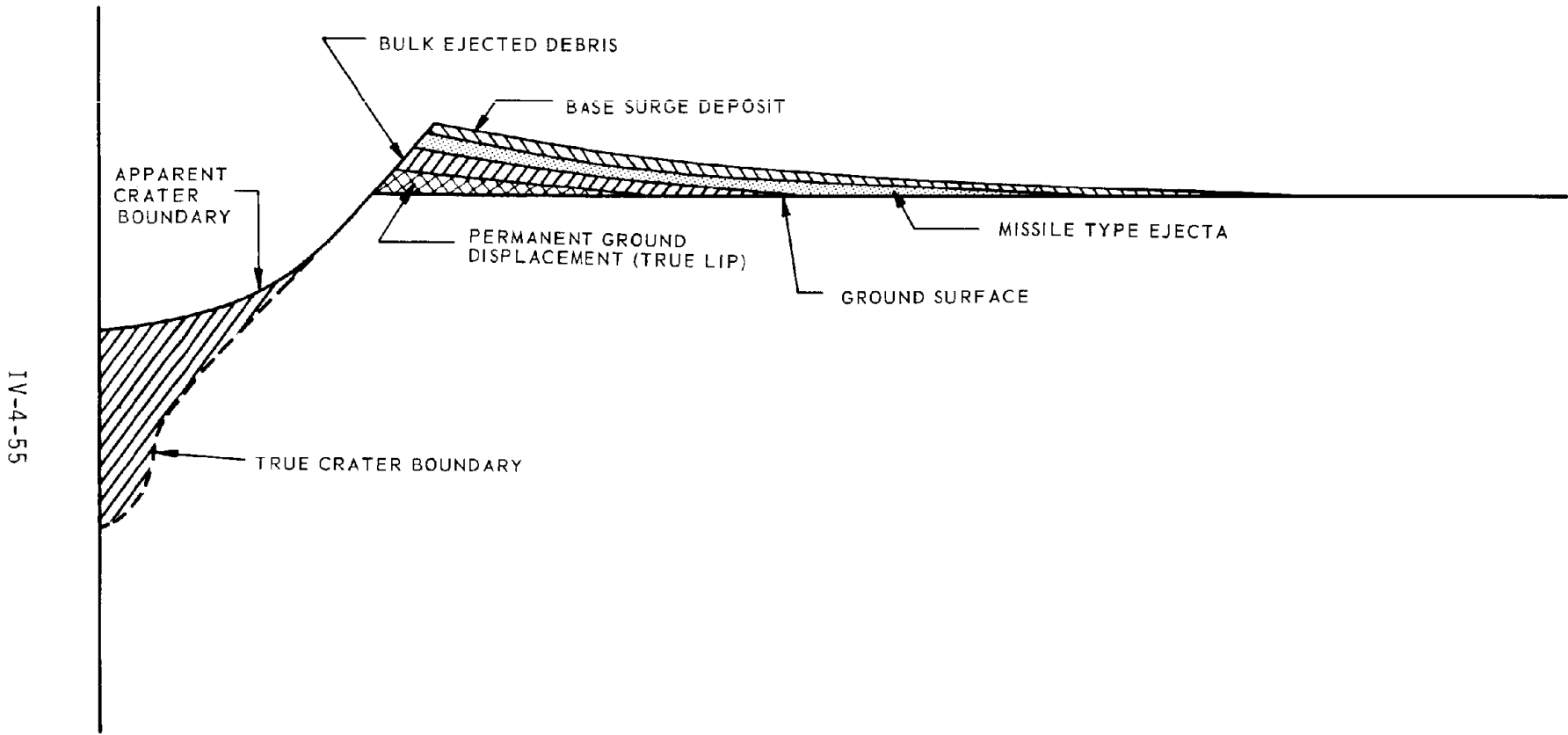
Figure IV-4.34. Diagrammatic section of SEDAN crater lip (Reference IV-4.16).
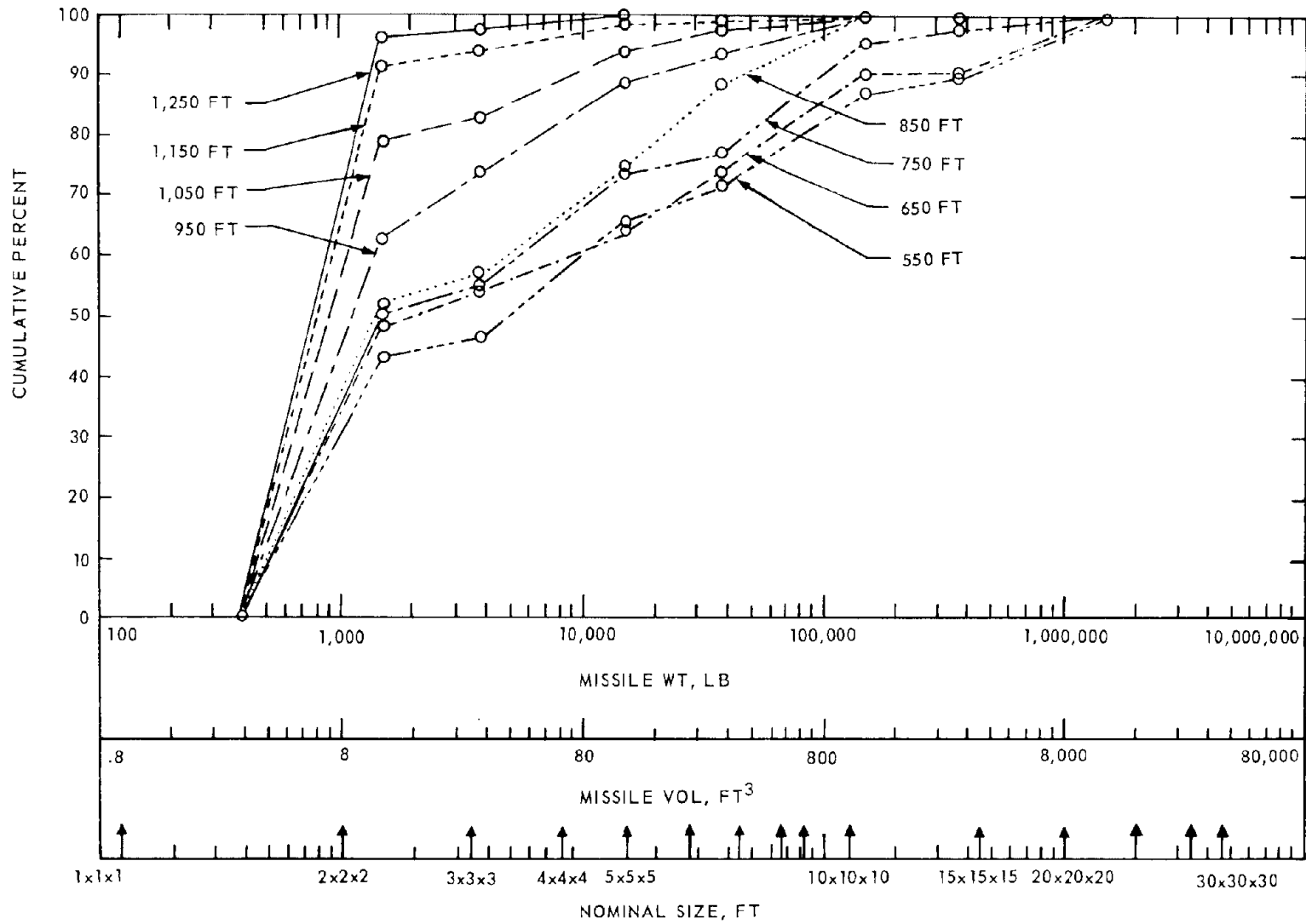
Figure IV-4.35. Size distribution of missiles 2 feet by 2 feet
and larger (Reference IV-4.14).
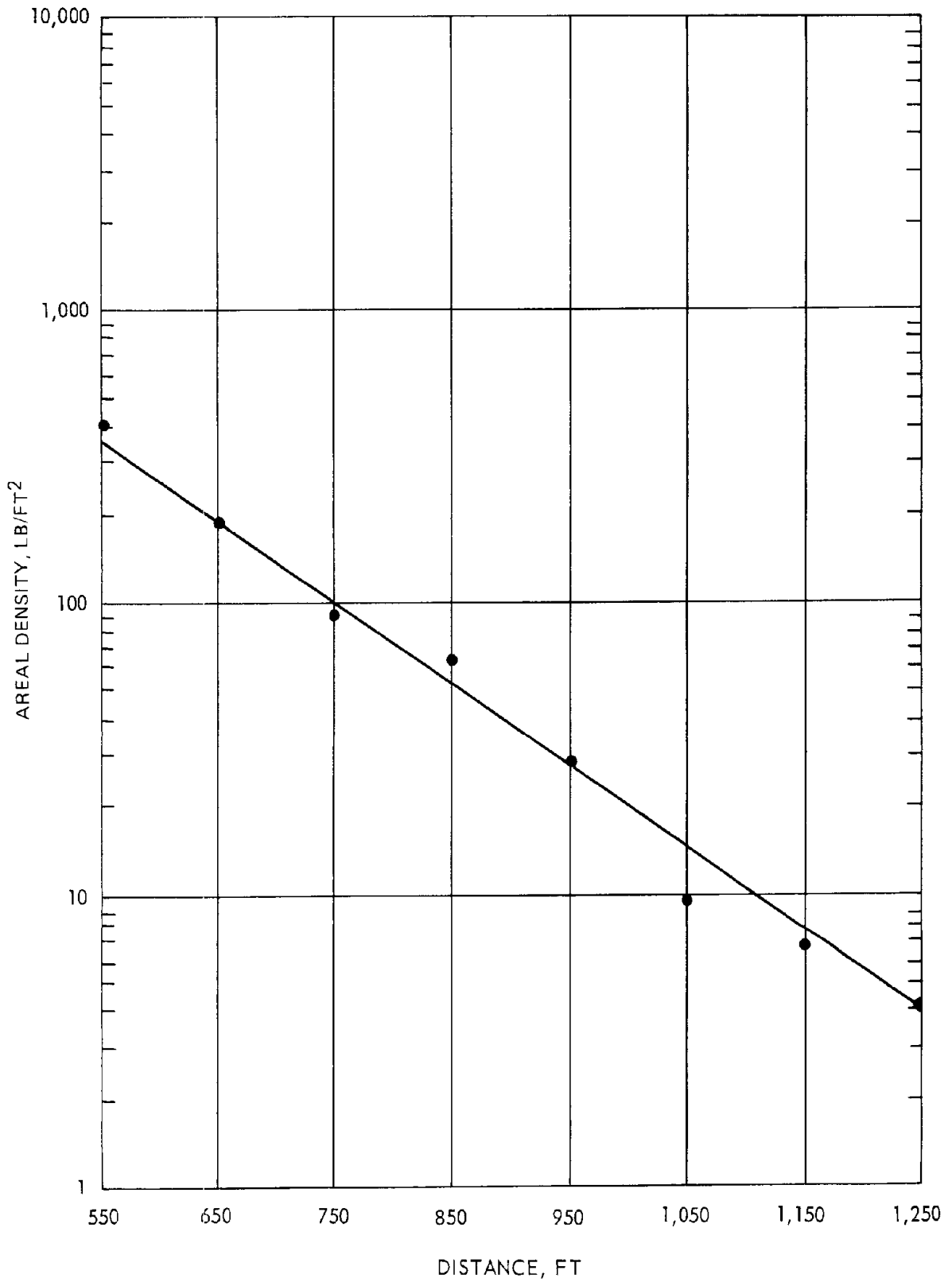
Figure IV-4.36. Areal density of missiles 2 feet by 2 feet
and larger (Reference IV-4.14).

IV-4-57

Henny (Reference IV-4.14) states that three incandescent missiles ranging in size from 1.5 to 3 meters were tracked with high-speed motion picture cameras as they exited from the fireball top and their velocities were then estimated to range from 335 to 365 m/sec. The lower layer of material was probably ejected from the crater in bulk, being relatively unaffected by the atmosphere during its flight. The thickness of this layer varied between 1 cm and 3.8 meters near the crater. This layer is referred to in Reference IV-4.16 as the bulk ejecta layer.

The upper layer varies in thickness between 1 and 15 cm, is poorly sorted, and contains considerable fused material in addition to pebbles, cobbles, sand, and silty material. This upper layer and the remaining portion of the base-surge deposit when combined were found to be equivalent in grain-size distribution to the bulk ejecta of the lower layer. The upper layer is usually referred to in Reference IV-4.16 as the missile ejecta layer. The bulk and missile ejecta were sampled separately. The cumulative percent curves for the samples taken from these two layers are shown in Figure IV-4.37 for three collector rings. The median grain size size is uniformly larger in the upper layer of missile ejecta while the fine-grained material, mostly silt-sized and light pumice-like fused material, has been locally redeposited.

The areal density as a function of range is plotted in Figure IV-4.38. The range of observations and the arithmetic mean are shown for each radial distance. A least-squares fit to the azimuthally averaged data points give the functions

$$\delta = \frac{6.98 \times 10^{14}}{R^{4.3}} \quad , \; kg/m^2 \qquad (IV-4.3)$$

and

$$t = \frac{4.65 \times 10^{13}}{R^{4.3}} \quad , \; cm \qquad (IV-4.4)$$

where δ is the areal density, t is the ejecta thickness where an ejecta density of 1.5 gm/cm^3 was assumed, and R is the range in meters from GZ. This fit appears to give the ejecta thickness within about a factor of three on the average. On the other hand, if three functions are used to fit the data, there results
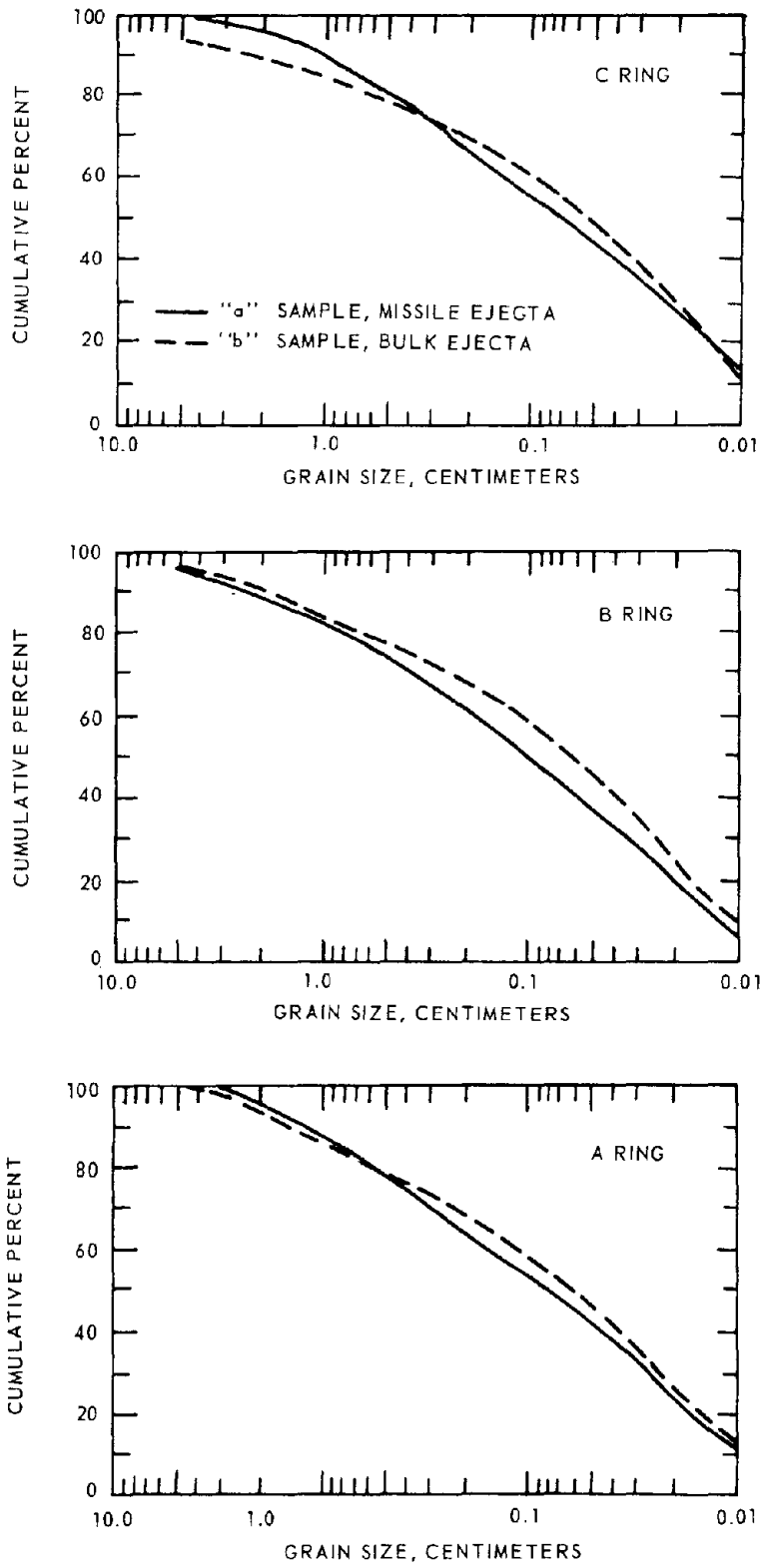
Figure IV-4.37. Grain-size distribution of the two distinct debris layers (Reference IV-4.16).

BAR SHOWS RANGE IN AREAL DENSITY OBSERVATIONS. TRIANGLE IS THE AVERAGE AREAL DENSITY. THE CIRCLED NUMBER SHOWS THE NUMBER OF STATIONS WHERE SAMPLES WERE RECOVERED.

AVERAGE AREAL DENSITY AT LIP CREST.

$$\frac{6.98 \times 10^{14}}{R^{4.3}}$$

EDGE OF CRATER

AREAL DENSITY (kg/m^2)

EJECTA THICKNESS, CM

RADIAL DISTANCE, IN
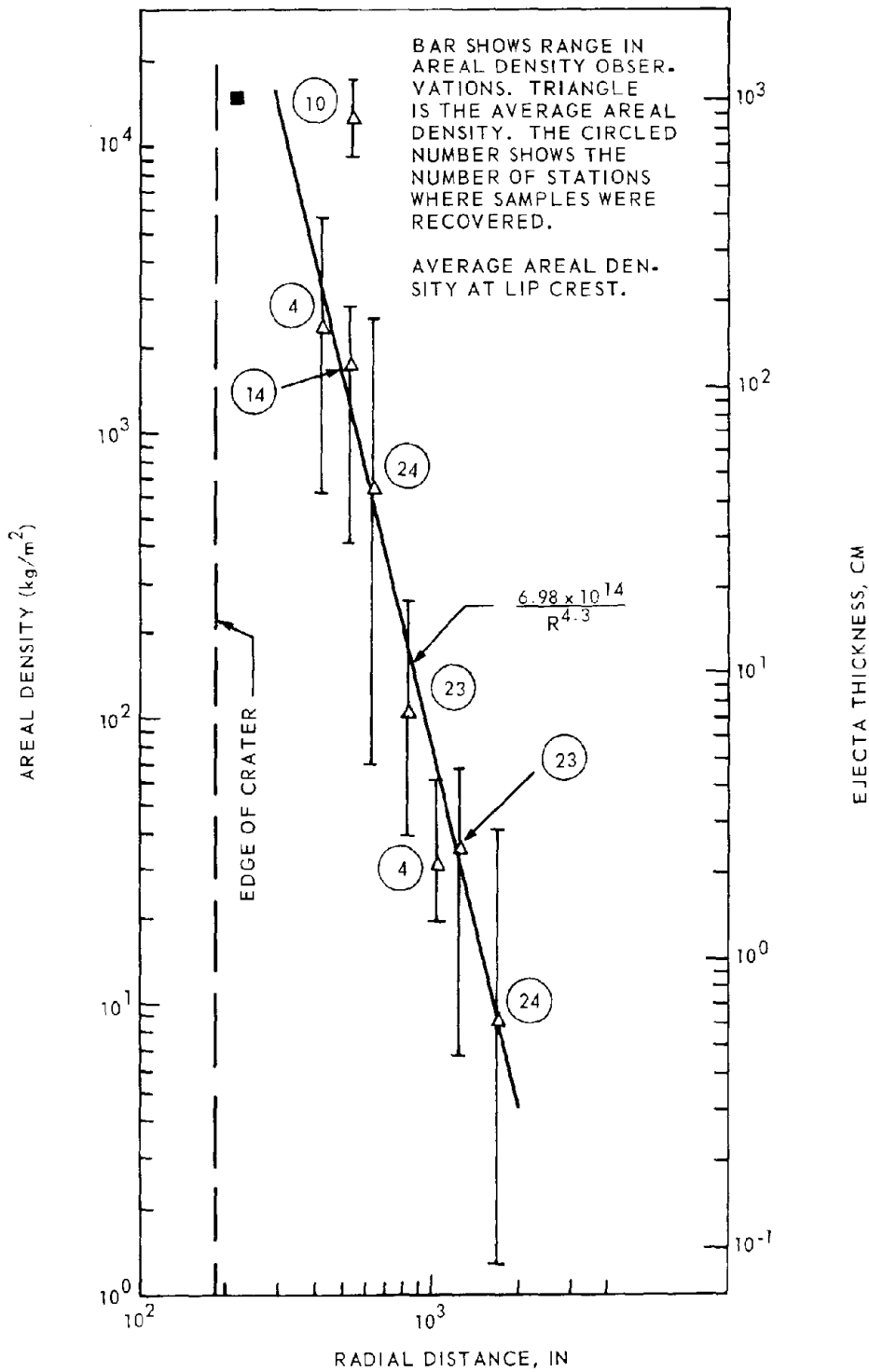
Figure IV-4.38.   Mass of material per unit areas as a function of range (Reference IV-4.18).

$$\delta_1 = \frac{2.26 \times 10^9}{R^{2.2}} \qquad 220 \leq R \leq 550 \ m$$

$$\delta_2 = \frac{3.88 \times 10^{19}}{R^{6.0}} \qquad 550 \leq R \leq 840 \ m \qquad (IV\text{-}4.5)$$

$$\delta_3 = \frac{2.60 \times 10^{12}}{R^{3.5}} \qquad 840 \leq R \leq 1710 \ m$$

These curve fits to the data are shown in Figure IV-4.39 and were used to compute the total ejecta mass deposition. This ejecta was computed by means of integrals of the type

$$M_p = 2\pi \int_{R_1}^{R_2} \delta(R) \ RdR \qquad (IV\text{-}4.6)$$

where M_p is that portion of the total ejecta mass falling within the radial range R_1 to R_2. By the use of the piecewise values of $\delta(R)$, the total ejecta mass was computed from

$$M_e = \sum_{p=1}^{n} M_p \qquad (IV\text{-}4.7)$$

These estimates include the bulk and the missile ejecta layers.

The distribution of ejecta mass relative to the crater is shown in Figure IV-4.40 with the TEAPOT ESS data plotted for comparison. (TEAPOT ESS is discussed in the next subsection.) In Figure IV-4.40 the ratio of M_i/M_e is plotted as the ordinate versus the ratio of the range over the crater radius (R/R_a). M_i is the cumulative ejecta mass between the crater edge and the distance of interest, and M_e is the total ejecta mass. This curve was obtained by integrating successive increments of the areal density versus the range curve shown in Figure IV-4.39. Figure IV-4.40 shows that 50, 79, and 92 percent of the total SEDAN ejecta mass was deposited between the crater edge and 2, 3, and 5 crater radii, respectively.
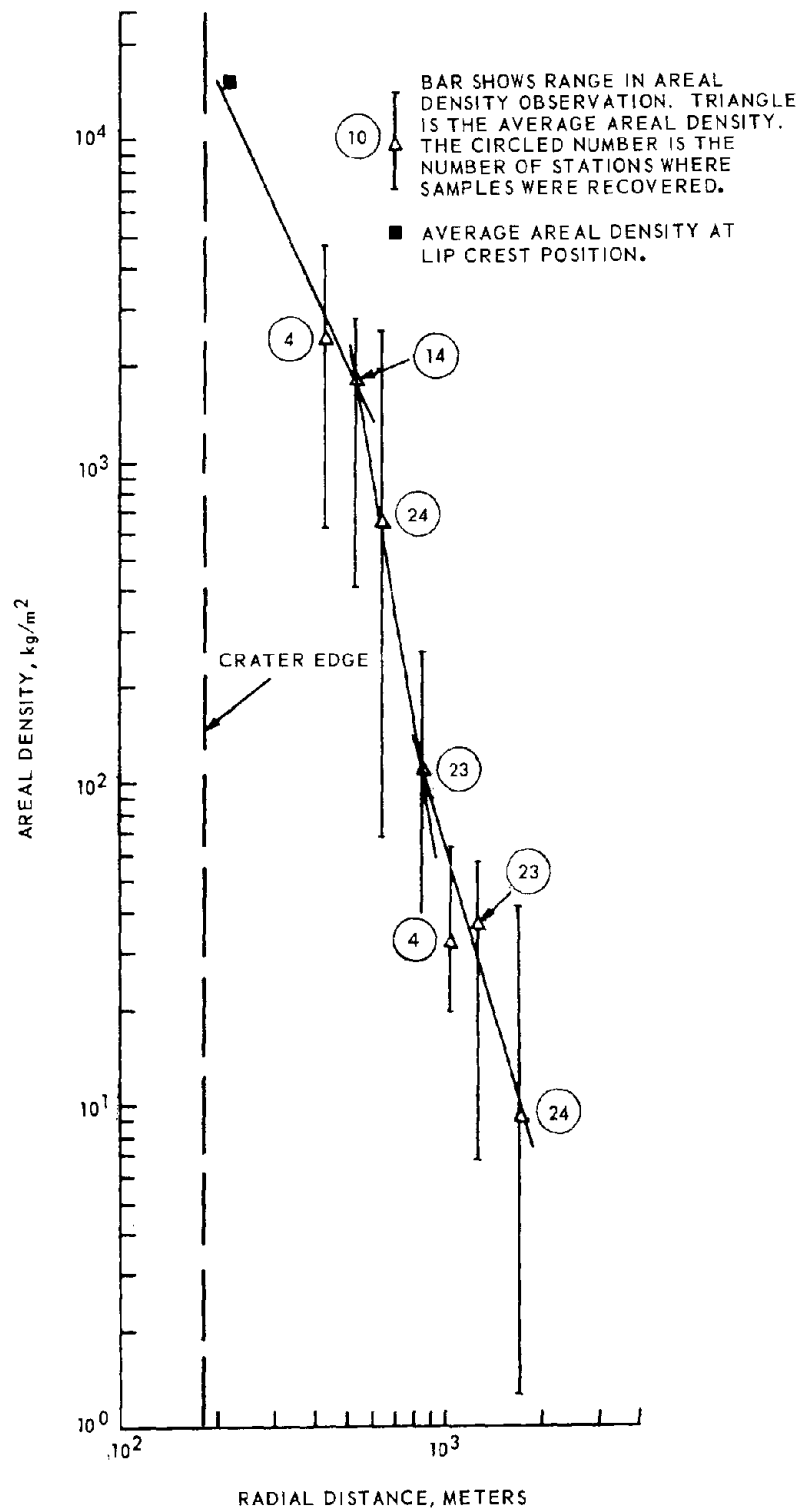
Figure IV-4.39. Areal density versus distance relation-
ships used for computation of ejecta
mass (Reference IV-4.18).

The chart shows data with y-axis labeled M_i/M_e ranging from 0 to 1.0, and x-axis labeled "INCREMENTS OF CRATER RADII, α, α = R/R$_a$" ranging from 1 to 100. Two curves labeled "TEAPOT ESS" and "SEDAN" are shown.

CALCULATED DATA POINTS

α	SEDAN $\dfrac{M_i}{M_e}$	TEAPOT $\dfrac{M_i}{M_e}$
1.14	.0424	−
1.2	.0869	.0492
1.4	.2150	.2294
1.6	.3231	.4208
1.8	.4152	.5542
2.0	.4957	.6463
2.3	.6001	.7366
2.7	.7143	.8135
3.0	.7872	.8495
3.3	.8309	.8755
3.7	.8722	.8999
4.0	.8913	.9131
5.0	.9210	.9402
6.0	.9379	.9541
7.0	.9489	.9628
8.0	.9566	.9688
10.0	.9660	.9764
30.0	.9859	.9913
70.0	.9891	.9937
100.0	.9896	.9944

Figure IV-4.40. Ejecta mass distribution relative to the crater (Reference IV-4.16).

Figure IV-4.41 is a sketch of the crater cross section and the distribution of the excavated mass. This mass may be attributed to various components. Part of the crater void is caused by displacing the original ground surface upward and radially outward to form the true crater lip. The remaining void may be caused by compaction of the medium surrounding it, and the ejection of vaporized material and ballistic debris. For mass computations, Carlson and Roberts (Reference IV-4.16) assumed that the vaporized material is included in the ejecta and long-range fallout quantities. The portion of the apparent crater volume caused by permanent upward distortions of the original ground surface surrounding the crater is equal to the volume of the true lip. The portion of the crater volume resulting from the compression of the medium is the remainder after the ejecta and true lip mass quantities have been subtracted from the mass inferred from the apparent crater volume. Calculations performed by Carlson and Roberts to determine the mass partitioning are summarized in Table IV-4.10. Note the large fraction of the crater content going into ejecta in the range between 220 and 1710 meters, and the large fraction involved in compaction.

Table IV-4.10. Component masses of crater and lip (Reference IV-4.16).

Component	Calculated Mass (kg)			Percentage of Apparent Crater Mass
	Maximum	Minimum	Estimated	
Apparent Crater			7.65×10^9	
True Lip	9.13×10^8	9.36×10^7	2.3×10^8	3
Ejecta (crater edge to 220 m)			1.9×10^8	3
Ejecta (220 m to 1710 m)			4.22×10^9	55
Fallout (1.7 to 4 km)			6.0×10^7	1
Fallout (beyond 4 km)	6.8×10^8	3×10^6	6.0×10^7	1
Compression	3.08×10^9	1.59×10^9	2.89×10^9	37

LONG-RANGE FALLOUT, (1.7 km TO INFINITY)

1.2×10^8 kg

EJECTA (CRATER EDGE TO 220 METERS)

1.9×10^8 kg

3.35 m
(ASSUMED)

CRATER
EDGE

EJECTA (220 METERS TO 1710 METERS)

4.22×10^9 kg

ORIGINAL
GROUND
SURFACE

DIP ANGLE 4.5°

TRUE LIP MASS:
2.3×10^8 kg

APPARENT CRATER MASS: 7.65×10^9 kg

FALLBACK
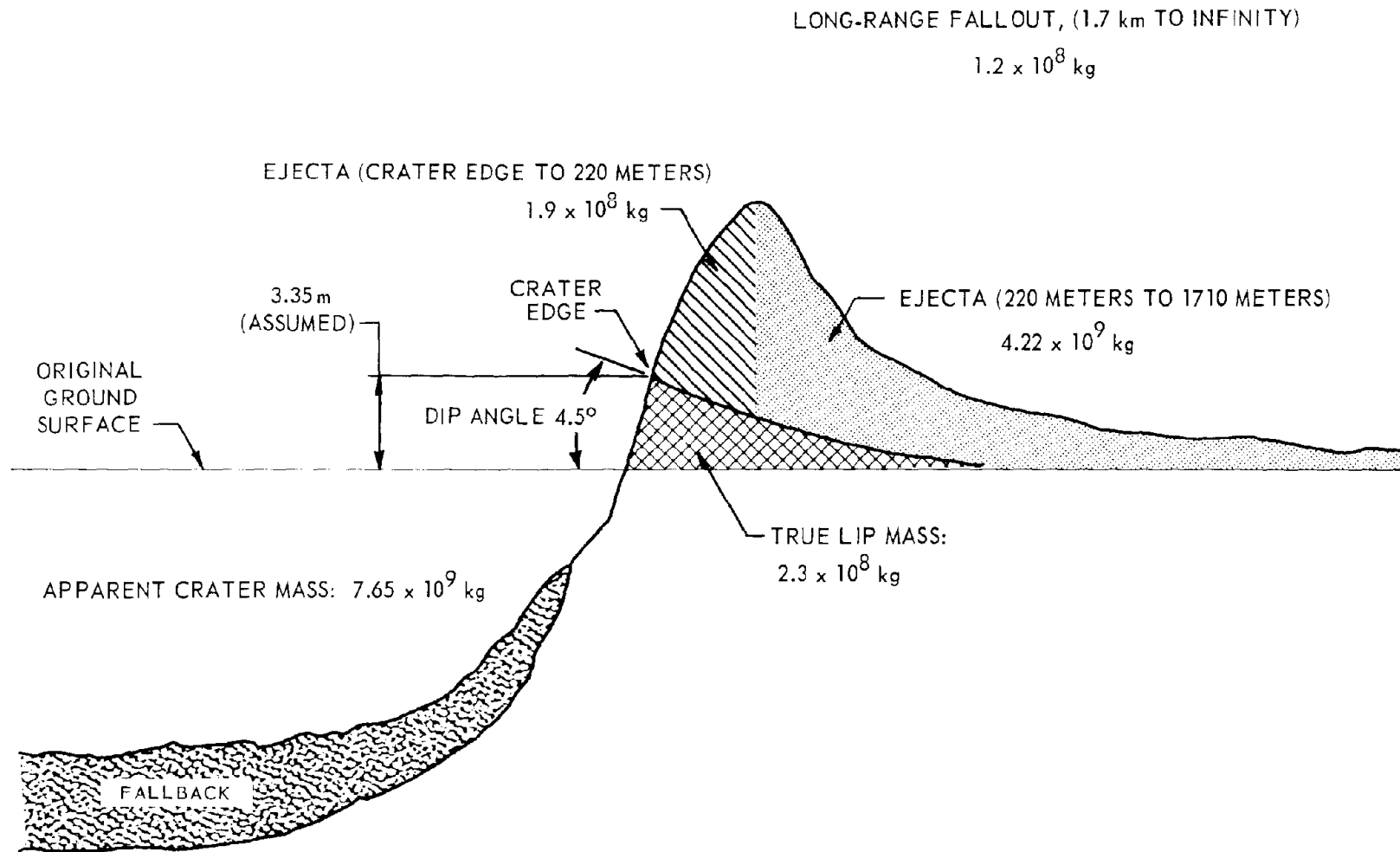
Figure IV-4.41. Sketch of SEDAN crater lip showing mass quantities (Reference IV-4.18).

Numerous impact craters were observed on the ground surface surrounding the detonation crater. Small craters having diameters on the order of 1 meter were located at ranges as great as 2140 meters from SGZ. Numerous impact craters with lip-to-lip diameters of several meters were found at radial distances of nearly 1300 meters. Many craters were clearly visible in the aerial photographs taken after the shot. A large impact crater with a diameter of approximately 7.3 meters was observed at a range of 1280 meters from GZ. The largest impact crater visible on aerial photographs was located at a radial distance of about 300 meters from GZ. The distribution of impact craters with a diameter greater than about 3 meters is shown in Figure IV-4.42. Nine impact craters were excavated to determine the nature of the missiles that formed them. A diagrammatic composite section of the impact craters that were excavated is shown in Figure IV-4.43. Most of these impact craters were formed by discrete masses of alluvium and a few were craters produced by single boulders or other kinds of debris. As with naturally occurring meteor craters on Earth and the Moon, several craters were found to have a central mound of ejecta. Carlson and Roberts (Reference IV-4.16) noted that a careful study of aerial photographs indicated no correlation for circumferential variability between impact craters and ejecta areal densities for the more distant sampling rings.

A missile survey was made along the four primary sampling radii. The missiles were recovered, weighed, and their approximate size determined. Their location at impact was also noted. The original portion in the crater region of these missiles is unknown. Nevertheless, Carlson and Roberts (Reference IV-4.16) postulated missile exit angles to be between 50 and 85 degrees. Using the classical vacuum ballistic trajectory equation, they inferred initial velocities for these two ejection angles for a number of the missiles recovered. They compared their results with Shoemaker's analysis for the ejecta from the Copernicus crater on the Moon (Reference IV-4.19). As would be expected, there is rough agreement. However, application of Sherwood's simple model (Reference IV-4.20) reveals the initial velocity to be much larger than that computed by Carlson and Roberts because Sherwood included the large drag produced by the atmosphere.

The ejecta deposition can be related to the device yield. Nordyke and Williamson (Reference IV-4.18) concluded that the yield dependence of the ejecta should be of the form
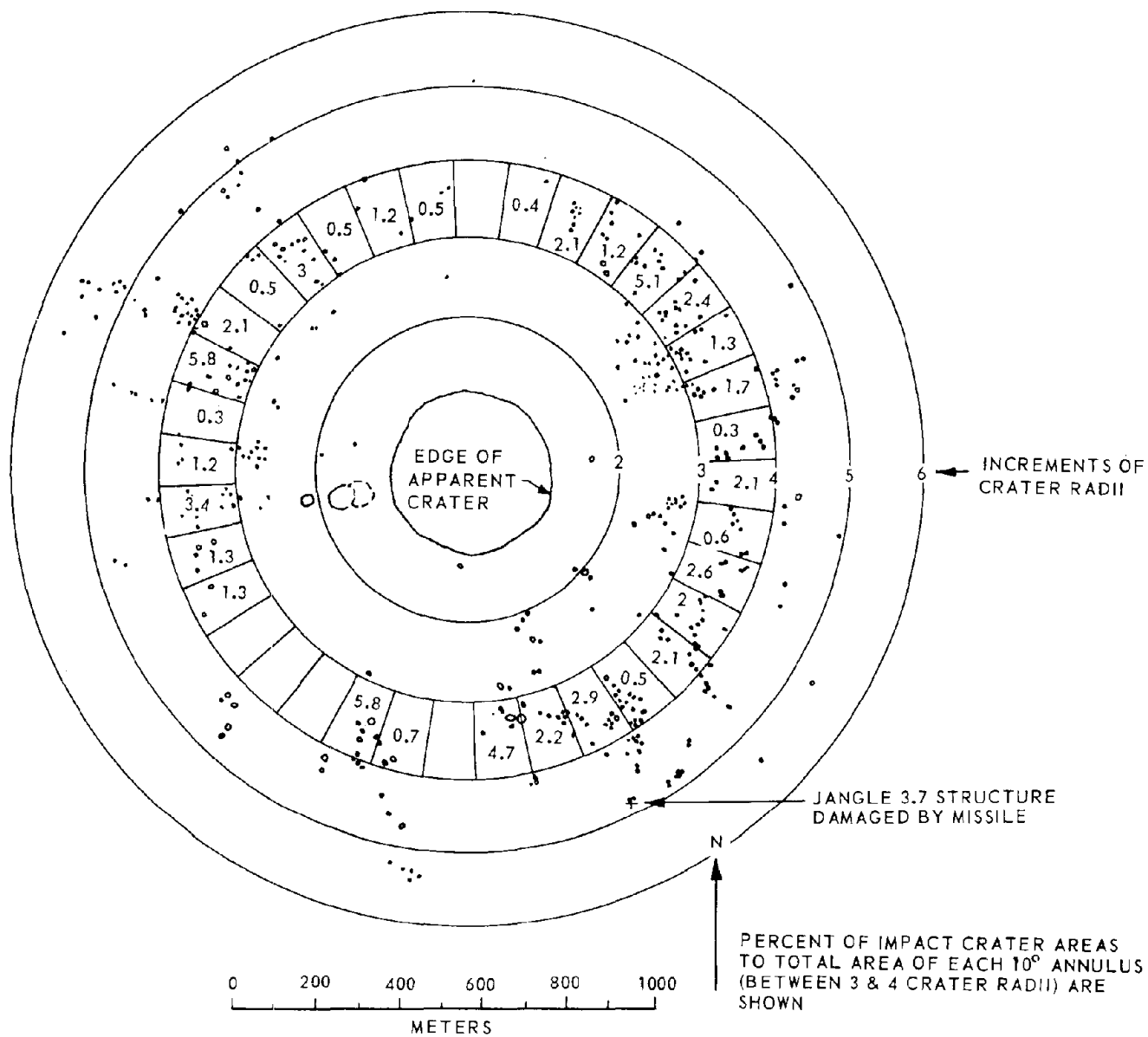
Figure IV-4.42. Distribution of large impact craters (Reference IV-4.18).
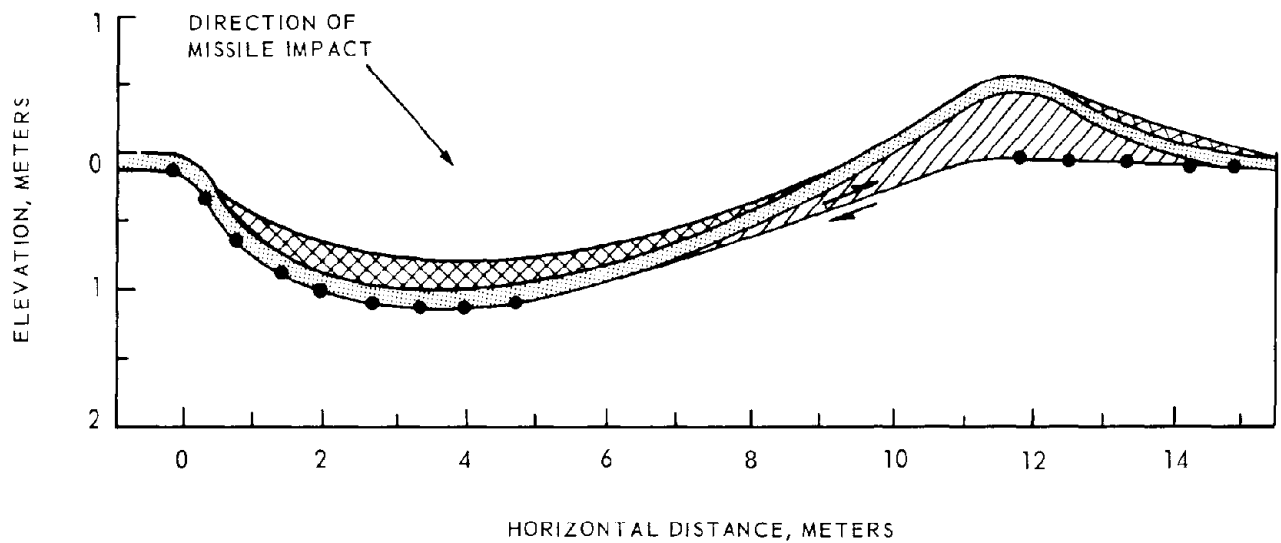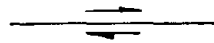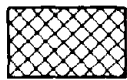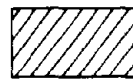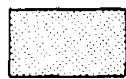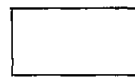
Figure IV-4.43.   Diagrammatic section of impact crater (Reference IV-4.18).

$$\frac{\delta}{W^{1/3.4}} = K (R/W^{1/3.4})^{-b} \qquad , \quad b > 2 \qquad \text{(IV-4.8)}$$

where W is the equivalent yield in kt and K is a constant to be determined. Normalizing this equation to the SEDAN Event they obtain an equation for the ejecta thickness in alluvium of

$$\frac{\delta}{W^{1/3.4}} = 5.3 \times 10^{11} \left(\frac{R}{W^{1/3.4}} \right)^{-4.3}$$

or

$$\delta = 5.3 \times 10^{11} \left(\frac{W^{1.56}}{R^{4.3}} \right) \qquad \text{(IV-4.9)}$$

They found that this function predicted the average ejecta distribution reported for the 0.5-kt SCOOTER Event (Reference IV-4.21) within a factor of 1.5 to 2.0.

IV-4.1.2.5 TEAPOT ESS. The TEAPOT ESS Event was detonated in the Yucca Flat area of the NTS at a depth of 20.4 meters (Reference IV-4.22), and had a yield of 1.2 kt. The soil characteristics for this event were nearly identical to that for the JANGLE U Event. The principal objective of this event was the investigation of the effect of charge depth on cratering (Reference IV-4.23). Some photography was made to measure the visible surface effects, including the radial throwout, the column, the smoke crown, and the jet and base surge (Reference IV-4.22). Preliminary crater measurements were obtained by aerial mapping procedures of the aerial markers that were emplaced in 12 positions around GZ before the detonation. These markers consisted of reinforced concrete crosses 2.5 by 1.8 meters painted black and yellow. Using these aerial markers and mapping techniques, a contour map of the apparent crater and continuous ejecta was obtained from aerial stereophotographs taken at 20.5 hours after detonation. From crater profiles the dimensions of the crater were determined.

Milligan and Young (Reference IV-4.22) give a general and brief discussion of the throwout observed from photographs taken during the event. The radial ejection of crater material was seen to be extremely pronounced and asymmetrical. The farthest ejecta reached the ground in about 15 seconds and was noted to have a

maximum extent of approximately 610 meters from GZ. The heavy concentration of dust streamers, due to the disintegration of the ejecta material during its return to the ground surface, completely obscured the initial formation of the base surge. The ejecta material reached a maximum height of approximately 220 meters. The maximum range of the ejecta measured from GZ at the indicated azimuths are given in Table IV-4.11. The material thrown out of the crater in the form of ejecta originated within the crater formed by the explosion (Reference IV-4.24).

Table IV-4.11. Maximum ejecta range.

Azimuth (deg)	Maximum Range (m)
97	549
172	515
277	615
352	586

The distribution of the ejecta mass relative to the crater is shown in Figure IV-4.40. This mass distribution curve was derived by integrating successive increments of the areal density versus range curve shown in Figure IV-4.44. In this figure, the areal density is best represented by three line segments having the following representation (Reference IV-4.25):

$$\delta_1 = 1.97 \times 10^{11} \ R^{-4.31} \ , \quad 65 \leq R \leq 245 \tag{IV-4.10}$$

$$\delta_2 = 3.25 \times 10^{9} \ R^{-3.57} \ , \quad 245 \leq R \leq 2650 \tag{IV-4.11}$$

$$\delta_3 = 2.12 \times 10^{1} \ R^{-1.17} \ , \quad 2650 \leq R \leq 14{,}500 \tag{IV-4.12}$$

where δ_i is the ejecta areal density in kg/m^2 for the range of interest, and R is the range in meters. Although a planned ejecta experiment was not part of the
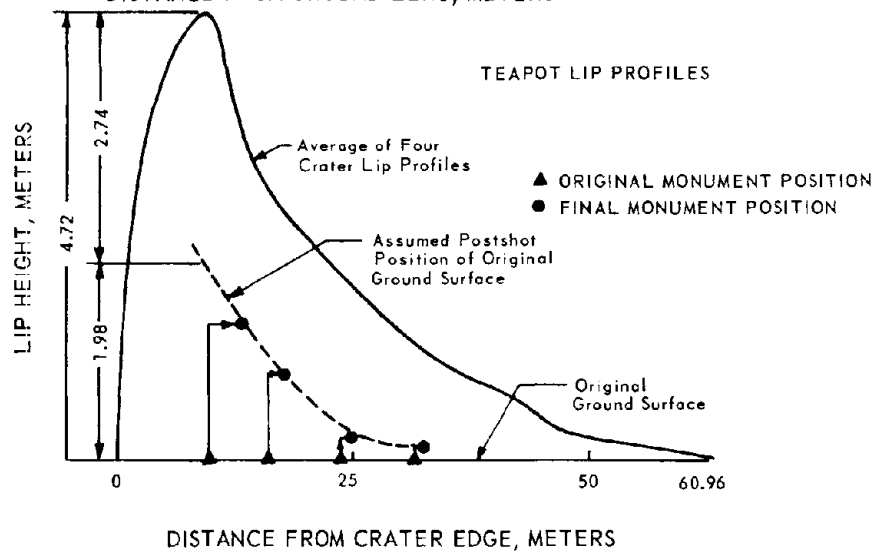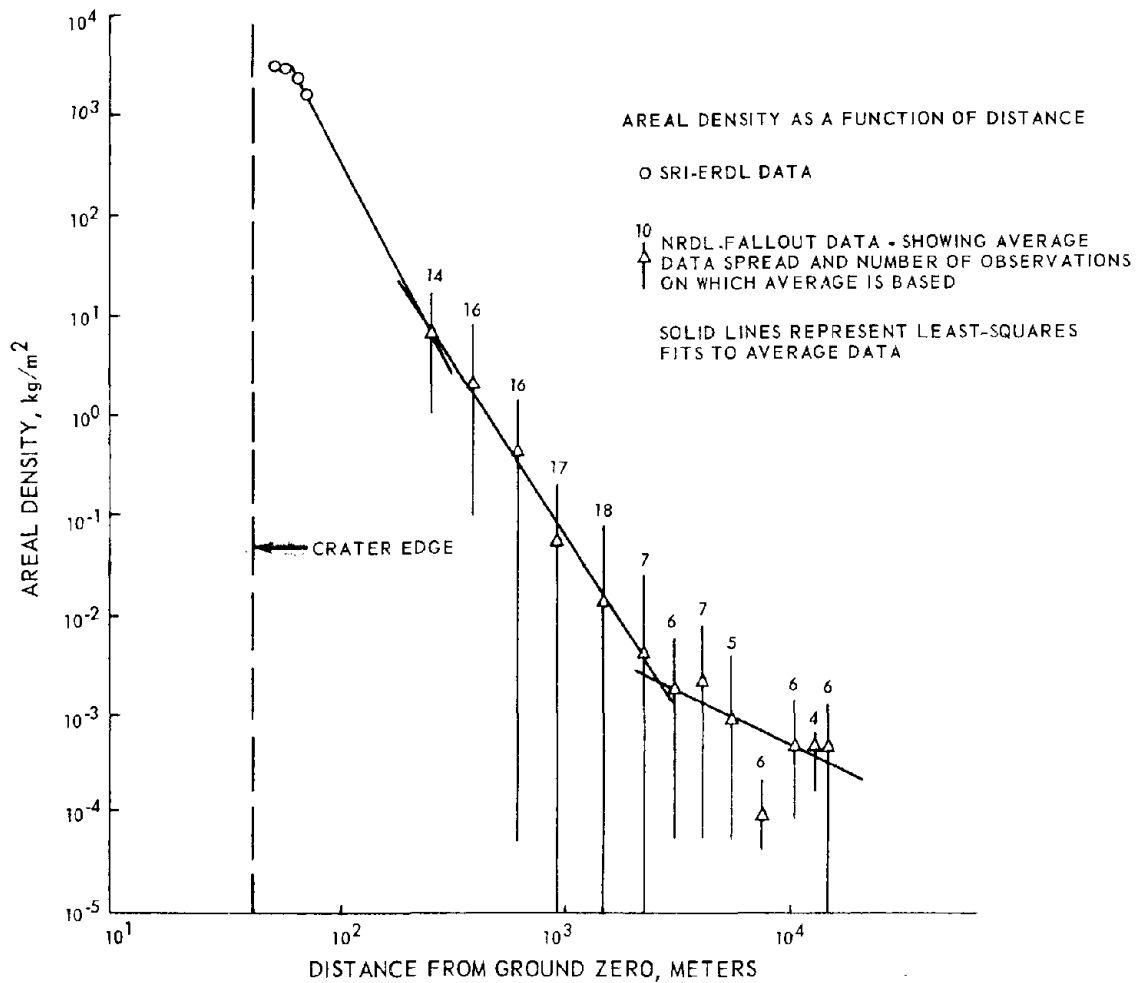
Figure IV-4.44. Ejecta areal density as a function of distance and lip profiles for the TEAPOT ESS crater.

TEAPOT ESS Event, there are data available that permit ejecta quantity as a function of range to be established. An extensive radioactive fallout experiment included circumferential stations commencing at a radial distance of approximately 270 meters from GZ and extending beyond approximately 15,000 meters (Reference IV-4.26). Fallback quantities at close-in ranges were also obtained from topographical profiles of the crater lip (Figure IV-4.44).

Component masses of the crater and the lip computed for the TEAPOT ESS Event, using the same techniques used for the SEDAN Event, are shown in Table IV-4.12. As indicated, 32 percent or less of the apparent crater volume can be attributed to compression of the surrounding medium. This value is less than for the SEDAN Event (41 percent) which seems reasonable because the TEAPOT ESS scaled DOB was less than for the SEDAN Event. However, the TEAPOT ESS true lip represents a much greater portion of the apparent crater mass (18 percent compared to 3 percent for SEDAN). This is also consistent with observation because greater ground distortion occurs for craters produced by shallow underground or near-surface detonations.

Table IV-4.12. TEAPOT ESS component masses of crater, ejecta, and lip.

Component	Calculated Mass (kg)	Apparent Crater Mass (%)
Apparent Crater	1.18×10^8	--
True Lip	2.1×10^7	18
Ejecta (crater edge to 53 m)	8.1×10^6	7
Ejecta (53 m to infinity)	5.12×10^7	43
Compression (also includes long range fallout mass)	3.8×10^7	32

IV-4.1.3 Summary

For convenience in discussing the ejecta data obtained from nuclear events, these events were arbitrarily separated into two groups: the near-surface events, and the deeply buried events. The separation of these events into two groups by means of the scaled DOB of 10 $m/kt^{1/3.4}$ was also arbitrary. The JANGLE S and U,

and the JOHNIE BOY Events are all near-surface detonations, either just above or just below the surface. The deeply buried events group begins with TEAPOT ESS at approximately 20 m/kt$^{1/3.4}$.

For the near-surface events, mostly crater data were found. The only event for which ejecta distribution measurements were made was for the JOHNIE BOY Event. Very little data are available for the near-surface events, primarily because the measurement of ejecta characteristics were of secondary importance.

For the deeply buried events, considerably more measurements of ejecta are available. All of the events cited, with the exception of the TEAPOT ESS Event, were part of the PLOWSHARE Program. Admittedly, not all of the events discussed were candidates for ejecta measurements. It was the author's intent to present only the well instrumented four events usually discussed, namely DANNY BOY, SCHOONER, SEDAN, and TEAPOT ESS.

Table IV-4.13 summarizes the apparent crater dimensions for each event discussed in subsections IV-4.1.1 and IV-4.1.2. The device yields and their depths of burst are also shown. For convenience, the apparent crater radii and depth were scaled by the yield in kt to the 1/3.4 power.

Table IV-4.14 summarizes the data available on the ejecta distribution for the events discussed. Ejecta distribution equations of the form

$$\delta(R) = aR^{\alpha} \qquad , \; kg/m^2 \qquad (IV-4.13)$$

were used, where a and α are constants and R is the radial range in meters. The equations shown in the table give a curve fit to average values of the ejecta distribution. The dashes indicate that no data are available. No curve fit could be found for the ejecta distribution for the CABRIOLET Event. Therefore, a crude fit was made by the author on the basis of a crater sectional profile. Figure IV-4.45 shows a composite of the cumulative ejecta distribution that were found in the data for all events.

Table IV-4.15 presents some relationships among various crater and ejecta quantities that are useful in determining the mass partitioning of the material excavated from the crater by the detonation. A curve fit was attempted for the ratio M_e/M_a including all events shown in the table. This fit showed a low value for the coefficient of determination (r^2), or in other words, a poor fit.

Table IV-4.13. Summary of scaled apparent crater dimensions.

Event	Yield (kt)	DOB $(m/kt^{1/3.4})$	Radius $(m/kt^{1/3.4})$	Depth $(m/kt^{1/3.4})$
NEAR SURFACE (<10 $m/kt^{1/3.4}$)				
JANGLE S	1.2	13.0	-1.07	4.9
JANGLE U	1.2	37.3	5.18	15.4
JOHNIE BOY	0.5	22.8	-0.39	11.4
DEEPLY BURIED (>10 $m/kt^{1/3.4}$)				
CABRIOLET	2.3	42.8	40.56	27.8
DANNY BOY	0.43	41.8	42.94	24.2
SCHOONER	35.	45.6	37.96	22.3
SEDAN	100.	47.8	50.07	25.4
TEAPOT ESS	1.2	42.2	19.34	26.0

However, considering the data for the yield from 0.43 kt (DANNY BOY) through 1.2 (TEAPOT ESS) only, the fit is given by

$$M_e/M_a = 0.323 \ W^{-1.26} \qquad\qquad\text{(IV-4.14)}$$

where W is the yield in kt, with $r^2 = 0.73$. No reasonable power law fit to the M_a/M_t data could be obtained.

Finally, Table IV-4.16 summarizes the availability of crater and ejecta data. It is separated into five categories for convenience. Note again that four events, JOHNIE BOY, DANNY BOY, SEDAN and TEAPOT ESS have been well instrumented in nearly all categories. Some continuous and missile ejecta data also exists for CABRIOLET, although some of these data are not too useful.

Table IV-4.14. Summary of ejecta distribution.

Event	Yield (kt)	DOB (m)	Equation $\delta = aR^{\alpha}$ (kg/m^2)
NEAR SURFACE (<10 m/kt$^{1/3.4}$)			
JANGLE S	1.2	-1.07	-
JANGLE U	1.2	5.18	-
JOHNIE BOY	0.5	-0.39	$\delta = 2.06 \times 10^8 R^{-3.65}$
DEEPLY BURIED (>10 m/kt$^{1/3.4}$)			
CABRIOLET	2.3	51.82	$\delta* = 2.45 \times 10^5 R^{-0.8}$, 68.6<R<137
DANNY BOY	0.43	33.50	$\delta = 2.69 \times 10^{18} R^{-8.55}$
SCHOONER	35.	108.0	$\delta = 2.01 \times 10^{15} R^{-5.43}$
SEDAN	100.	194.0	$\delta\dagger = 6.98 \times 10^{14} R^{-4.3}$
TEAPOT ESS	1.2	20.4	$\delta\dagger = 2.1 \times 10^{11} R^{-3.94}$

*This value was derived from a crude average for continuous ejecta above the upthrusted ground surface. An average density of 2.63 gm/cm^3 was assumed.
†Fit to average data.
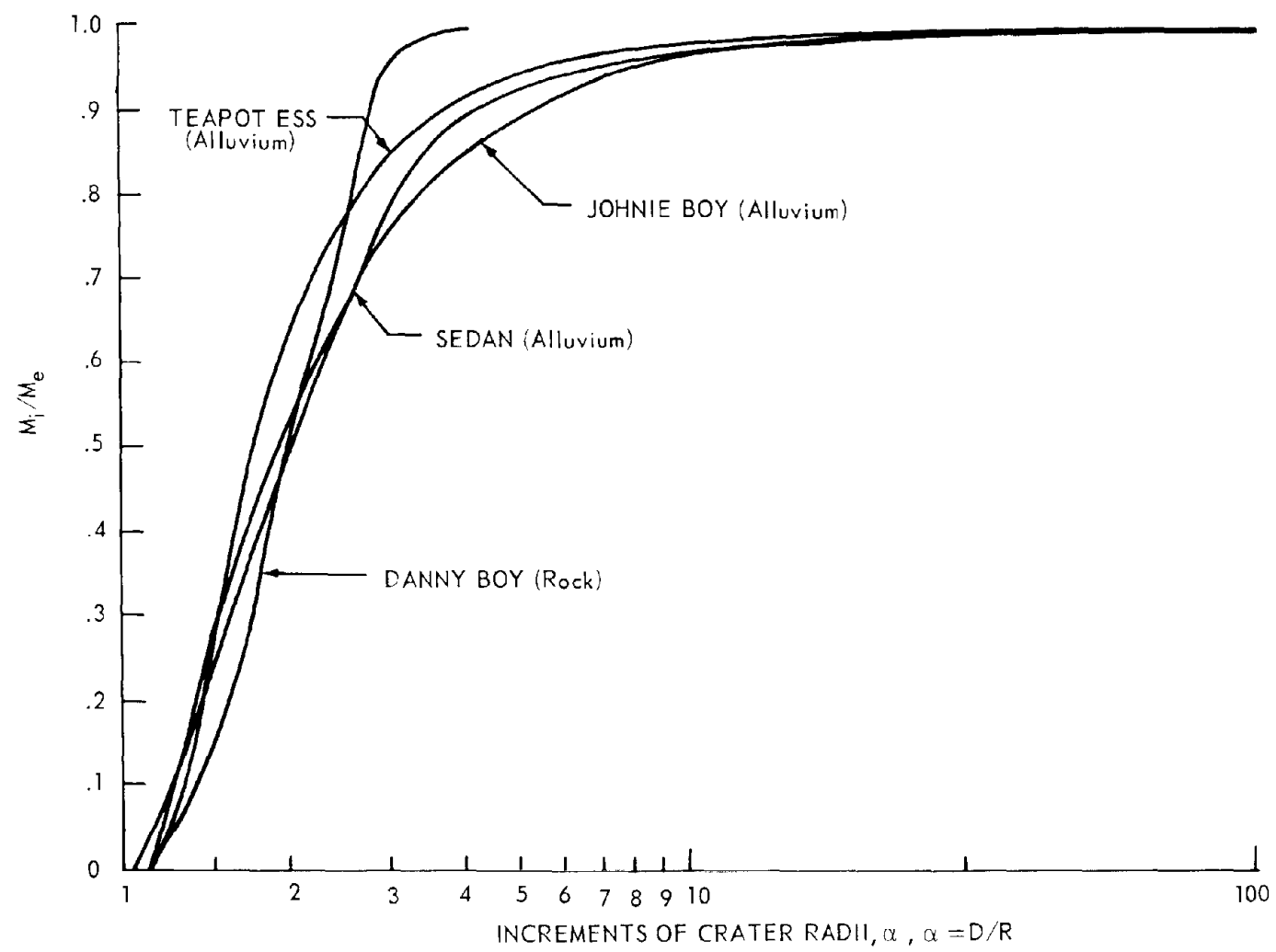
Figure IV-4.45. Ejecta mass distribution curve.

Table IV-4.15. Some ratio of crater masses.

Event	M_e/M_t	M_e/M_a	M_f/M_t	M_a/M_t
NEAR SURFACE ($<$10 m/kt$^{1/3.4}$)				
JANGLE S	-	0.25	-	-
JANGLE U	-	0.17	-	-
JOHNIE BOY	0.35	0.53	0.27	0.68
DEEPLY BURIED ($>$10 m/kt$^{1/3.4}$)				
CABRIOLET	-	1.34	-	-
DANNY BOY	0.55	1.29	0.45	0.43
SCHOONER	-	1.20	-	-
SEDAN	0.20	0.42	0.43	0.48
TEAPOT ESS	0.34	0.42	0.17	0.81

M_e = total ejecta mass.
M_t = total true crater mass.
M_a = apparent crater mass.
M_f = fallback mass.

IV-4.2 HIGH-EXPLOSIVE EVENTS

This section contains a discussion of some of the high-explosive (HE) events. There have been hundreds of single-burst events with a yield greater than 100 pounds as a cursory examination of Reference IV-4.31 will show. There have been also countless single-burst experiments in which the explosive yield ranged from grams up to 100 pounds. These experiments have been carried out in a wide variety of media. To discuss them all would constitute a staggering undertaking.

In addition, there have been a large number of experiments, covering as large a range in explosive yield as the single-burst events, carried out with multiple charges arranged in a wide variety of configurations. Some of these experiments

Table IV-4.16. Existence of crater and ejecta distribution data.

Event	Apparent Crater	True Crater	Upthrust	Ejecta	Missiles	References
NEAR SURFACE (<10 m/kt$^{1/3.4}$)						
JANGLE S	X	-	-	-	-	
JANGLE U	X	-	-	-	x*	
JOHNIE BOY	X	X	X	X	-	
DEEPLY BURIED (>10 m/kt$^{1/3.4}$)						
CABRIOLET	X	-	x	x	-	
DANNY BOY	X	X	X	x	-	IV-4.28, IV-4.29
SCHOONER	X	x	x	x	X	
SEDAN	X	X	X	X	x	
TEAPOT ESS	X	X	X	x	-	IV-4.27, IV-4.30
*Lower case "x" indicates that only partial data are available.						

were discussed in Chapter IV-3. Many of the multiple charge experiments were carried out by Sandia Laboratories (Reference IV-4.32). Some of these experiments, as for example the row cratering experiments conducted by Vortman (Reference IV-4.33), were very sophisticated in their cratering and ejecta instrumentation, and the postshot data collection and analysis.

In this section, only a few of the single-burst HE experiments with an explosive yield of 10 tons and greater have been chosen for discussion. This discussion represents the author's bias and is not intended to imply that other experiments yielded results of any less importance or value. Table IV-4.17 shows the single-burst events discussed.

IV-4.2.1 Single-Charge Events

This subsection discusses ejecta data obtained from a number of HE events in various media and at various depths of burst. Some of these events are discussed more thoroughly than others, depending on the quality of the data obtained from the event discussed.

IV-4.2.1.1 STAGECOACH. The STAGECOACH Program consisted of three events performed in alluvium at three different depths of burst: STAGECOACH I at 24.4 meters, STAGECOACH II at 5.2 meters, and STAGECOACH III at 10.4 meters. The charge yield was 40,000 pounds of TNT. Some of the experiments were designed to determine the ejecta mass and trajectories of discrete missiles produced by using labelled radioactive tracers (References IV-4.34 and IV-4.35).

From simple experiments, reliable data were obtained on the distribution and quantity of fine particulate ejected by these detonations. An empirical relationship was obtained by Perret et al. (Reference IV-4.36) that allows the total mass of particulate deposited to be estimated within an order of magnitude from crater volume alone. From this relationship, which appears also applicable to media other than desert alluvium, and from knowledge of crater volume as a function of yield and depth of burial, a scaling law for total particulate deposited was inferred.

To determine the trajectories of discrete missiles, 28 pellets tagged with radioactive Sb^{124} were buried around the explosive charge in the region of the crater. With these pellets, postshot location helped determine approximate ballistic trajectories and estimation of the initial velocity field of particles in the crater region.

Table IV-4.17. Single-charge chemical explosions.

Event Name	Date	Medium	Yield	Dob (m)	Areal Density Distribution		
					Radial	Circumferential	Tracers
STAGECOACH	1960	Alluvium	20 tons	5.2, 10.4, 24.4	Yes	No	Yes
SCOOTER	1960	Alluvium	500 tons	38.1	Yes	No	Yes
AIR VENT I	1963	Playa	20 tons	5.2	Yes	Yes	No
FLAT TOP I	1964	Limestone	20 tons	0	Yes	Yes	Yes
II	1964	Playa	20 tons	0	Yes	Yes	Yes
III	1964	Playa	20 tons	0	Yes	Yes	Yes
MIDDLE GUST	1971	Layered Media	20 and 100 tons	0 to 0.48	Yes	Yes	Yes
MIXED COMPANY	1972	Layered Media	20 and 500 tons	0, 1.4	Yes	Yes	Yes
ESSEX I, Phase I	1973		10 tons	6, 12	Yes	Yes	Yes

Reliable data were obtained on areal density of earth material deposited ballistically from the crater's edge and on the total mass of earth ejected from the crater by the explosion. The deeper STAGECOACH I explosion (24.4 meters) deposited more earth near the crater edge and considerably less at distances farther from the edge than did the shallower shots. Estimates of total mass of ejecta were made from Sb^{124} tracer data, from particulate collector data, and from true and apparent lip profiles.

The method of collecting ejecta samples was much the same as described in Section IV-4.2. The total debris per unit area decreased approximately as the square of the radial distance within the range sampled for STAGECOACH II and III. The approximate least squares fits for these two events are given by Roberts and Blaylock (Reference IV-4.35) as

$$\delta_{II} = 1.32 \times 10^5 R^{-2.03} \qquad\qquad (IV-4.15)$$

$$\delta_{III} = 1.46 \times 10^5 R^{-1.97} \qquad\qquad (IV-4.16)$$

where δ is the areal density in kg/m^2 and R is the radial distance in meters. Not enough data were obtained to determine how the inverse power of the radial distance changes as the DOB and the radial distance increase from GZ. However, on the basis of the data that were obtained tentative estimates of the power variations on R were obtained. These are summarized in Table IV-4.18.

Size and number of missiles ejected from the STAGECOACH craters found in alluvium depend upon the availability of pebbles and cobbles locally present at and adjacent to GZ. Missile-sized clods, poorly to well cemented by caliche, were collected on the tarps in addition to pebble and cobble fragments. Many of the missiles were fragments of larger, rounded pebbles with one or more fresh fracture surfaces. Film coverage of ejecta was made, but, because of uncertainties introduced by lack of reference point and lack of definition of the missiles, no trajectories were calculated. However, the films show that the higher ejection velocities occur close to GZ associated with higher ejection angles. Both the ejection angle and the velocity decrease outward from GZ.

Scattered missiles were noted beyond 335 meters (22 apparent crater radii) from GZ for STAGECOACH II and somewhat beyond 485 meters (about 27.5 apparent crater radii) for STAGECOACH III. Since both of these events were buried, this

Table IV-4.18.   Variation of inverse power of R with distance
(Reference IV-4.35).

Distance (Apparent Crater Radii)	Inverse Power of the Distance	Remarks
1.18 - 2.0	4.2	Data from lip profiles furnished by Sandia Laboratories.
2.0 - 4.0	2.33	Data from lip profiles furnished by Sandia Laboratories and extrapolation from areal density of debris curves.
4.0 - 20.0	2.0	Region sampled.
1.15 - 2.0	4.1	Data from lip profiles furnished by Sandia Laboratories.
2.0 - 4.0	2.39	Data from lip profiles furnished by Sandia Laboratories and extrapolation from areal density of debris curves.
4.0 - 20.0	2.0	Region sampled.

may be of some assistance in determining the origin of the missiles. Venting of the gases tends to include a much larger rock volume than that volume immediately adjacent to the buried HE.

IV-4.2.1.2 SCOOTER. Project SCOOTER was one of a series of chemical explosive cratering studies that was part of the PLOWSHARE Program. It had an explosive yield of 500 tons of TNT (Reference IV-4.36) arranged into an approximate sphere whose center was 38 meters below the surface of Yucca Flat at the NTS.

The extremely simple experiments of the SCOOTER explosion provided data on the distribution and quantity of earth material ejected by the explosion. By means of radioactive tracer techniques, measurements were made of the areal density of ballistic ejecta from the crater radius outward. Figure IV-4.46 presents all data obtained on ejecta density from the SCOOTER experiment. Crater lip profiles were converted to areal density assuming the in-situ density to be 1.6 gm/cm^3.
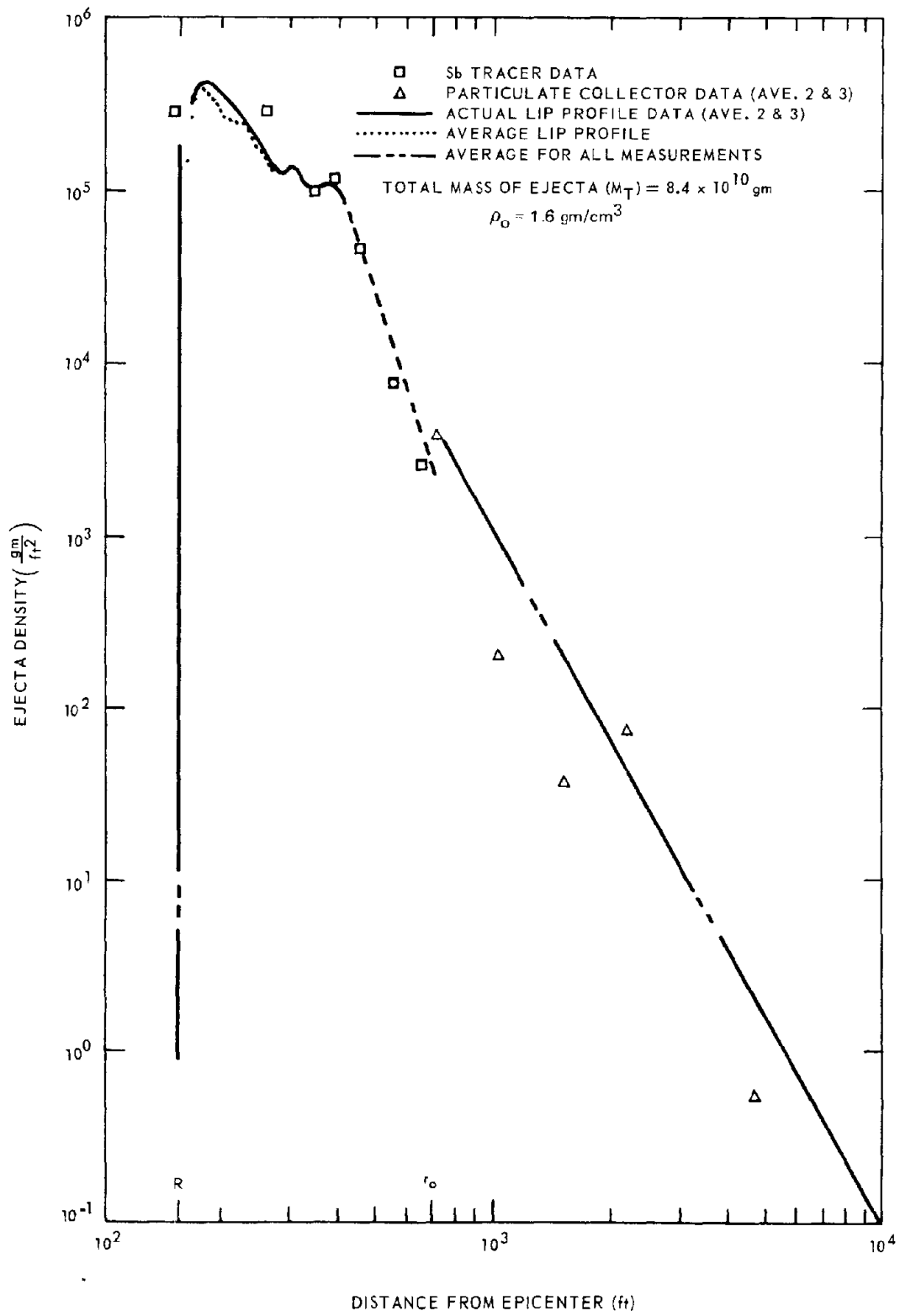
Figure IV-4.46. Ejecta density versus distance (Reference IV-4.36).

Lip profile data, radioactive antimony tracer data and fine particulate data taken together determine a fairly continuous curve for ejecta density as a function of distance.

The tracer method also leads to an estimate of the effective velocity field about the explosive charge and a determination of those regions of earth about the charge from which particular ejecta originated. Figure IV-4.47 compares the velocity field for the SCOOTER and STAGECOACH III Events at nearly the same cube-root-scaled depths.

At distances from the explosion epicenter beyond which ballistic ejecta were not deposited, dust from the explosion cloud or fine particulate was measured with collector pans. From these data, average areal density as a function of distance was determined, and that fraction of crater volume material which was deposited as fine particulate was established. An empirical scaling law for the mass of ejecta deposited as fine particulate, obtained from STAGECOACH experimental data, has been verified by the 500-ton SCOOTER experiment and from data available from the 100-kt SEDAN Event. This scaling law appears to give results for the mass of earth material deposited as fine particulate which are correct within a factor of about 2.

Data from tracer and fine particulate experiments were sufficient to determine the total mass of ejecta deposited by an explosion. Figure IV-4.48 shows total ejecta mass as a function of apparent crater volume. From this figure, a scaling law for total ejecta mass was obtained for desert alluvium as was done for mass of fine particulate. That part of crater volume mass which can be accounted for as ejecta was found to be 70 to 90 percent for chemical explosions at cube-root-scaled depths of 1/2 to 1. Data from the TEAPOT ESS nuclear explosion (scaled depth of 1/2) revealed that 40 percent of the crater volume mass was ejected. This fraction is about a factor of 2 less than that for a chemical explosion at the same scaled burst depth (20 tons at 5.18 meters). It would appear then that from ejecta data, chemical explosions are more energetic than nuclear explosives in ejecting earth material from the crater region.

The study of particles large enough to act as missiles was carried out to furnish data for empirical missile distribution equations. No data suitable for a missile distribution analysis were derived because the only material available was from a single collection pad.
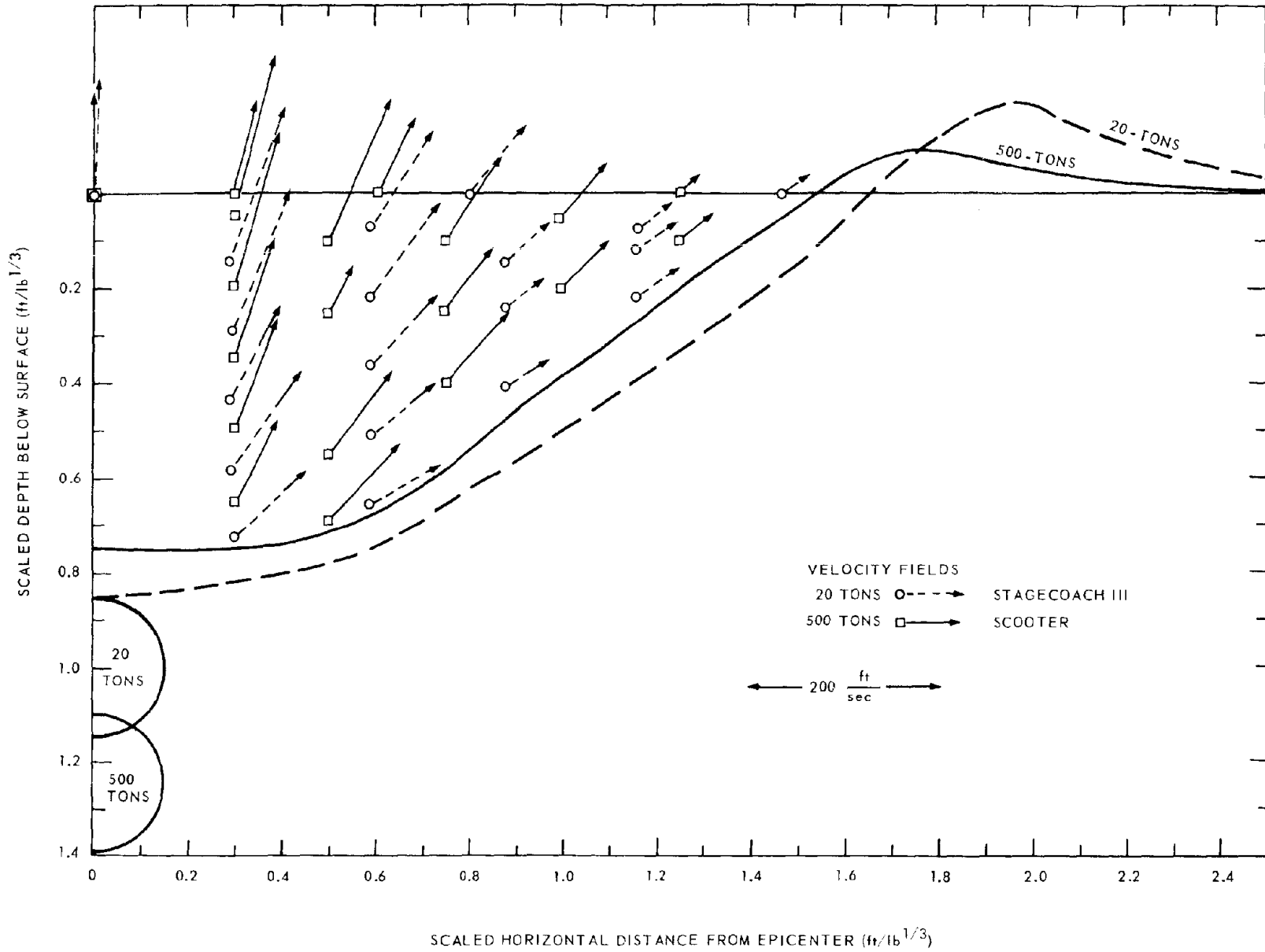
Figure IV-4.47. Comparison of STAGECOACH and SCOOTER effective velocity fields
(Reference IV-4.36).
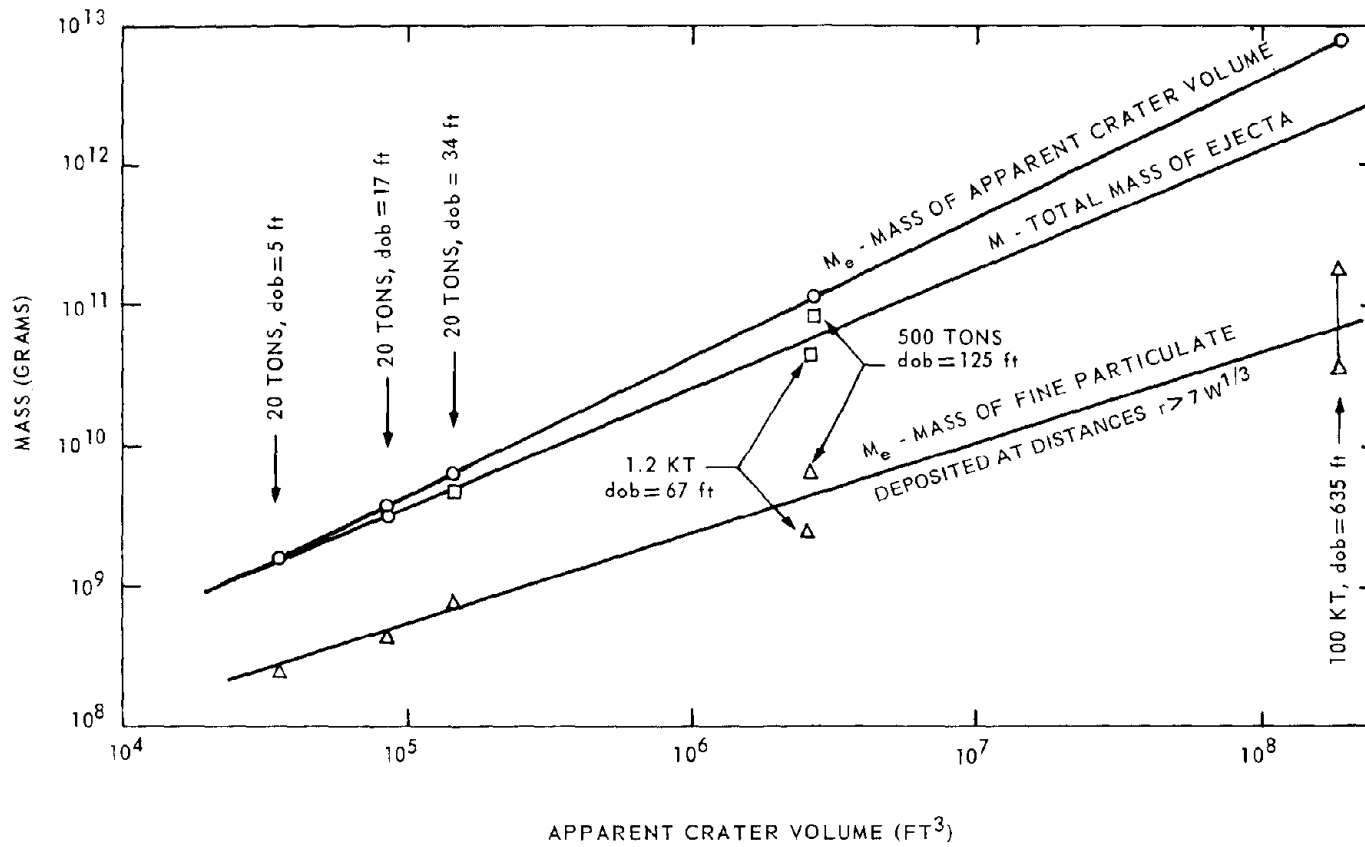
Figure IV-4.48. Comparison of crater volume mass and ejecta mass (Reference IV-4.35).

IV-4.2.1.3 AIR VENT I. Project AIR VENT consisted of a series of HE detonations fired in the playa of Frenchman's Flat at NTS (Reference IV-4.37). This project was divided into three phases. Each phase attempted to resolve one of the relevant questions concerning the difference in cratering properties between Area 10 alluvium and the Area 5 playa at the NTS. The discussion here only will be concerned with AIR VENT Phase I, which had as its objective the direct comparison with the STAGECOACH II Event. Both events were detonated at about the same depth: 5.21 meters for STAGECOACH II, and 5.24 meters for AIR VENT I.

The true crater was divided into four basic zones according to the material response thought necessary to satisfy postshot pellet positions and sand-column measurements. These zones are shown in Figure IV-4.49. The ballistic and scoured ejecta zones shown in Figure IV-4.49 were determined directly from final pellet positions. The initial criterion for distinguishing between ballistic and scoured pellets was to regard pellets recovered on top of and beyond the apparent lip as ballistic. Pellets recovered below the apparent lip surface during lip excavation are considered scoured. Ballistic and scoured ejecta zones were determined directly from final pellet positions. The true crater material was determined as the below-grade true crater volume minus the volume of permanent displacement, as determined from postshot sand-column measurements. The fallback zone is therefore a residual rather than a directly measured volume, determined by subtracting the ballistic and scoured ejecta zones from the true crater volume. Boundaries between these zones represent average or prevailing behavior rather than all-inclusive results.

Quantities of ejecta found at the various final ground range intervals are compared with masses of corresponding regions of the ballistic zone in Table IV-4.19. The two quantities differ at all ground ranges, and the ratios of these two quantities are as great as 4 to 1. It should be noted that the two quantities that were compared actually differ because: (1) measured ejecta at distant ground ranges include slowly falling airborne particulate from the dust cloud, and (2) the drag on ballistically thrown clods of ejecta is higher than for the polished spherical pellets, of the same mass and density, used in this experiment, causing them to fall to the ground surface at shorter ground ranges.

Recovery data on emplaced pellets were used to derive an initial velocity field for the ballistic zone according to the methods described in Reference IV-4.38. Since only initial and terminal positions of pellets were known,
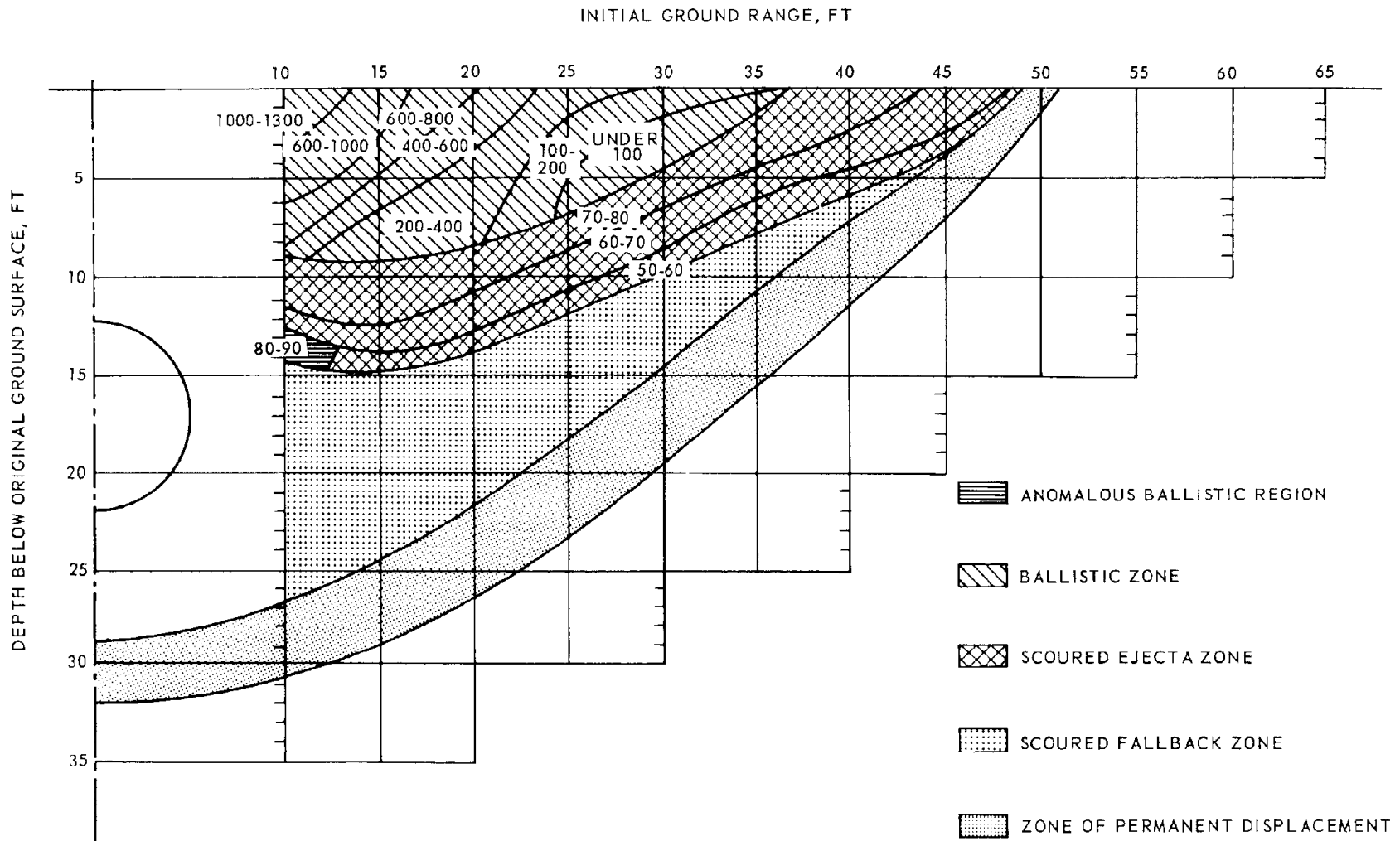
Figure IV-4.49.   Crater zones.   (Numbers in ballistic and scoured ejecta zones are ranges of mean values of final ground ranges, (R_E), for pellets initially placed within the outlined regions.)   (Reference IV-4.37).

Table IV-4.19. Comparison between far-out ejecta and masses of corresponding regions of ballistic zone.

	Ground Range Intervals (m)							
	400+	400-300	300-245	245-180	180-120	120-60	60-30	Under 30
Ballistic Zone Mass, kg		97,340	83,825	133,900	177,390	233,150	187,790	192,780
Percent of Total Ballistic Zone Mass		9.31	8.01	12.7	11.2	22.3	18.0	18.5
Percent of Total Above-Grade Fallback and Ejecta		4.52	3.90	6.18	5.46	10.8	8.73	8.96
Percent of Apparent Crater Mass		4.14	3.56	5.65	4.99	9.91	7.98	8.20
Cumulative Ballistic Zone Mass, kg		97,340	181,170	313,890	431,370	664,520	852,310	1,045,090
Percent of Total Ballistic Zone Mass		9.31	17.3	30.0	41.2	63.5	81.5	100.0
Percent of Total Above-Grade Fallback and Ejecta		4.52	8.42	14.6	20.1	30.9	39.6	48.6
Percent of Apparent Crater Mass		4.14	7.70	13.3	18.3	28.2	36.2	44.4
Ejecta, kg[a]	97,890[b]	23,320	23,040	35,060	62,370	159,670	291,670	
Percent of Above-Grade Fallback and Ejecta Beyond 30 m Ground Range	14.1	3.36	3.32	5.06	9.00	23.0	42.1	
Percent of Total Above-Grade Fallback and Ejecta	4.55	1.08	1.07	1.63	2.90	7.42	13.6	
Percent of Apparent Crater Mass	4.16	0.99	0.98	1.49	2.65	6.79	12.4	

Table IV-4.19. (continued).

	Ground Range Intervals (m)							
	400+	400-300	300-245	245-180	180-120	120-60	60-30	Under 30
Cumulative Ejecta, kg[a]	97,890[b]	121,200	144,250	179,170	241,770	401,440	693,100	
Cumulative Percent of Above-Grade Fallback and Ejecta Beyond 30 m Ground Range	14.1	17.5	20.8	25.9	34.9	57.9	100.0	
Percent of Total Above-Grade Fallback and Ejecta	4.55	5.63	6.70	8.33	11.2	18.66	32.2	
Percent of Apparent Crater Mass	4.16	5.15	6.13	7.62	10.3	17.1	29.5	

[a]Computed quantities from measurements of particulate include both ballistic and wind-blown material.

[b]Computed values from experimental result from extrapolation of logarithmic distribution curves to a ground range of 3,050 meters.

semistatistical methods were adopted to find an epicentral pattern defining a directional field of initial velocities which results in the best-curve fit for initial velocity magnitudes by the method of least-squares. Epicenter depths for pellet placement levels were computed and found to increase monotonically with pellet depths. This is radically different from the radial pattern of initial velocity directions assumed in computing pellet trajectories in the earlier DANNY BOY, STAGE-COACH and SCOOTER Events. Computed initial velocities for the various pellet placement levels are plotted in Figure IV-4.50. Computed velocities at most ground ranges within the ballistic zones were highest for pellets buried 0.3-meter deep, rather than the surface pellets. This is attributed more to placement conditions than to loading phenomena. Since zero-depth pellets were trowelled and tamped into the playa with their top surfaces tangent to the ground surface, they were not fully constrained in the medium in all directions. Their behavior may still be representative of equivalent natural objects.

Initial velocity curves ordered roughly according to pellet levels, but local departures from this trend are apparent. It was noted that a substantial vertical separation exists between initial velocity curves for the top 0.6 meter of the ballistic zone and curves for lower levels, particularly at the shorter ground ranges. This implies either the existence of a high-velocity region of limited depth and radial extent from which ejecta must arise to be capable of traveling the very long ground range observed. This high-velocity region corresponds to the shallow close-in region of pellets found at far-out ground ranges shown in Figure IV-4.49. Slopes of the initial velocity curves also show a pronounced radial attenuation of this high-velocity region.

The field of initial velocity magnitudes within the ballistic zone is plotted in Figure IV-4.51, showing initial velocity regions oriented roughly in the fashion of the final ground-range regions of the ballistic zone shown in Figure IV-4.49. The range of epicenters was found to correspond to epicenter depths from 0.25 to 0.76 of the DOB where the deepest epicenter corresponds to a pellet level of 2.4 meters below grade -- near the interface between the ballistic and scoured ejecta zones.

Ballistic pellets were ejected very close to the radial direction in contrast to the DANNY BOY AND FLAT TOP I Events (detonated in rock) where rotational effects in the horizontal plane were observed. On AIR VENT I, median values of the
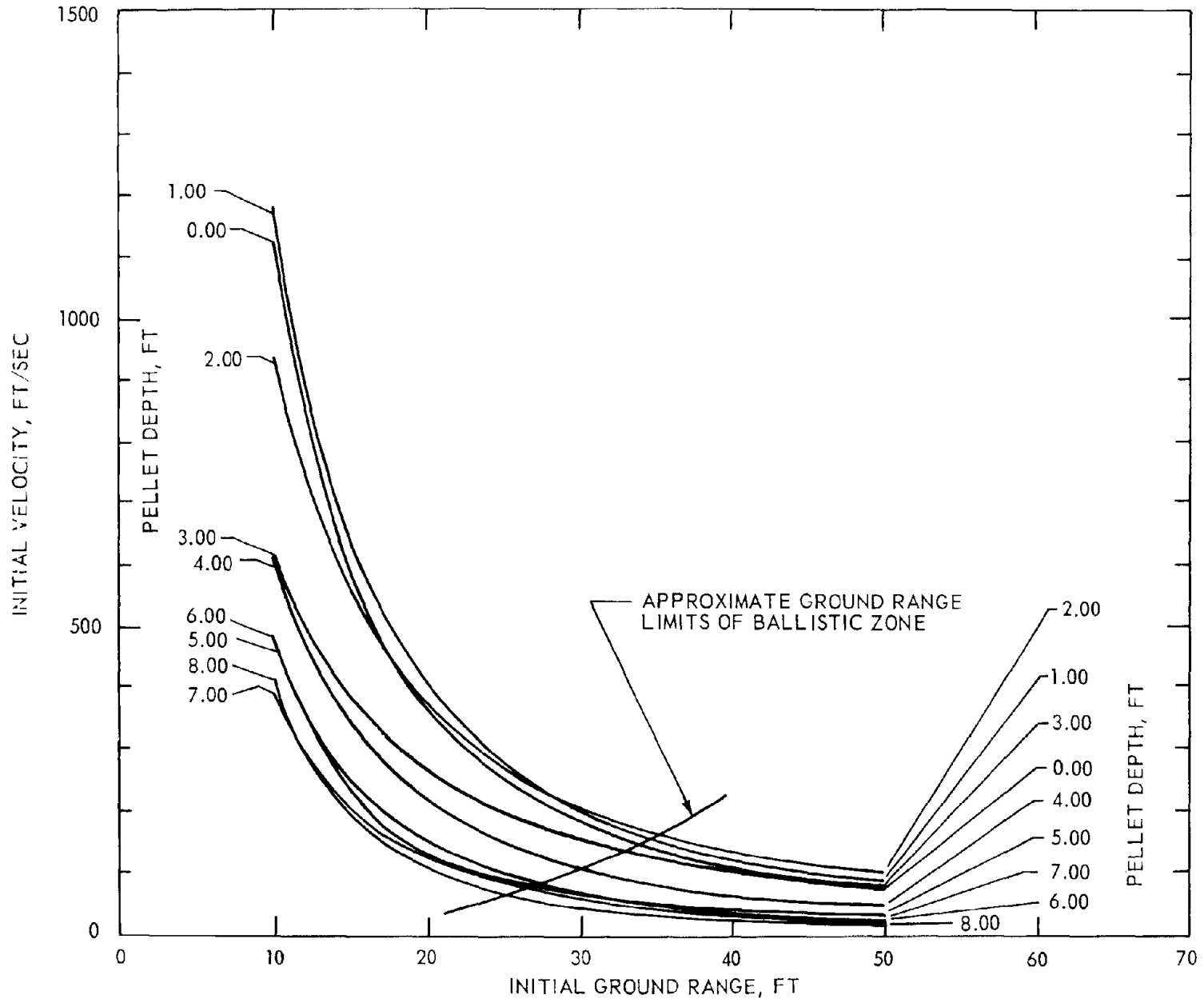
Figure IV-4.50. Estimated initial velocities of ballistic pellets (Reference IV-4.38).
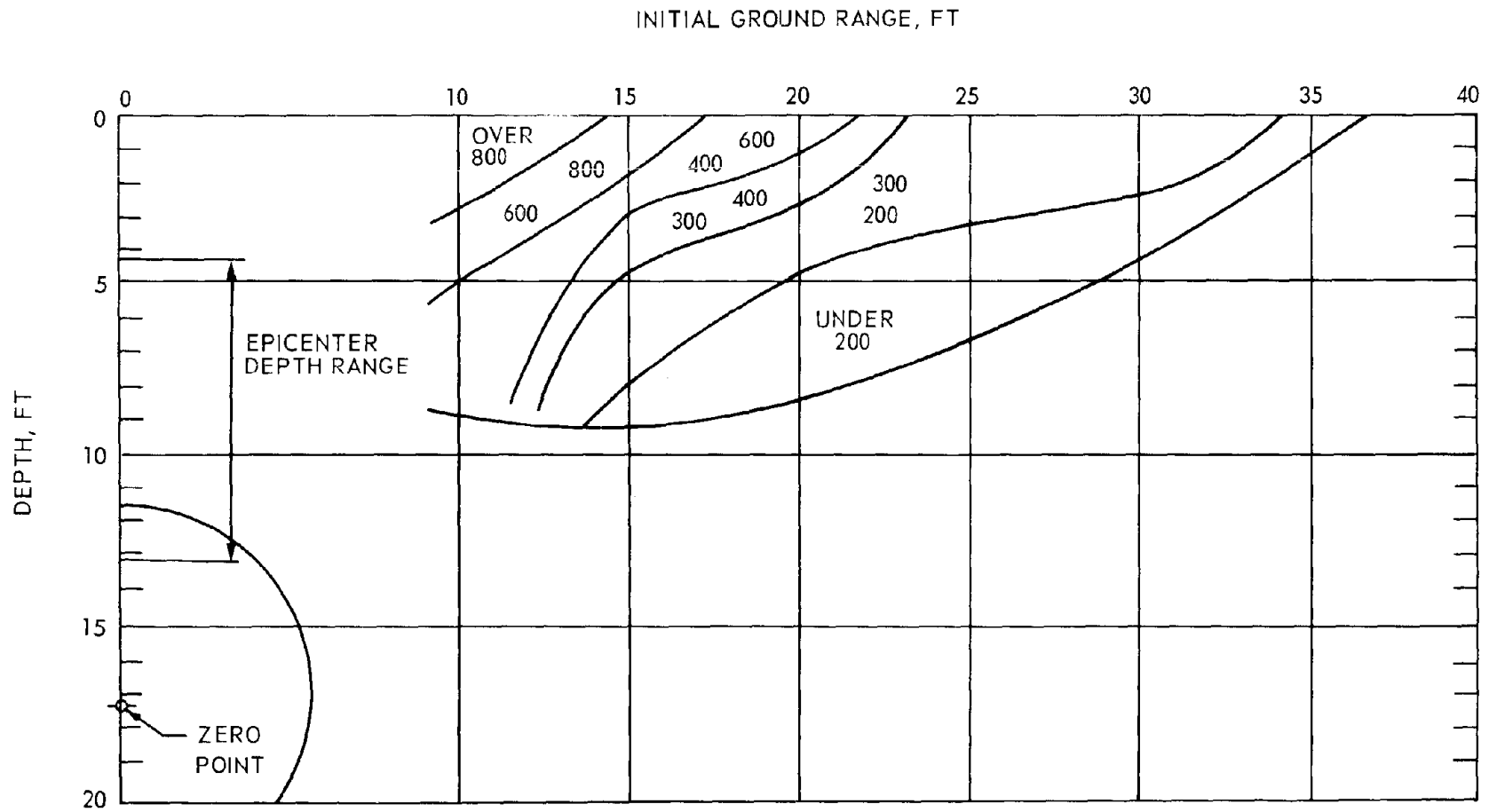
Figure IV-4.51.   Initial velocity magnitudes in ballistic zone (Reference IV-4.38).

horizontal trajectory angle are less than two degrees for pellets placed along any initial azimuth or circumference.

As shown in Figure IV-4.49, the scoured ejecta zone consisted of a 1.8-meter deep seam extending from 2.7 to 4.6 meters below grade at ground ranges from 3 to 4.6 meters, beyond which it sloped upwards at a 23 degree angle and out-cropped between 11.3 and 15.5-meter ground range. This zone is divided, in Figure IV-4.49, into three regions corresponding to postshot ground ranges of pellets. Isorange lines in the scoured ejecta zone represent arithmetic mean values of final ground ranges for pellets recovered in the apparent lip. Assuming pellet behavior to be representative of the flow of natural ejecta, the region between these lines defines the source of material found between various ground ranges. It is seen that a direct relationship exists between locations of source material and final ground range for scoured material forming the apparent lip. The uppermost region of the scoured ejecta zone corresponds to the tail of the apparent lip, while the material from the lowest region is found near the lip crest.

Scouring flow implied from the recovery of pellets found in the apparent lip is a decidedly regular pattern of simple overturning beyond the lip crest as shown in Figure IV-4.52. This overturning is a similar behavior to what was also observed on SEDAN.

Depth and areal density of ejecta are plotted for the region within ten apparent crater radii in Figure IV-4.53. Plotted curves are minima, maxima, and arithmetic means of 12 regression lines computed from sampling measurements. They do not represent the envelope of minimum and maximum field measurements, which would vary much more widely. As an envelope of regression line values, the high and low limits represent circumferential variations in depth and areal density to be expected as a result of ray-like behavior at the closer ground ranges, and from atmospheric winds in the far-out region. The curves of Figure IV-4.53 are based on quadratic expressions to represent the crater lip to about two crater radii, and power-law fits to ejecta measurements beyond this region.

Scaled cumulative above-grade ejecta distribution curves for AIR VENT I are compared with results from FLAT TOP II and III in Figure IV-4.54. Curves for the two FLAT TOP surface bursts are shown to be in excellent agreement except in the region from about 1.8 to 2.5 crater radii. It is seen that the AIR VENT curve departs significantly from the FLAT TOP curves with differences being greatest at the shorter ground ranges. Where 65 percent of above-grade ejecta is accumulated
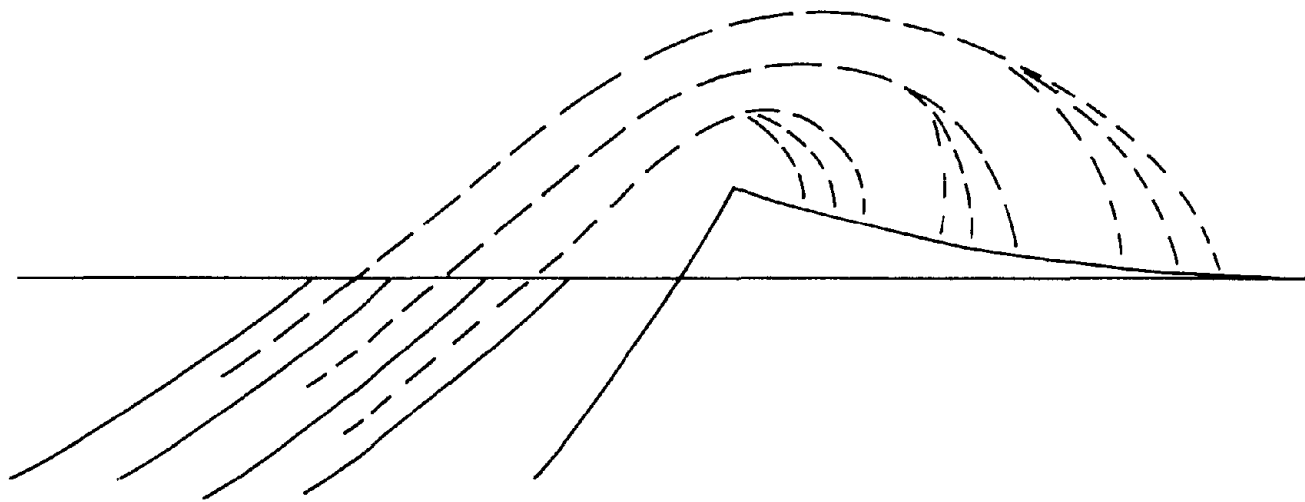
Figure IV-4.52.   Simple overturning flow of apparent lip source material
(Reference IV-4.38).
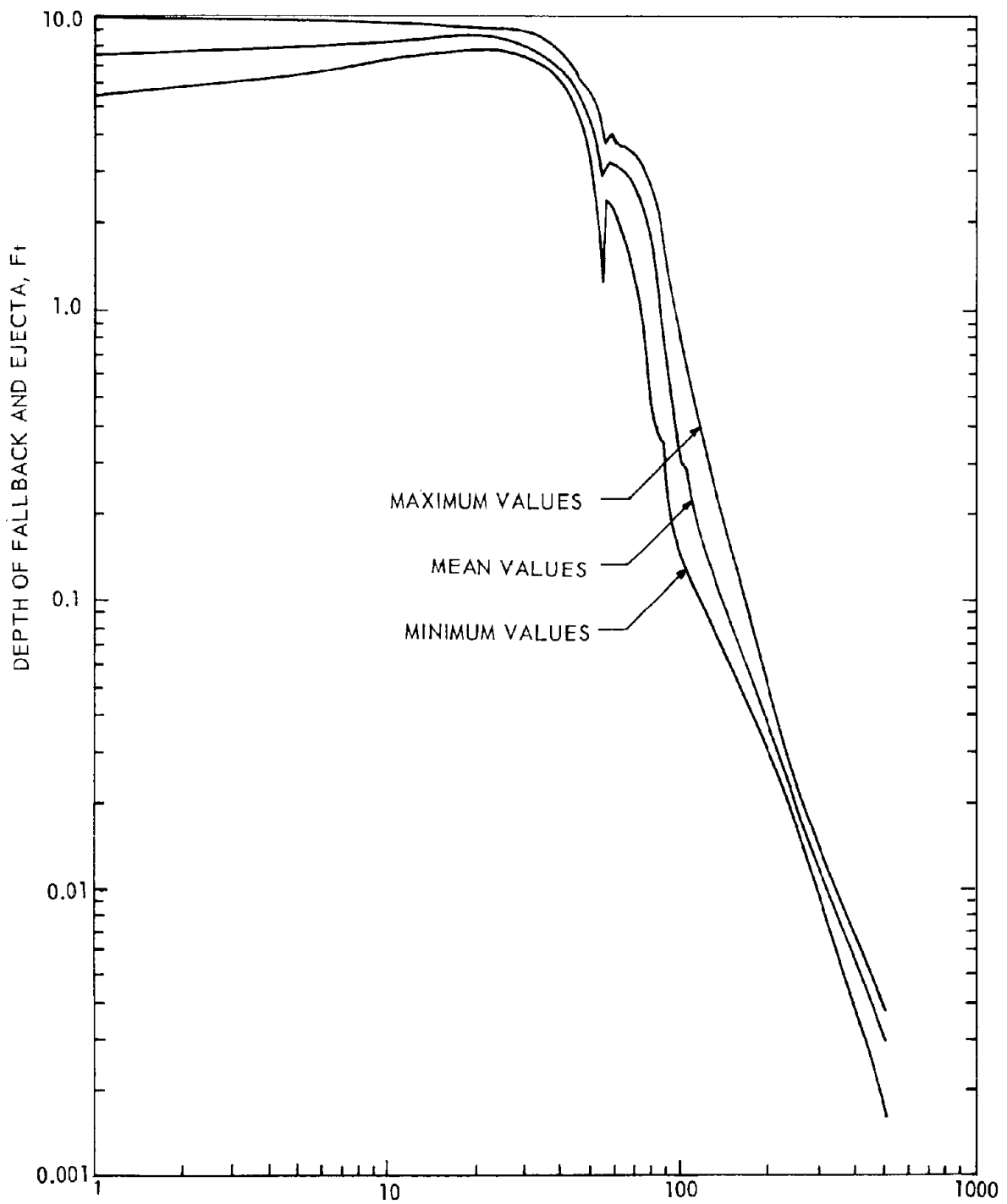
Figure IV-4.53. Depth and areal density of fallback and
ejecta (Reference IV-4.38).
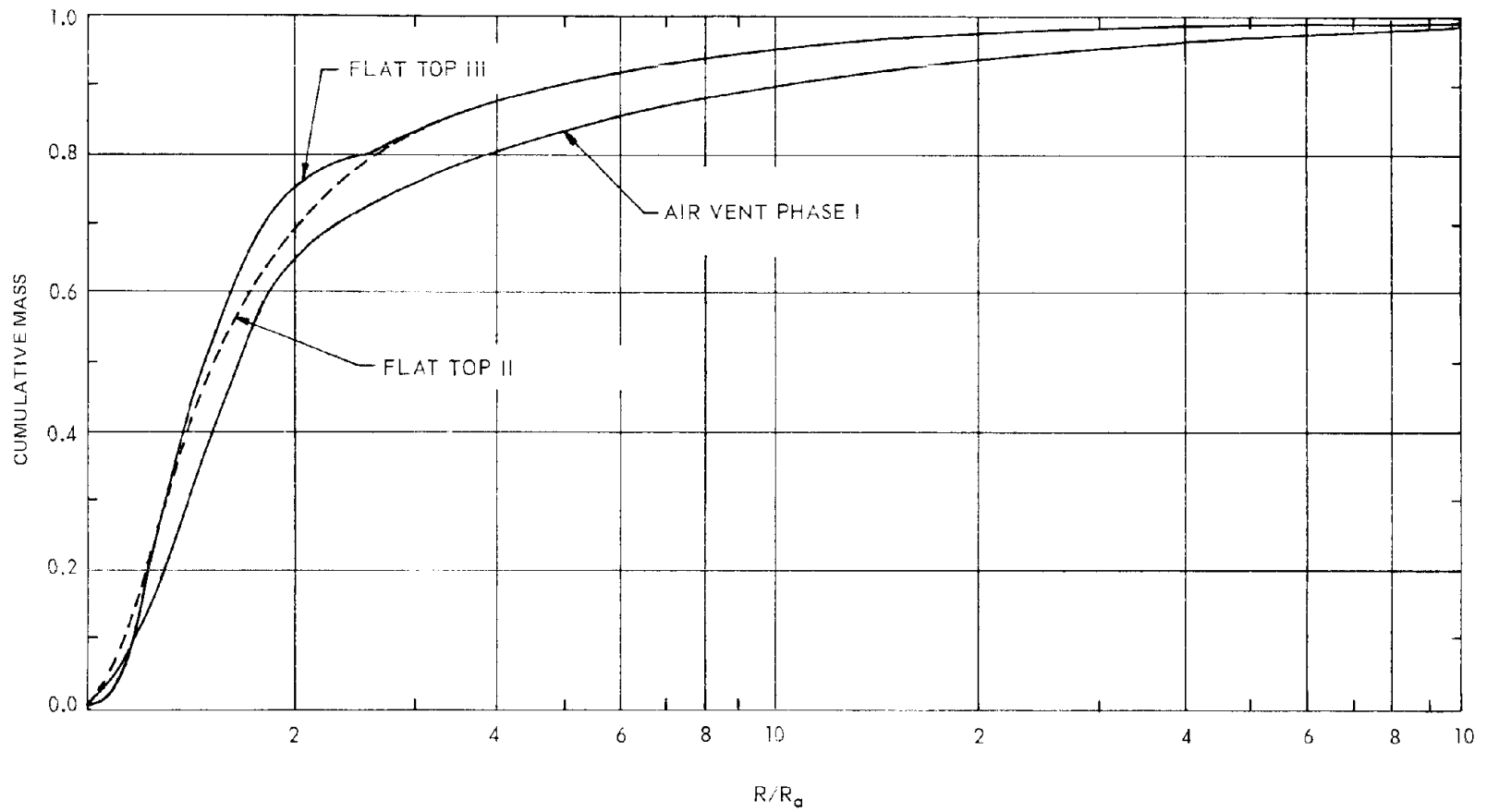
Figure IV-4.54. Scaled cumulative distribution of above-grade fallback and ejecta - AIR VENT and FLAT TOP (Reference IV-4.38).

within 2.0 crater radii on AIR VENT, the accumulation was 69 percent on FLAT TOP II and 75 percent on FLAT TOP III. The lower level of the AIR VENT cumulative distribution curve indicates that a substantially greater portion of the above-grade ejecta fell at greater scaled ground ranges. Coupled with the greater total volume of above-grade ejecta produced on AIR VENT the underground burst resulted in much more material distributed at far-out ground ranges.

IV-4.2.1.4. FLAT TOP I. The FLAT TOP I Event consisted of the detonation of 20 tons of TNT at the surface of a limestone outcrop at the NTS. The objectives of this test were to obtain information of: (1) ejecta areal density and thickness as a function of ground range, (2) the size distribution of ejecta particles, and (3) cratering and throwout mechanics from this explosion (Reference IV-4.39).

The crater configuration and ejecta distribution were strongly influenced by the site geology (Reference IV-4.39). The apparent crater was roughly elliptical with its major axis parallel to the strike of the outcrop and its minor axis perpendicular to that strike. The close-in ejecta were deposited in a rayed pattern, in addition to which six distinct rays were formed. It is possible that these rays were caused by secondary joint patterns. The rayed ejecta pattern is clearly visible on aerial photographs of the crater. The crater lip west of GZ was almost completely bare of ejecta.

Areal density as a function of distance from GZ was computed from determinations of ejecta thickness in the lip area. Figure IV-4.55 is a plot of the mean ejecta areal density as a function of distance from GZ based on a bulk density of 1.6 gm/cm^3. Ejecta mass through 30 meters from GZ was found to be 1.20×10^6 kg. This number includes a small adjustment for the uplift of a concrete pad used on an unrelated experiment as well as adjustment for the four uplift profiles. Integration of the area under the areal density versus distance curve of Figure IV-4.55 gave an ejecta mass of 1.03×10^6 kg through 30 meters from GZ. Ejecta mass from 30 to 160 meters was computed to be between 1.18×10^5 kg and 1.54×10^5 kg, depending on the analysis method used (Reference IV-4.39). Thus, calculations of ejecta mass through 160 meters give values ranging from about 1.14 to 1.35×10^6 kg, depending on the procedure used. With the ejecta sampling data that was available, it was not possible to compute the total ejecta mass with the accuracy hoped for when the project was planned.
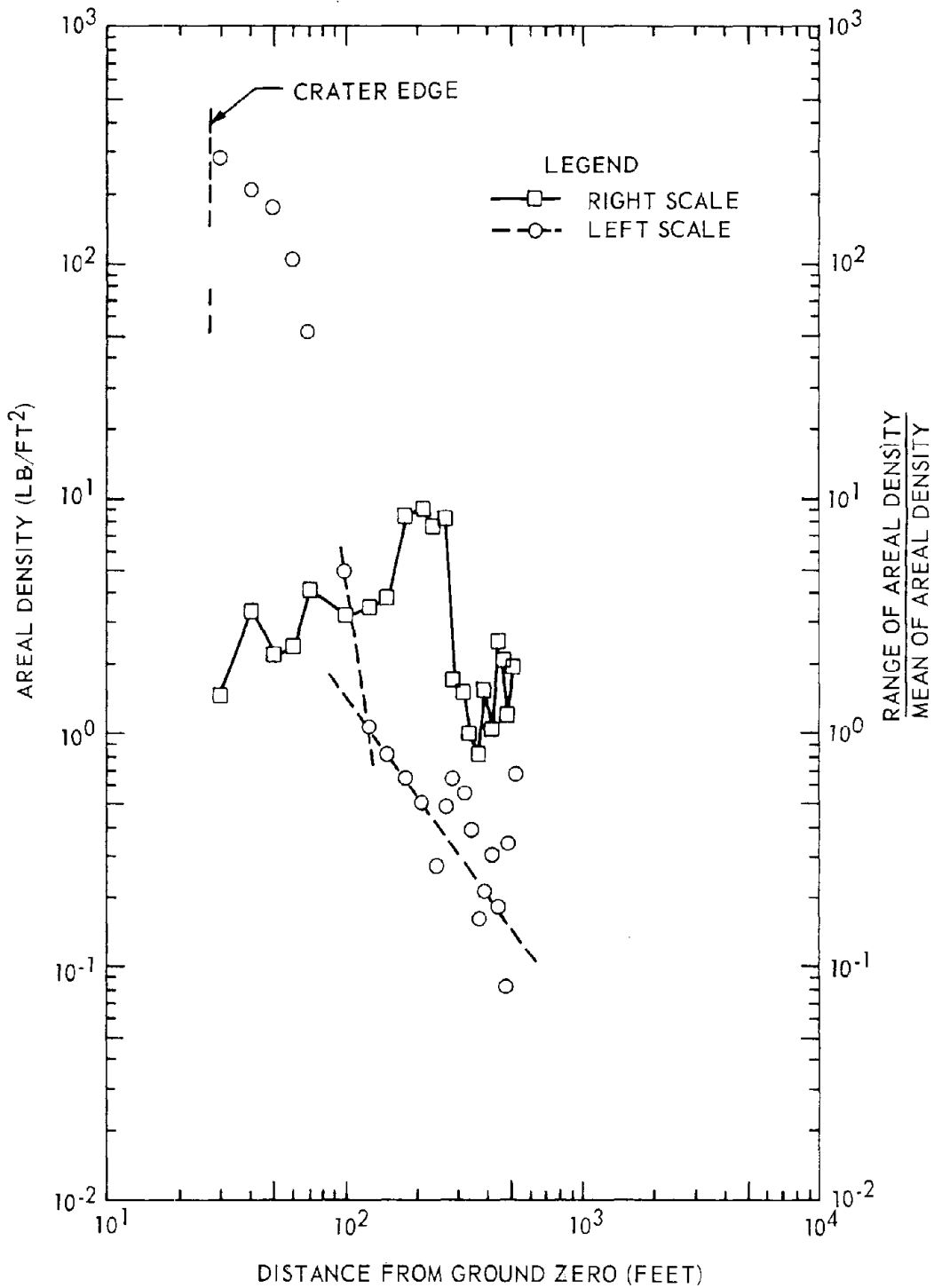
Figure IV-4.55. Ejecta areal density as a function of distance for FLAT TOP I (Reference IV-4.39).

The ratio of the range of areal density to mean areal density as a given radial distance is shown in Figure IV-4.55. This ratio, rather than the standard deviation, is given to emphasize that the distribution of areal density as a function of azimuth is unknown. The ratio of range to mean is seen to increase almost exponentially with distance from GZ through 80 meters, where the number of sampling stations per ring was decreased. The increase of sample scatter with distance was attributed to two factors. One factor was the increasing concentration with distance of ejecta mass in a relatively few large fragments. The likelihood of obtaining representative ejecta samples with a few small collector surfaces under these conditions was remote. An example illustrating this point was seen at the 80-meter sampling ring where over 80 percent of the mass collected from 10 pads was in a single fragment. The second factor concerned the concentration of the ejecta mass in rays. Intuition suggests that for a rayed deposition pattern the true probability density function for areal density at a given distance is at least bimodal. The sample array was inadequate to define differences in ejecta distribution as a function of azimuth. There was a complete hiatus in sampling of non-coded ejecta between 160 and 1130 meters.

The site geology caused differences in the size of lip ejecta. Large blocks of limestone parted along bedding planes, sliding up and away from GZ. Some blocks had dimensions of approximately 1.5 x 1.0 x 6.0 meters. It is a question of definition as to whether these upthrust blocks are ejecta or uplift. No fragments as large as the upthrust block of dimensions mentioned above were included in the ejecta along the western side of the crater. The beds dipped away from GZ in this direction, and large blocks separating along bedding planes tended to be displaced upward more or less as a unit. These blocks were defined as the uplift surface.

The largest ejecta fragment in the sector between 9 and 18 meters from GZ measured 1.2 x 0.7 x 0.6 meters, with an estimated weight of about 540 kg. The largest ejecta fragment between 18 and 27 meters from GZ measured 0.9 x 0.6 x 0.3 meter with an estimated weight of 330 kg.

Figure IV-4.56 shows the results of combining all the ejecta size data after weighting with respect to ejecta mass represented by each sample. The machine computation of ejecta mass using the areal density data plotted in Figure IV-4.55 was used in the weighting procedure. The hump in the size interval from 7.6 to 22 centimeters may be related to the spacing of fractures and bedding planes. From field observations it is likely that the hump would be more pronounced if the class intervals had been so chosen that one interval was intermediate between the
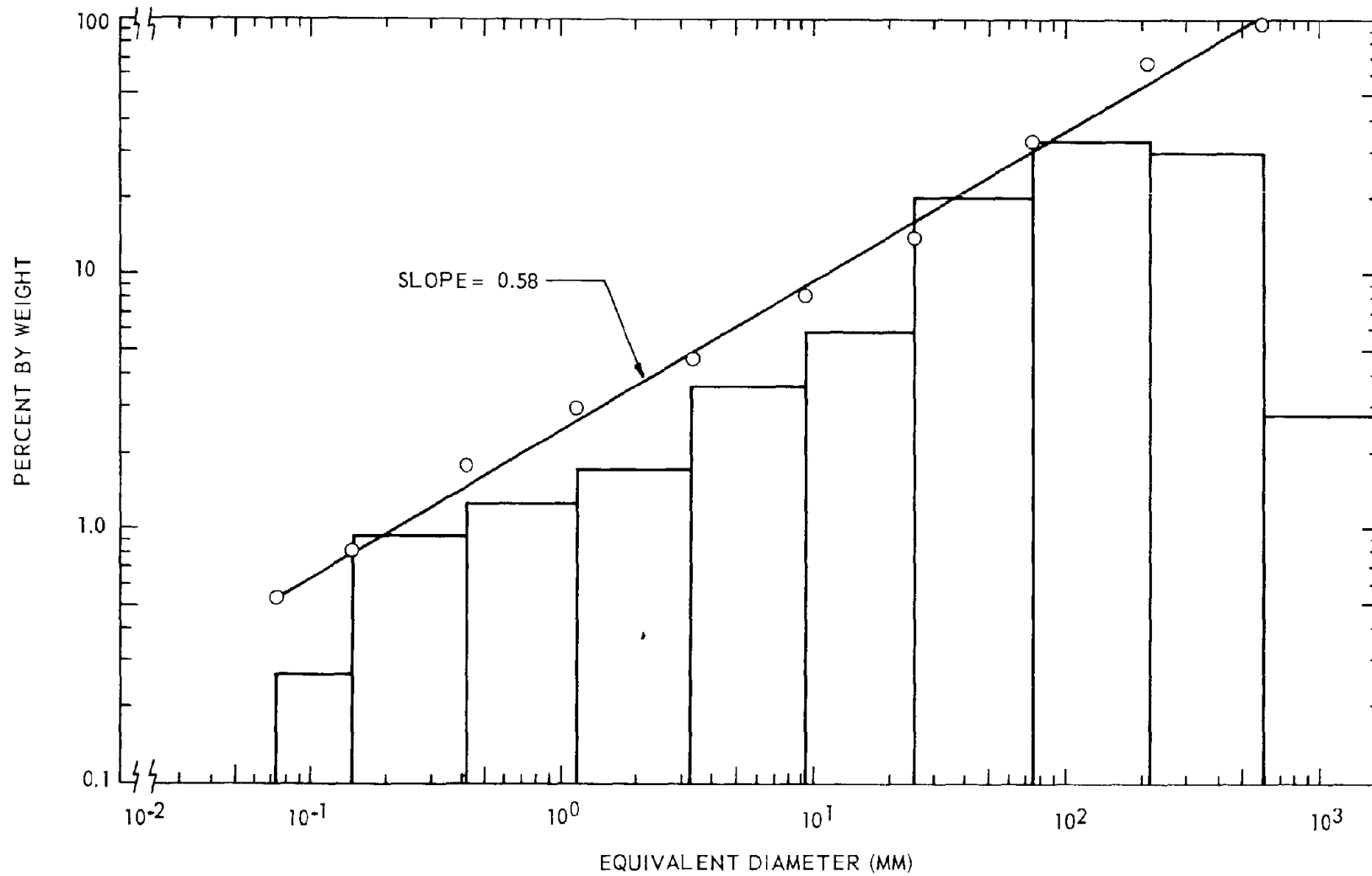
Figure IV-4.56. Size distribution of total ejecta through 160 meters (Reference IV-4.39).

7.6- to 22-centimeter and the 22- to 61-centimeter intervals. The relative proportions of intervals of fines were not accurately determined, but this had little effect on the proportions determined for the intervals of coarser material. The cumulative effect of all limitations of the size analysis resulted in an understatement of the true amount of comminution caused by the explosion.

No effort was made to collect data on noncoded ejecta distribution between 160 and 760 meters from GZ. Virtually all the ejecta found beyond 760 meters from GZ were in the form of shock comminuted but coherent masses of dust-size limestone particles. The massive fragments had considerable cohesive strength but were friable and could be powdered between the fingers. Figure IV-4.57 shows the distribution of missile impact points mapped by survey crews beyond 760 meters in the sector from S 12° E to S 72° E. When these data were plotted, it was thought unusual that the distribution of missiles was so uniform over the range of distances from GZ covered by the survey. Therefore, four areas, each covering about 2 acres, were selected for investigation. Two areas were chosen where impact points were relatively scarce and two where impact points were relatively concentrated. These areas are shown on Figure IV-4.57. From these data it appears that only about 50 to 75 percent of the impact points in areas of greatest concentration were mapped, whereas almost all of them were mapped in areas of low concentration. When the mapped frequency of impact points is corrected on the basis of these observations, a maximum concentration of three to four impact points per 930 m^2 is obtained for the sector from S 12° E to S 72° E beyond 760 meters from GZ. Little data could be collected on the size of impacting missiles in the far-out region because of the tendency for missiles to shatter on impact. The most spectacular impact point seen was to the northwest of GZ at an estimated distance of about 820 meters. This impacting missile fell on a limestone outcrop and splashed over and irregular, elongated area measuring about 38 meters by about 11 meters. The long axis of the splash paralleled the radial from GZ through the impact point. The impacting missile is estimated to have weighed at least a few hundred kilograms. The most distant missile in the southeast sector was found at a range of about 1240 meters horizontally from, and 100 meters vertically above, GZ. The largest fragment of this missile measured about 46 x 30 x 23 centimeters. The combined weight of all its fragments was estimated to be about 110 kilograms.

The cumulative frequencies of coded ejecta as a function of distance were found to be approximated by Gaussian distributions and Figure IV-4.58 shows probability plots of the cumulative frequency of the ejecta distributions.

N 12°W

N 72°W

2,500 FT (760 M)

AREAS CHECKED
AFTER MAPPING

○ FAR-OUT MISSILE

☐ ADDITIONAL MISSILES
FOUND

N

0   200   400   600

FEET

IV-4-103
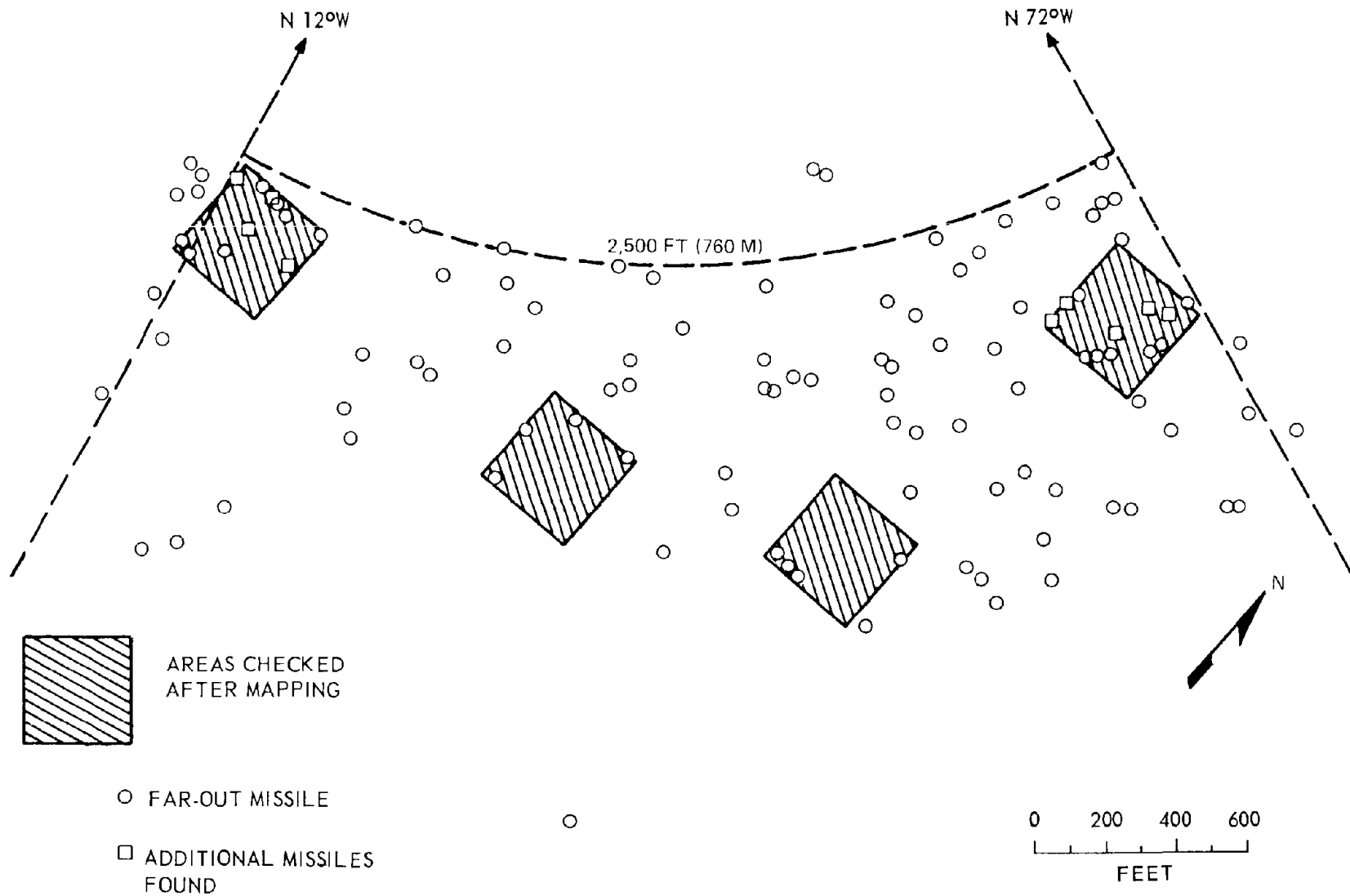
Figure IV-4.57.   Distribution of far-out missiles, FLAT TOP I   (Reference IV-4.39).
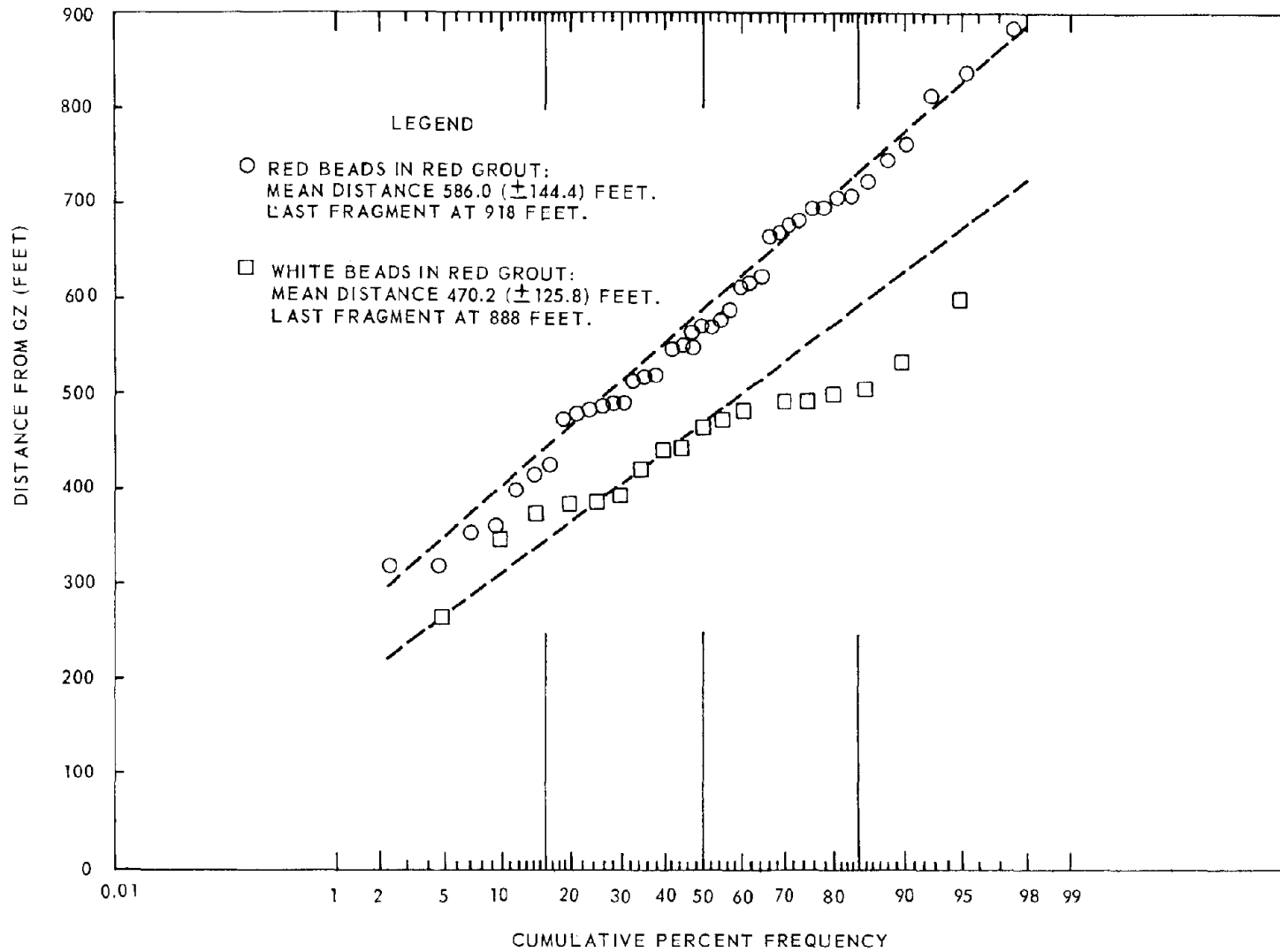
Figure IV-4.58. Cumulative frequency distribution of coded cylinder fragments (Reference IV-4.39).

Comparison with the straight lines representing Gaussian distributions having the sample means and standard distributions illustrates the goodness of fit. Both cylinders containing the coded ejecta from which these distributions of ejecta were found were emplaced 3.7 meters horizontally from the charge center. The upper distribution of fragments came from a cylinder emplaced with its center a vertical distance about 0.9 meter lower than the charge center. The lower distribution came from a cylinder with its center about 1.5 meters lower than the charge center. The general trend of ejecta distribution from individual cylinders was toward decreasing mean distance from GZ with increasing depth of emplacement.

IV-4.2.1.5 FLAT TOP II and III. The FLAT TOP II and III Events had identical yields (20 tons). Both were emplaced with their center of gravity coincident with the ground surface, with the charges being spherical in shape and emplaced in the playa alluvium of Frenchman Flat at the NTS. The charges were detonated approximately 300 meters from one another at approximately 4-week intervals. The differences in these two shots consisted mainly in the details of the preshot soil characteristics. Because of these slight differences but identical project objectives, these two events are discussed together. The overall objectives of these two events were to assist in the achievement of a fundamental understanding of the crater throwout problem by collecting and analyzing experimental data on initial and final positions of emplaced pellets. A second objective was to collect and analyze data on the distribution of natural ejecta material for use in empirical studies of ejecta distribution and its scaling. A detailed description of these objectives, of the studies of the behavior of discrete pellets, and of studies of the distribution of natural crater throwout material can be found in Reference IV-4.40. A brief description of some of the results obtained from these two events is as follows.

The true crater was divided into four basic zones according to the material response required to satisfy postshot pellet positions and sand-column measurements. These zones consisted of: (1) the ballistic zone, whose material was flung far from GZ and studied by trajectory analysis; (2) the scoured ejecta zone, determined from initial positions of pellets found buried in the apparent lip; (3) the scoured fallback zone, determined only partially from pellets recovered inside the crater; and (4) the zone of permanent displacement, determined from preshot and postshot positions of disks located in sand columns.

A detailed study of the volumes and masses of crater zones and corresponding measurements of fallback and ejecta is summarized in Tables IV-4.20 and IV-4.21. The ballistic and scoured ejecta zones were determined directly from final pellet positions. During analysis, abrupt changes in the progression of final ground range values among pellets placed along vertical and lateral lines were sought as a criterion for distinguishing between ballistic and scoured zone pellets. This was not markedly noticeable between the ballistic and scoured ejecta zones on FLAT TOP III where the isorange contours near the interface were observed to have similar directional patterns. Ballistic and scoured ejecta zones were determined directly from final pellet positions. The dissociated material was determined as the below-grade true crater volume minus the volume of permanent displacement, and was determined from postshot sand-column measurements. Therefore, the fallback zone is a residual rather than a directly measured volume, determined by subtracting the ballistic and scoured ejecta zones from the dissociated volume. Boundaries between these zones represent average or prevailing behavior rather than all-inclusive results. Local variations and anomalies were observed to occur within the limits of a single quadrant. Since apparent lip excavation was not performed on FLAT TOP II, the levels of nonrecovery of pellets emplaced in the crater zone became the lower limit of the ballistic zone and the scoured ejecta and scoured fallback zones were combined.

Approximate dimensions for the four crater zones compared with the AIR VENT I underground burst have already been shown in Table IV-4.19. Distribution of the dissociated mass among its constituent zones, compared with results from AIR VENT I, is shown in Table IV-4.22.

Noticeable different results were observed between FLAT TOP II and III. While the dissociated mass on FLAT TOP III was about twice that on FLAT TOP II, the ballistic zone mass was only one-half greater. No problem exists for pellets found considerably beyond the conventional lip, or buried deeply in the apparent lip. The mode of transport is uncertain for pellets lying on top or just under the apparent lip surface. The manner of collecting and preparing data in Reference IV-4.40 tended to overestimate the ballistic zone somewhat on AIR VENT I and FLAT TOP II and underestimate it on FLAT TOP III. If limitations on true crater measurements on FLAT TOP III resulted in a 20 percent overestimate of the dissociated volume, a corrected ballistic zone ratio would be 24.6 percent of the dissociated volume. On AIR VENT I, with a scaled DOB of 1/2, both the ballistic

Table IV-4.20. Mass distribution of crater, fallback, and ejecta zones, FLAT TOP II (Reference IV-4.40).

Regions	Volume (m^3)	Density (kg/m^3)	Mass $(kg \times 10^{-6})$	Percent of Dissociated Mass	Percent of Total Fallback and Ejecta Mass	Percent of True Crater Mass[a]	Percent of Apparent Crater Mass[a]
Apparent Crater, at Grade	650	1451	0.95	82.6	79.1	61.9	100.0
True Crater, at Grade	1050	1451	1.53	133.3	127.6	100.0	161.4
Apparent Crater, at True Lip Crest	740	1451	1.07	93.6	89.6	70.2	113.3
True Crater, at True Lip Crest	1150	1451	1.67	145.8	139.6	109.4	176.6
Below-Grade Volume of Charge	7.4	1451	-	-	-	-	-
Ballistic Zone[d]	230	1451	0.33	29.1	27.8	21.8	35.2
Scoured Ejecta Zone[d] Scoured Fallback Zone[d]	560	1451	0.81	70.9	67.9	53.2	85.9
Dissociated Volume[d]	790	1451	1.15	100.0	95.7	75.0	121.1
Below-Grade Permanent Deformation	265	1451	0.38	33.4	31.9	25.0	40.4
Pre-Crest True Lip[b]	2.2	1485	0.0032	0.3	0.3	0.21	0.34
Post-Crest True Lip[b]	173	1485	0.26	22.3	21.4	16.8	27.0
Total True Lip	175	1485	0.26	22.6	21.6	17.0	27.4
Net Permanent Deformation	89	-	0.12	10.8	10.3	8.1	13.0

CRATER AND LIP REGIONS

Table IV-4.20. (continued).

Regions	Volume (m^3)	Density (kg/m^3)	Mass $(kg \times 10^{-6})$	Percent of Disso-ciated Mass	Percent of Total Fallback and Ejecta Mass	Percent of True Crater Mass[a]	Percent of Apparent Crater Mass[a]
Below-Grade Fallback	399	1216	0.49	42.3	40.5	31.7	51.2
Above-Grade Fallback	12	1216	0.014	1.2	1.2	0.92	1.5
Total Fallback	410	1216	0.50	43.5	41.7	32.7	52.7
Pre-Crest Above-Grade Ejecta[b]	63	1216	0.077	6.7	6.4	5.0	8.1
Post-Crest Ejecta[b]	540	1181	0.64	55.5	53.1	41.6	67.1
Total Above-Grade Ejecta	602	-	0.71	62.1	59.5	46.6	75.2
Pre-Crest Ejecta Above True Lip	51	1216	0.063	5.5	5.2	4.1	6.6
Total Ejecta	1160	-	0.79	60.9	58.3	45.7	73.8
Conventional Lip[c]	630	-	0.80	69.4	66.4	52.0	84.0
Above-Grade Ejecta in Conventional Lip[c]	454	1181	0.54	46.7	44.7	35.1	56.6
Total Fallback and Ejecta		-	1.20	104.5	100.0	78.3	126.5

EJECTA REGIONS

[a]Percentage of Below-Grade Crater Volumes

[b]True Lip Crests

[c]True Lip Plus Above-Grade Ejecta to Two Apparent Crater Radii

[d]Does Not Include Below-Grade Volume of Charge

Table IV-4.21. Mass distribution of crater, fallback, and ejecta zones, FLAT TOP III (Reference IV-4.40).

Regions	Volume (m³)	Density (kg/m³)	Mass (kg x 10⁻⁶)	Percent of Disso-ciated Mass	Percent of Total Fallback and Ejecta Mass	Percent of True Crater Mass[a]	Percent of Apparent Crater Mass[a]
Apparent Crater, at Grade	1093	1608	1.76	69.5	96.4	57.6	100.0
True Crater at Grade	1898	1608	3.05	120.7	167.4	100.0	173.6
Apparent Crater, at True Lip Crest	1314	1608	2.11	83.6	115.9	69.2	120.2
True Crater, at True Lip Crest	1884	1608	3.03	119.9	166.2	99.3	172.3
Volume of Charge	7.4	1608	-	-	-	-	-
Ballistic Zone[d]	310	1608	0.498	19.7	27.3	16.3	28.3
Scoured Ejecta Zone[d]	426	1608	0.685	27.1	37.6	22.5	39.0
Scoured Fallback Zone[d]	836	1608	1.345	53.2	73.8	44.1	76.5
Dissociated Volume[d]	1572	1608	2.528	100.0	138.7	82.8	143.8
Below-Grade Permanent Deformation	319	1608	0.513	20.3	28.1	16.8	29.2
Pre-Crest True Lip[b]	10.1	1584	0.016	0.6	0.9	0.5	0.9
Post-Crest True Lip[b]	164	1584	0.260	10.3	14.2	8.5	14.8
Total True Lip	174	1584	0.276	10.9	15.1	9.0	15.7
Net Permanent Deformation	145	-	0.237	9.4	13.0	7.8	13.5

CRATER AND LIP REGIONS

Table IV-4.21. (continued).

	Regions	Volume (m^3)	Density (kg/m^3)	Mass $(kg \times 10^{-6})$	Percent of Disso- ciated Mass	Percent of Total Fallback and Ejecta Mass	Percent of True Crater Mass[a]	Percent of Apparent Crater Mass[a]
EJECTA REGIONS	Below-Grade Fallback	793	1216	0.964	38.1	52.9	31.6	54.8
	Above-Grade Fallback	59	1216	0.072	2.9	3.9	2.4	4.1
	Total Fallback	852	1216	1.036	41.0	56.8	33.9	58.9
	Pre-Crest Above-Grade Ejecta[b]	86	1216	0.104	4.1	5.7	3.4	5.9
	Post-Crest Ejecta[b]	640	1181	0.755	29.9	41.4	24.7	42.9
	Total Above-Grade Ejecta	725	-	0.859	34.0	47.1	28.1	48.9
	Pre-Crest Ejecta Above True Lip	26	1216	0.032	1.3	1.8	1.1	1.8
	Total Ejecta	666	-	0.787	31.1	43.2	25.8	44.8
	Conventional Lip[c]	676	-	0.869	34.4	47.7	28.5	49.4
	Above-Grade Ejecta in Conven- tional Lip	503	1181	0.593	23.5	32.6	19.4	33.7
	Total Fallback and Ejecta	1518	-	1.823	72.1	100.0	59.7	103.7

[a]Percentage of Below-Grade Crater Volumes

[b]True Lip Crests

[c]True Lip Plus Above-Grade Ejecta to Two Apparent Crater Radii

[d]Does Not Include Below-Grade Volume of Charge

Table IV-4.22. Dissociated mass comparison.

	Percent of Dissociated Mass		
	AIR VENT I	FLAT TOP II	FLAT TOP III
Ballistic Zone	27.8	29.1	19.7
Scoured Ejecta Zone	39.3	70.9	27.1
Scoured Fallback Zone	32.9	70.9	53.2

and scoured ejecta zones were about twice those of the FLAT TOP III surface event, and the ballistic zone was three times that of the FLAT TOP II surface event. In all cases, the mass of the ballistic zone was under 30 percent of the dissociated mass.

Throwout distances are based on behavior of 3.8-centimeter diameter phenolic spheres with polished surfaces. The distances these spheres were thrown do not necessarily coincide with distances to which soil particles from these regions were thrown, since the drag forces are different. Analysis of the data showed that the far-flung pellets originated in a relatively shallow near-surface region. This region extended to a depth of about 30 to 40 percent of maximum ballistic zone depth and to a maximum radius at the ground surface equivalent to about 65 percent of the maximum ballistic zone radius. The region is sufficiently pronounced on FLAT TOP II to imply the existence of two ballistic zones originating in a different phenomenological setting and at a different time period. Although the overall crater dimensions differ markedly between the two events, decided dimensional similarities exist between these high-range ballistic regions as shown in Table IV-4.23.

Recovery data on emplaced pellets have been used to derive an initial velocity field for the ballistic zone according to the methods described in Reference IV-4.40. Computed initial velocities are plotted for the various pellet placement levels in Figures IV-4.59 and IV-4.60 for FLAT TOP II and III. Initial velocity curves for the various pellet levels are ordered approximately according to pellet burial depths in both events, although local departures from this trend are apparent. On FLAT TOP II, pronounced vertical separation exists between initial velocity curves for the top half-meter of the ballistic zone and curves for the
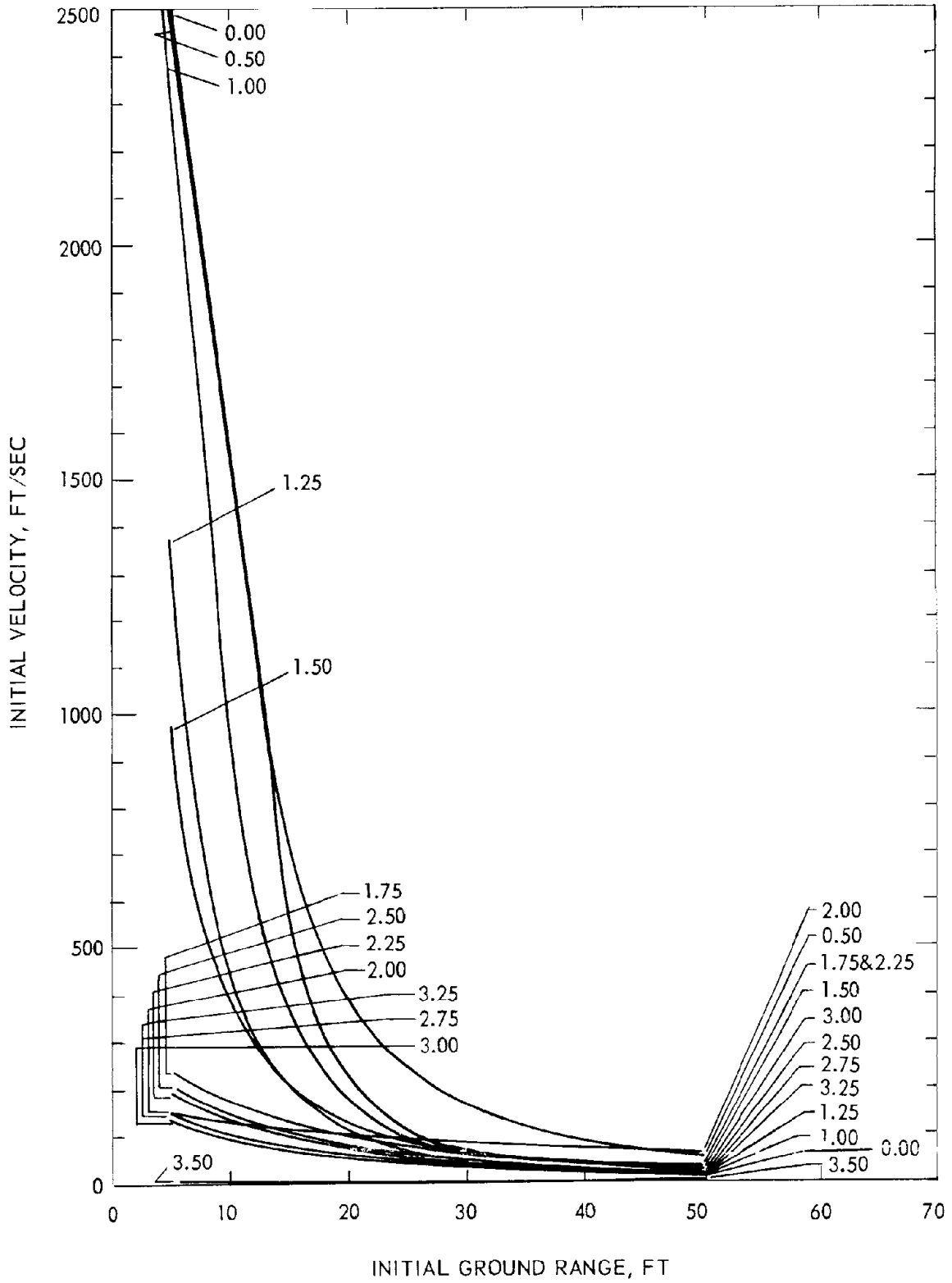
Figure IV-4.59. Computed values of pellet initial velocities, FLAT TOP II (Reference IV-4.40).
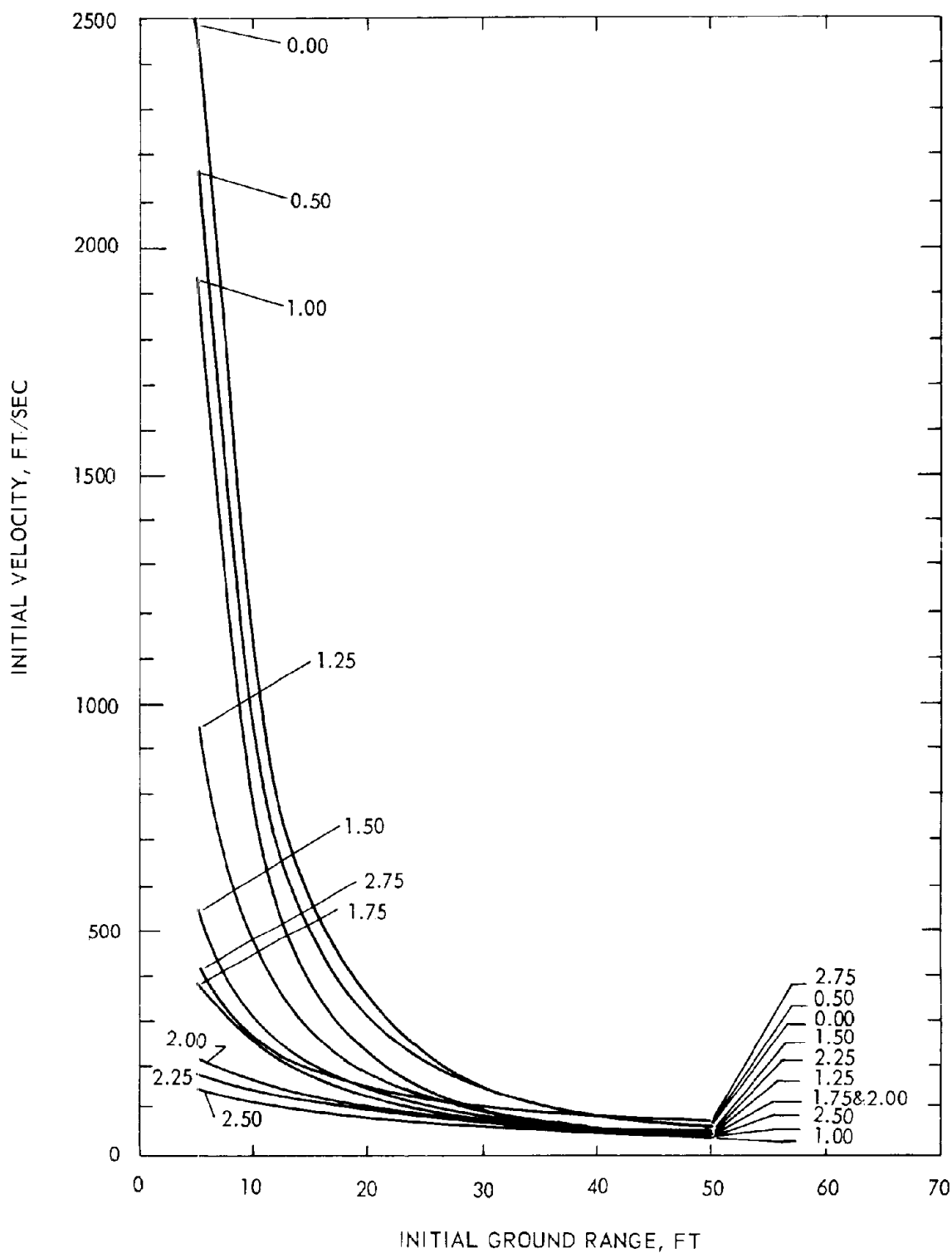
Figure IV-4.60. Computed values of pellet initial velocities,
FLAT TOP III (Reference IV-4.40).

Table IV-4.23. Similarity in range of throwout.

Throwout Distance Region (m)	Maximum Depth (m)		Maximum Radius (m)	
	FLAT TOP II	FLAT TOP III	FLAT TOP II	FLAT TOP III
Over 427	0.3	0.2	2.9	3.1
366 - 427	0.4	0.3	3.3	3.2
305 - 366	0.5	0.4	3.8	3.4
244 - 305	0.5	0.5	4.2	3.7
183 - 244	0.5	0.5	4.9	4.8
122 - 183*	0.5	0.7	6.9	6.6

*The high-range ballistic region is assumed to end at the 122-meter terminal ground range contour.

lower levels. This implies either the existence of a high-velocity region of limited depth and radial extent, from which ejecta must arise to be capable of traveling to very long ground ranges. This high-velocity region corresponds to the shallow close-in region of pellets found at far-out ground ranges. Slopes of the initial velocity curves also show a pronounced radial attenuation of this high-velocity field. Comparable behavior, though less pronounced, was observed on FLAT TOP III. Fields of initial velocity magnitudes within the ballistic zones are plotted in Figures IV-4.61 and IV-4.62 for FLAT TOP II and FLAT TOP III, respectively, showing initial velocity regions oriented roughly in the fashion of the final ground-range regions of the ballistic zones.

The depth and the areal density of ejecta for various levels of ejecta are plotted in Figures IV-4.63 and IV-4.64 for the region within about 10 apparent crater radii. The high and low limits represent circumferential variations in depth and areal density to be expected as a result of ray-like behavior at the closer ground ranges and from atmospheric wind effects in the far-out region. These curves are based on quadratic expressions to represent the crater lip to about 2 crater radii and power-law fits to ejecta measurements beyond this region.

The computer mass distributions of ejecta for FLAT TOP II and III are given in Table IV-4.24. A comparison of the cumulative distribution of total fallback and ejecta for AIR VENT I and FLAT TOP II and III is given in Table IV-4.25.

INITIAL GROUND RANGE, FT
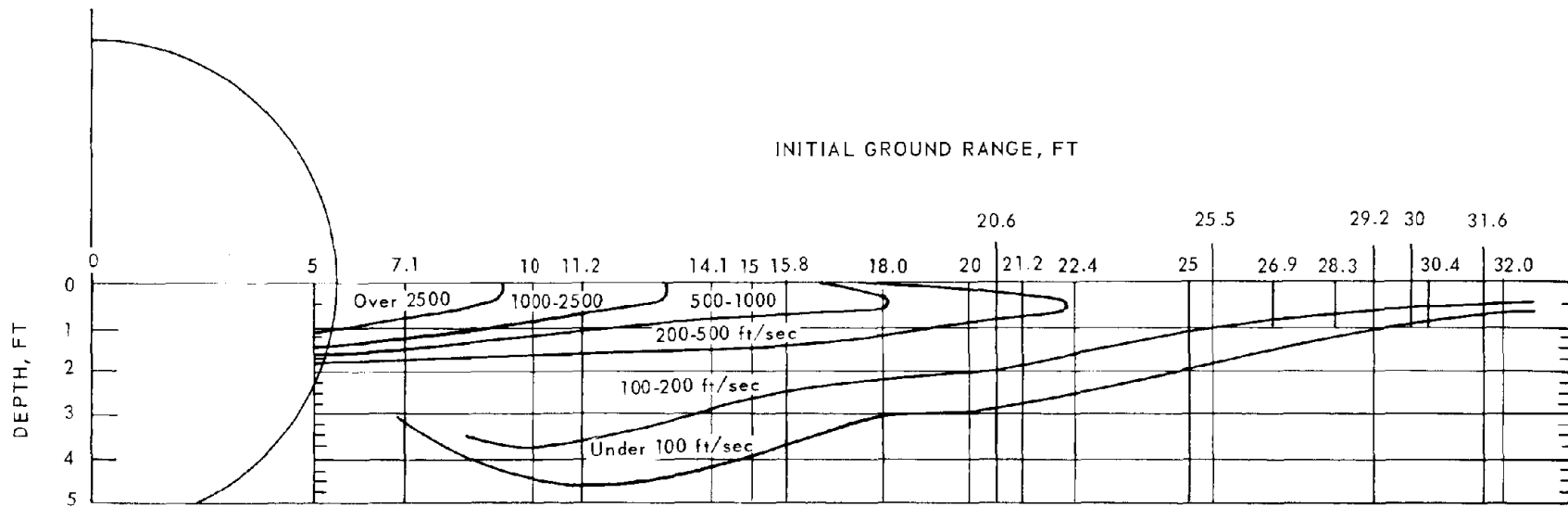
Figure IV-4.61.   Initial velocities in the ballistic zone, FLAT TOP II (Reference IV-4.40).

INITIAL GROUND RANGE, FT
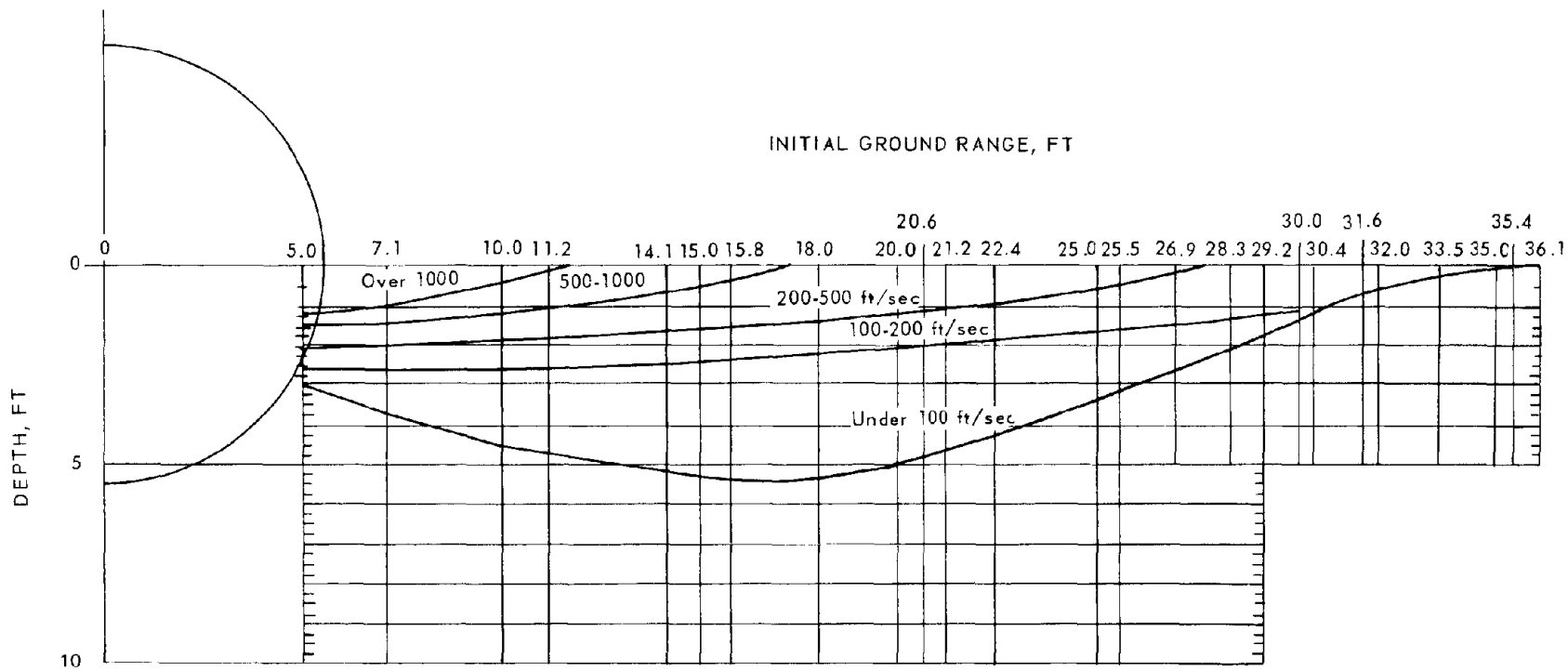
Figure IV-4.62. Velocity magnitudes in ballistic zone, FLAT TOP III (Reference IV-4.40).
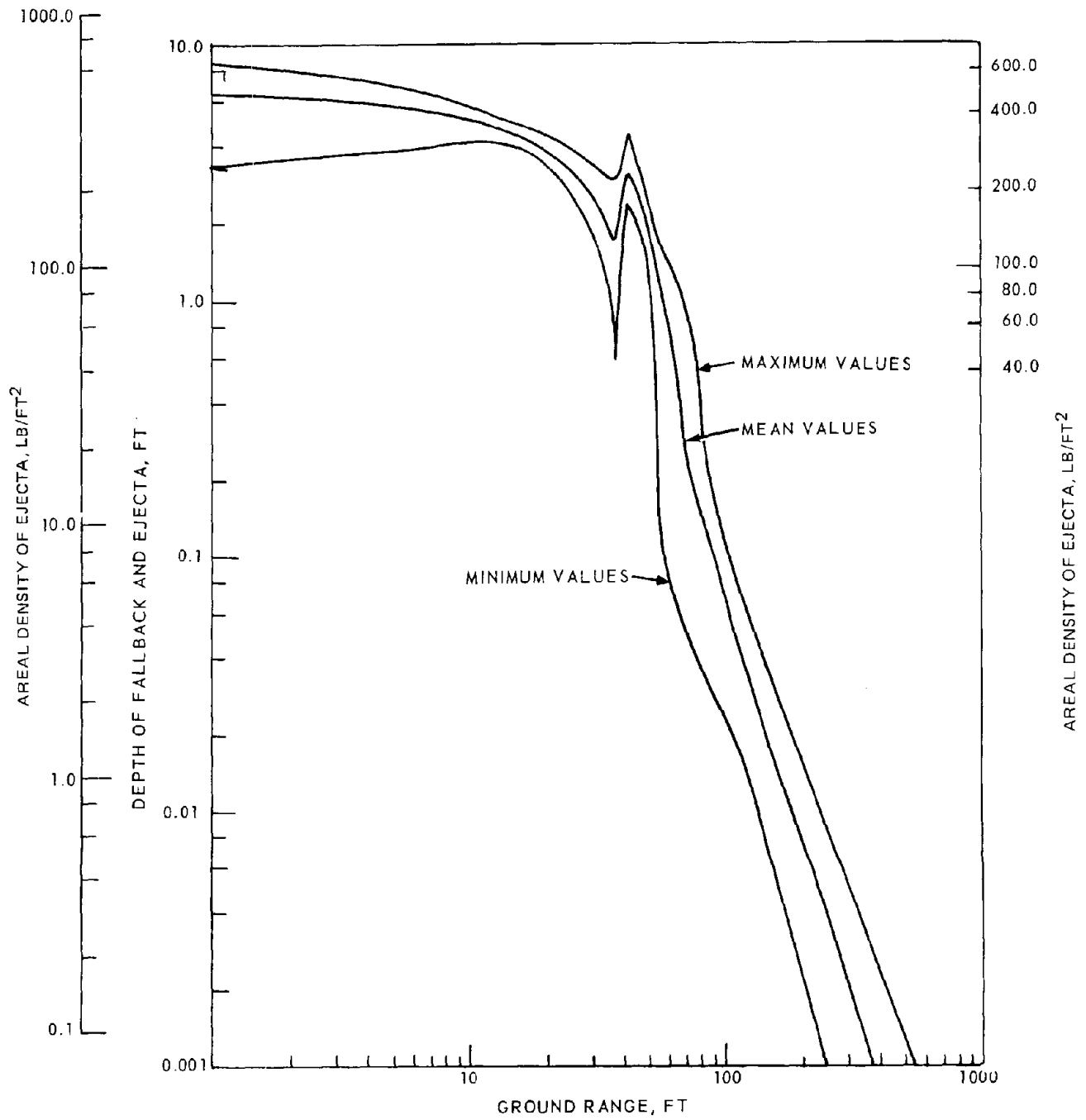
Figure IV-4.63. Depth and areal density of fallback and ejecta, FLAT TOP II. (Depths are based on quadratic expressions for apparent lip.) (Reference IV-4.40).
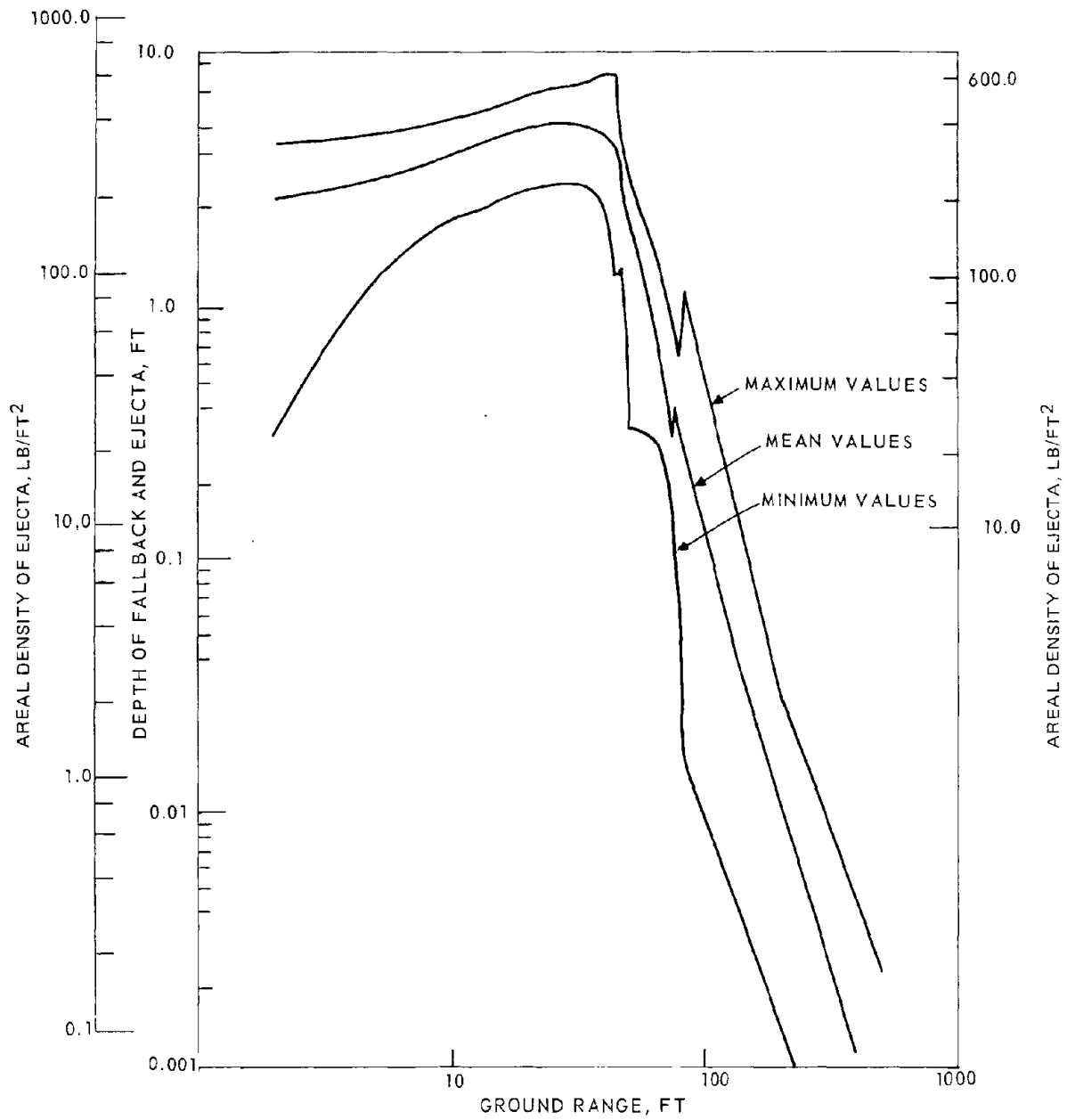
Figure IV-4.64. Depth and areal density of fallback and ejecta, FLAT TOP III. (Depths are based on quadratic expressions for apparent lip.) (Reference IV-4.40).

Table IV-4.24. Distribution of ejecta masses.

	FLAT TOP II		FLAT TOP III	
	Mass (kg)	Percent of Total	Mass (kg)	Percent of Total
Total Fallback	499,420	41.7	696,160	56.8
Total Ejecta	698,550	58.3	528,830	43.2
Below-Grade Fallback	326,140	40.5	647,700	52.9
Above-Grade Ejecta and Fallback	478,840	59.5	577,290	47.1

Table IV-4.25. Fallback and ejecta distribution comparisons.

Percent of Total Fallback Ejecta	Ground Range Intervals		
	FLAT TOP II	FLAT TOP III	AIR VENT I
20	Beyond 1.75 R_a*	Beyond 1.7 R_a	Beyond 2.0 R_a
14	Beyond 2.0 R_a	Beyond 2.0 R_a	
10	Beyond 3.0 R_a	Beyond 2.5 R_a	Beyond 4.4 R_a
5	Beyond 5.7 R_a	Beyond 4.5 R_a	Beyond 12.0 R_a
*R_a is the apparent crater radius measured at the preshot ground surface.			

Variations occurring in particle-size distribution in the ejecta with increasing ground range have been extensively discussed in Reference IV-4.40 and are discussed briefly here. Although precise measurements of the distribution of particulate fractions were not a primary objective of the FLAT TOP II and III program, the results are quite erratic, exhibiting nonmonotonic behavior, lack of regular ordering of curves, and frequent crossing-over between curves. Some irregularities in behavior are probably due to local wind effects prevailing at the time of tests, which were not of constant velocity and direction for the

duration of the fallback process. Variations in local effects at collector stations can exist that tend to increase or reduce the sample collection and this can even have a selective effect on various particulate distribution fractions. However, on AIR VENT I, where a dead calm atmospheric condition prevailed, a high degree of consistency in fractional deposition was found among sampling lines at 90-degree intervals.

IV-4.2.1.6 MIDDLE GUST. MIDDLE GUST was a series of HE detonations designed to provide free-field ground motion, cratering, and structure-medium interaction data for surface and near-surface explosions. This series consisted of five main events and fourteen 1000-pound calibration shots. These events were carried out in southeastern Colorado. The main events consisted of two 20-ton surface bursts, where the charge center was coincident with the ground surface; two 100-ton above-surface-tangent bursts, (the HOB was equal to one charge radius); and one 100-ton airburst with the HOB equal to two charge radii. Each charge of the main event series consisted of TNT blocks stacked into a spherical configuration (Reference IV-4.41).

The MIDDLE GUST Series charges were fired over a layered medium consisting of clay over shale. Two sites that differed only in their water table were chosen for these events. Site I, called the "wet" site, had a 3-meter overburden of sandy clay over weathered clay shale. The weathered shale/competent shale interface was approximately 5.5 meters below ground surface. A perched water table on top of the impervious competent shale extended upwards of about 1.2 meters below the ground surface. Site II, called the "dry" site, had no appreciable water table. It had a 0.9- to 1.2-meter clay overburden over weathered shale. At Site I, one surface burst, one above-surface-tangent burst, and the airburst were fired. The remaining surface burst and above-surface-tangent burst were fired at Site II.

This series had many projects that are outlined in the test plan and prediction report (Reference IV-4.42). The projects of interest here were the crater and ejecta studies under Program 4: Crater Investigations, Dynamic Ejecta Investigations, Photogrammetric Studies, and Technical Photography. The Crater/Ejecta Study objectives were, in part (Reference IV-4.41), to determine: (1) ejecta origins from the crater region, (2) the extent and depth of the continuous ejecta in the crater lip, (3) the distribution of the debris field and the hazardous range for the missile ejecta beyond the continuous ejecta boundary, and (4) photographically determine the terminal trajectory of natural missiles. Table IV-4.26 lists the apparent and true crater dimensions for the series.

Table IV-4.26. Apparent and true crater dimensions,
MIDDLE GUST Series.

Event No.	Charge		Average Radius (m)	Depth		Volume (m³)
	Weight (tons*)	Geometry		GZ (m)	Maximum (m)	
Apparent Crater						
I	20	S[a]	15.0	4.2	5.1	1943
II	100	A[b]	13.2	3.7	4.6	1407
III	100	ST[c]	15.8	6.6	7.3	2650
IV	100	ST	13.2	4.2	4.4	1235
V	20	S	10.4	3.7	4.0	603
True Crater						
I	20	S	15.7	4.6	5.3	2347
II	100	A	15.3	4.4	4.7	1702
III	100	ST	17.6	6.7	7.3	3455
IV	100	ST	13.9	5.4	5.5	1608
V	20	S	12.4	4.0	4.3	946

*Long tons
[a]Surface burst
[b]Airburst
[c]Above-surface-tangent burst

In MIDDLE GUST I, a 20-ton event, the continuous ejecta extended to distances between 55 and 110 meters from GZ. The maximum missile range was 730 meters to the southeast. This furthest missile was actually a concrete airblast gauge base originally located at ground surface 6.1 meters from GZ. The maximum range for a natural missile was 670 meters. Most of the natural ejecta for this event, and for the other events at Site I were cohesive particles of the clay overburden material. Very little shale was ejected out of the crater and the shale particles that were found were quite small. Missiles with linear dimensions slightly over 0.6 meter were found in the missile ejecta. Evidence of particle spray around impact craters indicated many clay missiles were much larger than this prior to impact. The artificial missile experiment was quite successful, with about 70 percent of the cylinders recovered in the debris field or still in place in columns where they served as permanent displacement markers. The maximum range for an artificial

missile was 392 meters to the southwest. The results showed ejecta origins giving maximum ranges originating from near ground surface to about 2 charge radii from GZ.

The continuous ejecta of the 100-ton MIDDLE GUST II Event extended to an average of about 76 meters from GZ. The missile ejecta field was much sparser than that of MIDDLE GUST I with a maximum missile range of only about 305 meters.

For the MIDDLE GUST III Event, a 100-ton event, the continuous ejecta extended to an average of 76 meters from GZ. Maximum natural missile range was 550 meters. About 50 percent of the artificial missiles were recovered, with a maximum range of 210 meters to the south.

For MIDDLE GUST IV, a 100-ton event, the continuous ejecta extended to an average of 85 meters from GZ. The maximum range of natural missiles was 670 meters to the northeast. Approximately 63 percent of the artificial missiles were recovered and a maximum range of 290 meters was observed.

Finally, on MIDDLE GUST V, a 20-ton event, the continuous ejecta extended to a range between 61 and 85 meters from GZ. The maximum range of natural missiles was about 550 meters. As with MIDDLE GUST IV, the ejecta was primarily from the over-burden. Approximately 60 percent of the artificial missiles were recovered, exhibiting a maximum range of 310 meters. The ejecta origin and range relationships observed were nearly identical to MIDDLE GUST I. Ejecta from MIDDLE GUST IV and V were characterized primarily by clumps of clay overburden and heavily weathered shale in the debris field beyond the lip crest. The small quantity of shale that was ejected outside the crater was in the form of small, thin flakes. The above data are summarized in Table IV-4.27.

Meyer (Reference IV-4.43) made the observation that it was on MIDDLE GUST V that the photographic experiment to determine terminal ejecta parameters was successful. A high-speed camera located about 180 meters from GZ photographed a sample of impacting missiles. While analysis of the film was not completed at the time of the MIXED COMPANY/MIDDLE GUST Results Meeting (Reference IV-4.41), obser-vations showed steep impact angles of about 60 to 80 degrees, with impact velocities estimated to be on the order of 60 m/sec. The complete ejecta data analysis is only now being released (Reference IV-4.43). Meyer concluded that the ejecta fields for all events were found to be similar to what might be expected from detonations in clay. The above-surface-tangent bursts gave ejecta fields similar to that observed on Event DIAL PACK. Maximum missile ranges were less than expected, but

Table IV-4.27. MIDDLE GUST Series ejecta characteristics.

Event Number	Yield (tons)	Continuous Ejecta Range (m)	Maximum Range of Artificial Ejecta (m)	Maximum Range of Natural Ejecta (m)
I	20	55-110	392	670
II	100	76		305
III	100	76	210	550
IV	100	85	290	670
V	20	61-85	310	550

this is probably due to the nature of the medium, which gave poor ballistic performance. Missiles of large size were produced, but there was a strong tendency for them to break up upon impact.

Wisotski (Reference IV-4.41) presented early results of dynamic ejecta behavior obtained with photographic data. The main objectives of this project were to record and analyze the dynamic ejecta phenomena from the main and calibration events of the MIDDLE GUST Series. A secondary objective was to record and analyze the early- and late-time detonation phenomena which included fireball and shockwave expansion, and cloud formation and rise. Only the dynamic ejecta information was presented in Reference IV-4.41. Dynamic ejecta information from HE detonations prior to the MINE SHAFT Series (References IV-4.44 and IV-4.45) was practically non-existent. The data obtained on the MINE SHAFT Series were limited to 2.2 seconds of recording time. Later, 29 separate events ranging in yield from 1000 pounds to 500 tons were photographed for durations of at least 25 seconds.

The most important parameters derived from the position-time data were the terminal impact velocity, angle, and distance and the initial crater escape velocity, angle, and origin. Of these two groups, less credence must be given to the escape parameters since their values are derived from position-time data relatively far removed from the point at which the escape parameters are determined. Also, certain assumptions were made for the in-flight ejecta when it was within the fireball. These assumptions were that each missile origin was at the ground surface, that each attained its maximum initial velocity at the same point, and that the decay

in the velocity of each missile was maintained throughout the turbulence of the fireball and the upheaval of crater material. These assumptions were made because there was no information on the manner in which the material around GZ erupted during the formation of the crater. Undoubtedly, there was some position-time value related to the acceleration phase reached by the particle when it attained its maximum escape velocity. Since it is not known what this value was because of the visual obstruction by the fireball, it was perceived that a position-time value at the ground surface was as valid as one assumed at a position above or below the ground surface. The results and discussion in Wisotski's preliminary report (Reference IV-4.41) cover the general procedures used to reduce part of the position-time data obtained from MIDDLE GUST Event I. It also includes some comparisons between MIDDLE GUST Events I and II obtained after a cursory analysis of the raw data. The MIDDLE GUST II data indicated asymmetrical throwout of the ejecta. This may have been due in part to the platform which held the charge above GZ.

Considering the amount of photographic data obtained from the MIDDLE GUST main and calibration events, the project effort was considered a success. Recently Linnerud (Reference IV-4.46) made an analysis of the in-flight ejecta data for MIDDLE GUST III. He presented bounding measurements of ejecta velocities, spire velocities, and ejecta area and diameter correlations. Both the bracketing observations and the detailed measurements reported should prove useful to the theoretician and modeler attempting to understand the energetics of these detonations. The results of this study are summarized as follows.

The MIDDLE GUST III spires were observed to emanate from the detonation point at an angle of some 45 degrees from the horizontal. Their velocities were observed to be some 120 to 180 m/sec. This velocity is fairly constant over the observation period. The spires were observed to be composed of small particles (maximum size 3 to 5 cm^2), with images just below the finite resolution limit of the camera/film system.

The horizontal component of ejecta velocities never exceeded approximately 60 m/sec. A good overall maximum horizontal velocity component was probably more like 30 m/sec. This in turn, assuming reasonable ejection angles, implies that ejecta velocities probably never exceeded about 90 to 120 m/sec.

It became obvious from a review of the films that recorded ejecta cover a wide range of shape factors --from nearly circular to extremely elongated. However,

measurements made by Linnerud would indicate that, as an overall representation, ejecta can probably be reasonably well approximated as spherical masses.

Measurements made do not support the currently used $a^{-3.5}$ power law for ejecta size distributions. However, it would not be appropriate at the present time to drop this size description in favor of another. More data from other detonation geometries and geological conditions should be obtained to help understand why this power law was not appropriate for MIDDLE GUST III. In-flight distribution of ejecta size is not expected to be the same as that for all particles as ejected because fallout differentiates the sizes thereby affecting the original size distribution.

IV-4.2.1.7 MIXED COMPANY. Operation MIXED COMPANY is the name given to the third 500-ton blast and shock experiment in the MIDDLE NORTH Series. The series was begun in Canada at the Defence Research Establishment Suffield (DRES) with the PRAIRIE FLAT Event in 1968 and continued in 1970 with the DIAL PACK Event. The 500-ton MIXED COMPANY III Event consisted of TNT charges arranged in a surface-tangent burst geometry on an alluvial soil over sandstone. Among the test objectives, ejecta deposition characteristics, maximum missile ranges, and debris translation experiments were carried out.

Tests have been conducted in the past on layered geologic systems. However, most of these were small-scale tests using concrete as the underlying layer and sand as the overburden. The surface or surface tangent geometries were not studied as extensively as those with the charge in contact with the underlying layer (References IV-4.46 and IV-4.47). The small scale also affects the reproducibility of shearing resistance at the interface. In addition, in other tests that were supposedly conducted on layered media, the layer was at a depth well below the crater depth. Therefore, the crater was almost unaffected by the layer. Thus, the MIXED COMPANY III shot conditions were untested previously. A rock interface can cause a blast to form a shallower and/or wider crater than will be formed in a homogeneous material. Shearing at the interface can cause large permanent differential displacements between the soil and the rock. A soil/rock interface can cause the maximum ejecta range to be decreased, and it can affect the type of material distributed in the lip and fallback zone. Ejecta missiles of the longest range normally originate near the surface at a distance from the charge of about one-half the apparent crater radius. Ejected pieces of soil that tend to break up in flight do not travel as far as identically shaped pieces of rock. Thus, a blast in or on a soil over a rock medium would have a maximum ejecta range about equal to

that of an equivalent blast in a similar homogeneous soil and pieces of underlying rock would be scattered throughout the area. On the other hand, an equivalent blast in a similar homogeneous rock would have a similar area with rock scattered about, but the maximum ejecta range would be greater.

Ejecta on the MIXED COMPANY Events appeared to be typical of ejecta on most HE detonations. Some raying occurred, but no specific anomalies were observed. A least-squares curve fit for the maximum range of natural missile ejecta showed that it scales as $W^{0.274}$ where W is the yield, as shown in Figure IV-4.65, with the MIDDLE GUST and DIAL PACK data. This exponent is comparable to the 0.3 exponent obtained from the MINE SHAFT Series data. The maximum ejecta range of 914 meters was somewhat greater than that for the DIAL PACK Event (686 meters), the difference probably being due to the difference in the geologies of the two sites. The MIDDLE GUST data fall close to the same curve as the MIXED COMPANY data.

Ejecta mass density δ plots for the MIXED COMPANY III Event are shown in Figure IV-4.66. Despite the fact that only a few samples were taken for MIXED COMPANY III, a reasonable mass density curve was obtained in which the density is seen to vary as R^{-4} for data in the continuous ejecta region. Data taken on missile count and size were used to obtain the second curve in Figure IV-4.66, the mass density in the missile ejecta region which varies as R^{-5}. These mass densities can be called typical, as mass densities for most events vary between R^{-2} and R^{-6}.

The artificial ejecta experiment that was planned for MIXED COMPANY III did not produce any results. The lack of results can be attributed to the fact that only one sand column was in the crater region where its components could be thrown out. The column array had been originally designed for a minimal crater study, and later was amended to include subsurface displacement and artificial ejecta measurements after the original array of holes had already been drilled. However, despite the problems, one piece of artificial ejecta was traced even though it was not part of this project. An airblast gauge mount, a concrete cylinder 0.9 meter in diameter and 0.9 meter high (total weight of approximately 1360 kg), was thrown about 915 meters to the northwest. Apparently, the concrete broke into two pieces just before impact, because two impact craters (about 1.8 meters wide and 0.3 meter deep) were found side by side. The gauge mount originated 5.5 meters northwest of GZ with the top of the cylinder flush with the ground surface.
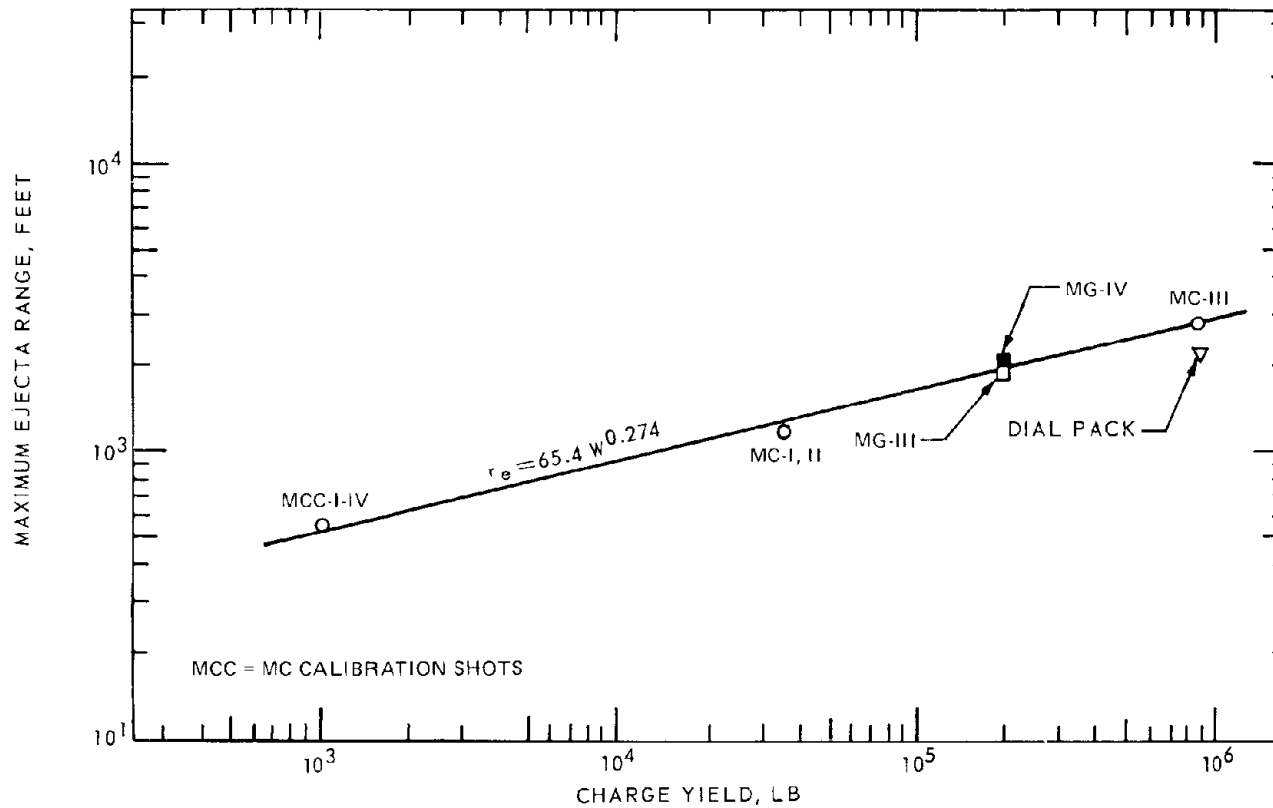
Figure IV-4.65. Maximum range of ejecta versus charge yield for the MIXED COM-
PANY Surface-Tangent (ST) Events with scaled overburden condi-
tions. (Data from the DIAL PACK and MIDDLE GUST ST Events are
shown for comparison. MIDDLE GUST III was on the MIDDLE GUST
"wet" site and MIDDLE GUST IV was on the MIDDLE GUST "dry"
site.) (Reference IV-4.47)
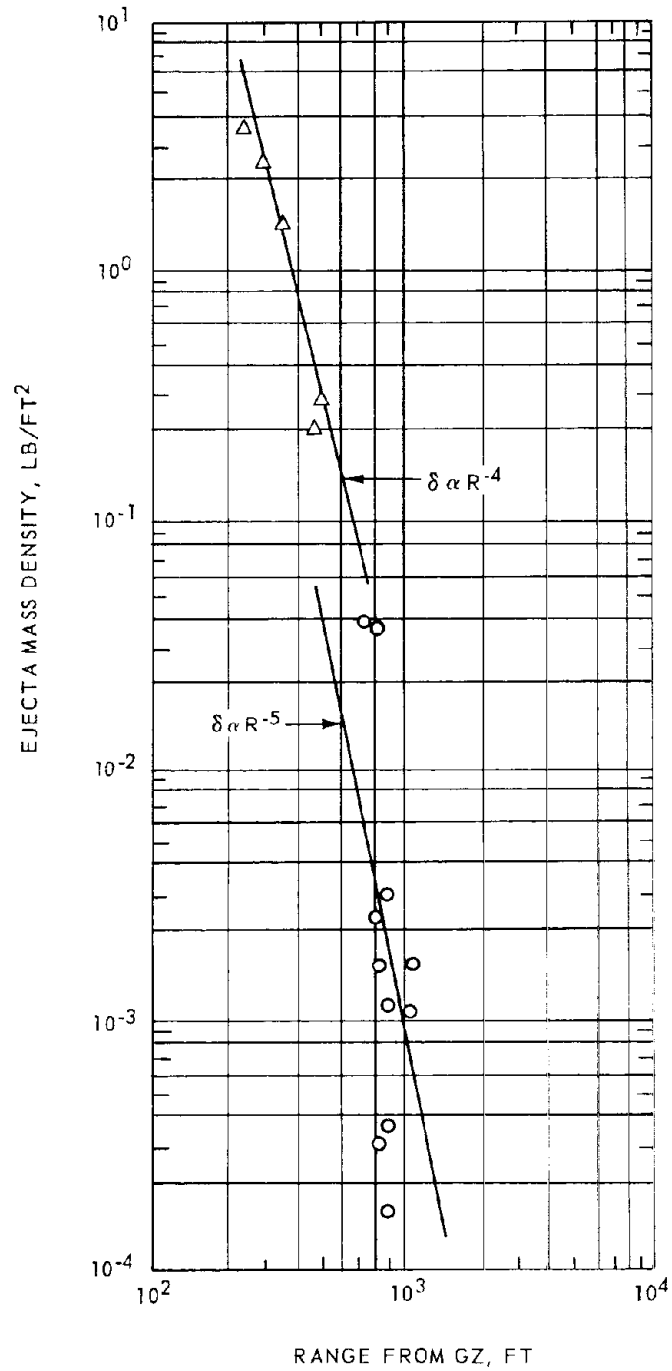
Figure IV-4.66.   Ejecta mass density versus range from GZ for MIXED COMPANY III. (Upper line is for crater lip area and lower line is for discontinuous region.) (Reference IV-4.47)

Wisotski (Reference IV-4.48) reported on the results of a photographic analysis of the 500-ton MIXED COMPANY Event III. Among the various aspects of the detonation covered by the photography, in-flight ejecta phenomenon was examined. Dynamic ejecta information was also obtained from the two 20-ton events.

The appearance of the photographed ejecta mass thrown out beyond the fireball debris from MIXED COMPANY Event III was both asymmetrical and sparse when compared to the throwout photographed from MIDDLE GUST Events I and III (Reference IV-4.49). Not only were the number of available trajectories low, but of those that were photographically tracked, very few had long trajectory paths with peak data points. Similar conditions existed for MIXED COMPANY Events I and II. Consequently, less credence can be given to the impact and escape parameters derived from the MIXED COMPANY Events data than were derived from the abundance of long-trajectory data obtained from the MIDDLE GUST Events. Photographs (Reference IV-4.48) show how sparse the ejecta were from MIXED COMPANY Event III. The spatial resolution was poor. Results derived from the MIDDLE GUST Series indicated that at least 40 to 50 trajectories are required in any one direction or in total to obtain reasonable least-squares parabolic fit to the data. The total number of trackable trajectories from anyone of the MIXED COMPANY Events was well below these numbers. Of those that were tracked there were very few that had long-trajectory paths with peaks.

The MIXED COMPANY Events data presented in Reference IV-4.48 were analyzed with a computer program developed to calculate the impact and escape parameters from position-time data of the MIDDLE GUST Events. A description of the method of data analysis used on the MIXED COMPANY Events is given in Reference IV-4.48.

Although the least-squares parabolic-curve fits of the impact parameters from MIXED COMPANY Events I, II, and III were quite different from what was expected when compared to the MIDDLE GUST Series results, a comparison of all three events for each impact parameter was made so that some relative idea of the differences between events could be obtained. The impact angular spread from about 30 to 60 degrees is much more than was obtained from five main events of the MIDDLE GUST Series. The velocity spread at long distances of about 98 m/sec down to about 40 m/sec is much greater than was recorded from the five main events of the MIDDLE GUST Series. Figure IV-4.67 shows the impact velocity versus impact distance from all events and all data. The maximum spread in time at long impact distances was smaller and the overall maximum impact times were less at 460 meters by 2 to 4 seconds when compared to the MIDDLE GUST Series.
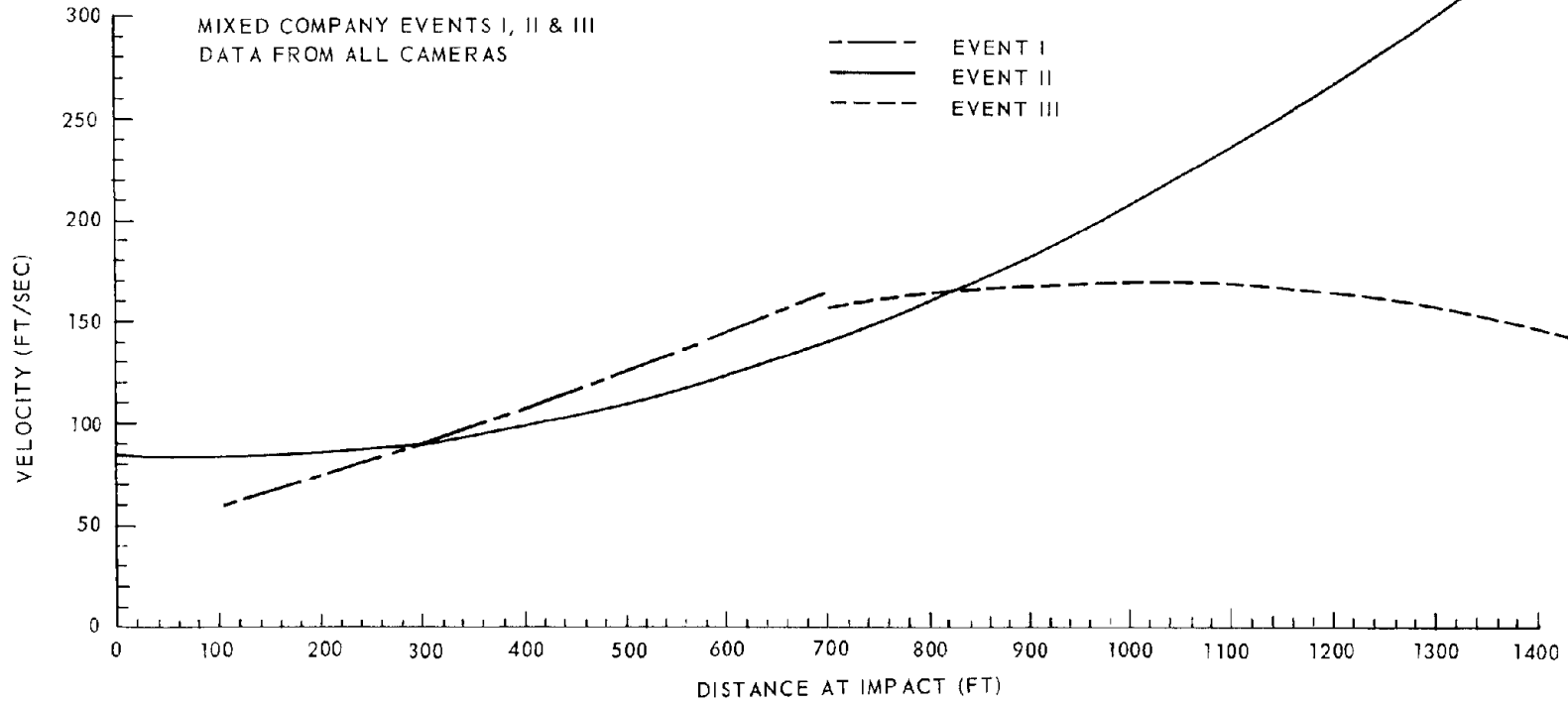
Figure IV-4.67.   Impact velocity versus impact distance from all events, all data (Reference IV-4.48).

IV-4.2.1.8 ESSEX. Project ESSEX Phase I, which stands for Effects of Subsurface Explosions, was initiated early in 1972 to determine the effects of different types of stemming, depths of burial, and geologic conditions on the explosion phenomenology, the crater size and the various effects produced by the subsurface detonation.

The ESSEX I Phase I test series consisted of four NM cratering events with a yield of approximately 10 tons of TNT. Each event was designated by its DOB and the degree of stemming. All events were detonated in the saturated sandy soil of the Peason Ridge area, Fort Polk Military Reservation in west-central Louisiana. Event 12 MS was a test whose DOB of the charge center was 12 meters below the surface and a yield of 10 tons of TNT equivalent, and was stemmed with a medium matching grout. Event 12 MPS had a center-of-charge DOB of 12 meters, a yield of 10-ton TNT equivalent,and was partially stemmed with a medium matching grout, leaving a 17.78-centimeter diameter, 10.86-meter access hole between the explosive-air interface and the surface GZ. Event 6 MS had a center-of-charge DOB of 5.85 meters and a yield of 10-ton TNT equivalent, and was stemmed with medium matching grout. Finally, Event 6 MU had a center-of-charge DOB of 5.85 meters and a yield of 8-ton TNT equivalent, and was partially stemmed with medium matching grout, leaving a 1.8-meter diameter, 5.24-meter access hole (partially blocked by a concrete lid) from the explosive-air interface to the surface GZ. The detailed results of these experiments will not be presented here as the interested reader can find them in Reference IV-4.50.

Reference IV-4.50 presents the results of the ejecta studies made during the ESSEX I Phase I test series. Included in that reference are the raw data that were collected, the techniques used to determine particle-size distribution and areal distribution of ejecta, the technique used to determine and to analyze the structure of the continuous ejecta field, and the techniques used to determine the bulking factor and the dimension of the continuous ejecta field. The investigation of the effects of depth of burial on ejecta distribution indicates that the probability of personnel and soft-target damage in the missile ejecta field can be maximized at all ranges by burying the explosive device at a scaled DOB of 76 $ft/kt^{1/3.4}$. The report also shows that the continuous ejecta field radius may be significantly increased while minimizing missile ejecta field hazards by using explosive devices buried at a scaled DOB of 152 $ft/kt^{1/3.4}$.

IV-4.3 SUMMARY OF EJECTA DATA

This section summarizes, in a general manner, the discussion of the previous sections. The approach taken is that of presenting information about the continuous and missile ejecta and its origin, the initial velocity and trajectories of ejecta, and the particle-size distribution.

IV-4.3.1 Ejecta Origin

There appear to be two distinct modes of ejecta formation, depending upon whether the explosive charge is buried or near the surface. The demarcation between these two conditions is not well defined (Reference IV-4.51). By "buried" is meant that the charge is deep enough into the ground to require a perceptible lag between detonation and venting of the explosion gases. If height or depth of burial is scaled by dividing the height or the depth from ground surface to the charge center of gravity by the cube root of charge weight W, the scaled height or depth is represented by $Z = HOB$ (or $DOB)W^{1/3}$*. Thus, a shallow buried charge would be at a scaled depth $-0.5 > Z > -1.0$ ft/lb$^{1/3}$†.

Ejecta formation for a buried explosion actually can be observed photographically. First a shock wave passes through the medium and reflects as a rarefaction wave at the surface causing initial fracturing and spalling, followed by a heaving action due to the expanding gases, and finally ejection. Ejection by a near-surface explosion, where the scaled depth is $0.3 > Z > -0.5$ ft/lb$^{1/3}$, is less well understood since the fireball precludes direct observation; it is probably the result of a crushing action by the shock front, followed by infiltration, and finally ejection by the scouring action of high-pressure gases.

Figure IV-4.68 shows the origin and relative range profiles obtained from studies of artificial ejecta, and provides qualitative information on the crater formation and ejection processes. While the fate of particles originating immediately above or below the charge is obscure, the remainder of the dissociated material follows a rather similar pattern despite differences in both shot geometry and cratered medium (Reference IV-4.52).

---

*This is called mass-gravity scaling, if the effect of gravity is considered (Reference IV-4.52). An alternative, still assuming gravity to be an important consideration, is the energy-gravity scaling, where $Z = HOB$ (or $DOB)/W^{1/4}$.

†Note that the convention used here is for HOB to be positive and DOB negative.
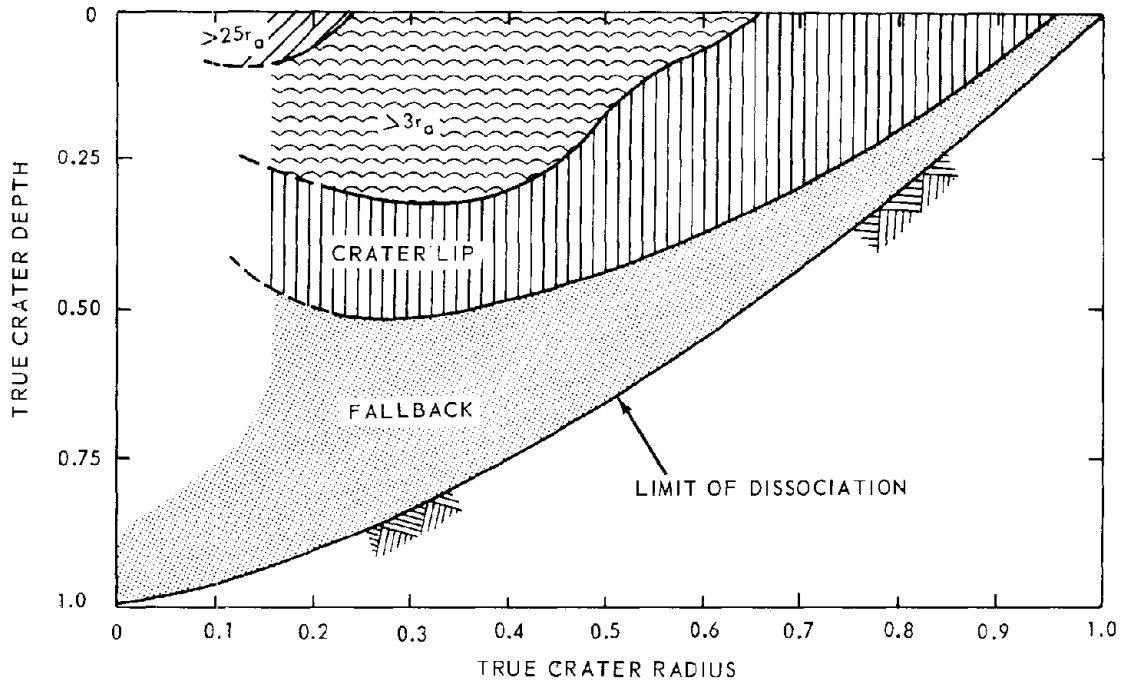
a. Buried detonation
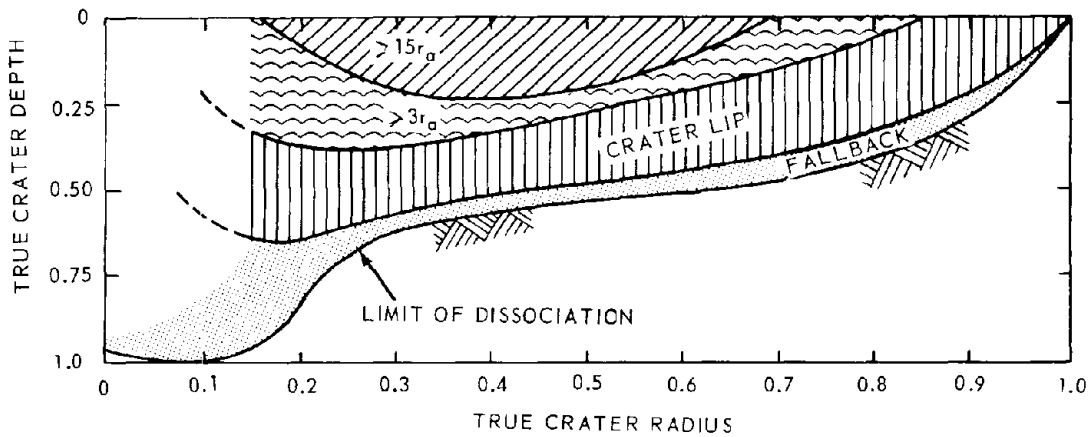
b. Near-surface detonation

Figure IV-4.68. Ejecta origin/relative range profiles. (To aid in comparison, crater profiles representing different explosive geometries and yields are shown with a common true crater radius.) (Reference IV-4.51)

Particles from near the charge are smaller than those originating near the outer reaches of the true crater. Pulverization may explain the lack of data on material near the charge. Accompanying this severe comminution are high-particle accelerations. Very small (grain-size) particles that manage to exit the crater under these conditions probably reach terminal velocities quickly as the result of drag. These particles undergo a short trajectory or become part of the dust cloud. Larger particles probably form the ejecta "spires" so often observed on near-surface detonations. These spires are thought to result from the break-up or ablation of fast-moving particles and the turbulence associated with their supersonic speeds. Larger particles which survive this portion of their trajectories should achieve a fairly long range, even though the initial angle of ejection, approximately 60 degrees or so, may be somewhat high to place them in the maximum range of the ejecta field.

Material nearest the true crater boundary tends to fall back into the crater, forming the apparent crater profile. This occurs mainly because the overburden does not permit it to escape. On the other hand, there is a near-surface zone for both buried and surface shots that produces the ejecta travelling the farthest, and between these two extremes lie two rather distinct zones that account for the continuous deposition of the ejecta which falls in the intermediate range. For all zones, the larger ejecta is thought to originate from positions nearest the outer edge of the crater. In rock, jointing is known to affect the size of the ejecta, but the significance of its influence is not well known.

It should be noted that Figure IV-4.68 shows that the long-range and missile ejecta come from zones near the surface and fairly close to the charge. This missile ejecta can be found at ranges beyond 15 crater radii for near-surface detonations and beyond 25 crater radii for buried detonations.

IV-4.3.2 Ejecta Areal Density

Tables IV-4.28 through IV-4.30 (Reference IV-4.51) show the ejecta data obtained from explosively formed craters in rock, clay, and layered media. In these tables ρ is the in-situ medium density, R_a is the apparent crater radius, and V_a is the apparent crater volume.

Table IV-4.28. Ejecta data from explosively formed craters in rock (Reference IV-4.51).

Event	Type	Explosive W (tons-TNT equivalent)	ρ^* (lb/ft³)	HOB** Actual (ft)	HOB** Scaled (ft/lb$^{1/3}$)	Crater R_a (ft)	Crater V_a (ft³)	δ (lb/ft²)	F_w (tons)	Particle Size Distribution	Particle Size m_t (lb)	Particle Size d_t (ft)	r_e (ft)	References/Remarks
Basalt														
Danny Boy	NE	420	169	-110	-1.17	107	1.026×10^6	$(1.42 \times 10^{19})R^{-8.86}$	4.256×10^3	Graph, table	~220,000	6	900	IV 4.53,54,55,56,57
Pre-Schooner D	HE	21.8	162	-41.8	-1.19	46.1	6.48×10^4	--	--	Graph	--	--	1550	IV-4.55,58
Pre-Schooner B	HE	21.7	162	-50.2	-1.43	49.0	7.398×10^4	--	--	--	--	--	984	IV-4.58
Pre-Schooner A	HE	21.6	162	-58.0	-1.66	50.3	7.587×10^4	--	--	Graph	--	8	507	IV 4.58,59
Buckboard 11	HE	20	162	-25.5	-0.75	44.6	5.422×10^4	$(1.320 \times 10^7)R^{-2.797}$	6.72×10^2 (author) (2.443×10^3 using δ equation)	Graph of fines	700	1.8++	4158	IV 4.60/Max. range achieved by largest particle
Buckboard 12	HE	20	162	-42.7	-1.25	57.0	1.35×10^5	$(6.707 \times 10^6)R^{-2.677}$	~2.09×10^3 (author) (1.89×10^3 using δ equation)	--	500	1.8++	~3500	IV-4.60
Buckboard 13	HE	20	162	-58.8	-1.72	36.8	2.32×10^4	$(6.904 \times 10^6)R^{-3.019}$	1.32×10^2 (author) (5.35×10^2 using δ equation)	--	--	--	3500	IV-4.60
Multiple-Threat Cratering Experiments:														
LS	HF	8	164	0	0	18.7	3.659×10^3	$(1.292 \times 10^5)R^{-2.853}$	1.115×10^2	Yes	1,700	--	~3300	IV-4.61/Conflict in data. Invalid δ equation.
SI (CI)	HE	2	164	0	0	12.1	7.73×10^2	--	5.25×10^1	--	--	--	--	IV-4.61
S2a	HE	2	164	0	0	10.7	6.72×10^2	$(2.310 \times 10^5)R^{-3.252}$	2.97×10^1	Yes	680	--	850	IV-4.61
S4a	HE	2	164	0	0	10.4	6.05×10^2	$(2.933 \times 10^3)R^{-2.477}$	5.49	Yes	350	--	750	IV-4.61/Conflict in data
C2	HE	2	164	-2.2	-0.14	14.0	1.500×10^3	$(4.251 \times 10^5)R^{-3.167}$	9.60×10^1	Yes	2,240	--	3292	IV-4.61/Invalid δ equation
ST1	HE	2	164	2.2	0.14	3.7	3.7×10^1	$(3.569 \times 10^4)R^{-3.459}$	1.14×10^1	Yes	9	--	250	IV-4.61/Questionable E_w
ST3a	HE	2	164	2.2	0.14	4.5	2.5×10^1	$(7.094 \times 10^7)R^{-4.953}$	8.89×10^2	Yes	10	--	180	IV-4.61/Questionable E_w
CS	HE	1	139	0	0	--	--	$(5.256 \times 10^3)R^{-2.645}$	--	Yes	170	--	450	IV-4.61

* Medium unit weight (in situ).
** (-) denotes burial (DOB).
† Means of expressing distribution of particle sizes, to include largest recorded particle(s) of weight m_t and diameter d_t.
++ Nominal size, that dimension which determines screen size through which particle will pass.

Table IV-4.28. (continued).

| | | Explosive | | | HOB | | Crater | | | | Ejecta | | | | |
| | | W | | | | | | | | | | Particle Size | | | |
Event	Type	(tons-TNT equivalent)	ρ (lbs/ft^3)	Actual (ft)	Scaled (ft/lb$^{1/3}$)	R$_a$ (ft)	V$_a$ (ft^3)	σ (lb/ft^2)	E$_w$ (tons)	Distribution	m, (lb)	d, (ft)	r$_e$ (ft)	References/ Remarks
Buckboard 4	HE	0.5	~162	-10	-1.00	--	--	--	--	--	--	--	1650	IV-4.60
Buckboard 5	HE	0.5	~162	-4.8	-0.48	15.0	1.89×10^3	--	--	--	37.5	--	3300	IV 4.60
Buckboard 10	HE	0.5	~162	-4.8	-0.48	15.8	2.66×10^3	--	--	--	--	--	--	IV-4.60
Buckboard 8	HE	0.5	~162	-14.7	-1.47	16.9	3.50×10^3	--	--	--	--	--	870	IV-4.60
Granitic Rock														
Mine Shaft														
Mine Under	HE	100	162	15.7	0.27	No measurable crater		--	--	--	--	>1.0	695	
Mine Ore	HE	100	162	7.1	0.12	23.0	5.94×10^3	$(3.90 \times 10^6)R^{-2.95}$	6.60×10^2	Yes	~3,100	~4	2300	
Mineral Rock	HE	100	162	7.1	0.12	31.5	8.10×10^3	$(1.85 \times 10^6)R^{-2.73}$	6.10×10^2	Yes	~36,000	--	2800	
Mineral Lode	HE	11.125	162	-100	3.56	--	--	--	--	Narrative	--	23.5	2150	IV-4.62
Mine Shaft Calibration:														
-2	HE	0.5	162	1.2	0.12	4.5	19	$(4.73 \times 10^7)R^{-4.57}$	1.21×10^3	Missile survey	81	--	450	IV-4.63
-5	HE	0.5	162	0	0	5.4	1.09×10^2	$(2.12 \times 10^1)R^{-1.22}$	--	Missile survey	310	--	1100	IV-4.63
-7	HE	0.5	162	-0.4	-0.04	9.4	2.46×10^2	--	--	Missile survey	1,400	--	1080	IV-4.63
Limestone														
Flat Top I	HE	20	~169	0	0	27.0	9.99×10^3	$\sim(3.62 \times 10^6)R^{-2.80}$	1.5×10^3	Graph	2,200	2.25*†	4059	IV-4.62,39
Rhyolite and Rhyolitic Rock														
Palanquin	NE	4,300	~137	-280.0	-1.37	119.1	1.25×10^6	--	--	--	--	--	1591	IV-4.64
Cabriolet	NE	2,300	137	-170.8	-1.03	179.4	5.401×10^5	--	--	Graph	--	9**	--	IV 4.65
Pre-Schooner II	HE	94.15	140	-71	-1.25	95.2	6.691×10^5	--	--	--	--	--	2240	IV 4.58,65
Sandstone														
Underground Explosion Test Program (UETP):														
817	HE	160	140	-25.0	-0.37	--	--	$(1.668 \times 10^{10})R^{-3.355}$	8.16×10^4	--	--	--	--	IV-4.66/r$_t$ = 94.8 ft
814	HE	20	140	-12.5	-0.37	--	--	$(2.263 \times 10^7)R^{-2.883}$	2.22×10^3	--	--	--	--	IV-4.66/r$_t$ = 56.4 ft
815	HE	20	140	-12.5	-0.37	--	--	$(2.554 \times 10^6)R^{-2.556}$	1.15×10^3	--	--	--	--	IV 4.66/r$_t$ = 70.5 ft

Table IV-4.28. (continued).

| | | Explosive | | | | Crater | | Ejecta | | | Particle Size* | | | |
Event	Type	W (tons TNT equivalent)	ρ (lb/ft³)	HOB Actual (ft)	HOB Scaled (ft/lb^1/3)	R_a (ft)	V_a (ft³)	δ (lb/ft²)	E_w (tons)	Distribution	n_f (lbs)	d_f (ft)	r_e (ft)	References/ Remarks
Middle Course I:														
B10	HE	1.4	156	3.8	0.27	6.1	6.21×10^1	--	--	Graph	-- }	3+*	350	
B11	HE	1.4	156	1.9	0.13	8.5	2.943×10^2	--	--	Graph	-- }		920	
B12	HE	1.4	156	0	0	12.2	1.042×10^3	--	--	Graph	-- }	3+*	1100	
B13	HE	1.4	156	-1.9	-0.13	16.9	2.055×10^3	--	--	Graph	-- }		1150	
B14	HE	1.4	156	-20.9	-1.48	27	1.512×10^4	--	--	Graph	--	3+*	800	
B15	HE	1.4	156	-20.9	-1.48	24	7.722×10^3	--	--	Graph	--	1.5	1000	/Unstemmed
Middle Course II:														
M3	HE	1.4	158	-15	-1.06	18.6	4.644×10^3	--	--	Graph	--	~1.0	1200	IV-4.67/Water stemmed
M4	HE	1.4	158	-20	-1.42	22.7	6.588×10^3	$(6.33 \times 10^{15})R^{-6.59\pm}$	$2.55 \times 10^{6\pm}$	Graph	--	~1.1	950	IV-4.67/Water stemmed
M5	HE	1.4	158	-24	-1.70	18.9	3.726×10^3	--	--	Graph	--	~2.0	>1600 (40 lb)	IV-4.67/Water stemmed
M6	HE	1.4	158	-28	-1.99	20.5	4.509×10^3	--	--	Graph	--	~1.3	1350	IV-4.67/Water stemmed
M7	HE	1.4	158	-33	-2.34	20.8	4.050×10^3	--	--	Graph	--	~1.3	800	IV-4.67/Water stemmed
M8	HE	1.4	158	-15	-1.06	21.8	6.102×10^3	--	--	Graph	--	~1.1	~1200	IV-4.67/Unstemmed
M9	HE	1.4	158	-20	-1.42	21.5	7.047×10^{13}	$(7.53 \times 10^{13})R^{-6.35\pm}$	$8.61 \times 10^{4\pm}$	Graph	--	0.75	750	IV-4.67/Unstemmed
M10	HE	1.4	158	-25	-1.77	18.3	3.618×10^3	--	--	Graph	--	0.75	500	IV-4.67/Unstemmed
M11	HE	1.4	158	-30	-2.13		Mound	--	--	Graph	--	~0.50	300	IV-4.67/Unstemmed
M12	HE	1.4	158	-33	-2.34		Mound	--	--	Graph	--	1.1	450	IV-4.67/Unstemmed
M13	HE	1.4	158	-20	-1.42	23.5	8.208×10^3	$(5.23 \times 10^{14})R^{-6.13\pm}$	$8.66 \times 10^{5\pm}$	Graph	--	~1.2	1100 (65 lb)	IV-4.67
M14	HE	1.4	158	-4	-0.28	17.5	3.132×10^3	--	--	Graph	--	2.0	~1750 (140 lb)	IV-4.67/Unstemmed
M15	HE	1.4	158	-8	-0.57	23.6	8.397×10^3	--	--	Graph	--	~1.8	>2200 (2 lb)	IV-4.67/Unstemmed
M16	HE	1.4	158	-20	-1.42	27.0	1.415×10^4	$(4.56 \times 10^{12})R^{-5.20\pm}$	1.18×10^5	Graph	--	~1.0	1000	IV-4.67/Reduced stemming. (Open 4-in.-dia. hole)
UETP:														
810	HE	1.28	140	-5.0	-0.37	--	--	$(4.477 \times 10^7)R^{-3.347}$	9.74×10^2	--	--	--	--	IV-4.66/r_t = 32.5 ft
811	HE	1.28	140	-5.0	-0.37	--	--	$(1.271 \times 10^6)R^{-2.904}$	2.34×10^2	--	--	--	--	IV-4.66/r_t = 25.3 ft

± Questionable. Derived from isodensity contours.

Table IV-4.28. (continued).

Event	Type	Explosive W (tons-TNT equivalent)	p (lb/ft³)	HOB Actual (ft)	HOB Scaled (ft/lb^1/3)	Crater R_a (ft)	Crater V_a (ft³)	δ (lb/ft²)	E_w (tons)	Ejecta Particle Size Distribution	m, (lb)	d, (ft)	r_e (ft)	References/ Remarks
Mixed Company Calibration (MCC):														
3	HE	0.5	142	1.35	0.135	3.4	1.5×10^1	--	0.9	--	--	--	160	IV-4.68
-4	HE	0.5	142	0	0	8.6	3.50×10^2	--	2.56×10^1	--	--	--	1300	IV-4.68
Coupling Efficiency of Near-Surface Explosions (CENSE):														
-2	HE	0.5	--	1.50	0.15	--	3.3×10^1	--	--	--	--	0.08	300	IV-4.69/Mound crater
-3	HE	0.5	--	0.75	0.075	5.8	4.6×10^1	--	--	--	44	0.8	400	IV-4.69
-4	HE	0.5	--	0	0	7.7	1×10^1	--	--	--	14	0.7	1000	IV-4.69
-5	HE	0.5	--	-0.75	-0.075	8.3	3.39×10^2	--	--	--	--	--	300	IV-4.69
-6	HE	0.5	--	-1.50	-0.15	12.3	6.36×10^2	--	--	--	--	--	750	IV-4.69
-7	HE	0.5	--	-13.50	-1.35	14.5	2.055×10^3	--	--	--	--	--	1300	IV-4.69
Tuffaceous Rock														
Schooner	NE	31,000	~125	-335.0	-0.846	426	6.164×10^7	--	--	Graph	2,343,750	20+	~7000	IV-4.70,71
Shale														
Middle Gust (MG) IV	HE	100	~120	7.9	0.14	43.3	4.36×10^4	$(2.13 \times 10^{12})R^{-5.06}$	2.15	--	--	--	2200	IV-4.43
Pre-Gondola I:														
-A	HE	22.39	135	-52.7	-1.48	76.1	2.353×10^5	--	--	Graph	--	2	545	IV-4.72
-D	HE	22.26	133	-56.9	-1.60	65.1	1.339×10^5	--	--	Graph	--	4	453	IV-4.72
-C	HE	21.58	135	-42.5	-1.21	80.4	2.776×10^5	--	--	Graph	--	2	800	IV-4.72
-B	HE	21.30	134	-46.2	-1.32	78.5	2.413×10^5	--	--	Graph	--	2	905	IV-4.72
MG V	HE	20	~120	0	0	34.1	2.13×10^4	$(1.11 \times 10^{10})R^{-4.30}$	4.52×10^3	--	--	--	1800	IV-4.43
Diamond Ore IIB:														
-6M	HE	~18.7	119	-19.7	-0.59	71.5	1.80×10^5	--	--	Graph	--	0.5	2733	IV-4.73
Diamond Ore IIA:														
-1	HE	13.4	119	-41.0	-1.37	67.6	1.536×10^5	$(2.481 \times 10^{14})R^{-5.217}$	8.82×10^9 (discontinuous field only)	Graph	--	--	1040	IV-4.74,75/Unstemmed, δ questionable, unreasonable E_w
-2	HE	12.5	119	-41.0	-1.40	65.1	1.285×10^5	--	--	Graph	--	--	1110	IV-4.74,75/Possible detonation malfunction
-3	HE	11.6	119	-19.7	-0.69	62.3	1.555×10^5	$(1.988 \times 10^{10})R^{-3.545}$	7.97×10^5 (discontinuous field only)	Graph	--	--	2180	IV-4.74,75/δ, E_w questionable

Table IV-4.28.   (continued).

Event	Type	Explosive W (tons-TNT equivalent)	ρ (lb/ft^3)	HOB Actual (ft)	HOB Scaled (ft/lb$^{1/3}$)	Crater R_a (ft)	Crater V_a (ft^3)	Ejecta δ (lb/ft^2)	Ejecta E_w (tons)	Particle Size Distribution	Particle Size m_t (lb)	Particle Size d_t (ft)	r_e (ft)	Reference/ Remarks
Diamond Ore IIB:														
-IT1	HE	1.1	119	-5	-0.38	20.2	4.44×10^3	--	--	Graph	--	0.6	1025	IV-4.73
-IT2	HE	1.1	119	-10	-0.77	25.8	1.05×10^4	--	--	Graph	--		1033	IV-4.73
-IT3	HE	1.1	119	-15	-1.15	22.5	6.90×10^3	--	--	Graph	--)		879	IV-4.73
-IT4	HE	1.1	119	-20	-1.54	22.8	5.30×10^3	--	--	Graph	-- }	0.6	785	IV-4.73
-IT5	HE	1.1	119	-25	-1.92	20.3	3.60×10^3	--	--	Graph	--)		820	IV-4.73
-IT6	HE	0.96	119	-18	-1.45	25.0	6.6×10^3	--	--	Graph	--	--	867	IV-4.73
Pre-Gondola:														
SC-1	HE	0.55	119	-19.1	-1.85	7.1	--	--	--	--	--	--	206	
SC-2	HE	0.55	119	-15.8	-1.53	27.3	--	--	--	--	--	--	333	
SC-3	HE	0.55	119	-23.3	-2.26	14.6	--	--	--	--	--	--	147	
SC-4	HE	0.55	119	-12.2	-1.18	24.5	--	--	--	--	--	--	500	
USAF Weapons Lab:														
AFWL-1	HE	0.50	120	2.68	0.27	3.8	2.79×10^1	--	--	Graph, table	--	--	624	IV-4.76
AFWL-2	HE	0.50	120	1.34	0.13	8.0	2.16×10^2	--	--	Graph, table	--	--	387	IV-4.76
AFWL-3	HE	0.50	120	0	0	12.0	1.328×10^3	--	--	Graph, table	--	--	458	IV-4.76
AFWL-4	HE	0.50	120	-1.34	-0.13	16.0	2.860×10^3	--	--	Graph, table	--	--	862	IV-4.76

Table IV-4.29. Ejecta data from explosively formed craters in clay (Reference IV-4.51).

Event	Type	W (tons-TNT equivalent)	ρ^* (lb/ft³)	HOB** Actual (ft)	HOB** Scaled (ft/lb^1/3)	R_a (ft)	V_a (ft³)	δ (lb/ft²)	E_w (tons)	Distribution	m_ℓ (lb)	d_ℓ (ft)	r_e (ft)	References/Remarks
Dry Clay														
Underground Explosion Test Program (UETP)														
318	HE	160	103	-35.0	-0.51	120	1.1×10^6	$(7.336 \times 10^8) R^{-3.032}$	1.55×10^4	Narrative description	--	6	3500	IV-4.77,78
315	HE	20	97	-17.5	-0.51	64	1.9×10^5	$(8.593 \times 10^{10}) R^{-4.172}$	1.48×10^4	Narrative description	--	3	>1050	IV-4.77,78
308	HE	1.28	79	-2.6	-0.19	20	5.4×10^3	$(5.232 \times 10^4) R^{-2.562}$	3.74×10^1	Narrative description	--	0.42	160	IV-4.77,78
309	HE	1.28	84	-7.0	-0.51	21.5	7.3×10^3	$(5.736 \times 10^7) R^{-3.757}$	4.58×10^2	Narrative description	--	0.50	200	IV-4.77,78
312	HE	1.28	93	-7.0	-0.51	26	1.3×10^4	$(2.939 \times 10^4) R^{-2.140}$	1.42×10^2	Narrative description	--	1.0	500	IV-4.77,78
302	HE	0.16	73	0	0	7.2	2.4×10^2	$(1.452 \times 10^4) R^{-2.824}$	1.06×10^1	Narrative description	--	0.42	--	IV 4.77,78
303	HE	0.16	81	-1.3	-0.19	9	6.0×10^2	$(3.755 \times 10^5) R^{-3.722}$	1.57×10^1	Narrative description	--	0.83	-	IV-4.77,78
304	HE	0.16	84	-3.5	-0.51	10.5	8.2×10^2	$(4.657 \times 10^5) R^{-3.247}$	6.2×10^1	Narrative description	--	1.50	--	IV-4.77,78
305	HE	0.16	83	-7.0	-1.02	11.8	1.3×10^3	$(5.783 \times 10^6) R^{-3.647}$	1.89×10^2	Narrative description	--	0.50	--	IV-4.77,78
306	HE	0.16	94	-14.0	-2.05	15	2.36×10^2	$(2.602 \times 10^1) R^{-2.251}$	0.055	Narrative description	--	0.50	75	IV-4.77,78
307	HE	0.16	92	-21.0	-3.07	--	--	--	--	Narrative description	--	0.50	45	IV-4.77,78
310	HE	0.16	90	-3.5	-0.51	11	9.0×10^2	$(2.222 \times 10^5) R^{-3.057}$	5.04×10^2	Narrative description	--	0.50	>250	IV 4.77,78
313	HE	0.16	91	-3.5	-0.51	12.8	1.5×10^3	$(7.243 \times 10^3) R^{-2.266}$	2.28×10^1	Narrative description	--	0.83	210	IV-4.77,78
Symmetry	HE	0.16	88	-7.0	-1.02	12.2	1.3×10^3	$(2.957 \times 10^5) R^{-3.005}$	7.30×10^1	--	--	--	--	IV-4.77
316	HE	0.055	88	-2.45	-0.51	9	7.4×10^3	$(1.355 \times 10^3) R^{-2.179}$	5.62	Narrative description	--	0.50	100	IV-4.77,78

Note: Except for the Sprint Event, all ejecta areal densities and total weights are based upon dry weights; actual weights would be higher.

* Medium unit weight (in situ).

** (-) denotes burial (DOB).

+ Means of expressing distribution of particle sizes, to include largest recorded particle(s) of weight m_ℓ and diameter d_ℓ.

Table IV-4.29.   (continued).

Event	Type	Explosive W (tons-TNT equivalent)	ρ (lb/ft³)	HOB** Actual (ft)	HOB** Scaled (ft/lb^{1/3})	Crater R_a (ft)	Crater V_a (ft³)	δ (lb/ft²)	E_w (tons)	Particle Size⁺ Distribution	m (lb)	d (ft)	r_e (ft)	References/ Remarks
Moist Clay														
Sprint	HE	~4	120–125	−20	−1.0	38	1.8×10^3	$(8.63 \times 10^7)R^{-3.42}$	3.11×10^3	Missile survey	~600	--	822	IV–4.79/Unstemmed cylindrical charge
Wet Clay														
UETP														
403	HE	1.28	107	−5.0	−0.37	41.8	2.906×10^4	$(8.323 \times 10^7)R^{-3.397}$	1.01×10^3	Narrative description	--	6	~1200	IV 4.77,78
402	HE	0.16	116	−2.5	−0.37	18.8	4.1×10^3	$1.192R^{-0.570}$	--	Narrative description	--	4.0	~250	IV 4.77,78,80
404	HE	0.16	116	−2.5	−0.37	17.5	3.9×10^3	$(3.646 \times 10^4)R^{-2.324}$	9.65×10^1	Narrative description	--	4	650	IV–4.77,78
1A-46	HE	0.16	111	−3.5	−0.51	--	--	--	--	Narrative description	--	4	~1500	IV–4.78
1A-48	HE	0.16	116	−2.5	−0.37	--	--	--	--	Narrative description	--	6	2000	IV–4.78

Table IV-4.30. Ejecta data from explosively formed craters in layered earth (Reference IV-4.51).

Event	Type	Explosive W (tons–TNT equivalent)	ρ^* (lb/ft^3)	HOB** Actual (ft)	HOB** Scaled (ft/lb$^{1/3}$)	Crater R_a (ft)	Crater V_a (ft^3)	δ (lb/ft^2)	E_w (tons)	Ejecta Particle Size Distribution	m_l (lb)	d_l (ft)	l_e (ft)	References/Remarks
Desert Alluvium Overlying Sandstone														
Mixed Company														
-3	HE	500	$\frac{130\dagger\dagger}{142}$	13.5	0.135	57.8	7.5×10^4	$(5.25 \times 10^{16})R^{-6.5}$	4.25×10^3	Table	--	--	~3000	IV-4.81/Depth overburden = 5.5 ft
-1	HE	20	$\frac{130}{142}$	0	0	24.9	1.06×10^4	$(1.93 \times 10^5)R^{-2.24}$	6.76×10^2	--	--	--	1000	IV-4.81/Depth overburden = 4.8 ft
-2	HE	20	$\frac{130}{142}$	4.60	0.135	20.4	2.1×10^3	$(2.88 \times 10^6)R^{-3.12}$	1.92×10^2	--	--	--	1100	IV-4.81/Depth overburden = 2.2 ft. Did not crater into rock
MCC														
-1	HE	0.5	$\frac{130}{142}$	1.35	0.135	4.6	4.3×10^1	--	1.4	--	--	--	190	IV-4.81/Depth overburden = 3 ft. Did not crater into rock
-2	HE	0.5	$\frac{130}{142}$	0	0	5.6	8.8×10^1	--	8.5	--	--	--	500	IV-4.81/Depth overburden = 6 ft. Did not crater into rock
-4	HE	0.5	$\sim\frac{120}{142}$	1.35	0.135	7.6	1.35×10^2	--	6.6	--	--	--	450	IV-4.81/Depth overburden = 0.65 ft
-5	HE													
Clay-Sand (9 ft) Overlying Shale (Water Table at 4 ft)														
Middle Gust														
II	HE	100	$\frac{131}{138}$	15.8	0.270	43.3	4.97×10^4	$(4.21 \times 10^6)R^{-3.04}$	$\sim 2.4 \times 10^2$	--	--	--	1000	IV-4.43/6 for discontinuous ejecta field only
III	HE	100	$\frac{131}{138}$	7.9	0.140	51.9	9.36×10^4	$(3.28 \times 10^7)R^{-2.92}$	2.85×10^3	* --	--	--	1800	IV-4.43
I	HE	20	$\frac{131}{138}$	0	0	49.1	6.86×10^4	$(8.72 \times 10^9)R^{-3.82}$	$\sim 1.3 \times 10^4$	--	--	~2	2200	IV-4.43/6 for discontinuous ejecta field only

* Medium unit weight (in situ).
** (-) denotes burial (DOB).
\+ Means of expressing distribution of particle sizes, to include largest recorded particle(s) of weight m_l and diameter d_l.
†† Overburden/rock.

Table IV-4.30. (continued).

Event	Type	W (tons-TNT equivalent)	ρ (lb/ft³)	HOB Actual (ft)	HOB Scaled (ft/lb$^{1/3}$)	R_a (ft)	V_a (ft³)	δ (lb/ft²)	E_w (tons)	Particle Size Distribution	m_l (lb)	d_l (ft)	r_e (ft)	References / Remarks
Alternating Layers of Clays, Silts, and Sands (Water Table at 10- to 30-ft Depth)														
Prairie Flat	HE	500	Variable	13.46	0.135	100	2.62×10^5	$(4.16 \times 10^{12})R^{-4.82}$	1.05×10^4	..	--	..		IV-4.82
Dial Pack	HE	500	Variable	13.46	0.135	95	3.00×10^5	--	--	--	--	--	2200	
Distant Plain 6	HE	100	Variable	7.9	0.135	42.6	--	$(10.32 \times 10^4)R^{-2.636}$	2.20×10^2	--	--	1-3	~1070	
Essex														
3MS	HE	11.5	Variable	-9.8	-0.34	70.7	1.514×10^5	--	--	...	--	..	2513	IV-4.83
12MS	HE	10	Variable	-39.4	-1.45	61.2	1.654×10^5	--	--	Graph, table	--	--	947	IV-4.84,50
6MWS	HE	10	Variable	-19.2	-0.71	67.7	1.953×10^5	--	--	--	--	--	2244	IV-4.83/Water stemmed
12MPS	HE	10	Variable	-39.4	-1.45	90.4	1.796×10^5	--	--	Graph, table	--	--	964	IV-4.84,50/Partially stemmed
6MS	HE	10	Variable	-19.2	-0.71	85.4	2.127×10^5	--	--	Graph, table	--		2476	IV-4.84,50
3MU	HE	9	Variable	-9.8	-0.37	67.5	1.555×10^5	--	--	--	--	--	2152	IV-4.83/Unstemmed
6MU	HE	8	Variable	-19.2	-0.76	79.1	1.811×10^5	--	--	Graph, table	--	--	1538	IV-4.84,50/Unstemmed. Maximum missile range based upon incomplete search
12MU	HE	8	Variable	-39.4	1.56	47.4	4.222×10^4	--	--	--	--	--	646	IV-4.83/Unstemmed
Interbedded Sandstone and Shale														
Middle Course														
M1	HE	1.4	--	-8	-0.57	20	4.725×10^3	--	--	--	--	--	>2100	IV-4.67
M2	HE	1.4	--	-12	-0.85	22	6.750×10^3	--	--	--	--	--	1800	IV-4.67

IV-4.3.3 Initial Velocities

The early experiments with near-surface and buried events did not include methods for determining the initial velocity of particles and their subsequent trajectories. This type of investigation was performed chiefly by Wisotski at Denver Research Institute in Colorado. Recently, the MIDDLE GUST III photographic data have been analyzed to determine the initial condition of the ejecta, and Wisotski (References IV-4.48 and IV-4.49) performed extensive data reduction for the MIXED COMPANY and MIDDLE GUST Events. The results of these analyses, the MIDDLE GUST III data analysis in particular, have been used by Seebaugh to construct ejecta environment computational tools. Figure IV-4.69 (from Reference IV-4.85) shows the MIDDLE GUST III ejection velocity as a function of fragment diameter. The data points are for four camera positions and the solid curve is the size-dependent ejection velocity limit, with the maximum fragment mass determined from the observed apparent crater volume (Reference IV-4.41). The symbols represent the results reported by Wisotski (Reference IV-4.49) for this event. The details of the camera placement are also discussed in Reference IV-4.49. The circular symbols correspond to the left (west) cameras while the square symbols correspond to the right (east) cameras. This distinction is made because 18-mph winds blowing from left to right affected the data acquisition and possibly perturbed the fragment trajectories. In Wisotski's (Reference IV-4.49) data reduction procedure, the segments of the trajectories from the fireball to the ground dust layer (near impact) were extrapolated back to determine the ejection conditions. Using this procedure, many fragments appeared to originate outside of the apparent crater. The problem was that the planes containing the trajectories relative to the plane normal to the camera axis were unknown. A correction was made by rotating each trajectory plane until the fragment origin equalled the apparent crater radius or made its closest approach to the apparent radius. The open symbols on Figure IV-4.69 denote trajectories that had, after data reduction, origins near the apparent crater radius. The solid symbols denote fragments with origins, after data reduction, at ranges other than the crater radius. The size-velocity limit curve on Figure IV-4.69 bounds 143 out of the 151 data points given in Reference IV-4.49 for the MIDDLE GUST III Event. However, this limit curve overpredicts the maximum ejecta range (Reference IV-4.85).
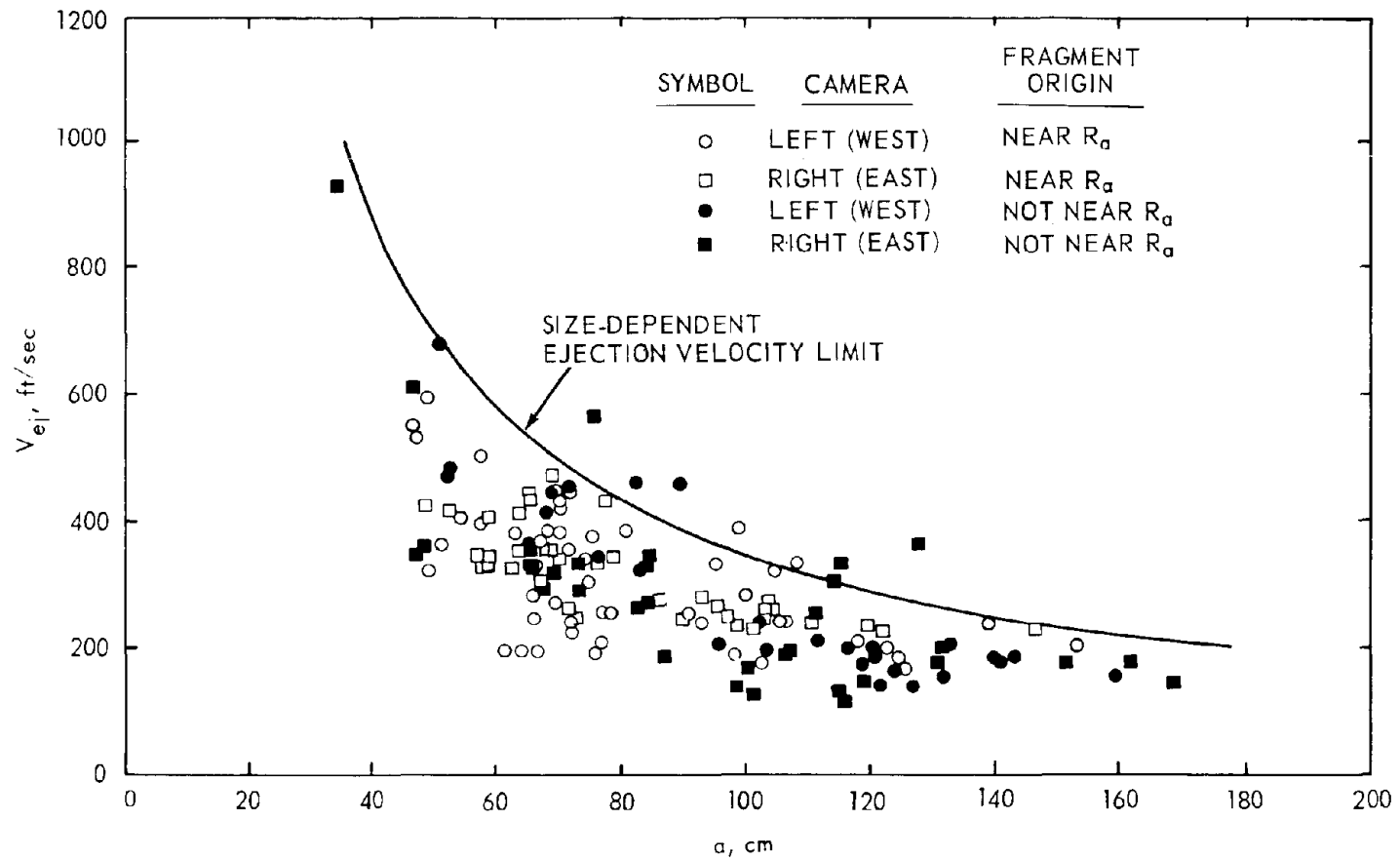
Figure IV-4.69.   Correlation of ejection velocity and fragment diameter,
Event MIDDLE GUST III (Reference IV-4.85).

Linnerud (Reference IV-4.46) made an analysis of the in-flight ejecta from the MIDDLE GUST III photographic coverage. He concluded that the horizontal component of ejecta velocities never exceeded approximately 60 m/sec. A good overall maximum horizontal velocity component was probably approximately 30 m/sec. Assuming reasonable ejection angles implies that ejecta velocities probably never exceeded some 90 to 120 m/sec.

One prominent early time feature of the MIDDLE GUST III Event, and this was also observed on other cratering shots, both HE and nuclear, is the formation of high-velocity spires. These spires form a "crown" around the fireball and the developing dust cloud. The spire angle for MIDDLE GUST III was approximately 50 degrees (Reference IV-4.84). The velocity of these spires was observed to vary between 120 and 180 m/sec and remained fairly constant up to about 1.5 seconds. From careful film analysis the estimated upper diameter of the spire material was about 2 to 3 centimeters (Reference IV-4.46).

IV-4.3.4 Particle Trajectories

A detailed treatment of ejecta particle trajectories between the immediate vicinity of the crater and impact is beyond the scope of this sourcebook. However, some of the major factors that influence particle range and impact velocity are briefly discussed.

During the early portions of their trajectories, particles may experience a severe environment in which high gas temperatures prevail and reflected airblast shock fronts affect their trajectories (Reference IV-4.86). In the case of buried explosions, venting of explosion gases overtake and accelerate ejecta masses.

Ejecta particles of interest here follow trajectories that are essentially ballistic, although the particles may suffer perturbations by gas acceleration and afterwinds. Excluding the effects of the atmosphere, that is drag that absorbs the kinetic energy of the particles, the paths are parabolic. For a parabolic trajectory, the maximum ground range is obtained from the expression

$$R_{max} = \frac{V_o^2}{g} \sin 2\alpha \qquad (IV-4.17)$$

where V_o is the initial particle speed, α is the particle elevation angle at exit, measured from the horizontal, and g is the gravitational constant.

The retarding force that the atmosphere exerts on any particle moving through it is computed from

$$D(t) = \frac{1}{2} C_D A \rho [V(t)]^2 \qquad (IV-4.18)$$

where C_D is the drag coefficient for the particle which is a function of the shape and the Mach number, ρ is the atmospheric density, A is the frontal area of the particle in the direction of motion, and $V(t)$ is the time-dependent particle velocity. Actually to compute $D(t)$ at any instant, the instantaneous particle velocity $V(t)$ is needed. The solution of the equations of motion that include the drag in the above form can be extremely complex.

The ballistic coefficient β is a measure of the effects of the atmospheric drag on the particle. It is usually represented by

$$\beta = \frac{W_p}{C_D A} \qquad (IV-4.19)$$

where W_p is the particle weight. For a spherical particle, the ballistic coefficient becomes

$$\beta_s = \frac{4 r \rho_p}{3 C_D} \qquad (IV-4.20)$$

where ρ_p is the particle density and r is its radius. Therefore, as r increases so does β. A particle with a high value of β is least affected by air drag. Hence, from the above, one can perceive that a complete solution of the equations describing the path of a particle from the crater to impact would involve these and other considerations. Using certain simplifying assumptions, a closed form solution can be obtained which has great practical utility. One of these methods due to Sherwood (Reference IV-4.20) is discussed in Section IV-4.4. Obviously, drag continues to change as the parameters representing the atmosphere and the particle change, especially in the early portion of the trajectory. For early trajectories of rock particles, experimentally measured values of β averaged approximately 1.08 (Reference IV-4.45).

Considering the gross comminution and the ejection velocity, including the ejection angle, there would appear to be a combination of particle size, shape, and origin that, for a given set of conditions such as explosive yield and position and cratered medium, would determine the maximum particle range. The origin of the ejecta was illustrated in Figure IV-4.68 and the shape and the size, based

upon field observations over a wide range of conditions, is a compact particle weighing on the order of one-half kilogram for rock and dry clay, and is probably larger for plastic clay.

Observations of terminal trajectories are available for small (less than one-half kilogram) particles of granite and for clay/shale particles up to 35 kilograms (Reference IV-4.43). The terminal velocities associated with the granite particles were inferred from penetrations into Styrofoam "traps." This included estimations of impact angles of about 80 degrees from the horizontal. The clay/shale data, which were obtained photographically, revealed similar impact angles. All particles appeared to have achieved or very nearly achieved terminal velocity prior to impact. A fit to these data was suggested by Rooke (Reference IV-4.51), and is shown in Figure IV-4.70. This figure takes into account terminal velocities of ideally shaped particles.

IV-4.3.5 Post-Impact Particle Statistics

The sizes and shapes of particles found in the ejecta field are determined by their origins, as discussed in subsection IV-4.3.1, by the characteristics of the cratered medium, possibly by occurrences in the early portion of their trajectories (e.g., erosion), interparticle collision, and by terminal impact including bounce and roll. In general, rock particles resulting from near-surface bursts exhibit three distinct dimensions of length, ℓ, width, w, and height, h, as opposed to the more compact shape of dense rock particles from buried explosions, in which width and height dimensions may be virtually identical (Figure IV-4.71 from Reference IV-4.51). This tendency toward an oblong particle has also been observed in buried detonations in layered rock (Reference IV-4.87). Figure IV-4.71 is based upon conclusions drawn from two studies of ejecta particles from a near-surface burst over granite. The curves are all visual fits intended to show data trends and to approximate average dimensions taken from numerous observations at various distances from GZ in the missile ejecta field. Each measured dimension represents a maximum in its own axis, that is, particle irregularities are not depicted; length is the longest and height is the shortest.

Practically all data linking particle dimensions to measured weight W_p are for particles less than or equal to 50 kilograms in dense rock. In Figure IV-4.72 (Reference IV-4.51), the granite data of Figure IV-4.71 are again employed to provide size-weight equivalency, based upon visual fits of measured weights and nominal sizes. For this, "nominal" sizes have been taken as the middle dimension
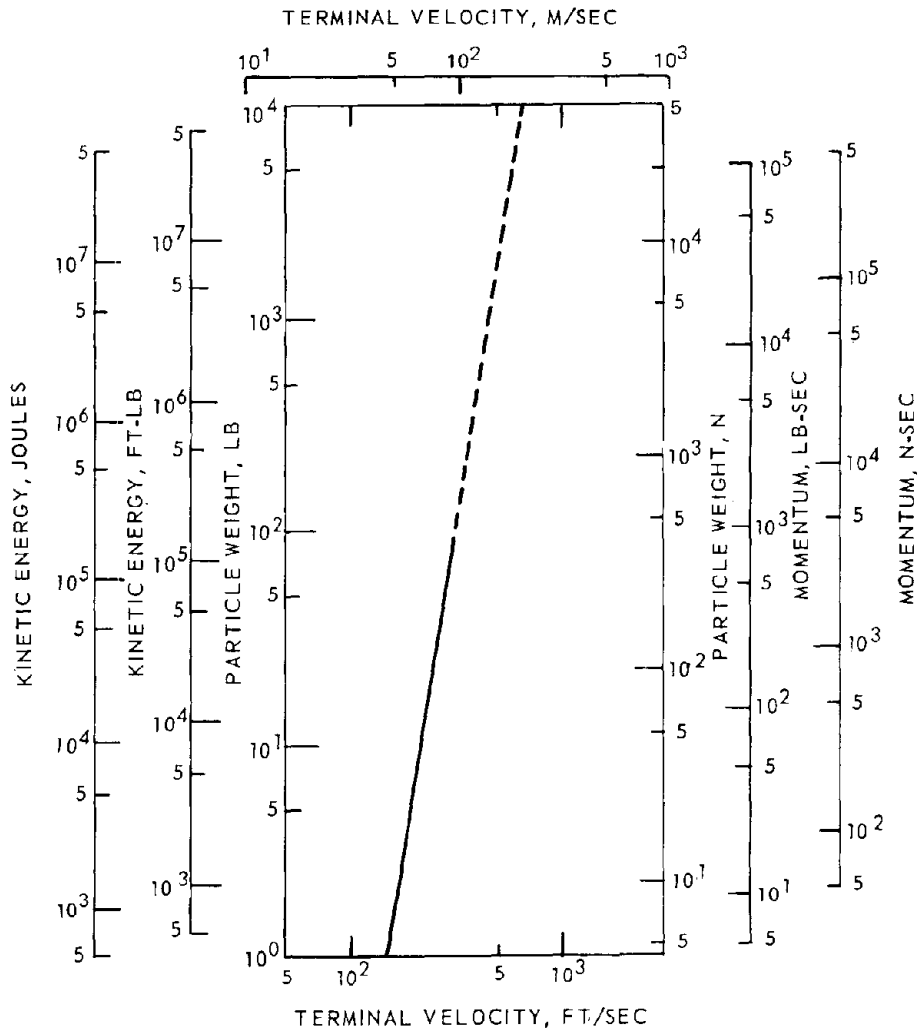
Figure IV-4.70.   Terminal velocity (speed) and associ-
ated kinetic energy and momentum for
ejecta particles (Reference IV-4.51).
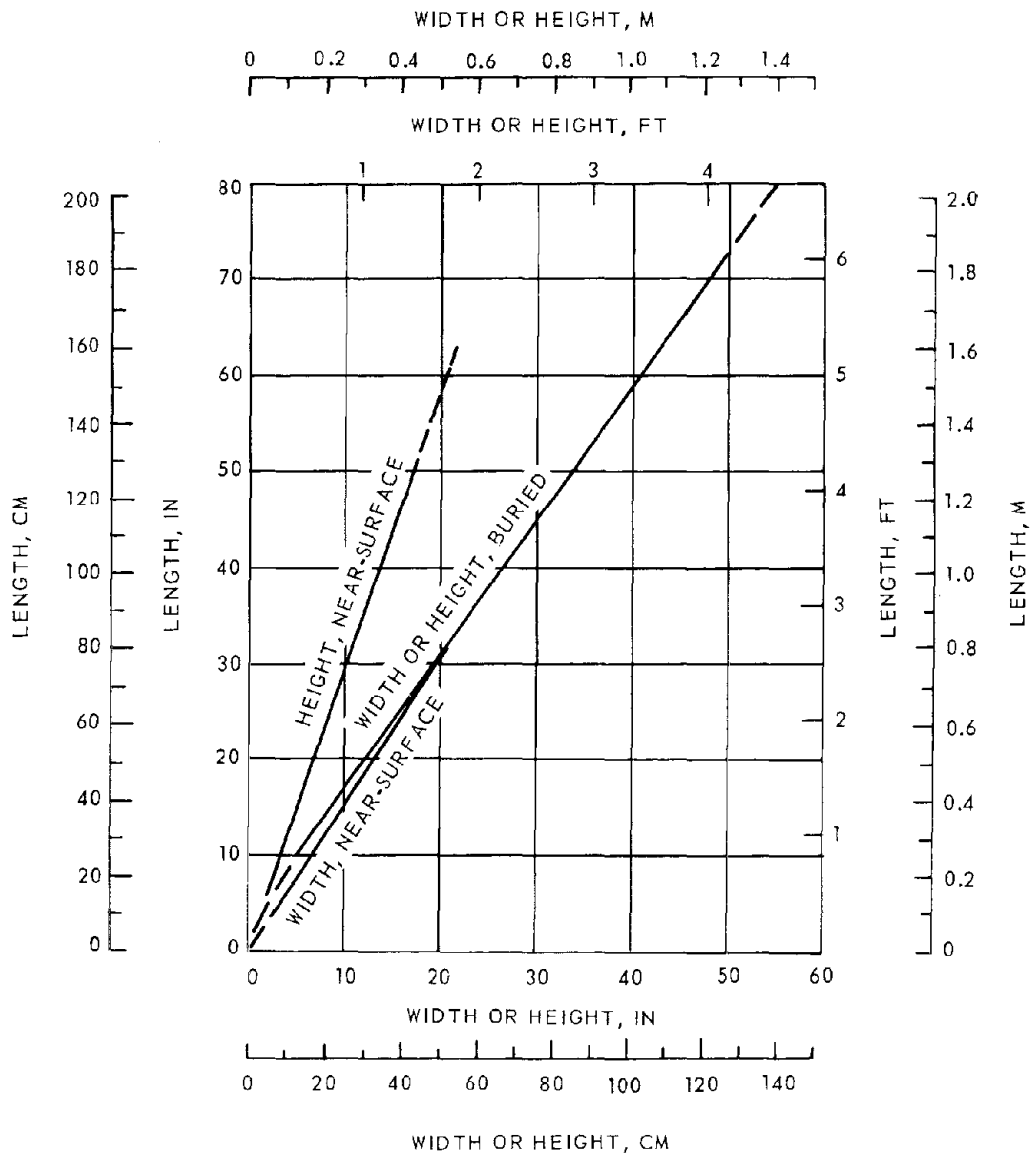
Figure IV-4.71. Ejecta particle dimensions for explosions in dense rock (Reference IV-4.51).
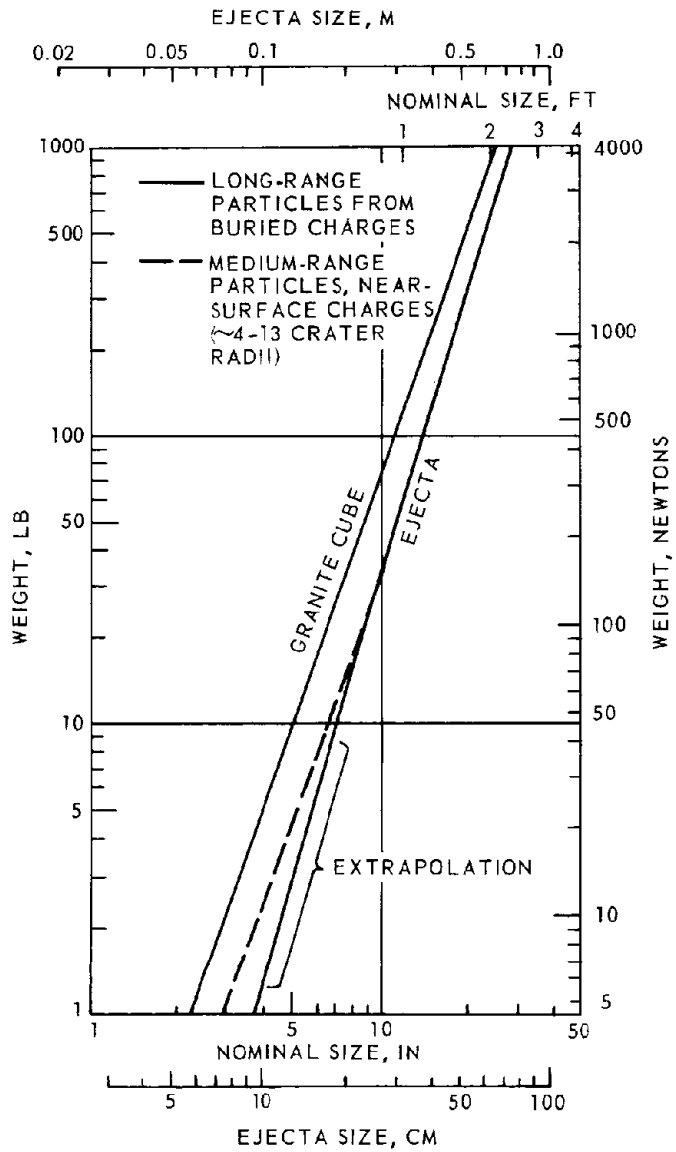
Figure IV-4.72. Ejecta size versus weight for dense rock (Reference IV-4.51).

(width), or that governing passage through a sieve. Hereafter, where no further description is given, the sizes shown are nominal. To these data have been added a few observations of large, fairly long-range particles of basalt from smaller, buried charges. This curve has been extrapolated below the 5 kilogram level. The differences exhibited by the two groups of data are insignificant above W_p perspective to 10 kilograms. Size-weight relations of a granite cube are included for comparison.

Analysis of post-impact missile ejecta indicate a trend toward increasing secondary breakage with increasing distance from GZ out to about 10 apparent crater radii, at which distance the breakage factor β (pre-impact size/post-impact size) appears to lie between 2 and 3. It is suspected that this ratio decreases at greater ranges, since particles found on the fringe of the ejecta field exhibit little evidence of secondary breakage. Only one published report on this topic is available for clay/shale (Reference IV-4.46), a photographic study of the in-flight ejecta field of the MIDDLE GUST III Event. Comparison of a rough average of the size versus numbers indicates a wide difference between pre- and post-impact size distributions, with $\beta \geq 4$. By contrast, unpublished results from a more recent experiment in a stratified, moist clay indicate $\beta \approx 4$ at similar ranges. Undoubtedly, moisture content influences secondary breakage, with relatively high moisture increasing particle plasticity, thereby decreasing secondary breakage. At this time, it only seems possible to say that secondary breakage is a significant consideration in the "as-found" ejecta fields of clay and shale media.

IV-4.3.6 Ejecta Deposition

The continuous ejecta usually extends from 2 to 4 apparent crater radii, R_a, from GZ, with maximum depth occurring at or near the lip crest. Maximum lip height above the original ground surface is approximately 1/5 to 1/4 the apparent crater depth, D_a, for buried bursts and 1/4 to 1/3 D_a for near-surface detonations. In general, the volume of ejecta deposited in the lip varies from about 40 to 90 percent of the total by weight, the latter value representing deeper burials. In the graphs developed by Rooke (Reference IV-4.51), the extent of the crater lip is estimated at 2.5 to 3 R_a.

Of the important parameters pertaining to the missile ejecta field, perhaps the simplest to determine, is the maximum recorded range for any particle.

Figure IV-4.73 (Reference IV-4.51) is one means of expressing this fact. Note that the range is scaled by the sixth root of charge weight W; this relation was first used by Vortman (Reference IV-4.88). No theoretical justification seems apparent. The graph has been constructed so that all data points fall below the curves. Relatively smooth envelopes were obtained by Rooke (Reference IV-4.51) despite the differences in cratered media. The maximum ordinates indicate an optimum DOB for scaled range $Z \approx -0.5$ ft/lb$^{1/3}$. A useful variation of the information contained in Figure IV-4.73 is that of maximum range as a function of post-impact particle size which is shown in Figure IV-4.74. Both ordinate and abscissa are dimensionless in this figure, thereby eliminating doubts associated with artificial scaling exponents. It contains a rough comparison of both dense rock and softer, cohesive material, as well as effects of DOB. For dense rock, the data base consists of a least-squares fit of near-surface data in basalt and granite,
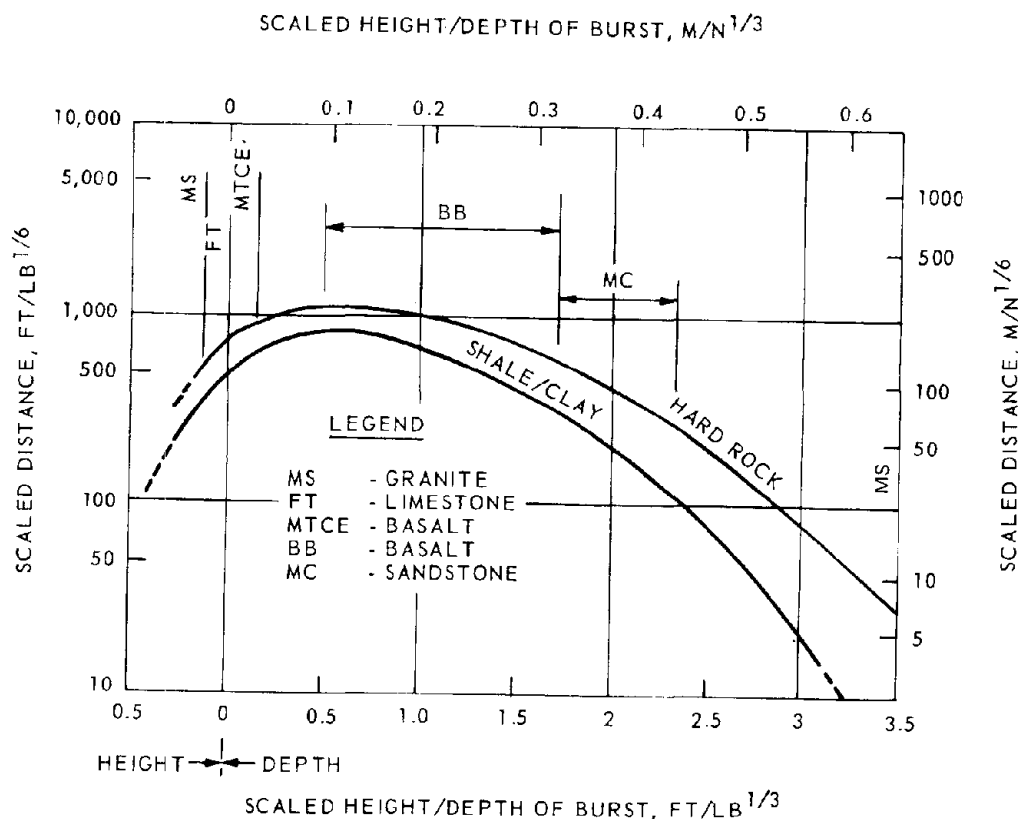
Figure IV-4.73. Maximum scaled distance for crater ejecta (Reference IV-4.51).
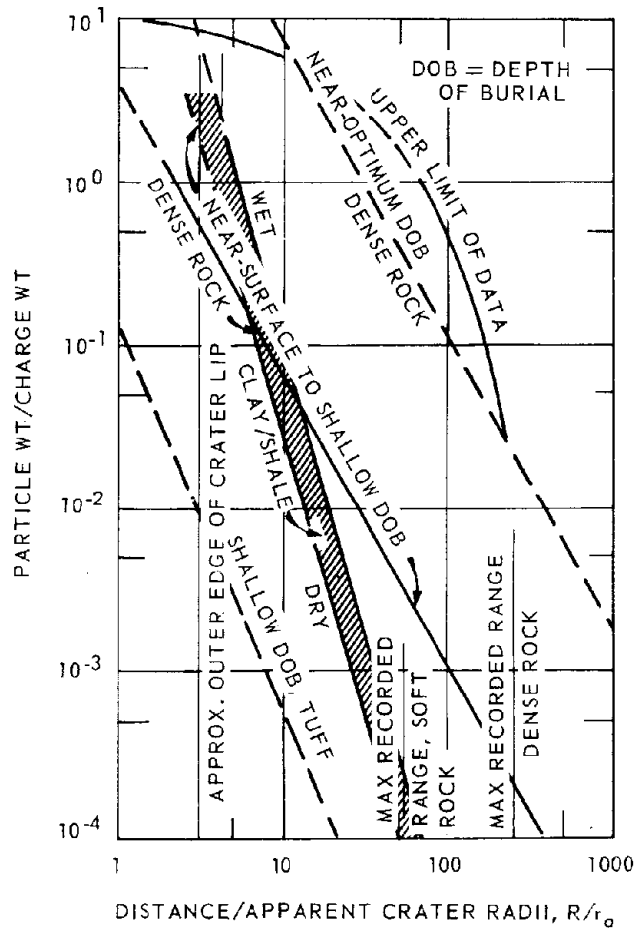
Figure IV-4.74. Maximum range versus size for
ejecta particles, all data.
(Except for the upper limit
envelope, average maxima are
depicted as obtained by fit-
ting curves to scattered data
points.) (Reference IV-4.51)

with the near-optimum curve ($Z \approx -1.5$ ft/lb$^{1/3}$, in this case) being visually fitted to a few data points in dense sandstone. The remaining data include "soft" rocks and clays, and consist of: (1) least-squares fits of observations in dry and wet clays, shales, and combinations of clays and shale, and (2) a visual fit of the SCHOONER tuff data based upon assumed nominal sizes and weights. The limitations of this graph typify those inherent in ejecta data in general. With the exception of the upper limit curve, enveloping all data, the curves are intended to depict <u>average</u> maxima, or the maximum ranges to be <u>expected</u>, as opposed to maximum ranges recorded.

IV-4.3.7 Areal Density and Total Ejecta Weight

A parameter often used for ejecta deposition is that of the areal density δ in units of weight-per-unit-area deposited beyond the crater lip. The areal density shown on Figure IV-4.75 is based on an earlier similar graph (Reference IV-4.53) with new data added (Reference IV-4.51).

Areal density measurements are usually made from prepared surfaces positioned in a circular pattern centered on GZ and at various radial distances. These measurements are subject to considerable errors especially at distances where dust deposition, other than ejecta, by the blast wave may represent a significant amount of the total deposit. Circumferential variations in the deposition can be large also. However, comparison of the averages of many such observations provide a recognizable pattern, and this sampling procedure is used as one means of determining the total weight of ejected material at a given location. A straight-line fit is constructed to fit the measured sample using a least-squares method, as shown in Figure IV-4.76, integrating the equation

$$\delta = CR^{-m} , \qquad\qquad\qquad\text{(IV-4.21)}$$

and mathematically rotating the integral through 2π radians. Here C and m are coefficients resulting from the least-squares fit to the data. The ejecta weight is then given by

$$M_e = 2\pi \int_{R_{econ}}^{R_{emax}} (CR^{-m}) R\,dR \qquad\qquad \text{(IV-4.22)}$$
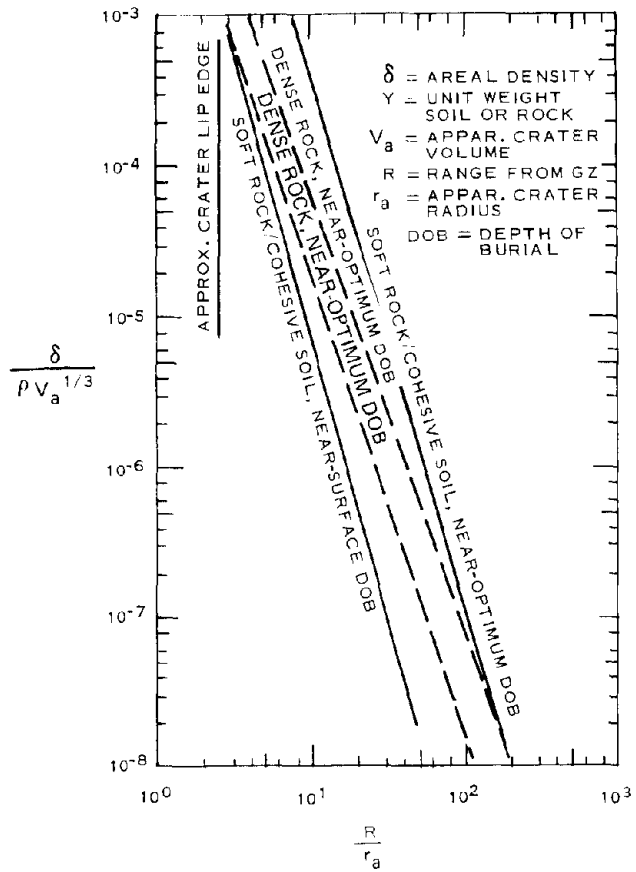
Figure IV-4.75. Ejecta areal density parameters (Reference IV-4.51).
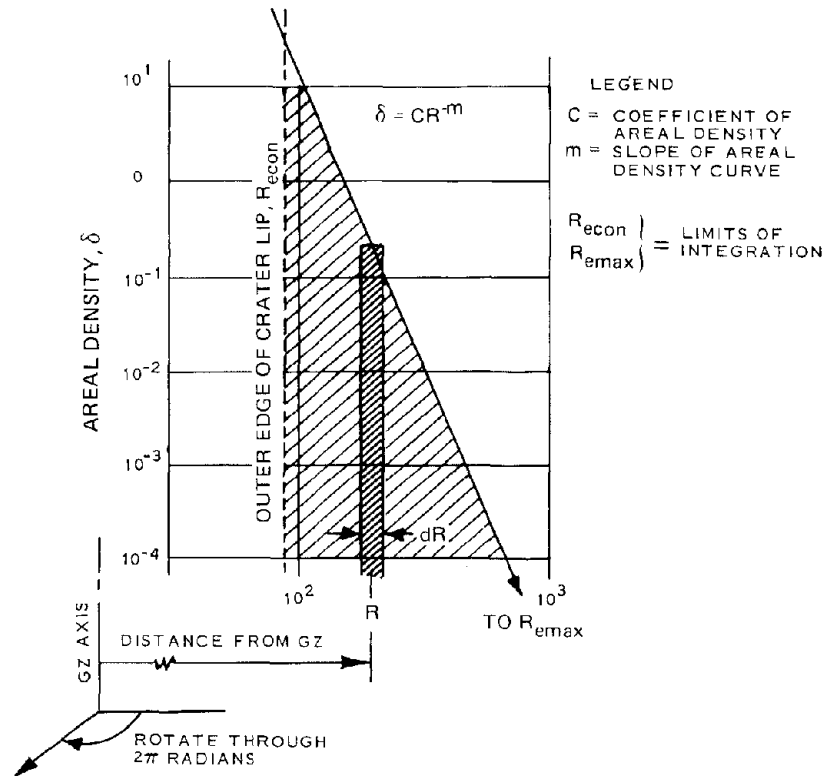
Figure IV-4.76. Concept of ejecta weight determinations (Reference IV-4.51).

where R_{econ} is the lower limit or the outer edge of the crater lip and R_{emax} is the maximum range of the continuous ejecta. This type of data fit is usually satisfactory between the outer edge of the crater lip and the range at which particulate material is essentially windborne. It is often necessary to obtain the lip volume or weight by isopach contours and the windborne material can then usually be neglected since the procedure itself introduces large uncertainties. The outer limit R_{emax} is the maximum recorded range of the ejecta. However, setting $R_{emax} = \infty$ usually introduces only a small error.

The other method of finding the total ejecta weight involves a complete study of the true crater and a balancing of volumes resulting from the crater-forming mechanisms of compaction, plastic flow, ejection, and for nuclear events, vaporization (Reference IV-4.53). When such a study can be conducted, it probably provides more reliable ejecta weight data than the sampling procedure. The best available data of this type are listed in Tables IV-4.28 through IV-4.30.

The integrand of Equation IV-4.22 giving M_e above can be arranged to solve for the range R_p within which some specified percentage of the total ejecta weight E_{wp} might be expected to fall, or

$$R_p = \left\{ \frac{(E_{wp})^{-m+2}}{2\pi C} + a^{-m+2} \right\}^{1/(-m+2)} \tag{IV-4.23}$$

where the symbols are as defined above and a represents the limit of integration designating the radial distance from GZ at which the integration begins.

This has been done by Rooke (Reference IV-4.51), and is shown in Figures IV-4.77 and IV-4.78 for dense rock and other cohesive materials, respectively, using the δ expressions given in Tables IV-4.28 through IV-4.30. A surprising number of these expressions yielded unrealistic results, casting doubts upon their validity. The graphical format chosen for this is that of logarithmic probability, long used in industrial rock crushing (Reference IV-4.89).
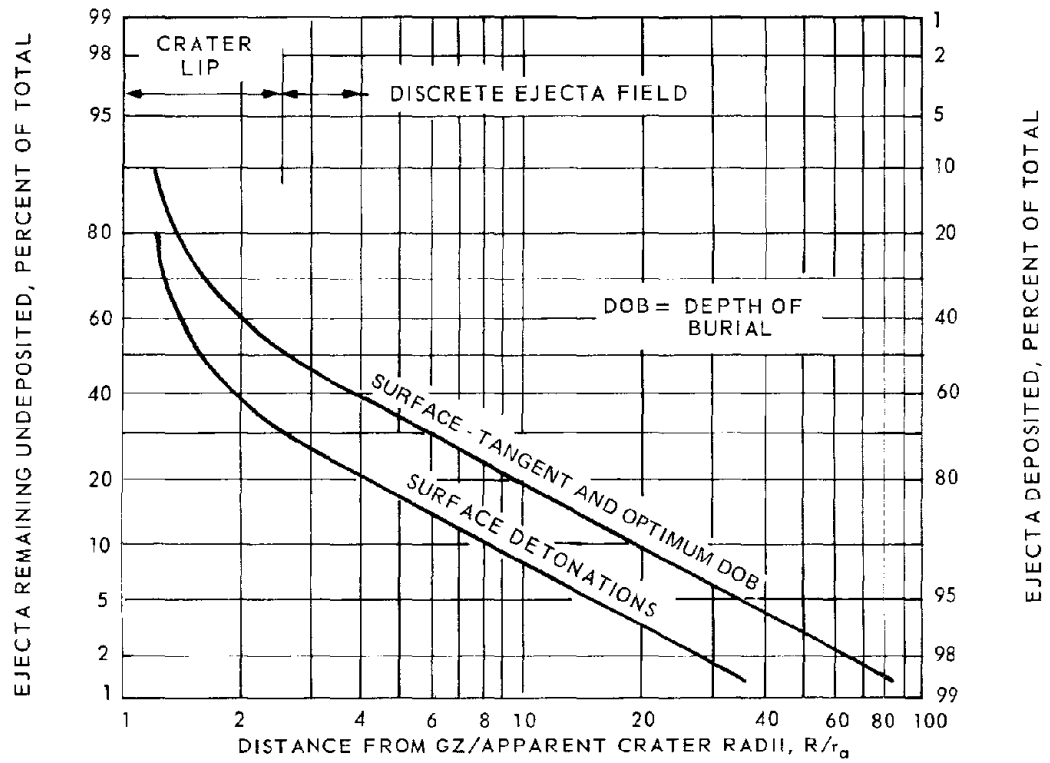
Figure IV-4.77.   Ejecta distribution in dense rock (Reference IV-4.51).
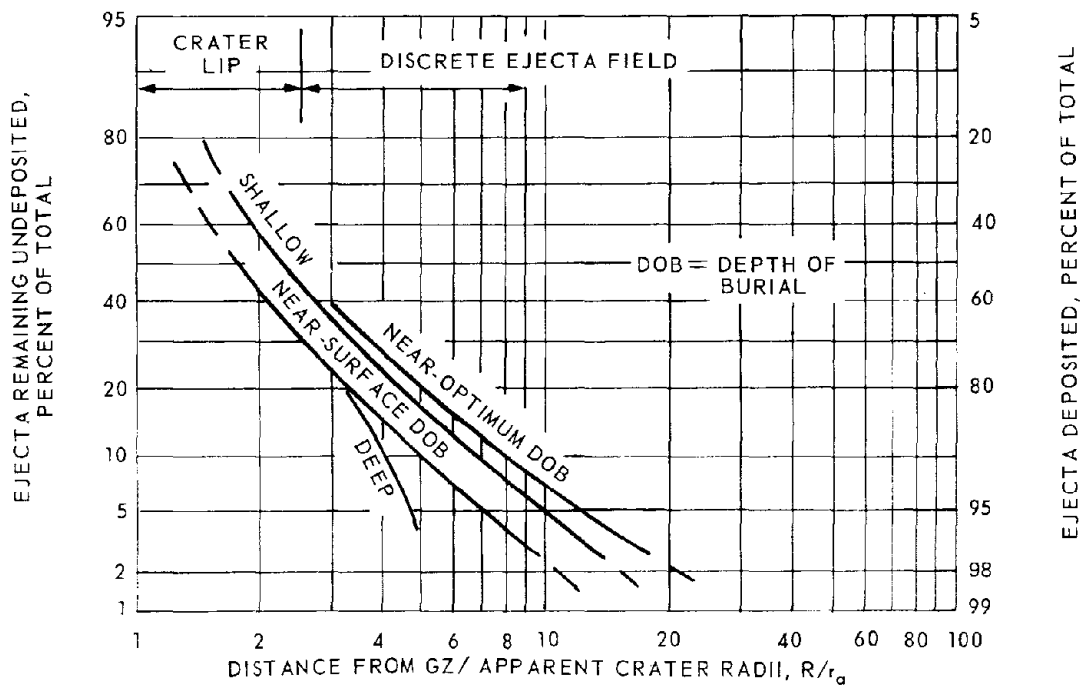
Figure IV-4.78.   Ejecta distribution in soft rock and cohesive
                  soil (Reference IV-4.51).

IV-4.3.8 Particle-Size Distribution

Post-impact particle sizes vary as a result of shot conditions and distance
from GZ, but no comprehensive research has attempted to embrace all of the varia-
bles, and the relations remain tenuous. A wide range of charge yields may produce
indiscernible differences in particle-size distributions. In order to compare
events of different conditions, several means of scaling nominal particle sizes
were investigated by Rooke (Reference IV-4.51) and the dimensionless parameter
$s/V_a^{1/3}$ was tentatively adopted, where V_a is the apparent crater volume and s is
the particle size. Again, the logarithmic probability graph was used for this
purpose in Figures IV-4.79 through IV-4.81, data points being fitted visually.
All events in Tables IV-4.28 through IV-4.30 having suitable size distribution data
were used. The results differed markedly from one event to the next, and the
curves of Figures IV-4.79 through IV-4.81 should be regarded as tentative indica-
tors of data trends only. More research is obviously needed to establish a better
scaling parameter (Reference IV-4.51).

The scaling procedure discussed above appears suitable, at least as an interim
measure, for the prediction of particle-size distributions. The graphs show that
scaled particle size for a given percentage on the ordinate decreases with
increasing charge size. The greatest variation in scaled particle size occurs in
near-surface detonations in dense rock and the least in buried explosions in soft
rock. In all cases, the data suggested logarithmic fitting between charge sizes.
The slopes which most nearly fit the data in both near-surface and near-optimum
DOB cases are quite similar, but differ between hard and soft rock. For the
smaller particles associated with the larger charges, the curves are observed to
bend in a concave, upward fashion. Here again, considerable difference was noted
in the data. Concerning the decrease in mean particle size which occurs with
increased range from GZ, the intervals shown in Figures IV-4.79 and IV-4.81 should
be applied; no suitable data could be found for the curves of Figure IV-4.80.
As an aid to obtaining a "feel" for the actual particle sizes represented by the
graphs, particle weights represented by the curves have been included. Thus,
Figure IV-4.79, for example, shows that for a 100-ton surface-tangent burst in
dense rock (explosive charge sphere resting on ground surface), more than 80 per-
cent by weight of the ejecta deposited beyond the outer edge of the crater lip but
within a distance of 15 crater radii from GZ are smaller than 5 kilograms. For
similar conditions at the 1-ton charge size, only 10 percent are smaller than 5
kilograms.
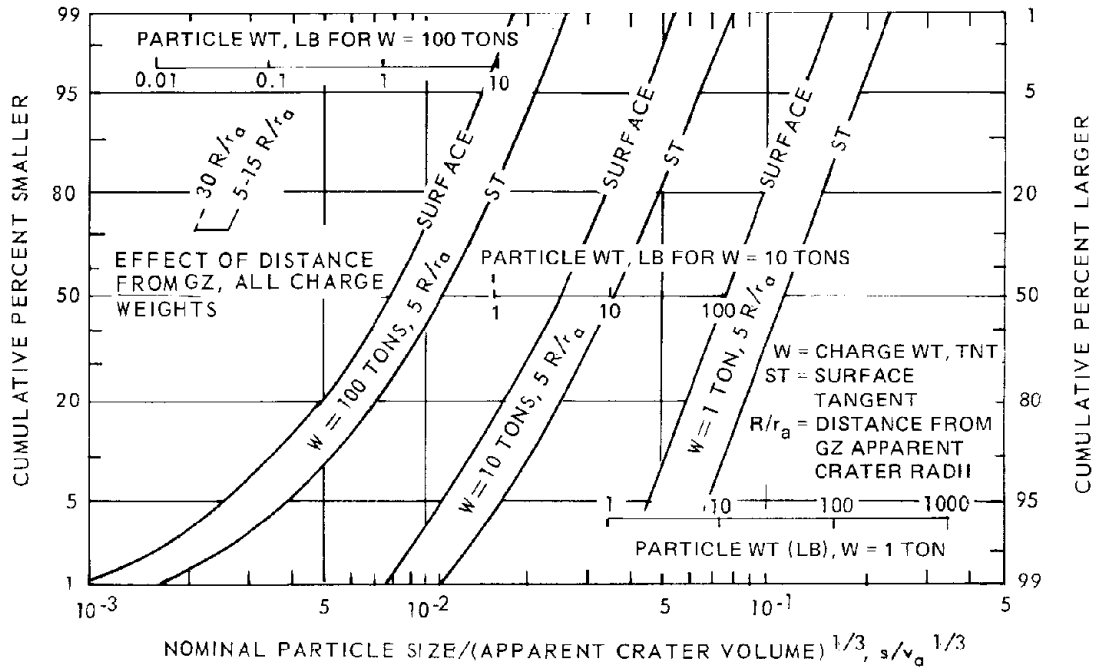
Figure IV-4.79. Ejecta size distributions, near-surface detonations in dense rock. (Graph illustrates general data trends only.) (Reference IV-4.51)
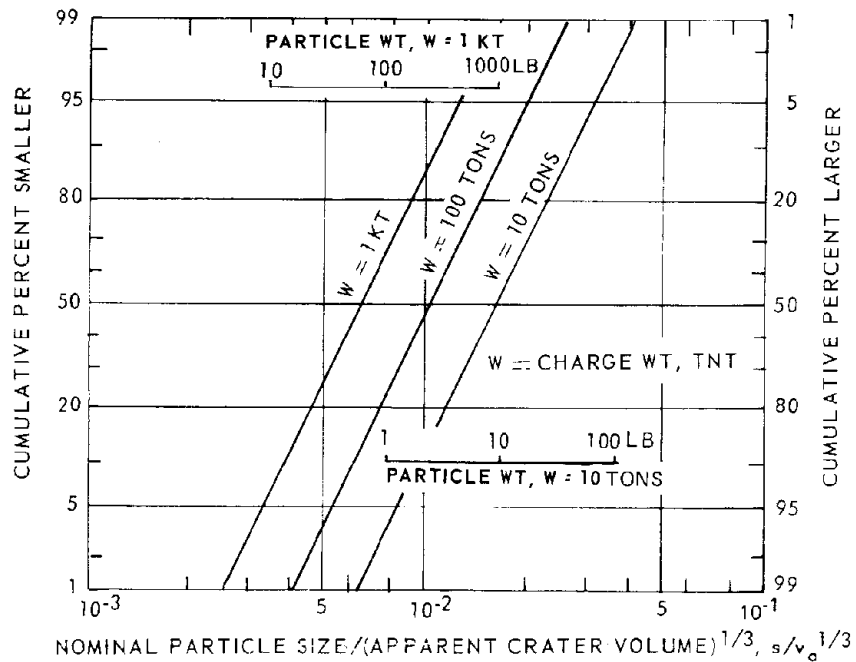
Figure IV-4.80. Ejecta size distributions, near-optimum depth of burial, dense rock. (Graph illustrates general data trends only.) (Reference IV-4.51)
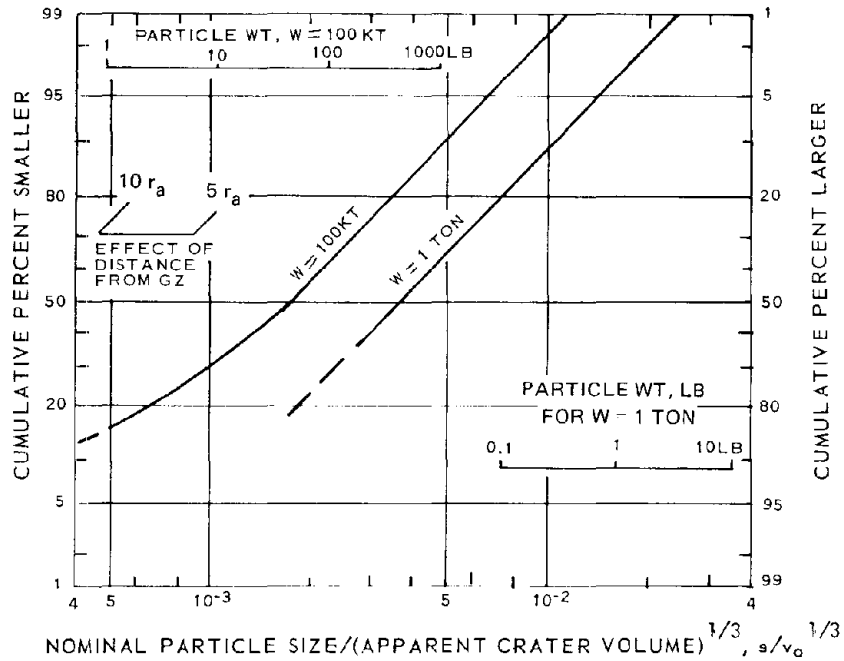
Figure IV-4.81. Ejecta size distributions, shallow to medium depth of burial, soft rock. (Graph illustrates general data trends only.) (Reference IV-4.51)

A detailed survey of size distributions of soil samples obtained from past nuclear and chemical explosions for surface or slightly buried devices was undertaken by Seebaugh (Reference IV-4.85). This survey is concerned only with the relative distribution of dust and ejecta mass with size and not with the total mass of crater material. A limitation on the survey is the soil type. Hence, studies of the size distributions from cratering shots in coral are excluded. A significant fraction of the data comes from HE simulations events which, while not reproducing the very high overpressure levels generated by a nuclear burst in crater formation, provide useful data.

At present, ejecta environment models utilize a power-law size distribution of the type a^{-n}. For a cohesive soil, such as clay, rock, basalt, and shale, the differential number density distribution is given by (Reference IV-4.85)

$$\frac{dn}{da} \sim a^{-3/5}.$$

(IV-4.24)

Assuming that the particles are spherical with a size-independent bulk density, the differential mass density distribution becomes

$$\frac{dm}{da} \sim a^{-0.5}.$$

(IV-4.25)

The cumulative mass $M(a)$, that is, the mass of all particles smaller than a given diameter, is obtained from

$$M(a) = \int_{a_{min}}^{a} (\frac{dm}{da}) \, da' \sim (\sqrt{a} - \sqrt{a_{min}})$$

(IV-4.26)

where a_{min} is the minimum size in the distribution.

The size distributions that resulted from analyzing the data from five cratering shots at the NTS were compared in Reference IV-4.59. These events were DANNY BOY, CABRIOLET, SULKY, PRE-SCHOONER, CHARLIE, and DUGOUT. Samples of ejecta fragments or crater fallback material were analyzed. The size distributions are shown in Figure IV-4.82 as cumulative weight fraction versus particle diameter. Except for CABRIOLET, which was detonated in rhyolite, the soil type was basalt. Except for DANNY BOY, the lower limit on particle size was 3 centimeters. In all five cases considered, the curves are approximately linear below 20 centimeters, which indicates a power-law dependence of the form

$$CM = Ka^b$$

(IV-4.27)

where CM is the cumulative weight fraction, K is a constant, and a is the particle diameter. Currently, ejecta models use b = 0.5 for cohesive soils. In contrast, these data indicate that b ranges from 0.39 for CABRIOLET to 1.1 for PRE-SCHOONER, CHARLIE and SULKY. As noted from the burst parameters indicated on the figure, there is no apparent correlation of b with the type of explosion, that is, nuclear or HE. The data for DANNY BOY offer the most convincing evidence for a simple power-law distribution. However, Linnerud (Reference IV-4.46) points out in Figures IV-4.83 and IV-4.84, which present data from two HE tests, DIAL PACK and MIDDLE GUST III, that the power law discussed by Seebaugh is not valid for these two events because these distributions have been modified during flight by
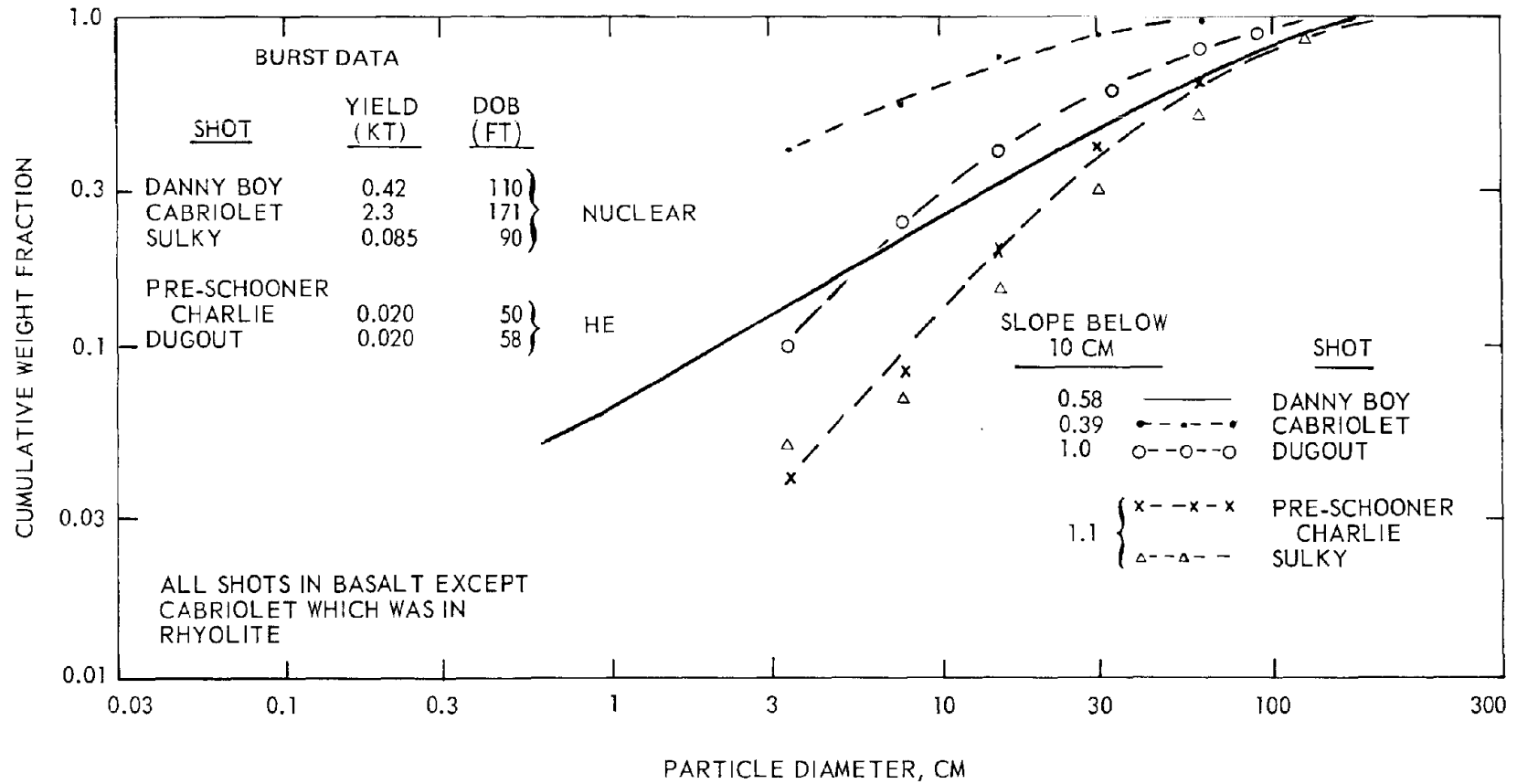
Figure IV-4.82. Size distributions for five NTS shots (Reference IV-4.85).

The graph shows:

- Y-axis: CUMULATIVE MASS FRACTION (from 0.003 to 1.0)
- X-axis: DIAMETER, CM (from 0.001 to 1.0)

AIRCRAFT SAMPLE
PASS #1

DASHED CURVE - LOG NORMAL

$x_o = \log_{10} (0.003)$

$\sigma = 0.3$

$$CM \, (a < 0.018) = 0.0208 \int_{-\infty}^{y} \frac{1}{\sqrt{2\pi}} e^{-y^2/2} dy$$

$$y = \frac{\log_{10}(a) - x_o - 3 \ln 10 \sigma^2}{\sigma}$$

SOLID CURVE - POWER LAW

$Slope = 0.5$
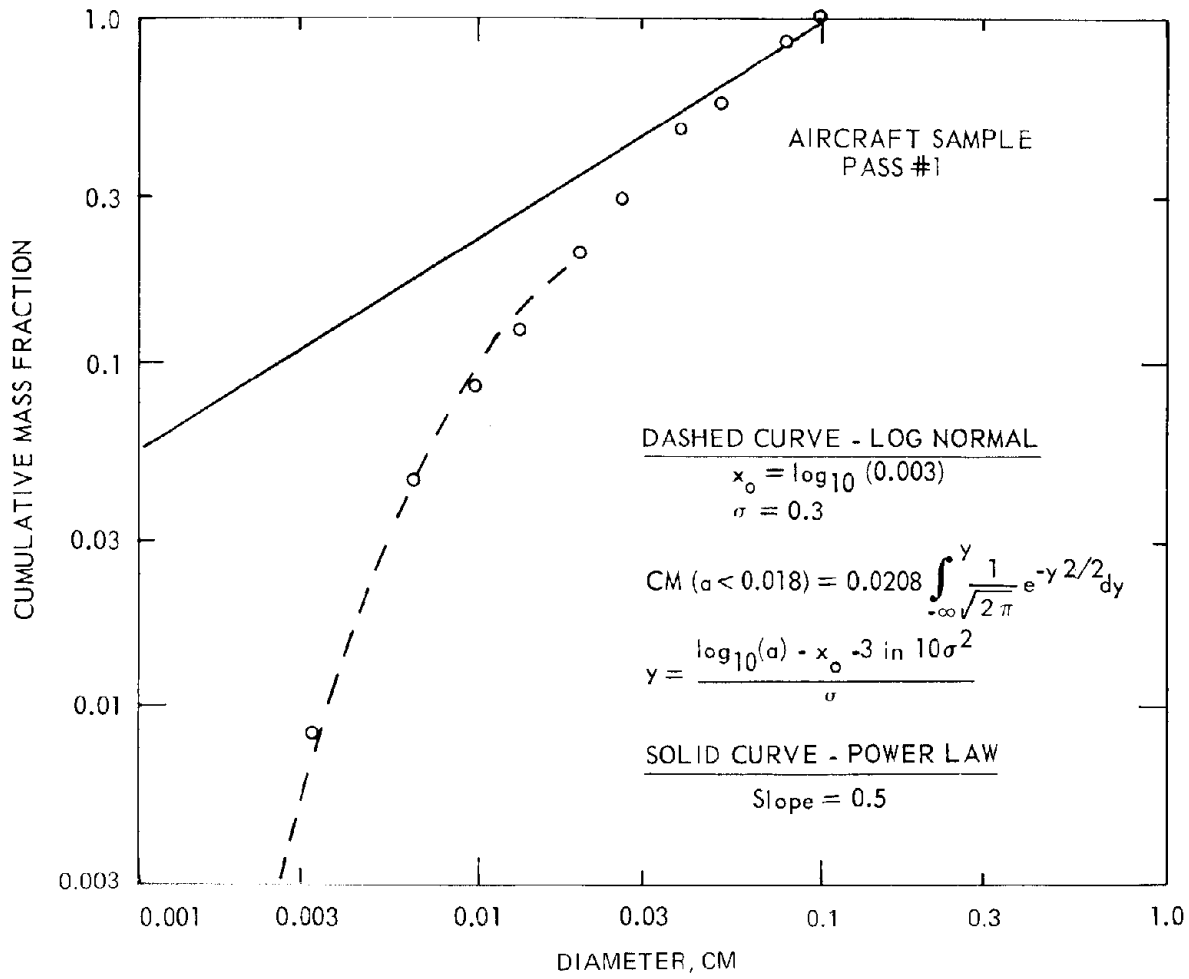
Figure IV-4.83. MIDDLE GUST III size distribution (Reference IV-4.46).

AIRCRAFT SAMPLING
(LASL-288, PASS #2)

SOLID CURVE - LOG NORMAL
$x_o = \log_{10} (0.002)$
$\sigma = 0.3$

DASHED CURVE - LOG NORMAL
$x_o = \log_{10} (0.003)$
$\sigma = 0.3$

DOT-DASHED CURVE - POWER LAW
Slope $= 0.5$
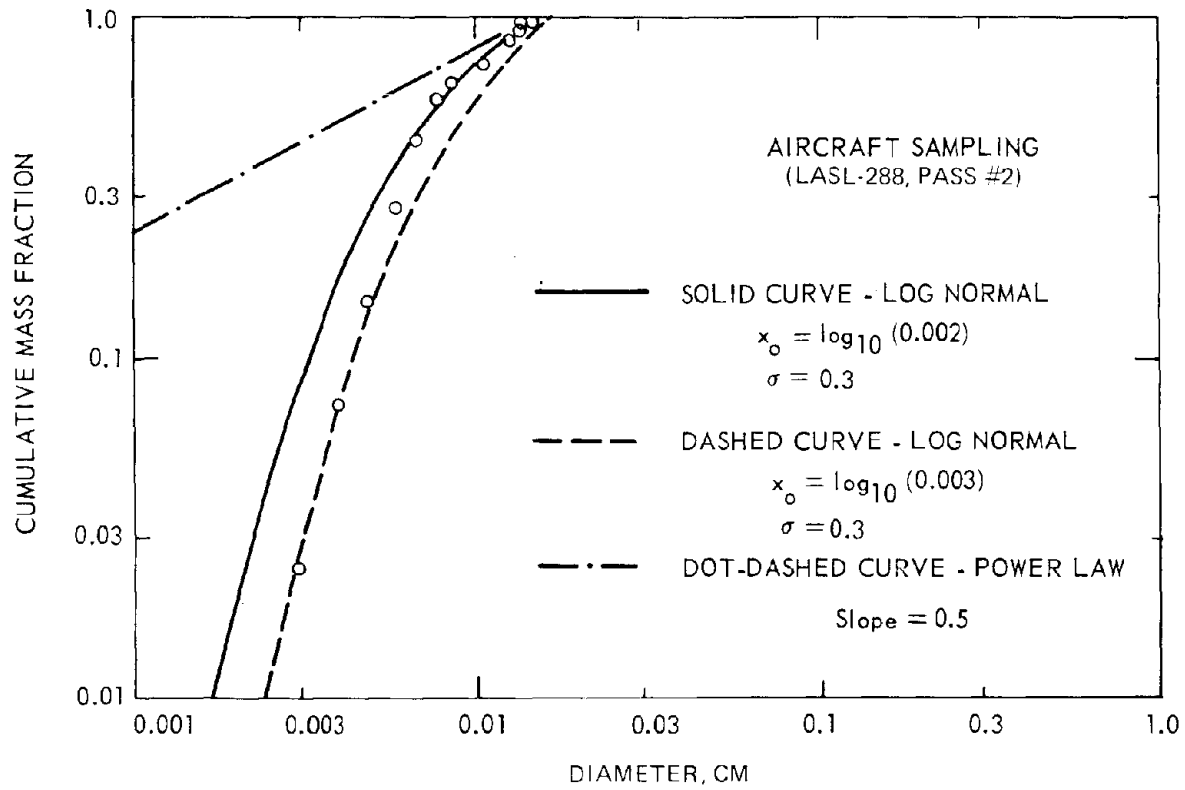
Figure IV-4.84. DIAL PACK size distribution (Reference IV-4.46).

particle differential settling. (DIAL PACK was a 500-ton surface-tangent sphere of HE.) The data presented in these figures do not lend support to the currently employed power law $a^{-3.5}$ for the ejecta-size distribution. (See subsection IV-4.2.1 which discusses the MIDDLE GUST Events.)

Event MINERAL ROCK of the MINE SHAFT Series was a 100-ton HE shot in granite at an HOB equal to 90 percent of the charge radius. Ejecta samples (Reference IV-4.90) were obtained at 3-meter intervals, starting at a ground range of 34 meters. After attempting to eliminate preshot contamination by visual estimates, the samples were sieved into five intervals with end points of 0.0041, 0.083, 0.17, 0.47, 0.72, and 1.44 centimeters. A mean size was determined for each interval for an equivalent sphere (by weight) after analyzing the shapes of the ejecta particles. A simple power law does not adequately describe the size distributions for any of the individual samples. The value of b (defined in Equation IV-4.27) for the second and third intervals combined (0.083 to 0.47 cm) is much higher than expected and higher than that observed for the first and second intervals (0.0041 to 0.17 cm) and for the third and fourth intervals (0.17 to 0.72 cm). This is shown in Figure IV-4.85, where the ground range dependence of the three slopes is indicated. From 0.0041 to 0.17 centimeter the average value of b is 0.69 ± 0.22, while from 0.17 to 0.72 centimeter it is 0.75 ± 0.40. In this latter size range there is some indication of a ground range dependency. The anomaly in the intermediate size range is probably due to a bias in the experimental procedure.

The PILEDRIVER Event was an underground nuclear detonation at a depth of 457 meters in granite with a yield of 61 kt. Two samples of chimney rubble were sized (Reference IV-4.91) and the resulting cumulative weight fractions are shown in Figure IV-4.86. This analysis covers a much wider particle-size interval and $\sigma = 0.3$. This is indicated on Figure IV-4.87 by the dashed curve for less than 0.018 centimeter. This type of behavior has been observed in other experiments. There is strong evidence that the lower end of the spectrum exhibits a steeper slope in the cumulative mass versus size that is best fit by a log-normal distribution with a median diameter of 0.002 centimeter and a standard deviation of 0.3.

IV-4.3.9 Maximum Particle Size

In the previous subsection it has been shown that the fragment-size distribution function for cratering in hard rock has a fixed form. The possible variation in exponent is reasonably well bounded. Another question is related to the large particle cutoff of the distribution, that is, what is the maximum particle
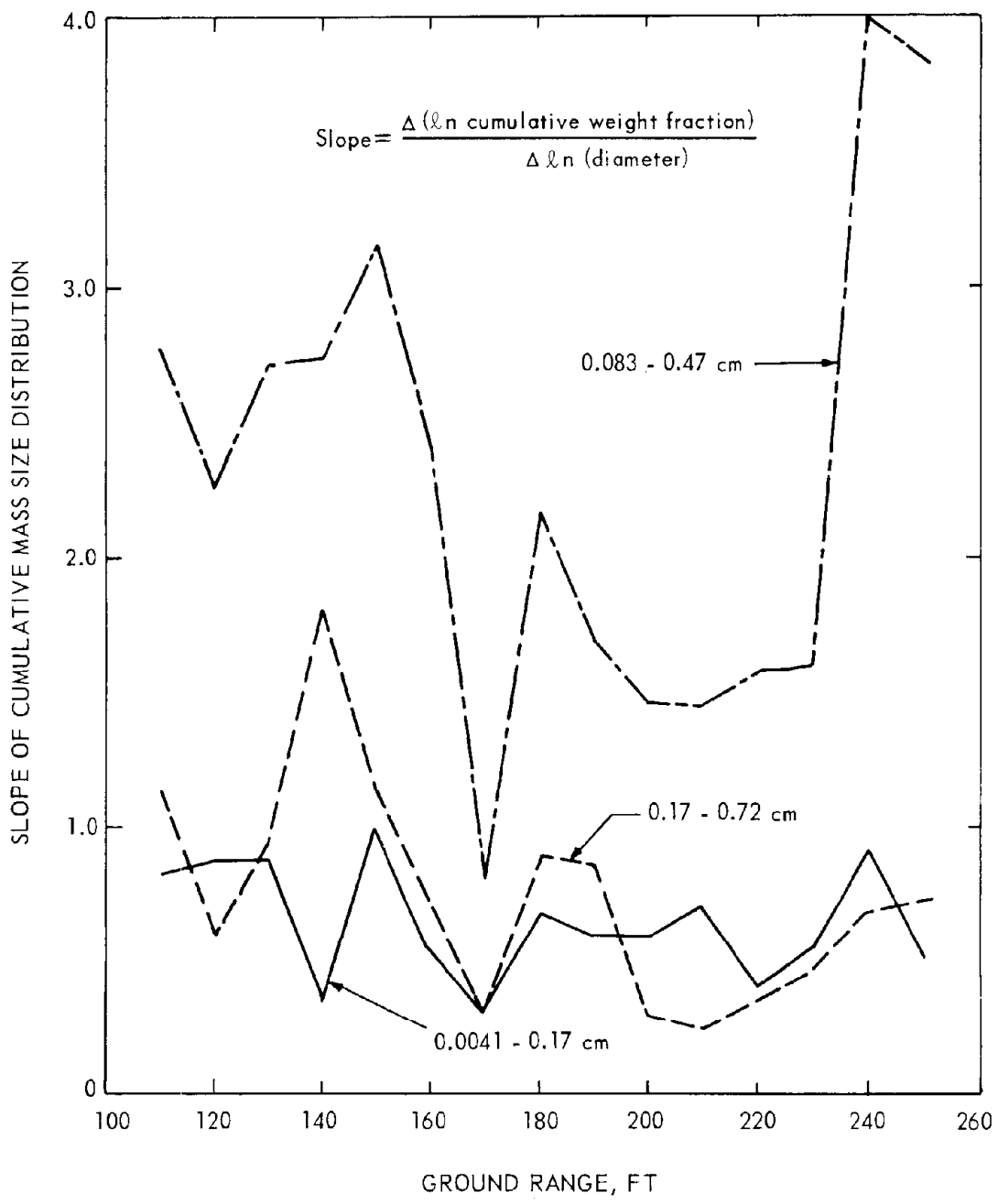
Figure IV-4.85. Slope of MINERAL ROCK size distributions (Reference IV-4.85).
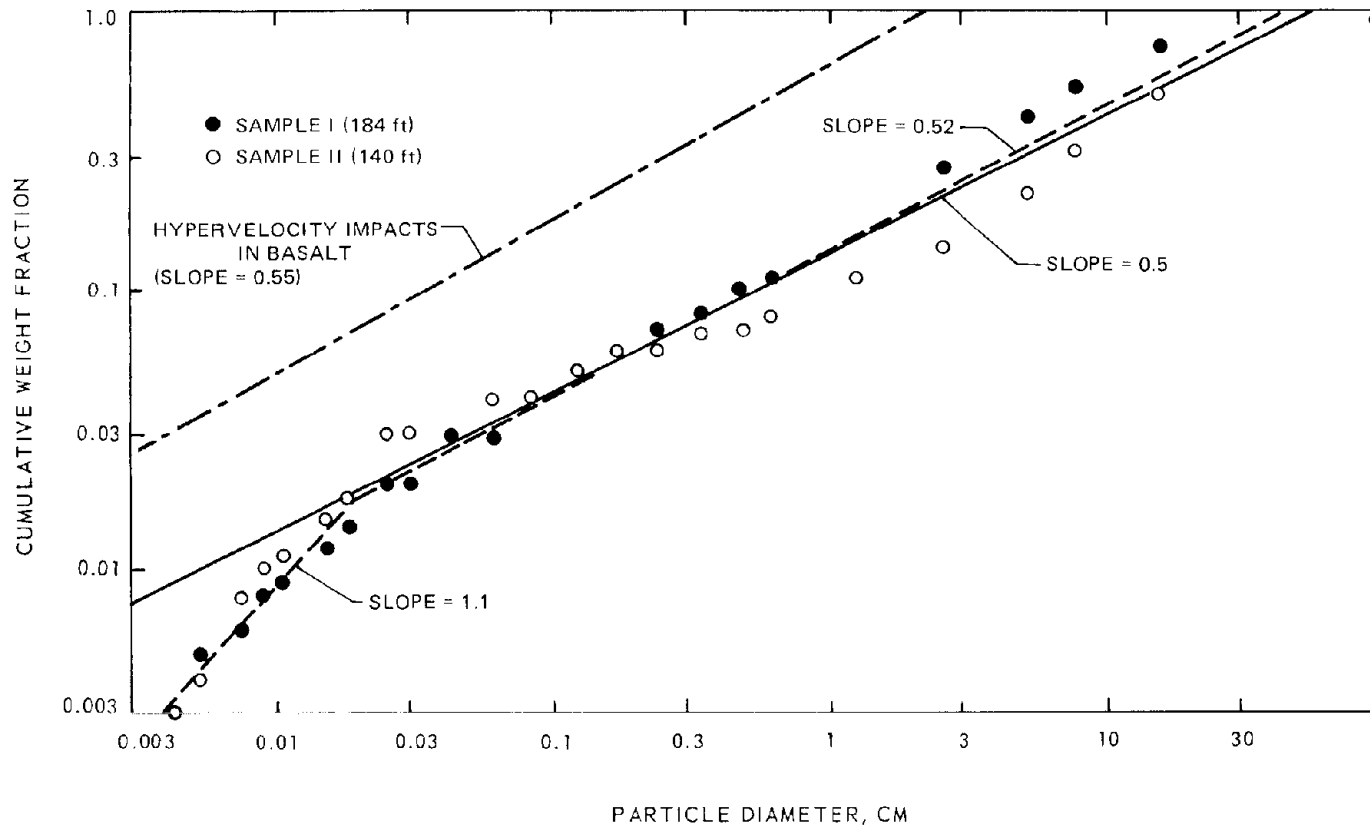
Figure IV-4.86. Size distribution for PILEDRIVER chimney rubble (Reference IV-4.85).
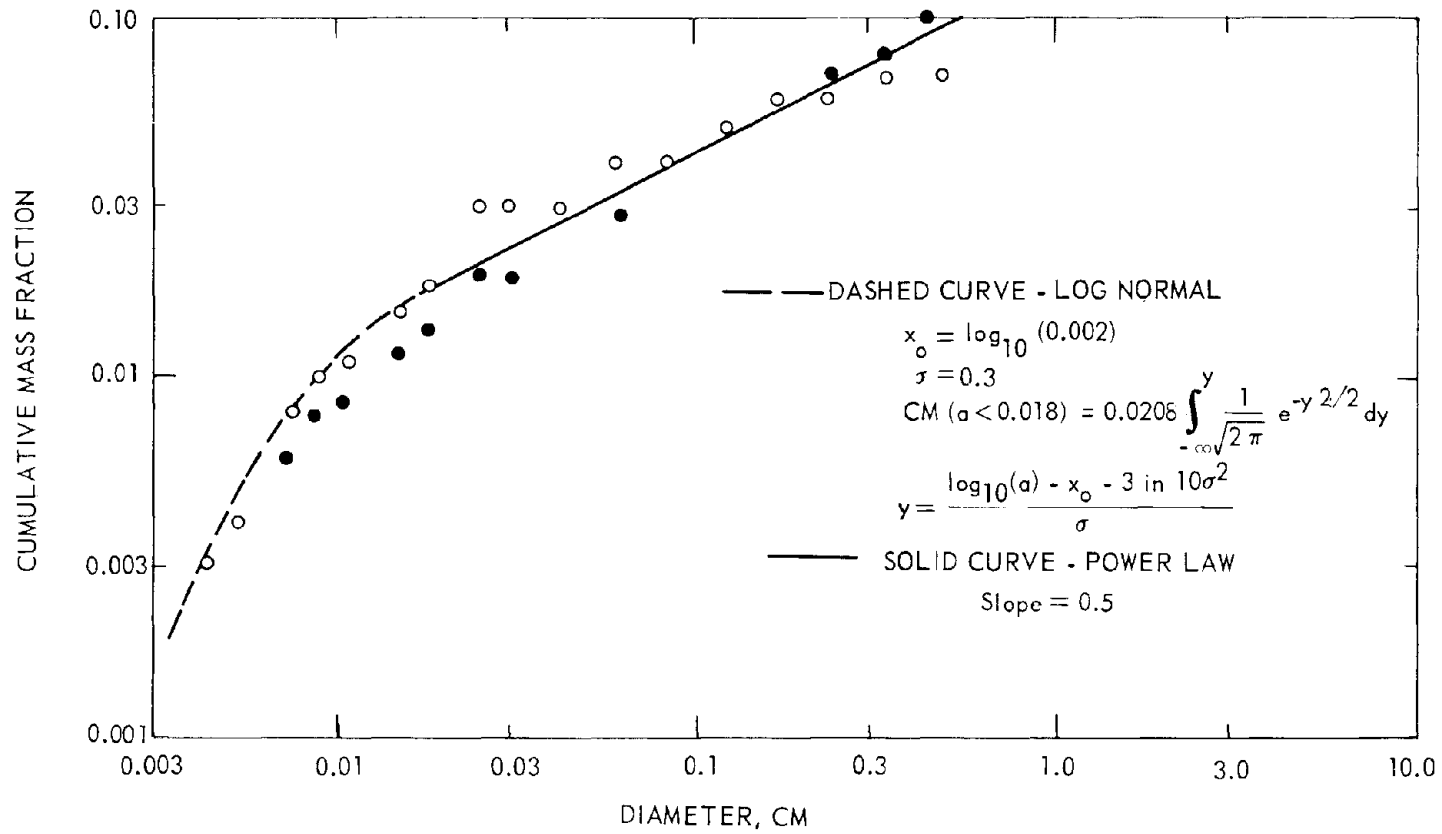
Figure IV-4.87.   PILEDRIVER size distribution (Reference IV-4.85).

size which can be expected for given cratering conditions? Fortunately, this question has a rather precise answer for cratering in hard rock. Gault (Reference IV-4.92) and Moore et al. (Reference IV-4.93) compiled relevant data from hypervelocity impact experiments, HE and nuclear detonation events, and natural meteor craters on earth have demonstrated that for kiloton and megaton explosive yields the maximum particle size, m_{max}, is given by

$$m_{max} \ (g) \simeq 0.2 \ [M_e \ (g)]^{0.8}, \qquad\qquad (IV-4.28)$$

where masses are in grams. More recent data from exploration of lunar craters by Surveyor confirms this relationship. Figure IV-4.88 illustrates the above relationship.

There is no suggestion from the data that the maximum particle size for soil crater ejecta is yield-dependent. Material properties dominate instead. In the case of a compressive and cohesive soil, the production of large particles is understandable. For desert alluvium, some of the large particles may simply be rock boulders which were present initially. However, in soil, such large particles occur with very-low frequency. The explosion may increase the number of large particles slightly, but most of the ejecta mass consists of subcentimeter particles. The concept of maximum particle size in soil does not have the same importance it has for cratering in hard rock.

IV-4.4 SUMMARY OF SOME COMPUTATIONAL METHODS

This section presents a discussion of some of the computational tools available to determine the ejecta field. The discussion proceeds with a description of the ejecta models and computer codes that may be of interest to the reader. This discussion is sometimes unavoidably sketchy because little detailed information was available to the author at the time of writing. However, with the use of the references, the reader can find the full description of the codes of interest to him. In some cases, while the modeling could be discussed adequately, little or no information was available to the author about the computer codes themselves.

The ejecta models discussed are, with some exceptions, restricted in their use to homogeneous and isotropic soil or rock and assume the burst to occur very near the surface. All models are based on HE test data. They are then extrapolated in their use to megaton-size weapon yields, usually a few megatons.
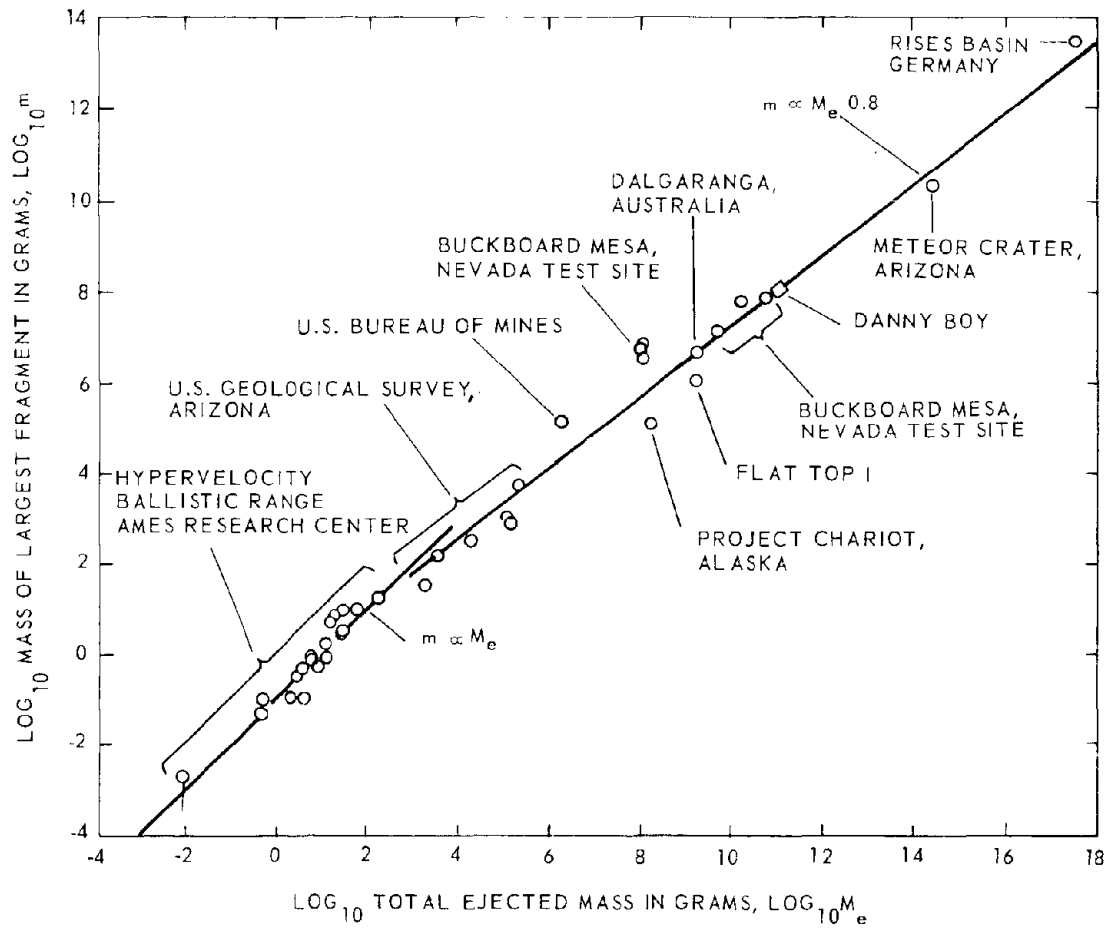
Figure IV-4.88. Mass of the largest fragment versus total ejected mass for explosive and impact cratering events (Reference IV-4.92).

Now, this kind of extrapolation is very large indeed considering that the data pertain to detonations involving at the most 500 tons of TNT. In some models the data base is the 20-ton FLAT TOP I and II Events. Recently, however, some attempts have been made to use early near-surface events as the data base for detailed ejecta computations. This obviously imperfect state of affairs in extrapolating to megaton yield results from the fact that there is no data for ejecta from megaton-size detonations on or near the ground. The work done under the PLOWSHARE Program is only peripherally applicable because it mainly concerns shots buried at a depth to maximize crater dimension.

The problem of the description of particle trajectories in a gravitational force field has interested mathematicians, physicists and military engineers since the invention of guns. The problem of finding the trajectory of a point mass where the only force is that of gravitation is a simple one. When the effects of air drag are included in the equations of motions, no easy analytical solution is possible. A simple analytical solution is obtained only after some simplifying assumptions have been made in the equations of motions and their integrals. MacMillan (Reference IV-4.94) describes the difficulties aptly by saying:

> "But if a projectile is moving in a medium such as the air,
> the surface of the projectile is acted upon by the pressure
> of the medium, and the nature of that pressure varies in a
> very complicated way with the nature of the medium, the
> shape of the projectile, the distribution of the mass within
> it, its orientation, its rate of spin, and its axis of spin.
> The problem is an extremely complicated one and forms the
> subject matter of exterior ballistics.

> If, however, the projectile is a homogeneous sphere not rota-
> ting, and the resisting medium is at rest, the projectile can
> be regarded as a particle which is acted upon by a force which
> in magnitude is some function of the speed of the projectile
> and which has a direction opposite to the velocity of the
> projectile."

According to the last paragraph then, the balance of forces on the particle gives

$$\frac{dv}{dt} = -g\,[\sin\theta + \phi(v)] \qquad\qquad (IV\text{-}4.29)$$

and

$$v\frac{d\theta}{dt} = -g \cos \theta \qquad \text{(IV-4.30)}$$

where v is the instantaneous velocity, θ is the instantaneous angle the velocity vector of the projectile makes with the horizontal, and $\phi(v)$ is the velocity function. The time can be eliminated between these two equations to give

$$\frac{1}{v}\frac{dv}{d\theta} = \tan \theta + \phi(v) \sec \theta \qquad \text{(IV-4.31)}$$

Legendre, in the early 19th century, analyzed the integrable case when the function $\phi(v)$ is of the form (Reference IV-4.99)

$$\phi(v) = \frac{1}{n}(a + bv^n)$$

where a and b are constants and n may or may not be an integer. By substitution of $\sin \theta = \tanh w$ and by setting $v^n = u^{-1}$, there results the linear equation

$$\frac{du}{dw} + (a + n \tanh w)u = -b \qquad \text{(IV-4.32)}$$

which after integration gives

$$u = \frac{b}{n^2 - a^2}[a - \tanh w] - \frac{bn(n-1)}{n^2 - a^2} e^{-aw}\operatorname{sech}^n w \int e^{aw}\cosh^{n-2} w\, dw$$

$$\text{(IV-4.33)}$$

The problem is then one of choosing n.

A method easily amenable to computation was developed by Sherwood (Reference IV-4.19). The forces on the particle are resolved along the vertical y-axis and the horizontal x-axis, or

$$m \frac{dU_y}{dt} = -mg - F_{D_y} \qquad \text{(IV-4.34)}$$

$$m \frac{dU_x}{dt} = -F_{D_x} \qquad \text{(IV-4.35)}$$

where U_y and U_x are the velocities along the y- and x-axis, respectively. For a Newton type drag force which is proportional to the velocity squared, $F_{D_y} \sim U^2_y$ csc θ and $F_{D_x} \sim U^2_x$ sec θ so that the above equations are coupled by the trajectory angle θ. For a simple uncoupling approximation, Sherwood writes $F_{D_y} \sim U^2_y$ and $F_{D_x} \sim U^2_x$ which is equivalent to understating the correct total drag force at each point along the trajectory by the factor $(\sin^4 \theta + \cos^4 \theta)^{\frac{1}{2}}$. Using these assumptions and using a dimensionless velocity, position, and time as

$$x = Xg/U^2_0$$

$$y = Yg/U^2_0$$

$$u = U/U_0 \qquad \text{(IV-4.36)}$$

$$t = tg/U_0$$

where U_0 is the initial velocity, then Equations IV-4.34 and IV-4.35 become

$$\frac{dU_y}{dt} = -1 - BU^2_y \qquad \text{(IV-4.37)}$$

$$\frac{dU_x}{dt} = -BU^2_x \qquad \text{(IV-4.38)}$$

where B is the dimensionless ballistic coefficient

$$B = \frac{1}{2} C_D \frac{A\rho U^2_0}{mg} \qquad \text{(IV-4.39)}$$

which reduces to

$$B = \frac{3}{4} C_D \frac{\rho}{\rho_p} \frac{U_0^2}{Dg} \qquad (IV-4.40)$$

for a spherical particle. Here C_D is the drag coefficient, ρ is the air density, ρ_p is the particle density, D is the characteristic particle diameter. Equation IV-4.37 may be integrated twice to find the time of flight and integrating the Equation IV-4.38 twice, based on $X_0 = Y_0 = 0$, gives

$$\tau_f = \frac{2}{\sqrt{B}} \tan^{-1} (\sqrt{B} \sin \theta_0) \qquad (IV-4.41)$$

and

$$x = \frac{1}{B} \ln [1 + B\tau \cos \theta_0] \qquad (IV-4.42)$$

where θ_0 is the initial or ejection angle above the horizontal. Note that τ, τ_f and x are dimensionless. The maximum particle range is obtained by substituting Equation IV-4.41 into Equation IV-4.42 so that

$$x_r = \frac{1}{B} \ln \left[1 + 2\sqrt{B} \cos \theta_0 \tan^{-1}(\sqrt{B} \sin \theta_0) \right] \qquad (IV-4.43)$$

If B is small, the expression for the maximum ground range can be expanded in a series to give

$$x_R = \sin (2\theta_0) \left[1 - B \sin \theta_0 \left(\cos \theta_0 + \frac{1}{3} \sin \theta_0 \right) \right] + \ldots \qquad (IV-4.44)$$

which gives the correct vacuum ballistic result in the limit of B → o. The range calculated with Equation IV-4.43 is always somewhat higher than those obtained by numerically integrating the equations of motion. However, the calculated values are usually within 20 percent of the numerical results except for high angles of elevation.

While Sherwoods' method is a convenient way of computing particle trajectories, the initial conditions of these particles must be known. These conditions can only be inferred since no direct measurements are available. Photographic analyses have yielded this type of information by an examination of that part of the trajectory that could be seen outside the fireball on high-yield TNT shots.

Sogge and Stroeberger (Reference IV-4.95) performed a study whose objective was to develop a procedure to determine trajectory parameters of ejecta particles based on high-speed motion pictures. They examined many large particles throughout their trajectories, and their investigation was specifically directed at the determination of positions, velocities, accelerations, and angles at various points along the particle trajectories. Selected cratering events from projects PRE-GONDOLA I and BUCKBOARD were used to obtain ejecta trajectory characteristics. These events were documented on high-speed motion picture film. However, these films were not expressly made to observe crater ejecta as were later film coverage made during the MIDDLE GUST and MIXED COMPANY Events. Because of the nature of the films of PRE-GONDOLA I and BUCKBOARD, methods to determine the relationships between true three-dimensional motion of the particles and its recorded two-dimensional motion were required. The large rock ejecta studied by Sogge and Stroeberger had sizes up to approximately 2.1 x 2.4 x 3.1 meters.

In their report, Sogge and Stroeberger studied only those particles observed to impact on an imaginary horizontal line through GZ and perpendicular to the camera line of sight to GZ. A method was presented whereby the trajectory data of particles with varying directions of ejection could be analyzed.

A number of simple empirical ejecta models have been described by Schoutens (Reference IV-4.96). Among the models to be described here (Reference IV-4.96) is the EJECTA model developed by Schoutens.

EJECTA is a semiempirical computer code designed to calculate the distribution and the instantaneous ground deposition of debris ejected from a crater produced by a burst on or near the surface. This model allows computations to be made of the ejecta from bursts over soil, rock, or a combination of horizontally stratified layers of soil and rock. Rock is treated as discrete particles ranging in size from centimeters to meters. Soil is assumed to be fine-grained sand deposited as continuous ejecta around the crater and exhibiting a radially decreasing thickness.

For stratified media, soil and rock deposition is treated separately. The model also allows the burst to be placed above or below the ground surface in soil, rock, or layered media. The crater profile is assumed parabolic and shape invariant with burst height or depth between $\pm$ 5 ft/kt$^{1/3}$.

The mass of ejecta, composed of particles assumed spherical and having a diameter between a_1 and a_2 meters, deposited at a ground range, r, in units of crater radii is given by

$$ m = \frac{K\rho_R}{2\pi r\, R_{ar}^2} \left\{ r^{0.125}\, W^{0.65} \left(a_2^{0.515} - a_1^{0.515} \right) \right\} \frac{d}{dr} F(r) \qquad \text{(IV-4.45)} $$

where K is a scaling crater volume parameter obtained from high-yield detonations, ρ_R is the in-situ rock density, R_{ar} is the apparent crater radius in rock, W is the yield in megatons, and F(r) is a function describing the cumulative ejecta rock mass as a function of ground range r. The function F(r) was fitted to the FLAT TOP I data for hard rock. In dealing with soil, K is somewhat different in magnitude and F(r) is fitted to the FLAT TOP II data for soil. To obtain the number of particles contained in this mass range, spherical particles are assumed with density ρ_R so that their number is

$$ N = \frac{6K}{2\pi^2 r\, R_{ar}^2} \left\{ r^{0.125}\, W^{0.65} \left(a_1^{-2.485} - a_2^{-2.485} \right) \right\} \frac{d}{dr} F(r) . \qquad \text{(IV-4.46)} $$

Equation IV-4.46 gives the number of ejecta particles per square meter ranging in size from a_1 to a_2 meters ejected to a ground range r due to a ground burst having a yield of W megatons. The derivative of the function F(r) is computed at the value of r between r_1 and r_2 of interest. The particle-size distribution is computed from the power law given by Equation IV-4.24 so that

$$ M(a) = C\, r^{0.125}\, a^{0.515}\, W^{-0.35}, \qquad \text{(IV-4.47)} $$

where spherical particles have been assumed and C is a constant. The constant C and the exponents are so adjusted as to give the maximum particle size that agrees with the results of Gault (Reference IV-4.92).

The model includes a velocity cutoff for small particles to eliminate those particles which by reason of aerodynamic drag cannot reach the impact point of interest.

When small particles and soil are considered, the deposition per unit area is computed by

$$M = K_1 \, f_e \, \rho_s \, W^{1/3} \, \frac{1}{2\pi r} \, \frac{d}{dr} \, F_s(r) \qquad\qquad (IV-4.48)$$

where K_1 is another crater volume scaling constant, f_e is a scaling factor to obtain only the ejecta mass from the crater mass, ρ_s is the soil in-situ density, and $F_s(r)$ is the function $F(r)$ for soil based on FLAT TOP II soil data, describing the cumulative ejecta soil mass as a function of ground range. To obtain the soil deposition at r, Equation IV-4.48 is divided by ρ_s or

$$\delta(r) \;=\; K_1 \, f_e W^{1/3} \, \frac{1}{2\pi r} \, \frac{d}{dr} \, F_s(r) \; . \qquad\qquad (IV-4.49)$$

The geology model in EJECTA allows the user to consider alternative layers of soil and rock in horizontal stratification by specifying one soil density and one rock density for all layers, and any number of rock layer thicknesses and depths. The model then computes the fraction that is rock in the crater by the equation

$$f_R \;=\; \frac{\displaystyle\sum_1^h \left(2ht_i - 2d_i t_i - t_i^2\right)}{\displaystyle\sum_1^h \left\{ (d_{i-1} + t_{i-1})^2 - (d_i + t_i)^2 + 2h\,(d_i - d_{i-1}) + 2h\,(t_i - t_{i-1}) \right\}} \qquad (IV-4.50)$$

where h is the true crater depth, d_i is the depth of the top of ith rock layer and t_i is its thickness. The true crater depth is obtained by considering the crater volume to be a paraboloid of revolution containing material with an average density ρ_{av} determined by

$$\rho_{ar} = \frac{\rho_R \sum\limits_{1}^{h-1} t_{i-1} + \rho_R t_n' + \rho_s \sum\limits_{1}^{h} d_i}{\sum\limits_{1}^{h-1} (t_{i-1} + d_i) + t_n'} \qquad (IV\text{-}4.51)$$

where t_n' is the thickness of the last rock layer within the crater. The true crater depth for a true contact burst is given by

$$h = \frac{2}{\pi} (1 + \frac{\beta}{\alpha}) M_a \left(\frac{1}{\rho_{av} R_{amix}^2} \right) \qquad (IV\text{-}4.52)$$

where M_a is the apparent crater mass, R_{amix} is the apparent crater radius for a soil-rock stratified combination of average density ρ_{av}. The constants α and β are determined from experimental data for HE bursts in hard rock and soil. These constants represent the fraction of soil or rock that is thrown out of the crater from the true crater mass.

The HOB and DOB effects computations are based on known HOB data. The crater depth computations needed above are modified as follows for soil or rock:

$$D_{ts}(H) = D_{ts}(0) \frac{\Phi(H)}{[\psi(H)]^2} \qquad (IV\text{-}4.53)$$

$$D_{tr}(H) = D_{tr}(0) \frac{\Phi(H)}{[\psi(H)]^2} \qquad (IV\text{-}4.54)$$

where the subscripts ts and tr refer to true soil and true rock crater depths, respectively. The function $\Phi(H)$ is a curve fit to the curve describing the variation in the crater volume with HOB or DOB, and $\psi(H)$ is a similar function for the variations in the crater radius.

In the case of alternate layers of soil and rock, the true crater depth needed in Equation IV-4.50 is

$$D_{tmix}(H) = \frac{2}{\pi} \frac{M_{mix}(0)}{\rho_{av}} \left(\frac{1}{R^2_{amix}(0)} \right) \frac{\Phi(H)}{[\psi(H)]^2} \qquad (IV-4.55)$$

where $M_{mix}(0)$ is the excavated crater mass for soil-rock layers given that the DOB is zero.

The EJECTA model was compared with computations performed with other models and found to agree well. Comparisons were also made with available data and the results EJECTA agree well with data.

The Air Force Design Manual (Reference IV-4.97) presents simple models for computing crater sizes and ejecta deposition. Because these models are simple we felt it would be useful to the reader to include the section on ejecta from Reference IV-4.97 in toto, with minor modifications.

It should be recalled that since the total volume of ejecta is related to the total volume of the crater, uncertainties in crater volume are directly reflected in uncertainties in the ejecta distribution. In addition, there are uncertainties with regard to the mechanisms causing the crater. Compaction, for example, produces a crater but no ejecta. Because ejecta results from cratering, it is reasonable to expect that the total ejecta mass is closely related to the crater volume. Test data substantiates this relation, except for bursts occurring far enough above the surface to produce a depression crater without ejecta. The prediction method for ejecta depth, areal density and azimuthal variation presented herein is based upon Reference IV-4.98 wherein apparent crater volume is used to scale range and ejecta depth. The following equations taken from that reference may be used to calculate maximum, median, and minimum and average ejecta depths (D_{max}, D_{med}, D_{min}, and $\overline{D}$) at any range, R, outside the crater in soil and soft rock geologies:

$$D_{max} = V_a^{1/3} [0.767 \exp(-2.121R_S) + 0.0443 \exp(-0.3793R_S)] \qquad \text{(IV-4.56)}$$

$$D_{med} = V_a^{1/3} [0.8914 \exp(-2.549R_S) + 0.01668 \exp(-0.5359R_S)] \qquad \text{(IV-4.57)}$$

$$D_{min} = V_a^{1/3} [1.036 \exp(-2.978R_S) + 0.00628 \exp(-0.6925R_S)] \qquad \text{(IV-4.58)}$$

$$\overline{D} = V_a^{1/3} [0.749 \exp(-2.30R_S) + 0.0168 \exp(-0.423R_S)] \qquad \text{(IV-4.59)}$$

where $R_S = R/V_a^{1/3}$. All dimensions are in feet. The distribution of ejecta depth at a given range may be approximated from

$$D(k) = \left(D_{min} \right)^{\frac{95-k}{90}} \text{ or } \left(D_{max} \right)^{\frac{k-5}{90}}, \text{ feet} \qquad \text{(IV-4.60)}$$

where k is the probability of obtaining an ejecta depth less than D(k) at a given range and $D(95) = D_{max}$; $D(50) - D_{med}$; $D(5) = D_{min}$. For hard rock geologies (basalt) calculated ejecta depths should be multiplied by a factor of 2. The maximum ejecta thickness relation, Equation IV-4.56, results in a value that is larger than about 95 percent of the ejecta measurements at a given range from a cratering burst. The median thickness (Equation IV-4.57) is larger than 50 percent of the measurements, and the minimum ejecta thickness (Equation IV-4.58) is smaller than 95 percent of the measurements. The variation of maximum, median and minimum ejecta depth with range is shown in Figure IV-4.89.

The parameters of yield, HOB, explosive source characteristics, and geology are assumed to influence the ejecta distribution through their influence on the crater volume. The variation in ejecta depth at a given range (ejecta raying is an example) is intrinsic in the ejecta problem and cannot be decreased significantly by more exact knowledge of ejecta phenomenology. ' The equations presented are primarily intended for nuclear cratering bursts, but they can be used with reasonable validity for HE bursts as well.
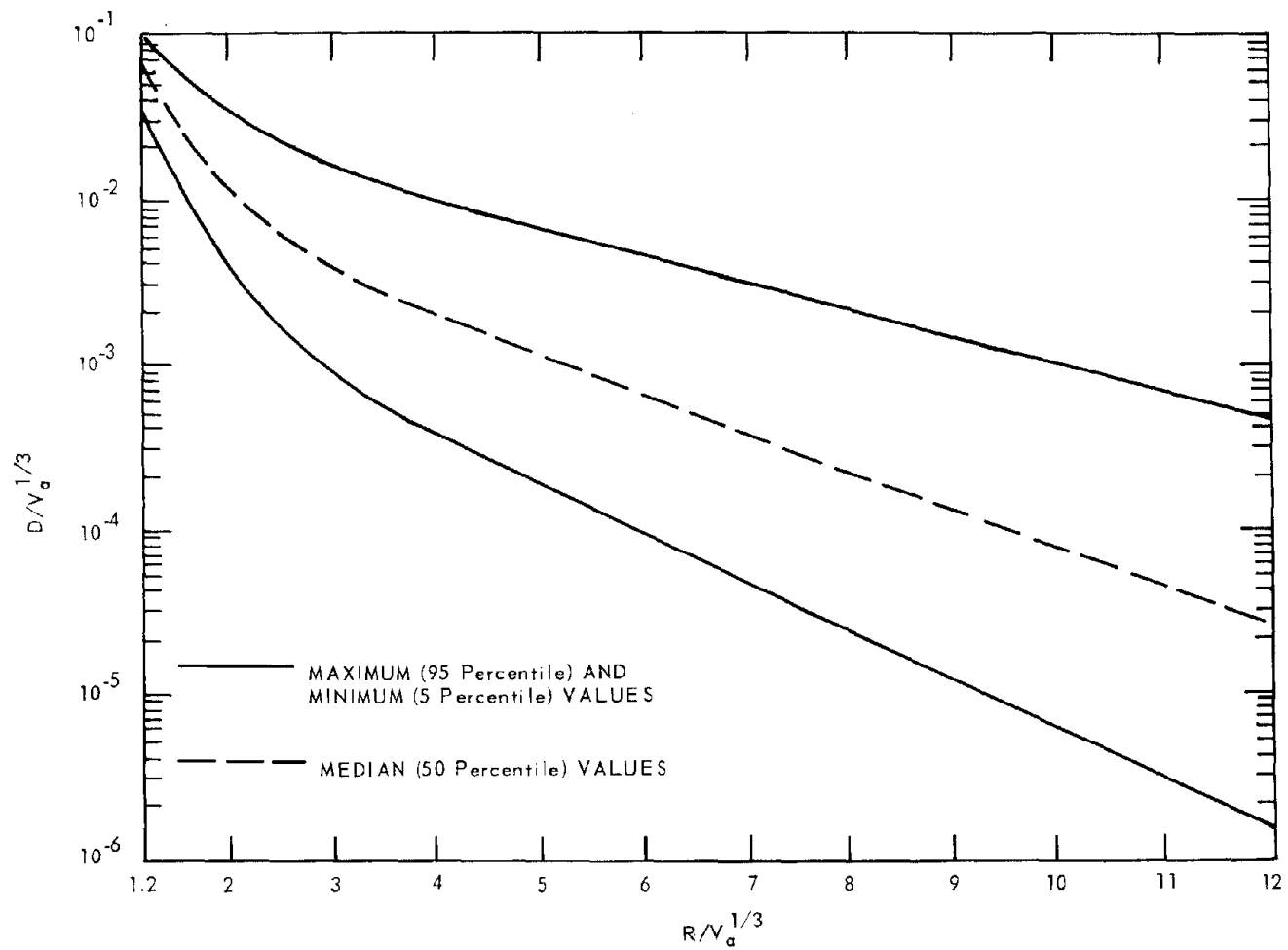
Figure IV-4.89. Ejecta depth as a function of ranges for nuclear bursts
                 (Reference IV-4.97).

Equations IV-4.56 through IV-4.59 are valid for any range beyond the crater lip, for above-surface bursts, and for below-surface bursts down to scaled depths of burst $(HOB/V_0^{1/3})$ of 0.2. The validity of Equations IV-4.56 through IV-4.59 for more deeply buried bursts is uncertain, and use for scaled depths of burst greater than 0.2 is not recommended.

Areal weight density may be estimated from ejecta depth by the relation

$$\delta = \rho D \qquad\qquad (IV-4.61)$$

where δ is the areal density, ρ is the bulk unit weight of ejecta, and D is the ejecta depth. A bulk ejecta density of 1.6 gm/cm^3 may be assumed. It should be noted that the measurements upon which Equations IV-4.56 through IV-4.59 are based were taken over physical areas which vary with scaled range. On the crater lip, the measurement may average over a negligible area on the order of one square meter. In the missile ejecta region, the averaging may be over several thousand square meters. The measurements in the continuous ejecta region, when scaled up to a high-yield nuclear burst, might correspond to an area of about 3.0 x 3.0 meters. In the missile ejecta region, the measurements would correspond to an area on the order of 300 x 300 meters.

Crater volumes for use in Equations IV-4.56 through IV-4.59 may be estimated with the relations:

High-Yield Bursts ($W \gtrsim 1$ kt)

$$V_a = 0.04V_0 \exp(-55.1 \; HOB/V_0^{1/3}), \; HOB/V_0^{1/3} > 0.002 \qquad (IV-4.62)$$

$$V_a = 0.05V_0 \exp(-166.0 \; HOB/V_0^{1/3}), \; 0 < HOB/V_0^{1/3} < 0.002 \qquad (IV-4.63)$$

$$V_a = 4.07V_0 \exp(0.0033 + DOB/V_0^{1/3}), \; 0 < DOB/V_0^{1/3} \leq 0.2 \qquad (IV-4.64)$$

Below-Surface Low-Yield Burst ($W < 1$ kt)

$$V_a = 4.39V_0(DOB/V_0^{1/3} + 0.0216)^{0.88}, \; 0 \leq DOB/V_0^{1/3} < 0.055 \qquad (IV-4.65)$$

$$V_a - 4.07V_0(0.0033 + DOB/V_0^{1/3})^{0.77}, \; 0.055 \leq DOB/V_0^{1/3} < 0.2 \qquad (IV-4.66)$$

where V_o is the crater volume in ft^3 due to a half-buried sphere of TNT. Above-surface apparent crater volumes from Figure IV-4.90 should not be used since most of the crater volume for $HOB/V_o^{1/3} > .02$ is thought to result from compaction. Equations IV-4.62 through IV-4.66 estimate the crater volume resulting primarily from excavational processes. Equations IV-4.64 through IV-4.66 are fits to the buried nuclear curves of Figure IV-4.90.

The ratio of total ejecta mass* to apparent crater mass can be determined to an excellent approximation with (Reference IV-4.98):

$$M_t/M_a = 0.54FW^{-0.0477} \quad , \quad (W > 1 \text{ kt}) \quad\quad\quad (IV-4.67)$$

$$M_t/M_a = 0.54F \quad\quad\quad , \quad (W < 1 \text{ kt}) \quad\quad\quad (IV-4.68)$$

where M_t is the total ejecta mass, M_a is the apparent crater mass, $F = 2$ for hard rock and unity for all other geologies and W is the yield in kilotons. Figures IV-4.91, IV-4.92, and IV-4.93 present ejecta distributions for a variety of conditions. Figure IV-4.91 shows ejecta depth as a function of overpressure level for 1-Mt, 5-Mt, and 25-Mt yields and an assumed cratering efficiency of 2.8 m^3/ton. Figure IV-4.92 gives scaled ejecta depth as a function of cratering efficiency at the 1000- and 600-psi levels. The D(90), D(50), and D(10) values are shown. Figure IV-4.93 plots ejecta thicknesses at the 1000-psi level for nuclear-surface bursts on layered sites as a function of scaled depth to water table and bedrock.

Knowledge of the missile-size distribution is important from the standpoint of proper design of debris removal systems and as a necessary input in determining the expected number of missile impacts on a given area. The general form for the ejecta missile-size distribution for cratering events in rock (Reference IV-4.39) is given by

$$M/M_t = (a/a_{max})^n \quad\quad\quad (IV-4.69)$$

where M/M_t is the cumulative mass fraction of ejecta, M is the cumulative ejecta mass at all ranges with equivalent diameters less than or equal to the value a,

---

*The normal convention of ejecta literature in which the word "mass" is loosely defined to mean "weight" is used herein.
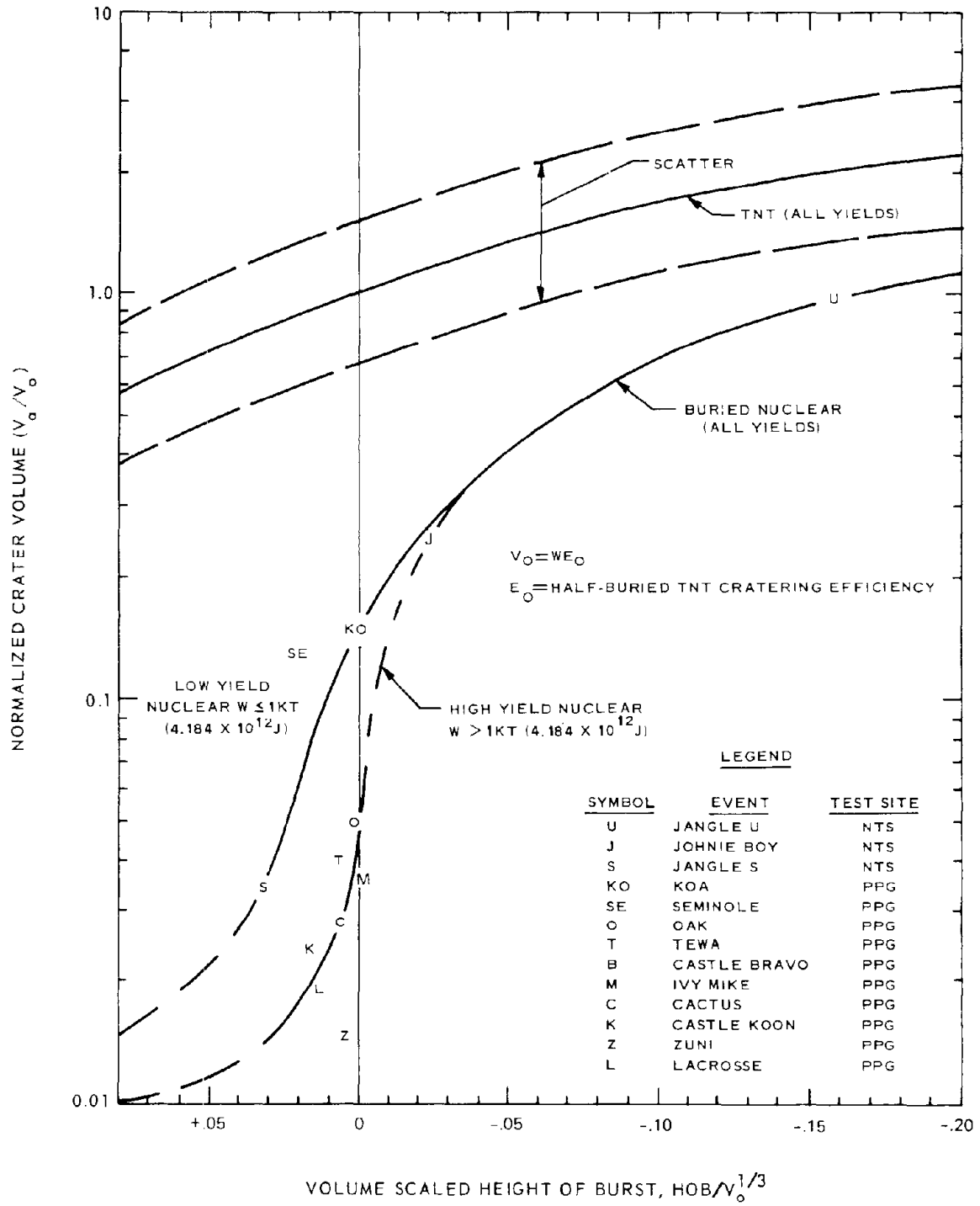
Figure IV-4.90.   Height of burst effects in the near-surface region
(Reference IV-4.97).
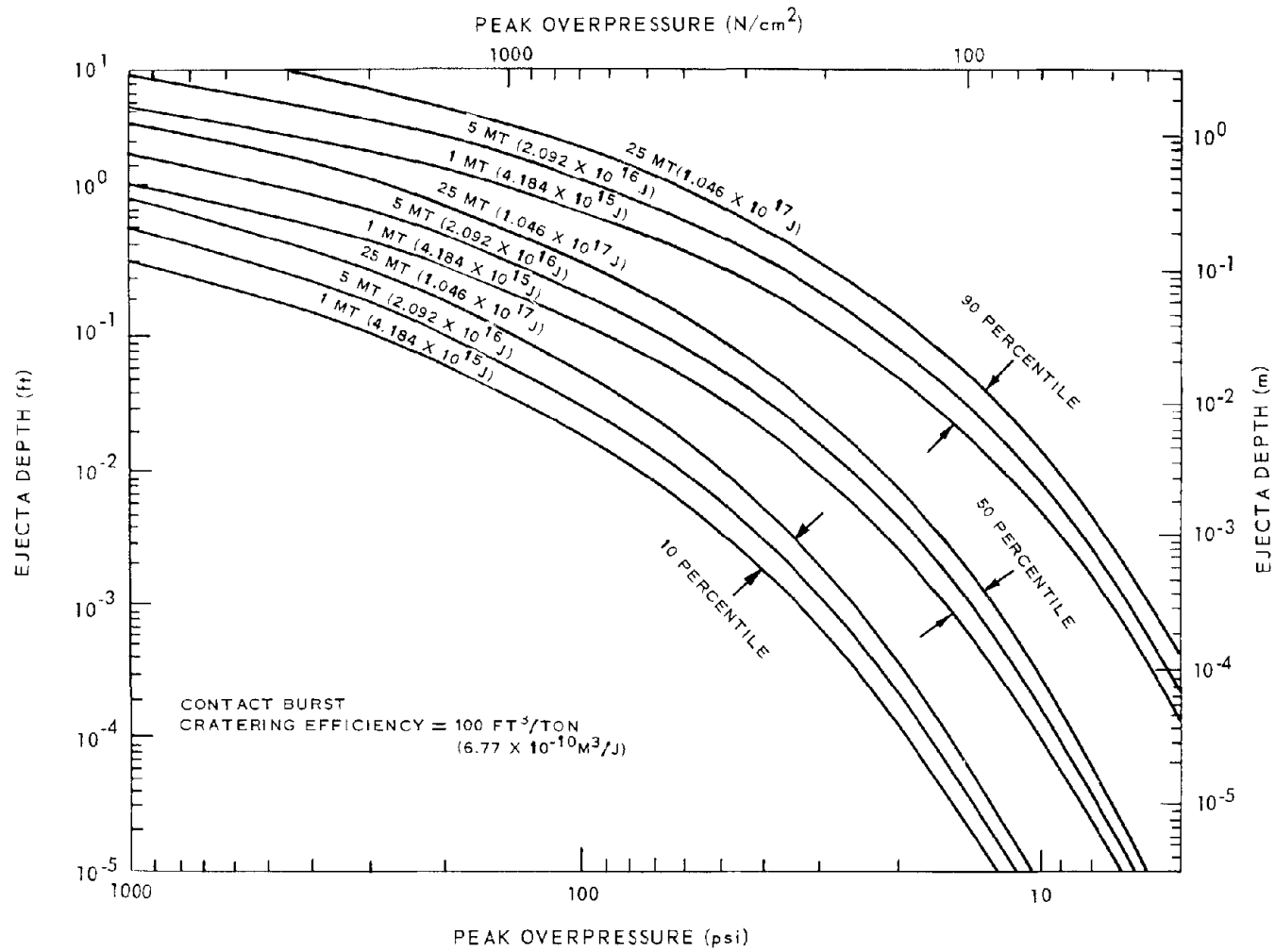
Figure IV-4.91. Ejecta depth as a function of overpressure (Reference IV-4.97).
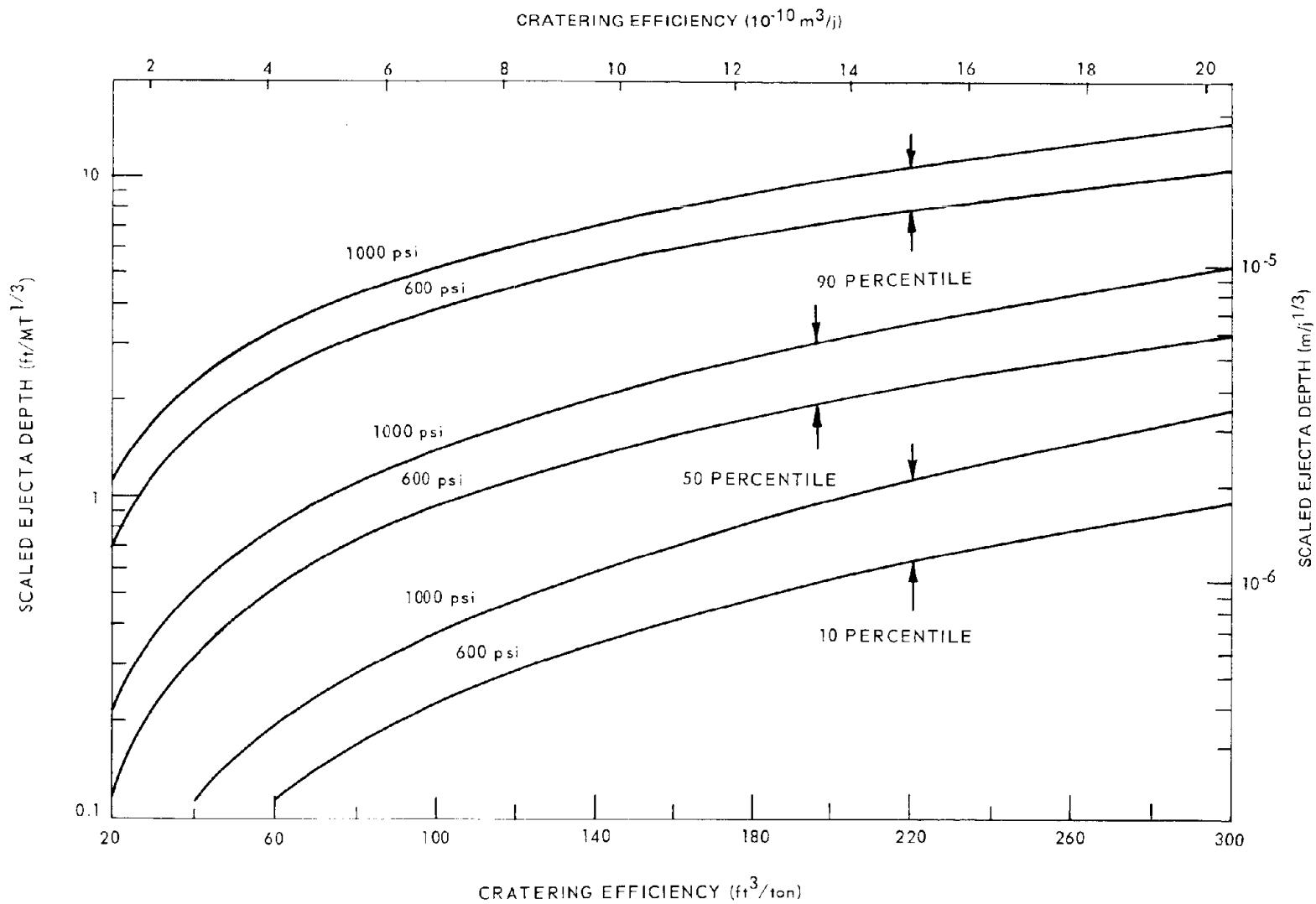
Figure IV-4.92.   Scaled ejecta depth at 1000 psi (689 N/cm²) and 600 psi (414 N/cm²)
levels as a function of cratering efficiency (Reference IV-4.97).
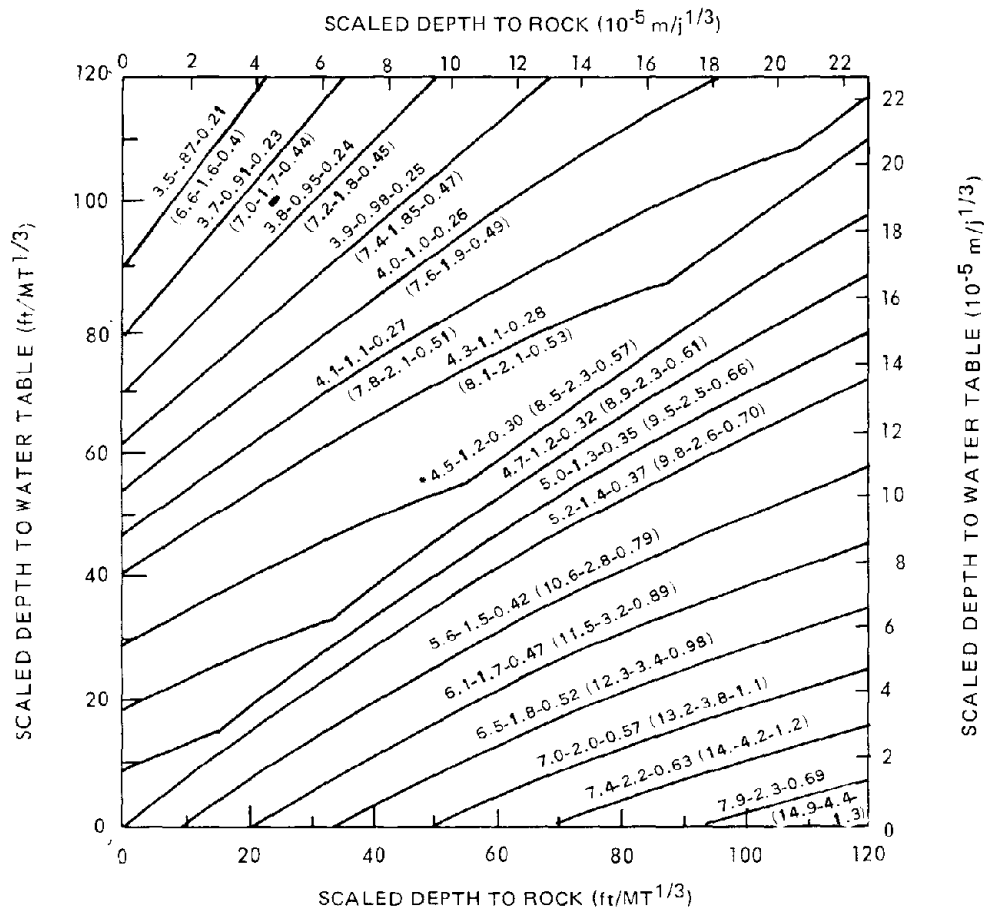
Figure IV-4.93. Ejecta thickness at 1000-psi (690 N/cm²)
level from high-yield surface burst in
layered geology (Reference IV-4.97).

M_t is the total ejecta mass, a_{max} is the absolute maximum equivalent missile diameter, and n is an exponent that is approximately equal to 0.5. The equivalent missile diameter and the missile mass are related by the expression

$$m = \pi \rho_p a^{3}/6 \qquad \text{(IV-4.70)}$$

where m is the missile mass, a is the missile diameter, and ρ_p is the preshot material density. From Equations IV-4.67 and IV-4.68, M_t is

$$M_t = 0.54 F \rho_p W^{-0.0477} V_a, \qquad (W > 1 \text{ kt}) \qquad \text{(IV-4.71)}$$

$$M_t = 0.54 F \rho_p V_a, \qquad (W \leq 1 \text{ kt}) . \qquad \text{(IV-4.72)}$$

The absolute maximum missile mass of a single missile from a cratering event is related to the total missile mass by (Reference IV-4.97)

$$m_{max} = 0.05884 M_t^{0.8}, \qquad \text{lbs} \qquad \text{(IV-4.73)}$$

where m_{max} is the absolute maximum mass of a single missile, and M_t is the total ejecta mass. However, the maximum missile size at a given range and azimuth will be less than the absolute maximum missile size for the following reasons: (1) the maximum missile size at a given range decreases as the range increases (the absolute maximum missile size will be found at or near the crater lip), and (2) the limited area of measurement at a given range and azimuth means that in general the maximum missile size at that range will not be found in the measurement area. Similar considerations apply to the median missile size (50 percent cumulative ejecta mass fraction) as well. The maximum median missile mass, m_m, found at a given range is given by the expression

$$m_m = 0.1094 M_t^{0.8} R_s^{-1.644}, \qquad \text{lbs} \qquad \text{(IV-4.74)}$$

where $R_s = R/V_a^{1/3}$. Equation IV-4.74 was derived from limited test data from the five large MIDDLE GUST Events, the FLAT TOP I Event, and the MIXED COMPANY III

Event. The actual maximum missile mass found in a given measurement area at some scaled range depends on the measurement area and the azimuthal coverage. For areas of several hundred to several thousand square meters on a large HE event (crater volume of several thousands cubic meter), a median value for observed missile mass may only be 5 or 10 percent of that predicted by Equation IV-4.74. An important observation is that when the effect of range is taken into account, the particle-size distributions in rock and many cohesive stiff soils may not be significantly different, especially when it is noted that the maximum missile size for large cratering events in rock will probably be controlled by the joint spacing in the rock. However, the dynamic missile-size distribution for unconsolidated, weak, noncohesive soils differs significantly from that in rock, and the static missile-size distribution differs even more. The dynamic missile-size distribution refers to the size distribution of the missiles in flight. Static distribution refers to sizes after all missiles have fallen to the ground. In the case of hard rock missiles, the dynamic and static particle-size distributions may be very similar. For noncohesive soils, the difference may be substantial, as shock-agglutinated soil clods will break on impact. Analysis of secondary impact craters from the 100-kt SEDAN Event indicate that the dynamic missile-size distribution (shock-agglutinated soil clods) at missile sizes about 1-meter diameter may follow the form of Equation IV-4.69 with n = 0.00147, and an m_{max} consistent with Equation IV-4.73.

For unconsolidated weak soils (NTS alluvium), the following dynamic particle and missile-size distribution is recommended (Reference IV-4.97):

$$M/M_t = (a/a_{max})^{0.00147} \qquad \text{(IV-4.75)}$$

for a $\geq$ 0.1 meter, and

$$M/M_t = 1.1434 - 0.0038 \log (a_{max}) + [0.2995 - 0.0011 \log (a_{max})]$$

$$\cdot \log(a), \qquad \text{(IV-4.76)}$$

for a < 0.10 meter,

where a_{max} is given by Equation IV-4.70 using m_{max} from Equation IV-4.73. For the static particle-size distribution use Equation IV-4.76 for all particle sizes. To determine the particle-size distributions in soil ($a \geq 1.10$ m) and rock at a given range use the relation

$$F(a) = (a/a_m)^n \qquad (IV-4.77)$$

where $F(a)$ is the cumulative mass fraction over a given measurement area and a_m is the equivalent diameter of m_m as defined in Equations IV-4.70, IV-4.75, and IV-4.76. The exponent n may be taken as 0.5 for hard rock geologies and 0.00147 for unconsolidated alluvial soil. For cohesive soil or layered geologies, $n = 0.5$ is recommended as a conservative estimate. From Equations IV-4.70, IV-4.71 and IV-4.74

$$a_m = 0.504K(\rho_p)^{-0.0667} (V_a)^{0.267} (W)^{-0.0127} R_S^{-0.548} ; \quad ft.$$

$$(W > 1kt) \qquad (IV-4.78)$$

$$a_m = 0.504K(\rho_p)^{-0.0667} (V_a)^{0.267} R_S^{-0.548} ; \qquad (W \leq 1 kt) \quad (IV-4.79)$$

where ρ_p is in lb/ft^3, and V_a in ft^3, and K is 1.2 for hard rock geologies and 1 for layered and cohesive soil geologies.

The expected number of impacts per unit area of missiles with equivalent diameters between a_1 and a_2 is given by the expression

$$I(a_1,a_2) = 6\delta n(a_2^{n-3} - a_1^{n-3})/\pi\rho_p a_m^n(n-3) \qquad (IV-4.80)$$

where δ is the ejecta areal density and n is the exponent in the particle-size-distribution equation (Equation IV-4.77). To calculate I at a given range, R, taking into account the azimuthal distribution of Equation IV-4.61, let $\delta = \rho\bar{D}$, where the average ejecta depth is calculated from Equation IV-4.59. To find the expected number of missile impacts per square foot of missiles equal to or larger in equivalent diameter than a, let $a_1 = a$, and $a_2 = a_m$ in Equation IV-4.80,

IV-4-191

where a_m is calculated from Equation IV-4.78 or IV-4.79. The probability of impact on a given area of missiles with equivalent diameters between a_1 and a_2 can be estimated by

$$P = 1 - \exp \left[-I(\ell_1 + a_1)(\ell_2 + a_1) \right] \qquad \text{(IV-4.81)}$$

where ℓ_1 and ℓ_2 are the length and width, respectively, of the given area.

Computer code calculations of the trajectories of 1-, 10-, and 100-centimeter diameter spheres through 0.1-Mt and 10-Mt nuclear surface-burst environments are presented in Reference IV-4.99. The results are given by the following equations:

$$V_i = 5.673(R/\sin2\theta)^{0.5} \exp(-\frac{R}{R_0}); \qquad \text{ft/sec,} [R < R_0/2] \qquad \text{(IV-4.82)}$$

$$V_i = 23.08 \left[\frac{a \rho_p}{C_d} \right]^{0.5}; \qquad \text{ft/sec } [R > R_0/2] \qquad \text{(IV-4.83)}$$

where V_i is the impact velocity, $R_0 = 90\rho_p a \sin(2\theta/C_d)$, ft, where R is the ejecta impact range, a is the effective missile diameter, ρ_p is the density of material in the cratered region, θ is the initial ejection angle measured from the horizontal and C_d is the drag coefficient.

A nominal value of $C_d = 0.6$ is recommended, with a possible range in drag coefficients between 0.3 and 1.2. A value of $\theta = 45$ degrees can be taken as a nominal ejection angle, with $\theta = 15$ degrees and $\theta = 75$ degrees as reasonable bounding values.

Although explosive yield affects the range at which a given missile will impact, all missiles with the same value of θ, a, ρ_p and C_d that impact at a given range will do so with about the same velocity, regardless of the yield and initial ejection velocity. Impact angles tend to have about the same magnitude as ejection angles at the higher overpressure levels. At the lower overpressure levels (several psi and less) the angles are more nearly vertical. For low-yield nuclear bursts, the impact and ejection angles should be nearly the same at nearly all ranges.

Shockey et al. (Reference IV-4.100) have recently published a report dealing with the prediction of cratering and fragmentation behavior in rock. They point out that previous attempts to calculate cratering behavior in rock have met with limited success. Observed crater shapes are often not well predicted, and ejecta-size distributions are not predicted at all (Reference IV-4.101). Their work represents an attempt to make more accurate calculations by including in the computational modeling the behavior of inherent flaws and faults in the material. The SRI NAG/FRAG fracture and fragmentation model (References IV-4.102 through IV-4.108) which simulates the activation, growth, and coalescence of flaws and cracks and, thereby, the formation of fragments, was incorporated into the Sandia TOODY3 wave propagation code to simulate the conditions of cratering experiments performed in rock.

In laboratory experiments, craters were produced in hard, dense quartzite rock by detonation of surface explosives and by impact of steel projectile cylinders. Crater dimensions, subcrater fracture damage, and ejecta size, velocity and angle distributions were measured and compared with the calculated results. The agreement was good and encouraged Shockey and his coworkers to apply the approach to a large-scale cratering event. Of particular interest was the fact that the predicted and observed craters were shallow and broad, thus proving the ability of the NAG/FRAG model to predict high aspect ratio craters.

The NAG/FRAG fracture and fragmentation model was also used to simulate the 20-ton buried-explosive cratering event, PRE-SCHOONER DELTA, and the calculated results were compared with measurements. Good agreement was achieved by selecting a physically reasonable, but as yet unmeasured, crack growth law. This result supports the contention that when the mechanisms underlying crater formation are understood and modeled in a physically realistic way, cratering and ejecta formation behavior can be accurately predicted. They also suggest that when cratering occurs in hard rock, flaw activation and growth processes are the dominant mechanisms. Furthermore, the NAG/FRAG model appears to provide an adequate treatment of these processes.

A description of the ejecta source is required to calculate the ejecta environment and the contribution of the crater to the dust cloud loading. The source description must include the mass ejection rate, the ejection velocity (speed and angle),and the fragment size distribution as functions of ground range and time. Attempts to construct an ejecta source model completely from experimental data

have been unsuccessful. Data exist on some HE shots for total ejecta mass, but not for the rate of ejection (see, for example, References IV-4.109 and IV-4.110). The inflight ejecta trajectory analyses discussed in Reference IV-4.86 give representative fragment ejection velocities, but do not relate mass to velocity. Thus, it is necessary to incorporate results of theoretical calculations into the ejecta source model to complete the source description.

A number of two-dimensional hydrocode calculations using advanced elastic-plastic material models have been performed recently (References IV-4.111 through IV-4.114). With the exception of the recent JOHNIE BOY calculations (Reference IV-4.112), these codes have not been successful in predicting the final crater dimensions. It appears that the poor agreement for the final crater size is a result of failure to properly predict the late-time motion, which occurs at low velocities (below about 9 m/sec). In fact, analysis shows that most cratering calculations agree among themselves at early times, and only begin to disagree at times when the higher-velocity ejecta have already left the developing crater. At the time that this occurs, that is, at the time when hydrocode calculations begin to show disagreement in the description of the final crater growth, and when the material model for strength and plastic flow begins to have a strong effect on the subsequent motion, the radius of the instantaneous crater is smaller than the computed final crater radius.

There is qualitative evidence that the hydrocodes are correctly predicting the higher-velocity motions. In Figure IV-4.94, the initial location and final range of marked grout columns for the MINE SHAFT test are shown (taken from Reference IV-4.110). The ejecta origins and the final crater contour for the ELK 64 JOHNIE BOY calculation (Reference IV-4.112) are also shown in this figure. Comparison of the two results shows that the ejecta origin relative to the apparent crater contours are in qualitative agreement and also that the predicted contours of the apparent and true craters are in qualitative agreement with the measured contours. In the calculation, the ejecta leaves the crater from the lip of the developing crater. This phenomenon is well known in hypervelocity impact studies and in the ejection of water from projectile impacts (Reference IV-4.113). Finally, very little ejecta comes from the region near the vertical axis in the calculation. This result is in agreement with HE test observations. The main assumption for the construction of a crater ejecta model is that the early crater-ing motion in the hydrocodes is substantially correct, and that only the late-time

(a) JOHNIE BOY CALCULATION

(b) MINE SHAFT EXPERIMENT
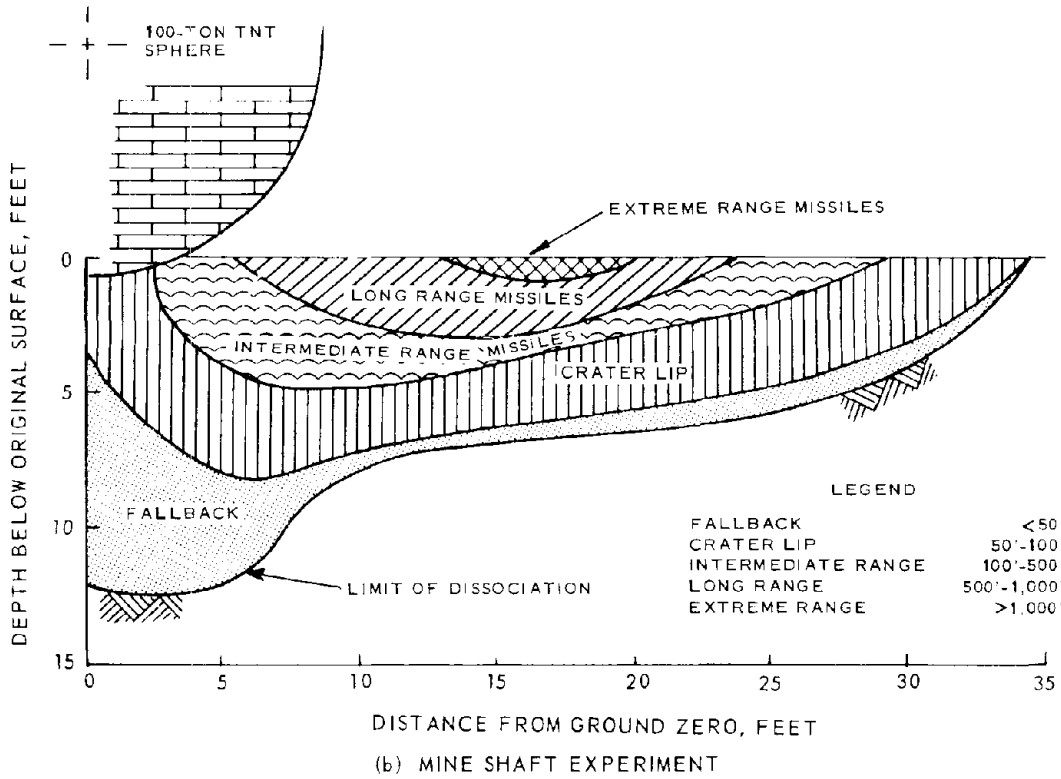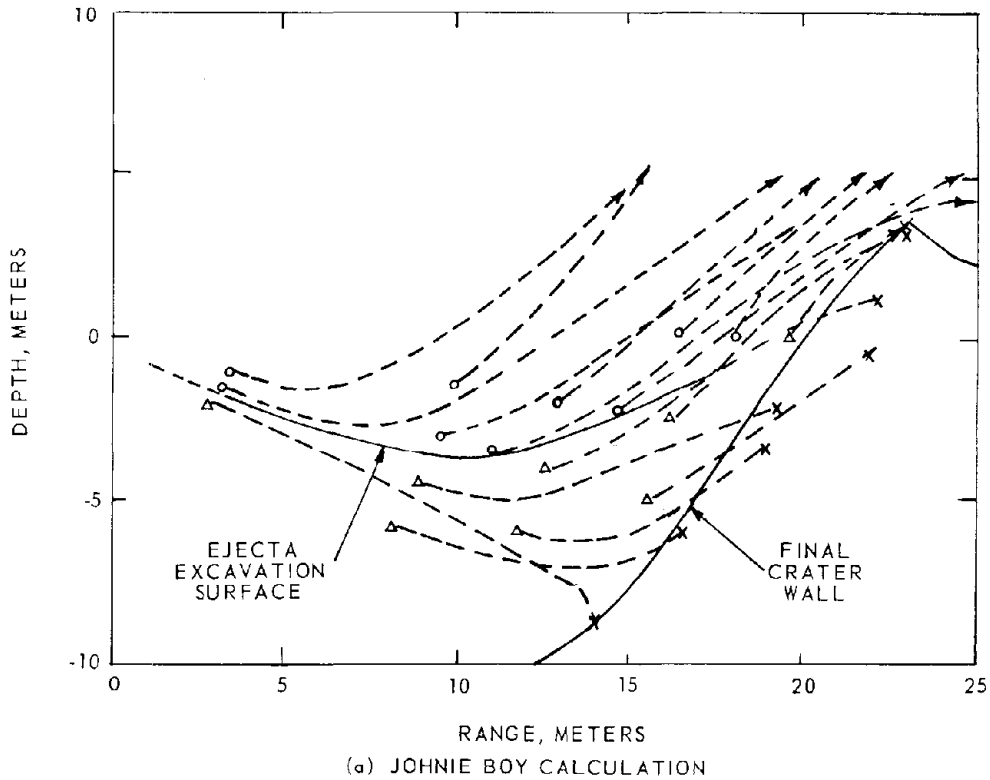
Figure IV-4.94. Origin of crater ejecta (References IV-4.110 and IV-4.112).

motion, which is unimportant for the ejecta problem, is not being correctly calcu-
lated. Therefore, early-time hydrocode cratering calculations can be used to
construct a realistic ejecta source.

The initial step in constructing an ejecta source from hydrocode data was to
identify existing cratering calculations having sufficiently detailed output. The
output required was determined to be the density and vector velocity of ejecta
passing the original ground surface as a function of radius and time. The reason
ejecta velocity is an important parameter to examine can be seen from the behavior
of the crater lip in practically all the calculations examined. As the crater
grows, the preponderance of high-velocity ejecta comes out at the lip of the
instantaneous crater. A small amount of very-low-density material leaves from
near the center of the crater. But beyond the lip of the growing crater, the
ground surface is raised slightly and at a relatively low velocity. Effectively
the soil surface appears to be peeled back as the crater grows. In the SHEP calcu-
lation of JOHNIE BOY, at 150 milliseconds, the growing crater had a radius of 13.7
meters, and a large amount of ejecta was passing the original ground surface
between 13.7 and 18.3 meters. But beyond 18.3 meters and extending well beyond
30.5 meters, the ground surface was raised about 1 foot . As the crater grows to
its final radius of about 21.3 meters, a time comes when the lip material gets
caught up in the flow and is ejected. That is, the first third of a meter of
material at a radius of about 21.3 meters should be ejected toward the very end
of the crater growth. But, practically all the calculations examined report total
ejecta mass defined as mass that has crossed the original ground surface. There-
fore, the lip material just discussed will be counted as ejecta at a very early
time. In fact, the surface material near the final crater radius of 21.3 meters
was raised above the original ground surface as early as 40 milliseconds in the
SHEP calculation. For this reason, reported plots of ejecta mass versus time
could be seriously misleading when higher-velocity ejecta is considered. These
plots often have an artificially high rate of mass ejection because the lip is
counted as ejecta too early in the calculation. Because of this difficulty, and
because ejecta velocity itself was a required output, existing cratering calcula-
tions were examined to see if the required output (that is, density and velocity
as a function of position and time) was available. It was initially determined
that eight such calculations were available. These are identified in Table
IV-4.31 and described in References IV-4.111 and IV-4.112. Later, two other
calculations were examined, the MIXED COMPANY calculation reported by Ialongo

Table IV-4.31. Survey of existing hydrocode calculations.

Contractor*	Yield	Code Used	Material Model	Source	Yield Coupling
SHI	1 Mt	SHEP	Alluvium (bad EOS)	0	0.04
ATI	1 Mt, 15-ft DOB	AFTON	Granite	Radiation diffusion	1.00
S^3	5 Mt	?	Wet tuff	1	0.03
ATI	1 Mt (3102)	AFTON	Granite	2	0.055
ATI	5 Mt (3114)	AFTON	Granite (no strength)	2	0.055
ATI	5 Mt (3115)	AFTON	Granite	2	0.055
SHI	JOHNIE BOY	SHEP	Alluvium	Cold	0.33
PI	JOHNIE BOY	ELK 64	Alluvium	Cold	0.33

*SHI = Shock Hydrodynamics, Inc.   Yield range 0.5 - 5000 kt
 ATI = Applied Theory, Inc.   Stress range 0 - 17 kbar
 S^3 = Systems, Science and Software Coupling range 0.04 - 1.00
 PI = Physics International   DOB range 0 - 4.6 meter

(Reference IV-4.114) and the MIDDLE GUST calculation reported by Trulio (Reference IV-4.111). At a given output time in the calculation, the density and velocity components of material crossing the original ground surface as a function of radius are input into a simple analysis program. The ejecta flow at radius R is then calculated as:

$$\frac{\partial^2 M}{\partial A \partial t} = \rho v. \tag{IV-4.84}$$

Each radial zone is examined and the incremental mass

$$dM = \rho v \, dA \, dt \tag{IV-4.85}$$

is accumulated in the appropriate vertical velocity bin, giving a distribution of ejecta mass versus velocity. A noteworthy feature of this distribution as it develops in time is that the high-velocity ejecta comes out at early times, and vice versa, so that successively lower and lower bins are populated. This is illustrated in Figure IV-4.95, which compares this histogram with the average velocity at the time the total ejecta mass is reached on the abscissa. This average vertical velocity is defined as momentum flux/mass flux or

$$<v> = \frac{\sum v \, dm}{\sum dm} \tag{IV-4.86}$$

where the sum is over the radial zones. Note both methods of associating ejecta mass with velocity agree well. The analysis program output is then examined to determine if false ejecta past the crater lip is being counted in the total. If so, a velocity cutoff of a few meters per second is imposed on the mass ejected. The results of this analysis showed an unexpected consistency. In certain of the calculations, the mass ejection rate was very nearly constant over a long time, usually three decades of time. For the 1-Mt cases studied, this constant mass ejection rate persisted past 0.5 second, where the average vertical velocity was about 10 m/sec. This property was especially noticeable for the 1-Mt calculation
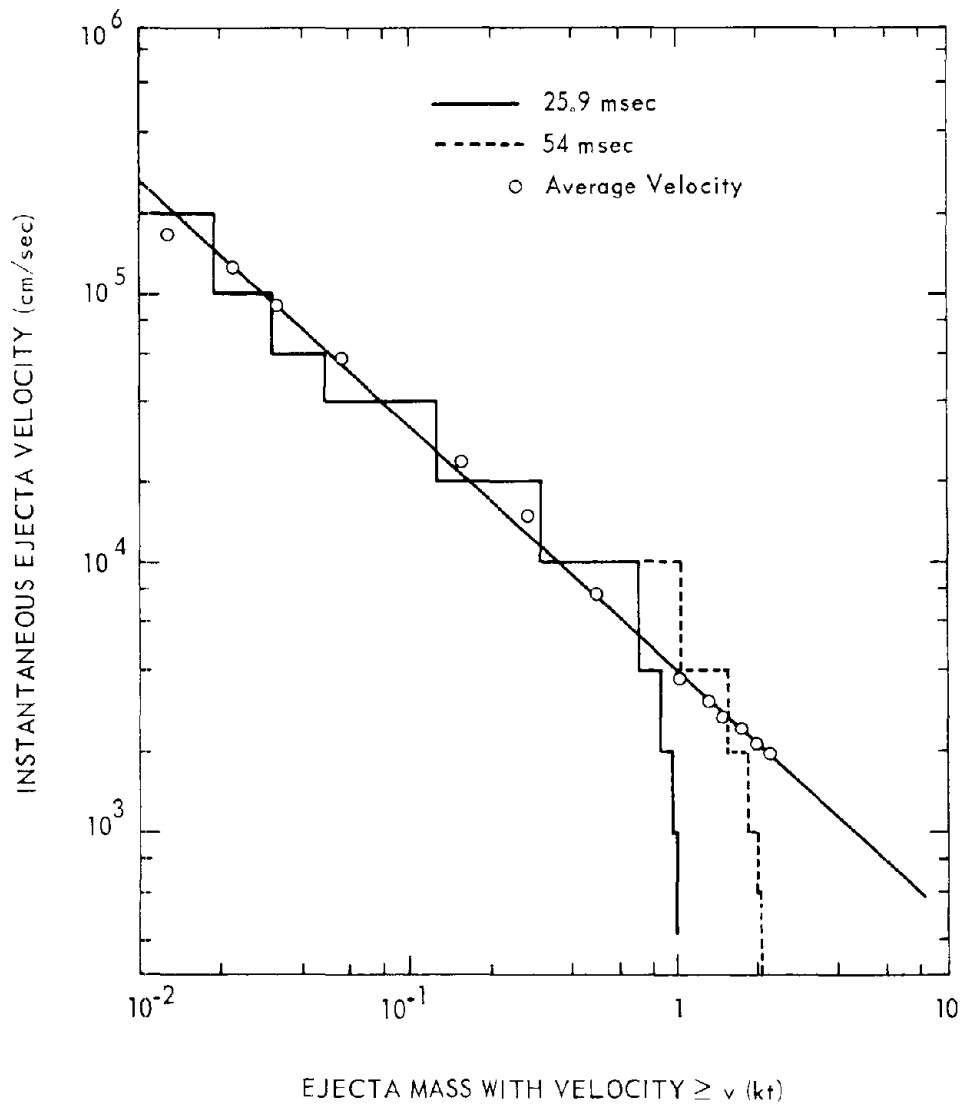
Figure IV-4.95. SHEP velocity distribution for JOHNIE BOY.

for JOHNIE BOY and for the ATI 3102 (1 Mt) calculation. This behavior is shown in Figure IV-4.96.

In the other calculations examined, this linear behavior is not so evident. These calculations differ from the three just mentioned in that data were available at more widely spaced times. Thus, the probability of inaccurate estimation of the mass lofting calculations is increased. For these calculations, a best-fit straight line to the data was calculated, weighting the data between 0.001 and 0.1 second in the fit. In one calculation, 1 Mt at 4.6 meters DOB, the ejecta points between 0.01 and 0.1 second were weighted. The ejecta from this calculation fell below the best-fit line by a factor of 5 at 0.001 second, by far the greatest variance from a constant lofting rate observed. This is believed to be caused by the overburden relief which is an inherently slower process than the early-time hydrodynamic blowoff seen in surface-burst calculations.

The slopes of the linear fits to ejecta time histories are the mass ejection rates. From the curve fits to these computer code results, the mass lofting rates were calculated and are shown in Table IV-4.32. Note the considerable range of these values. One questionable point in these values is that the ATI 3114 rate on strengthless granite is considerably lower than the rate for granite with strength described in ATI 3115. The reason for this is suspected to be that the data used to assemble these rates were available at only five times.

Table IV-4.32. Mass ejection rates.

Calculation*	Yield (kt)	$\dot{M}$(kt/sec)
S^3	5000	4500 $\pm$ 1500
SHI 1 MT	1000	1460
SHI JOHNIE BOY	0.5	37.5
ATI 3102	1000	1800
ATI 3114	5000	3400
ATI 3115	5000	4800
ATI 15' DOB	1000	12,500
*S^3 = Systems, Science and Software SHI = Shock Hydrodynamics, Inc. ATI = Applied Theory, Inc.		
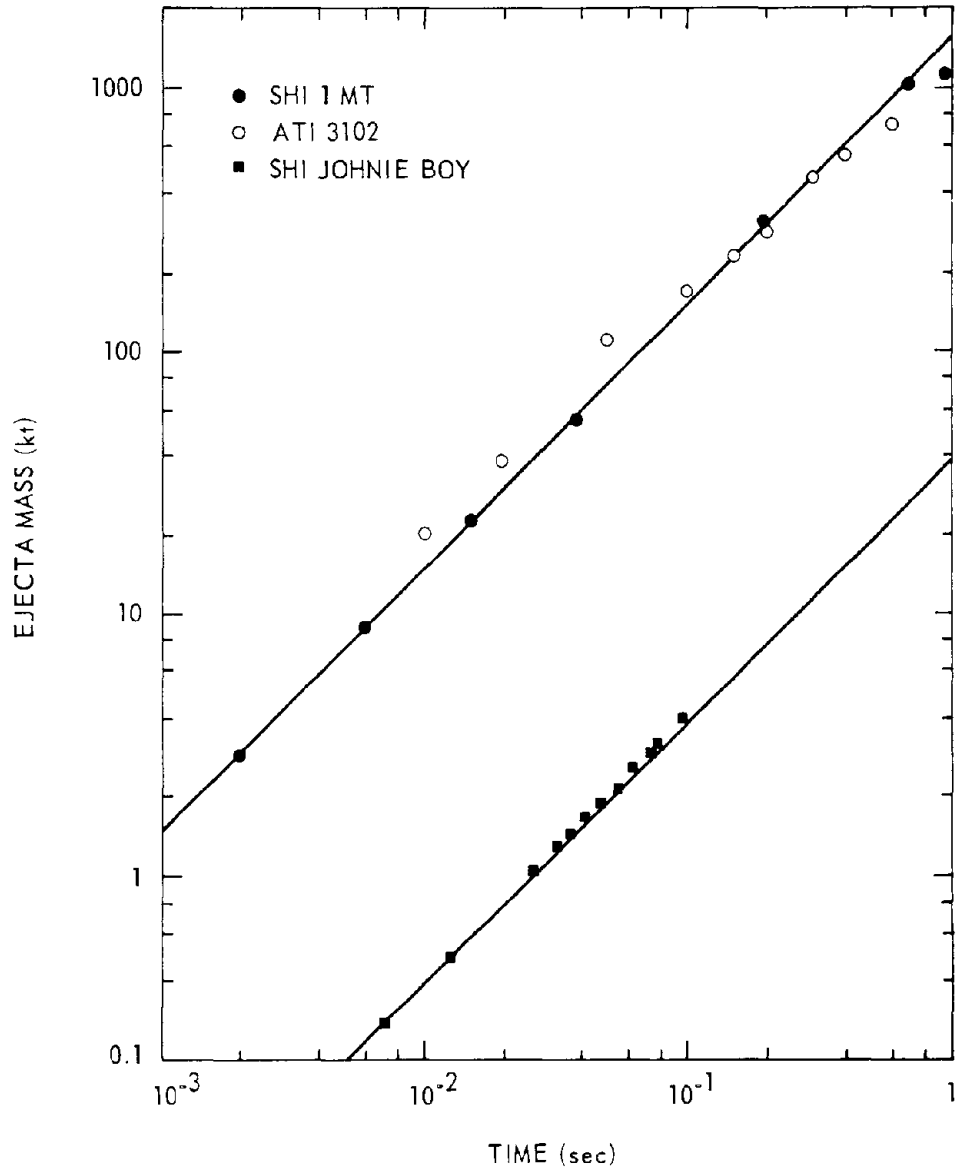
Figure IV-4.96. Ejection history for three calculations.

Since Tables IV-4.31 and IV-4.32 were completed, two other calculations have been analyzed. These were the MIXED COMPANY III calculation reported by Ialongo (Reference IV-4.114) and the MIDDLE GUST III calculation reported by Trulio.

MIXED COMPANY III was a 500-ton TNT surface-tangent burst over a layered geology of soil over sandstone over granite (Reference IV-4.114). The calculation was done with the SHESAM/SHEP code using an advanced plasticity model for the portion of the motion where strength became important. This calculation was in substantial agreement with stress measurements made at the shot and with postshot crater measurements. Total ejecta-mass histories were determined from the ejecta flux given as a function of radius and time by the method outlined above. The derived ejecta mass so obtained is shown in Figure IV-4.97. It can be seen that the early-time ejection rate persists only for ejecta with velocities greater than 50 m/sec. Presumably, a large amount of low-velocity mass associated with the outside of the lip of the growing crater is counted in the low-velocity ejecta mass. This is due to the definition of ejecta as all mass passing the original air-ground interface. The instantaneous crater lip includes a ramp extending some 6 meters beyond the "true" lip of high-velocity ejecta. Since this relatively slow-moving ramp is above the original interface, it is counted as ejecta. It is felt that to include this low-velocity mass as ejecta is unrealistic. It may not even be detached from the ground at the time that it crosses the interface and is counted as ejecta. At any rate, it will most probably fall back before the time that vertical motion begins to loft the ejecta. Accordingly, an ejection cutoff velocity was sought such that mass exterior to the lip would not be counted as ejecta. A vertical velocity of 50 m/sec was found adequate to exclude this mass. When ejecta mass with velocity greater than this cutoff was plotted against time, it was found that the ejection rate remained substantially constant from the earliest time to about 35 milliseconds. Thus, the dramatic increase in ejection rate is associated with the low-velocity ejecta outside the instantaneous crater. The lofting histories associated with velocity cutoffs are also shown in Figure IV-4.97.

The second calculation that was examined after Tables IV-4.31 and IV-4.32 were assembled is the MIDDLE GUST III calculation. Unfortunately, data were not available before 0.1 second, and peak-ejecta velocities were below 30 m/sec. Accordingly, it was concluded that these data would not be as useful for establishing mass lofting rates so they were omitted. From this discussion of eight
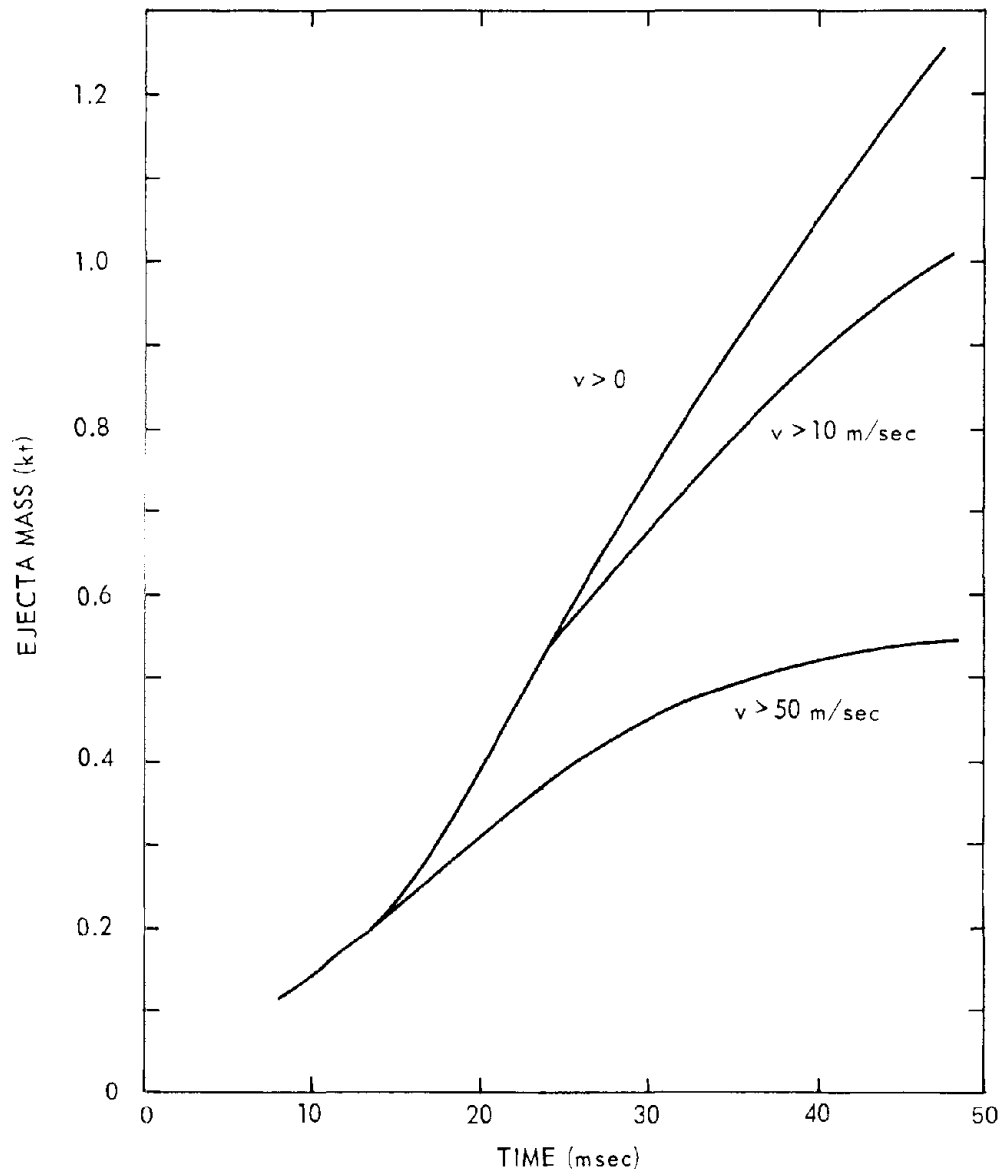
Figure IV-4.97. Calculated MIXED COMPANY ejecta.

very different hydrocode cratering calculations, it can be concluded that the ejection rate for high-velocity ejecta is effectively constant. This observation is useful for developing a dust and ejecta source.

IV-4.5   REFERENCES

IV-4.1   Sager, R.A., C.W. Denzel, and W.B. Tiffany, "Cratering from High Explosive Charges, Compendium of Crater Data," U.S. Army Engineer Waterways Experiment Station, Vicksburg, Mississippi, Technical Report No. 2-547, Report 1, May 1960.

IV-4.2   Rooke, A.D., Jr. and L.K. Davis, "Project PRE-BUGGY, Emplacement and Firing of High-Explosive Charges and Crater Measurements," U.S. Army Engineer Waterways Experiment Station, Vicksburg, Mississippi, Miscellaneous Paper No. 1-663, February 1965.

IV-4.3   Cook, M.A., The Science of High Explosives, Robert E. Krieger Publishing Company, Inc., 1971.

IV-4.4   Rooke, A.D., Jr., B.L. Carnes, and L.K. Davis, "Cratering by Explosions: A Compendium and an Analysis," U.S. Army Engineer Waterways Experiment Station, Vicksburg, Mississippi, Technical Report N-74-1, January 1974.

IV-4.5   Vortman, L.J., "Maximum Missile Ranges from Surface and Buried Explosions," Sandia Laboratories, Albuquerque, New Mexico, Report No. SC-RR-67-616, September 1967.

IV-4.6   Bishop, J.A. and F.E. Lowance, "Operation JANGLE, Project 4.2-Physical Characteristics of Crater and Lip," U.S. Naval Civil Engineering Research and Evaluation Laboratory, Port Hueneme, California, Report No. WT-399, May 1952.

IV-4.7   Vaile, R.B., Jr. and V. Salmon, "Operation JANGLE - Project 4.5-Evaluation of Missile Hazard, Underground Shot," Stanford Research Institute, Menlo Park, California, Report No. WT-338, May 1952.

IV-4.8   Frandsen, A.D., "Engineering Properties Investigation of the CABRIOLET Crater," Army Engineer Nuclear Cratering Group, Livermore, California, Report PNE-957, October 1969.

IV-4.9   Hughes, B.C., "The Challenge of Military Nuclear Construction," U.S. Army War College, USAWC Research Paper, 8 March 1972.

IV-4.10   Ahlers, E.B., "Project DANNY BOY - Project 1.5: Throwout Study of an Underground Nuclear Detonation, Final Report," POR 1814 (WT-1814), September 1962.

IV-4.11   Hess, W.N., "Throwout Calculations," Paper O in Proceedings of the Geophysical Laboratory - Lawrence Radiation Laboratory Cratering Symposium, UCRL-6438 Part II, March 28 - 29, 1961.

IV-4.12   Rooke, A.D., Jr. and L.K. Davis, "Project DANNY BOY - Project 1.6: Mass Distribution Measurements of Crater Ejecta and Dust, Final Report," POR 1815 (WT-1815) July 1963.

IV-4.13 Tewes, H.A., "Experimental Plan for Project SCHOONER," Lawrence Radiation Laboratory, Livermore, California, August 1968.

IV-4.14 Henny, R.W., "SCHOONER Observations and Early Results (Interim Report)," Air Force Weapons Laboratory, Report No. AFWL-TR-69-133, October 1969.

IV-4.15 Henny, R.W., "Project SCHOONER - Site, Crater, Ejecta, Missile and Cloud Investigation Technical Program (Revised)," Eric H. Wang Civil Engineering Research Facility, University of New Mexico, Albuquerque, New Mexico, December 1968.

IV-4.16 Carlson, R.H. and W.A. Roberts, "Mass Distribution and Throwout Studies - Project SEDAN," The Boeing Company, Seattle, Washington, Report No. PNE-217F, May 1963.

IV-4.17 Allen, J., "Radioactive Pellet Trajectory Study - Project SEDAN," Lawrence Livermore Laboratory, Livermore, California, Report No. PNE-218F, April 1965.

IV-4.18 Nordyke, M.D. and M.M. Williamson, "The SEDAN Event - Final Report," Report No. PNE-242F, April 1965.

IV-4.19 Shoemaker, E.M., "Ballistic and Throwout Calculations for the Lunar Crater Copernicus," Paper Q of Proceedings of the Geophysical Laboratory - Lawrence Radiation Laboratory Cratering Symposium, UCRL-6438 Part II, March 1961.

IV-4.20 Sherwood, A.E., "Effect of Air Drag on Particles Ejected During Explosive Cratering," Journal of Geophysical Research, 72, No. 6, pp 1783 - 1791, 1967.

IV-4.21 Perret, W.R. et al., "Project SCOOTER, Final Report," Sandia Corporation, SC-4602 (RR), October 1963.

IV-4.22 Milligan, M.L. and G.A. Young, "Operation TEAPOT - Underground Shot - Base Surge Analysis," U.S. Naval Ordnance Laboratory, White Oak, Maryland, NAVORD Report 4153 (AFSWP-876), 31 January 1956.

IV-4.23 Doll, E.B. and Col H.K. Gilbert, USAF, "Summary Report of the Technical Director, Operation TEAPOT Preliminary Report," ITR-1153, June 1955.

IV-4.24 Young, G.A., "Base Surge Analysis - HE Tests," Operation JANGLE Project 1 (9)-4, NOL Report 1169 (WT-339), May 1952.

IV-4.25 Carlson, R.H. and G.D. Jones, "Distribution of Ejecta from Cratering Explosions in Soils," Journal of Geophysical Research, 70, No. 8, pp 1897 - 1910, 1965.

IV-4.26 Stetson, R.L. et al., "Distribution and Intensity of Fallout from the Underground Shot," Project 2.5.2, Operation TEAPOT, U.S. Naval Radiological Defense Laboratory, San Francisco, California, Report No. WT-1154, March 1958.

IV-4.27   Lewis, J.G., "Crater Measurements, Operation TEAPOT," WT-1105, Armed Forces Special Weapons Project, July 18, 1955.

IV-4.28   Nordyke, M.D. and W.R. Wray, "A Nuclear Cratering Experiment," J. Geophys. Res., Vol. 69, 4, February 15, 1964.

IV-4.29   Leisck, J.F., "Postshot Geologic Investigations of the DANNY BOY Nuclear Cratering Experiment in Basalt," Lawrence Radiation Laboratory, Livermore, California, UCRL-7803, March 1964.

IV-4.30   Sachs, D.C. and L.M. Swift, "Underground Explosion Effects," Operation TEAPOT, Project 1.7, Stanford Research Institute, Menlo Park, California, WT-1106, July 1959.

IV-4.31   "Guide to High-Explosive Field Tests with Military Applications (Yields of 100 Pounds or More)," General Electric-TEMPO, DASIAC, Report No. DASIAC SR 159, July 1976.

IV-4.32   Vortman, L.J., "Ten Years of High Explosive Cratering Research at Sandia Laboratory," Nuclear Applications and Technology, Vol. 7, pp 269-304, September 1969.

IV-4.33   Vortman, L.J. and J.W. Long, "Ejecta from a Row-Charge Cratering Explosion," Sandia Laboratories, Albuquerque, New Mexico, Report No. SC-RR-72-0001, March 1972.

IV-4.34   Vortman, L.J. and H.R. MacDougall, "Project STAGECOACH - 20-Ton HE Cratering Experiments in Desert Alluvium - Final Report," Sandia Laboratories, Report No. SC-4596(RR), May 1962.

IV-4.35   Roberts, W.A. and J.A. Blaylock, "Distribution of Debris Ejected by the STAGECOACH Series of High Explosive Cratering Bursts," The Boeing Company, Seattle, Washington, Report No. D2-6955-1, October 1961.

IV-4.36   Perret, W.R., A.J. Chabai, J.W. Reed, and L.J. Vortman, "Project SCOOTER, Final Report," Sandia Laboratories, Report No. SC-4602(RR), October 1963.

IV-4.37   Flanagan, J.J., "Project AIR VENT," Sandia Laboratories, Report No. SC-RR-64-1704.

IV-4.38   Ahlers, E.B., "Crater Ejecta Studies - AIR VENT Phase I," IIT Research Institute, Chicago, Illinois, Report No. IITRI M-6072-FR, Final Report, May 1965.

IV-4.39   Anthony, M.V., T.P. Day, and C.R. Wauchose, "FERRIS WHEEL Series, FLAT TOP I Event - Ejecta Distribution from FLAT TOP I Event," The Boeing Company, Seattle, Washington, Report No. POR 3007, October 1965.

IV-4.40   Ahlers, E.B. and C.A. Miller, "FERRIS WHEEL Series, FLAT TOP Event, Project Officers Report - Project 1.5a, Crater Ejecta Studies," IIT Research Institute of Illinois, Chicago, Illinois, Report No. POR 3006, November 21, 1966.

IV-4.41 "Proceedings of the MIXED COMPANY/MIDDLE GUST Results Meeting, 13-15 March 1973, Volume II, Sessions 2B and 3B," General Electric Company-TEMPO, DASIAC, Santa Barbara, California, DNA 3151P2, 1 May 1973.

IV-4.42 Melzer, L.S., "MIDDLE GUST Test Series, Events I, II, III, Test Plan and Prediction Report," Air Force Weapons Laboratory, Report No. AFWL-TR-71-147, November 1971.

IV-4.43 Meyer, J.W., "MIDDLE GUST Series: Crater and Ejecta Studies," (in preparation) U.S. Army Engineer Waterways Experiment Station, CE, Vicksburg, Mississippi.

IV-4.44 Wisotski, J., "Technical Photography from MINE UNDER and MINE ORE Events of the MINE SHAFT Series," Denver Research Institute, Report No. DRI 2495 or DASA 2268, May 1969.

IV-4.45 Wisotski, J., "Analysis of In-Flight Ejecta From Photography of a 100-Ton TNT Detonation on Granite," Denver Research Institute, Report No. DRI 2538, May 1970.

IV-4.46 Linnerud, H.J., "In-Flight Ejecta Size Distributions for MIDDLE GUST III," Science Applications, Inc., Bedford, Massachusetts, Report No. DNA 3574F, March 1975.

IV-4.47 Carnes, B.L., "MIDDLE NORTH Series, MIXED COMPANY Event - Craters and Ejecta from Near-Surface Bursts on Layered Media," U.S. Army Engineer Waterways Experiment Station, Vicksburg, Mississippi, Report No. POR 6612, 17 September 1975.

IV-4.48 Wisotski, J., "MIDDLE NORTH Series, MIXED COMPANY Events, Technical Photography," Denver Research Institute, Denver, Colorado, Report No. POR 6625, 7 August 1975.

IV-4.49 Wisotski, J., "MIDDLE GUST Dynamic Ejecta Measurements," Denver Research Institute, Denver, Colorado, Report No. AFWL-TR-75-104, 1975.

IV-4.50 Dishon, J.F., "ESSEX-DIAMOND ORE Research Program: Ejecta Measurement Report, ESSEX I, Phase I," U.S. Army Engineer Waterways Experiment Station, Livermore, California, Report No. DNA PR 0009, February 1975.

IV-4.51 Rooke, A.D., Jr., "Graphic Portrayal of Discrete Explosion-Produced Crater-Ejecta Characteristics," U.S. Army Engineer Waterways Experiment Station, Vicksburg, Mississippi, Miscellaneous Paper N-76-7, June 1976.

IV-4.52 Chabai, A.J., "Scaling Dimensions of Craters Produced by Buried Explosions," Sandia Corporation, Albuquerque, New Mexico, Report No. SC-RR-65-70, February 1965.

IV-4.53 Rooke, A.D., Jr., B.L. Carnes, and L.K. Davis, "Cratering by Explosions: A Compendium and an Analysis," U.S. Army Engineer Waterways Experiment Station, CE, Vicksburg, Mississippi, Technical Report N-74-1, January 1974.

IV-4.54 Davis, L.K. and A.D. Rooke, Jr., "DANNY BOY Event, Project 1.6, Mass Distribution Measurements of Crater Ejecta and Dust; Volumetric Equalities of the Crater," U.S. Army Engineer Waterways Experiment Station, CE, Vicksburg, Mississippi, Miscellaneous Paper No. 1-754, Appendix B, December 1965.

IV-4.55 Sherman, W.C., "Particle-Size Analysis by Photo-Grid Method," U.S. Army Engineer Waterways Experiment Station, CE, Vicksburg, Mississippi, Letter Report, 20 November 1964.

IV-4.56 Kley, R.J. and R.J. Lutton, "A Study of Selected Rock Excavations as Related to Large Nuclear Craters," U.S. Army Engineer Waterways Experiment Station, CE, Vicksburg, Mississippi, Miscellaneous Paper No. 3-991, October 1967.

IV-4.57 Banks, D.C. and R.T. Saucier, "Geology of Buckboard Mesa, Nevada Test Site," U.S. Army Engineer Waterways Experiment Station, CE, Vicksburg, Mississippi, Preliminary Report PNE-5001, July 1964.

IV-4.58 Benfer, R.H., "Project PRE-SCHOONER II, Apparent Crater Studies," U.S. Army Engineer Nuclear Cratering Group, Lawrence Radiation Laboratory, Livermore, California, Final Report PNE-508, May 1967.

IV-4.59 Anderson, B.D., "A Simple Technique to Determine the Size Distribution of Crater Fallback and Ejecta," U.S. Army Engineer Nuclear Cratering Group, Lawrence Radiation Laboratory, Livermore, California, Technical Report No. 18, March 1970.

IV-4.60 Chabai, A.J. and R.H. Bishop, "Project BUCKBOARD, 20-Ton and 1/2-Ton High Explosive Cratering Experiments in Basalt Rock," Sandia Corporation, Albuquerque, New Mexico, SC-4675(RR), Chapters 4 and 8, August 1962.

IV-4.61 Henny, R.W. and R.H. Carlson, "Natural Missile Distributions for High Explosive Craters in Hard Rock - Volume III, Multiple Threat Cratering Experiment," Air Force Weapons Laboratory, Report No. AFWL-TR-67-8, June 1970.

IV-4.62 Strange, J.N. and W.H. McAnally, Jr., "Operation MINE SHAFT; Surface Effects and Cavity Resulting from the Detonation of a 16-Ton Charge Deep in Granite," U.S. Army Engineer Waterways Experiment Station, CE, Vicksburg, Mississippi, Technical Report N-70-4, July 1970.

IV-4.63 Davis, L.K., "MINE SHAFT Series; Subtask N123, Calibration Cratering Series," U.S. Army Engineer Waterways Experiment Station, CE, Vicksburg, Mississippi, Technical Report N-70-4, February 1970.

IV-4.64 Videon, F.F., "Project PALANQUIN, Studies of the Apparent Crater," U.S. Army Engineer Nuclear Cratering Group, Lawrence Radiation Laboratory, Livermore, California, Final Report PNE-904, July 1966.

IV-4.65 Frandsen, A.D., "Engineering Properties Investigations of the CABRIOLET Crater," U.S. Army Engineer Nuclear Cratering Group, Lawrence Radiation Laboratory, Livermore, California, Final Report PNE-957, March 1970.

IV-4.66   "Underground Explosion Test Program: Rock, Final Report, Volume II,"
          Engineering Research Associates, Inc., St. Paul, Minnesota, 30 April 1953.

IV-4.67   Sprague, K.E., "MIDDLE COURSE II Cratering Series," Explosive Excavation
          Research Laboratory, U.S. Army Engineer Waterways Experiment Station, CE,
          Vicksburg, Mississippi, Technical Report E-73-3, July 1973.

IV-4.68   Carnes, B.L., "MIXED COMPANY: Crater and Ejecta from Near-Surface Bursts
          on Layered Media," (in preparation) U.S. Army Engineer Waterways Experiment
          Station, CE, Vicksburg, Mississippi.

IV-4.69   Ingram, J.K., J.L. Drake, and L.F. Ingram, "Influence of Burst Position on
          Airblast, Ground Shock, and Cratering in Sandstone," U.S. Army Engineer
          Waterways Experiment Station, CE, Vicksburg, Mississippi, Miscellaneous
          Paper N-75-3, May 1975.

IV-4.70   Henny, R.W., "SCHOONER Observations and Early Results," Air Force Weapons
          Laboratory, Kirtland Air Force Base, New Mexico, Technical Report No. AFWL-
          TR-69-133, October 1969.

IV-4.71   Henny, R.W., "SCHOONER Ejecta Studies," Air Force Weapons Laboratory,
          Kirtland Air Force Base, New Mexico, Technical Note DE-TN-70-014, January,
          1971.

IV-4.72   Fisher, P.R., R.J. Kley, and H.A. Jack, "Project PRE-GONDOLA I, Geologic
          Investigations and Engineering Properties of Craters," U.S. Army Engineer
          Nuclear Cratering Group, Lawrence Radiation Laboratory, Livermore,
          California, Final Report PNE-1103, May 1969.

IV-4.73   O'Connor, J.M., "Preliminary Results, Phase IIb, Project DIAMOND ORE,"
          Explosive Excavation Research Laboratory, U.S. Army Engineer Waterways
          Experiment Station, CE, Livermore, California, Memorandum for Record,
          24 November 1972.

IV-4.74   O'Connor, J.M., "Preliminary Results, Phase IIa, Project DIAMOND ORE,"
          Explosive Excavation Research Laboratory, U.S. Army Engineer Waterways
          Experiment Station, CE, Livermore, California, Memorandum for Record,
          26 November 1971.

IV-4.75   O'Connor, J.M., T.J. Donlan, and D.E. Burton, "Explosive Selection and
          Fallout Simulation Experiments, Nuclear Cratering Device Simulation
          (Project DIAMOND ORE)," Explosive Excavation Research Laboratory, U.S.
          Army Engineer Waterways Experiment Station, CE, Livermore, California,
          Technical Report E-73-6, October 1973.

IV-4.76   Harvey, W.T., "1000-Pound Near Surface Cratering Experiments, Fort Peck,
          Montana," Explosive Excavation Research Laboratory, U.S. Army Engineer
          Waterways Experiment Station, CE, Livermore, California, Preliminary
          Report E-73-5 (later renumbered E-73-6), April 1973.

IV-4.77   "Underground Explosion Test Program: Soil, Final Report, Volume I,"
          Engineering Research Associates, Inc., St. Paul, Minnesota, 30 August
          1952.

IV-4.78 "Instrumentation for Underground Explosion Test Program: Dry Clay, Dry Sand, Wet Clay, Volume I, Supplement to Interim Technical Report No's. 1, 2 and 3," Engineering Research Associates, Inc., St. Paul, Minnesota, 1 June 1952.

IV-4.79 Rooke, A.D., Jr. and T.D. Chew, "Crater and Ejecta Measurements for a Full-Scale Missile Detonation in an Underground Cell," U.S. Army Engineer Waterways Experiment Station, CE, Vicksburg, Mississippi, Miscellaneous Paper No. 1-853, November 1966.

IV-4.80 "Instrumentation for Underground Explosion Test Program: Wet Clay," Engineering Research Associates, Inc., St. Paul, Minnesota, Interim Technical Report No. 3, November 1951.

IV-4.81 Carnes, B.L., "MIXED COMPANY: Craters and Ejecta from Near-Surface Bursts on Layered Media," Defense Nuclear Agency, Field Command, Kirtland Air Force Base, New Mexico, DNA POR 6612, 17 September 1975.

IV-4.82 Jones, G.H.S. et al., "Operation PRAIRIE FLAT, Project Officers Report-Project LN 3.01, Crater and Ejecta Study," Defence Research Establishment Suffield, Ralston, Alberta, Canada, POR 2115 (WT-2115), 10 December 1970.

IV-4.83 Miller, A.E., "ESSEX-DIAMOND ORE Research Program Preliminary Combined Results Report - ESSEX I, Phase 2, Nuclear Cratering Device Simulation (Project ESSEX)," Explosive Excavation Research Laboratory, U.S. Army Engineer Waterways Experiment Station, CE, Vicksburg, Mississippi, Preliminary Report E-75-1 (DNA PR 0016), 21 March 1975.

IV-4.84 Miller, G.M., Jr., "ESSEX-DIAMOND ORE Research Program Test Execution Report - ESSEX I, Phase 1, Nuclear Cratering Device Simulation (Project ESSEX)," Explosive Excavation Research Laboratory, U.S. Army Engineer Waterways Experiment Station, CE, Vicksburg, Mississippi, Preliminary Report E-75-6 (DNA PR 0001), April 1975.

IV-4.85 Seebaugh, W.R., "Studies of the Nuclear Crater Ejecta Environment," Science Applications, Inc., McLean, Virginia, Report No. DNA 3640F, 24 June 1975.

IV-4.86 Wisotski, J., "Technical Photography of a 100-Ton TNT Detonation on Granite, MINERAL ROCK Event," Denver Research Institute, Denver, Colorado, DRI-2543 (MS 2166), June 1970.

IV-4.87 Bechtell, W.R., "Project R. D. Bailey Experimental Excavation Program," Explosive Excavation Research Laboratory, U.S. Army Engineer Waterways Experiment Station, CE, Vicksburg, Mississippi, Technical Report E-75-2, June 1975.

IV-4.88 Vortman, L.J., "Maximum Missile Ranges from Surface and Buried Explosions," Sandia Laboratories, Report No. SC-RR-67-616, September 1967.

IV-4.89 Austin, J.B., "Methods of Representing Distribution of Particle Size," Industrial and Engineering Chemistry, Volume II, No. 6, pp. 334-339, 15 June 1939.

IV-4.90   Stroeberger, D.E., "Operation MINE SHAFT-MINERAL ROCK Ejecta Study,"
          The Boeing Company, Seattle, Washington, Report No. DNA 2743P, December
          1971.

IV-4.91   Rabb, D., "Particle-Size Distribution Study: PILEDRIVER Event," U.S.
          Atomic Energy Commission, Engineering with Nuclear Explosives, Volume 2,
          Proceedings (unpublished).

IV-4.92   Gault, D.E., "Spray Ejected from the Lunar Surface by Meteoroid Impact,"
          Ames Research Center, NASA TN D-1767, April 1963.

IV-4.93   Moore, H.J., D.E. Gault, and R.V. Lugn, "Experimental Impact Craters in
          Basalt," Society of Mining Engineering Transaction, September 1963.

IV-4.94   MacMillan, W.D., Theoretical Mechanics - Statics and the Dynamics of a
          Particle, Dover Publications, Inc., New York, p. 254, 1958.

IV-4.95   Sogge, R.L. and D.E. Stroeberger, "Transient Ejecta Analysis," The
          Boeing Company, Technical Report No. AFWL-TR-70-64, 1970.

IV-4.96   Schoutens, J.E., General Electric Company-TEMPO (unpublished).

IV-4.97   Crawford, R.E., C.J. Higgins, and E.H. Bultman, "The Air Force Manual
          for Design and Analysis of Hardened Structures," Civil Nuclear Systems
          Corporation, Albuquerque, New Mexico, Report No. AFWL-TR-74-102, October
          1974.

IV-4.98   Post, R.L., "Ejecta Distributions from Near-Surface Nuclear and HE
          Bursts," Air Force Weapons Laboratory, Albuquerque, New Mexico, Report
          No. AFWL-TR-74-51, May 1974.

IV-4.99   Ganong, G.P. and W.A. Roberts, "The Effects of the Nuclear Environment
          on Crater Ejecta Trajectories for Surface Bursts," Air Force Weapons
          Laboratory, Albuquerque, New Mexico, Report No. AFWL-TR-68-125,
          October 1968.

IV-4.100 Shockey, D.A., M. Austin, D.R. Curran, and L. Seaman, "Development of
          a Capability for Predicting Cratering and Fragmentation Behavior in
          Rock," Stanford Research Institute, Menlo Park, California, Report No.
          DNA 3730F, May 1975.

IV-4.101 Ferritto, J.M. and J.B. Forrest, "Ground Motions from Pacific Cratering
          Experiments 1000-Pound Explosive Shots," Civil Engineering Laboratory,
          Naval Construction Battalion Center, Port Hueneme, California, Technical
          Report No. R808, January 1975.

IV-4.102 Shockey, D.A., C.F. Petersen, D.R. Curran, and J.T. Rosenberg, "Failure
          of Rocks Under High Rate Tensile Loads," in New Horizons in Rock Mechanics,
          Proceedings of the 14th Symposium on Rock Mechanics, H.R. Hardy, Jr. and
          R. Stefanko, Eds., (American Society of Civil Engineers, New York, 1973).

IV-4.103 Shockey, D.A., D.R. Curran, L. Seaman, J.T. Rosenberg, and C.F. Petersen,
          "Fragmentation of Rock Under Dynamic Loads," Int. J. Rock Mech. Sci.
          Geomech. Abstr., 11, pp. 303-317, 1974.

IV-4.104 Barbee, T.W. et al., "Dynamic Fracture Criteria for Ductile and Brittle Metals," Journal of Materials, JMLSA, 7, pp. 393-401, 1972.

IV-4.105 Shockey, D.A., L. Seaman, D.R. Curran, et al., "A Computational Model for Fragmentation of Armor Under Ballistic Impact," U.S. Army Ballistic Research Laboratories, Aberdeen Proving Ground, Maryland, December 1973.

IV-4.106 Seaman, L. and D.A. Shockey, "Models for Ductile and Brittle Fracture for Two-Dimensional Wave Propagation Calculations," Final Report to AMMRC, December 1973.

IV-4.107 Shockey, D.A., L. Seaman, and D.R. Curran, "Dynamic Fracture of Beryllium under Plate Impact and Correlation with Electron Beam and Underground Test Results, Air Force Weapons Laboratory, Report No. AFWL-TR-73-12, 1973.

IV-4.108 Curran, D.R., D.A. Shockey, and L. Seaman, "Dynamic Fracture Criteria for a Polycarbonate," J. Appl. Phys. 44, pp. 4025-4038, 1973.

IV-4.109 Davis, L.K., "MINE SHAFT Series, Events MINE UNDER and MINE ORE," U.S. Army Engineer Waterways Experiment Station, Vicksburg, Mississippi, Technical Report No. N-70-8, 1970.

IV-4.110 Davis, L.K. et al., "Operation MINE SHAFT," U.S. Army Engineer Waterways Experiment Station, Vicksburg, Mississippi, Report MS-2151, 1972.

IV-4.111 Trulio, J.G., "Calculations of Cratering, Ejecta and Dust Lofting," Applied Theory, Inc., DASA 2507, 1970.

IV-4.112 Maxwell, D. et al., "JOHNIE BOY Crater Calculations," Physics International Company, DNA 3048F, 1973.

IV-4.113 Johnson, W.E., "Code Correlation Study," AFWL-TR-70-144, 1971.

IV-4.114 Ialongo, G., "Prediction Calculations for the MIXED COMPANY III Event," DNA 3206T, November 1973.

APPENDIX IV-4A

BIBLIOGRAPHY*

This appendix contains a listing of reference material which is mostly drawn upon by researchers in the field of ejecta. It is divided into general subjects and, therefore, note that a few entries appear here and in the list of specific references cited in this chapter.

---

*This bibliography was taken in part from Reference IV-4.3.

IV-4A.0   EJECTA MEASUREMENTS FROM HE SPHERES

IV-4A.1   Carlson, R.H. and G.D. Jones, "Project AIR VENT, Ejecta Distribution
           Studies," The Boeing Company, Seattle, Washington, D2-90575, November
           1964.

IV-4A.2   Wisotski, J., "Analysis of In-Flight Ejecta from Photography of a 100-Ton
           TNT Detonation on Granite," Denver Research Institute, Denver, Colorado,
           DRI-2538, May 1970.

IV-4A.3   Vortman, L.J. et al., "Project BUCKBOARD, 20-Ton and 1/2-Ton High Explo-
           sive Cratering Experiments in Basalt Rock," Sandia Corporation, Albuquer-
           que, New Mexico, SC-4675(RR), August 1962.

IV-4A.4   Rappleyea, C.A., "Crater, Ejecta, and Air-Blast Studies from Five High-
           Explosive Charges in a Horizontal Square Array," Sandia Corporation,
           Albuquerque, New Mexico, SC-RR-66-480, April 1967.

IV-4A.5   Ahlers, E.B., "Crater Ejecta Studies, AIR VENT, Phase I," IIT Research
           Institute, Chicago, Illinois, IITRI-Proj. M6072, May 1965.

IV-4A.6   Fienstein, D.I., "Debris Distribution," IIT Research Institute, Chicago,
           Illinois, IITRI-Proj. M6066, March 1966.

IV-4A.7   Meyer, J.W., "Event DIAL PACK, Project 3.01, Crater and Ejecta Studies,"
           U.S. Army Engineer Waterways Experiment Station, CE, Vicksburg, Missis-
           sippi (unpublished).

IV-4A.8   Rooke, A.D., Jr. et al., "Participation in Operation DISTANT PLAIN,
           Apparent Crater and Ejecta Measurements," U.S. Army Engineer Waterways
           Experiment Station, CE, Vicksburg, Mississippi, Miscellaneous Paper
           No. 1-901, May 1967.

IV-4A.9   Henny, R.W. and R.H. Carlson, "Distribution of Natural Missiles Resulting
           from Cratering Explosions in Hard Rock," The Boeing Company, Seattle,
           Washington, October 1966.

IV-4A.10   Sherwood, A.E., "The Effect of Air Drag on Particles Ejected During Ex-
           plosive Cratering," Lawrence Radiation Laboratory, Livermore, California,
           UCRL-14974, June 1966.

IV-4A.11   Carlson, R.H. and R.T. Newell, "Ejecta from Single-Charge Cratering
           Explosions: Volume I," Sandia Corporation, Albuquerque, New Mexico,
           SC-RR-69-1, June 1970.

IV-4A.12   Anthony, M.V. et al., "FERRIS WHEEL Series, FLAT TOP Event, Ejecta
           Distribution from FLAT TOP I Event, Project 1.5b, The Boeing Company,
           Seattle, Washington, POR 3007 (WT-3007), October 1965.

IV-4A.13   Ahlers, E.B. and C.A. Miller, "Crater Ejecta Studies, Project 1.5a, FLAT
           TOP Event," IIT Research Institute, Chicago, Illinois, POR 3006 (WT-3006),
           November 1966.

IV-4A.14   Bishop, J.A. and F.E. Lowance, "Operation JANGLE, Project 4.2, and
            Missile Phenomena, Physical Characteristics of Crater and Lip," U.S.
            Naval Civil Engineering Research and Evaluation Laboratory, Port Hueneme,
            California, WT-399 (in WT-375), May 1952.

IV-4A.15   Vortman, L.J., "Maximum Missile Ranges from Surface and Buried Explo-
            sions," Sandia Corporation, Albuquerque, New Mexico, SC-RR-67-616,
            September 1967.

IV-4A.16   Wisotski, J.,"Technical Photography of a 100-Ton TNT Detonation on
            Granite, MINERAL ROCK Event," Denver Research Institute, Denver, Colorado,
            DRI-2543, June 1970.

IV-4A.17   Meyer, J.W. and A.D. Rooke, Jr., "MINE SHAFT Series, Events MINE UNDER and
            MINE ORE Ejecta Studies," U.S. Army Engineer Waterways Experiment Station,
            CE, Vicksburg, Mississippi, Miscellaneous Paper N-69-2, September 1969.

IV-4A.18   Henny, R.W. and R.H. Carlson, "Natural Missile Distributions for High
            Explosive Craters in Hard Rock, Multiple Threat Cratering Experiment,"
            Air Force Weapons Laboratory, Kirtland Air Force Base, New Mexico, Tech-
            nical Report No. AFWL-TR-67-8, Volume III, June 1970.

IV-4A.19   Day, W.C., Editor, "Project PRE-GONDOLA II, Summary Report," U.S. Army
            Engineer Nuclear Cratering Group, Lawrence Radiation Laboratory, Liver-
            more, California, PNE-1112, February 1971.

IV-4A.20   Mellsen, S.B., "Correlation of Drag Measurements in Operation PRAIRIE
            FLAT with Known Steady Flow Values," Defence Research Establishment
            Suffield, Ralston, Alberta, Canada, Suffield Memorandum No. 12/69,
            April 1969.

IV-4A.21   Mellsen, S.B., "Development of the Free Flight Method for the Measure-
            ment of Drag on Cylinders in Operation PRAIRIE FLAT," Defence Research
            Establishment Suffield, Ralston, Alberta, Canada, Suffield Memorandum
            No. 119/68, January 1969.

IV-4A.22   Carlson, R.H. and W.A. Roberts, "Rayed Debris Distribution Systems
            Associated with Explosion Craters," The Boeing Company, Seattle, Wash-
            ington, D2-09151, March 1962.

IV-4A.23   Roberts, W.A. and E.N. York, "Outer Crater Lip Debris Ejected by
            SCOOTER - A Buried High Explosive Cratering Shot," The Boeing Company,
            Seattle, Washington, D2-90086, April 1962.

IV-4A.24   Anderson, B.D., "A Simple Technique to Determine the Size Distribution
            of Crater Fallback and Ejecta," U.S. Army Engineer Nuclear Cratering
            Group, Lawrence Radiation Laboratory, Livermore, California, Technical
            Report No. 18, March 1970.

IV-4A.25   Roberts, W.A. and J.A. Blaylock, "Distribution of Debris Ejected by the
            STAGECOACH Series of High Explosive Cratering Bursts," The Boeing
            Company, Seattle, Washington, D2-6955-1, October 1961.

IV-4A.1   EJECTA MEASUREMENTS FROM HE HEMISPHERES

IV-4A.26   Carlson, R.H. and W.A. Roberts, "Ejecta Study of 100-Ton Suffield Explosive Cratering Shot," The Boeing Company, Seattle, Washington, D2-90203, September 1962.

IV-4A.27   Carlson, R.H. and W.A. Roberts, "Local Distribution of Material Ejected by Surface Explosions: White Tribe Interim Report," The Boeing Company, Seattle, Washington, D2-6955-2, August 1961.

IV-4A.28   Kaplan, K., "Techniques for Preventing Damage from Ejecta Missiles for a Test with a 500-Ton Hemispherical Charge," Defense Atomic Support Agency, Washington, D.C., Report No. 655-81, December 1965.

IV-4A.2   EJECTA MEASUREMENTS FROM NUCLEAR EXPLOSIONS

IV-4A.29   Davis, L.K. and A.D. Rooke, Jr., "DANNY BOY Event, Project 1.6, Mass Distribution Measurements of Crater Ejecta and Dust, Volumetric Equalities of the Crater," U.S. Army Engineer Waterways Experiment Station, CE, Vicksburg, Mississippi, Miscellaneous Paper No. 1-754, Appendix B, December 1965.

IV-4A.30   Ahlers, E.B., "DANNY BOY Event, Project 1.5, Throwout Study of an Underground Nuclear Detonation," Armour Research Foundation of the Illinois Institute of Technology, Chicago, Illinois, POR 1814 (WT-1814), February 1964.

IV-4A.31   Rooke, A.D., Jr. and L.K. Davis, "DANNY BOY Event, Project 1.6, Mass Distribution Measurements of Crater Ejecta and Dust," U.S. Army Engineer Waterways Experiment Station, CE, Vicksburg, Mississippi, POR 1815 (WT-1815), February 1964.

IV-4A.32   Ganong, G.P. and W.A. Roberts, "The Effect of the Nuclear Environment on Crater Ejecta Trajectories for Surface Bursts," Air Force Weapons Laboratory, Kirtland Air Force Base, New Mexico, Technical Report No. AFWL-TR-68-125, October 1968.

IV-4A.33   Allen, J., "Project SEDAN, Radioactive Pellet Trajectory Study," Lawrence Radiation Laboratory, Livermore, California, PNE-218F, July 1965.

IV-4A.34   Carlson, R.H. and W.A. Roberts, "Project SEDAN, Mass Distribution and Throwout Studies," The Boeing Company, Seattle, Washington, PNE-217F, August 1963.

IV-4A.35   Roberts, W.A., R.H. Carlson, and G.L. Keister, "Ejecta Studies, SEDAN Event," The Boeing Company, Seattle, Washington, D2-90296, December 1962.

CHAPTER IV-5

REVIEW OF THE SOVIET WORK IN CRATERING AND
ASSOCIATED GROUND MOTION*

IV-5.0 INTRODUCTION

For many years the U.S. and the U.S.S.R. have been independently investi-
gating the effects of explosions for civil and military applications. One of
the particular areas of interest is that of explosively produced craters and
the resulting ground motion. A cursory examination of the Soviet literature
indicates a divergence in scientific emphasis and techniques from those of
the U.S. Because of these differences, a careful review and study of the
foreign work can lead to important new insights into the phenomenology and
theory on the subject. Furthermore, such a study should expand the data base
upon which future predictive capabilities must stand.

Several limitations have been imposed on this review. Since this work is
intended for English-speaking readers, only documents that are available in
translations will be referenced. Additionally, reports dealing exclusively
with the seismic detection problem or with material properties are not re-
viewed. The primary source of information was the Foreign Technology Division
of Wright Patterson Air Force Base, Ohio. Contributions were also obtained
from the Lawrence Livermore Laboratory and the Defense Documentation Center.
Soviet Physics "DOKLADY" and J.E.T.P. are translation journals offered by the
American Physical Society and a substantial representation of all of these
sources (available from the Slavic Library of the Battelle Memorial Institute)
were used.

The impression gained from reviewing the Soviet literature is that a well
balanced scientific attack on the problems of explosive crater formation and
the associated motions has been carried out in the U.S.S.R. Large-scale
field experiments to test the problems of airblast, ground motion and crater-
ing were performed. Coupled with these experiments, theoretical and empirical
analyses were also conducted. To examine particular questions which could not

---

*Author: T.F. Stubbs (Physics International)

be answered by the large-scale experiments and by theoretical analyses, small-scale modeling experiments were performed. For example, the influence on cratering of variations in atmospheric pressure and acceleration of gravity were investigated. The major point of difference between the analysis performed in the U.S. and the U.S.S.R. was the almost total lack of reference in the Soviet literature to numerical calculations, such as the multi-dimensional machine computations routinely performed in the United States. Moreover, the U.S. does not appear to rely nearly so heavily on the small-scale modeling techniques as does the U.S.S.R.

Justifications for performing the various cratering experiments have had a strong influence on the experimentation philosophies of the U.S. and the U.S.S.R. Although the justifications for the work in the U.S.S.R. are a point of conjecture, the results are not. For the most part, the Soviet experimentation philosophy appears to have been aimed at obtaining basic scientific understanding of the processes involved in large scale cratering events. Although few such experimental programs were undertaken, they were instrumented to the fullest possible extent. Ground motion data were obtained from ground zero to teleseismic distances. Airblast overpressure was measured along the ground surface and apparently at various elevations above the ground plane. Crater dimensions were obtained and a relatively complete set of measurements of the ejecta field were also obtained. Most of these data were for varying yields and depths-of-burst. The existence of much of the data is inferred because it is not directly reported in the translated literature available to the author. References are made in the literature to untranslated documents containing such information. Taken at face value, the translated literature would seem to indicate that most of these experiments were conducted without regard to any specific military or civilian programs. By the mid-1960's the Soviets had a good understanding of the cratering process and the ground motion. On the other hand, the U.S. has justified the execution of its various cratering events only insofar as it could be shown to pertain to whatever military or civilian program was then under consideration. Only recently has the U.S. recognized the importance of fundamental knowledge of the effects of cratering explosions.

This review will be separated into three overlapping sections. The first section will discuss the large-scale field experiments while the second section will discuss the small-scale modeling experiments. The overlap between these two sections will become apparent in the course of the presentation. For

example, included in the small-scale experiments are yields up to 200 kg of explosive while the large-scale field experiments discussed will consider yields as low as 80 kg. Included in the section on large-scale experiments are some data from the U.S.S.R. equivalent to the U.S. PLOWSHARE program. The third section will include a discussion of the theoretical and the empirical analyses performed. The overlap between this section and the section on small-scale modeling experiments will also become evident. Most of the small-scale experiments were designed to answer questions concerning the empirical analyses.

Unless otherwise specified, dimensions in the following sections will be in the MKS system.

IV-5.1 LARGE YIELD FIELD EXPERIMENTS

IV-5.1.1 Nuclear Cratering Experiments

A summary of four nuclear cratering events conducted by the Soviets for the study of peaceful uses of nuclear explosives was forwarded to the United States as part of an information exchange agreement on the peaceful uses of nuclear explosives. Reference IV-5.1 is a compendium of the documents received by the United States during this exchange. Table IV-5.1 summarizes this information for three single charge cratering events.

The results of the explosion conducted in hole 1004 are almost identical to those of the U.S. nuclear cratering event SEDAN. However, the geology of the experiment was very different from that of SEDAN as is shown in Figure IV-5.1.* Interestingly, the resulting craters have very nearly the same dimensions.

The fourth nuclear cratering event (T-2) discussed was a multiple charge experiment much like the U.S. event BUGGY. In this Soviet experiment, three charges each having a yield of 0.2 kt were emplaced at a depth of 31.4 meters with horizontal separation of 40 meters. The resulting crater is shown in plan and in cross section views in Figure IV-5.2. The quoted crater dimensions are given in Table IV-5.2.

Although ground motion was carefully measured along at least two radial lines on each of the experiments, not all of the empirical fits to the resulting ground motion data were quoted. For example, only the peak velocity and displacement in the vertical component of the compressional or

---

*SEDAN was detonated in a deep, uniform bed of NTS alluvium having a low moisture content.

p-wave and the peak horizontal velocity and displacement in the Rayleigh wave were quoted. For all three of the single charge explosions, it was found that the following relationships held:

$$A_p^z = 40 \left(\frac{y^{1/3}}{r} \right)^{1.4} \quad , \text{ mm} \qquad \text{(IV-5.1)}$$

$$U_p^z = 590 \left(\frac{y^{1/3}}{r} \right)^{1.6} \quad , \text{ cm/sec} \qquad \text{(IV-5.2)}$$

Table IV-5.1. Summary of cratering measurements from reported Soviet single charge nuclear cratering experiments.

Label	Dimension	T-1	"1003"	"1004"
Yield	kt	0.2	1.1	> 100
DOB	M	31.4	48	~ 200
R_a	M	34-40	62	200-215
D_a	M	21	20	83
R_1	M	41-52	71	260
H_1	M	8-10	9	20-35
R_{eb}	M	55-70	140	647
Slope	Deg	35	40	30-55
V_a	M^3		1.11×10^5	6.4×10^6
R_m	M	190		900-1000

DOB - Depth of burst

R_a - Mean apparent crater radius at original ground surface

D_a - Mean apparent crater depth at original ground surface

R_1 - Mean crater radius at the crest of the lip

H_1 - Mean height of lip above original ground surface

R_{eb} - Mean maximum range of the continuous ejecta blanket

V_a - Apparent crater volume below original ground surface

R_m - Maximum range of ejecta missiles
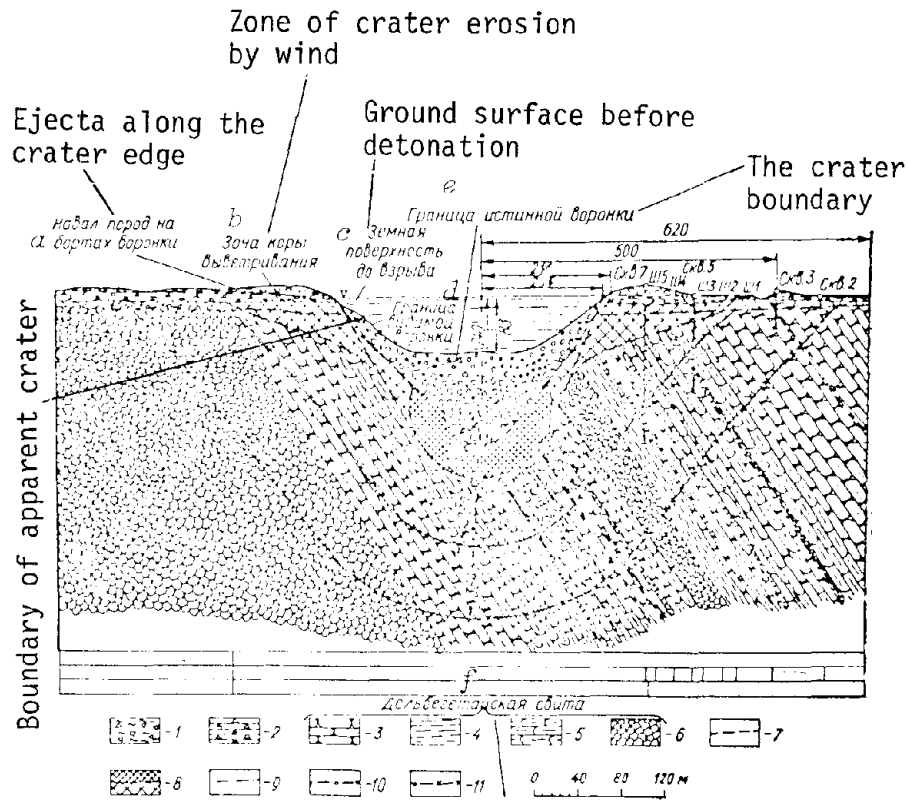
Figure IV-5.1. Geologic section of the crater produced by the explosion in hole 1004.

Table IV-5.2. Results of the T-2 experiments.

Parameter	Values*
Half width of the trench	30 to 35
Trench depth	16
Lip height on the side	between 9 and 16
Lip height on the ends	7
Width of the ejecta blanket on the sides of the trench	95
Width of the ejecta blanket on the ends of the trench	65
Maximum distance of an ejecta projectile	170
Total excavation volume	7.7×10^4

*Linear dimensions in meters, volume dimensions in cubic meters.

1 План траншеи
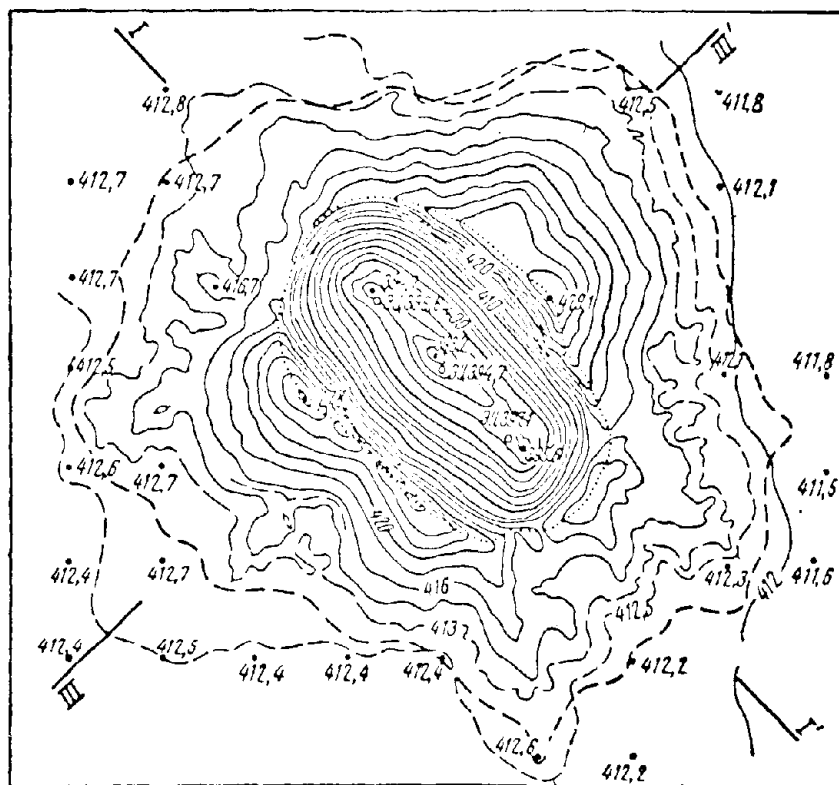
2 Условные обозначения

3 ············ Контур воронки   4 ——————— Граница зоны навала
по гребню навала   выброшенного грунта

5 Разрезы
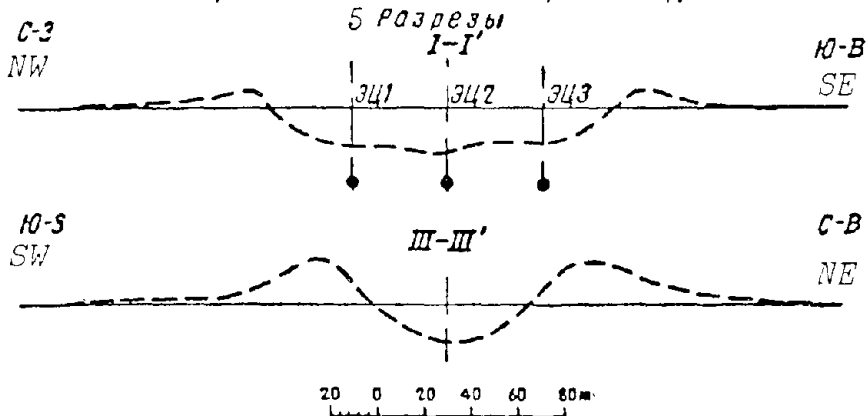
1 - Plan view of trench
2 - Legend
3 - Crater contour along the lip crest
4 - Zone boundary of continuous ejecta
5 - Cross section

Figure IV-5.2.   Contours of trench and throwout material
produced by explosion T-2.

where A_p^Z is the vertical amplitude of the p-wave and U_p^Z is the vertical particle velocity. For the Rayleigh waves the following two relationships held:

$$A_R^X = 165 \left(\frac{Y^{1/3}}{r} \right)^{1.25} \quad , \text{mm} \quad \text{(IV-5.3)}$$

$$U_R^X = 425 \left(\frac{Y^{1/3}}{r} \right)^{1.4} \quad , \text{cm/sec} \quad \text{(IV-5.4)}$$

where A_R^X is the horizontal amplitude of the Rayleigh wave, U_R^X is the horizontal particle velocity, and r is the epicentral distance. Along a direction normal to the axis of the multiple burst explosion (T-2), it was found that the vertical component of the p-wave velocity had exactly the same form as the above equation. However, the peak displacement is given by:

$$A_p^Z = 27 \left(\frac{Y^{1/3}}{r} \right)^{1.2} \quad , \text{mm} \quad \text{(IV-5.5)}$$

and the horizontal components of the Rayleigh waves are given by:

$$A_R^X = 90 \left(\frac{Y^{1/3}}{r} \right)^{1.25} \quad , \text{mm} \quad \text{(IV-5.6)}$$

$$U_R^X = 240 \left(\frac{Y^{1/3}}{r} \right)^{1.4} \quad , \text{cm/sec} \quad \text{(IV-5.7)}$$

It was also claimed that along the axis of the experiment, the displacement amplitudes were between a factor of 1.4 and 1.6 lower than the values given by the above equations while the velocity amplitudes were a factor of 2.2 lower. The geology in which these experiments were conducted is said to be a silty, sandy deposit with sandstone, silt stone and a substantial amount of organic material in the rock structure. In all cases the depths of burst were substantially below the water table.

Other close-in ground motion data from a Soviet nuclear explosion is contained in Reference IV-5.2. Comparisons are made between the two U.S. explosions in salt, SALMON and GNOME, and the 1.1 kt explosion in salt at a depth of 160 meters. Figure IV-5.3 shows a comparison between peak velocity data obtained from the SALMON shot, the Soviet shot, and the expressions

$$U_{max} = 10 \left(\frac{C^{1/3}}{r} \right)^{1.5} \qquad , \text{m/sec} \qquad (IV-5.8)$$

$$A_{max} = 1.35 \, C^{1/3} \left(\frac{C^{1/3}}{r} \right)^{1.6} \qquad , \text{m} \qquad (IV-5.9)$$

where C is the yield in kg. Peak and permanent displacement data are shown scaled in Figure IV-5.4. The peak velocity data from event GNOME are shown as the dashed line in Figure IV-5.3. Evidently the Soviet and U.S. experiences of completely contained underground explosions (camouflet explosion) in salt are the same. It is interesting to note that the peak scaled displacement from all three explosions fall on the same curve. Since the GNOME experiment was a de-coupled shot (it was detonated in a 30 cubic meter room), this would indicate that peak displacement is related more to the late time, gas pressure-induced motion than to the shock-induced motion. One of the interesting results of the work of Rodionov and Tsvetkov (Reference IV-5.2) came about from comparing the calculated maximum volume with the final volume of the camouflet. Two different methods of calculating the maximum volume were used, one in which the yield surface was described as a Mohr-Coulomb function and the other in which a constant yield surface, that is a von Mises condition, was assumed. Using the Coulomb yield condition led to inconsistencies, such as the maximum dynamic volume in one calculation being less than the final experimental volume. Using a constant yield (von Mises condition) stress led to a computed maximum volume which was consistent with the measured final cavity volume. Therefore, it could be concluded that salt behaves as a von Mises solid under the conditions of a camouflet explosion.

IV-5.1.2 Large-Yield High-Explosive Experiments

Three major single charge high explosive test series were conducted by the Soviets. The first was performed in southern Kazakhstan during 1957. The purpose of this series was to investigate scaling laws and their relationship to cratering explosions. A second series used charges of the same weight and investigated the effects of depth of burst. The third series, conducted near Moscow in 1959, was chiefly concerned with the ground motion resulting from fully contained detonations. Scaling laws for the latter events were investigated by using a series of different charge masses detonated at about the same scaled
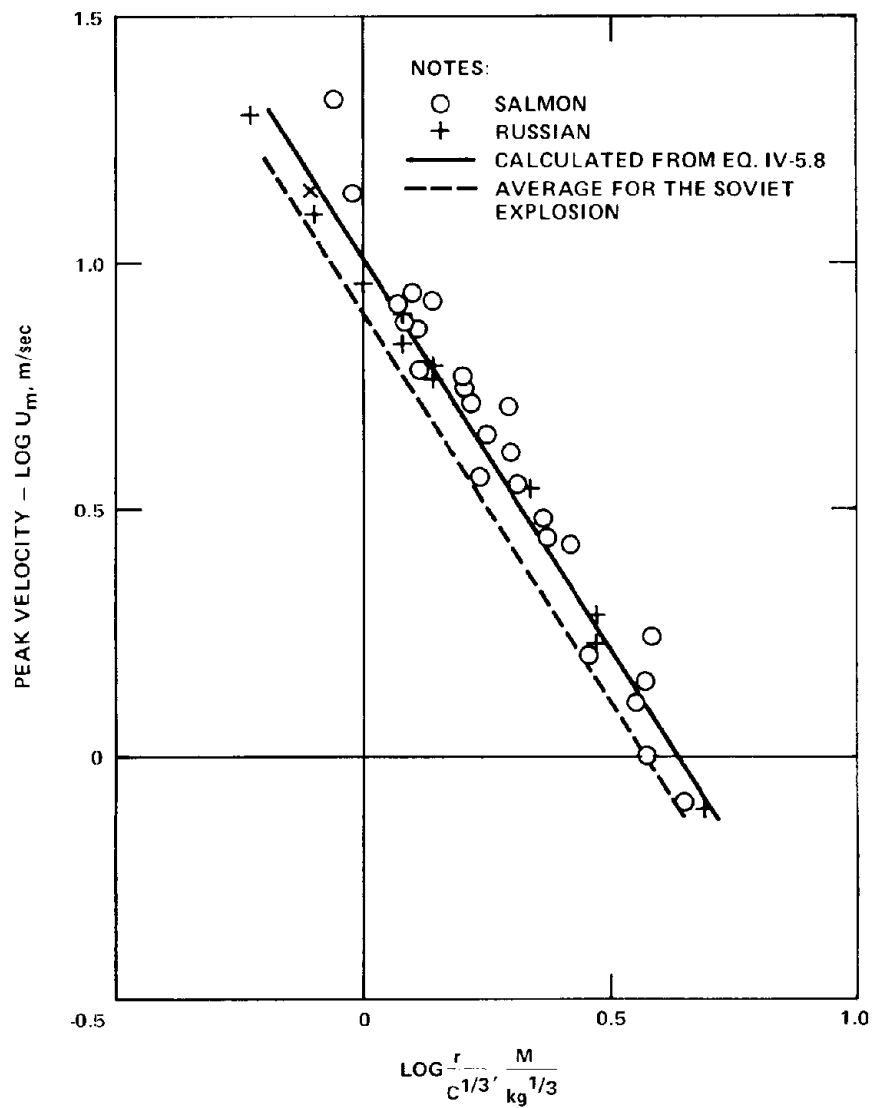
Figure IV-5.3. Maximum mass velocity of the medium as a function of distance.
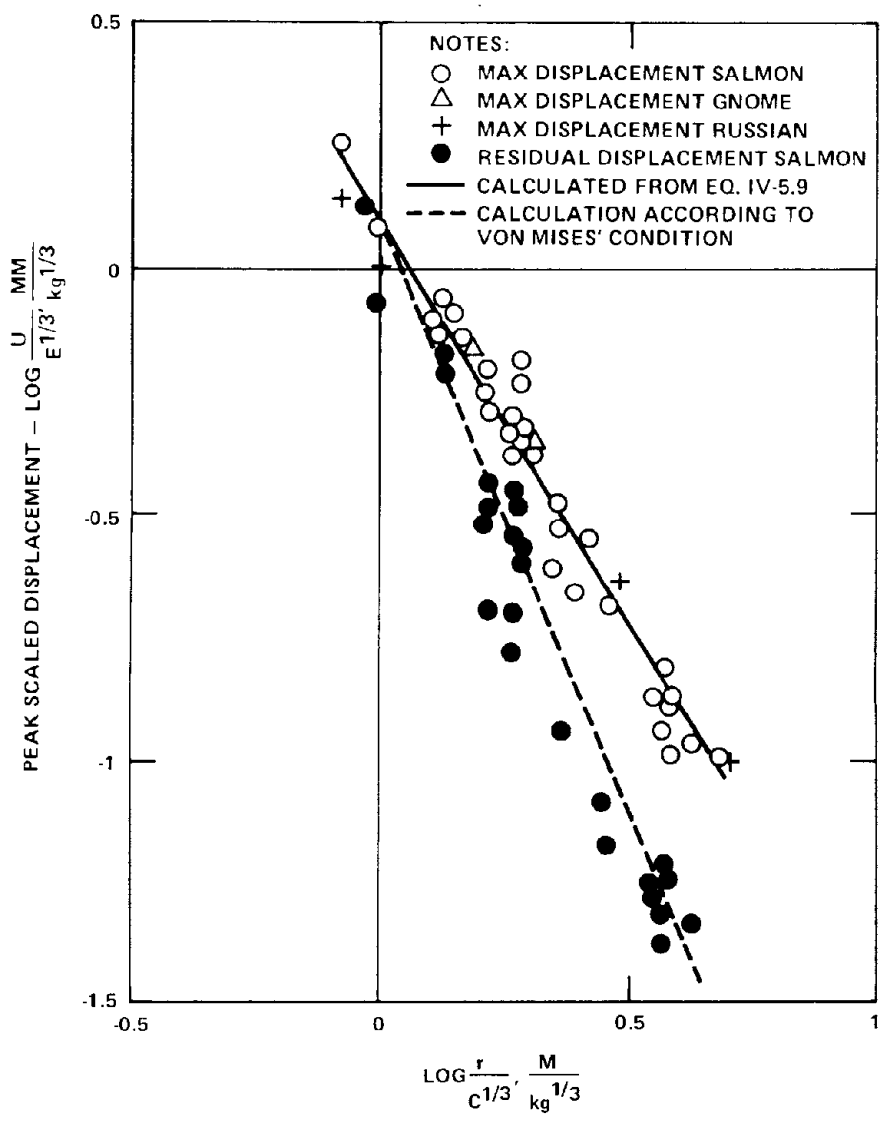
Figure IV-5.4. Medium displacement as a function of distance.

depth of burst, between 1.6 and 1.7 m/kg$^{1/3}$. There are numerous translated documents discussing the first series of events. There are a few translated articles discussing the third series of events with some passing corroborative evidence in other articles. Data from the third series, that is the depth-of-burst events, is essentially unavailable in translated form except for one or two data points appearing on various plots. The article by Garnov and Kharin (Reference IV-5.3) gives reference to all three series.

Conceptually, the simplest configuration of an explosion is one at such a depth that it remains completely contained. Ostensibly to assess safety limits in relation to underground civil work, a series of tests spanning a rather wide range of yield and depth of burst, and employing two different explosive types, was reported by Kharin, Kuz'mina and Danilova (Reference IV-5.4). The experiments were conducted in an area that can be characterized as consisting of an upper layer of loam of high calcium content overlying a quartz sand and sandstone, most probably overlying a hard impervious deposit. (This latter is an assumption as it was stated that the water supply is "kremastic water." Judging from the context this may mean a perched water table.) The tests were conducted throughout the spring, summer and autumn of 1963. Figure IV-5.5 shows the peak velocity measured near the surface of the ground resulting from the explosion at a scaled depth between 2.64 and 2.37 m/kg$^{1/3}$. By "three-dimensional wave" is meant the velocity vector while the term "surface wave" indicates the vertical component of the velocity at the surface. It was found that the peak magnitude of the velocity vector in the compressional wave can be approximated in the scaled range between 2 and 100 m/kg$^{1/3}$ by

$$\overline{V}_p = 100 \left(\frac{C^{1/3}}{r} \right)^{2.20} \qquad , \text{ cm/sec} \qquad \text{(IV-5.10)}$$

where $\overline{V}_p$ is the p-wave velocity vector and C is the yield in kg. As shown in Figure IV-5.5 the peak vertical component of the velocity does not attenuate nearly as rapidly as $\overline{V}_p$. It can be approximated by

$$V_R^z = 100 \left(\frac{C^{1/3}}{r} \right)^{1.30} \qquad , \text{ cm/sec} \qquad \text{(IV-5.11)}$$

where V_R^z is the vertical component of the Rayleigh particle velocity. In Figure IV-5.6 the data of the peak vertical displacement on the surface resulting from
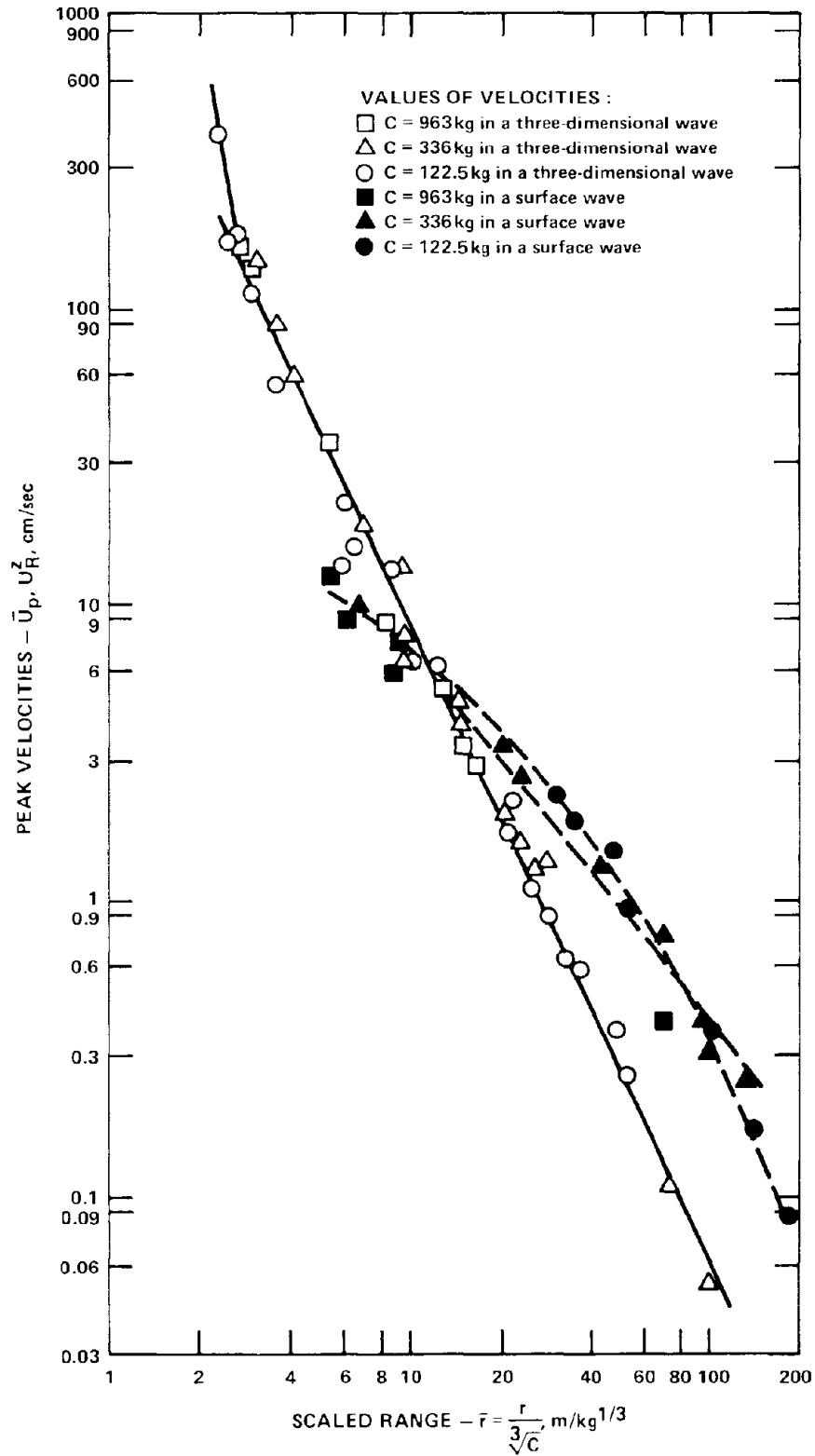
Figure IV-5.5. Relationship of maximum velocities on reduced
hypocentric distance.

The chart shows:

Y-axis: PEAK VELOCITIES $-\bar{U}_P$, U_R^Z, cm/sec

X-axis: SCALED RANGE $-\bar{r} = \dfrac{r}{\sqrt[3]{c}}$, m/kg$^{1/3}$

VALUES OF VELOCITIES :
- □ C = 963 kg in a three-dimensional wave
- △ C = 336 kg in a three-dimensional wave
- ○ C = 122.5 kg in a three-dimensional wave
- ■ C = 963 kg in a surface wave
- ▲ C = 336 kg in a surface wave
- ● C = 122.5 kg in a surface wave
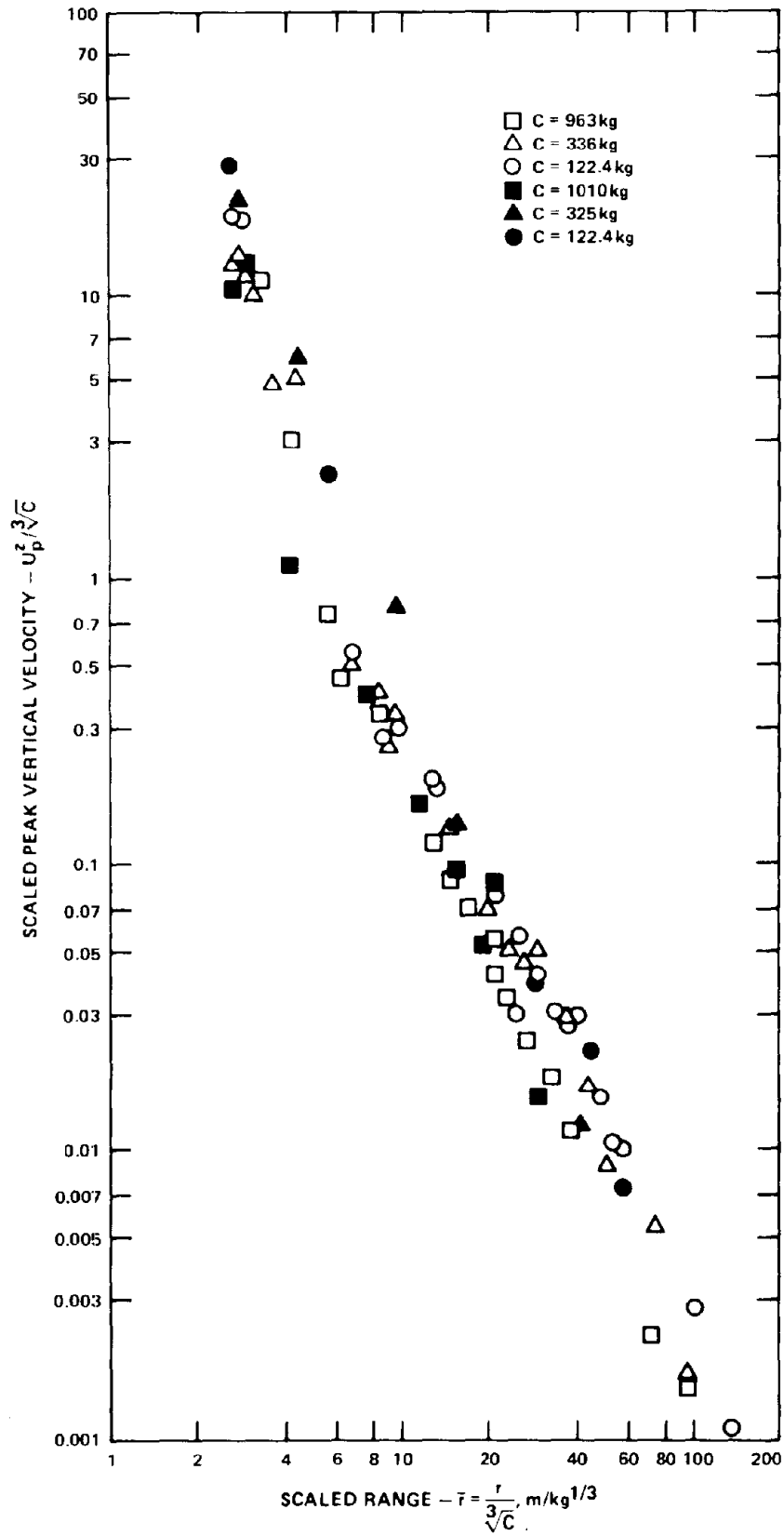
Figure IV-5.6. Dependence of reduced displacement amplitude in
a three-dimensional wave on reduced distance.

the series of six experiments is reproduced, all at a scaled depth of burst of approximately 2.5 m/kg$^{1/3}$. It should be noted that the data from the higher yield experiments systematically show a lower scaled displacement. It would be interesting to investigate the behavior of these data under some other forms of scaling such as Cauchy or Froude yield scaling.*

Three additional questions were simultaneously answered by Kharin, Kuz'mina and Danilova: the effect of scaled depth of burst, the effect of the type of explosive, and the effect of the depth of the gauge station. The analysis is quite involved and beyond the scope of this review, therefore, only a summary will be presented here. No essential difference was noted in the ground motion as a result of the different types of explosive. Figure IV-5.7 shows the effect of depth of burst on the peak vertical velocity and vertical displacement as a function of depth of burst. The subscript "p" stands for the compressional wave portion of the signal and the "R" represents the Rayleigh wave. Some attenuation with depth at a given epicentral range was noted. However, the essential characters of the waves were not altered. Included in the data of Figure IV-5.7 are further experiments conducted with TNT at the same location but the following year. These data are not available in untranslated form except as points on this particular graph.

By far the most extensively reported series of experiments was a group of cratering explosions conducted in 1957. Four general geographic locations, all relatively close to one another, were employed. Area 1 is a fairly dry site of sandy loam. Areas 2, 3 and 4 are a clay to clay-shale sort of material that appears to be either saturated or quite wet. All experiments were conducted at or near what was expected to be the optimum depth of burst for producing a crater. Charge masses ranged from approximately 80 kg up to a kiloton. The explosive used was an ammonium nitrate slurry. In addition to the standard high speed photography, measurements of the ejecta trajectories through special techniques, post-shot ejecta measurements, crater dimensions, and ground motion in the range of a few crater diameters to far teleseismic distances were recorded. A fairly complete discussion of the experimental techniques used is given by Dokuchayev, Rodionov and Romashov (Reference IV-5.5). Included in their discussion are such descriptions as charge emplacement techniques, data on the

---

*Cauchy scaling is a cube root of yield scaling which represents an active elastic restoring force. Froude scaling is a quarter power of yield scaling to account for restoring forces due to gravity.
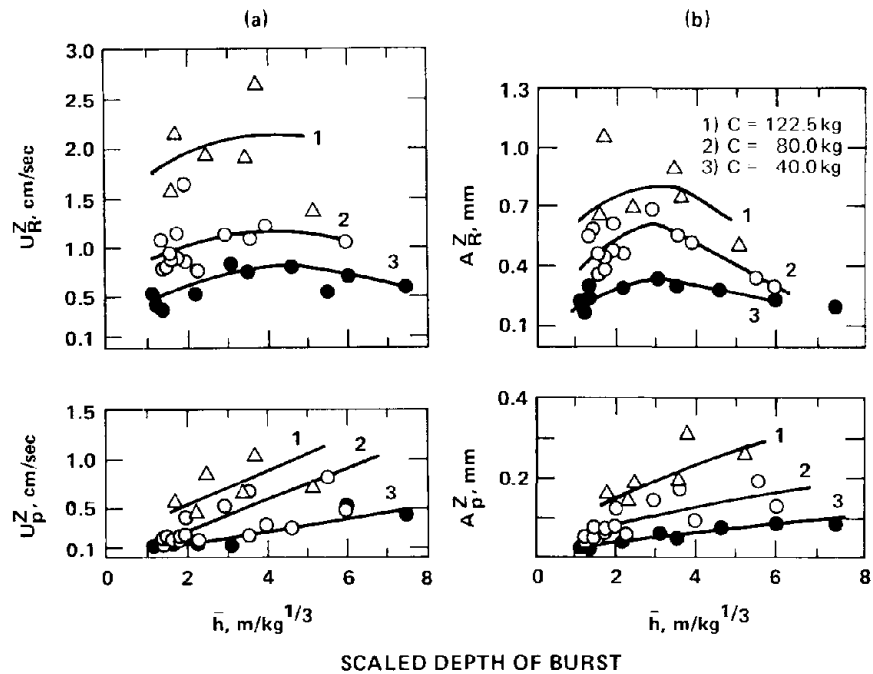
Figure IV-5.7. Peak vertical velocity and displacement.

instrumentation, a minimal amount of information on the geology of the four test sites, and a summary of the data and ground motion measurements. The four test sites were all closely related geologically and geographically. It was claimed that the 1000-ton blast was conducted in a "dense and dry" green to blue-green clay with thin sandstone intercalations. The density of this material was between 1.8 and 2.05 gm/cm^3 and had a moisture content of 15 and 30 percent (the term "dry" is perhaps exaggerated). Overlaying this dense clay was a sandy loam containing quantities of loose breccia to a depth of about 10 meters. In order to conduct the lower yield explosions in a geology which was roughly scaled to that of the kiloton shot, an area was required in which the dense clays were nearly exposed. Two sites satisfying this condition were found in the immediate vicinity of the kiloton epicenter. It was claimed that uniaxial compression tests of this dense clay led to a volume change of 5% under pressure of 180 bar. The fourth test site, labeled "Site No. 1" in the

literature, consisted of an area in which the loam reached a depth of 20 meters. The maximum depth of burst for any shot at this location was 7 meters. This loam was said to be dry (moisture content 4.5%), highly porous (16%) with a density of 1.58 gm/cm³.

As mentioned above, all of these experiments were conducted with depth of burst near the optimum. Reference IV-5.5 made clear that all experiments were designed around the kiloton explosion yield with one of the primary objectives being the investigation of the scaling rules for the crater geometry and associated ground motion. The depth of burst of the kiloton shot was as close to optimum as predictable. The lower yield charges were set at depths of burst covering the range given by Cauchy and Froude scaling. It would appear that at least 36 explosions were conducted throughout the four test sites. Table IV-5.3 lists these explosions, the test sites and the shot numbers corresponding to those given in Reference IV-5.6. Strong motion seismograms and velocity histories are presented in Reference IV-5.6 for several of the shots shown in Table IV-5.3.

In addition to high speed photography showing the rising mound above the explosion, careful study of the ejecta pattern was made on most of these shots. In addition to topological mapping of the resulting ejecta field, two separate but very similar methods were used to obtain a measure of the trajectories of the ejecta. The standard technique of emplacing radioactive pellets in the crater region of the ground was performed. Most of the explosions were labeled by this technique. One typical result is shown in Figure IV-5.8. As shown, a continuous mapping was possible of the material from the source to the final impact point on the ground. Beside each of the solid rays emanating from the indicated explosive charge is a number denoting the epicentral range at which that column was found. This is somewhat at variance with the U.S. experience from event SCOOTER. As seen from the published ejecta source profile (Reference IV-5.7) for SCOOTER (Figure IV-5.9), no such continuous mapping is possible. Another unique method of estimating the trajectory of the mass points within the ejecta field of the crater was to place small brilliant flares in the ground in place of the radioactive pellets. The fuel composition of the flare is color coded so that the initial location of each photographed flare is known. The flares and the explosive are simultaneously ignited at night and the resulting trajectories recorded on color film. A reproduction of a time exposure is shown in Figure IV-5.10.

Table IV-5.3. High explosive cratering tests during the 1957 series in southern Kazakhstan.

Test Site	Shot*	Notes	Charge Mass (kg)	DOB (m)	R_a (m)	D_a (m)	H_ℓ (m)	V (m³)
Porous Loam (dry)	#1	a	10	0.6	1.5	0.9	-	-
	16		10	0.65	1.7	0.95		
	17		10	0.95	1.75	0.8		
	12	b,c	10	1.0	1.75	0.8		
		a	10	1.2	1.8	0.75		
	23		10	1.55	1.8	0.7		
		a	80	2.0	3.25	1.8	0.2-0.6	27
		a	80	2.5	3.85	1.9	0.3-0.5	36
		a	80	2.75	3.7	1.7	0.3	32
	27	b,c	80	3.4	3.75	0.5	0.2	17
	1		10^3	4.0	8.0	3.4	0.8	385
	2	b	10^3	5.0	7.0	2.85	0.7-1.4	225
	3	b	10^3	6.0	8.4	3.95	1.1	425
	4	b,c	10^3	7.0	8.5	3.1	0.4-1.2	315
	5	b	10^3	15.0	-----	Subsidence ---		
	#2	7	b,c	10^3	4.5	9.2	4.5	1.1-2.0	530
	6	b,c	10^3	5.0	8.8	4.85	1.6-1.8	500
	10		10^3	5.9	8.3	2.95	0.7-1.3	300
	9	b	10^3	7.0	10.0	$0^{(d)}$	0.7-1.3	$0^{(d)}$
	8	b	10^3	15.0				
Clay	#3	28		120	1.95	3.5	1.9	1.4-1.6	26
	29		115	2.65	4.8	2.75	0.7-0.8	66
		a	120	3.1	4.5	2.0	0.8-1.2	48
	32		105	3.4	3.6	1.7	0.4-0.8	26
	30		90	3.35	3.0	1.0	0.8-1.0	14
	35		10^3	4.4	8.4	3.9	1.3-2.5	320
		a	10^3	5.4	8.6	4.8	1.3-2.0	420
	33		10^4	9.25	18.5	7.5	2.4-3.0	3750
		a	10^4	11.0	19.0	9.7	2.4-2.6	4200
		a	10^4	13.0	17.5	9.0	1.0-2.5	3800
	#4	36		981000	40.0	75.0	32.0	8-13	237900

(a) No corresponding data in Reference IV-5.6; cannot make a definite correspondence.

(b) Displacement history presented in Reference IV-5.6.

(c) Velocity history presented in Reference IV-5.6.

(d) Ejecta refilled this crater.

*Reference IV-5.6.
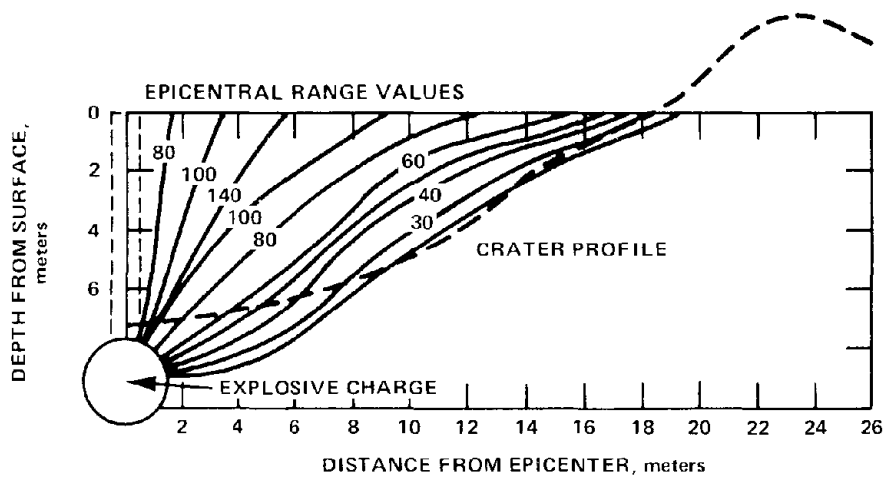
Figure IV-5.8. Lines of equal scatter of the ground material
following the explosion of a 10-ton charge in
clay at a depth of 9 meters.
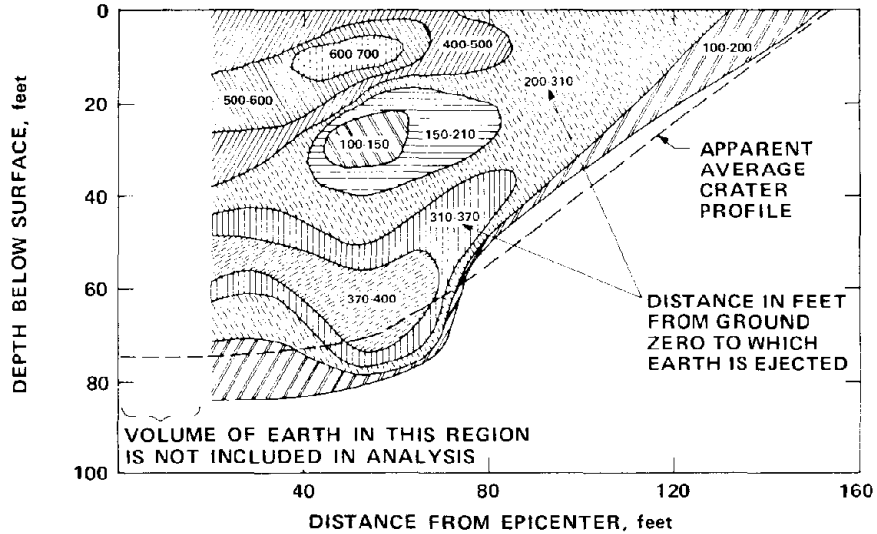
Figure IV-5.9. Source map of ejecta from tracer pellet data -
Event SCOOTER.
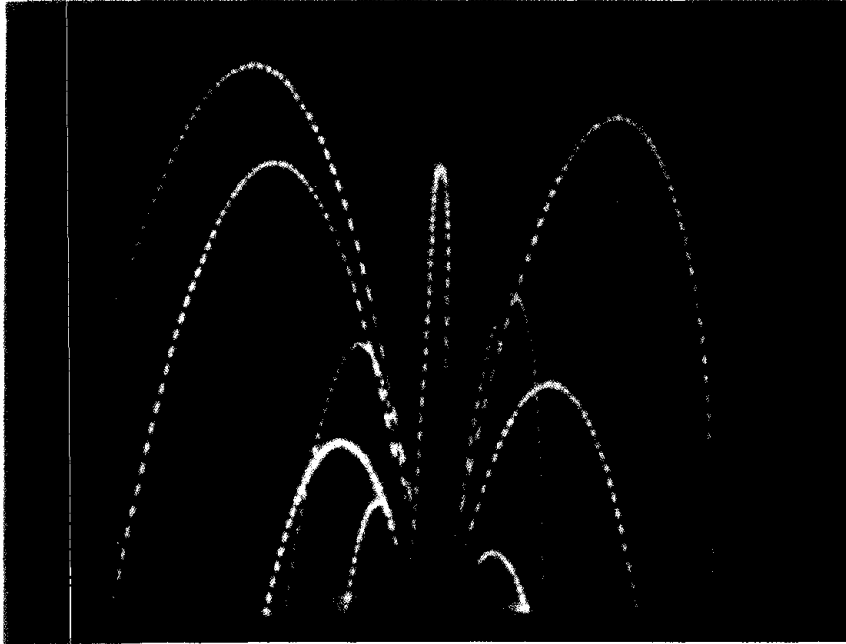
Figure IV-5.10. Multiple exposure photograph of trajectories of artificial ejecta (flares) during a night-time cratering explosion.
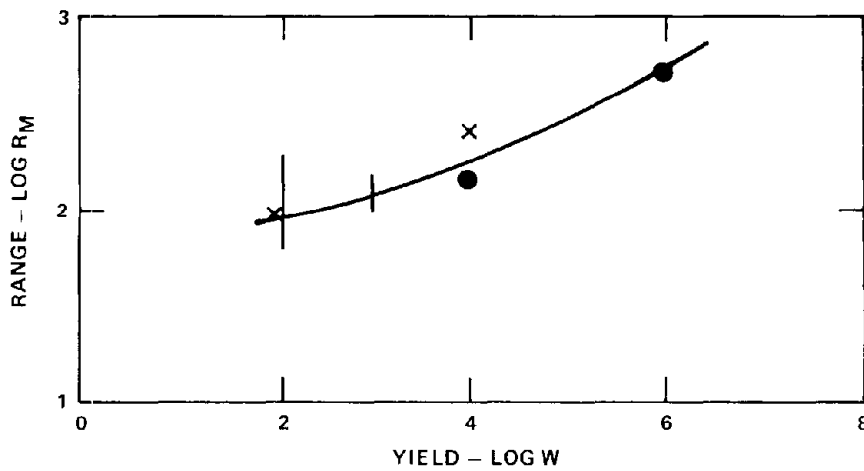
Figure IV-5.11. Maximum range of ejecta.

One very interesting conclusion drawn from this study is that the trajectory of the surface-origin ejecta appear to emanate from a point in the ground approximately twice the depth of burst. The maximum range of ejecta was obtained by filming these explosions. Figure IV-5.11 shows a plot of maximum ejecta range as a function of yield. The scaled depth of burst for all yields was approximately 0.4 $m/kg^{1/3}$. Included in Figure IV-5.11 are two data points from an experiment carried out in 1959. Other than the few data points that appear as crosses in Figure IV-5.11 and two passing references, there are no data presently available from this test series.

The basic reference on ground motion from this 1957 series of cratering explosions is that of Medvedev (Reference IV-5.6). As indicated in Table IV-5.3, many of the ground motion records resulting from the 1957 experiments are represented in that collection of articles. The same data are presented in somewhat greater details in Reference IV-5.8. A typical set of such records is shown in Figure IV-5.12 which represents some of the data taken from the kiloton charge detonated at a depth of 40 meters. Very careful attention was given to observing the developing phases of the waves. The components represented by p are the compressional waves. Many phases at late times in the records are denoted by R. These correspond to the Rayleigh waves and the various wavelets within the Rayleigh wave group. Observation of Figure IV-5.12 shows that the Rayleigh wave is recognized as close to surface ground zero as 500 meters. However, the wave is not fully developed until an epicentral range of 2000 to 3200 meters is attained. Peak amplitudes of these various phases are shown in Figure IV-5.13. It is seen that, although each of the wavelets appears (at least within the accuracy of the data) to attenuate at the same rate, the envelope covering all of the wavelets attenuates with range at a much slower rate. A summary of the peak vertical displacements from these experiments is shown in Figure IV-5.14. This figure is an almost direct copy from Figure IV-5.3; however, the abscissa has been corrected by one order of magnitude. The rise time-to-peak displacement in the compressional wave is plotted when scaled according to Froude and according to Cauchy (Figures IV-5.15a and IV-5.15b, respectively). It is the contention of Rulev (Reference IV-5.8) that the vertical component of motion
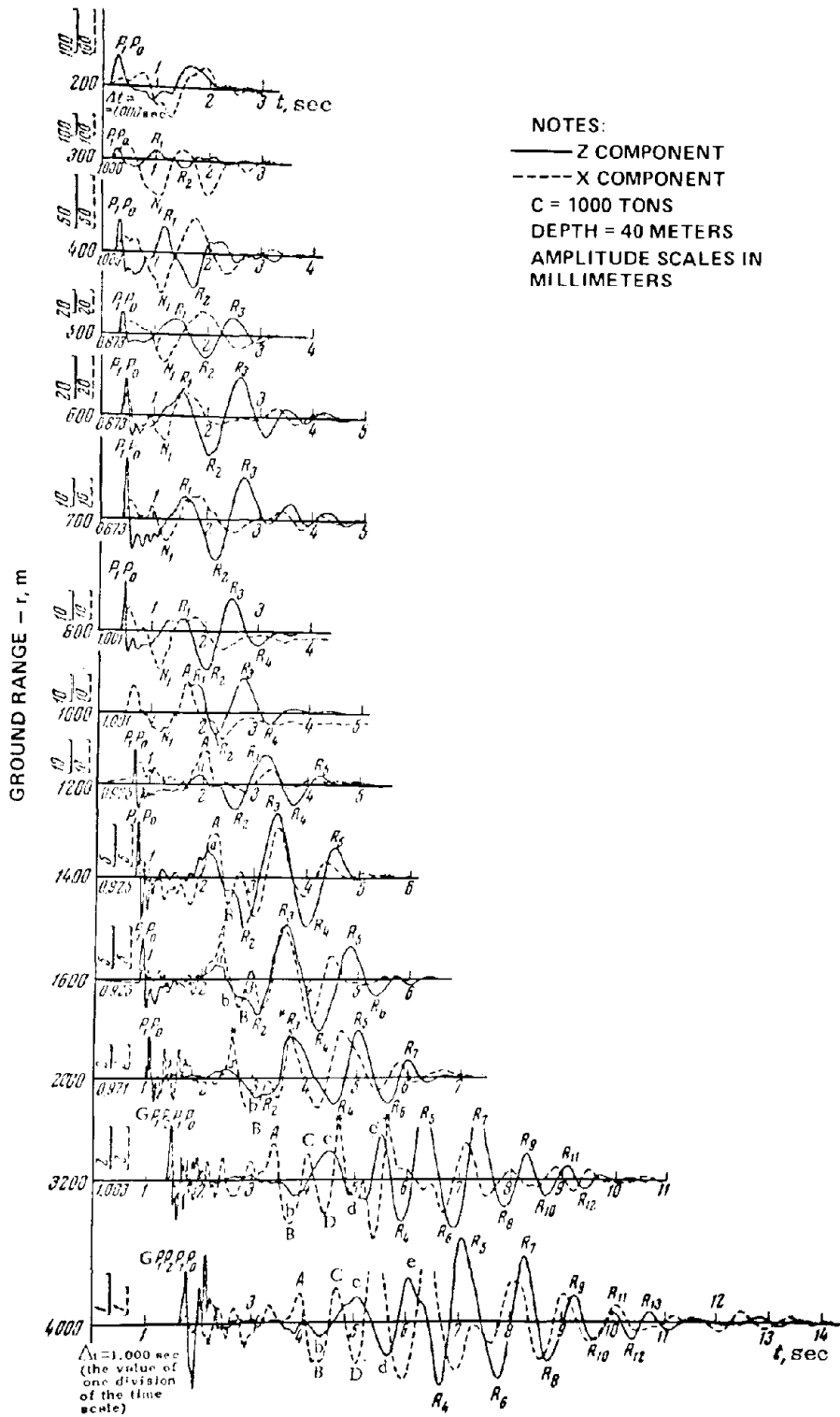
Figure IV-5.12.   Ground motion at various epicentral distances.
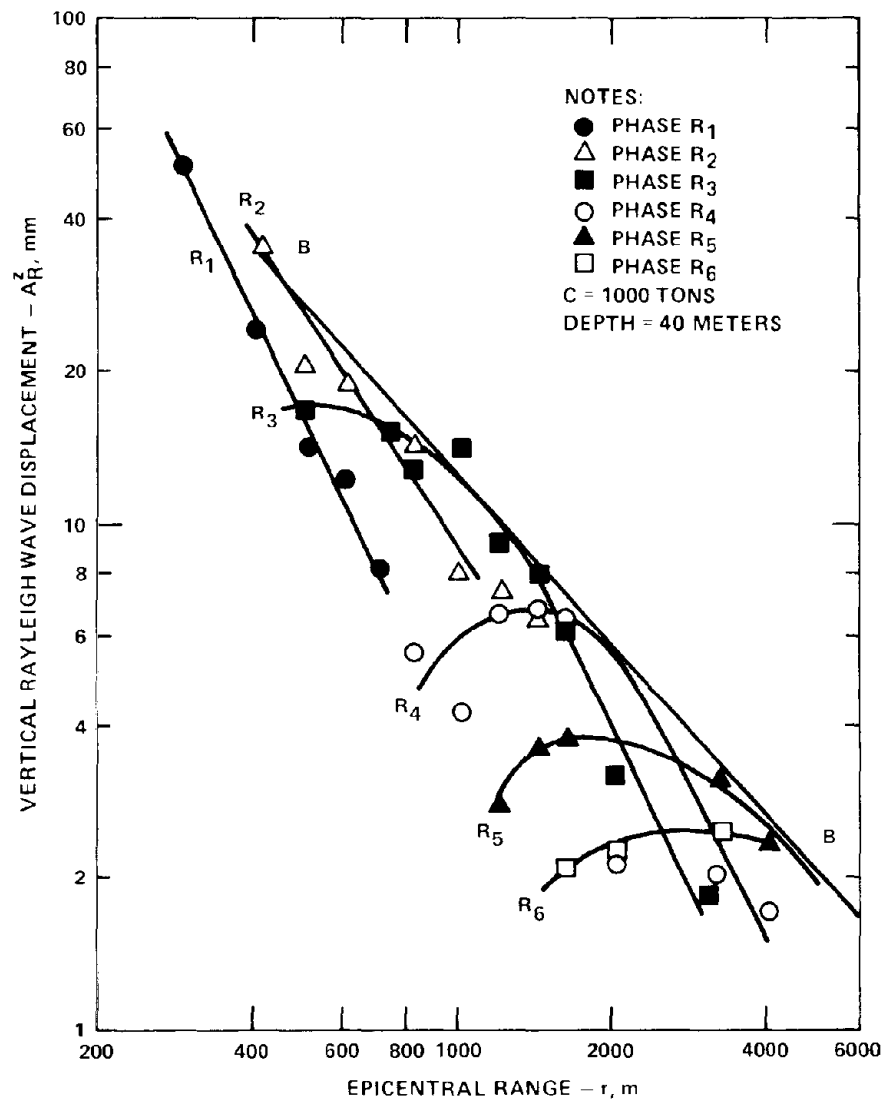
Figure IV-5.13.   Ground displacement on the vertical component A_R^Z in different phases of the Rayleigh wave versus epicentral distance.
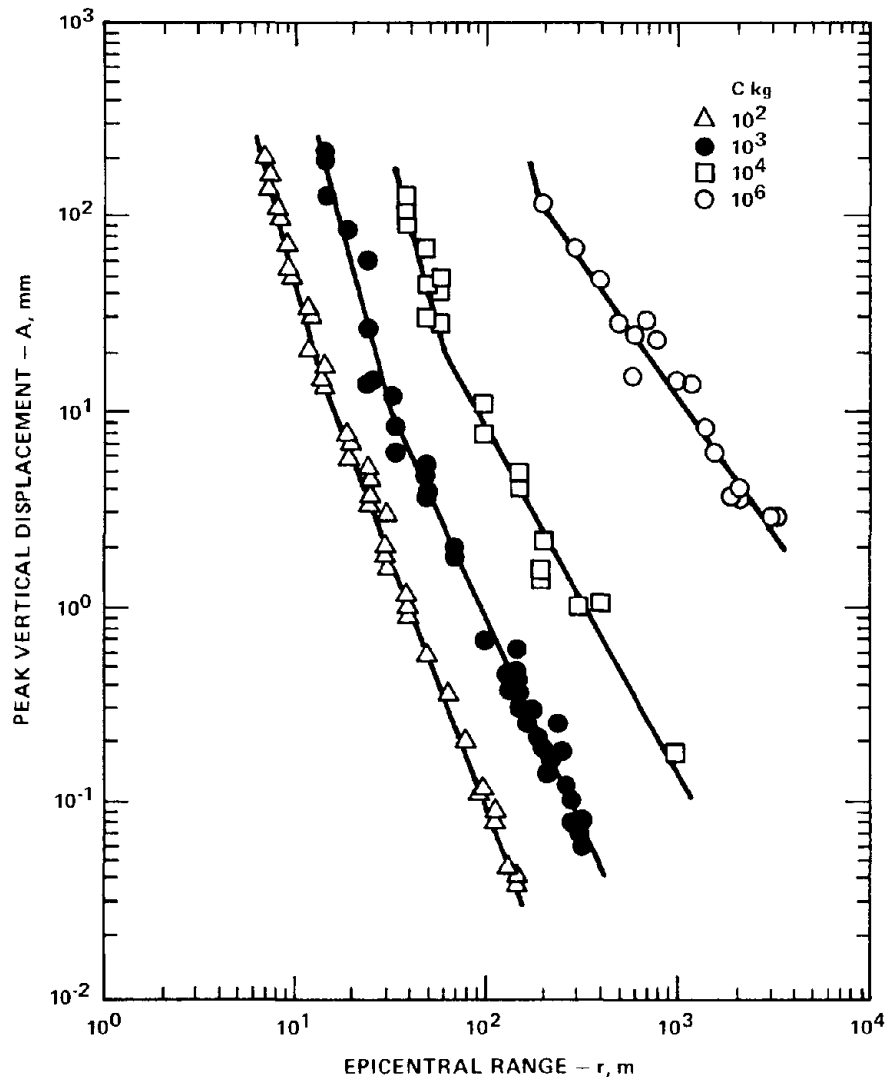
Figure IV-5.14. Peak vertical displacement (A) as a
                function of yield (C) and range (r)
                for near optimally buried charges.

scales best according to Froude. Scaling of the horizontal components of
displacement and the rise time to maximum displacement in the p-wave (when
scaled according to Cauchy and Froude) are seen in Figure IV-5.16. From
these data it was concluded by Kuz'mina (Reference IV-5.9) that the horizontal
displacements scale best according to Froude while the time-to-peak displace-
ments scale best according to Froude close to the source of the explosion and
according to Cauchy far from the epicenter. Although the data may appear to
scale according to Froude, Kuz'mina clearly points out that this may be induced
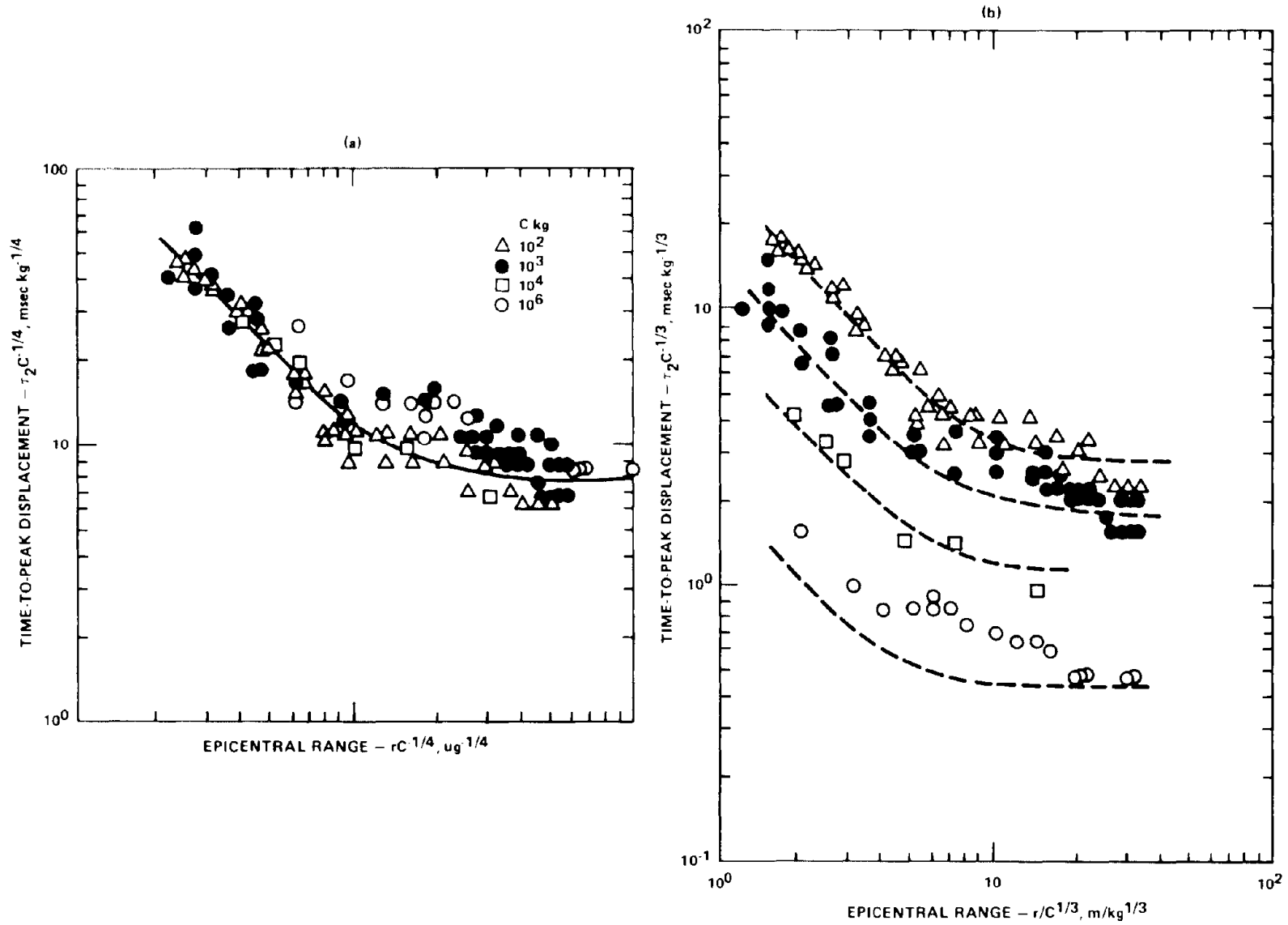
Figure IV-5.15. Time-to-peak displacement in compressional wave when scaled according to the Froude (a) and Cauchy (b) rules.
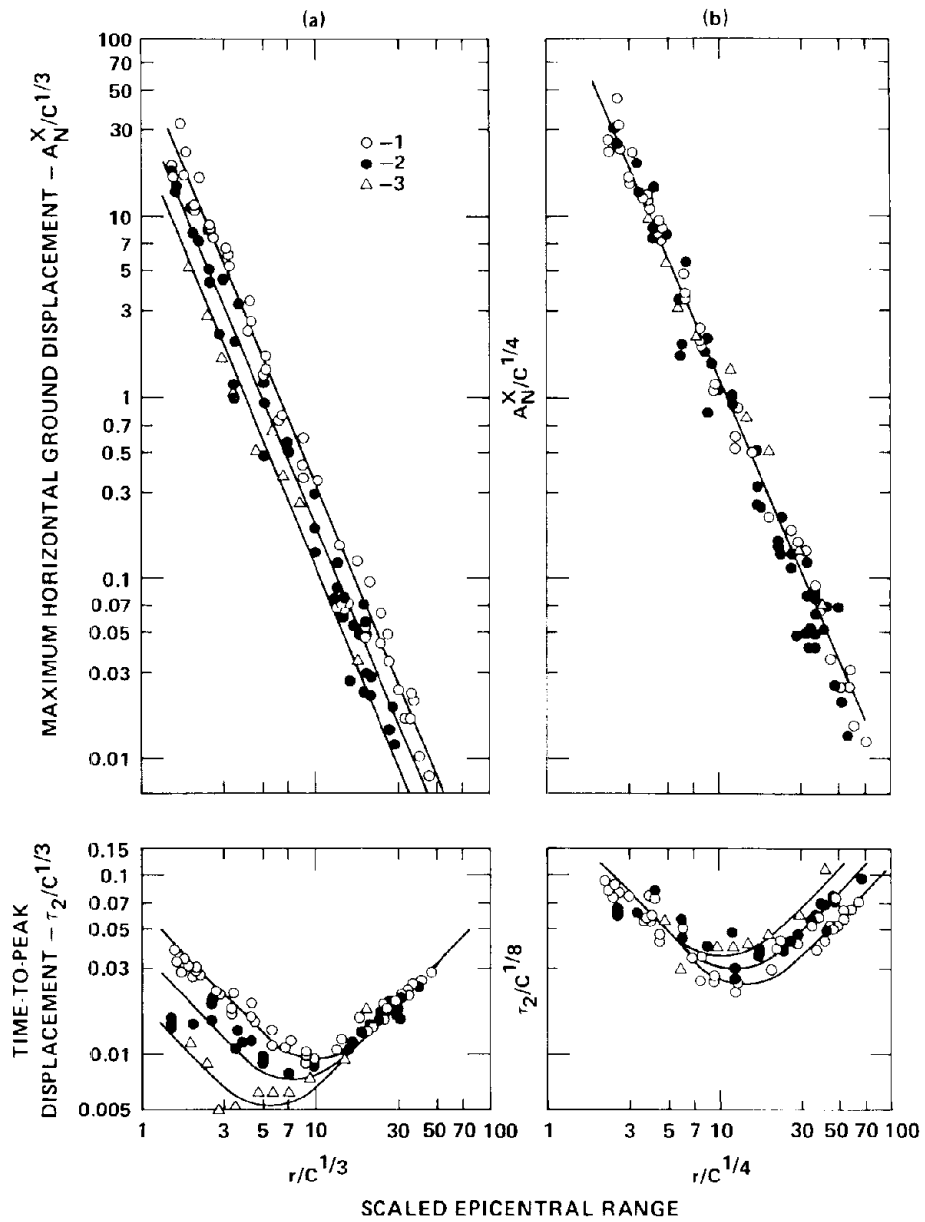
Figure IV-5.16. Maximal ground displacement along the horizontal component and the time of its increase versus epicentral distance in modeling after Cauchy (a) and after Froude (b). [Areas 2 and 3: (1) C = 100 kg, (2) C = 1000 kg, (3) C = 10,000 kg.]

by the layering of the test site. He then gives empirical formulae for relating the oscillatory period, T, the group amplitude, A_{gr}, and the peak particle velocity, U, as function of range. The group amplitude is the envelope of all the individual wave amplitudes shown in Figure IV-5.13. These values are given by

$$A_{gr} = 10 \frac{C^{1/2}}{r} \qquad , mm$$

$$T = 0.06 \ C^{1/5} \qquad , sec \qquad (IV-5.12)$$

$$U = 100 \frac{C^{1/3}}{r} \qquad , cm/sec$$

where C is the yield in kg and r is the epicentral range in meters.

Kuz'mina (Reference IV-5.9) also reports an extensive study of the frequency spectra resulting from the cratering explosions of 1957 and the fully contained explosions in the Moscow area in 1959. Two different frequencies are reported in this work. The first is called the visible recording frequency, the frequency that one would obtain by an examination of the oscillogram, and the second is the spectral maximum obtained by performing a Fourier analysis of the oscillogram. Shown in Table IV-5.4 are the reduced data obtained from the experiments at the two sites. Remember that the Kazakhstan area experiments consisted of cratering explosions while the Moscow area experiments were fully contained explosions. The wave notation is as follows: R denotes the vertical component of the Rayleigh wave, p denotes the compressional wave and K denotes both components of the head wave. This table is shown graphically in Figure IV-5.17. Variation of the frequency content with material properties is shown in Figure IV-5.18. Kuz'mina also claims that the horizontal component of the ground motion produced by cratering explosions has a lower frequency than the vertical component. Data presented indicate that the ratio f_H/f_V of the maximum frequencies for the two components is between 1.5 and 2. The variations of the spectral maxima and the width of the spectrum as functions of yield for both the cratering and the fully contained explosions are presented in Table IV-5.5.

Table IV-5.4.   Reduced data from Kazakhstan and Moscow area experiments.*

Wave	q (kg)	$\bar{r}$ $(m/kg^{1/3})$	Oscillation-Recording Duration (sec)	T^{vis} (sec)	T^{max} (sec)	f^{vis} (Hz)	f^{max} (Hz)	$\Delta f/f^{max}$ (%)
			KAZAKHSTAN					
K_z	10^4	2.31	0.595	0.460	0.740	2.17	1.35	119
	10^3	2.50	0.555	0.340	0.345	2.94	2.90	110
	10^3**	2.50	0.445	0.280	0.475	3.57	2.10	120
	120	2.54	0.475	0.440	-	2.27	-	-
K_x	10^4	2.31	0.655	0.600	0.740	1.67	1.35	119
	10^3	2.50	0.535	0.460	0.715	2.17	1.40	130
	10^3**	2.50	0.525	0.380	0.690	2.63	1.45	120
	120	2.54	0.475	0.440	0.605	2.27	1.65	113
P	10^4	9.25	0.160	0.260	-	3.85	-	-
	-	-	-	0.132	-	7.37	-	-
	10^3	10.00	0.070	0.128	-	7.80	-	-
	10^3**	10.00	0.075	0.200	-	5.00	-	-
	120	8.13	0.040	0.084	-	11.90	-	-
	10^4	19.20	0.175	0.100	0.208	10.00	4.78	-
	10^3	20.00	0.100	0.112	-	8.90	-	-
	10^3**	20.00	0.090	0.200	-	5.00	-	-
	120	19.30	0.075	0.072	-	13.90	-	-
	-	-	-	0.120	-	8.35	-	-
R	10^4	19.20	0.875	0.550	0.590	1.82	1.70	44
	10^3	20.00	0.500	0.240	0.300	4.17	3.35	88
	10^3**	20.00	0.470	0.250	0.308	4.00	3.25	81
	120	19.30	0.260	0.240	0.312	4.17	3.20	118
			MOSCOW AREA					
K_z	330	3.62	0.510	0.430	0.590	2.33	1.70	114
	120	4.20	0.445	0.420	0.512	2.38	1.95	113
K_x	330	3.62	0.570	0.380	0.590	2.63	1.70	114
	120	4.20	0.435	0.310	0.490	3.22	2.05	114
P	10^3	9.10	0.090	0.200	-	5.00	-	-
	330	9.75	0.067	0.160	-	6.25	-	-
	120	10.00	0.057	0.140	-	7.15	-	-
R	10^3	9.10	0.625	0.390	0.480	2.56	2.10	76
	330	9.75	0.740	0.330	0.480	3.03	2.10	86
	120	10.00	0.360	0.200	0.455	5.00	2.20	98

*Explosions set off on site I.
**Superscript implies the value obtained by visual inspection of records; maximum is the peak obtained by a Fourier analysis.
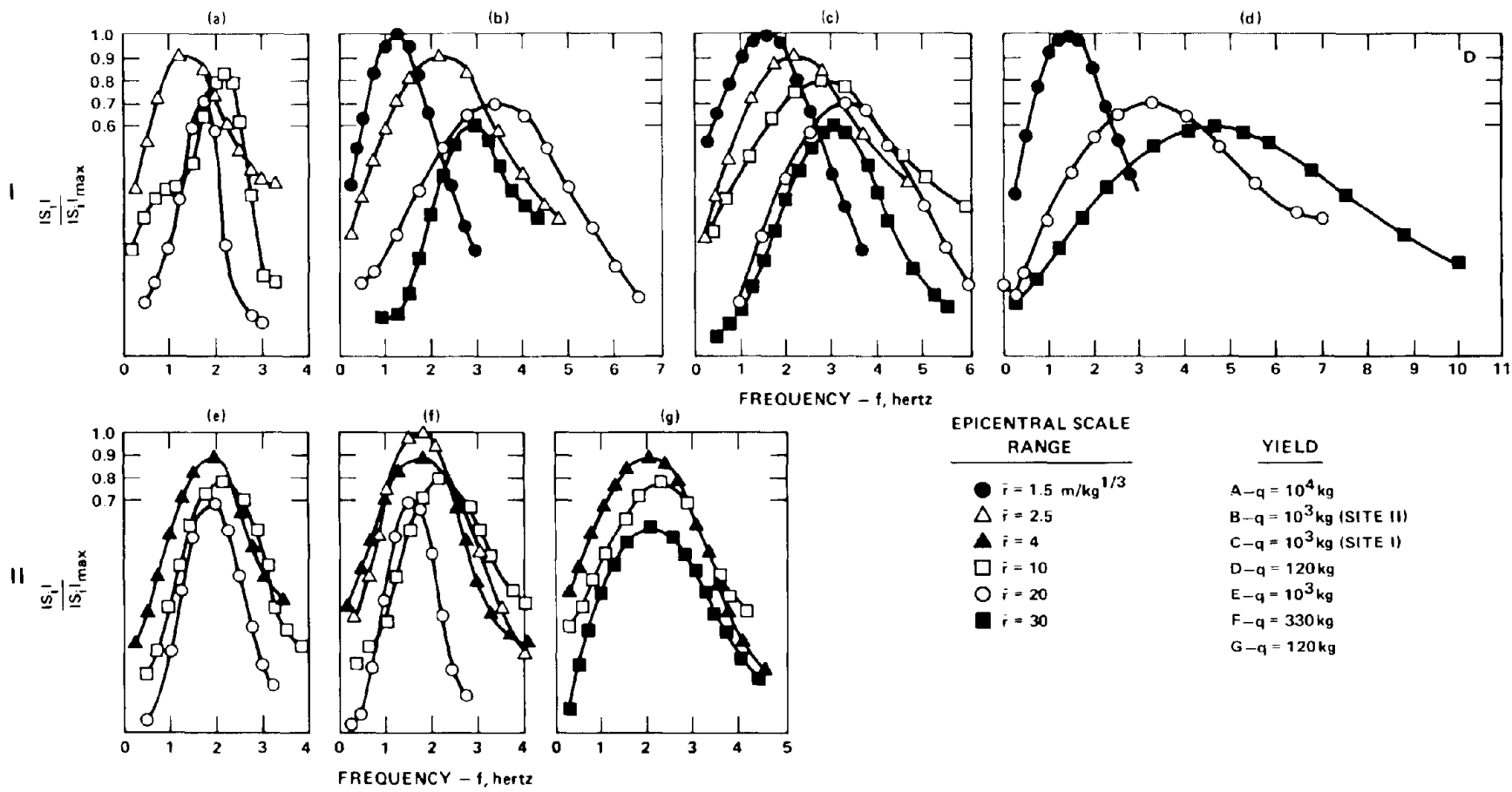
Figure IV-5.17. The changing frequency spectra of surface wave, R, and total ground movement, K, depending on the scaled distance.
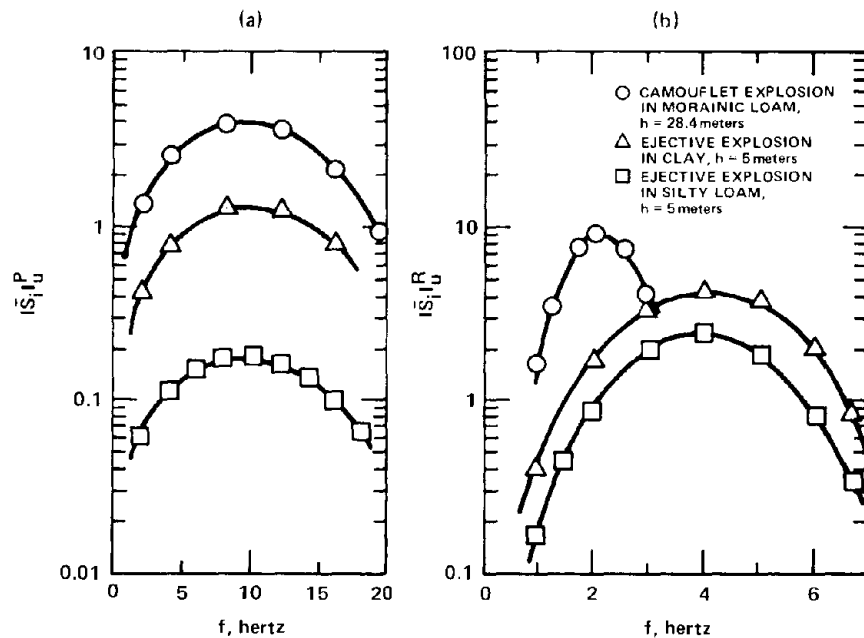
Figure IV-5.18. Velocity spectra of ground particle in the p-wave at a distance of r = 100 meters from the epicenter (a) and in the R-wave at a distance of r = 200 meters (b), when the explosions are set off by charges weighing 1000 kg.

The Soviet experience in explosive cratering is substantial as indicated in Reference IV-5.10 where the data of the 1957 test series are compared with other cratering explosions in a geology described as a rocky soil overlying a hard bedrock. Two sources of shock waves are distinguished in this report. The first is the compression wave produced by the explosion itself. A second source of ground motion is produced by the venting of the gases during the cratering process. High pressure gas within the expanding cavity is rapidly released to the atmosphere. This then allows the elastic stresses around the cavity to be released in a relatively short time, radiating ground waves. The ground motion from this second energy source is termed the decompression wave. The compressional wave resulting from the shock front of

Table IV-5.5. Variation of spectral maxima and spectral width
as functions of yield.

	Explosion Site						
	Kazakhstan				Moscow Area		
Yield (kg)	120	10^3	10^3	10^4	120	330	10^3
f^{max}(Hz) Vertical Velocity	23	9.5	10	4	16.8	11.6	9.4
$\dfrac{\Delta f}{f^{max}}$ (%)	-	100	102	108	104	108	102
f^{max} (Hz) Vertical Displacement R-Wave	3.2	3.3	335	1.7	2.2	2.1	2.1
$\dfrac{\Delta f}{f^{max}}$ (%)	115	78	90	43	98	85	76
p-wave Horizontal f^{max} (Hz) Displacement	1.65	1.4	-	1.3	-	-	-

the explosion is longitudinal in character.* The decompression wave has longitudinal and transverse components. The production of transverse waves from cratering explosions is as follows: shear and tensile stresses are built up in the material above the rising gas bubble. For the material remaining in place on the lower portion of the gas bubble, stresses will remain compressional. Upon venting of the gases to the atmosphere, the shear and tension waves are radiated simultaneously with the compression waves, thus introducing longitudinal and transverse motion into the ground surrounding the forming crater.

Attenuation with distance of the horizontal component of the compressional wave was found to be quite rapid. However, the attenuation of this wave with depth at a given range was found to be quite small. Data supporting this statement is given in Table IV-5.6. The opposite was found to hold for the

*See Chapter IV-1, Section IV-1.1 for a description of the origin of elastic waves.

Table IV-5.6. Peak velocity and displacements in
compression wave*.

Gage Depth (m)	U_x (cm/sec)	U_z (cm/sec)	A_x (mm)	A_z (mm)
0	1.4	1.4	0.120	0.110
6.0	0.9	0.4	0.108	0.037
11.4	0.8	0.5	0.110	0.033
20.0	0.9	0.3	0.120	0.022

*Range = 245 m, yield = 10^3 kg, DOB = 12 m

decompression wave. The characteristics of compression and decompression
waves have led to the identification of the decompression wave with a Rayleigh
wave. It is Romashov's contention that the identification of the long period
high amplitude late time waves with a Rayleigh wave is incorrect; these dis-
turbances are stress relief waves induced by the crater (what has been identi-
fied in the U.S. as cratering-induced motion). Oscillation periods of these
waves are found to be material-dependent. Romashov quotes the period in rocky
soil as $T = 6.5\ C^{1/3}$ sec and for clay, $T = 60\ C^{5/2\,4}$ µsec.

One of the articles in Reference IV-5.3 by Rulev and Kharin addresses the
question of the azimuthal asymmetry of the radiated ground motion from the
detonation of row charges.* For this series, the maximum explosive mass de-
tonated in any experiment was 160 kg. All experiments were conducted at
depths of burst to insure full containment of the explosion. Each experiment
was conducted with the charges equally spaced. However, from experiment to
experiment the spacing was varied between 2.5 and 20 meters. Furthermore,
experiments were also conducted in which the number of charges in a row varied
from 1 through 8. Figure IV-5.19 shows the resulting contours of equal velocity
for one particular experiment in which each of 8 individual charges weighing
20 kg were separated by 8 meters.

---

*Translated documents to date have been limited to linear arrays of charges.
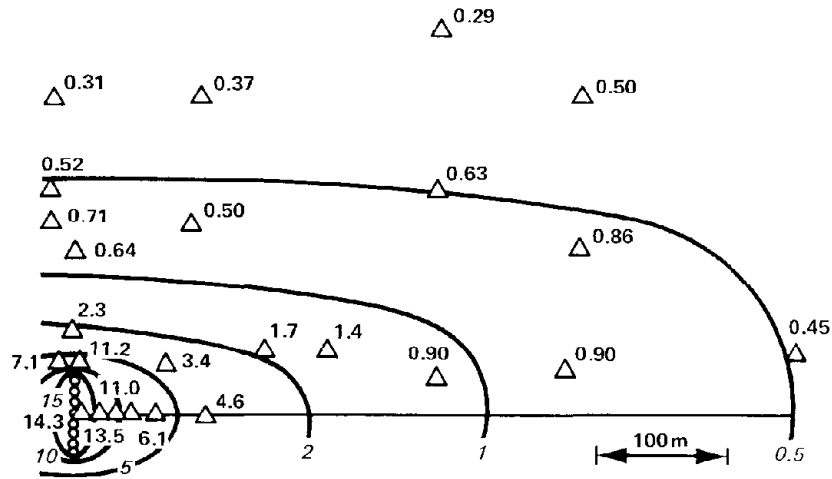
Figure IV-5.19.   Lines of equal velocities for linear
                  explosion No. 17. (The numbers near
                  the triangles, which mark the place
                  where the instruments were located,
                  indicate the measured velocities U_x,
                  cm/sec.)

Multiple-burst cratering explosions were briefly discussed in
Reference IV-5.1 by Myasnikov, et al. For these experiments, 5 or 6 charges
were placed in a row at a depth between 5.6 and 5.7 meters. Each individual
charge weighed between 600 and 650 kg. The cavities in which these charges
of granulated TNT were emplaced were created by the hole-springing technique
and the resulting cavities were not all exactly of uniform volume resulting
in some variation in charge weights. Parenthetically, it should be noted
that the hole-springing technique most likely alters the material properties
of the medium and the resulting craters are in a material which cannot be
considered to be truly representative of the virgin medium. However, the
effects of the hole-springing operation on the material properties of the

medium are unknown and may very well be minimal. Separation between charges
was varied between 1.1 and 1.8 times the depth of burst and the total number
of charges was varied between 5 and 25. Results of these experiments are
shown in Figure IV-5.20. It is seen that complete line charge equivalence*
is obtained for the relative separation of 1.1 times the depths of burst.
Increasing the separation distance between the charges increases the distinc-
tion between the effects of the individual charges. In other words, the
distinction between the crater dimensions at a position between the charges
and the crater dimensions at the charge positions increases with charge
separation. This is indicated by the three lines drawn for the relative
depth and width of the trench in Figure IV-5.20.

Although numerical values of the ground motion are not presented, the
general results are as follows. It was noted that when five charges comprised
the linear array, the intensity of the ground surface vibrations is essentially
the same as from a single explosion of the same total yield. However, when
the number of charges in the line is increased to about 25, the intensity
at axis normal to the line charge axis is between 20 and 50 percent greater
than with a single charge of the same total weight. Moreover, it was noted
that along the axis of the crater, the vibration intensity decreases by a
factor between 3 and 7 for a large number of charges in the linear array
compared to a single charge. At large epicentral ranges the difference be-
tween the on-axis and axis-normal vibration intensity decreases.** This is
somewhat in contradiction to the conclusion to be drawn from Figure IV-5.19.

IV-5.3 MODELING EXPERIMENTS

The two major processes of importance in crater production are sur-
face spall and gas acceleration. At depths of burst less than optimum,
these processes are not completely separable. Three different techniques
have been employed to investigate the effects of the gas acceleration
phase in the absence of the shock front.

The article by Lebedev, et al. in the collection of documents of
Reference IV-5.3 describes such a method. In this method, the explosion
was simulated by a combustion front rather than a deflagration front. This

---

*Line charge equivalence means a crater having completely uniform depth and
  width as if produced by a continuous linear charge at constant depth.
**At large enough distances, the line charges look like a single larger charge.
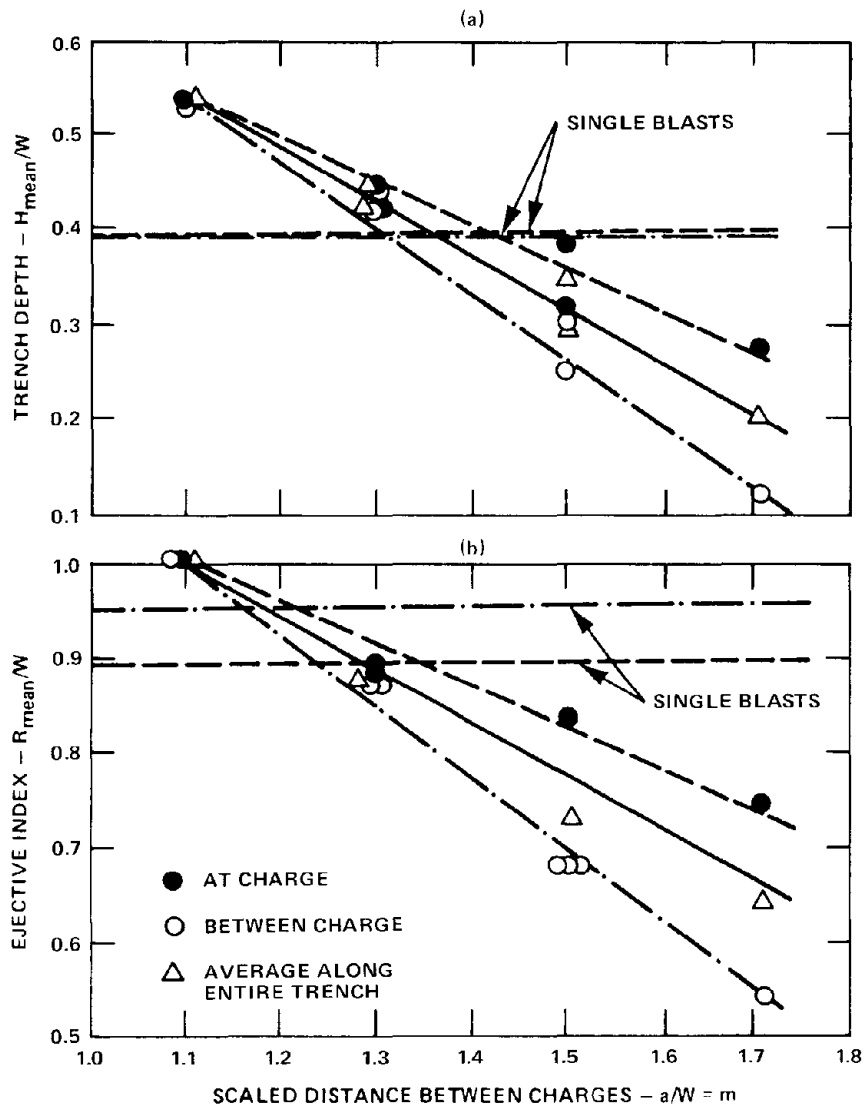
Figure IV-5.20. Relative trench depth (a) and ejective index (b) as functions of the relative distance between charges (W is the depth of burst).

yielded a large amount of gas in a time long compared to a shock front generation, but in a time short compared to the crater production time. Velocities were measured by using small coils emplaced in the cratering medium and by placing the entire experiment in a magnetic field. Quite significantly, the first motion in these oscillograms was vertically up-ward and horizontally inward. Clearly no detectable compression wave was generated. It was pointed out that the oscillograms resulting from

cratering explosions could be divided into two qualitatively different parts. In the initial part the motion proceeds along a horizontal direction away from the explosion and vertically upward toward the surface. The velocity of propagation identifies this motion as a compressional wave. Soon after the compressional wave reaches the free surface, motion can be identified as that resulting from the gas acceleration phase and is superimposed on the compressional wave. The motion due to the gas acceleration phase appears to be even stronger than the initial compressional wave. Lebedev, et al., further pointed out that the frequency of the signal resulting from the gas acceleration phase may have had a period several times greater than that of the compression wave. This particular phenomenon was claimed to be a transverse wave propagating in a layer near the free surface whose thickness increases as the wave spreads out. By the nature of its source, this must be a shear wave and, therefore, has all of the properties of classical Rayleigh waves.

A second method of generating a crater by the gas acceleration phase only was to introduce a small amount of vaporizing chemical (boron carbide) at the proper depth of burst (Reference IV-5.1). Energy was then fed into this chemical through the discharge of an electrical spark. A schematic diagram of the experimental arrangement is shown in Figure IV-5.21. The data thus generated were compared to craters produced by the explosion of a spherical charge of PETN explosive placed at the same depth of burst. The energy in the electric discharge is easily measured from the circuit parameters while the energy in the PETN charge is a known quantity. Scaled crater radii and volume as a function of the energy released are shown in Figure IV-5.22 and Figure IV-5.23. It was shown that by taking into account the energy of vaporization of the various chemicals introduced at the focus of the spark gap and computing the energy expended by starting from the initial pressure in the cavity, the data could be collapsed to a reasonable single curve. Particle velocity was measured by implanting small coil pickups in the sand and impressing a magnetic field across the entire test bed. Peak particle velocities were seen to have roughly the same behavior as the displacement (Figure IV-5.24). In other words, for a given range, the chemical explosion gave the largest velocity and the boron carbide material at the spark focus gave the smallest velocity at the same range. From these data it was concluded that with proper knowledge of the chemical properties of the substance introduced at the focus of a high energy spark gap, craters
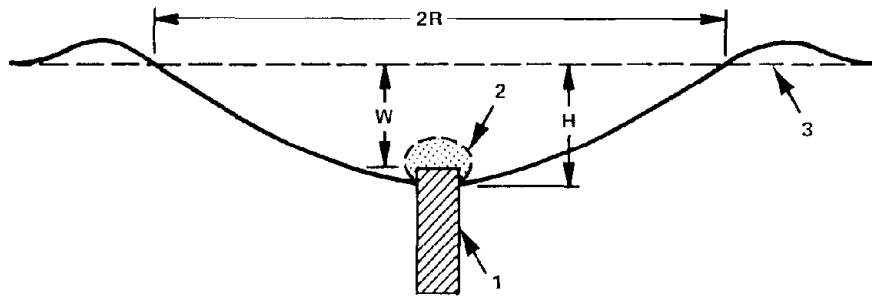
NOTES: 1 - ELECTRODES, 2 - VAPORIZING COMPOUND,
3 - ORIGINAL TEST-BED SURFACE.

Figure IV-5.21.   Experimental setup and cross section of
ejecta crater in which the explosion, W,
is reckoned from the center of the charge.
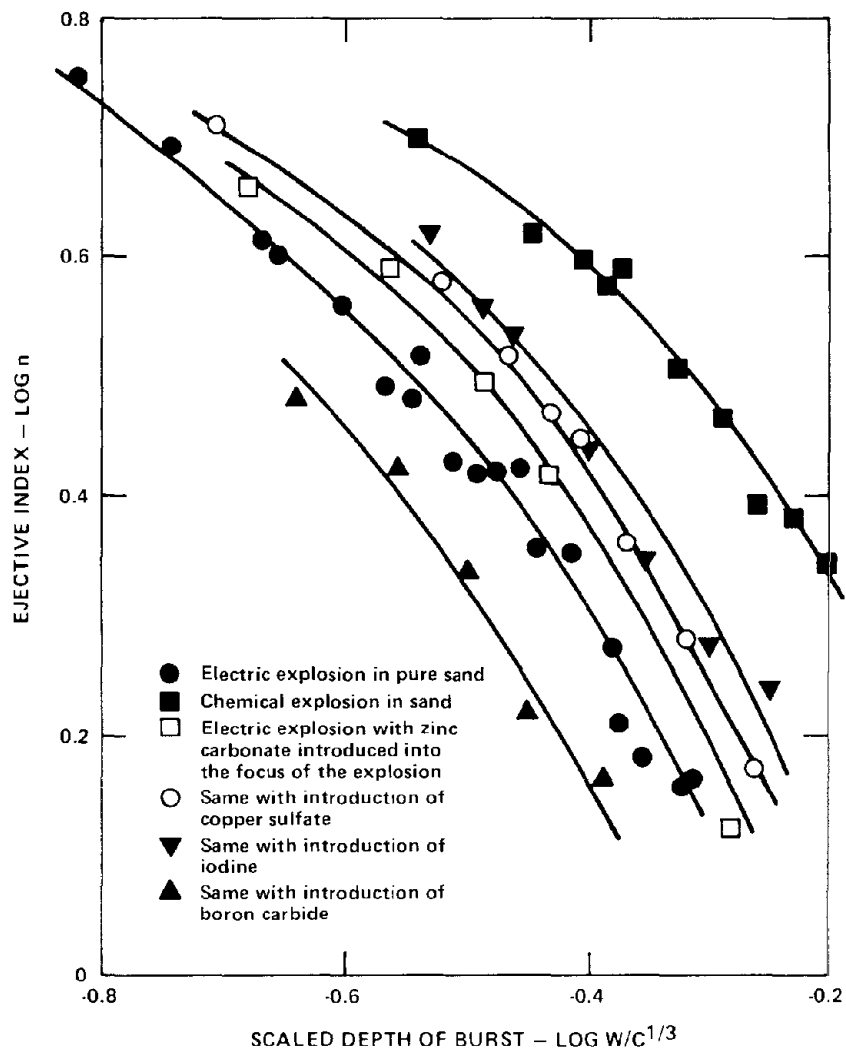
Figure IV-5.22.   Ejective index as a function of the scaled
explosion-source emplacement depth.
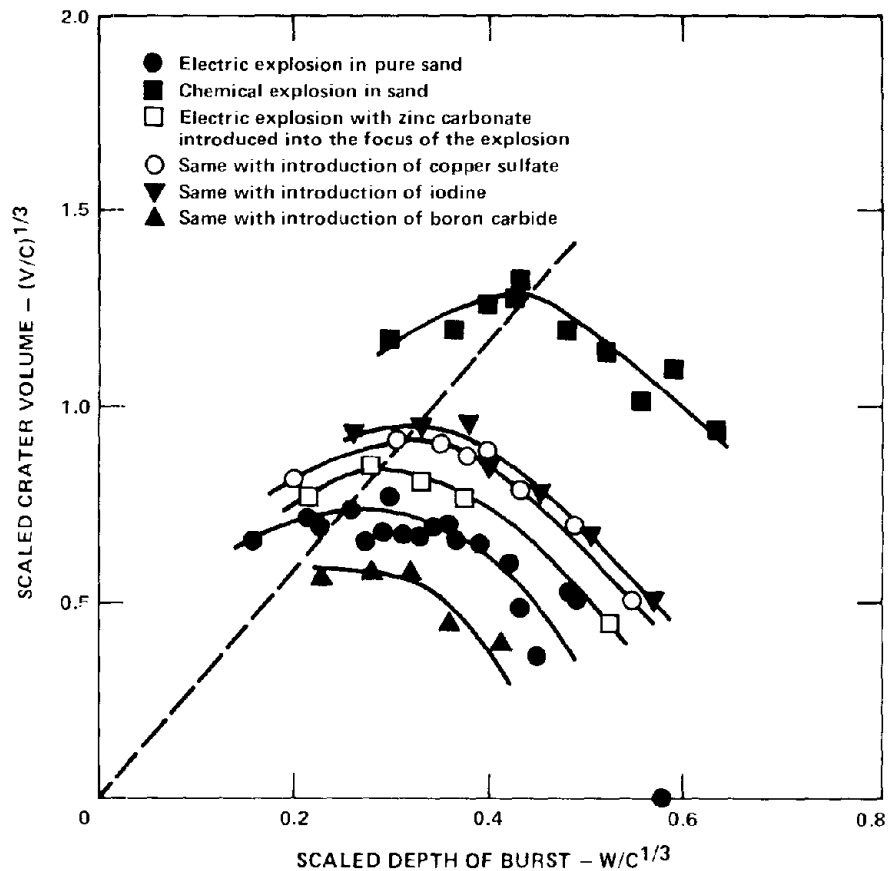
Figure IV-5.23. Ejection-crater volume, referred to the unit of
                 blast energy, as a function of the scaled explo-
                 sion-source emplacement depth.

produced by explosives could be modeled quite well by this technique.

The third and most extensively reported method of studying the gas acceleration phase of cratering is to place a gas-filled balloon at the required depth of burst in a prepared test bed. The gas pressure in the balloon is varied by adjusting the wall thickness of the balloon. This maintains a constant volume. Not only can this technique be used to investigate the gas acceleration phase, but it can also be used to investigate the effect of the atmospheric overpressure on cratering. This was accomplished by placing the entire test bed in a vacuum chamber (Reference IV-5.3). From this very extensive, and apparently continuing series of tests, the surface deformation velocities and the resulting crater dimensions were obtained. The velocities were obtained by means of high speed photographic techniques. This yielded a good estimate of the velocity history at
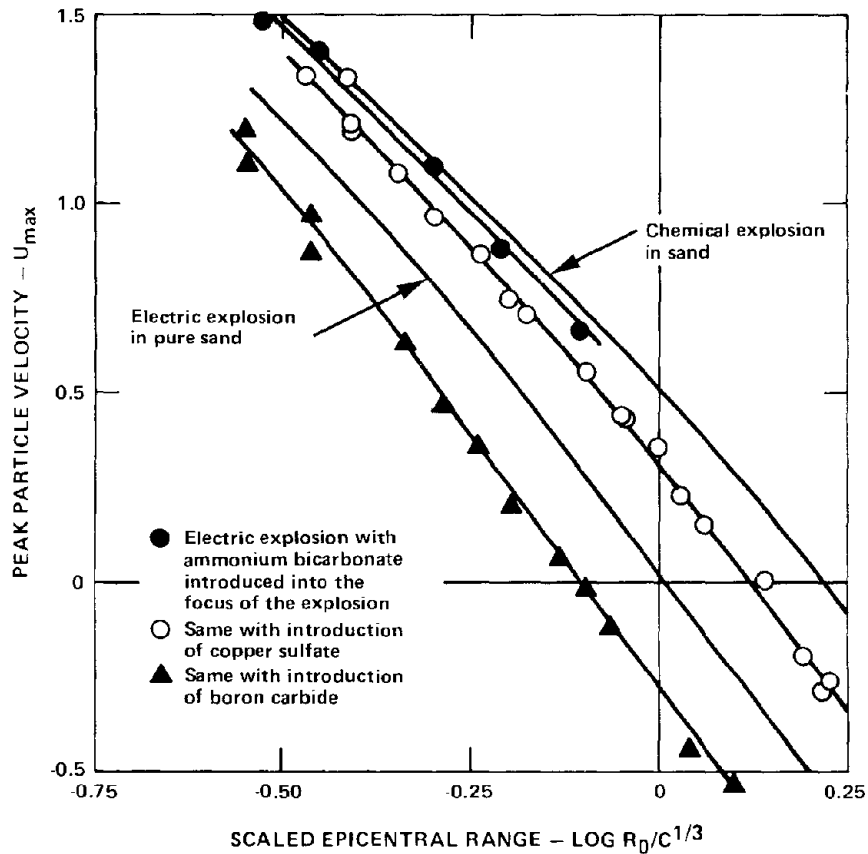
Figure IV-5.24. Maximum particle velocity (m/sec) as a function
of the scaled distance from the center of the
explosion $(m/kg^{1/3})$.

the epicenter. The cratering medium for all these tests was dry sand. We
define E to be the total energy change of the gas bubble in expanding from
its initial pressure to the ambient vacuum chamber pressure. A dimension-
less variable, $\bar{E}$, may then be given by the ratio of E to the product of the
cube of the depth of burst and the total pressure at the shot point.* Results
of these experiments led to the empirical equation:

$$R_a/DOB = 0.5 + 0.85 \ \ln \bar{E} \qquad\qquad (IV-5.13)$$

*The vacuum chamber pressure and the lithostatic pressure, so that

$$\bar{E} = \frac{E}{(p_0 + \rho gD) \ D^3}$$

(see equation IV-3.14)

The line representing this equation is compared with experimental data from U.S. experiments for yields from 256 pounds of HE to the 100 kt SEDAN event (Figure IV-5.25). A reasonably good correlation is seen to
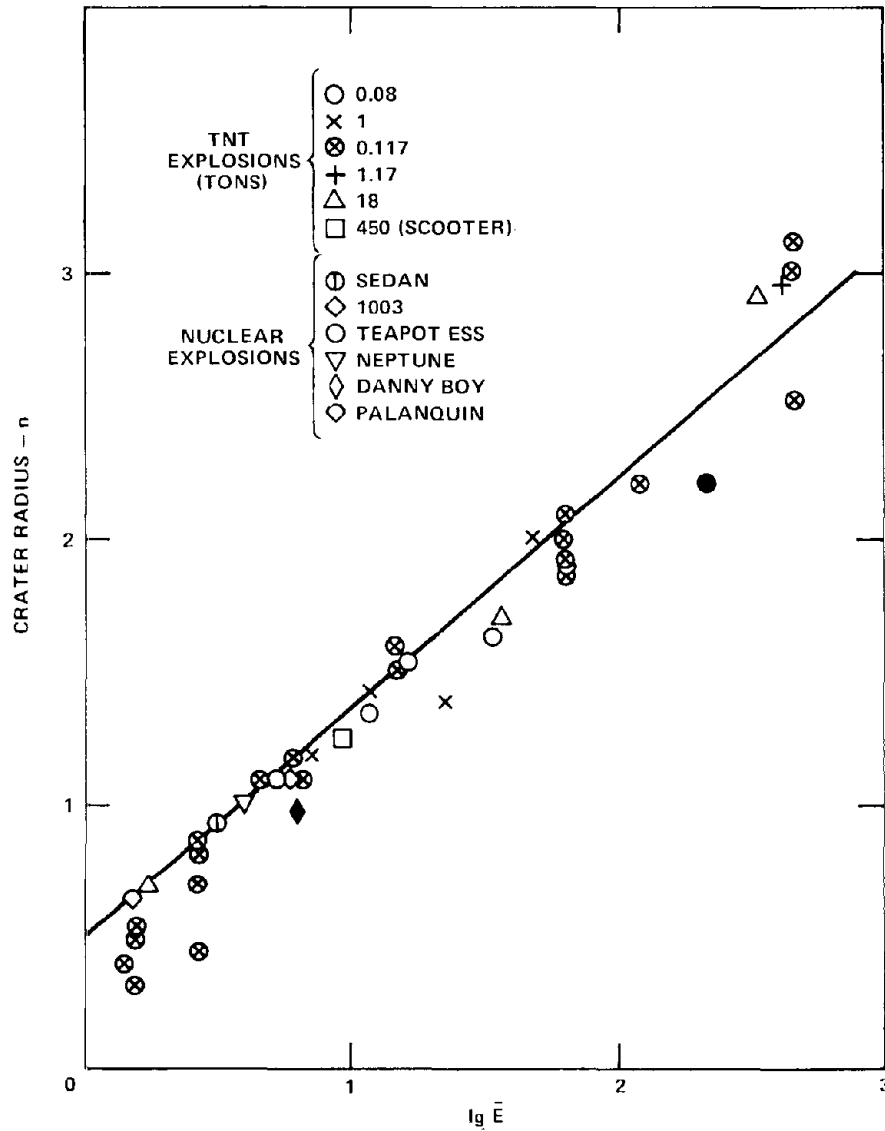
Figure IV-5.25. Comparison of crater dimensions in model experiments (solid line) with experimental results.

exist for crater radius. An attempt was also made to show the scaling of
the rate of rise above the shot point. This is shown in Figure IV-5.26
and the data are from Reference IV-5.11. Although the term was never
included in any of the translated Soviet analyses, it was quickly
recognized (Reference IV-5.12) that the strength of the material above
the expanding gas bubble should be included as a term to be added to the
atmospheric overpressure. Thus, a more appropriate dimensionless number
would be the total energy expended divided by the sum of the work required
to raise the material through the gravitational potential, the work done
against the atmospheric overpressure, and the work done against the shear
strength for a von Mises solid.
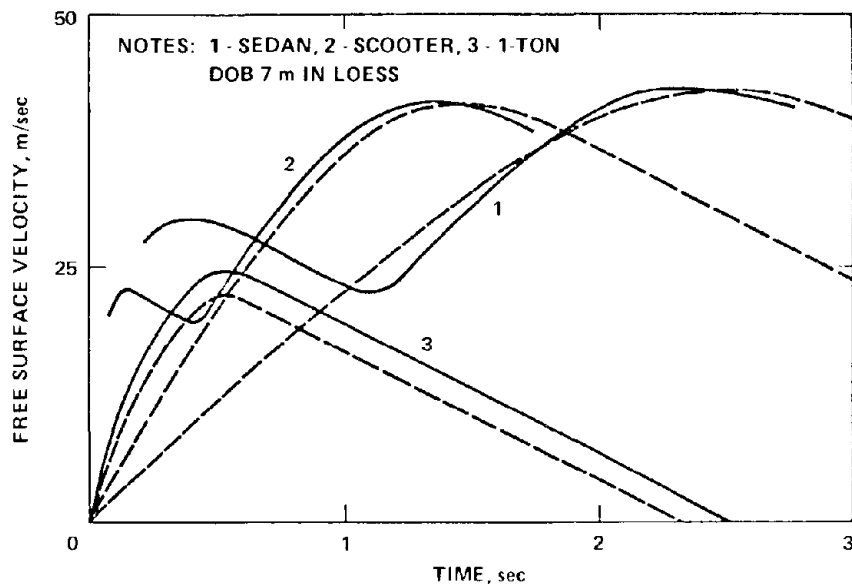
Figure IV-5.26. Comparison of curves for the rate of rise
of the free surface above the shot point
as a function of time in field experiments
(solid lines) and model experiments
(dashed lines).

Model experiments of explosively produced craters are many and varied. One interesting set of experiments was performed by Bakhrakh, et al. (Reference IV-5.13). They made a comparison between the behavior of explosive cratering in natural clay and in a water solution of zinc chloride. The initial densities of these materials were the same. Shock measurement of the equation of state indicated that both materials had nearly the same pressure-volume Hugoniots. Results of experiments indicated that the clay behaved in the classic manner in which the rising dome maintained its integrity throughout the full recording time. In contrast, the zinc chloride solution established three different zones above the expanding cavity. The first two were made up of cleavage layers of different thicknesses propagating at different velocities. The third zone was a layer of the solution directly adjacent to the lower portion of the cavity. The authors also claimed that they observed the same effect in water.

An article by Romashov and Simonov in Reference IV-5.3 describes small scale (0.2 gm) explosions in plasticene, either in preparation for, or as a result of, the 1957 series of tests. The interesting results of these tests show that the final center of curvature of the bottom of the crater is displaced upwards from the true center of the explosion. The displacement for these shots is given in Table IV-5.7.

Table IV-5.7. Upward displacement of center
of curvature of bottom half of
camouflet from center of explo-
sive.

h_{DOB}, mm	24	33	40	45
Ar, mm	21.5	22.5	17.5	18
	20.5	18.0	17.5	18
	16.0	18.0	19.0	17
	14.0	16.0	19.5	--
	--	18.0	19.0	--

Reference IV-5.5 describes two modeling experiments conducted with explosives. In the first experiment the objective was to measure the shock and flow characteristics of sand in a spherical geometry. Explosive weights from 1 to 24 gm using a 50/50 mixture of TNT and hexogene were used. The sand was a very fine grain material with a density of 1.55 gm/cm^3 with about 8% by weight of moisture. The particle velocities were measured by placing a metal foil in the sand and shorting out rigid pins as the metal foil passed by them. Residual displacements were measured in much the same manner. Small pieces of foil were placed with their initial positions carefully recorded. The final positions were also obtained and carefully measured. The explosions were conducted in a very large container of sand to insure that the motions were spherically symmetric. A summary of the more important results of these experiments is given. The peak velocity "U" in the shock front at the position "r" is given by

$$U = 3.4 \left(\frac{C^{1/3}}{r} \right)^{1.8} \qquad\qquad (IV-5.14)$$

The particle velocity "U_p" at the position "r" behind the shock front is given by

$$U_p = U \left(\frac{R}{r} \right)^{3/2} \qquad\qquad (IV-5.15)$$

where R is the crater radius. Equation (IV-5.15) implies there is expansion upon release of stress that is greater than would be predicted from pure elasticity theory. It is claimed that for a density greater than some critical value, the sand increases its volume upon shear deformation, that is, there is shear dilitancy in the sand. The reason stated for this effect is that the sand cannot reach its densest packing during the shear process. Another important observation is that the bulk deformation behind the shock front is such that the density measured in the Eulerian coordinate system is nearly constant.

The same diagnostic techniques were used to determine the ground motion from cratering explosions. In this series of tests the same explosive charges of 24 gm were detonated at depths of 10, 15, 20 and 30 cm. Additional measurements included photographic coverage and the use of a foil placed on the ground surface

at ground zero to short out contacts in a mandrel supported above the test bed. The rise velocity of the dome above the expanding gas bubble was measured by this technique. From a knowledge of Hugoniot properties of sand measured with one-dimensional spherically symmetric shots, an estimate was made of the total kinetic energy delivered by the shock front to the material at the ground surface. Measurements were made of the total kinetic energy in the material ejected from the crater. It was noted that the total energy of the ejecta is several times greater than the energy transmitted by the compression wave. It was concluded that the primary ejection mechanism of an explosion in sand could be represented as a process of expulsion by the gas acceleration phase.

The influence of the ratio of the tangential to the radial stress, σ_θ/σ_r, was also investigated by using modeling clay as a cratering medium. For sand, this ratio was one-half while for the modeling clay the ratio was between 0.7 and 0.9. The ejecta velocities from a completely spherical detonation were found to be proportional to this ratio. On the basis of these results it was concluded that the most important characteristic of the ground material in determining the kinetic energy of the displaced medium is the ability of the ground to resist shear deformation.

A series of high explosive cratering experiments was reported by Alekseyenko (Reference IV-5.14) in which the goal was to obtain a measure of the stress histories in the entire solid half-space surrounding the explosion. A general schematic of the experimental arrangement is shown in Figure IV-5.27. Cubic TNT charges weighing from 1.6 to 12.8 kg were detonated tangent to the surface. Stresses were measured along three principal axes. One stress deviator was also measured. For the gauge system near the axis of symmetry a single shock front was observed. However, for those gauge stations near the free surface, two stress maxima were observed and their sources were analyzed (Reference IV-5.15). To determine the true source of the double maximum near the ground surface, several different experiments were performed. In the first experiment, a near-surface gauge location was shielded from the direct air-blast. In a second set of experiments the direct ground shock resulting from the explosion was prevented from reaching the gauge by digging a trench between

the gauge and the shotpoint. These tests demonstrated that the first maximum was a direct manifestation of the airblast pressure, while the second maximum was induced exclusively by the shock front transmitted through the ground from ground zero. Figure IV-5.28 shows a cross section of the wave front at various distances from the shot point. Times of arrival of the shock front have been mapped from these measurements. In those regions where the arrival time was not a function of the angle between the axis of symmetry and the gauge coordinate, the wave front had a spherical shape. Near the surface, however, it was found that the arrival times of the two maxima indicated a wave front which was no longer spherical. The first stress maximum is directly related to the arrival of the airblast. The second stress maximum showed a wave front deviating slightly from sphericity. This is clearly a result of the ground shock resulting from the point loading at ground zero. The dashed lines in Figure IV-5.28 indicate the first arrival of a signal while the solid lines indicate the arrival of the stress maximum. The deviation from sphericity of the stress maximum is indicated by the extension of the spherical surface to the ground surface. Careful examination of this stress field, and a comparison with the stress field generated by a spherically symmetric shock, leads to the conclusion that the greatest influence of the free surface is in the surface region itself. It must be pointed out that the work performed did not consider epicentral ranges such that outrunning of the ground shock could have occurred. Indeed, the authors point out that the stress state created by the traveling airblast differed insignificantly from the stress field of a plane wave on the surface of the ground.

Concurrent with these investigations, airblast measurements were also made. One of the very significant results of these measurements was an estimate of the fraction of the explosive yield that is coupled into the ground (Reference IV-5.16). Starting from theoretically derived hodographs for a contact explosion in air on an incompressible half-space, corresponding experimental data can be used to obtain the effective yield at a given position. Since the airblast must obey geometric similarity (this was also shown by Brode in the U.S.), all that is needed are data on the explosive yield and curves of the time of arrival. Knowing the effective yield from a charge over a compressible half space and the true yield of that charge, it is possible to obtain the total amount of energy radiated to the air. It is assumed that the
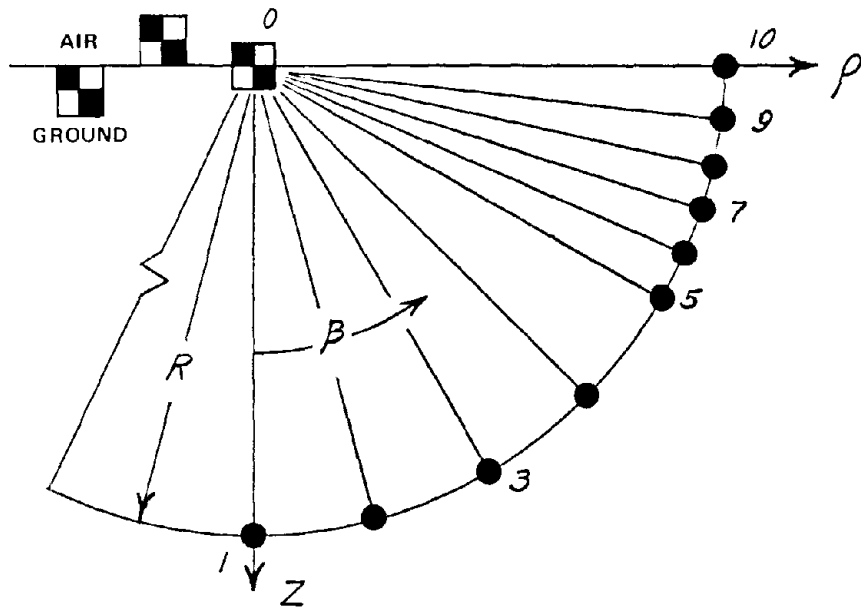
Figure IV-5.27. Schematic layout of high explosive
experiment and gauge stations.
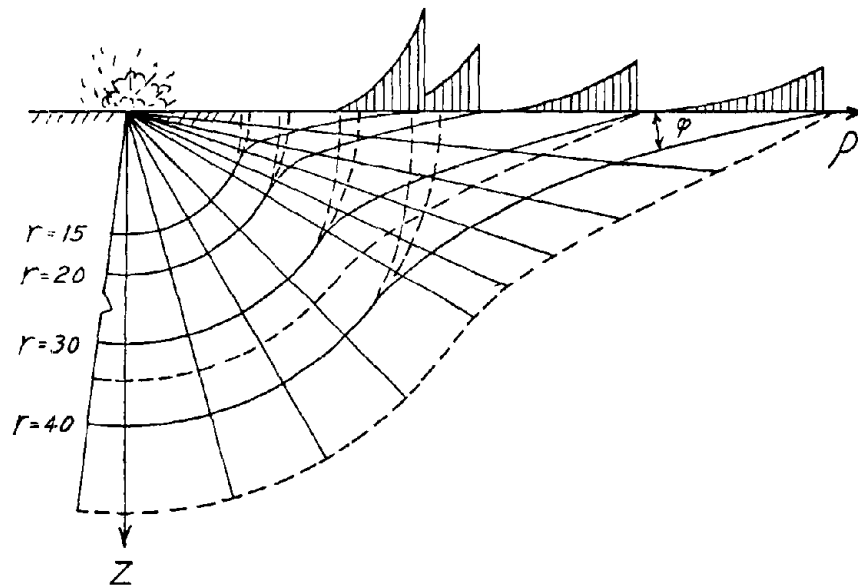
Figure IV-5.28. Shock front contours at various times
after detonation.

rest of the energy is then radiated into the earth. Table IV-5.8 shows the dependence of this partition of energy on the material composition of the half space and depth of burst of the charge. Yields used in constructing these data varied from 1.6 to 25 kg.

Several other modeling experiments are worth mentioning. Lyakov and Dubova (Reference IV-5.17) conducted a series of experiments that appear to have been performed earlier than that reported by Alekseyenko. Half-buried spheres of TNT weighing 0.2, 0.4, 0.8, and 1.6 kg were detonated in dry sand. They reported that the strain gauges were placed below the charge along a line at 30 degrees from the vertical axis, another at 45 degrees, another at 60 degrees, and the last one in the surface. (From the data reported - pressure - it must be assumed that the sensors were not strain gauges but stress gauges.) One of the first results of this work was that the front of the stress disturbance loses its discontinuous shock character at a range greater than 0.34 m/gm$^{1/3}$. A second result was that stresses measured along radii within an angle of 45 degrees of the axis of symmetry can be approximated by

$$\sigma_r(\phi) = \sigma_r(0)\cos\phi$$

$$\sigma_\theta(\phi) = K_\theta \sigma_r(\phi)$$

(IV-5.16)

where σ_r and σ_θ are the radial and tangential stresses respectively, K_θ is a constant, and ϕ is the angle from the vertical. As ϕ increases from zero to about 45 degrees, the radial and tangential stresses decrease. However, it was found that the opposite effect occurred for angles near 90 degrees: stresses attenuate with depth in the near-surface region. Based on the experimental evidence that the stress in the near-surface region decreases with increasing depth, Lyakov and Dubova proposed that the stress field created in the soil is a super-position of two waves. These are precisely the waves discussed by Alekseyenko. Interestingly, Alekseyenko makes no reference to the work of Lyakov and Dubova and vice versa.

Flash X-ray techniques have been used to observe the development of a camouflet in a sandy medium (Reference IV-5.18). The experiments consisted of a cube of sand 2.5 meters on the side with the high explosive charge in

Table IV-5.8. Partition of energy between air and ground in a contact burst.

Quantity	Explosion on Concrete. Charge on Surface	Explosion on Undisturbed Sand			Explosion on Loose Sand	
		Charge on Surface	Charge Level with Surface	Center of Charge 1 Radius below Surface	Charge at Surface	Center of Charge Level with Surface
E_a	0.9	0.8	0.65	0.53	0.7	0.56
E_h	0.1	0.2	0.35	0.47	0.3	0.44

E_a = Energy radiated into the air.

E_h = Energy radiated into the half space.

the geometric center. X-ray shadow images of the expanding cavity were
recorded. The cavity growth proceeds by basically three different stages.
The first is a regular expansion of the spherical cavity from the initial
size of the high explosive charge to a volume between 9 and 10 times as
large. It was estimated that the pressure in the cavity at this stage is
around 1 kbar because the sand around this cavity has been strengthened
through compaction. The second stage is characterized by the appearance
and growth of large radial cracks that destroy the stengthened layer of
sand. During this process the volume expansion occurs primarily through
the development of fissures, while the inner radius of the cavity slightly
decreases. In the third and final stage, following the breakup of the
strong layer of material, an acceleration in the enlargement of the cavity
is observed as result of compression of the sand located beyond the
strengthened crust. The remainder of the paper (Reference IV-5.18) dis-
cusses an equation of state which will model this behavior.

Today there still exists considerable controversy over the proper
form of scaling laws for the cratering process, and over the existence of
any true scaling laws. The equations of motion may be made dimensionless
under two mutually exclusive conditions. The first condition (dynamic or
geometric similarity) is characterized by the restoring forces due to the
elastic properties of the medium. This is commonly called Cauchy scaling.
The second condition of scaling arises when the only restoring force is that
due to gravity. This is commonly called Froude scaling. In any cratering
process both of these restoring forces are operative. However, it is
important to know which of the two predominates in any given situation.
Therefore, it becomes highly desirable to obtain experimental information
on craters produced in gravitational fields other than that of the earth's
surface.

The last experiment that will be discussed in this chapter, and perhaps
the most innovative of the modeling experiments, was performed by Viktorov
and Stepanov (Reference IV-5.19). Their experiments were intended to deter-
mine the scaling laws in the pressure of different acceleration fields.
Viktorov and Stepanov employed a linear acceleration sled to simulate gravi-
tational accelerations of 25, 45, and 66 g's. Craters were blasted in a low
moisture content (3 to 4 percent) fine-grained sand (grain density of
2.60 gm/cm^3) using various charge masses at various depths of burst. A

summary of the resulting experimental data is given in Table IV-5.9. They showed that, within the range of the high acceleration data, the apparent crater radii vary according to $g^{-1/8}$. However, when the two data points at 1 g are included from the analysis the exponent becomes -1/12.

Table IV-5.9. Crater data from high-g linear acceleration sled experiments.

DOB (cm)	Charge Mass (gm)	Acceleration (g's)	Apparent Crater Dimensions		
			Depth (cm)	Radius (cm)	Volume (cm^3)
10	3.06	25	7.5	13.4	1800
10	4.59	25	8.5	16.6	2900
10	6.12	25	9.5	17.5	3950
15	4.59	25	4.0	12.3	900
15	6.12	25	5.0	16.0	1500
15	7.65	25	4.0	18.0	2050
20	6.12	25	3.1	19.7	300
20	9.18	25	3.6	13.5	950
10	3.06	45	5.4	13.0	1000
10	4.59	45	6.5	14.1	1600
10	6.12	45	8.0	16.4	2250
15	4.59	45	2.8	9.4	350
15	6.12	45	3.1	10.5	700
15	7.65	45	3.5	14.5	1000
20	7.65	45	2.5	8.4	100
20	9.18	45	3.0	9.5	300
10	3.06	65	5.0	12.0	700
10	4.59	66	3.0	13.6	1000
10	6.12	66	3.4	15.3	1450
15	4.59	66	1.0	9.0	150
15	6.12	66			
15	7.65	66			
10	3.06	1	12.5	17.0	
10	6.12	1	14.7	21.4	

IV-5.4 EMPIRICAL AND THEORETICAL ANALYSES

Because of the great proliferation of theoretical work and the close interrelationships between the various fields of investigation, the organization of this chapter is somewhat fluid. First we will consider some of the work dealing with first-principal solution of the equations of motion where varying sophistications of the material constitutive properties are employed. This is followed by a brief look at the theoretical behavior of multicomponent systems. Lyakhov has extensively used the "pseudo-integration" technique, mentioned below, to solve the equations of motion. In particular, the method of characteristics is used extensively to determine the interaction of shock waves with buried and surface structures. Finally, the analyses of miscellaneous special problems will be discussed.

Because of the limitations imposed by the lack of translated key papers, this review can in no way be considered to be comprehensive. It is, instead, intended to be a general overview giving some of the aspects and scope of the research that has been conducted in the Soviet Union on cratering and ground motion.

A standard Soviet technique for solving the equations of motion is to use empirical curve fits obtained from experimental data to estimate the derivatives in the equations of motion. This approach may be termed "pseudo-integration." As an example, the peak radial stress as a function of range measured in a given experiment can lead to the stress gradient as a function of range. Furthermore, peak displacement and vertical velocity data may also be used in a similar fashion. With the inclusion of sufficient empirical data, a detailed knowledge of the equation of state of the material becomes unnecessary.

IV-5.4.1 Basic Theoretical Work

The general equations of soil and rock mechanics have been discussed and used by Grigoryan (References IV-5.20 through IV-5.22). Of greatest relevance to cratering and ground motion is Reference IV-5.21 where the effects of a spherically-symmetric explosion in a compacting medium are calculated. The assumption is made that flow behind the shock front is plastic and incompressible. The shock attenuates with range, and at some particular range, "R_e," the peak stress in the shock front is equal to the elastic limit of the solid. From that point the wave is assumed to propagate in an elastic solid. The solution of the equations of motion for the material

behind the shock front is assumed to be a power series in the compression. Experimental data on the attenuation of the peak stress with range in the shock front were used to obtain an analytic approximation to the stress gradient for ranges less than R_e. Particle velocities and stresses are matched on either side of the "boundary" R_e. The full solution to the problem is found to be nonlinear and is solved numerically on a computer.

One very interesting piece of work was done by Gurvich (Reference IV-5.23). He calculated the frequency spectrum of a source in an infinite solid. The peak spectral amplitude dependence on total explosive yield is found to be the following. For small yields, the amplitude increases linearly with the charge weight while for large yields the amplitude increases as the cube root of the yield.* Throughout, the frequency of the maximum of the spectrum is proportional to the cube root of the yield. Gurvich also found that the natural frequency of the spherical radiator depends only upon the radius of the cavity and the shear wave velocity of the infinite medium.† The damping of the waves is determined only by Poisson's ratio. Inclusion of a free surface boundary transforms this problem to that of the Lamb solution. This was described by Shemyakin (Reference IV-5.25). In order that surface motions from the analytic solution may be compared with experimental data, Shemyakin shows analytically derived oscillograms and particle trajectories for material near the surface.

A generalization of the Lamb solution for a point-source above a free surface is given by Kogan in Reference IV-5.26. One of the major conclusions of that work is that the spectrum of the radiated energy in a perfect medium differs from the spectrum of the source function in the suppression of the low

---

*In Chapter IV-2.0, see Section IV-2.1.6 discussing cavity decoupling. There, reference is made to a paper published by Latter, Martinelli and Teller in The Physics of Fluids in 1959, which discusses the amplitude as a function of yield.

†See Equation IV-2.12 (Section IV-2.1.6 of Chapter IV-2) which states that the natural frequency of the radiator depends on the cavity radius and the compressional wave speed. Latter et al. (Reference IV-5.24) states that the natural frequency is proportional to the speed of sound, that is, the compressional wave speed, while Gurvich states that it is proportional to the shear wave speed (Editor's note).

frequencies and the displacement of the frequency maximum to higher values. In the case of an absorbing medium, that band of frequencies which is absorbed is removed from the radiated spectrum.

N. V. Zvolinsky (References IV-5.27 and IV-5.28) obtained the solutions to the one-dimensional propagation of explosively generated waves in a non-ideal ground. Both spherical elastic waves and plane elastic-plastic waves were investigated. In this work the pressure-volume equation of state was considered to be piece-wise linear on loading and linear on unloading. In Reference IV-5.27 the initial slope of the pressure-volume loading curve is given by the elastic properties of the medium. The soil then is allowed to compact at constant stress and when fully compacted is assumed to be incompressible. Points below the loading curve are reached through an incompressible process. In Reference IV-5.28 a slightly more sophisticated equation of state was assumed. The fully compacted material was not considered to be incompressible in that it had a measurable, but high, bulk modulus. Compaction proceeded with a bulk modulus considerably less than that of the initial elastic value. States below the loading curve and the fully compacted point were reached through a bulk modulus equal to the initial elastic loading curve. For points greater than the fully compacted condition, loading and unloading below the loading curve was again assumed to be incompressible. Assuming a simple Mohr-Coulomb plasticity condition, analytic solutions of the equations of motion for one dimensional plane propagation were found.

Propagation of disturbances in multi-component materials was investigated by Lyakhov and Polyakova in Reference IV-5.29 and by Nikolayevski in Reference IV-5.30. Reference IV-5.29 concentrates on the pressure-volume equation of state of a material that has a skeletal structure which may or may not be filled with water or air. Two compressibility mechanisms were postulated wherein the first consisted of the collapse of the skeletal structure and the second assumed an equilibrium between the three components of the material, that is, the solid rock, the water, and the air. Reference IV-5.30 is a much more definitive work on the propagation of sound through a two-phase material in which one of the phases is a solid and the other can be a liquid. Both phases may exhibit viscosity (or strain-rate) effects. Two

limiting cases of disturbances are considered. The first is that of the propagation of a small perturbation such as an acoustic wave. It is assumed that, for this condition, strain and stress rates are low enough that complete equilibrium can be maintained between the two phases. The second limiting case is that in which a high intensity shock wave is transmitted through the medium. In this case, stress and strain rates are so high that the material acts as one in which no exchange of momentum or heat between the two phases can take place and each of the two phases follows its own adiabat on compression. A careful application of the Onsager relations of irreversible thermodynamics leads to relationships between the kinetic coefficients of the thermodynamic processes and the plasticity conditions on the yield surface. A particular example is given in which this approach is applied to the flow rule given by the Drucker-Prager model.

IV-5.4.2 The Method of Characteristics

Use of the method of characteristics in estimating the interaction of shock waves and boundaries and structural inclusions has been the prime concern of Lyakhov (References IV-5.17 and IV-5.31 through IV-5.33). As a simple introduction in Reference IV-5.31, he derives the transmission and reflection coefficients for a shock incident on several different types of barriers. This is expanded by Lyakhov and Polyakova (Reference IV-5.33) where the response of a buried structure (represented as a simple spring-mass-damper system) is calculated. The equation of state of the ground surrounding their model was described as a fairly simple loading surface much like that of Nikolayevski with states below the loading curve being reached through an incompressible mechanism. Comparison of their computed results with experimental data yielded a reasonably good correlation. It was claimed, however, that good correlation is only possible when the influence of a free surface can be neglected. In a situation where there is a sizeable reflection or an arrival of the rarefaction wave from the free surface, it is necessary to properly include all of the plastic properties of the surrounding medium. Reference IV-5.33 is an extensive compendium of the methods of approximating shock waves and their interaction through the method of characteristics. It embodies a great deal of information on the field determination of the equation of state and the behavior

of a great many materials. This compendium compares quite favorably with the contents of Nuclear Geoplosics, Volume II. All of the work included in their compendium describes equations of state and equations of motion that are amenable to analytical or graphical solution. No detailed mention is made of direct numerical methods of solution of the equations of motion.

IV-5.4.3 Specialized Problems

Estimating the growth of a cavity resulting from an underground explosion is valuable not only for the estimation of the driving function in ground motion computations, but also for the determination of the total cavity volume produced which is of use in engineering applications. This problem was addressed by Krivtsov (References IV-5.34 and IV-5.35). The expansion of the explosion products was assumed to be almost adiabatic. Based on previous work, the adiabatic gas constant was assumed to be 3 for very high pressures decreasing to 4/3 at low pressures. In Reference IV-5.35 Krivtsov makes two further assumptions that led to a solution of the equations of motion. These were that the velocity field behind the shock front decayed with range to an exponent that depends on the compressibility of the soil. The second assumption was that of a Mohr-Coulomb plasticity condition with non-associated flow. The analytic solutions obtained were compared with experimental results obtained through photographs of the expansion of a cavity in sand. It was seen that there was a substantial difference between his predictions and the experimental data in the initial growth of the cavity. However, the experimental data and the analytic solution converged to the same value at late times.

Experimental data collected on surface waves resulting from cratering explosions was carefully analyzed by Rulev (Reference IV-5.36). It had been claimed by Lebedev (Reference IV-5.3) that the transverse waves resulting from cratering explosions should not be considered Rayleigh waves but were directly related to the cratering process itself. What Rulev showed was that, for most of the data considered, the wave motion is elliptical, counterclockwise and attenuates exponentially with depth.* Data for both granite and loess

*This is in fact a Rayleigh wave (Figure 5.7 of Reference IV-5.37 and related text) (Editor's note).

are presented. From these data Rulev concludes that the surface wave, as measured in the Soviet experiments, is truly a Rayleigh wave. He furthermore found that the scaling of these waves obeys dynamic similarity. The range of yields that were detonated in granite is between 1 and 115 tons. Depth-of-burst effects were also examined and it was found that the energy in the surface wave is a function of the depth of burst. From this, an effective yield is determined as a function of depth of burst. In Figure IV-5.29 data is reproduced from Reference IV-5.36 showing the ratio of the effective-to-true charge weight as a function of scaled depth of burst. The scaled depth of burst is measured in $m/(ton)^{1/3}$. The following statement is made in Reference IV-5.36: "An explosion of one ton carried out on a granite surface will produce the same effect as a 20 kilogram explosion at a depth of 3.5 to 4 meters. The energy released into a surface wave will be one-fiftieth of that released during a one-ton explosion at the optimum depth." The solid line in Figure IV-5.29 represents the data for granite while the dashed line represents equivalent data for a soft compactable material like loess or alluvium.

The problem of an airburst has been attacked by Kogan (Reference IV-5.38). Three basic assumptions were made. First, that the dimensions of the explosives were very small compared to the dimensions of the problem. Second, it was assumed that the earth surface is absolutely rigid and smooth. Finally, that the earth medium in which the seismic energy is transmitted is isotropic, homogeneous, and absorbing. It was further assumed that the radiation of spectral energy would be in cylindrical symmetry so that solutions to the equations of motion would be expressible in terms of Bessel functions. The Fourier transform of the driving function is then given by the Fourier convolution of the applied pressure with the Bessel function. For a surface burst the pressure as a function of radius and time is taken to be that resulting from an explosion twice the yield of the one in free air. Extension of this work to non-zero heights of burst, including estimates of the Mach reflection effect, are beyond the scope of this review. However, as shown in Figure IV-5.30 , there is good agreement between the theoretically computed energy in the Rayleigh wave of the epicentral range, Λ, and the height of burst as a function of yield. A decisive conclusion of this report
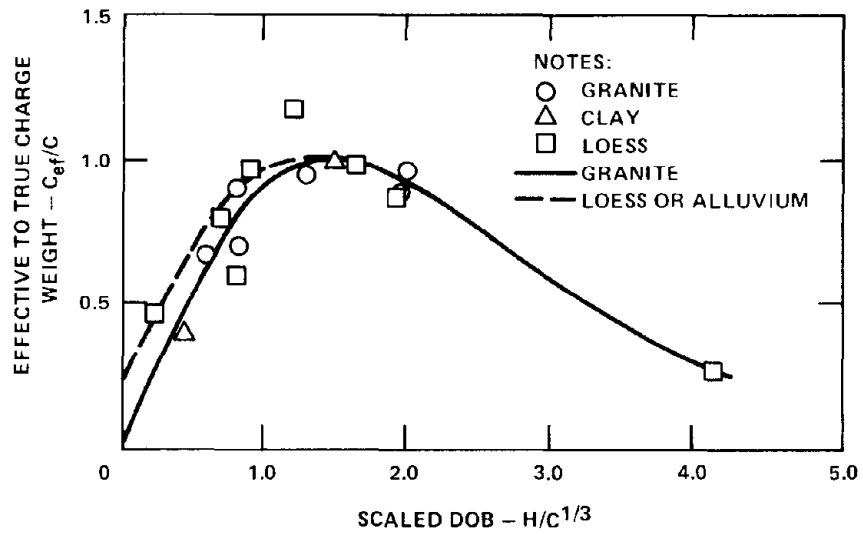
Figure IV-5.29. Dependence of the seismic effect of the scaled depth of burst.
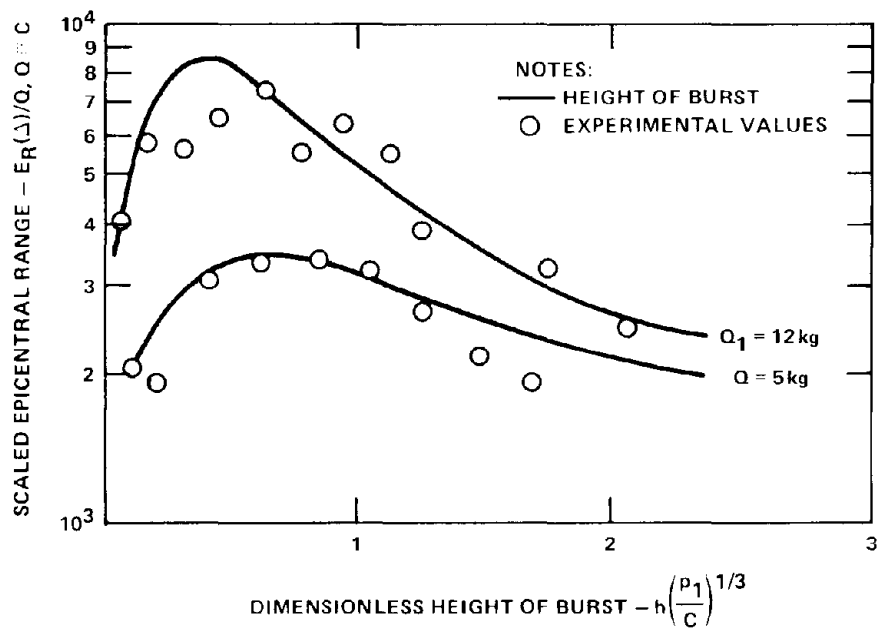
Figure IV-5.30. Energy in transmitted Rayleigh wave, E_R, as a function at height of burst, h. (Continuous lines are theoretical curves of $E_R(\Lambda)/C$ and points are experimental values.)

is that there is a detonation height for each yield and fixed epicentral distance at which the seismic energy observed will be a maximum.

The inclusion of either discontinuous surfaces or processes in analytic and numerical solutions is often quite difficult and has received a good deal of attention. The well known Hugoniot condition across a shock front, and the Von Neumann-Richtmyer artificial viscosity used in the numerical solutions of shock propagation problems are two examples. Barrenblatt and Chernyi (Reference IV-5.39) have developed a generalized technique for obtaining the continuity conditions across a wide class of discontinuities. The method is most easily explained by reference to a particular example. Consider the idealized situation of a fluid flow in which one part of the fluid is moving and the other part is not. Integration of the forces across this discontinuity may be zero. However, the integral of the first moment of the forces is non-zero. Simply stated, the resultant of the forces in the problem may be zero while the torque is not zero. Such arguments were extended directly to a very wide class of discontinuities in dissipative media in which the stress, strain, and strain-rate tensors can be arbitrarily related. The only conditions imposed upon the relationships is that they are sufficiently continuous to admit whatever invariance is required in the problem under consideration. Hugoniot equations for the conservation of mass, energy, and momentum across a shock front are derived as a special case.

Finally, a description of a finite difference calculation to determine the stress and velocity histories near the source of a spherical explosion is given in Reference IV-5.40. A Mie-Grueneisen equation of state was assumed for the material with the pressure-volume relationship being derived from uniaxial shock experiments. The boundary condition was that of a spherical cavity upon the surface of which was imposed the stress due to the gas within the cavity. Two source functions were considered. The first was that of a gas within the cavity expanding adiabatically from some initial peak pressure. The second source function differed only in the early time history of the pressure. It was an extension of the point-blast solution where the total energy of the explosion was converted to kinetic energy of the gas. The momentum of the gas was then obtained and transferred to the wall as the gas reflected from it. Further changes within the cavity continued as adiabatic processes. The finite difference scheme used was a standard forward

differencing technique. There is clearly more to the calculations than is
published because a fairly good agreement in the calculations was obtained
for the peak stress as a function of radius and time, coupled with good
estimates of the cavity growth as a function of time for the shots RAINIER
HARD HAT and SHOAL conducted in the United States. The success seen in
this calculation indicates that the Soviets are well advanced in the appli-
cation of large computers to rock mechanics calculation.

IV-5.5 SUMMARY

The picture that emerges from this review is that of a carefully
thought-out and broad attack on the basic scientific question associated
with cratering and ground motion. Three separate series of single-charge
tests were conducted. The first was to answer the questions about the
scaling laws pertaining to craters and their associated ground motion.
The second series investigated the effects of depth of burst and the
third was associated exclusively with contained explosions. Additional
experiments were conducted in soils other than the alluvium and clay
materials of the above three series. In particular, granitic soils were
examined. Measurements of triaxial stress, vector displacement histories,
velocity vector histories, airblast and cratering-associated phenomena
such as ejecta sources and trajectories were performed. Epicentral ranges
in which the ground motion data were taken from one to two crater radii to
teleseismic distances was also reported. Similar experimentation were also
carried out for multiple-burst tests with primary emphasis on row charge
detonation.

Careful theoretical analyses were made of the resulting experimental
data and, where further clarification was required for a greater under-
standing of the phenomena, extensive modeling experiments were conducted.

Unique experimentation techniques were developed and employed. As
a particular example we should mention the use of flares for night-time
cratering explosions to measure the trajectories of the ejecta. In the
modeling techniques, the observation of the gas acceleration phase was
performed by the rapid release of high pressure gas in a cavity in a sand
test bed within a vacuum chamber.

As stated previously, this work shows a concentrated effort to under-
stand the basic physics of the process of explosion coupling to the earth.
In a relatively few series of tests, the Soviets have gained an impressive
understanding of the phenomena associated with cratering and ground motion.

IV-5.6   REFERENCES

IV-5.1   "Nuclear Explosions for Peaceful Purposes," A Collection of
          Seven Documents, Atomizdat, Moscow 1970; Translated by R. Addis,
          February (1971).

IV-5.2   Rodionov, V.N. and Tsvetkov, V.M., "Some Results of Obser-
          vations of Underground Nuclear Explosions," UDC 621.039.9.

IV-5.3   "Blasting Practice," Collection No. 64/21, Romashov, A.N.
          and Kharin, D.A., eds., "Nedra" Moscow, 1968 UCRL-Trans-10441.
          (A collection of seven translated reports.)

IV-5.4   Kharin, D.A., Kuz'mina, I.V. and Danilova, T.I., "Ground
          Vibrations During Camouflet Blasts," FTD-HT-23-453-72.

IV-5.5   Dokuchayev, M.M., Rodionov, V.N., and Romashov, A.N., "Crater-
          ing Blasts," UCRL-TRANS-10420.

IV-5.6   Medvedev, S.V., "Problems of Engineering Seismology," Library
          of Congress, Catalog Card No. 63-17635, USSR Academy of Science
          Press, Moscow (1962). (A collection of six reports.)

IV-5.7   Perret, W., et al., "Project SCOOTER," SC-4602(RR), Sandia
          Corp. Report, October (1963).

IV-5.8   Rulev, D.B.G., "Similarity of Compression Waves During Explo-
          sions in Grounds," FTD-MT-64-87, Page 166.

IV-5.9   Kuz'mina, V.N., "Spectra of Seismic Waves from Underground
          Explosions from Observation in the Near Zone," FTD-HC-23-594-
          70. (This document also appears as part of Reference IV-5.3.)

IV-5.10   Romashov, A.M., "On the Nature of Certain Ground Waves Excited
          by an Underground Explosion," FTD-HC-23-87-70. (This document
          is included in Reference IV-5.3.)

IV-5.11   Rodionov, V.N., "Methods of Modeling Ejection with Considera-
tion of the Force of Gravity," U.S.S.R. State Committee on
the Uses of Atomic Energy, Moscow (1970), UCRL-TRANS-10476.

IV-5.12   Sadovskii, M.A., Adushkin, V.V., Rodionov, V.N., and
Startsev, G.N., "A Method of Modeling Large Cratering Explo-
sions," Fiz. Goreniya i Vzryva 3,119 (1967).

IV-5.13   Bakhrakh, S.M., Trunin, R.F., Balabanov, A.V., Kovalev, N.P.,
Kotov, V.A., and Orekin, Yu, K., "The Initial Stage of an
Explosion with Ejection," Izv. Earth Physics, 12, 32-38 (1971).

IV-5.14   Alekseyenko, V.D., "Experimental Investigation of Dynamic
Stress Field in Soft Earth During Contact Explosion," FTD-
MT-64-61.

IV-5.15   Alekseyenko, V.D., "Waves in Surface Region of a Ground Half
Space During the Contact Explosion," FTD-MT-64-87.

IV-5.16   Alekseyenko, V.D., "Experimental Investigation of the Energy
Distribution in a Contact Explosion," UDC-662.21 Physics of
Combustion and Explosions, 3, 1 (1967).

IV-5.17   Lyakov, G.N., and Dubova, R.I., "Waves in Soil during a Surface
Blast and their Interaction with Obstacles," FTD-HT-23-744-72.
Translated from the 1965 Fifth Session of the Scientific Council
on the National Economic Utilization of Explosion.

IV-5.18   Al'tshuler, L.V., Balabanov, A.V., Rodionov, V.A., and
Terasov, D.M., "X-Ray Examination of the Initial Development
State of a Camouflet Cavity in a Sandy Soil," FTD-HF-314-73.

IV-5.19   Viktorov, V.V. and Stepenov, R.D., "Modeling of the Action of
an Explosion with Concentrated Charges in Uniform (Homogeneous)
Ground," Engineering Collection of the Institute of Mechanics
of the Academy of Sciences of the U.S.S.R., Vol. XXVIII,
p. 87-96 (1960).

IV-5.20   Grigoryan, S.S., "On Some Special Problems of Thermodynamics
           of Continuous Media," PMM 24, 651 (1960).

IV-5.21   Grigoryan, S.S., "On a Solution of a Problem of an Underground
           Explosion in Soft Soils," PMM 28, 1070 (1964).

IV-5.22   Grigoryan, S.S. and Chernous'ko, F.L., "One-Dimensional Quasi-
           Statical Motions of Soil," PMM, 25, 86 (1961).

IV-5.23   Gurvich, I.I., "The Theory of Spherical Radiators and Seismic
           Waves," Earth Physics, Series No. 10, page 45 (1965), UDC
           534.1: 550.834.

IV-5.24   Latter, A.L., LeLevier, R.E., Martinelli, E.A., and McMillan,
           W.G., "A Method of Concealing Underground Nuclear Explosions,"
           The RAND Corporation, Report No. R-348, 30 March 1959.

IV-5.25   Shemyakin, E.I., "The Lamb Problem for an Internal Source,"
           Doklady Soviet Physics, 6, 10, 930 (1962).

IV-5.26   Kogan, S. Ya., "The Seismic Energy Generated by a Surface
           Source," IZV Series, p. 1000 (1963), UCD 550.834.

IV-5.27   Zvolinsky, N.V., "On the Emission (Radiation) of an Elastic
           Wave from a Spherical Explosion in the Ground," PMM, 24, 126
           (1960).

IV-5.28   Zvolinsky, N.V., "Plain Explosion Waves in an Elastoplastic
           Medium," Doklady Soviet Physics, 9, 400 (1964).

IV-5.29   Lyakhov, G.M. and Polyakova, N.I., "The Calculations of Two
           Compressibility Mechanisms in Equations of Soil Dynamics,"
           All Union Symposium on the Propagation of Elasto-Plastic Waves
           in Solids, Izd-vo AN Azer SSR, (1964), FTD-HT-23-749-72.

IV-5.30   Nikolayevsky, V.N., "The Theory of Shock Wave Propagation
           in Soft Water Saturated Soils," All Union Symposium on
           Elasto-Plastic Wave Propagation in Continuous Media (1966),
           p. 269, FTD-HC-23-240-71.

IV-5.31   Lyakhov, G.M., "On the Interaction of Shock Waves in a
           Water Saturated Earth and in Water," Iz. Mechanics and
           Engineering News, 1, p. 155 (1961), FTD-HT-23-872-70.

IV-5.32   Lyakhov, G.M., "The Interaction of Shock Wave in a Plastic
           Medium with an Edifice," Izd-vo AN, Azer SSR, BAKU, p. 245
           (1966), FTD-HT-23-748-72.

IV-5.33   Lyakhov, G.M. and Polyakova, M.I., "Waves in Solid Media and
           Loads on Structures," NEDRA, 1 (1967), FTD-MT-24-1137-71.

IV-5.34   Krivtsov, V.A., "Determining the Radius of the Cavity from the
           Underground Explosion in the Presence of Residual Pressure from
           Explosion Products," Izd-vo Naukova Dumka. Kiev (1969) p. 28,
           FTD-HT-23-750-72.

IV-5.35   Krivtsov, V.A. and Semenova, L.A., "The Approximate Determina-
           tion of Cavity Development in an Underground Explosion of a
           Spherical Charge in Soil," Prikladnaya Mekhanika, 3 (1967),
           UDC 624.131.

IV-5.36   Rulev, B.G., "The Energy in a Rayleigh Surface Wave from
           Explosions in Different Kinds of Rocks," Izv. Earth Physics
           Series 4, 23 (1965), UDC-534.222.2.

IV-5.37   Tolstoy, I., Wave Propagation, McGraw-Hill Book Company, 1973.

IV-5.38   Kogan, S. Ya., "The Connection Between the Parameters of an
           Aerial Explosion and Seismic Energy," Izv. Earth Physics Series,
           p. 9 (1965), UDC 534.222.2.

IV-5.39   Barrenblatt, G.I. and Chernyi, G.G., "On Moment Relations on Surfaces of Discontinuity in Dissipative Media," PMM 27, 784 (1963).

IV-5.40   Koryavov, V.P., and Vilenskaya, G.G., "Calculation of the Motion in the Near Field of an Explosion in a Solid Medium," PMTF, 9, 76 (1968).

DISTRIBUTION LIST

DEPARTMENT OF DEFENSE

Assistant to the Secretary of Defense
Atomic Energy
ATTN: Executive Assistant

Defense Advanced Rsch Proj Agency
ATTN: TIO

Defense Intelligence Agency
ATTN: DB-4C2, C. Wiehle
ATTN: RDS-3A
ATTN: DB-4C2, B. Morris
ATTN: DB-4C3
ATTN: DB-4C1

Defense Nuclear Agency
ATTN: STSP
2 cy ATTN: SPSS
2 cy ATTN: SPAS
4 cy ATTN: TITL

Defense Technical Information Center
12 cy ATTN: DD

Field Command
Defense Nuclear Agency
ATTN: FCT
ATTN: FCPR
ATTN: FCTMOF

Field Command
Defense Nuclear Agency
Livermore Branch
ATTN: FCPRL

Field Command Test Directorate
Defense Nuclear Agency
ATTN: FCTC

Interservice Nuclear Weapons School
ATTN: TTV

Joint Strat Tgt Planning Staff
ATTN: NRI-STINFO Library
ATTN: DOXT
ATTN: JLA
ATTN: JLTW-2
ATTN: XPFS

NATO School (SHAPE)
ATTN: U.S. Documents Officer

Undersecretary of Def for Rsch & Engrg
ATTN: Strategic & Space Sys (OS)

DEPARTMENT OF THE ARMY

BMD Advanced Technology Center
Department of the Army
ATTN: 1CRDABH-X
ATTN: ATC-T

BMD Systems Command
Department of the Army
ATTN: BMDSC-H, N. Hurst

DEPARTMENT OF THE ARMY (Continued)

Chief of Engineers
Department of the Army
ATTN: DAEN-RDL
ATTN: DAEN-MCE-D

Construction Engineering Rsch Lab
Department of the Army
ATTN: CERL-SOI-L

Deputy Chief of Staff for Ops & Plans
Department of the Army
ATTN: DAMO-NC

Deputy Chief of Staff for Rsch Dev & Acq
Department of the Army
ATTN: DAMA-CSS-N

Engineer Studies Center
Department of the Army
ATTN: DAEN-FES, LTC Hatch

Harry Diamond Laboratories
Department of the Army
ATTN: DELHD-I-TL
ATTN: DELHD-N-P

U.S. Army Armament Material Readiness Cmd
ATTN: MA Library

U.S. Army Ballistic Research Labs
ATTN: DRDAR-BLT, C. Kingery
ATTN: DRDAR-BLT, W. Taylor
ATTN: DRDAR-BLT, A. Ricchiazzi
ATTN: DRDAR-BLV
ATTN: DRDAR-BLT, J. Keefer
ATTN: Tech Library

U.S. Army Communciations Command
ATTN: Tech Reference Division

U.S. Army Concepts Analysis Agency
ATTN: CSSA-ADL

U.S. Army Engineer Center
ATTN: ATZA

U.S. Army Engineer Div, Huntsville
ATTN: HNDED-SR

U.S. Army Engineer Div, Ohio River
ATTN: ORDAS-L

U.S. Army Engineer School
ATTN: ATZA-DTE-ADM
ATTN: ATZA-CDC

U.S. Army Foreign Science & Tech Ctr
ATTN: DRXST-SD

U.S. Army Mat Cmd Proj Mngr for Nuc Munitions
ATTN: DRCPM-NUC

Dist-1

DEPARTMENT OF THE ARMY (Continued)

U.S. Army Engr Waterways Exper Station
    ATTN: WESSE, L. Ingram
    ATTN: WESSD, J. Jackson
    ATTN: J. Strange
    ATTN: J. Zelasko
    ATTN: F. Brown
    ATTN: Library
    ATTN: WESSA, W. Flathau
    ATTN: WESSS, J. Ballard

U.S. Army Material & Mechanics Rsch Ctr
    ATTN: DRXMR, J. Mescall
    ATTN: DRXMR-TE, R. Shea
    ATTN: Technical Library

U.S. Army Materiel Dev & Readiness Cmd
    ATTN: DRCDE-D, L. Flynn
    ATTN: DRXAM-TL

U.S. Army Missile R&D Command
    ATTN: RSIC
    ATTN: DRDMI-XS

U.S. Army Mobility Equip R&D Cmd
    ATTN: DRDME-HT, A. Tolbert
    ATTN: DRDME-WC

U.S. Army Nuclear & Chemical Agency
    ATTN: Library

U.S. Army War College
    ATTN: Library

U.S. Military Academy
Department of the Army
    ATTN: Document Library

DEPARTMENT OF THE NAVY

Marine Corps
Department of the Navy
    ATTN: POM

David Taylor Naval Ship R&D Ctr
    ATTN: Code 1700, W. Murray
    ATTN: Code 177, E. Palmer
    ATTN: Code 2740
    ATTN: Code 1740, R. Short
    ATTN: Code 1740.5
    ATTN: Code L42-3

Marine Corp Dev & Education Command
Department of the Navy
    ATTN: D091, J. Hartneady

Naval Construction Battalion Center
    ATTN: Code L51, J. Crawford
    ATTN: Code L51, S. Takahashi
    ATTN: Code L51, W. Shaw
    ATTN: Code L51, R. Odello

Naval Electronic Systems Command
    ATTN: PME 117-21

Naval Electronics Systems Command
    ATTN: Commander

Naval Explosive Ord Disposal Fac
    ATTN: Code 504, J. Petrousky

DEPARTMENT OF THE NAVY (Continued)

Naval Facilities Engineering Command
    ATTN: Code 04B

Naval Material Command
    ATTN: MAT 08T-22

Naval Ocean Systems Center
    ATTN: Code 013, E. Cooper
    ATTN: Code 4471

Naval Postgraduate School
    ATTN: Code 1424 Library
    ATTN: G. Lindsay

Naval Research Laboratory
    ATTN: Code 2627
    ATTN: Code 8404, H. Pusey
    ATTN: Code 8403, R. Belsham
    ATTN: Code 8440, G. O'Hara

Naval Sea Systems Command
    ATTN: SEA-09G53
    ATTN: SEA-033
    ATTN: SEA-06J, R. Lane
    ATTN: SEA-0351
    ATTN: SEA-9931G

Naval Surface Weapons Center
    ATTN: Code F31
    ATTN: Code R10
    ATTN: Code R14
    ATTN: Code U401, M. Kleinerman

Naval Surface Weapons Center
    ATTN: Tech Lib & Info Svcs Br
    ATTN: W. Wishard

Naval War College
    ATTN: Code E-11

Naval Weapons Center
    ATTN: Code 266, C. Austin
    ATTN: Code 233
    ATTN: Code 3263, J. Bowen

Naval Weapons Evaluation Facility
    ATTN: Code 10
    ATTN: R. Hughes

Office of Naval Research
    ATTN: Code 474, N. Perrone

Office of the Chief of Naval Operations
    ATTN: OP 982
    ATTN: OP 982E, M. Lenzini
    ATTN: OP 981
    ATTN: OP 654C3, R. Piacesi
    ATTN: OP 098T8
    ATTN: OP 03EG

Strategic Systems Project Office
Department of the Navy
    ATTN: NSP-272
    ATTN: NSP-273
    ATTN: NSP-43

DEPARTMENT OF THE AIR FORCE

Aerospace Defense Command
Department of the Air Force
    ATTN: XPX

Air Force Armament Laboratory
    ATTN: DLYV, J. Collins

Air Force Geophysics Laboratory
    ATTN: LWW, K. Thompson

Air Force Institute of Technology
    ATTN: Library
    ATTN: Commander

Air Force Office of Scientific Research
    ATTN: NA, B. Wolfson

Air Force Systems Command
    ATTN: DLW
    ATTN: R. Cross

Air Force Weapons Laboratory
Air Force Systems Command
    ATTN: NTES-C, R. Henny
    ATTN: NTE, M. Plamondon
    ATTN: SUL
    ATTN: NTED
    ATTN: NTES, J. Lee
    ATTN: NTES, R. Jolley

Assistant Chief of Staff
Intelligence
Department of the Air Force
    ATTN: IN

Ballistic Missile Office
Air Force Systems Command
    ATTN: DEB

Ballistic Missile Office
Air Force Systems Command
    ATTN: MNN
    ATTN: MNNX
    ATTN: MNNXH

Deputy Chief of Staff
Research, Development, & Acq
Department of the Air Force
    ATTN: AFRDQI
    ATTN: R. Steere

Deputy Chief of Staff
Logistics & Engineering
Department of the Air Force
    ATTN: LEEE

Foreign Technology Division
Air Force Systems Command
    ATTN: SDBF, S. Spring
    ATTN: TQTD
    ATTN: NIIS Library
    ATTN: SDBG

Rome Air Development Center
Air Force Systems Command
    ATTN: TSLD
    ATTN: RBES, R. Mair
    ATTN: Commander

DEPARTMENT OF THE AIR FORCE (Continued)

Strategic Air Command
Department of the Air Force
    ATTN: NRI-STINFO Library
    ATTN: XPFS

United States Air Force Academy
    ATTN: DFCEM, W. Fluhr

DEPARTMENT OF ENERGY

Department of Energy
Albuquerque Operations Office
    ATTN: CTID

Department of Energy
    ATTN: OMA/RD&T

Department of Energy
Nevada Operations Office
    ATTN: Mail & Rec for Tech Library

OTHER GOVERNMENT AGENCIES

Central Intelligence Agency
    ATTN: OSWR/NED
    ATTN: OSR/SE/F

Department of the Interior
Bureau of Mines
    ATTN: Tech Lib

Department of the Interior
U.S. Geological Survey
    ATTN: D. Roddy

Federal Emergency Management Agency
    ATTN: Hazard Eval & Vul Red Div

NASA
AMES Research Center
    ATTN: R. Jackson
    ATTN: F. Nichols

U.S. Nuclear Regulatory Commission
    ATTN: R. Whipp for Div of Sec for L. Shao

DEPARTMENT OF ENERGY CONTRACTORS

Lawrence Livermore National Lab
    ATTN: L-200, T. Butkovich
    ATTN: L-90, R. Dong
    ATTN: Tech Info Dept Library
    ATTN: J. Goudreau
    ATTN: M. Fernandez
    ATTN: T. Gold
    ATTN: H. Glenn
    ATTN: L-205, J. Hearst
    ATTN: L-437, R. Schock
    ATTN: L-90, D. Norris
    ATTN: L-7, J. Kahn

Los Alamos National Scientific Lab
    ATTN: MS 364
    ATTN: A. Davis
    ATTN: R. Sanford
    ATTN: M/S 632, T. Dowler
    ATTN: MS 670, J. Hopkins
    ATTN: G. Spillman

DEPARTMENT OF ENERGY CONTRACTORS (Continued)

Oak Ridge National Laboratory
        ATTN: Central Research Library
        ATTN: Civil Def Res Proj

Sandia National Laboratories
Livermore National Laboratory
        ATTN: Library & Sec Class Div

Sandia National Lab
        ATTN: 3141
        ATTN: L. Vortman

DEPARTMENT OF DEFENSE CONTRACTORS

Acurex Corp
        ATTN: J. Stockton
        ATTN: C. Wolf

Aerospace Corp
        ATTN: L. Selzer
        ATTN: P. Mathur
        ATTN: H. Mirels
2 cy ATTN: Tech Info Services

Agbabian Associates
        ATTN: C. Bagge
        ATTN: M. Agbabian

Analytic Services, Inc
        ATTN: G. Hesselbacher

Applied Research Associates, Inc
        ATTN: H. Auld
        ATTN: N. Higgins
        ATTN: J. Bratton

Applied Theory, Inc
        ATTN: J. Trulio

Artec Associates, Inc
        ATTN: S. Gill

AVCO Research & Systems Group
        ATTN: W. Broding
        ATTN: Library A830
        ATTN: J. Atanasoff
        ATTN: D. Henderson

BDM Corp
        ATTN: A. Lavagnino
        ATTN: T. Neighbors
        ATTN: Corporate Library

BDM Corp
        ATTN: R. Hensley

Bell Telephone Labs
        ATTN: J. White

Boeing Co
        ATTN: M/S 42/37, R. Carlson
        ATTN: Aerospace Library
        ATTN: R. Holmes
        ATTN: R. Hager
        ATTN: R. Dyrdahl
        ATTN: J. Wooster

Boeing Co
        ATTN: M/S 42/37, K. Friddell

DEPARTMENT OF DEFENSE CONTRACTORS (Continued)

California Institute of Technology
        ATTN: T. Ahrens

California Research & Technology, Inc
        ATTN: K. Kreyenhagen
        ATTN: Library
        ATTN: M. Rosenblatt
        ATTN: S. Schuster

California Research & Technology, Inc
        ATTN: D. Orphal

Calspan Corp
        ATTN: Library

Center for Planning & Rsch, Inc
        ATTN: R. Shnider

University of Denver
        ATTN: J. Wisotski

Effects Technology, Inc
        ATTN: K. Narasimhan

EG&G Washington Analytical Svcs Ctr, Inc
        ATTN: Library
        ATTN: Director

Electric Power Research Institute
        ATTN: G. Sliter

Electromechanical Sys of New Mexico, Inc
        ATTN: R. Shunk

Eric H. Wang
Civil Engineering Rsch Fac
University of New Mexico
        ATTN: N. Baum
        ATTN: D. Calhoun

Franklin Institute
        ATTN: Z. Zudans

Gard, Inc
        ATTN: G. Neidhardt

General Dynamics Corp
        ATTN: R. Dibrell

General Electric Co
        ATTN: M. Bortner

General Electric Co
        ATTN: A. Ross

General Electric Company—TEMPO
        ATTN: DASIAC

General Research Corp
        ATTN: TIO

Geocenters, Inc
        ATTN: E. Marram

H-Tech Labs, Inc
        ATTN: B. Hartenbaum

Honeywell, Inc
        ATTN: T. Helvig

IIT Research Institute
    ATTN: A. Longinow
    ATTN: Documents Library

Institute for Defense Analyses
    ATTN: Classified Library
    ATTN: Director

J. H. Wiggins Co, Inc
    ATTN: J. Collins

Kaman AviDyne
    ATTN: G. Zartarian
    ATTN: Library
    ATTN: R. Ruetenik
    ATTN: N. Hobbs

Kaman Sciences Corp
    ATTN: Library
    ATTN: F. Shelton
    ATTN: D. Sachs

Karagozian and Case
    ATTN: J. Karagozian

Lockheed Missiles & Space Co, Inc
    ATTN: B. Almroth
    ATTN: T. Geers

Lockheed Missiles & Space Co, Inc
    ATTN: TIC-Library

Management Science Associates
    ATTN: K. Kaplan

Martin Marietta Corp
    ATTN: G. Fotieo
    ATTN: A. Cowan

Martin Marietta Corp
    ATTN: J. Donathan

University of Massachusetts
    ATTN: W. Nash

McDonnell Douglas Corp
    ATTN: R. Halprin

Merritt CASES, Inc
    ATTN: Library
    ATTN: J. Merritt

Meteorology Research, Inc
    ATTN: W. Green

Mitre Corp
    ATTN: Director

Nathan M. Newmark Consult Eng Svcs
    ATTN: J. Haltiwanger
    ATTN: W. Hall
    ATTN: N. Newmark

University of New Mexico
    ATTN: G. Triandafalidis

University of Oklahoma
    ATTN: J. Thompson

Pacific-Sierra Research Corp
    ATTN: H. Brode

Pacifica Technology
    ATTN: R. Bjork
    ATTN: Tech Library
    ATTN: G. Kent

Physics Applications, Inc
    ATTN: C. Vincent

Physics International Co
    ATTN: L. Behrmann
    ATTN: Technical Library
    ATTN: J. Thomsen
    ATTN: E. Moore
    ATTN: F. Sauer

University of Pittsburgh
    ATTN: M. Willims, Jr

R & D Associates
    ATTN: P. Rausch
    ATTN: J. Lewis
    ATTN: W. Wright, Jr
    ATTN: A. Field
    ATTN: R. Port
    ATTN: Tech Info Center
    ATTN: P. Haas

Rand Corp
    ATTN: A. Laupa
    ATTN: C. Mow
    ATTN: Library

Science Applications, Inc
    ATTN: Tech Library

Science Applications, Inc
    ATTN: S. Oston

Science Applications, Inc
    ATTN: D. Bernstein
    ATTN: D. Maxwell
    ATTN: R. Hoffmann

Science Applications, Inc
    ATTN: W. Layson
    ATTN: J. Cockayne
    ATTN: B. Chambers III
    ATTN: G. Binninger

Southwest Research Institute
    ATTN: W. Baker
    ATTN: A. Wenzel

SRI International
    ATTN: G. Abrahamson
    ATTN: W. Wilkinson

Systems, Science & Software, Inc
    ATTN: K. Pyatt
    ATTN: D. Grine
    ATTN: R. Sedgewick
    ATTN: T. McKinley
    ATTN: T. Riney
    ATTN: T. Cherry
    ATTN: Library

DEPARTMENT OF DEFENSE CONTRACTORS (Continued)

TeleDyne Brown Engineering
    ATTN: J. Ravenscraft

Terra Tek, Inc
    ATTN: A. Abou-Sayed
    ATTN: Library
    ATTN: S. Green
    ATTN: A. Jones

Tetra Tech, Inc
    ATTN: L. Hwang

Texas A & M University System
    ATTN: H. Coyle

Weidlinger Assoc, Consulting Engineers
    ATTN: J. McCormick
    ATTN: M. Baron

DEPARTMENT OF DEFENSE CONTRACTORS (Continued)

TRW Defense & Space Sys Group
    ATTN: P. Bhutta
    ATTN: B. Sussholtz
    ATTN: A. Narevsky
    ATTN: D. Jortner
    ATTN: A. Feldman
    ATTN: Tech Info Center
2 cy ATTN: N. Lipner

TRW Defense & Space Sys Group
    ATTN: F. Pieper
    ATTN: G. Hulcher
    ATTN: E. Wong
    ATTN: P. Dai

Weidlinger Assoc, Consulting Engineers
    ATTN: J. Isenberg